

POLISH SOCIETY OF THEORETICAL AND APPLIED MECHANICS

**JOURNAL OF THEORETICAL
AND APPLIED MECHANICS**

No. 3 • Vol 55

Quarterly

WARSAW, JULY 2017

JOURNAL OF THEORETICAL AND APPLIED MECHANICS

(until 1997 Mechanika Teoretyczna i Stosowana, ISSN 0079-3701)

Beginning with Vol 45, No. 1, 2007, *Journal of Theoretical and Applied Mechanics* (JTAM) has been selected for coverage in Thomson Reuters products and custom information services. Now it is indexed and abstracted in the following:

- Science Citation Index Expanded (also known as SciSearch®)
- Journal Citation Reports/Science Edition

Advisory Board

MICHAŁ KLEIBER (Poland) – Chairman

- JORGE A.C. AMBROSIO (Portugal) ★ ANGEL BALTOV (Bulgaria) ★ ROMESH C. BATRA (USA)
★ ALAIN COMBESCURE (France) ★ JÜRI ENGELBRECHT (Estonia) ★ WITOLD GUTKOWSKI (Poland)
★ JÓZEF KUBIK (Poland) ★ ZENON MRÓZ (Poland) ★ RYSZARD PARKITNY (Poland)
★ EKKEHARD RAMM (Germany) ★ EUGENIUSZ ŚWITOŃSKI (Poland) ★ HISAAKI TOBUSHI (Japan)
★ ANDRZEJ TYLIKOWSKI (Poland) ★ DIETER WEICHERT (Germany) ★ JOSE E. WESFREID (France)
★ JÓZEF WOJNAROWSKI (Poland) ★ JOSEPH ZARKA (France)
★ VLADIMIR ZEMAN (Czech Republic)

Editorial Board

WŁODZIMIERZ KURNIK – Editor-in-Chief,

PIOTR CUPIAŁ, KRZYSZTOF DEMS, WITOLD ELSNER, KURT FRISCHMUTH (Germany),
PIOTR KOWALCZYK, ZBIGNIEW KOWALEWSKI, TOMASZ KRZYŻYŃSKI, STANISŁAW KUKLA,
TOMASZ ŁODYGOWSKI, EWA MAJCHRZAK, WIESŁAW NAGÓRKO, JANUSZ NARKIEWICZ,
BŁAŻEJ SKOCZEŃ, ANDRZEJ STYCZEK, UTZ VON WAGNER (Germany), JERZY WARMIŃSKI,
ELŻBIETA WILANOWSKA – Secretary, PIOTR PRZYBYŁOWICZ – Language Editor,
EWA KOISAR – Technical Editor



Articles in JTAM are published under Creative Commons Attribution – Non-commercial 3.0. Unported License <http://creativecommons.org/licenses/by-nc/3.0/legalcode>. By submitting an article for publication, the authors consent to the grant of the said license.



Crossref
Similarity Check
Powered by iThenticate

The journal content is indexed in Similarity Check, the Crossref initiative to prevent plagiarism.

* * * * *

Editorial Office

Al. Armii Ludowej 16, room 650
00-637 Warszawa, Poland
phone (+48 22) 825 7180, (+48) 664 099 345, e-mail: biuro@ptmts.org.pl

www.ptmts.org.pl/jtam.html

* * * * *



Ministerstwo Nauki
i Szkolnictwa Wyższego

Publication supported by Ministry of Science and Higher Education of Poland

(Journal of Theoretical and Applied Mechanics: 1) digitalizacja publikacji i monografii naukowych w celu zapewnienia i utrzymania otwartego dostępu do nich przez sieć Internet, 2) stworzenie anglojęzycznych wersji wydawanych publikacji, 3) wdrożenie procedur zabezpieczających oryginalność publikacji naukowych oraz zastosowane techniki zabezpieczeń – są finansowane w ramach umowy 715/P-DUN/2017 ze środków Ministra Nauki i Szkolnictwa Wyższego przeznaczonych na działalność upowszechniającą naukę)

STABILITY ANALYSIS AND DYNAMIC BEHAVIOUR OF A FLEXIBLE ASYMMETRIC ROTOR SUPPORTED BY ACTIVE MAGNETIC BEARINGS

MOLKA ATTIA HILI, SLIM BOUAZIZ, MOHAMED HADDAR

*Laboratory of Mechanical Modeling and Production (LA2MP), National School of Engineers of Sfax (ENIS),
University of Sfax, Tunisia; e-mail: Molka.hili79@gmail.com*

The objective of this work is to show the influence of dynamic characteristics of Active Magnetic Bearings (AMBs) on the stability and dynamic response of an asymmetric and unbalanced rotor. Indeed, AMBs have been successfully applied in several industrial machinery facilities. Their main advantages are the contactless working principle, frictionless suspension and operation in very high speeds. Firstly, the AMBs dynamic support parameters have been obtained through electromagnetic theory. Then, a generalized system equations of motion have been derived using the finite element method. The motion of a rotor the shaft cross-section of which is asymmetric is generally governed by ordinary differential equations with periodic coefficients. Floquet's theory is used to investigate the stability of this system of equations. Finally, numerical simulation results are presented and discussed.

Keywords: asymmetric rotor, finite element, Floquet's theory, dynamic coefficients, stability

1. Introduction

A spinning system serves as a model for many rotating machinery elements. It is generally composed of a flexible shaft on which a flexible or rigid disk is mounted and supported by bearings. Bearings have a considerable effect on the dynamic behaviour of such systems. Recently, AMBs are increasingly used, especially in machines operating at very high rotational speeds, because of their many advantages (no lubrication, very long life, supporting hard environments, precise control, low power use and high-speed operating) compared to rolling elements, hydrodynamic or elasto-hydrodynamic bearings.

On the other hand, the presence of defects is a major concern in rotating machinery; they generate some important loads and vibrations and also stability problems. Asymmetric cross section of the shaft is among commonly encountered defects, it is usually due to machining defects.

The study of rotating systems supported by AMBs bearings and analysis of machine faults has resulted in an extensive body of publications.

Lei and Palazzolo (2008) presented an approach for the analysis and design of magnetic suspension systems with a large flexible rotor dynamic model including dynamics, control and simulation. Inayat-Hussain (2007) presented a numerical study to investigate the response of an unbalanced rigid rotor supported by AMBs. The mathematical model of the rotor-bearing system used in that study incorporated non-linearity arising from the electromagnetic force-coil and current-air gap relationship, and the effects of geometrical cross-coupling. The response of the rotor was observed to exhibit a rich variety of dynamical behaviour including synchronous, sub-synchronous, quasi-periodic and chaotic vibrations. Inagaki *et al.* (1980) studied a multi-disk fully asymmetric rotor with longitudinal variation of the shaft cross section. The temporal equations of motion were obtained using the transfer matrix method. The unbalance response was deduced by the harmonic balance method.

Oncescu *et al.* (2001) proposed modifications into a classical finite element procedure developed for rotors with symmetry to incorporate the effect of shaft asymmetry and used Floquet's theory to investigate the stability of a general system of differential equations with periodic coefficients.

Recently, Inayat-Hussain (2010) studied the dynamics of a rigid rotor supported by load-sharing between magnetic and auxiliary bearings for a range of realistic design and operating parameters. Numerical results of that work show that the unbalance parameter is the main factor that influences the dynamics of the rotor-bearing system. It was also shown that the non-synchronous vibration response amplitude of the rotor with a relatively small unbalance magnitude can be reduced by decreasing the magnitude of the friction coefficient. Tsai *et al.* (2011) developed a wavelet transform algorithm to identify magnetic damping and stiffness coefficients of the driving rod with a set of 4-pole AMBs. This work further revealed that the identified second-order damping coefficient is negative for a specific rod displacement and speed. The dynamics of the rotor-AMBs system in the axial direction is unstable. Bouaziz *et al.* (2011) investigated the dynamic response of a rigid misaligned rotor mounted in two identical AMBs. Three simplified models of current biased radial AMBs were presented, where four, six and eight electromagnets were powered by a bias current and the respective control current. Results of that work show that angular misalignment is such that the $2\times$ and $4\times$ running speed components are predominant in spectra of vibration. Their magnitudes vary with the number of magnets in the bearing. Bouaziz *et al.* (2016), proposed a dynamical analysis of a high speed AMB spindle in the peripheral milling process. The time history of the response, orbit, FFT diagram at the tool-tip center and the bearings dynamic coefficients were plotted to analyze dynamic behavior of the spindle.

Most of the papers found in the literature concerning magnetic bearings are interested in the dynamic response of unbalanced or misaligned rotors. The shaft is generally considered rigid or massless.

On the other hand, the papers dealing with asymmetric shafts, consider that the shaft is supported by two identical elastic bearings. The coefficients of stiffness and damping are given arbitrarily. Stability study is very limited.

In this paper, dynamic characteristics of Active Magnetic Bearings (AMBs) is first be determined. Then a model of an asymmetric rotor supported by two magnetic bearings is presented using the finite element procedure. A stability analysis will be conducted while showing the influence of various parameters of the bearings on stability areas. In the same way, the dynamic response of the asymmetric shaft will be calculated and analyzed.

2. Bearing modelling

The electromagnetic bearing studied is formed by four electromagnets ($n = 4$) placed in the bearing around the rotor and producing an attractive force (Fig. 1).

Using the electromagnetic theory, the electromagnetic resultant forces produced by every pair of the electromagnets in x and y directions are expressed as (Inayat-Hussain, 2010)

$$F_x = \lambda \left[\left(\frac{I_0 - i_x}{C_0 - u_x} \right)^2 - \left(\frac{I_0 + i_x}{C_0 + u_x} \right)^2 \right] \quad F_y = \lambda \left[\left(\frac{I_0 - i_0 - i_y}{C_0 - u_y} \right)^2 - \left(\frac{I_0 + i_0 + i_y}{C_0 + u_y} \right)^2 \right] \quad (2.1)$$

where C_0 is the nominal air gap, i_0 is the bias current (to produce neutralizing force due to weight of the rotor), I_0 is the steady state current in the coil, u_x and u_y are respectively the shaft displacements in the x and y directions, λ is the global magnetic permeability expressed as

$$\lambda = \frac{\mu_0 AN^2}{4} \cos \theta \quad (2.2)$$

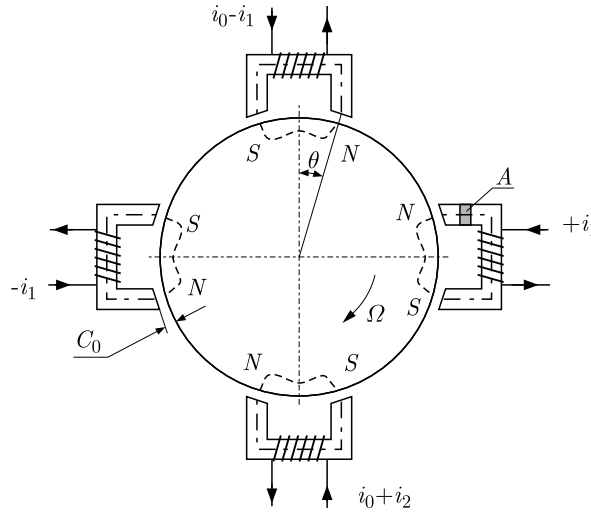


Fig. 1. Electromagnetic bearing

where A , μ_0 , θ and N represent, respectively, cross section area of an electromagnet, permeability of vacuum, half angle between the poles of the electromagnet and the number of windings in the coil, and i_j ($j = x, y$) represents the control current expressed using a proportional-differential (PD) controller as

$$i_j = k_p u_j + k_d \dot{u}_j \quad j = x, y \quad (2.3)$$

where \dot{u}_j is shaft velocity in the j direction, k_p is the proportional gain and k_d is the differential gain.

By replacing (2.3) respectively in (2.1), we obtain

$$F_x = a \left[\left(\frac{1 - \frac{k_p u_x - k_d \dot{u}_x}{I_0}}{1 - \frac{u_x}{C_0}} \right)^2 - \left(\frac{1 + \frac{k_p u_x + k_d \dot{u}_x}{I_0}}{1 + \frac{u_x}{C_0}} \right)^2 \right] \quad (2.4)$$

$$F_y = a \left[\left(\frac{1 - \frac{i_0}{I_0} - \frac{k_p u_y - k_d \dot{u}_y}{I_0}}{1 - \frac{u_y}{C_0}} \right)^2 - \left(\frac{1 + \frac{i_0}{I_0} + \frac{k_p u_y + k_d \dot{u}_y}{I_0}}{1 + \frac{u_y}{C_0}} \right)^2 \right]$$

where $a = \lambda I_0^2 C_0^2$.

Electromagnetic forces that depend on the shaft centre displacement and velocity are linearized (first order) around the equilibrium position (Bouaziz *et al.*, 2016). This will provide the classic model of a bearing with four stiffness and damping coefficients (Fig. 2)

$$\begin{Bmatrix} f_x \\ f_y \end{Bmatrix} = -\mathbf{K}_B \begin{Bmatrix} u_x \\ u_y \end{Bmatrix} - \mathbf{C}_B \begin{Bmatrix} \dot{u}_x \\ \dot{u}_y \end{Bmatrix} \quad (2.5)$$

where \mathbf{K}_B is the bearing stiffness matrix expressed as

$$\mathbf{K}_B = \begin{bmatrix} K_{xx} & K_{xy} \\ K_{yx} & K_{yy} \end{bmatrix} = - \begin{bmatrix} \left(\frac{\partial F_x}{\partial u_x} \right)_0 & 0 \\ 0 & \left(\frac{\partial F_y}{\partial u_y} \right)_0 \end{bmatrix} \quad (2.6)$$

and \mathbf{C}_B is the bearing stiffness matrix expressed as

$$\mathbf{C}_B = \begin{bmatrix} c_{xx} & c_{xy} \\ c_{yx} & c_{yy} \end{bmatrix} = - \begin{bmatrix} \left(\frac{\partial F_x}{\partial \dot{u}_x} \right)_0 & 0 \\ 0 & \left(\frac{\partial F_y}{\partial \dot{u}_y} \right)_0 \end{bmatrix} \quad (2.7)$$

In this model, the stiffness and damping cross-coefficients of the bearings are neglected. Numerical differentiation method is selected for determination of the dynamic coefficients. The partial derivatives are evaluated by the finite difference central method.

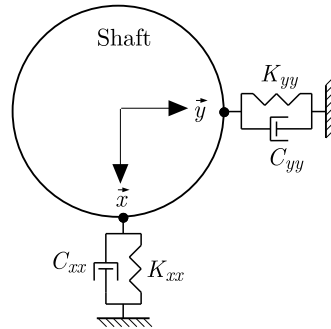


Fig. 2. Two DOF bearing model

3. Equation of motion

The mathematical model (Fig. 3) consists of a flexible asymmetric shaft, one rigid disk and two active magnetic bearings.

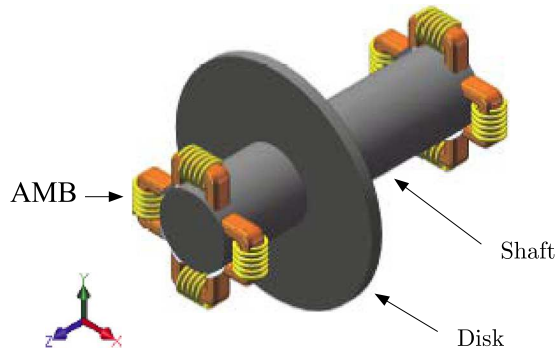


Fig. 3. Rotor bearing system with AMBs

The finite element procedure for rotors with the symmetric shaft is considered. Modifications are made to accommodate the effect of shaft asymmetry (Oncescu *et al.*, 2001).

3.1. Equation of motion of the shaft

The shaft is considered to be flexible. It is characterized by its kinetic and deformation energies. Its motion results from transverse displacement (u_x, u_y) and bending deformations (θ_x, θ_y) in the x - and y -planes (Fig. 4).

Because of the shaft asymmetry, the sectional moments of inertia I_x and I_y are not identical, consequently, the kinetic energy of the shaft can be represented by Oncescu *et al.* (2001)

$$\begin{aligned}
 T_s = & \frac{\rho S}{2} \int_0^L (\dot{u}_x^2 + \dot{u}_y^2 + \dot{u}_z^2) dz + \frac{\rho I_m}{2} \int_0^L (\dot{\theta}_x^2 + \dot{\theta}_y^2) dz + 2\rho I_m \Omega \int_0^L \dot{\theta}_x \theta_y dz \\
 & + \frac{\rho I_d}{2} \int_0^L (\dot{\theta}_x^2 + \dot{\theta}_y^2) dz \cos(2\Omega t) + \rho I_d \int_0^L (\dot{\theta}_x \theta_y) dz \sin(2\Omega t)
 \end{aligned} \tag{3.1}$$

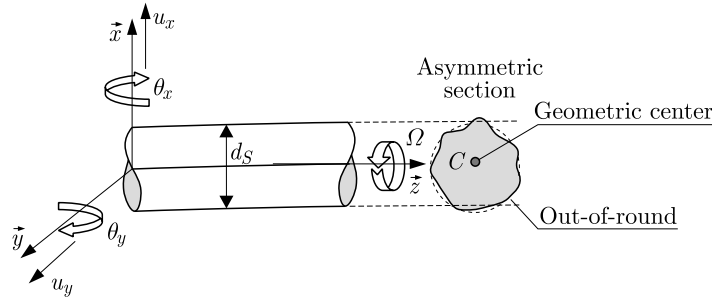


Fig. 4. Shaft modelling and corresponding DOF

where ρ is material density, $I_m = (I_x + I_y)/2$, $I_d = (I_x - I_y)/2$ are respectively deviatoric and mean area moments of inertia of the shaft cross-section (I_x and I_y are the second moments of area about the principal axes x and y of the shaft).

Rayleigh's dissipation function of the disk is (Gosiewski, 2008)

$$E_d = \frac{1}{2} \int_0^L c_s (\dot{u}_x^2 + \dot{u}_y^2) dz + \frac{1}{2} \int_0^L c_i [(\dot{u}_x + \Omega u_y)^2 + (\dot{u}_y - \Omega u_x)^2] dz \quad (3.2)$$

where c_s and c_i are respectively coefficients of external and internal damping.

If shear deformations are neglected, the strain energy of the shaft is (Onicescu *et al.*, 2001)

$$U = \frac{1}{2} \int_0^L EI_d \left\{ \left[\left(\frac{\partial^2 u_y}{\partial z^2} \right)^2 - \left(\frac{\partial^2 u_x}{\partial z^2} \right)^2 \right] \cos(2\Omega t) - 2u_x u_y \sin(2\Omega t) \right\} dz \\ + \frac{1}{2} \int_0^L EI_m \left[\left(\frac{\partial^2 u_x}{\partial z^2} \right)^2 + \left(\frac{\partial^2 u_y}{\partial z^2} \right)^2 \right] dz \quad (3.3)$$

where E is Young's modulus.

The finite element used to discretize the shaft consists of two node beam elements where each node has four degrees of freedom: two lateral displacements and two bending rotation angles. Applying Lagrange's formalism to this system permits the development of the equations of motion of asymmetric shaft (Onicescu *et al.*, 2001)

$$\mathbf{M}_s(t) \ddot{\boldsymbol{\delta}}_s + (\Omega \mathbf{G}_s + \mathbf{C}_s) \dot{\boldsymbol{\delta}}_s + \mathbf{K}_s(t) \boldsymbol{\delta}_s = \mathbf{0} \quad (3.4)$$

with

$$\mathbf{M}_s(t) = \mathbf{M}_{ss} + \mathbf{M}_{d,c} \cos(2\Omega t) + \mathbf{M}_{d,s} \sin(2\Omega t) \\ \mathbf{K}_s(t) = \mathbf{K}_{ss} + \mathbf{K}_{d,c} \cos(2\Omega t) + \mathbf{K}_{d,s} \sin(2\Omega t)$$

where \mathbf{M}_{ss} is the mass matrix of the symmetric shaft (Batoz and Gouri, 1990), $\mathbf{M}_{d,c}$ and $\mathbf{M}_{d,s}$ are mass matrices induced by the asymmetry of the shaft, \mathbf{G}_s is the gyroscopic matrix of the shaft, \mathbf{C}_s is the damping matrix, \mathbf{K}_{ss} is the stiffness matrix of the symmetric shaft (Batoz and Gouri, 1990), $\mathbf{K}_{d,c}$ and $\mathbf{K}_{d,s}$ are stiffness matrices induced by the asymmetry of the shaft, $\boldsymbol{\delta}_s$ is the vector of shaft DOFs.

3.2. Equation of motion of the disk

The center of mass of the rigid disk coincides with the elastic center of the shaft cross-section. The nodal displacements vector of the disk in fixed co-ordinates is given by:

$$\boldsymbol{\delta}_D = \{u_{d,x}, u_{d,y}, \theta_{d,x}, \theta_{d,y}\}.$$

The kinetic energy of the disk, by considering the effect of the unbalance, is expressed as (Oncescu *et al.*, 2001)

$$T_d = \frac{1}{2}M_d(\dot{u}_{d,x} + \dot{u}_{d,y}^2) + \frac{1}{2}J(\dot{\theta}_{d,x}^2 + \dot{\theta}_{d,y}^2) + 2J\dot{\theta}_{d,x}\theta_{d,y} + m_u d\Omega[\dot{u}_{d,x} \cos(\Omega t) + \dot{u}_{d,y} \sin(\Omega t)] \quad (3.5)$$

where M_d and J are mass and moment of inertia of the disk, Ω is angular speed of the rotor, m_u is unbalance mass (assumed to be small if compared with M_d), d is the radius defining location of the unbalance.

Rayleigh's function of the disk energy dissipation is (Gosiewski, 2008)

$$E_d = \frac{1}{2}c_s(\dot{u}_{d,x}^2 + \dot{u}_{d,y}^2) + \frac{1}{2}c_i[(\dot{u}_{d,x} + \Omega u_{d,y})^2 + (\dot{u}_{d,y} - \Omega u_{d,x})^2] \quad (3.6)$$

where c_s and c_i are respectively the coefficients of external and internal damping.

The application of Lagrange's equations for the disk only gives

$$\mathbf{M}_D \ddot{\boldsymbol{\delta}} + \dot{\boldsymbol{\delta}}(\Omega \mathbf{G}_D + \mathbf{C}_D) + \mathbf{K}_D \boldsymbol{\delta} = \mathbf{F}_u(t) \quad (3.7)$$

where \mathbf{M}_D , \mathbf{G}_D , \mathbf{C}_D and \mathbf{K}_D are respectively mass, gyroscopic, damping and stiffness matrices of the disk, $\mathbf{F}_u(t)$ is the unbalance vector.

3.3. General equation of motion of the rotor

By assembling the elementary matrices of shaft elements, disks and bearings (as expressed in Section 2), we obtain a system of n second order differential equations and n unknown functions, where n is the number of DOFs of the rotor. The global equations of motion are

$$\mathbf{M}(t)\ddot{\boldsymbol{\delta}} + (\mathbf{C} + \Omega \mathbf{G})\dot{\boldsymbol{\delta}} + \mathbf{K}(t)\boldsymbol{\delta} = \mathbf{F}_u(t) \quad (3.8)$$

where $\mathbf{M}(t)$ and $\mathbf{K}(t)$ are periodic matrices of period $T_1 = \pi/\Omega$, for which the time dependency is due to shaft asymmetry, \mathbf{C} is a constant matrix including damping effects of AM bearings, \mathbf{G} is the gyroscopic matrix, $\mathbf{F}_u(t)$ – unbalance vector of period $T_2 = 2\pi/\Omega$ and $\boldsymbol{\delta}$ is the vector of global DOFs.

The equations of motion are therefore parametric in nature, which usually causes a stability problem. Floquet's theory will be used to determine the zones of instability.

4. Floquet's theory

Floquet's method is a mathematical tool for solving parametric differential equations, such as (3.8). It involves computation of a transfer matrix over one period of motion (Dufour and Berlioz, 1998).

The study of stability of the steady state solution of system (3.8) can be reduced to study of stability of the trivial solution of the associated homogeneous system.

A state-space model for system (3.8) (with $\mathbf{F}_u(t) = \mathbf{0}$) has the form

$$\dot{\mathbf{X}} = \mathbf{A}(t)\mathbf{X} \quad (4.1)$$

where $\mathbf{A}(t)$ is a $m \times m$ ($m = 2n$) periodic matrix called the dynamic matrix of period T , and $\mathbf{X} = \{\delta, \dot{\delta}\}^{-1}$ is the state variable vector.

The transfer matrix $\boldsymbol{\Phi}(T, t_0)$ (Bauchau and Nikishkov, 2001) is by definition a matrix that relates the initial solution $\mathbf{X}(t_0)$ to the solution $\mathbf{X}(T)$ obtained at $t = T$, so

$$\mathbf{X}(T) = \boldsymbol{\Phi}(T, t_0)\mathbf{X}(t_0) \quad (4.2)$$

The period T of the matrix $\mathbf{A}(t)$ is divided into n intervals of equal length $h = T/n$ ($t_0 < t_1 < \dots < t_{n-1} < t_n$). Between the two solutions of (Eq. (3.7)) $\mathbf{X}(t_{i+1})$ and $\mathbf{X}(t_i)$, there is a relation

$$\mathbf{X}(t_{i+1}) = \mathbf{\Phi}(t_{i+1}, t_i)\mathbf{X}(t_i) \quad (4.3)$$

where $\mathbf{\Phi}(t_{i+1}, t_i)$ is the elementary transfer matrix. We can easily notice that

$$\mathbf{\Phi}(T, t_i) = \mathbf{\Phi}(T, t_{i+1})\mathbf{\Phi}(t_{i+1}, t_i) \quad (4.4)$$

The matrix $\mathbf{\Phi}(T, t_0)$ can be obtained by iterative calculation based on relation (4.4). We start with $\mathbf{\Phi}(T, T) = \mathbf{I}_m$ and gradually gets $\mathbf{\Phi}(T, t_{n-1}), \mathbf{\Phi}(T, t_{n-2}), \dots, \mathbf{\Phi}(T, t_0)$.

To determine the elementary transfer matrix $\mathbf{\Phi}(t_{i+1}, t_i)$, several methods have been proposed. In this work, Newmark's method is used.

Furthermore, it is shown that the stability of the trivial solution of equation (3.7) is fully defined by the eigenvalues of the transfer matrix over one period $\mathbf{\Phi}(T, t_0)$, known as the characteristic multipliers of system. The trivial solution is asymptotically stable if the modulus of all m eigenvalues is less than one, and is unstable if the modulus of at least one of the eigenvalues is greater than one.

5. Numerical results

The spinning system investigated in this paper is shown in Fig. 4. The disk is mounted on the shaft at $3L/4$. The system parameters are given in Table 1.

Table 1. System parameters

Parameter	Symbol	Value
Permeability of vacuum	μ_0	$4\pi \cdot 10^{-7}$ Wb/Am
Number of windings around core	N	300
Half angle between poles of electromagnet	θ	22.5 deg
Bias current	i_0	0.5 A
Differential gain	k_d	42.4 A·s/m
Proportional gain	k_p	14869 A/m
Rotor length	L	300 mm
Shaft diameter	d_S	10 mm
Disk diameter	d_D	100 mm
Young's modulus	E	$2.1 \cdot 10^{11}$ Pa
Density	ρ	7.85 gm/cm ³
Poisson's ratio	ν	0.28
Unbalance mass	M_u	5 gm
Moment of inertia	J	0.005 Kg·m ²
Rotor running speed	Ω	–

Figures 5 and 6 show respectively the dependency of stiffness and damping coefficients of AMBs on the air gap C_0 between the stator and the rotor for different values of the steady state current in the coil I_0 . Figures 7 and 8 show respectively the dependency of stiffness and damping coefficients of AMBs on the air gap C_0 between the stator and the rotor for different values of cross-sectional area of one electromagnet A .

K_{xx}, K_{yy}, C_{xx} and C_{yy} are strongly influenced by C_0, I_0 and A . Indeed, their values decrease considerably with C_0 , but regularly increase respectively with I_0 and A . This observation was proven by Bouaziz *et al.* (2011) when they determine the dynamic coefficients of AMB with

four, six and eight magnets. It is clear that the four coefficients become constant for large values of C_0 (from $C_0 = 2$ mm and irrespective of I_0 and A). It should also be noted that the values of damping coefficients are significant compared to those frequently encountered in literature for modeling of elastic bearings.

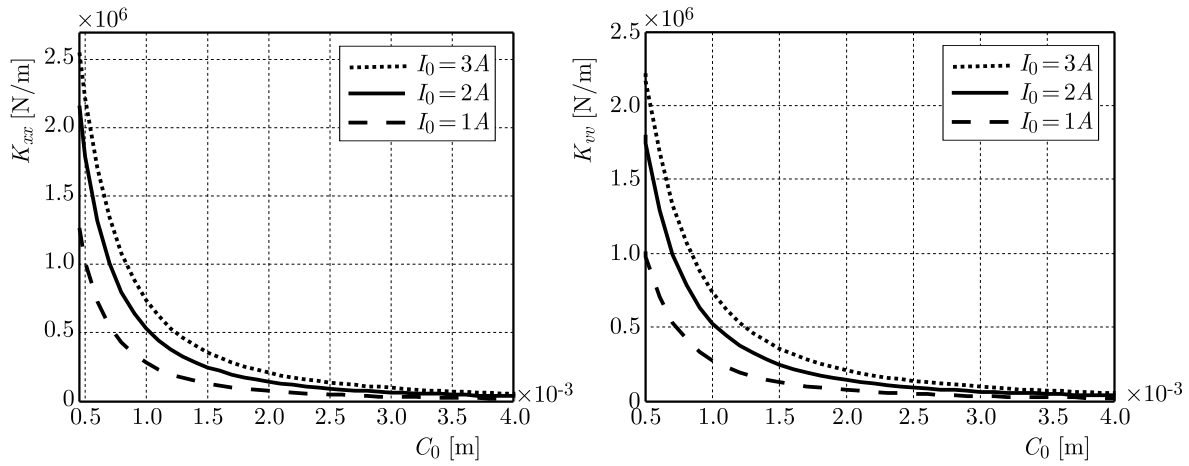


Fig. 5. Stiffness coefficients ($A = 200 \text{ mm}^2$)

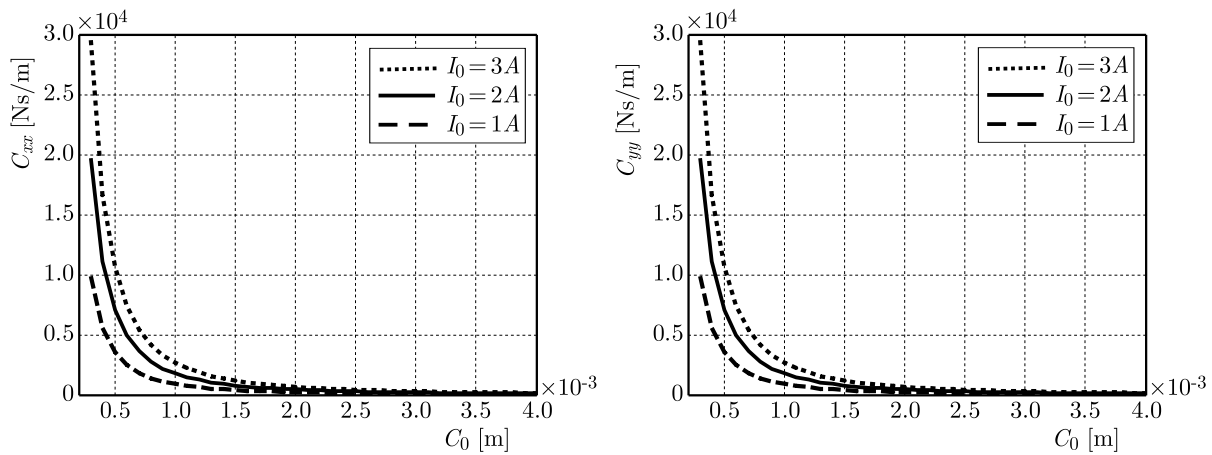


Fig. 6. Damping coefficients ($A = 200 \text{ mm}^2$)

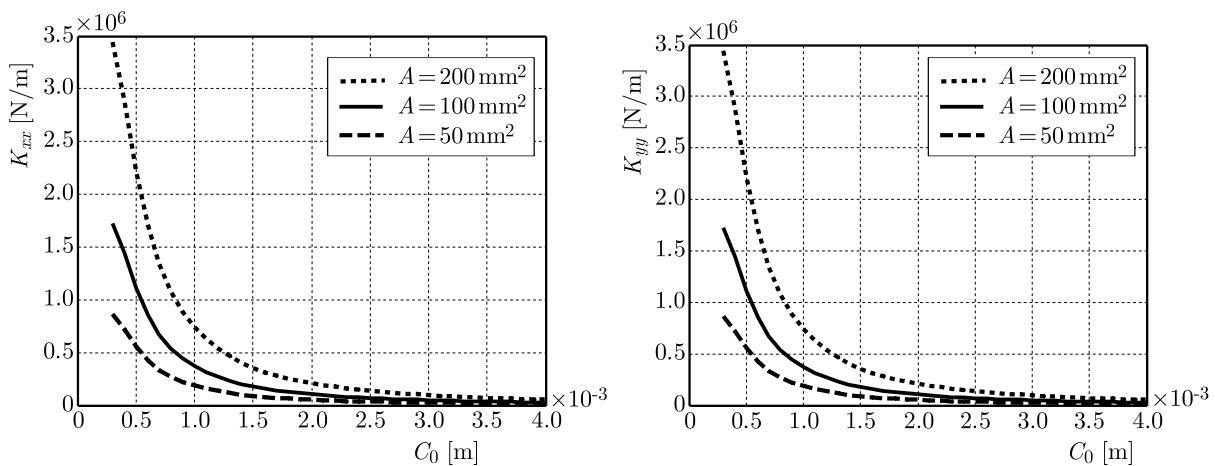


Fig. 7. Stiffness coefficients ($I_0 = 3 \text{ A}$)

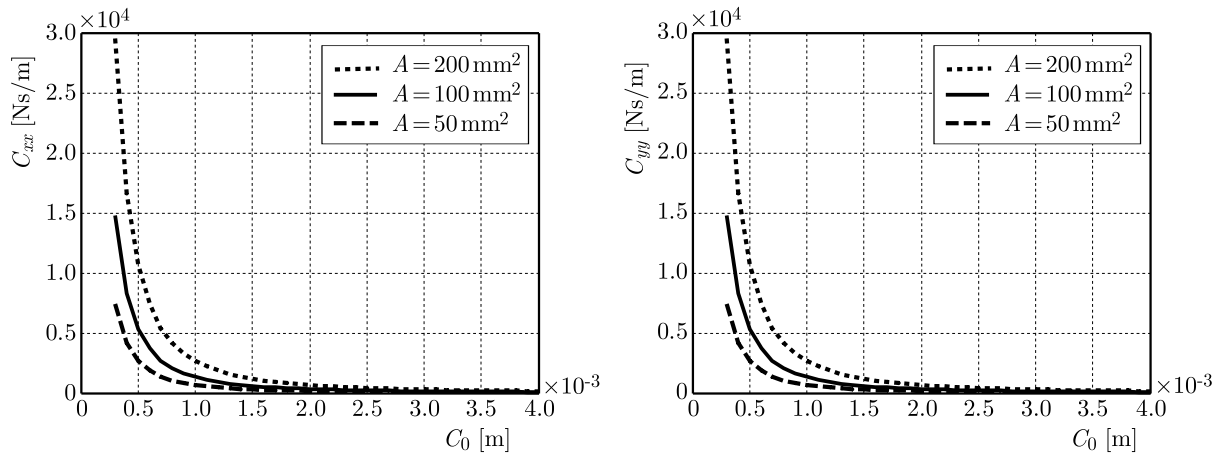


Fig. 8. Damping coefficients ($I_0 = 3 A$)

Since the coefficients of stiffness and damping are variable according to the parameters of the bearings, the stability of the studied asymmetric rotor varies as well. So try from the layout of different regions of stability to find the optimal parameters providing better system behavior (a minimum of regions of instability). The variable parameter is the factor of shaft asymmetry defined as the rate between the deviatory (I_d) and the mean area moments of inertia of the shaft cross-section (I_m): $f_{sa} = I_d/I_m$.

We are interested in the range of higher speeds because electromagnetic bearings are used in applications at high speeds.

Figure 9a shows regions of instability obtained for the studied system for factors of shaft asymmetry varying from 0 to 0.3 with increments by 0.05. The results have been obtained by varying the rotational speed between 10000 and 80000 rpm, with increments by 100 rpm. The air gap C_0 is 0.5 mm, the steady state current in the coil I_0 is 3A, and the effective cross-sectional area of one electromagnet A is 200 mm².

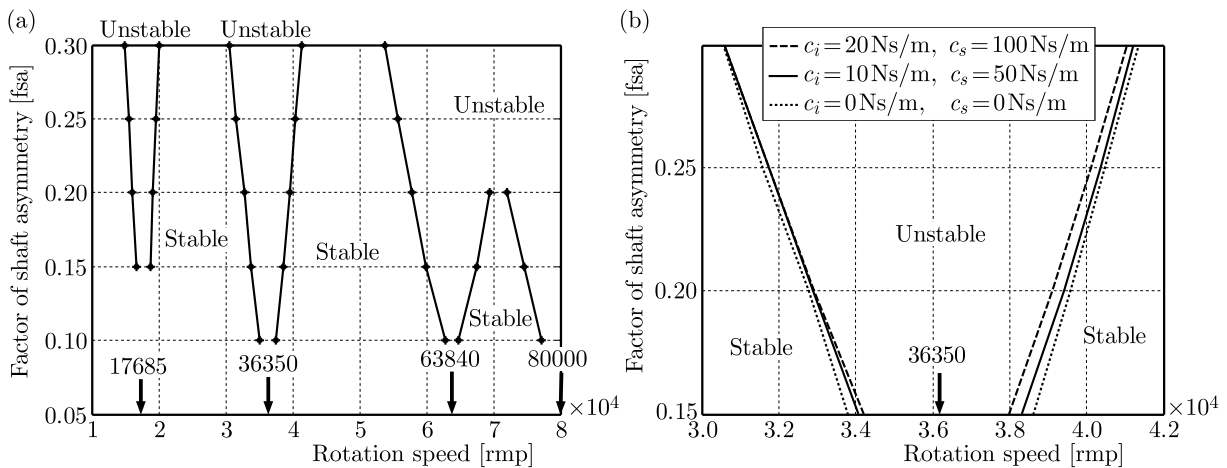


Fig. 9. Instability regions: (a) $C_0 = 0.5$ mm, $I_0 = 3$, $A = 200$ mm, (b) [30000-40000rpm], $C_0 = 0.5$ mm, $I_0 = 3$, $A = 200$ mm

For the symmetric shaft, no instability interval has been identified around the four shaft critical speeds: 17685, 36350, 63840 and 80100 rpm (according to the Campbell diagram). For the asymmetric shaft, four regions of instability appear for a factor of shaft asymmetry of 0.1 and for widths increasing with the shaft asymmetry. For a shaft asymmetry of 0.25, there are 5 critical speeds delimiting the three regions of instability: 15492, 19639, 31600, 40475, and 55765 rpm.

Figure 9b shows the influence of internal and external damping on the instability region [30000-40000 rpm]. The width of the stability zone decreases substantially by introducing the internal and external damping. This behavior is also observed for the other two instability regions. These coefficients are generally negligible compared to those provided by AMBs and cannot in this case considerably influence the stability of the system studied.

Figure 10 depicts the regions of instability respectively obtained for three different values of C_0 : 0.5 mm, 1.5 mm and 3 mm.

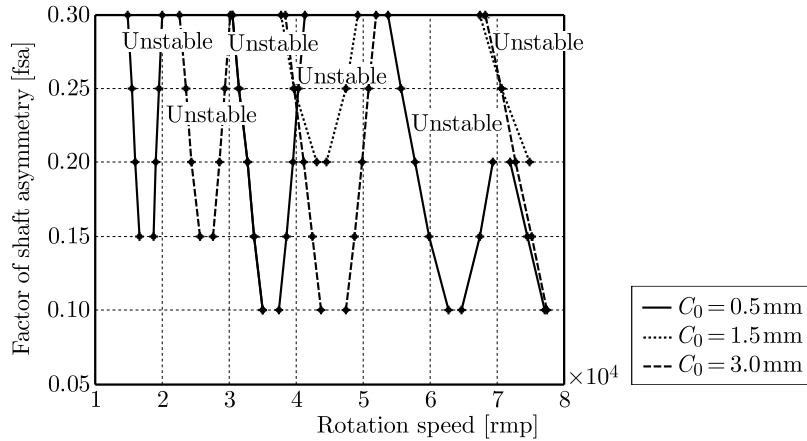


Fig. 10. Instability regions, $I_0 = 3$, $A = 200$ mm

It is evident that the instability regions are highly dependent on the air gap C_0 . Indeed, for a small value of C_0 ($C_0 = 0.5$ mm), the stiffness coefficients of AMBs are very important (Fig. 5). They increase the critical speed of the system and, therefore, the stability regions are also affected.

We note the presence of three regions of instability for $C_0 = 3$ mm against two for $C_0 = 1.5$ mm.

The second region of instability begins from a factor of shaft asymmetry of 0.2 for $C_0 = 1.5$ mm, while it starts from a factor of shaft asymmetry of 0.1 for $C_0 = 3$ mm. In fact, for greater values of C_0 , the stiffness coefficients of AMBs undergo a slight decrease. The positions of instability regions remain therefore almost unchanged, while their size and numbers increase with C_0 . This last behavior is explained by a decrease in damping coefficients of the AMBs.

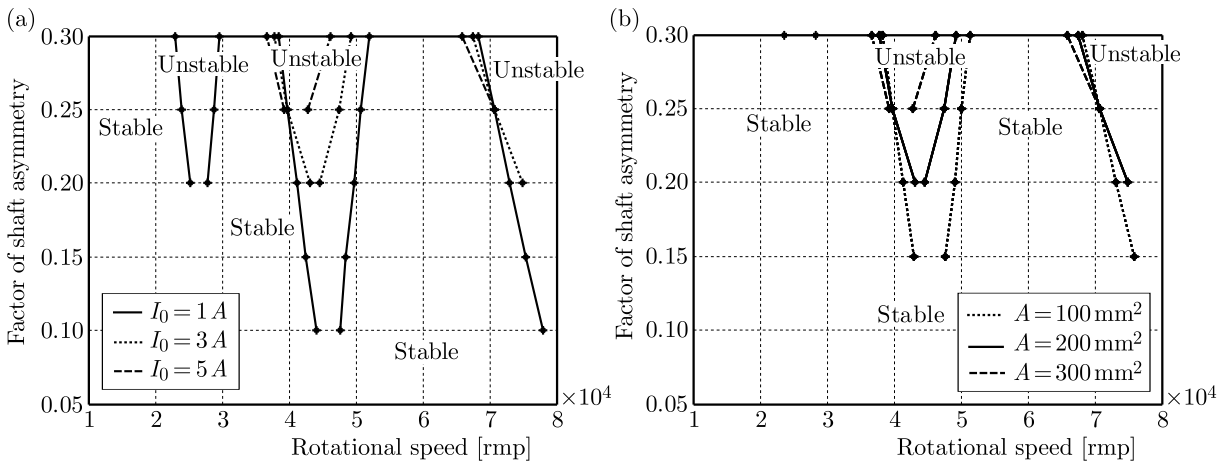


Fig. 11. Instability regions: (a) $C_0 = 1.5$ mm, $A = 200$ mm, (b) $C_0 = 1.5$ mm, $I_0 = 3$ A

Figure 11a shows regions of instability obtained for three values of I_0 . It is observed that regions of instability decreases with the increasing I_0 . By increasing I_0 , we can also remove a

region of instability, which proves the importance of control. Figure 11b presents the regions of instability obtained for three values of A . It is also observed that regions of instability decrease with the increasing A .

We can conclude that the stability is strongly linked with the dynamic coefficients of the bearings. A significant change of stiffness coefficients results in a change of the critical speed of the system and, consequently, a change in the positions of instability areas. At the same time, an increase in the damping coefficients, automatically leads to a decrease in the size of instability regions. C_0 and I_0 are the most influential parameters on the rotor stability. Based on this analysis, the parameters of AMBs that offer greater stability to the asymmetric rotor are: $C_0 = 1.5$ mm, $A = 200$ mm and $I_0 = 5$ A.

To better understand the instability phenomenon of asymmetric rotors, it is important to calculate and analyze the dynamic response. The dynamic response is observed at the disk-to-shaft attachment. A spectral method is used to estimate the dynamic response (Attia Hili *et al.*, 2006).

The frequency response along the x direction (power spectral density) of the rotor in the frequency range of 0 to 250 Hz is shown in Fig. 12a. The factor of asymmetry is 0.25 when the shaft running speed is 420 rpm.

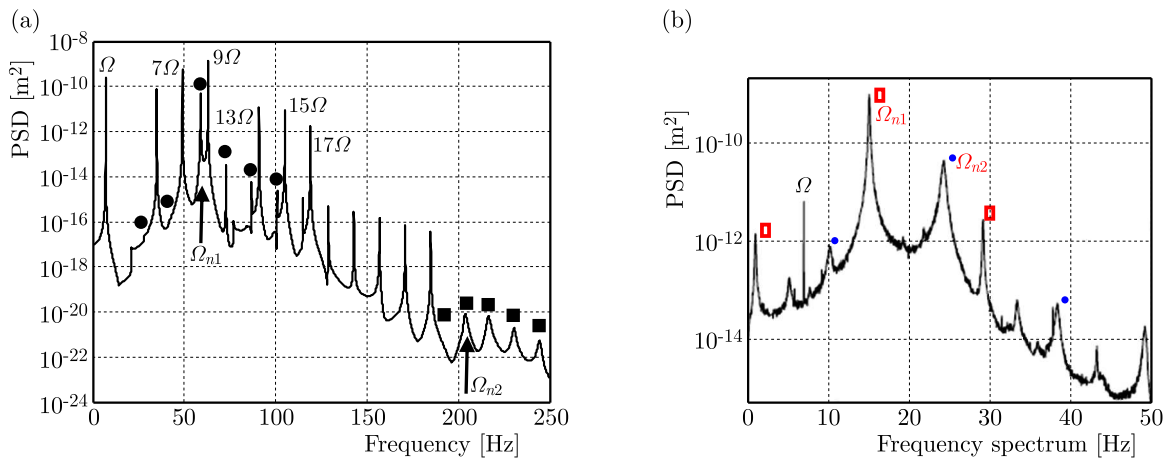


Fig. 12. (a) Frequency response, $C_0 = 1.5$ mm, $I_0 = 3$ A, $A = 200$ mm². (b) Experimental frequency response, Lazarus *et al.* (2010)

The frequency response is essentially characterized by:

- A dominant peak at the rotational frequency ($\Omega = 7$ Hz) indicating the presence of an unbalance.
- Several peaks located at frequencies of odd multiples of the rotational frequency ($3\Omega, 5\Omega, 7\Omega, \dots$) indicating the simultaneous presence of an unbalance and shaft asymmetry as well as representing the modulation phenomenon. Indeed, the mass and stiffness terms are time variables having the frequency equal to two times of that of rotation, whereas the excitation frequency (unbalance force) being equal to the rotational frequency.
- Two peaks presenting the first and second natural frequencies of the rotor (in xz -plane): $\Omega_{n1} = 59$ Hz and $\Omega_{n2} = 203$ Hz. Supplementary harmonics emerge in the frequency response and are located following the relation: $\Omega_j = \Omega_{ni} \pm 2j\Omega$ ($j > 1, i = 1, 2$). The fundamental and first secondary harmonics related to the natural frequencies F_{n1} and F_{n2} are respectively marked with spots and square marks. These peaks correspond to parametric quasi-modes characterizing every linear time-varying system like an asymmetric shaft. These results are in good agreement with the experimental results given in Fig. 12b and found by Lazarus *et al.* (2010). Indeed, the authors measured the frequency response of

an asymmetrical shaft. These experimental results are filtered to remove the spin speed subharmonics. The fundamental and first secondary harmonics related to the natural frequencies $\Omega_{n1} = 15$ Hz and $\Omega_{n2} = 23$ Hz are, respectively, marked with red square marks and with blue pots.

We deliberately chose a low speed rotation (although magnetic bearings operate at high speeds) to validate the numerical simulations. Finally, we note that the same behavior is observed in the yz -plane. The parametric quasi-modes also appear regardless of the running speed used.

6. Conclusion

In this paper, a finite element procedure for rotor-AMBs systems is generalized to include the effects of shaft asymmetry.

Firstly a model describing electromagnetic bearings (with four electromagnets) has been developed allowing to calculation of the dynamic coefficients which are mainly influenced by the air gap C_0 between the stator and the shaft, the effective cross-sectional area A and the bias current I_0 . Then, analysis of the stability by Floquet's theory shows that the stability is strongly dependent on the parameters of the bearings (which allow determination of the optimum parameters providing better behavior). The stability of the system is improved by the choice of AMBs parameters leading to an increase in the damping coefficients.

The dynamic response identifies the asymmetry of the shaft by the presence of odd harmonics of the rotational frequency and parametric quasi-modes in frequency spectra. These features could be useful in the detection of shaft faults in diagnosis of rotating machines.

References

1. ATTIA HILI M., FAKHFAKH T., HADDAR M., 2006, Failure analysis of a misaligned and unbalanced flexible rotor, *Journal of Failure Analysis and Prevention*, **6**, 4, 73-82
2. BATOZ J.L., GOURI D., 1990, *Modelisation des structures par éléments finis*, Paris Editions Hermès
3. BAUCHAU O.A., NIKISHKOV Y.G., 2001, An implicit Floquet analysis for rotorcraft stability evaluation, *Journal of The American Helicopter Society*, **46**, 200-209
4. BOUAZIZ A., BARKALLAH M., BOUAZIZ S., CHOLEY J.-Y., HADDAR M., 2016, Cutting parameters and vibrations analysis of magnetic bearing spindle in milling process, *Journal of Theoretical and Applied Mechanics*, **54**, 3, 691-703
5. BOUAZIZ S., BELHADJ MESSAOUD N., MATAAR M., FAKHFAKH T., HADDAR M., 2011, A theoretical model for analyzing the dynamic behaviour of spatial misaligned rotor with active magnetic bearings, *Mechatronics*, **21**, 899-907
6. DUFOUR R., BERLIOZ A., 1998, Parametric instability of a beam due to axial excitations and boundary conditions, *ASME Journal of Vibration and Acoustics*, **120**, 461-467
7. GOSIEWSKI Z., 2008, Control-oriented modeling and control of rotor vibration, *Acta Mechanica et Automatica*, **2**, 2, 21-38
8. INAGAKI T., KANKI H., SHIRAKI K., 1980, Response analysis of a general asymmetric rotor-bearing system, *Journal of Mechanical Design*, **102**, 147-157
9. INAYAT-HUSSAIN J.I., 2007, Chaos via torus breakdown in the vibration response of a rigid rotor supported by active magnetic bearings, *Chaos, Solitons and Fractals*, **31**, 4, 912-927
10. INAYAT-HUSSAIN J.I., 2010, Nonlinear dynamics of a magnetically supported rigid rotor in auxiliary bearings, *Mechanism and Machine Theory*, **45**, 11, 1651-1667

11. LAZARUS A., PRABEL B., COMBESCURE D., 2010, A 3D finite element model for the vibration analysis of asymmetric rotating machines, *Journal of Sound and Vibration*, **329**, 3780-3797
12. LEI S.G., PALAZZOLO A., 2008, Control of flexible rotor systems with active magnetic bearings, *Journal of Sound and Vibration*, **314**, 19-38
13. NELSON H.D., McVAUGH J.M., 1976, The dynamics of rotor-bearing systems using finite elements, *Journal of Engineering for Industry*, **98**, 593-600
14. ONCESCU F., LAKIS A.A., OSTIGUY G., 2001, Investigation of the stability and steady state response of asymmetric rotors using finite element formulation, *Journal of Sound and Vibration*, **245**, 2, 303-328
15. TSAI N.-C., LI H.-Y., LIN C.-C., CHIANG C.-W., WANG P.-L., 2011, Identification of rod dynamics under influence of active magnetic bearing, *Mechatronics*, **21**, 6, 1013-1024

Manuscript received August 24, 2016; accepted for print January 5, 2017

EFFECT OF INDUCED TEMPERATURE FIELD ON DEVELOPMENT OF CURVILINEAR CRACK WITH BONDS BETWEEN THE FACES IN END ZONES

VAGIF M. MIRSAALIMOV

*Azerbaijan Technical University and Institute of Mathematics and Mechanics of NAS of Azerbaijan, Baku,
Azerbaijan Republic; e-mail: vagif.mirsalimov@imm.az*

AZER B. MUSTAFAYEV

Institute of Mathematics and Mechanics of NAS of Azerbaijan, Baku, Azerbaijan Republic; e-mail: azer_bm@list.ru

Temperature changes near the end of a curvilinear cohesive crack and their influence on crack growth are investigated. The problem of local temperature changes consists in a delay or retardation of the cohesive crack growth. The bonds between the curvilinear crack faces in the end zones are modeled by application to the crack surface cohesive forces caused by the presence of bonds. The boundary value problem of equilibrium of the curvilinear crack with interfacial bonds in the end zones under action of external tensile loads, induced temperature field and tractions in the bonds preventing to its opening, is reduced to a system of singular integral equations with a Cauchy-type kernel. From the solution of this equation system, normal and tangential tractions in the bonds are found. Analysis of the limit equilibrium of the crack using the end zone model is performed on the basis of a criterion of bonds limiting stretching and includes: 1) establishment of tractions depending on opening of the crack faces; 2) evaluation of the stress state near the curvilinear crack with taking into account tensile loads, induced temperature field, tractions in the bonds; 3) determination of the critical external tensile loads.

Keywords: curvilinear crack with interfacial bonds, thermoelastic stress field, cohesive forces

1. Introduction

Creating reliable emergency response systems is a vital issue, especially when we talk about unique installations and safety of people. One of the effective means of crack growth retardation may be temperature and thermoelastic fields (Finkel, 1977; Parton and Morozov, 1985; Potthast and Herrmann, 2000; Fu *et al.*, 2001; Qin *et al.*, 2007; Liu, 2008, 2011a,b, 2014a,b; Georgantzinos and Anifantis, 2014; Liu *et al.*, 2015). In fracture mechanics, the healing problem existing in the crack body is of significant importance (Dimaki *et al.*, 2010). As seen from the results of the papers (Kadiev and Mirsalimov, 2001; Mirsalimov and Kadiev, 2004; Liu, 2008, 2011a,b; Itou, 2014; Liu, 2014a,b; Mirsalimov and Mustafayev, 2015a,b), the influence of the thermal source reduces strain of the stretching plane in the direction perpendicular to the crack, and because of what the stress intensity factor near the crack end lowers. In most of the existing papers, Griffith's model of a crack is used. In the present paper, we use a bridged crack model ([4], Mirsalimov, 2007; Mirsalimov and Mustafayev, 2016).

The crack retardation problem is of scientific and significant practical value as its solution enables one to extend the lifetime and, the main thing, to avoid accidents associated with sudden fracture. Evaluation of efficiency of application of thermal sources in crack growth retardation in thin-walled structural elements is of interest. Fracture of a construction may be prevented by creating a thermal field in the path of crack growth. Creation of thermal fields was justified by their ease of preparation and multilateral nature of influence on the fracture process.

Technical ease of obtaining in an extended object temperature and thermoelastic field in any size and distribution creates wide opportunities of change of the direction and retardation of crack growth. The experiments (Finkel, 1977) show that by heating the crack path to 70-100°C, we observe delay and retardation of a crack.

The effect of the temperature field on the retardation of a curvilinear crack with bonds between the faces still has not been investigated. In this connection, studying the influence of the reduced thermal stress field on curvilinear crack propagation in a stretchable plane with regard to the bonds between the faces in the crack end areas is of scientific and practical interest. The goal of the paper is to develop a mathematical model of curvilinear interfacial crack retardation by means of temperature fields.

2. Formulation of problem

Let us consider an unbounded elastic plane weakened with a crack of length $2\ell = b - a$ at the origin of coordinates. In real materials, due to structural and technological factors, crack surfaces have roughnesses and curvings. A fracture mechanics problem on a curvilinear crack in a plane assuming that the crack contour has roughnesses (small deviations from a linear form) is considered. It is assumed that there are areas at which the cohesion forces of the material continuously distributed at the end area of the crack, ect. It is considered that these areas adjoin to the crack tips, their sizes are comparable with the crack length [4]. Models of the crack with end zones were proposed for brittle materials in (Barenblatt, 1961) and for plastic flow state under constant stress in (Leonov and Panasyuk, 1959; Dugdale, 1960). The end zones of the curvilinear crack were simulated by the areas with weakened interparticle bonds in the material.

The model of a crack with interfacial bonds at the end zones may be used in different scales of fracture. Intensive development of crack models with explicit account of nonlinear laws of interaction in conformity to elasto-visco-plastic behavior of materials and various kinds of loading is connected with this fact. Bibliography on this subject may be found in papers of the special issue of *Engineering Fracture Mechanics* (2003).

When the length of the end zone of the crack is not small compared with the crack length, the methods for evaluating the fracture toughness of the material based on consideration of a crack with a small end zone are not applicable. In these cases, simulation of the stress state at the crack end zone should be carried out with regard to deformational characteristics of the bonds.

The crack faces outside the end zones are free from external loads. At infinity, the strengthened plane is subjected to uniform tension along the ordinate axis by a stress $\sigma_y^\infty = \sigma_0$ (Fig. 1). For retardation of the crack, on the path of its propagation a zone of compressible stresses is formed by means of heating the domain S by a thermal source to temperature T_0 . The following assumptions are accepted:

- a) All thermoelastic characteristics of the plate material are temperature independent.
- b) The plate material is homogeneous and isotropic.

It is assumed that at the moment $t = 0$ an arbitrary domain $S = S_1 + S_2$ on the crack growth path in the plane instantly heats up to a constant temperature $T = T_0$. The remaining part of the plate at the initial moment has zero temperature.

For many metallic materials (steels, aluminum alloy and so on) at the temperature change to 300°C-400°C, the dependence of thermoelastic characteristics weakly changes according to temperature. This fact was experimentally established. Thus, for all structural materials there exists such a temperature range in which the assumption on steadiness of characteristics of the material is correct. It is established on the basis of temperature dependence of the modulus of elasticity.

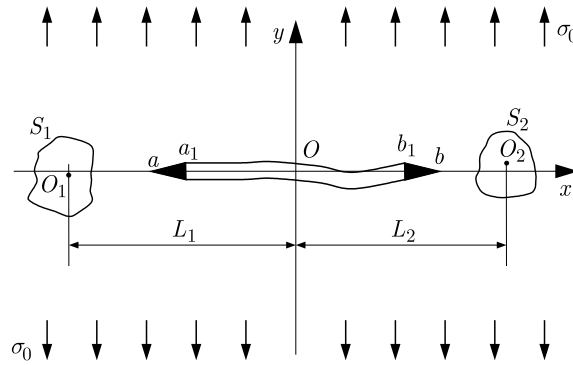


Fig. 1. Computational diagram of the problem

Let us distinguish a part of the crack of length $d_1 = a_1 - a$ and $d_2 = b - b_1$ (end zones) adjoining to its tips at which the crack faces interact. The interaction of the crack faces in the end zones is modeled by introducing between the crack faces the bonds (cohesive forces) having the given deformation diagram. The physical nature of such bonds and sizes of the end zones in which the interaction of crack faces is realized, depends on kind of the material. A crack existing in the plane is assumed to be close to a rectilinear form admitting only small deviations of the crack line from the straight line $y = 0$. The crack line equation is accepted in the form: $y = f(x)$, $a \leq x \leq b$. Based on the accepted assumption on the form of the crack line, functions $f(x)$ and $f'(x)$ are small quantities.

The end zones are small compared with another part of the plane. Therefore, the end zones may be mentally removed having changed by cuts whose surfaces interact between themselves by some law corresponding to the action of the removed material.

Under the action of external power and thermal loads on the plane, in the bonds connecting the crack faces in the end zones, there will arise in the general case, normal $q_y(x)$ and tangential $q_{xy}(x)$ forces. Consequently, to the crack faces in the end zones there will be applied normal and tangential stresses equal to $q_y(x)$ and $q_{xy}(x)$, respectively. The quantities of these stresses are not known in advance and they are to be determined.

The boundary conditions of the considered problem have the following form ($y = f(x)$)

$$\sigma_n - i\tau_{nt} = \begin{cases} 0 & \text{for } a_1 < x < b_1 \\ q_y - iq_{xy} & \text{for } a \leq x \leq a_1 \wedge b_1 \leq x \leq b \end{cases} \quad (2.1)$$

where n, t are natural coordinates. The stress state is represented in the form

$$\sigma_x = \sigma_{x_0} + \sigma_{x_1} \quad \sigma_y = \sigma_{y_0} + \sigma_{y_1} \quad \tau_{xy} = \tau_{xy_0} + \tau_{xy_1} \quad (2.2)$$

where $\sigma_{x_0}, \sigma_{y_0}, \tau_{xy_0}$ is the solution to the thermoelasticity problem for a crackless plane; $\sigma_{x_1}, \sigma_{y_1}, \tau_{xy_1}$ is the stress state of the plane with an interfacial crack on the faces on which the stresses equal in value and opposite in sign, defined by the stress state $\sigma_{x_0}, \sigma_{y_0}, \tau_{xy_0}$ for $y = 0$, are additionally applied.

3. The method of solution of the boundary-value problem

For determining the stresses $\sigma_{x_0}, \sigma_{y_0}, \tau_{xy_0}$, we solve a thermo-elasticity problem for a solid plane. At first, we find temperature distribution in the plane. For that we solve the following boundary value problem of heat theory

$$\frac{\partial T}{\partial t} = a_* \Delta T \quad T = \begin{cases} T_0 & \text{for } t = 0 \wedge x, y \in S \\ 0 & \text{for } t = 0 \wedge x, y \notin S \end{cases} \quad (3.1)$$

where Δ is the Laplace operator; a_* is the coefficient of thermal conductivity of the plane material.

For a generalized plane stress state, it is assumed that the plate is thermally insulated on lateral surfaces. When determining the temperature field, for simplifying the problem, we do not take into account a perturbed temperature field caused by the existence of the crack. Let the heated by heat source areas S_1 and S_2 from each vertex are arbitrary and simply connected regions with centers $O_k(L_k, c_k)$ (Fig. 1).

The solution to the thermal conductivity problem has the form

$$T(x, y, t) = \frac{T_0}{4\pi a_* t} \iint_{S_1} \exp\left(-\frac{R^2}{4a_* t}\right) d\xi d\eta + \iint_{S_2} \exp\left(-\frac{R^2}{4a_* t}\right) d\xi d\eta \quad (3.2)$$

where $R^2 = (x - \xi)^2 + (y - \eta)^2$.

For the thermoelastic potential of displacement, we find

$$F(x, y, t) = \frac{(1 + \nu)\alpha T_0}{4\pi} \left[\int_0^t \frac{1}{\tau} \iint_S \exp\left(-\frac{R^2}{4a_* \tau}\right) d\xi d\eta - 2 \iint_S \ln \frac{1}{R} d\xi d\eta \right] \quad (3.3)$$

where $S = S_1 + S_2$; ν is the Poisson ratio of the material; α is the coefficient of linear temperature expansion.

The components of the stress tensor are expressed through thermoelastic potential of displacement by the known formulas (Parkus, 1959) and have the form

$$\begin{aligned} \sigma_{x_0} &= -\mu(1 + \nu)\alpha T_0 \\ &\cdot \left\{ 1 + \frac{1}{\pi} \iint_S \frac{1}{R^4} \left[(x - \xi)^2 - (y - \eta)^2 + 2(y - \eta)^2 \Gamma\left(2, \frac{R^2}{4a_* t}\right) - R^2 \exp\left(-\frac{R^2}{4a_* t}\right) \right] d\xi d\eta \right\} \\ \sigma_{y_0} &= -\mu(1 + \nu)\alpha T_0 \\ &\cdot \left\{ 1 + \frac{1}{\pi} \iint_S \frac{1}{R^4} \left[-(x - \xi)^2 + (y - \eta)^2 + 2(x - \xi)^2 \Gamma\left(2, \frac{R^2}{4a_* t}\right) - R^2 \exp\left(-\frac{R^2}{4a_* t}\right) \right] d\xi d\eta \right\} \\ \tau_{xy_0} &= -\frac{\mu(1 + \nu)\alpha T_0}{2\pi} \iint_S \frac{4(x - \xi)(y - \eta)}{\pi} \frac{1}{R^4} \left[1 - \Gamma\left(2, \frac{R^2}{4a_* t}\right) \right] d\xi d\eta \\ \Gamma(\alpha, x) &= \int_x^\infty e^{-t} t^{\alpha-1} dt \end{aligned} \quad (3.4)$$

where μ is the shear modulus of the material.

Boundary conditions (2.1) on the crack with end zones on the basis of (2.2) take the form ($y = f(x)$)

$$\sigma_{n_1} - i\tau_{n_1} = \begin{cases} -[\sigma_{y_0}(x, 0) - i\tau_{xy_0}(x, 0)] & \text{for } a_1 < x < b_1 \\ q_y(x, 0) - iq_{xy}(x, 0) - [\sigma_{y_0}(x, 0) - i\tau_{xy_0}(x, 0)] & \text{for } a \leq x \leq a_1 \wedge b_1 \leq x \leq b \end{cases} \quad (3.5)$$

Let us consider some arbitrary realization of the curved (with small deviations from the rectilinear form) surface of crack faces.

As the functions $f(x)$ and $f'(x)$ are small quantities, the function $f(x)$ may be represented in the form

$$f(x) = \varepsilon H(x) \quad a \leq x \leq b$$

where ε is a small parameter for which we can accept the greatest height of the bulge of irregularity of the upper crack surface related to the crack length.

The stress and the displacement values and tractions in the bonds are sought in the form of an expansion in the small parameter

$$\begin{aligned} \sigma_{x_1} &= \sigma_x^{(0)} + \varepsilon\sigma_x^{(1)} + \dots & \sigma_{y_1} &= \sigma_y^{(0)} + \varepsilon\sigma_y^{(1)} + \dots & \tau_{xy_1} &= \tau_{xy}^{(0)} + \varepsilon\tau_{xy}^{(1)} + \dots \\ u &= u_0 + \varepsilon u_1 + \dots & v &= v_0 + \varepsilon v_1 + \dots \\ q_y &= q_y^0 + \varepsilon q_y^1 + \dots & q_{xy} &= q_{xy}^0 + \varepsilon q_{xy}^1 + \dots \end{aligned}$$

where the terms with ε of higher orders are neglected for simplification. Here $\sigma_x^{(0)}, \sigma_y^{(0)}, \tau_{xy}^{(0)}, u_0, v_0, q_y^0, q_{xy}^0$ and $\sigma_x^{(1)}, \sigma_y^{(1)}, \tau_{xy}^{(1)}, u_1, v_1, q_y^1, q_{xy}^1$ are the stresses, displacements and tractions in the bonds of zero and first approximations, respectively.

The values of stresses for $y = f(x)$ can be found by expanding in series the expressions for stresses in the vicinity of $y = 0$. Using the procedure of the perturbation method, allowing for previous formulas, we find boundary conditions for $y = 0, a \leq x \leq b$:

— in the zero approximation ($y = 0$)

$$\sigma_y^{(0)} - i\tau_{xy}^{(0)} = \begin{cases} -(\sigma_{y_0} - \tau_{xy_0}) & \text{for } a_1 < x < b_1 \\ q_y^0 - iq_{xy}^0 - (\sigma_{y_0} - \tau_{xy_0}) & \text{for } a^0 \leq x \leq a_1 \quad \wedge \quad b_1 \leq x \leq b^0 \end{cases} \quad (3.6)$$

— in the first approximation ($y = 0$)

$$\sigma_y^{(1)} - i\tau_{xy}^{(1)} = \begin{cases} N - iT & \text{for } a_1 \leq x \leq b_1 \\ q_y^1 - iq_{xy}^1 + N - iT & \text{for } a^1 \leq x \leq a_1 \quad \wedge \quad b_1 \leq x \leq b^1 \end{cases} \quad (3.7)$$

where for $y = 0$

$$\begin{aligned} N &= \tau_{xy}^{(0)} \frac{dH}{dx} - H \frac{\partial \sigma_y^{(0)}}{\partial y} & T &= (\sigma_y^{(0)} - \sigma_x^{(0)}) \frac{dH}{dx} - H \frac{\partial \tau_{xy}^{(0)}}{\partial y} \\ a &= a^0 + \varepsilon a^1 + \dots & b &= b^0 + \varepsilon b^1 + \dots \end{aligned} \quad (3.8)$$

The basic relations of the stated problem should be complemented by the equation connecting the crack faces opening and tractions in the bonds in the end zones of the crack. Without loss of generality, we can represent this equation in the form

$$(v^+ - v^-) - i(u^+ + u^-) = \Pi_y(x, \sigma)q_y(x) - i\Pi_x(x, \sigma)q_{xy}(x) \quad (3.9)$$

where the functions $\Pi_y(x, \sigma)$ and $\Pi_x(x, \sigma)$ are effective compliances of the bonds dependent on the tension of the bonds, $\sigma = \sqrt{q_y^2 + q_{xy}^2}$ is the modulus of the bonds traction vector; $(v^+ - v^-)$ are normal and $(u^+ + u^-)$ are tangential components of the opening of the crack faces in the end zones.

At constant values of Π_y, Π_x in (3.9), we have a linear law of deformation. In the general case, the deformation law is nonlinear and is given.

The stress strain state $\sigma_x^{(0)}, \sigma_y^{(0)}, \tau_{xy}^{(0)}$ and u_0, v_0 at an infinite plane and conditions of a plane problem with a cut along the abscissa is described by two piecewise-analytical functions $\Phi(z)$ and $\Omega(z)$ (Muskhelishvili, 2010)

$$\begin{aligned} \sigma_x^{(0)} + \sigma_y^{(0)} &= 2[\Phi_0(z) + \overline{\Phi_0(z)}] & \sigma_y^{(0)} - i\tau_{xy}^{(0)} &= \Phi_0(z) + \Omega_0(\bar{z}) + (z - \bar{z})\overline{\Phi_0'(z)} \\ 2\mu \frac{\partial}{\partial x}(u_0 + iv_0) &= \kappa\Phi_0(z) - \overline{\Phi_0(z)} - z\overline{\Phi_0'(z)} - \overline{\Psi_0(z)} \\ \Omega(z) &= \overline{\Phi}(z) + z\overline{\Phi'}(z) + \overline{\Psi}(z) \end{aligned} \quad (3.10)$$

where $\kappa = 3 - 4\nu$ for plane deformation, and $\kappa = (3 - \nu)/(1 + \nu)$ for a plane stress state.

For determination of the functions $\Phi_0(z)$ and $\Omega_0(z)$ on the basis of boundary conditions and the superposition principle, we have a linear conjugation problem (Muskhelishvili, 2010)

$$\begin{aligned} [\Phi_0(x) + \Omega_0(x)]^+ + [\Phi_0(x) + \Omega_0(x)]^- &= 2p_0(x) \\ [\Phi_0(x) - \Omega_0(x)]^+ - [\Phi_0(x) - \Omega_0(x)]^- &= 0 \end{aligned} \quad (3.11)$$

where $a \leq x \leq b$, x is the affix of the points of the contour of the crack with end zones

$$p_0(x) = \begin{cases} -(\sigma_{y_0} - \tau_{xy_0}) - \sigma_0 & \text{on free faces of the crack} \\ q_y^0 - iq_{xy}^0 - (\sigma_{y_0} - \tau_{xy_0}) - \sigma_0 & \text{on faces of the crack end zones} \end{cases}$$

Since the stresses in the plate are restricted, we should look for the solution to boundary value problem (3.11) in the class of everywhere bounded functions. The sought for solution to the boundary value problem is written in the form

$$\Phi_0(z) = \Omega_0(z) = \frac{\sqrt{(z - a^0)(z - b^0)}}{2\pi i} \int_{a^0}^{b^0} \frac{p_0}{\sqrt{(t - a^0)(t - b^0)(t - z)}} dt \quad (3.12)$$

Moreover, all the following solvability conditions of boundary value problem (3.11) should be fulfilled

$$\int_{a^0}^{b^0} \frac{p_0(t)}{\sqrt{(t - a^0)(b^0 - t)}} dt = 0 \quad \int_{a^0}^{b^0} \frac{tp_0(t)}{\sqrt{(t - a^0)(b^0 - t)}} dt = 0 \quad (3.13)$$

These relations serve for determination of the unknown parameters a^0 and b^0 .

For the final determination of the complex potentials $\Phi_0(z)$ and $\Omega_0(z)$, it is necessary to find the tractions in the bonds q_y^0 and q_{xy}^0 . Using the relation

$$2\mu \frac{\partial}{\partial x}(u_0 + iv_0) = \kappa \Phi_0(z) - \Omega_0(\bar{z}) - (z - \bar{z})\overline{\Phi_0'(z)}$$

and the boundary values of the functions $\Phi_0(z)$ and $\Omega_0(z)$ on the segment $a^0 \leq x \leq b^0$, we get the following equality

$$\Phi_0^+(x) - \Phi_0^-(x) = \frac{2\mu}{1 + \kappa} \left[\frac{\partial}{\partial x}(u_0^+ - u_0^-) + i \frac{\partial}{\partial x}(v_0^+ - v_0^-) \right] \quad (3.14)$$

Using the Sokhotski-Plemelj formulas (Muskhelishvili, 2010) and taking into account formula (3.12) we find

$$\Phi_0^+(x) - \Phi_0^-(x) = -\frac{i\sqrt{(x - a^0)(b^0 - x)}}{\pi} \int_{a^0}^{b^0} \frac{p_0(t)}{\sqrt{(t - a^0)(b^0 - t)(t - x)}} dt \quad (3.15)$$

The obtained expression, (3.15), is substituted into the left side of (3.14), and by taking into account relation (3.9) in the zero approximation we get the system of nonlinear integro-differential equations with respect to the unknown functions q_y^0 and q_{xy}^0

$$\begin{aligned} -\frac{\sqrt{(x - a^0)(b^0 - x)}}{\pi} \int_{a^0}^{b^0} \frac{q_y^0(t) + f_y(t)}{\sqrt{(t - a^0)(b^0 - t)(t - x)}} dt &= \frac{2\mu}{1 + \kappa} \frac{d}{dx} [II_y(x, \sigma^0) q_y^0(x)] \\ -\frac{\sqrt{(x - a^0)(b^0 - x)}}{\pi} \int_{a^0}^{b^0} \frac{q_{xy}^0(t) + f_{xy}(t)}{\sqrt{(t - a^0)(b^0 - t)(t - x)}} dt &= \frac{2\mu}{1 + \kappa} \frac{d}{dx} [II_x(x, \sigma^0) q_{xy}^0(x)] \end{aligned} \quad (3.16)$$

Here $f_y(t) = -\sigma_{y_0}(t) - \sigma_0$, $f_{xy}(t) = -\tau_{xy_0}(t)$.

4. Numerical solution and analysis

As expected, the stated problem in the zero approximation is decomposed into two independent problems: Eq. (3.16)₁ for mode I crack and Eq. (3.16)₂ for mode II crack.

Each of equations (3.16)₁ or (3.16)₂ is a nonlinear integro-differential equation with a Cauchy-type integral and may be solved only numerically. For their solution, one can use a collocation scheme (Panasyuk *et al.*, 1976; Mirsalimov, 1987; Ladopoulos, 2000, 2013) with an approximation of unknown functions.

Now pass to algebraization of integro-differential equations (3.16). At first, in integro-differential equations (3.16) all integration segments are reduced to one interval $[-1, 1]$. For that, we make a change of variables

$$t = \frac{1}{2}(a^0 + b^0) - \frac{1}{2}(a^0 - b^0)\tau \quad x = \frac{1}{2}(a^0 + b^0) - \frac{1}{2}(a^0 - b^0)\eta$$

At such a change of variables, the left side of integro-differential equation (3.16)₁ admits the following form

$$-\frac{1}{\pi}\sqrt{1-\eta^2} \left[\int_{-1}^1 \frac{q_y^0(\tau)}{\sqrt{1-\tau^2}(\tau-\eta)} d\tau + \int_{-1}^1 \frac{f_y(\tau)}{\sqrt{1-\tau^2}(\tau-\eta)} d\tau \right]$$

Respectively, for the left side of equation (3.16)₂ we get

$$-\frac{1}{\pi}\sqrt{1-\eta^2} \left[\int_{-1}^1 \frac{q_{xy}^0(\tau)}{\sqrt{1-\tau^2}(\tau-\eta)} d\tau + \int_{-1}^1 \frac{f_{xy}(\tau)}{\sqrt{1-\tau^2}(\tau-\eta)} d\tau \right]$$

Replace the derivative in the right hand side of equation (3.16)₁ for an arbitrary internal i -th node by a finite-difference approximation

$$\frac{d}{dx}[\Pi_y(x, \sigma^0)q_y^0(x)]_i = \frac{\Pi_y(x_{i+1}, \sigma^0(x_{i+1}))q_y^0(x_{i+1}) - \Pi_y(x_{i-1}, \sigma^0(x_{i-1}))q_y^0(x_{i-1})}{2\Delta x}$$

where $\Delta x = (b^0 - a^0)/M$.

In the similar way we do it with the right hand side of equation (3.16)₂. Therewith we take into account boundary conditions for $\eta = \pm 1$: $q_y^0(a^0) = q_y^0(b^0) = 0$, $q_{xy}^0(a^0) = q_{xy}^0(b^0) = 0$ (this corresponds to the conditions $v_0^+(a^0, 0) - v_0^-(a^0, 0) = 0$, $v_0^+(b^0, 0) - v_0^-(b^0, 0) = 0$, $u_0^+(a^0, 0) - u_0^-(a^0, 0) = 0$, $u_0^+(b^0, 0) - u_0^-(b^0, 0) = 0$).

Using the quadrature formula

$$\frac{1}{2\pi} \int_{-1}^1 \frac{g(\tau)}{\sqrt{1-\tau^2}(\tau-\eta)} d\tau = -\frac{1}{M \sin \theta} \sum_{k=1}^M g_k \sum_{m=1}^{M-1} \cos(m\theta_k) \cos(m\theta)$$

where

$$\tau = \cos \theta \quad \eta_m = \cos \theta_m \quad \theta_m = \frac{2m-1}{2M}\pi \quad (m = 1, 2, \dots, M)$$

all the integrals in (3.16) are replaced by finite sums, and the derivatives in the right hand sides of the equations are replaced by finite-difference approximations.

The above formulae enable one to reduce each integro-differential equation to a finite system of algebraic equations with respect to approximate values of the sought for function, respectively, at the nodal points. As a result, we get

$$\begin{aligned}
& -\frac{2}{M} \left[\sum_{\nu=1}^M q_{y,\nu}^0 \sum_{k=1}^{M-1} \sin(k\theta_m) \cos(k\theta_k) + \sum_{\nu=1}^M f_{y,\nu} \sum_{k=1}^{M-1} \sin(k\theta_m) \cos(k\theta_k) \right] \\
& = \frac{M(1+\kappa)}{4\mu(b^0-a^0)} \left[\Pi_y(x_{m+1}, \sigma^0(x_{m+1})) q_{y,m+1}^0(x_{m+1}) - \Pi_y(x_{m-1}, \sigma^0(x_{m-1})) q_{y,m-1}^0(x_{m-1}) \right] \\
& -\frac{2}{M} \left[\sum_{\nu=1}^M q_{xy,\nu}^0 \sum_{k=1}^{M-1} \sin(k\theta_m) \cos(k\theta_k) + \sum_{\nu=1}^M f_{xy,\nu} \sum_{k=1}^{M-1} \sin(k\theta_m) \cos(k\theta_k) \right] \\
& = \frac{M(1+\kappa)}{4\mu(b^0-a^0)} \left[\Pi_x(x_{m+1}, \sigma^0(x_{m+1})) q_{xy,m+1}^0(x_{m+1}) - \Pi_x(x_{m-1}, \sigma^0(x_{m-1})) q_{xy,m-1}^0(x_{m-1}) \right]
\end{aligned} \tag{4.1}$$

where

$$\begin{aligned}
m = 1, 2, \dots, M_1 & \quad q_{y,\nu}^0 = q_y^0(\tau_\nu) & \quad q_{xy,\nu}^0 = q_{xy}^0(\tau_\nu) \\
\sigma_{y0,\nu} = \sigma_{y0}(\tau_\nu) & \quad \tau_{xy0,\nu} = \tau_{xy0}(\tau_\nu) & \quad x_{m+1} = \frac{a^0+b^0}{2} + \frac{b^0-a^0}{2} \eta_{m+1}
\end{aligned}$$

If we take into account the equality

$$2 \sum_{k=0}^{M-1} \cos(k\theta_\nu) \sin(k\theta_m) = \cot \frac{\theta_m \mp \theta_\nu}{2}$$

the systems will take the following forms

$$\begin{aligned}
\sum_{\nu=1}^M A_{m\nu} (q_{y,\nu}^0 + f_{y,\nu}) & = \frac{M(1+\kappa)}{4\mu(b^0-a^0)} \left[\Pi_y(x_{m+1}, \sigma^0) q_{y,m+1}^0 - \Pi_y(x_{m-1}, \sigma^0) q_{y,m-1}^0 \right] \\
\sum_{\nu=1}^M A_{m\nu} (q_{xy,\nu}^0 + f_{xy,\nu}) & = \frac{M(1+\kappa)}{4\mu(b^0-a^0)} \left[\Pi_x(x_{m+1}, \sigma^0) q_{xy,m+1}^0 - \Pi_x(x_{m-1}, \sigma^0) q_{xy,m-1}^0 \right]
\end{aligned} \tag{4.2}$$

where

$$\begin{aligned}
m = 1, 2, \dots, M_1 & \quad q_{y,\nu} = q_y^0(\tau_\nu) & \quad q_{xy,\nu} = q_{xy}^0(\tau_\nu) \\
f_{y,\nu} = f_y(\tau_\nu) & \quad f_{xy,\nu} = f_{xy}(\tau_\nu) & \quad A_{m\nu} = -\frac{1}{M} \cot \frac{\theta_m \mp \theta_\nu}{2}
\end{aligned}$$

the upper sign is taken when the number $|m - \nu|$ is odd, the lower sign when it is even.

Now pass to algebraization of the solvability conditions of boundary value problem (3.13). Separating in them the real and imaginary parts, using the change of variables and Gauss's quadrature formula, we get the solvability conditions of the problem in the following form

$$\begin{aligned}
\sum_{\nu=1}^M f_y^*(\cos \theta_\nu) = 0 & \quad \sum_{\nu=1}^M \tau_\nu f_y^*(\tau_\nu) = 0 \\
\sum_{\nu=1}^M f_{xy}^*(\cos \theta_\nu) = 0 & \quad \sum_{\nu=1}^M \tau_\nu f_{xy}^*(\tau_\nu) = 0
\end{aligned} \tag{4.3}$$

where $f_y^* = q_y^0 + f_y$, $f_{xy}^* = q_{xy}^0 + f_{xy}$.

As a result of algebraization, instead of each integro-differential equation with corresponding additional conditions, we get $M_1 + 2$ (M_1 is the number of nodal points belonging to the crack end zones) algebraic equations to determine stresses at nodal points and the end zone sizes. Even in the special case of linear elastic bonds, the obtained system of equations becomes nonlinear because of the unknown size of the end zone. In this connection, for solving the obtained systems, in the case of linear bonds the method of successive approximations has been used.

In the case of a deformation law of nonlinear bonds, to define tractions in the end zones it is advisable to use an iterative scheme similar to the method of elastic solutions (Il'yushin, 2003).

It is accepted that the law of deformation of interparticle bonds (cohesive forces) is linear for $V = \sqrt{(v_0^+ - v_0^-)^2 + (u_0^+ - u_0^-)^2} \leq V_*$. The first step of iterative calculations is solving the system of equations (4.2) and (4.3) for linear-elastic interparticle bonds. The subsequent iterations are fulfilled only in the case when the relation $V(x) > V_*$ holds on a part of the end zone. For such iterations, the system of equations is solved at each approximation for quasi-brittle bonds with effective compliance variable along the crack end zone and dependent on the size of modulus of the fraction vector obtained in the previous step of calculation. Effective compliance analysis is conducted through the definition of the secant modulus in elasticity parameters. The successive approximations process ends as the forces along the end zone, obtained at two successive iterations, differ a little from each other.

The nonlinear part of the strain curve of interparticle bonds is represented in the form of a bilinear dependence whose ascending portion corresponds to elastic deformation of the bonds ($0 < V(x) < V_*$) with their maximum tension. For $V(x) > V_*$, the deformation law is described by a non-linear dependence determined by two points (V_*, σ_*) and (δ_c, σ_c) . And for $\sigma_c \geq \sigma_*$, we have a descending linear dependence (linear hardening corresponding to elastic-plastic deformation of bonds). Here σ_* is the maximum elastic stress in the bonds, δ_c is the characteristic of fracture toughness of the material determined experimentally. In numerical calculations, it has been assumed $M = 30$, which corresponds to partition of the integration interval into 30 Chebyshev nodal points.

After finding stress components in the zero approximation, we find the functions N and T from formulas (3.8). The sequence of solution of problem (3.7) in the first approximation is similar to the solution of the problem in the zero approximation. The solution of the problem on the definition of piecewise-analytic functions $\Phi_1(z)$ and $\Omega_1(z)$ is of the form

$$\Phi_1(z) = \Omega_1(z) = \frac{\sqrt{(z - a^1)(z - b^1)}}{2\pi i} \int_{a^1}^{b^1} \frac{p_1(t)}{\sqrt{(t - a^1)(t - b^1)(t - z)}} dt \quad (4.4)$$

where

$$p_1(t) = \begin{cases} N - iT & \text{on free crack faces} \\ q_y^1 - iq_{xy}^1 + N - iT & \text{on faces of the crack end zones} \end{cases}$$

Moreover, all the following solvability conditions of the boundary value problem should be fulfilled

$$\int_{a^1}^{b^1} \frac{p_1(t)}{\sqrt{(t - a^1)(b^1 - t)}} dt = 0 \quad \int_{a^1}^{b^1} \frac{tp_1(t)}{\sqrt{(t - a^1)(b^1 - t)}} dt = 0 \quad (4.5)$$

These relations serve for determination of the unknown parameters a^1 and b^1 .

Using the formula and boundary values of the functions $\Phi_1(z)$, $\Omega_1(z)$ on the segment $a^1 \leq x \leq b^1$, we find the equality

$$\Phi_1^+(x) - \Phi_1^-(x) = \frac{2\mu}{1 + \kappa} \left[\frac{\partial}{\partial x} (u_1^+ - u_1^-) + i \frac{\partial}{\partial x} (v_1^+ - v_1^-) \right] \quad (4.6)$$

Using the Sokhotski-Plemelj (Muskhelishvili, 2010) and taking into account formula (4.4), we find

$$\Phi_1^+(x) - \Phi_1^-(x) = -\frac{i}{\pi} \sqrt{(x - a^1)(b^1 - x)} \int_{a^1}^{b^1} \frac{p_1(t)}{\sqrt{(t - a^1)(b^1 - t)(t - x)}} dt \quad (4.7)$$

Substituting obtained expression (4.7) into the left part of equation (4.6) and taking into account relation (3.9) for the first approximation, after some transformations we get a system of nonlinear integro-differential equations with respect to the unknown functions q_y^1 and q_{xy}^1

$$\begin{aligned} -\frac{\sqrt{(x-a^1)(b^1-x)}}{\pi} \int_{a^1}^{b^1} \frac{q_y^1(t) + N(t)}{\sqrt{(t-a^1)(b^1-t)(t-x)}} dt &= \frac{2\mu}{1+\kappa} \frac{d}{dx} [\Pi_y(x, \sigma^1) q_y^1(x)] \\ -\frac{\sqrt{(x-a^1)(b^1-x)}}{\pi} \int_{a^1}^{b^1} \frac{q_{xy}^1(t) + T(t)}{\sqrt{(t-a^1)(b^1-t)(t-x)}} dt &= \frac{2\mu}{1+\kappa} \frac{d}{dx} [\Pi_x(x, \sigma^1) q_{xy}^1(x)] \end{aligned} \quad (4.8)$$

where $\sigma^1 = \sqrt{(q_y^1)^2 + (q_{xy}^1)^2}$.

Similarly, in the first approximation, in obtaining the algebraic systems all integration intervals are reduced to one interval $[-1, 1]$. Then, using the quadrature formulas of the Gauss type the integrals are replaced by finite sums. As a result we get the zero approximation while obtaining algebraic systems all integration intervals are reduced to one interval $[-1, 1]$. Then, the integrals are replaced by finite sums by means of Gauss-type quadrature formulas. As a result, we get

$$\begin{aligned} \sum_{\nu=1}^M A_{m\nu} [q_{y,\nu}^1 + N_\nu] &= \frac{\mu M}{(1+\kappa)(b^1-a^1)} [\Pi_y(x_{m+1}^1, \sigma^1) q_{y,m+1}^1 - \Pi_y(x_{m-1}^1, \sigma^1) q_{y,m-1}^1] \\ \sum_{\nu=1}^M A_{m\nu} [q_{xy,\nu}^1 + T_\nu] &= \frac{\mu M}{(1+\kappa)(b^1-a^1)} [\Pi_x(x_{m+1}^1, \sigma^1) q_{xy,m+1}^1 - \Pi_x(x_{m-1}^1, \sigma^1) q_{xy,m-1}^1] \end{aligned} \quad (4.9)$$

where

$$\begin{aligned} m = 1, 2, \dots, M_1 & \quad x_{m+1}^1 = \frac{1}{2}(a^1 + b^1) - \frac{1}{2}(a^1 - b^1)\eta_{m+1} & \quad q_{y,\nu}^1 = q_y^1(\tau_\nu) \\ q_{xy,\nu}^1 = q_{xy}^1(\tau_\nu) & \quad N_\nu = N(\tau_\nu) & \quad T_\nu = T(\tau_\nu) \end{aligned}$$

As a result of algebraization of the boundary problem solvability conditions (4.5), we obtain

$$\begin{aligned} \sum_{\nu=1}^M f_y^{*1}(\tau_\nu) = 0 & \quad \sum_{\nu=1}^M \tau_\nu f_y^{*1}(\tau_\nu) = 0 \\ \sum_{\nu=1}^M f_{xy}^{*1}(\tau_\nu) = 0 & \quad \sum_{\nu=1}^M \tau_\nu f_{xy}^{*1}(\tau_\nu) = 0 \end{aligned} \quad (4.10)$$

where $f_y^{*1} = q_y^1 + N$, $f_{xy}^{*1} = q_{xy}^1 + T$.

As a result of algebraization, as in the zero approximation, instead of each integro-differential equation we get a system of $M_1 + 2$ algebraic equations for determining stresses at nodal points of the crack end zones and end zones sizes.

A solving algorithm for algebraic systems (4.9) and (4.10) is similar to the solution of the systems for the zero approximation. The opening of the crack in the end zones may be determined from the relations

$$\begin{aligned} v^+(x, 0) - v^-(x, 0) &= \Pi_y(x, \sigma) q_y(x) \\ u^+(x, 0) - u^-(x, 0) &= \Pi_x(x, \sigma) q_{xy}(x) \\ a \leq x \leq a_1 & \quad b_1 \leq x \leq b \end{aligned} \quad (4.11)$$

Calculations show that for the linear law of deformation of bonds, tractions in the bonds have always maximal values at the edge of the end zone. The similar picture is observed for

the quantities of crack openings. Opening of a crack at the edge of end zone has maximum for linear and nonlinear laws of deformation, and with an increasing compliance of the bonds. To determine the limit state at which the crack growth occurs, we use the critical condition

$$|(v^+ - v^-) - i(u^+ + u^-)| = \delta_c \tag{4.12}$$

The joint solution of the obtained equations and condition (4.12) enable determination of the critical value of external loads, forces in the bonds and the size of the end zone for the limit equilibrium state under the given characteristics of bonds.

The function $H(x)$ describing roughness of the crack surface are considered as a determinate set of the rough surface of the profile contour and also as a stationary random function. In this case, the random function $H(x)$ is given by the canonical expansion

$$H(\theta) = \sum_{k=-\infty}^{\infty} v_k \varepsilon^{ik\theta}$$

where v_k are independent zero random values of the mathematical expectation and dispersions D_k .

Calculations show that the heated zone promotes flow of plastic deformations in the bonds.

In Fig. 2a, plots of distribution of normal forces q_y in the bonds of the crack end zones are depicted for the following values of free parameters $t_* = 4a_*t/L_1^2 = 10$; $c_1/L_1 = -0.2$; $c_2/L_2 = 0.1 = 0.1$; $\nu = 0.3$; $L_1 = L_2 = L$; $M = 30$; $E = 1.8 \cdot 10^5$ MPa; $V_* = 10^{-6}$ m; $\sigma_* = 75$ MPa; $\sigma_c/\sigma_* = 2$; $\delta_c = 2.5 \cdot 10^{-6}$ m; $C = 2 \cdot 10^{-7}$ m/MPa (C is the effective compliance of the bonds). There, curves 1 correspond to the bilinear law of strains of the bonds, and curves 2 correspond to the linear law of strains. In the computations, we used the dimensionless coordinates $x = (a + b)/2 + (b - a)x'/2$.

The compliance of the bonds in the normal and tangential directions is assumed to be equal.

Graphs of the distribution of tangential forces q_{xy} in the bonds of the crack end zones are shown in Fig. 2b.

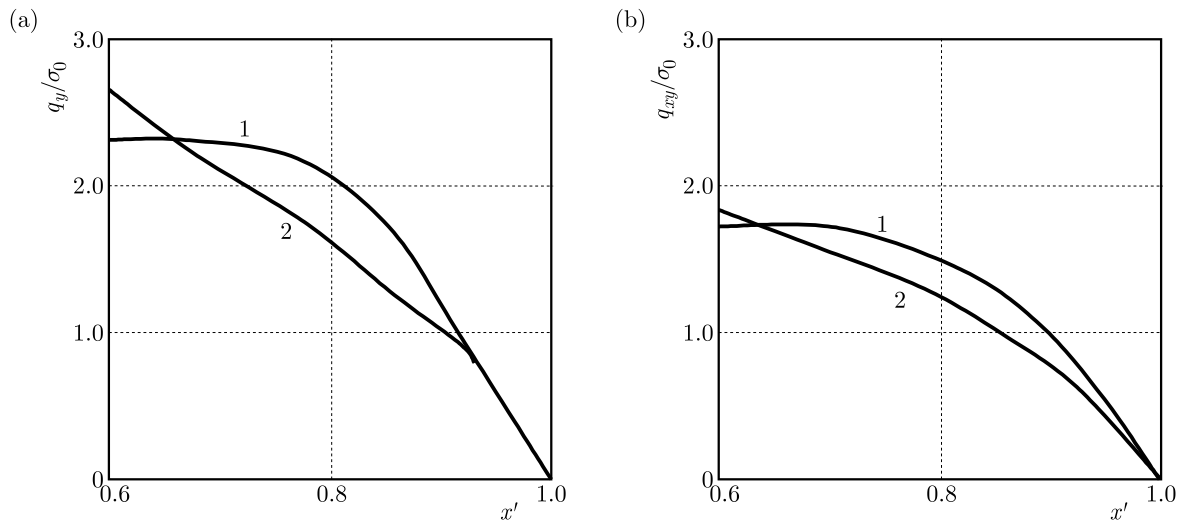


Fig. 2. Distribution of normal forces q_y/σ_0 (a) and tangential forces q_{xy}/σ_0 (b) in the bonds of the crack end zones

Graphs of the length of the crack end zone $(b - b_1)/(b - a)$ for the plate against the dimensionless value of the tensile stress σ_0/σ_* are shown in Fig. 3 for different crack lengths $\ell_* = (b_1 - a_1)/(b - a) = 0.5, 0.7$.

The dependence of the critical load σ_0/σ_* on the dimensionless length of the crack $(b - a)/R$ is shown in Fig. 4. There R is the typical linear size of the plate.

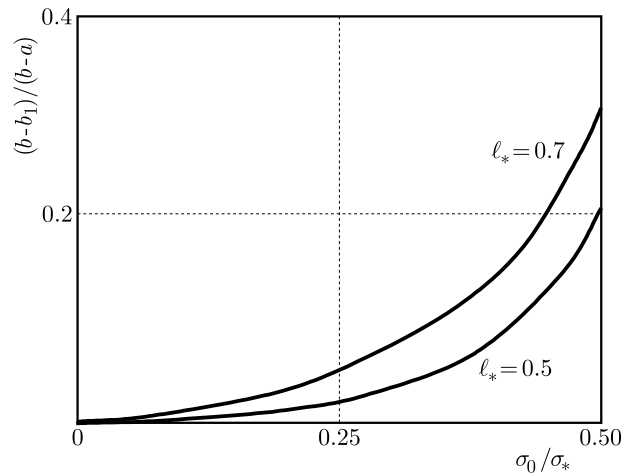


Fig. 3. Dependency of the length of the end zone $(b - b_1)/(b - a)$ on the dimensionless value σ_0/σ_* for different crack lengths

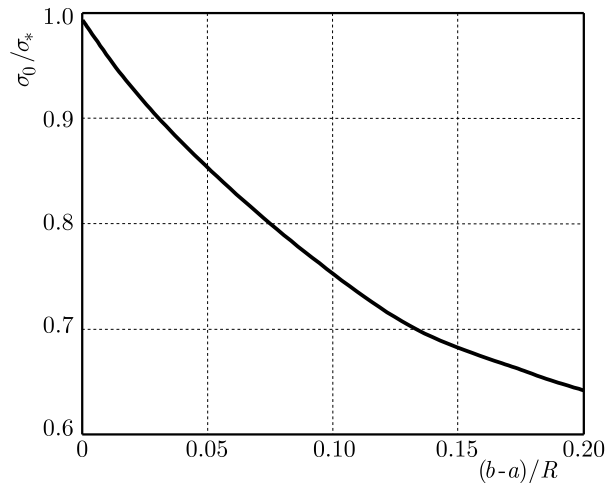


Fig. 4. Distribution of the critical load on the dimensionless length of the crack

Theoretical and experimental investigations show that the created temperature field in the course of some limited time for the purpose of crack retardation is an insurmountable barrier (Finkel, 1977) on the path of its propagation. Subsequent removal of the temperature field ($t \rightarrow \infty$) will gradually decrease the value of compressive stresses and crack retardation efficiency. The crack faces opening at the bottom of the end zone, having attained reduction, will gradually grow to the size stipulated by mechanical load.

Under action of the temperature field, simultaneously with the reduction of maximum tensile stress, there happens its unfolding towards the thermal source. This reduces (Morozov, 1969; Finkel, 1977) the displacement of the fracture plane observed in the experiment. After removing the temperature field, this circumstance will help ensuring that for crack propagation, an increase of the external tensile load is necessary. Note that the perturbed temperature field amplifies the inhibitory effect of the induced temperature field of stresses. In conclusion, note that plate-like elements have found wide application in constructions of different kind transport systems (aircraft). Based on experimental data and numerical results of this paper, we can recommend the following schemes of effective retardation of crack propagation:

- On the path of possible fracture of a plate-like construction, it is necessary to create stable temperature fields. If a crack grows in the direction of temperature increase, then velocity of its growth will decrease, and sooner or later it will stop.

- Creating no temperature fields beforehand, heating on the path of crack propagation may be conducted impulsively, for example, by means of explosive wires. In this case, the crack tip is found in the site of explosion. As a result of simultaneous action of impact waves of thermoelastic stress and plastic deformations of the heated material, the crack growth slows down and the fracture stops.

5. Conclusions

Theoretical investigation of the retardation problem for a curvilinear crack with interfacial bonds by temperature fields has been carried out. An effective calculation scheme of the retardation of the curvilinear crack with interfacial bonds in a plane under action of external tensile loads is suggested. Based on the obtained results, we can consider that the temperature field created in the vicinity of the crack tip is a barrier to its propagation way. Relations for tractions in the bonds and opening of curvilinear crack faces in the end zone depending on the applied load, intensity of thermal source, crack length, and geometrical sizes of the heated zone are obtained. The dependence of the crack length on the applied stretchable load, intensity of the heated zone and also on physical and geometrical parameters of the plate at monotone loading is established.

In the case of a crack with bonds in the end zones and temperature stresses induced by heat sources, the analysis of the limiting equilibrium state of the plane reduces to a parametric study of the solution of algebraic systems (4.2), (4.3) and (4.9), (4.10) for various laws of deformation of the bonds, sizes of end zones and thermal and elastic constants of the plane material. The normal and tangential stresses in the bonds and the crack opening are directly determined by solving the resulting algebraic systems in each approximation. The crack opening in the end zones can also be determined from relation (4.11).

References

1. BARENBLATT G.I., 1961, The mathematical theory for equilibrium cracks formed on brittle fracture (in Russian), *Journal of Applied Mechanics and Technical Physics*, **2**, 4, 3-56
2. DIMAKI A.V., MEL'NIKOV A.G., PLESHANOV V.S., SIZOVA O.V., 2010, Theoretical and experimental study of the healing of surface cracks using induction heating, *Inorganic Materials: Applied Research*, **1**, 4, 353-358
3. DUGDALE D.S., 1960, Yielding of steel sheets containing slits, *Journal of the Mechanics and Physics of Solids*, **8**, 100-108
4. *Engineering Fracture Mechanics, The special issue: Cohesive Models*, 2003, **70**, 15, 1741-1987
5. FINKEL V.M., 1977, *Physical Basis of Fracture Retardation* (in Russian), Metallurgiya, Moscow
6. FU Y.-M., BAI X.-Z., QIAO G.-Y., HU Y.-D., LUAN J.-Y., 2001, Technique for producing crack arrest by electromagnetic heating, *Materials Science and Technology*, **17**, 1653-1656
7. GEORGANTZINOS S.K., ANIFANTIS N.K., 2014, Crack closure, [In:] *Encyclopedia of Thermal Stresses*, R.B. Hetnarski (Edit.), Springer Netherlands, ISBN 978-94-007-2738-0, 774-779
8. IL'YUSHIN A.A., 2003, *Plasticity* (in Russian), Logos, Moscow
9. ITOU S., 2014, Thermal stresses around two upper cracks placed symmetrically about a lower crack in an infinite orthotropic plane under uniform heat flux, *Journal of Theoretical and Applied Mechanics*, **52**, 617-628
10. KADIEV R.I., MIRSAIIMOV V.M., 2001, Effect of heat source on the dynamics of crack growth (in Russian), *Vestnik Dagestanskogo Universiteta*, **4**, 69-73
11. LADOPOULOS E.G., 2000, *Singular Integral Equations, Linear and Non-linear Theory and its Applications in Science and Engineering*, Springer Verlag, Berlin

12. LADOPOULOS E.G., 2013, Non-linear singular integro-differential equations in Banach spaces by collocation evaluation methods, *Universal Journal of Integral Equations*, **1**, 28-38
13. LEONOV M.YA., PANASYUK V.V., 1959, Propagation of fine cracks in solid body (in Russian), *Prikladnaya Mekhanika*, **5**, 391-401
14. LIU T.J.C., 2008, Thermo-electro-structural coupled analyses of crack arrest by Joule heating, *Theoretical and Applied Fracture Mechanics*, **49**, 171-184
15. LIU T.J.C., 2011a, Finite element modeling of melting crack tip under thermo-electric Joule heating, *Engineering Fracture Mechanics*, **78**, 666-684
16. LIU T.J.C., 2011b, Fracture mechanics of steel plate under Joule heating analyzed by energy density criterion, *Theoretical and Applied Fracture Mechanics*, **56**, 154-161
17. LIU T.J.C., 2014a, Compressive stresses near crack tip induced by thermo-electric field, *International Journal of Mechanical, Aerospace, Industrial, Mechatronic and Manufacturing Engineering*, **8**, 11, 1799-1802
18. LIU T.J.C., 2014b, Crack detection/arrest with Joule heating, [In:] *Encyclopedia of Thermal Stresses*, R.B. Hetnarski (Edit.), Springer Netherlands, ISBN 978-94-007-2738-0, 779-791
19. LIU T.J.C., TSENG J.F., CHEN P.H., 2015, Analysis of thermo-electric field in steel strip with multiple cracks, *Proceedings of the 3rd International Conference on Industrial Application Engineering*, 408-412
20. MIRSALIMOV V.M., 1987, *Non-one Dimensional Elastoplastic Problems* (in Russian), Nauka, Moscow
21. MIRSALIMOV V.M., 2007, The solution of a problem in contact fracture mechanics on the nucleation and development of a bridged crack in the hub of a friction pair, *Journal of Applied Mathematics and Mechanics*, **71**, 120-136
22. MIRSALIMOV V.M., KADIEV R.I., 2004, Closing of a crack in the sheet element under action of local thermal field, *Journal of Machinery Manufacture and Reliability*, **33**, 6, 69-75
23. MIRSALIMOV V.M., MUSTAFAYEV A.B., 2015a, A contact problem on partial interaction of faces of a variable thickness slot under the influence of temperature field, *Mechanika*, **21**, 19-22
24. MIRSALIMOV V.M., MUSTAFAYEV A.B., 2015b, Solution of the problem of partial contact between the faces of a slot of variable width under the action of temperature fields, *Materials Science*, **51**, 96-103
25. MIRSALIMOV V.M., MUSTAFAYEV A.B., 2016, Influence of local temperature field on propagation of a curvilinear crack with interfacial bonds, *ZAMM – Journal of Applied Mathematics and Mechanics*, **96**, 1339-1346
26. MOROZOV E.M., 1969, On the strength analysis by the stage of fracture (in Russian), *Deform. Razrush. Term. Mekh. Vozdeistv*, **3**, 87-90
27. MUSKHELISHVILI N.I., 2010, *Some Basic Problem of Mathematical Theory of Elasticity*, Springer, Amsterdam
28. PANASYUK V.V., SAVRUK M.P., DATSYSHYN A.P., 1976, *The Stress Distribution Around Cracks in Plates and Shells* (in Russian), Naukova Dumka, Kiev
29. PARKUS H., 1959, *Instationäre Wärmespannungen*, Springer-Verlag, Wien
30. PARTON V.Z., MOROZOV E.M., 1985, *Elastic-Plastic Fracture Mechanics* (in Russian), Nauka, Moscow
31. POTTHAST B., HERRMANN K.P., 2000, Asymptotic analysis for temperature fields induced by dynamic crack growth in pressure-sensitive materials, *International Journal of Fracture*, **106**, 57-64
32. QIN Z, LIBRESCU L., HASANYAN D., 2007, Joule heating and its implications on crack detection/arrest in electrically conductive circular cylindrical shells, *Journal of Thermal Stresses*, **30**, 623-637

CHAOTIC VIBRATION OF AN AUTOPARAMETRICAL SYSTEM WITH THE SPHERICAL PENDULUM¹

DANUTA SADO, JAN FREUNDLICH, ANNA BOBROWSKA

Warsaw University of Technology, Institute of Machine Design Fundamentals, Warsaw, Poland

e-mail: dsado@poczta.onet.pl

In the paper, the dynamics of a three degree of freedom vibratory system with a spherical pendulum in the neighbourhood of internal and external resonance is considered. It has been assumed that the spherical pendulum is suspended to the main body which is then suspended to the element characterized by some elasticity and damping. The system is excited harmonically in the vertical direction. The equation of motion has been solved numerically. The influence of initial conditions on the behaviour of the spherical pendulum is investigated. In this type of the system, one mode of vibration may excite or damp another one, and for different kinds of periodic vibrations there may also appear chaotic vibrations. For characterization of an irregular chaotic response, time histories, bifurcation diagrams, power spectral densities, Poincaré maps and the maximum Lyapunov exponents have been calculated.

Keywords: spherical pendulum, energy transfer, coupled oscillators, chaos

1. Introduction

The subject of this work is investigation of the effect of initial conditions on the dynamics of a three degree of freedom system with a spherical pendulum. Dynamical systems having an element in the form of a mathematical or physical pendulum have important applications. Different kinds of coupled autoparametric oscillators with simple pendulums are presented in the book by Sado (2010). Furthermore, the numerical and analytical methods of researching the dynamics of two degree and three degree of freedom vibratory systems with the pendulums are presented in this book. There are shown: the influence of initial conditions on the behaviour of the vibratory system, the characteristic of vibrations, and how to manipulate the vibrations.

The real pendulum is of spherical type. The spherical pendulum was investigated by many researches. The spherical pendulum subjected to parametric excitation was studied by Miles and Zou (1993). They investigated the non-linear response of a slightly detuned spherical pendulum with natural frequencies. In that model, no stable harmonic motion was possible, therefore the motion of the system was either periodically modulated by a sinusoid or becomes chaotic. The numerical integration was supported by analytical predictions, which also uncovered that the limit cycles and chaotic motions overlapped those of stable harmonic motion.

In paper by Naprstek and Fischer (2009), the pendulum vibration damper modelled as a two degree of freedom strongly non-linear auto-parametric system was investigated. There was a kinematic external excitation applied to a point. In that model the excitation was considered to be horizontal and harmonically variable in time. The solution and the stability were analysed. Therefore, the biggest attention was paid to the resonance domain. In certain domains of the

¹The paper was presented at the 27th Symposium on Vibrations in Physical Systems, May 9-13, Poznań-Będlewo, Poland.

pendulum and excitation parameters, the semi-trivial solution did not exist in that domain and various post-critical three-dimensional regimes occurred. Some of them were non-stationary despite the harmonic excitation. Three different types of the resonance domain were investigated. Their main properties depended on dynamic parameters of the pendulum and the external excitation amplitude. An analytical and numerical study brought some recommendations for designers of such devices. Their aim was to avoid any post-critical response rules risking the pendulum functionality.

The bifurcation behaviour of a spherical pendulum where the suspension point is harmonically excited in both vertical and horizontal directions was presented by Leung and Kung (2006). The equations of motion for a lightly damped spherical pendulum were considered. The point of the suspension was harmonically excited in both vertical and horizontal directions. The equations were solved with approximation in the neighbourhood of resonance by including the third order terms in the amplitude.

A mathematical model of the spherical pendulum with a moving pivot was suggested by Mitrev and Grigorov (2009) and later developed. Such a model allowed studying the influence of different kinematic excitations applied to the pivot point. That required the kinematical and dynamical parameters of the pendulum which also determined the force in the rope. A numerical simulation for spatial curvilinear and planar with straight line motions trajectories was performed. The stochastic analysis of a spring spherical pendulum was done by Viet (2015). The vibration was reduced by a spring and damper installed in the radial direction between the point mass and the cable. Under the sway motion, the centrifugal force resulted in the radial motion, which in its turn produced the Coriolis force to reduce the sway motion.

The dynamics of coupled spherical pendulums (where two lower pendulums were mounted at the end of the upper pendulum) was considered by Witkowski *et al.* (2014). The analysis showed that three rotating modes existed. The linear modes helped to understand the nonlinear normal modes, which were later visualized in plots. When there was an increase of energy in one mode, we could see a symmetry pitchfork bifurcation. In the second part of the paper, the energy transfer between pendulums was investigated. The results for co-rotating (all pendulums rotated in the same direction) and counter-rotating motion (one of lower pendulum rotated in the opposite direction) were presented.

In the present paper, it is assumed that the spherical pendulum is suspended on a flexible element, thus in this system there may occur an autoparametric excitation as a result of inertial coupling.

2. A model of an autoparametric system with a spherical pendulum

The investigated system is shown in Fig. 1. The system consists of a body of mass m_1 suspended to the flexible element. This flexible element is characterised by the stiffness k and damping c . This system also consists of the spherical pendulum of the length l and mass m_2 which is suspended to the body of mass m_1 . The body of mass m_1 is subjected to the harmonic vertical excitation $F_1(t)$ and the spherical pendulum is subjected to the horizontal excitation $F_2(t)$.

The spherical pendulum is similar to the simple pendulum but it moves in 3D space, so we need to introduce a new variable φ in order to describe rotation of the pendulum in the plane XY . The position of the body of mass m_1 is described only by the coordinate z . However, the position of the pendulum is described by the coordinate z and two angles: θ and φ . The angle θ is the deflection of the pendulum measured from the vertical line. This system has three degrees of freedom. The equations of motion are derived as Lagrange's equations.

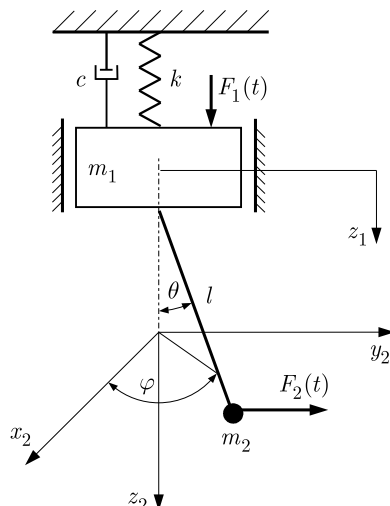


Fig. 1. A model of an autoparametric system with a spherical pendulum

The kinetic energy T is the sum of the energy of the two bodies

$$T = \frac{m_1 v_1^2}{2} + \frac{m_2 v_2^2}{2} = \frac{m_1 \dot{z}_1^2}{2} + \frac{m_2 (\dot{x}_2^2 + \dot{y}_2^2 + \dot{z}_2^2)}{2} \tag{2.1}$$

where

$$\begin{aligned} x_2 &= l \sin \theta \cos \varphi & y_2 &= l \sin \theta \sin \varphi & z_2 &= z_1 + l \cos \theta \\ z_1 &= z + z_{st} & z_{st} &= \frac{(m_1 + m_2)g}{k} \end{aligned} \tag{2.2}$$

The kinetic energy T is given by the expression

$$T = \frac{1}{2}(m_1 + m_2)\dot{z}^2 + \frac{1}{2}m_2(l\dot{\theta}^2 + l^2\dot{\varphi}^2 \sin^2 \theta - 2l\dot{z}\dot{\theta} \sin \theta) \tag{2.3}$$

The potential energy V is given by the expression

$$V = -(m_1 + m_2)g(z + z_{st}) + m_2g(l - l \cos \theta) + \frac{k(z + z_{st})^2}{2} \tag{2.4}$$

Assuming that the exciting forces are in the form: $F_1(t) = P_1 \cos(\nu_1 t)$, $F_2(t) = P_2 \cos(\nu_2 t)$, the dissipation function $D = c\dot{z}^2/2$, the equations of motion of the system are as follows

$$\begin{aligned} (m_1 + m_2)\ddot{z} - m_2l\ddot{\theta} \sin \theta - m_2l\dot{\theta}^2 \cos \theta + kz + c\dot{z} &= P_1 \cos(\nu_1 t) \\ m_2l^2\ddot{\theta} - m_2l\ddot{z} \sin \theta - m_2l^2\dot{\varphi}^2 \sin \theta \cos \theta + m_2gl \sin \theta &= l \cos \theta \sin \varphi P_2 \cos(\nu_2 t) \\ m_2l^2\ddot{\varphi} \sin^2 \theta + 2m_2l^2\dot{\varphi}\dot{\theta} \sin \theta \cos \theta &= l \sin \theta \cos \theta P_2 \cos(\nu_2 t) \end{aligned} \tag{2.5}$$

By introducing the dimensionless time and parameters

$$\begin{aligned} \tau &= \omega_1 t & \omega_1^2 &= \frac{k}{m_1 + m_2} & \omega_2^2 &= \frac{g}{l} & \beta &= \frac{\omega_2}{\omega_1} \\ \gamma &= \frac{c}{(m_1 + m_2)\omega_1} & \bar{z} &= \frac{z}{l} & a &= \frac{m_2}{m_1 + m_2} \\ A_1 &= \frac{P_1}{(m_1 + m_2)\omega_1^2} & A_2 &= \frac{P_2}{m_2 l \omega_1^2} & \mu_1 &= \frac{\nu_1}{\omega_1} & \mu_2 &= \frac{\nu_2}{\omega_1} \end{aligned} \tag{2.6}$$

after transformation (2.5) into the dimensionless form we obtain

$$\begin{aligned} \ddot{z} - a\ddot{\theta} \sin \theta - \dot{\theta}^2 \cos \theta + z + \gamma\dot{z} &= A_1 \cos(\mu_1 \tau) \\ \ddot{\theta} - \bar{z} \sin \theta - \dot{\varphi}^2 \sin \theta \cos \theta + \beta^2 \sin \theta &= A_2 \cos \theta \sin \varphi \cos(\mu_2 \tau) \\ \ddot{\varphi} \sin \theta + 2\dot{\varphi}\dot{\theta} \cos \theta &= A_2 \cos \theta \cos(\mu_2 \tau) \end{aligned} \tag{2.7}$$

where the overbars denoting non-dimensionalisation are omitted for convenience.

After transformation, the equations of motion can be written in a simpler form for numerical calculations:

$$\begin{aligned}\ddot{z} &= \frac{1}{1 - a \sin^2 \theta} [(A_1 \cos(\mu_1 \tau) + \dot{\theta}^2 \cos \theta - z - \gamma \dot{z}) + a \sin \theta (\dot{\varphi}^2 \sin \theta \cos \theta - \beta^2 \sin \theta)] \\ \ddot{\theta} &= \frac{1}{1 - a \sin^2 \theta} \left\{ \dot{\varphi}^2 \sin \theta \cos \theta - \beta^2 \sin \theta \right. \\ &\quad \left. + [A_1 \cos(\mu_1 \tau) + a \dot{\theta}^2 \cos \theta - z - \gamma \dot{z} + a \sin \theta (\dot{\varphi}^2 \sin \theta \cos \theta - \beta^2 \sin \theta)] \sin \theta \right\} \\ \ddot{\varphi} &= \frac{1}{\sin^2 \theta} (A_2 \sin \theta \cos \varphi \cos(\mu_2 \tau) - 2\dot{\varphi} \dot{\theta} \sin \theta \cos \theta)\end{aligned}\quad (2.8)$$

3. Numerical simulation results

The equations of motion of the given model are solved numerically using Runge-Kutta method with a variable step length. The calculations are carried out for different values of parameters of the system and for different initial conditions. Exemplary time histories of the displacements z and θ are obtained for parameters of the system $a = 0.8$, $\beta = 0.5$, $\gamma = 0$, $A_1 = A_2 = 0$ and for the initial conditions: $z(0) = 0.1$, $\theta(0) = 0.005^\circ$, $\varphi(0) = 0$, $\dot{z}(0) = \dot{\theta}(0) = \dot{\varphi}(0) = 0$ are presented in Fig. 2, where we can observe the energy transfer between the modes of vibration in a closed cycle. In this case, the spherical pendulum behaves in the same way as a simple pendulum, and motion of the pendulum is in the vertical plane (angle φ is constant and it depends on the initial conditions, so it is equal to 0 for $\varphi(0) = 0$).

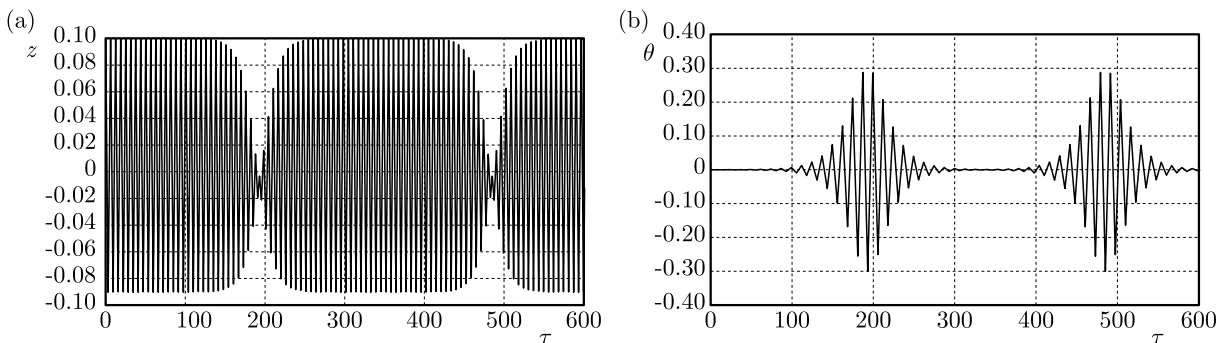


Fig. 2. Time history for (a) oscillator, (b) pendulum for $a = 0.8$, $\beta = 0.5$, $\gamma = 0$, $A_1 = A_2 = 0$, $z(0) = 0.1$, $\theta(0) = 0.005^\circ$, $\varphi(0) = 0$

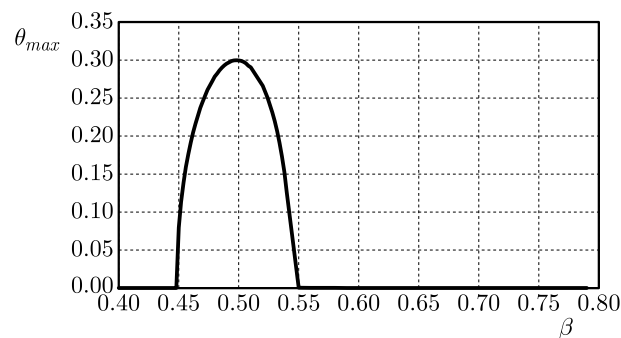


Fig. 3. Internal resonance for: $a = 0.8$, $\gamma = 0$, $A_1 = A_2 = 0$, $z(0) = 0.1$, $\theta(0) = 0.005^\circ$, $\varphi(0) = 0$

The diagram of internal resonance for the same initial conditions put on the displacements is presented in Fig. 3, and it is similar to a simple pendulum presented in the work (Sado, 2010).

We observe the resonance excitation for the frequency ratio $\beta = 0.5$. In this case, there is an assumption that the simple pendulum results are good.

On the other hand, when the initial conditions are put on the displacements and also on the velocities (in this example: $z(0) = 0, \dot{z}(0) = 0, \theta(0) = 5^\circ, \dot{\theta}(0) = -0.04, \varphi(0) = 0, \dot{\varphi}(0) = -0.96$), we can observe the influence of angle φ (Fig. 4). For these initial conditions, we observe the oscillation displacements z and θ with the same frequency.

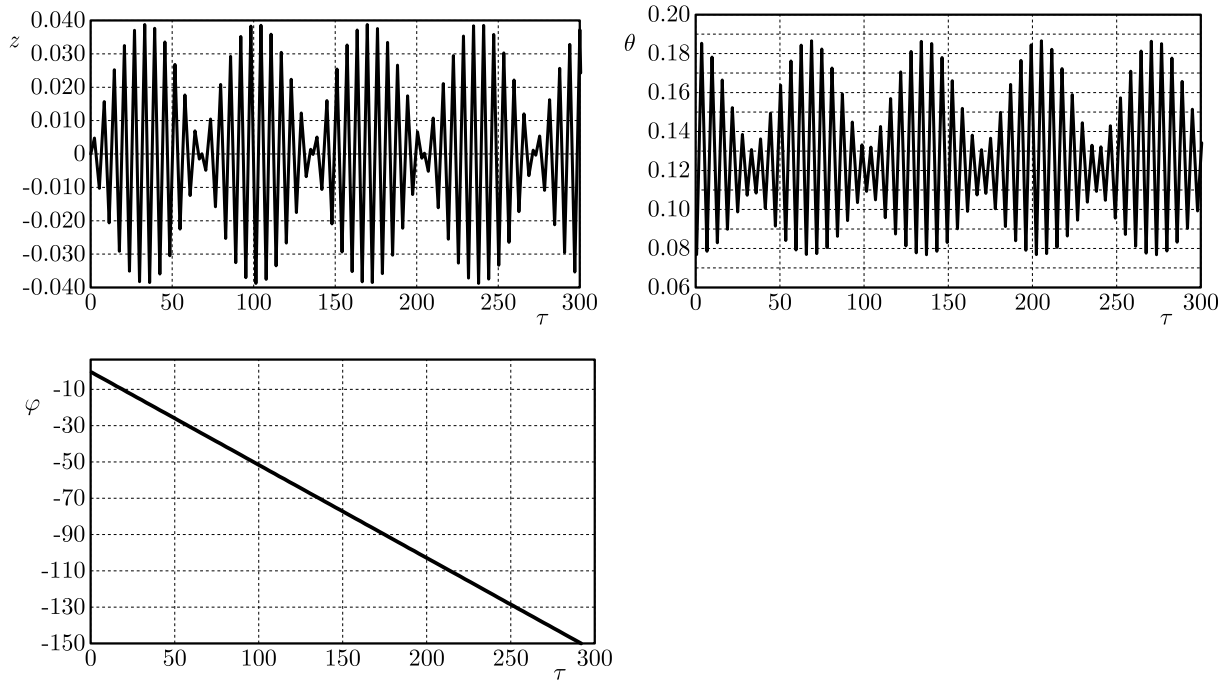


Fig. 4. Time history for: $a = 0.5, \beta = 0.51, \gamma = 0, A_1 = A_2 = 0, z(0) = 0, \dot{z}(0) = 0, \theta(0) = 5^\circ, \dot{\theta}(0) = -0.04, \varphi(0) = 0, \dot{\varphi}(0) = -0.96$

With the same initial conditions for displacements and velocities, the internal resonance is observed for the frequency ratio $\beta = 0.51$ (shown in Fig. 5a).

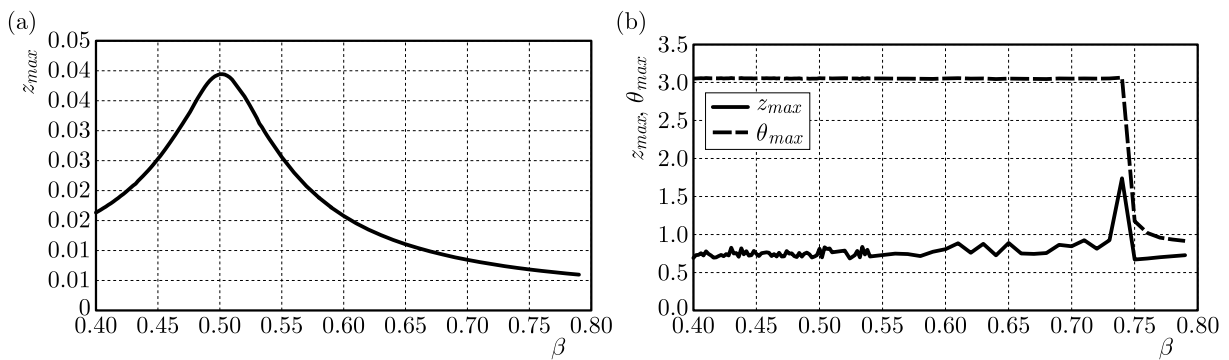


Fig. 5. Internal resonance for: (a) $a = 0.5, \gamma = 0, A_1 = A_2 = 0, z(0) = 0, \dot{z}(0) = 0, \theta(0) = 5^\circ, \dot{\theta}(0) = -0.04, \varphi(0) = 0, \dot{\varphi}(0) = -0.96$; (b) $a = 0.2, \gamma = 0, A_1 = A_2 = 0, z(0) = 0, \dot{z}(0) = 0.65, \theta(0) = 50^\circ, \dot{\theta}(0) = -0.04, \varphi(0) = 0, \dot{\varphi}(0) = -0.296$

For different parameters of the system: $a = 0.2, \gamma = 0, A_1 = A_2 = 0, \beta = 0.75$ and for initial conditions which are put on the displacements and also on the velocities ($z(0) = 0, \dot{z}(0) = 0.65, \theta(0) = 50^\circ, \dot{\theta}(0) = -0.04, \varphi(0) = 0, \dot{\varphi}(0) = -0.296$) there is visible an influence of the angle φ , and the internal resonance area is observed for the frequency ratio near $\beta = 0.75$ (Fig. 5b). In this example, the angle φ describes rotation of the pendulum around the axis z .

Assuming the model of the pendulum as a spherical pendulum, we obtain results more similar to the real system.

Next we prepare diagrams of the external resonance. An example is considered when the initial conditions are imposed on the displacements: $a = 0.8$, $\beta = 0.5$, $\gamma = 0$, $A_1 = 0.001$, $A_2 = 0$, $z(0) = 0$, $\theta(0) = 0.005^\circ$, $\varphi(0) = 0$. In that case, the diagram shows the external resonance for both the coordinate z and the angle θ with the vertical excitation force $F_1(t)$.

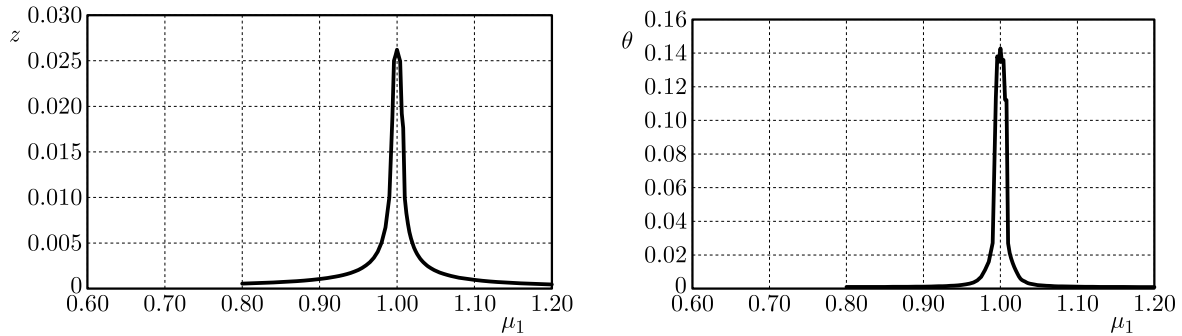


Fig. 6. External resonance for the coordinates z and θ for: $a = 0.2$, $\beta = 0.5$, $\gamma = 0$, $A_1 = 0.0001$, $z(0) = 0$, $\gamma = 0$

Near the internal and external resonances depending on the selection of physical parameters, the amplitudes of vibrations of the coupled system may be related differently. The motion in terms of z and θ are periodic or quasi-periodic vibrations, but sometimes the motion of the body of mass m_1 and the pendulum are chaotic. To characterize an irregular chaotic response, bifurcation diagrams are constructed.

Exemplary bifurcation diagrams for the displacements z and θ versus bifurcation parameter A_1 with parameters of the system: $a = 0.2$, $\beta = 0.5$, $\gamma = 0.00081443$, $\mu = 0.99$ are presented in Fig. 7 (it is assumed that the bifurcation parameter is the amplitude of excitation A_1).

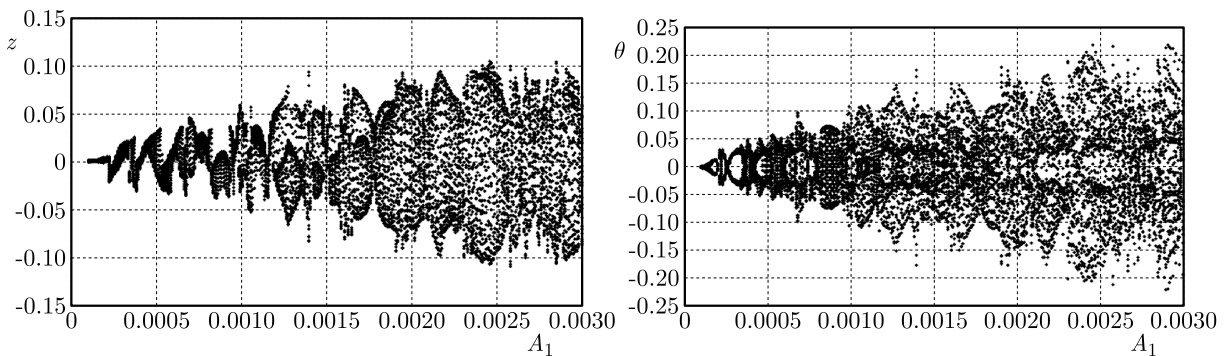


Fig. 7. Bifurcation diagrams for the coordinates z and θ for: $a = 0.2$, $\beta = 0.5$, $\gamma = 0.00081443$, $\mu_1 = 0.99$

As it can be seen from the bifurcation diagrams, motion of the oscillator and the spherical pendulum depends of the amplitude of excitation A_1 and can be of different character: it maybe periodic, quasi-periodic or chaotic. Several phenomena can be observed: the existence of a simple or a chaotic attractor, and various bifurcations. All these phenomena have to be verified in the phase space. Therefore, the Poincaré maps and Lyapunov exponents are then constructed. Exemplary results of the Poincaré maps (Fig. 8) and the maximum Lyapunov exponents (Fig. 9) are presented for the amplitude of excitation $A_1 = 0.0029$.

It is visible that the Poincaré maps trace strange attractors and the maximum Lyapunov exponents are positive, so the motions with respect both coordinates are chaotic.

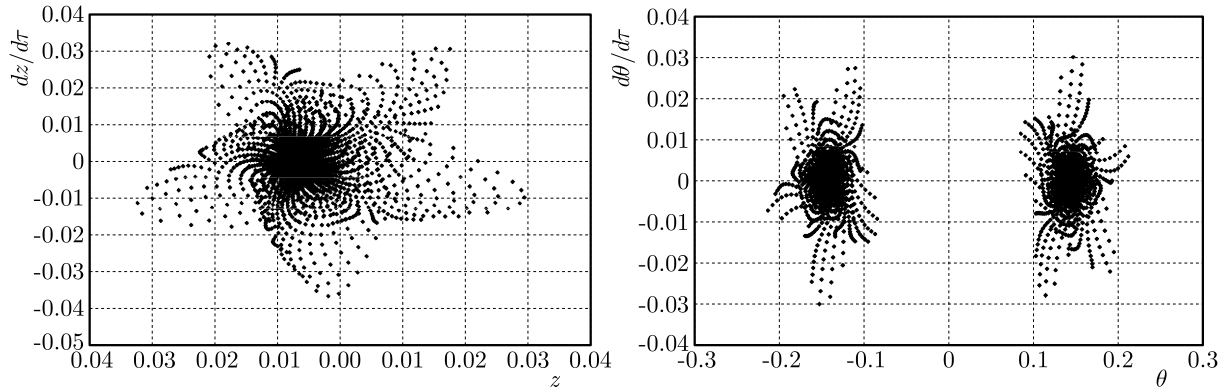


Fig. 8. Poincaré maps for the coordinates z (a) and θ (b) for $a = 0.2$, $\beta = 0.5$, $\gamma = 0.00081443$, $\mu_1 = 0.99$, $A_1 = 0.0029$

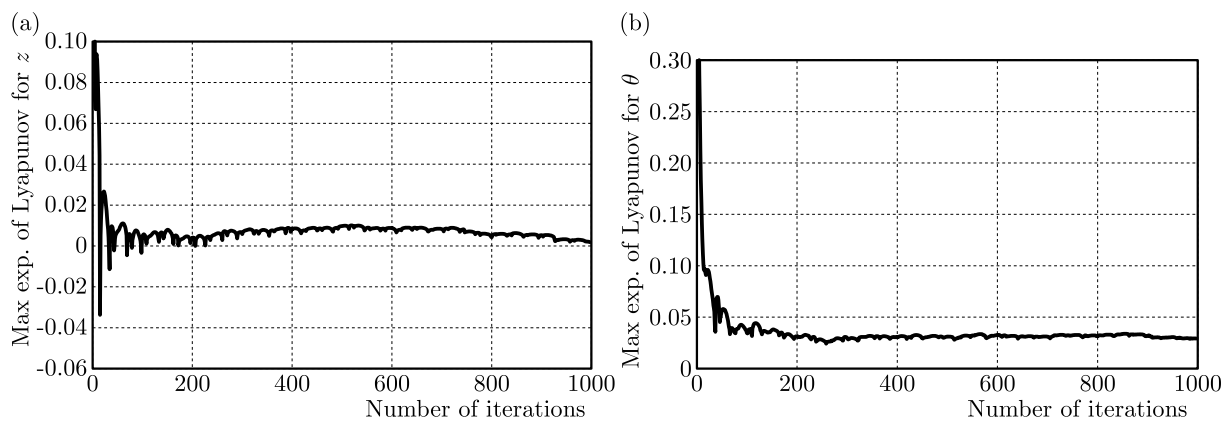


Fig. 9. Maximum Lyapunov exponent for the coordinates z (a) and θ (b) for $a = 0.2$, $\beta = 0.5$, $\gamma = 0.00081443$, $\mu_1 = 0.99$, $A_1 = 0.0029$

4. Conclusions

The influence of initial conditions on the behaviour of an autoparametric system with a spherical pendulum is very interesting, because sometimes when the initial conditions are imposed on the displacements of the spherical pendulum it behaves similarly to a simple pendulum (angle φ is constant), but when the initial conditions are put also on the velocities, we observe some influence of the angle φ . It is important, because near the internal and external resonance area there may appear different motion – regular or chaotic. Autoparametric systems are very sensitive to nonlinearities and the energy is transferred between modes of vibrations in a closed cycle. The time of this cycle depends on the values of parameters, and numerical calculations should be carried for a satisfactorily long time. Assuming the model of the pendulum as the spherical pendulum, the obtained results are more similar to those obtained for the system with the simple pendulum.

References

1. LEUNG A.Y.T., KUANG J.L., 2006, On the chaotic dynamics of a spherical pendulum with a harmonically vibrating suspension, *Nonlinear Dynamics*, **43**, 213-238
2. MILES J.W., ZOU Q.P., 1993, Parametric excitation of a detuned spherical pendulum, *Journal of Sound and Vibration*, **164**, 2, 237-250

3. MITROV R., GRIGOROV B., 2009, Dynamic behaviour of a spherical pendulum with spatially moving pivot, *Zeszyty Naukowe Politechniki Poznańskiej*, **9**, 81-91
4. NAPRSTEK J., FISCHER C., 2009, Auto-parametric semi-trival and post-critical response of a spherical pendulum damper, *Computers and Structures*, **87**, 1204-1215
5. SADO D., 2010, *Regular and Chaotic Vibration in Selected Pendulum Systems* (in Polish), WNT, Warsaw
6. VIET L.D., 2015, Partial stochastic linearization of a spherical pendulum with Coriolis damping produced by radial spring and damper, *Journal Vibration and Acoustics*, **137**, 5, 1-9, DOI: 10.1115/1.4030663
7. WITKOWSKI B., PERLIKOWSKI P., PRASAD A., KAPITANIAK T., 2014, The dynamics of co- and counter rotating coupled spherical pendula, *The European Physical Journal Special Topics*, **223**, 4, 707-720

Manuscript received September 20, 2016; accepted for print January 16, 2017

FINITE ELEMENT IMPLEMENTATION OF SLIGHTLY COMPRESSIBLE AND INCOMPRESSIBLE FIRST INVARIANT-BASED HYPERELASTICITY: THEORY, CODING, EXEMPLARY PROBLEMS

CYPRIAN SUCHOCKI

Warsaw University of Technology, Department of Mechanics and Armament Technology, Warsaw, Poland
e-mail: c.suchocki@imik.wip.pw.edu.pl

The present study is concerned with the finite element (FE) implementation of slightly compressible hyperelastic material models. A class of constitutive equations is considered where the isochoric potential functions are based on the first invariant of the right Cauchy-Green (C-G) deformation tensor. Special attention is paid to the most recently developed model formulations. The incremental form of hyperelasticity and its numerical implementation into both commercial and non-commercial FE software are discussed. A Fortran 77 UMAT code is attached which allows for a simple implementation of arbitrary first invariant-based constitutive models into Abaqus and Salome-Meca FE packages. Several exemplary problems are considered.

Keywords: hyperelasticity, finite element method, UMAT, elasticity tensor

1. Introduction

The hyperelastic constitutive equations are nowadays available in every advanced FE program. However, the material libraries of FE software usually include only a number of standard hyperelastic models such as: neo-Hooke, Mooney-Rivlin, Ogden or Yeoh. Less celebrated or newly developed constitutive models can be implemented into a FE program by taking advantage of a proper user subroutine. The FE package Abaqus provides three user subroutines which allow one to define a custom hyperelastic model, i.e. UHYPER (for isotropic hyperelastic materials), UANISOHYPER (for anisotropic hyperelastic materials) and UMAT (a general purpose subroutine which can be utilized for implementing any kind of constitutive equation), cf. Hibbit *et al.* (2008). Due to the method of FE implementation used for slightly compressible hyperelasticity in Abaqus, it is not recommended to utilize the subroutine UHYPER for all kinds of finite elements (cf. Jemioło, 2002). Thus, in the case of slightly compressible hyperelastic materials, i.e. the materials with decoupled volumetric and isochoric responses, the subroutine UMAT might be preferred. Both UHYPER and UANISOHYPER subroutines can be utilized to define nonlinear viscoelastic models based on the viscoelasticity theory used by Abaqus. Alternatively, a proper option allows one to simulate the Mullins effect in a hyperelastic material defined by the aforementioned subroutines¹. On the other hand, the subroutine UMAT is a much more powerful tool which enables one to define an arbitrary constitutive theory, including those based on hyperelasticity such as nonlinear viscoelasticity (e.g. Suchocki 2013) or growth models (e.g. Young *et al.*, 2010), so that the user is not limited by the built-in options of Abaqus.

The subroutine UMAT is a Fortran 77 code which is called during every iteration of the Newton-Raphson numerical procedure to calculate components of the stress tensor and the material Jacobian which is also referred to as tangent modulus or (in the case of elastic materials)

¹The nonlinear viscoelasticity and the Mullins effect must be used separately as Abaqus does not allow for combining these behaviors.

the elasticity tensor, cf. Hibbit *et al.* (2008). The material Jacobian may be defined either in an approximate or (if possible) an analytical form, which is usually very difficult to determine. The approximate material Jacobians always worsen the rate of convergence of the numerical calculations. It was demonstrated by Stein and Sagar (2008) that for the neo-Hooke hyperelastic model, the quadratic rate of convergence² is obtained only when the analytical material Jacobian is used. The utilization of the approximate material Jacobians resulted in worsening the convergence rate and, in the case of some of the considered problems and finite element types, it caused lack of convergence. Thus, it is always recommended to use an analytical material Jacobian whenever it is available.

In this study, the FE implementation of slightly compressible isotropic hyperelastic constitutive models that are not included in any of the commercial and non-commercial CAE packages is discussed. The stored energy functions that are based on the first invariant of the isochoric right C-G tensor are considered. The focus is on the recently developed models for polymeric materials (Gent, 1996; Jemioło, 2002; Lopez-Pamies, 2010; da Silva Soares, 2008; Khajehsaeid *et al.*, 2013) and on some model formulations used in soft tissue biomechanics (Demiray, 1972; Demiray *et al.*, 1988). The general framework for deriving an analytical material Jacobian is presented. A subroutine UMAT is attached allowing for using the newly developed exponential-logarithmic model (Khajehsaeid *et al.*, 2013) in both Abaqus and Salome-Meca FE packages. The code structure is universal so that any other first invariant-based slightly compressible or incompressible hyperelastic model can be easily implemented by simply changing the expressions for the stored energy derivatives. A number of exemplary problems were solved for selected energy potentials. The presented UMAT code can be upgraded to define nonlinear viscoelastic, elastoplastic, viscoplastic or other behavior using arbitrary constitutive theory.

2. Slightly compressible hyperelastic materials

In the following derivations, the multiplicative split of the deformation gradient tensor into the volumetric and isochoric component is utilized (e.g. Jemioło, 2016), i.e.

$$\mathbf{F} = \mathbf{F}_{vol} \bar{\mathbf{F}} \quad \mathbf{F}_{vol} = J^{\frac{1}{3}} \mathbf{1} \quad \bar{\mathbf{F}} = J^{-\frac{1}{3}} \mathbf{F} \quad \bar{\mathbf{C}} = \bar{\mathbf{F}}^T \bar{\mathbf{F}} = J^{-\frac{2}{3}} \mathbf{C} \quad (2.1)$$

where $J = \det \mathbf{F}$ and $\bar{\mathbf{C}}$ is the isochoric right C-G tensor with the following set of algebraic invariants

$$\bar{I}_1 = \text{tr} \bar{\mathbf{C}} \quad \bar{I}_2 = \frac{1}{2} \left((\text{tr} \bar{\mathbf{C}})^2 - \text{tr} \bar{\mathbf{C}}^2 \right) \quad \bar{I}_3 = \det \bar{\mathbf{C}} = 1 \quad (2.2)$$

In the case of slightly compressible hyperelastic materials, the stored energy function is considered to be the sum of the volumetric contribution U and the isochoric part \bar{W} , thus

$$W(\mathbf{C}) = U(J) + \bar{W}(\bar{I}_1, \bar{I}_2) \quad \mathbf{S} = 2 \frac{\partial W}{\partial \mathbf{C}} \Big|_{\mathbf{C}=\mathbf{C}^T} \quad (2.3)$$

where the most general form of the constitutive equation is given by Eq. (2.3)₂³. After substituting Eq. (2.3)₁ into Eq. (2.3)₂, the decoupled form of the constitutive equation is found

$$\mathbf{S} = Jp \mathbf{C}^{-1} + J^{-\frac{2}{3}} \text{DEV} \left[\bar{\mathbf{S}} \right] \quad p = \frac{\partial U}{\partial J} \quad \bar{\mathbf{S}} = 2 \frac{\partial \bar{W}}{\partial \bar{\mathbf{C}}} \Big|_{\bar{\mathbf{C}}=\bar{\mathbf{C}}^T} \quad (2.4)$$

with $\text{DEV}[\bullet] = [\bullet] - \frac{1}{3}([\bullet] \cdot \bar{\mathbf{C}}) \bar{\mathbf{C}}^{-1}$ being a deviator in the reference configuration.

²The quadratic convergence means that the error at the current iteration is proportional to the square of the error from the previous iteration.

³The adopted notation emphasizes the fact that symmetrization is carried out after calculating a derivative.

3. Material Jacobian tensor

Taking a directional derivative of Eq. (2.4)₁ with respect to \mathbf{C} , an incremental constitutive relation is found, see e.g. Jemioło and Gajewski (2014)

$$\Delta \mathbf{S} = \mathbf{c} \cdot \frac{1}{2} \Delta \mathbf{C} \quad \mathbf{c} = 2 \frac{\partial \mathbf{S}}{\partial \mathbf{C}} \Big|_{\mathbf{C}=\mathbf{C}^T} = 4 \frac{\partial^2 W}{\partial \mathbf{C} \otimes \partial \mathbf{C}} \Big|_{\mathbf{C}=\mathbf{C}^T} \quad \mathbf{c} = \mathbf{c}^{vol} + \mathbf{c}^{iso} \quad (3.1)$$

Assuming $U = U(J)$ and $\bar{W} = \bar{W}(\bar{I}_1)$, the expressions for the volumetric and the isochoric parts of the elasticity tensor can be derived

$$\begin{aligned} \mathbf{c}^{vol} &= J \frac{\partial U}{\partial J} (\mathbf{C}^{-1} \otimes \mathbf{C}^{-1} - 2\mathbf{I}_{\mathbf{C}^{-1}}) + J^2 \frac{\partial^2 U}{\partial J^2} \mathbf{C}^{-1} \otimes \mathbf{C}^{-1} \\ \mathbf{c}^{iso} &= -\frac{4}{3} J^{-\frac{2}{3}} \frac{\partial \bar{W}}{\partial \bar{I}_1} \left[\mathbf{1} \otimes \mathbf{C}^{-1} + \mathbf{C}^{-1} \otimes \mathbf{1} - I_1 \left(\mathbf{I}_{\mathbf{C}^{-1}} + \frac{1}{3} \mathbf{C}^{-1} \otimes \mathbf{C}^{-1} \right) \right] + J^{-\frac{4}{3}} \bar{\mathbf{c}}_{\bar{W}} \\ \bar{\mathbf{c}}_{\bar{W}} &= 4 \frac{\partial^2 \bar{W}}{\partial \bar{I}_1^2} \left[\mathbf{1} \otimes \mathbf{1} - \frac{1}{3} I_1 (\mathbf{1} \otimes \mathbf{C}^{-1} + \mathbf{C}^{-1} \otimes \mathbf{1}) + \frac{1}{9} I_1^2 \mathbf{C}^{-1} \otimes \mathbf{C}^{-1} \right] \end{aligned} \quad (3.2)$$

where

$$\mathbf{I}_{\mathbf{C}^{-1}} = \frac{1}{2} \left[(\mathbf{C}^{-1} \otimes \mathbf{C}^{-1}) \overset{(2,3)}{\mathbf{T}} + (\mathbf{C}^{-1} \otimes \mathbf{C}^{-1}) \overset{(2,4)}{\mathbf{T}} \right] = \frac{1}{2} (C_{IK}^{-1} C_{JL}^{-1} + C_{IL}^{-1} C_{JK}^{-1}) \mathbf{E}_I \otimes \mathbf{E}_J \otimes \mathbf{E}_K \otimes \mathbf{E}_L$$

is the fourth order identity tensor in the reference configuration with the Cartesian base $\{\mathbf{E}_K\}$ ($K = 1, 2, 3$)⁴, see e.g. Suchocki (2011).

The incremental constitutive law given by Eq. (3.1)₁ can be transformed into a form relating the incremental Oldroyd (convected) rate of the Kirchhoff stress to the increment of the strain rate tensor, i.e.

$$\mathcal{L}_v \boldsymbol{\tau} = \Delta \boldsymbol{\tau} - \Delta \mathbf{L} \boldsymbol{\tau} - \boldsymbol{\tau} \Delta \mathbf{L}^T = \mathbf{c}^{\tau c} \cdot \Delta \mathbf{D} \quad (3.3)$$

where $\Delta \mathbf{L} = \Delta \mathbf{F} \mathbf{F}^{-1}$ is the increment of the velocity gradient, whereas $\mathbf{c}^{\tau c}$ is the pushed-forward form of the material Jacobian

$$\mathbf{c}^{\tau c} = F_{iP} F_{jQ} F_{kR} F_{lS} C_{PQRS} \mathbf{e}_i \otimes \mathbf{e}_j \otimes \mathbf{e}_k \otimes \mathbf{e}_l \quad (3.4)$$

with $\{\mathbf{e}_k\}$ ($k = 1, 2, 3$) being the Cartesian base in the current configuration. The elasticity tensor takes the following form

$$\begin{aligned} \mathbf{c}^{\tau c} &= \frac{4}{3} \frac{\partial \bar{W}}{\partial \bar{I}_1} \left[\bar{I}_1 \left(\mathbf{I} - \frac{1}{3} \mathbf{1} \otimes \mathbf{1} \right) - (\mathbf{1} \otimes \text{dev}(\bar{\mathbf{B}}) + \text{dev}(\bar{\mathbf{B}}) \otimes \mathbf{1}) \right] + 4 \frac{\partial^2 \bar{W}}{\partial \bar{I}_1^2} \text{dev}(\bar{\mathbf{B}}) \otimes \text{dev}(\bar{\mathbf{B}}) \\ &+ J \left[\left(\frac{\partial U}{\partial J} + J \frac{\partial^2 U}{\partial J^2} \right) \mathbf{1} \otimes \mathbf{1} - 2 \frac{\partial U}{\partial J} \mathbf{I} \right] \end{aligned} \quad (3.5)$$

where

$$\mathbf{I} = \mathbf{1} \diamond \mathbf{1} = \frac{1}{2} \left[(\mathbf{1} \otimes \mathbf{1}) \overset{(2,3)}{\mathbf{T}} + (\mathbf{1} \otimes \mathbf{1}) \overset{(2,4)}{\mathbf{T}} \right] = \frac{1}{2} (\delta_{ik} \delta_{jl} + \delta_{il} \delta_{jk}) \mathbf{e}_i \otimes \mathbf{e}_j \otimes \mathbf{e}_k \otimes \mathbf{e}_l$$

and $\text{dev}[\bullet] = [\bullet] - \frac{1}{3}([\bullet] \cdot \mathbf{1})\mathbf{1}$.

⁴The following notation is used: $[\bullet] \overset{(\mu, \nu)}{\mathbf{T}} = ([\bullet]_{ijkl} \mathbf{e}_i \otimes \underbrace{\mathbf{e}_j}_{\mu} \otimes \mathbf{e}_k \otimes \underbrace{\mathbf{e}_l}_{\nu}) \overset{(\mu, \nu)}{\mathbf{T}} = [\bullet]_{ijkl} \mathbf{e}_i \otimes \underbrace{\mathbf{e}_l}_{\mu} \otimes \mathbf{e}_k \otimes \underbrace{\mathbf{e}_j}_{\nu}$.

The FE software Abaqus utilizes the incremental constitutive equation written in terms of the incremental Zaremba-Jaumann rate of the Kirchhoff stress (cf. Hibbit *et al.* 2008), i.e.

$$\boldsymbol{\tau}^\nabla = \Delta\boldsymbol{\tau} - \Delta\mathbf{W}\boldsymbol{\tau} - \boldsymbol{\tau}\Delta\mathbf{W}^\text{T} = J\mathbf{C}^{MJ} \cdot \Delta\mathbf{D} \quad (3.6)$$

where, respectively

$$\mathbf{C}^{MJ} = \frac{1}{J}(\mathbf{C}^{\tau c} + \mathbf{1} \diamond \boldsymbol{\tau} + \boldsymbol{\tau} \diamond \mathbf{1}) \quad \boldsymbol{\tau} = Jp\mathbf{1} + 2\frac{\partial\bar{W}}{\partial\bar{I}_1} \text{dev}(\bar{\mathbf{B}}) \quad (3.7)$$

and

$$\mathbf{1} \diamond \boldsymbol{\tau} = \frac{1}{2} \left[(\mathbf{1} \otimes \boldsymbol{\tau}) \begin{matrix} (2,3) \\ \text{T} \end{matrix} + (\mathbf{1} \otimes \boldsymbol{\tau}) \begin{matrix} (2,4) \\ \text{T} \end{matrix} \right] \quad \boldsymbol{\tau} \diamond \mathbf{1} = \frac{1}{2} \left[(\boldsymbol{\tau} \otimes \mathbf{1}) \begin{matrix} (2,3) \\ \text{T} \end{matrix} + (\boldsymbol{\tau} \otimes \mathbf{1}) \begin{matrix} (2,4) \\ \text{T} \end{matrix} \right]$$

and

$$\Delta\mathbf{W} = \frac{1}{2}(\Delta\mathbf{L} - \Delta\mathbf{L}^\text{T}) \quad \Delta\mathbf{D} = \frac{1}{2}(\Delta\mathbf{L} + \Delta\mathbf{L}^\text{T}) \quad (3.8)$$

The fourth order tensor \mathbf{C}^{MJ} is the material Jacobian which should be coded in the subroutine UMAT. For the considered class of hyperelastic materials, it takes the form

$$\begin{aligned} \mathbf{C}^{MJ} = & \frac{2}{J} \frac{\partial\bar{W}}{\partial\bar{I}_1} \left[\mathbf{1} \diamond \text{dev}(\bar{\mathbf{B}}) + \text{dev}(\bar{\mathbf{B}}) \diamond \mathbf{1} + \frac{2}{3}\bar{I}_1 \left(\mathbf{I} - \frac{1}{3}\mathbf{1} \otimes \mathbf{1} \right) \right. \\ & \left. - \frac{2}{3}(\mathbf{1} \otimes \text{dev}(\bar{\mathbf{B}}) + \text{dev}(\bar{\mathbf{B}}) \otimes \mathbf{1}) \right] + \frac{4}{J} \frac{\partial^2\bar{W}}{\partial\bar{I}_1^2} \text{dev}(\bar{\mathbf{B}}) \otimes \text{dev}(\bar{\mathbf{B}}) + \left(\frac{\partial U}{\partial J} + J \frac{\partial^2 U}{\partial J^2} \right) \mathbf{1} \otimes \mathbf{1} \end{aligned} \quad (3.9)$$

4. Finite element implementation

4.1. General

In Fig. 1, the interaction of the subroutine UMAT with the Abaqus package is illustrated for the Newton-Raphson iterative procedure during a single time increment (cf. Hibbit *et al.* 2008).

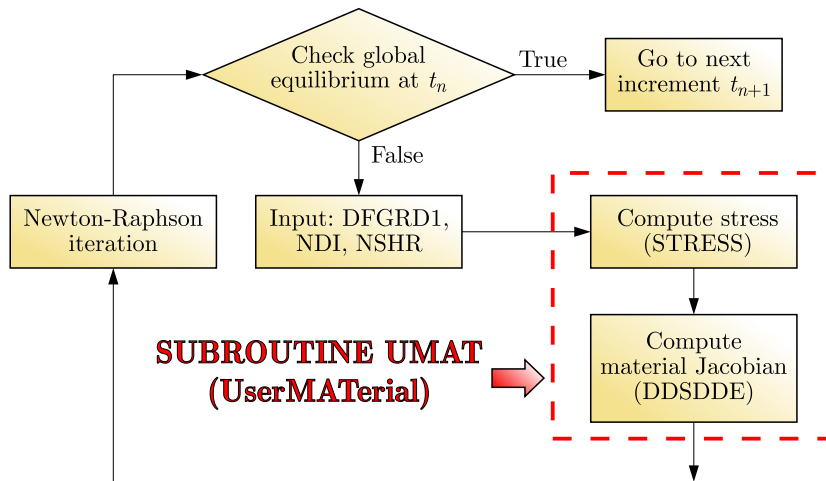


Fig. 1. Flow chart for the interaction of Abaqus and UMAT

The subroutine UMAT calculates the components of Cauchy stress and material Jacobian for each Gauss integration point. These quantities are subsequently used by Abaqus to form up the element stiffness matrix. Finally, the global stiffness matrix is assembled by Abaqus using the element stiffness matrices. The user subroutines used in other FE packages to define custom constitutive equations are integrated with the remainder of the program in a similar way and play the same role.

4.2. Variables and dimensions

In the following table, the meaning of the variables used in the Fortran 77 code has been explained. The dimensions of array variables have been specified in proper indices. The lengthy definitions of the auxiliary variables have been skipped.

Number of direct stress components	NDI
Number of shear stress components	NSHR
Array of material constants	PROPS(I)
Deformation gradient tensor $\mathbf{F}_{3 \times 3}$	DFGRD1(I,J)
Jacobian determinant	DET
Isochoric deformation gradient matrix $\bar{\mathbf{F}}_{3 \times 3}$	DISTGR(I,J)
Isochoric Left C-G deformation tensor matrix $\bar{\mathbf{B}}_{6 \times 1}$	BBAR(I)
Trace of $\bar{\mathbf{B}}$ divided by 3	TRBBAR
First partial derivative $\partial_J U$	DUDJ
Second partial derivative $\partial_{J_2}^2 U$	DDUDDJ
First partial derivative $\partial_{I_1} \bar{W}$	DWDI1
Second partial derivative $\partial_{I_1}^2 \bar{W}$	DDWDDI1
Cauchy stress tensor matrix $\boldsymbol{\sigma}_{6 \times 1}$	STRESS(I)
Material Jacobian matrix $\mathbf{C}_{6 \times 6}^{MJ}$	DDSDDE(I,J)
Auxiliary variables	EK, PR, SCALE, TERM1, TERM2, TERM3

According to the rule adopted in Abaqus, the column matrix components 1, 2, ..., 6 correspond to the scalar components of the second order tensor: 11, 22, 33, 12, 13, 23, respectively.

4.3. User subroutine UMAT

Algorithm for the implementation in ABAQUS

Input data: $\mathbf{F}_{3 \times 3}$ (DFGRD1), NDI, NSHR

1. Calculate Jacobian determinant J (DET)

$$J = \det \mathbf{F}_{3 \times 3}$$

2. Calculate isochoric deformation gradient $\bar{\mathbf{F}}_{3 \times 3}$ (DISTGR)

$$\bar{\mathbf{F}}_{3 \times 3} = J^{-\frac{1}{3}} \mathbf{F}_{3 \times 3}$$

3. Calculate left C-G deformation tensor $\bar{\mathbf{B}}_{6 \times 1}$ (BBAR)

$$\bar{\mathbf{B}}_{3 \times 3} = \bar{\mathbf{F}}_{3 \times 3} \bar{\mathbf{F}}_{3 \times 3}^T \quad \bar{\mathbf{B}}_{6 \times 1} = \{\bar{B}_{11} \bar{B}_{22} \bar{B}_{33} \bar{B}_{12} \bar{B}_{13} \bar{B}_{23}\}^T$$

4. Calculate Cauchy stress matrix $\boldsymbol{\sigma}_{6 \times 1}$ (STRESS)

5. Calculate Material Jacobian matrix $\mathbf{C}_{6 \times 6}^{MJ}$ (DDSDDE).

4.4. Coding in Fortran 77

```

SUBROUTINE UMAT(STRESS,STATEV,DDSDDE,SSE,SPD,SCD,
1 RPL,DDSDDT,DRPLDE,DRPLDT,STRAN,DSTRAN,
2 TIME,DTIME,TEMP,DTEMP,PREDEF,DPRED,MATERL,NDI,NSHR,NTENS,
3 NSTATV,PROPS,NPROPS,COORDS,DROT,PNEWDT,CELENT,
4 DFGRD0,DFGRD1,NOEL,NPT,KSLAY,KSPT,KSTEP,KINC)
!
!   INCLUDE 'ABA_PARAM.INC'
!
CHARACTER*8 MATERL
DIMENSION STRESS(NTENS),STATEV(NSTATV),
1 DDSDDE(NTENS,NTENS),DDSDDT(NTENS),DRPLDE(NTENS),
2 STRAN(NTENS),DSTRAN(NTENS),DFGRD0(3,3),DFGRD1(3,3),
3 TIME(2),PREDEF(1),DPRED(1),PROPS(NPROPS),COORDS(3),DROT(3,3)
!
!   LOCAL ARRAYS
! -----
!   BBAR - DEVIATORIC RIGHT CAUCHY-GREEN TENSOR
!   DISTGR - DEVIATORIC DEFORMATION GRADIENT (DISTORTION TENSOR)
! -----
!
REAL*8 BBAR,DISTGR
DIMENSION BBAR(6),DISTGR(3,3)
!
PARAMETER(ZERO=0.DO, ONE=1.DO, TWO=2.DO, THREE=3.DO, FOUR=4.DO)
!
! -----
!   UMAT FOR COMPRESSIBLE EXPONENTIAL-LOGARITHMIC HYPERELASTICITY
!
!           WARSAW UNIVERSITY OF TECHNOLOGY
!           CYPRIAN SUCHOCKI, JULY 2015
!
!           CANNOT BE USED FOR PLANE STRESS
! -----
!   PROPS(1) - A
!   PROPS(2) - A1
!   PROPS(3) - B
!   PROPS(4) - D1
! -----
REAL*8 A, A1, B, D1, TERM1, TERM2, TERM3, DUDJ, DDUDDJ,
1 DWDI1, DDWDDI1, TRBBAR, DET, SCALE
!
ELASTIC PROPERTIES
!
A=0.195
A1=0.018 ! originally a
B=0.22
D1=0.000000033
!
JACOBIAN AND DISTORTION TENSOR
!
DET=DFGRD1(1, 1)*DFGRD1(2, 2)*DFGRD1(3, 3)
1 -DFGRD1(1, 2)*DFGRD1(2, 1)*DFGRD1(3, 3)
IF(NSHR.EQ.3) THEN
DET=DET+DFGRD1(1, 2)*DFGRD1(2, 3)*DFGRD1(3, 1)
1 +DFGRD1(1, 3)*DFGRD1(3, 2)*DFGRD1(2, 1)
2 -DFGRD1(1, 3)*DFGRD1(3,1)*DFGRD1(2, 2)
3 -DFGRD1(2, 3)*DFGRD1(3, 2)*DFGRD1(1, 1)
END IF
SCALE=DET**(-ONE/THREE)
DO K1=1, 3
DO K2=1, 3
DISTGR(K2, K1)=SCALE*DFGRD1(K2, K1)
END DO
END DO
!
!   CALCULATE LEFT CAUCHY-GREEN TENSOR
!
BBAR(1)=DISTGR(1, 1)**2+DISTGR(1, 2)**2+DISTGR(1, 3)**2

```

```

BBAR(2)=DISTGR(2, 1)**2+DISTGR(2, 2)**2+DISTGR(2, 3)**2
BBAR(3)=DISTGR(3, 3)**2+DISTGR(3, 1)**2+DISTGR(3, 2)**2
BBAR(4)=DISTGR(1, 1)*DISTGR(2, 1)+DISTGR(1, 2)*DISTGR(2, 2)
1   +DISTGR(1, 3)*DISTGR(2, 3)
  IF(NSHR.EQ.3) THEN
    BBAR(5)=DISTGR(1, 1)*DISTGR(3, 1)+DISTGR(1, 2)*DISTGR(3, 2)
1   +DISTGR(1, 3)*DISTGR(3, 3)
    BBAR(6)=DISTGR(2, 1)*DISTGR(3, 1)+DISTGR(2, 2)*DISTGR(3, 2)
1   +DISTGR(2, 3)*DISTGR(3, 3)
  END IF
!
!  CALCULATE THE STRESS
!
  TRBBAR=(BBAR(1)+BBAR(2)+BBAR(3))/THREE
  DUDJ=2/D1*(DET-ONE)
  DDUDDJ=2/D1
  DWDI1=A*(exp(A1*(THREE*TRBBAR-THREE)))
1  -B*log(THREE*TRBBAR-TWO)
  DDWDDI1=A*(A1*exp(A1*(THREE*TRBBAR-THREE)))
1  -B*(THREE*TRBBAR-TWO)**(-ONE)
  TERM1=-FOUR/(THREE*DET)*DWDI1
  TERM2=FOUR/DET*DDWDDI1
  TERM3=DET*DDUDDJ

  CALL CALCSTRESS(BBAR,TRBBAR,DET,DUDJ,DWDI1,NDI,NSHR,
1  STRESS)
!
!  CALCULATE THE STIFFNESS
!
  CALL CALCTANGENT(DDSDDE,STRESS,BBAR,TRBBAR,DUDJ,
1  DWDI1,DDWDDI1,TERM1,TERM2,TERM3,DET,NTENS,NSHR)
!
  RETURN
  END
! -----
SUBROUTINE CALCSTRESS(BBAR,TRBBAR,DET,DUDJ,DWDI1,NDI,NSHR,
1  STRESS)

  REAL*8  BBAR,TRBBAR,DET,DUDJ,DWDI1,STRESS
  DIMENSION  BBAR(6),STRESS(6)

  PARAMETER(TWO=2.D0)

  INTEGER  NDI,NSHR,K1

  DO K1=1,NDI
    STRESS(K1)=TWO/DET*DWDI1*( BBAR(K1)-TRBBAR)+DUDJ
  END DO
  DO K1=NDI+1,NDI+NSHR
    STRESS(K1)=TWO/DET*DWDI1*BBAR(K1)
  END DO

  RETURN
  END
! -----
SUBROUTINE CALCTANGENT(DDSDDE,STRESS,BBAR,TRBBAR,DUDJ,
1  DWDI1,DDWDDI1,TERM1,TERM2,TERM3,DET,NTENS,NSHR)

  REAL*8  DDSDDE,STRESS,BBAR,TRBBAR,DUDJ,DWDI1,DDWDDI1,
1  TERM1,TERM2,TERM3,DET
  DIMENSION  DDSDDE(6,6),STRESS(6),BBAR(6)

  INTEGER  NTENS,NSHR,K1,K2

  PARAMETER(TWO=2.D0, THREE=3.D0, FOUR=4.D0)

  DDSDDE(1, 1)=-DUDJ+TERM3+TWO*TERM1*(BBAR(1)-TWO*TRBBAR)+
1  TERM2*(BBAR(1)**TWO+TRBBAR*(-TWO*BBAR(1)+TRBBAR))+

```

```

2 TWO*STRESS(1)
  DDSDE(2, 2)=-DUDJ+TERM3+TWO*TERM1*(BBAR(2)-TWO*TRBBAR)+
1 TERM2*(BBAR(2)**TWO+TRBBAR*(-TWO*BBAR(2)+TRBBAR))+
2 TWO*STRESS(2)
  DDSDE(3, 3)=-DUDJ+TERM3+TWO*TERM1*(BBAR(3)-TWO*TRBBAR)+
1 TERM2*(BBAR(3)**TWO+TRBBAR*(-TWO*BBAR(3)+TRBBAR))+
2 TWO*STRESS(3)
  DDSDE(1, 2)=DUDJ+TERM3+TERM1*(BBAR(1)+BBAR(2)-TRBBAR)+
1 TERM2*(BBAR(1)*BBAR(2)-TRBBAR*(BBAR(1)+BBAR(2)))+
2 TRBBAR**TWO)
  DDSDE(1, 3)=DUDJ+TERM3+TERM1*(BBAR(1)+BBAR(3)-TRBBAR)+
1 TERM2*(BBAR(1)*BBAR(3)-TRBBAR*(BBAR(1)+BBAR(3)))+
2 TRBBAR**TWO)
  DDSDE(2, 3)=DUDJ+TERM3+TERM1*(BBAR(2)+BBAR(3)-TRBBAR)+
1 TERM2*(BBAR(2)*BBAR(3)-TRBBAR*(BBAR(2)+BBAR(3)))+
2 +TRBBAR**TWO)
  DDSDE(1, 4)=FOUR/DET*BBAR(4)*(-DWDI1/THREE+
1 DDWDDI1*(BBAR(1)-TRBBAR))+STRESS(4)
  DDSDE(2, 4)=FOUR/DET*BBAR(4)*(-DWDI1/THREE+
1 DDWDDI1*(BBAR(2)-TRBBAR))+STRESS(4)
  DDSDE(3, 4)=FOUR/DET*BBAR(4)*(-DWDI1/THREE+
1 DDWDDI1*(BBAR(3)-TRBBAR))
  DDSDE(4, 4)=-DUDJ+TWO/DET*(TRBBAR*DWDI1+
1 TWO*DDWDDI1*BBAR(4)**TWO)+(STRESS(1)+STRESS(2))/TWO
  IF(NSHR.EQ.3) THEN
    DDSDE(1, 5)=FOUR/DET*BBAR(5)*(-DWDI1/THREE+
1 DDWDDI1*(BBAR(1)-TRBBAR))+STRESS(5)
    DDSDE(2, 5)=FOUR/DET*BBAR(5)*(-DWDI1/THREE+
1 DDWDDI1*(BBAR(2)-TRBBAR))
    DDSDE(3, 5)=FOUR/DET*BBAR(5)*(-DWDI1/THREE+
1 DDWDDI1*(BBAR(3)-TRBBAR))+STRESS(5)
    DDSDE(1, 6)=FOUR/DET*BBAR(6)*(-DWDI1/THREE+
1 DDWDDI1*(BBAR(1)-TRBBAR))
    DDSDE(2, 6)=FOUR/DET*BBAR(6)*(-DWDI1/THREE+
1 DDWDDI1*(BBAR(2)-TRBBAR))+STRESS(6)
    DDSDE(3, 6)=FOUR/DET*BBAR(6)*(-DWDI1/THREE+
1 DDWDDI1*(BBAR(3)-TRBBAR))+STRESS(6)
    DDSDE(5, 5)=-DUDJ+TWO/DET*(TRBBAR*DWDI1+
1 TWO*DDWDDI1*BBAR(5)**TWO)+(STRESS(1)+STRESS(3))/TWO
    DDSDE(6, 6)=-DUDJ+TWO/DET*(TRBBAR*DWDI1+
1 TWO*DDWDDI1*BBAR(6)**TWO)+(STRESS(2)+STRESS(3))/TWO
    DDSDE(4,5)=TERM2*BBAR(4)*BBAR(5)+STRESS(6)/TWO
    DDSDE(4,6)=TERM2*BBAR(4)*BBAR(6)+STRESS(5)/TWO
    DDSDE(5,6)=TERM2*BBAR(5)*BBAR(6)+STRESS(4)/TWO
  END IF
DO K1=1, NTENS
  DO K2=1, K1-1
    DDSDE(K1, K2)=DDSDE(K2, K1)
  END DO
END DO

RETURN
END

```

5. Exemplary problems

A number of exemplary FE simulations have been prepared in order to verify the performance of the developed UMAT code. Seven different types of the isochoric stored energy potential $\overline{W}(\overline{I}_1)$ and two types of the volumetric function $U(J)$ have been tested (see Tables 1 and 2). Two different approaches were used in order to simulate the material near incompressibility, i.e. the penalty method and the hybrid formulation (e.g. Liu *et al.* 1994). The results obtained for the material near incompressibility in the case of homogenous deformations were compared to the analytical solutions available in the fully incompressible case.

Table 1. Material parameter values

Material	Constitutive parameters	Units
Jemioło (2002) – Lopez-Pamies (2010)	$\mu_1 = 2.228$	[MPa]
	$\mu_2 = 1.919$	[MPa]
	$\alpha_1 = 0.6 [-], \alpha_2 = -68.73$	[-]
Gent (1996)	$\mu = 0.27$ $J_m = 85.91$	[MPa] [-]
Khajehsaeid <i>et al.</i> (2013)	$A = 0.195$	[MPa]
	$a = 0.018$	[-]
	$b = 0.22$	[-]
Demiray (1971)	$c = 0.2$	[MPa]
	$\beta = 16$	[-]
Demiray <i>et al.</i> (1988)	$\alpha = 10.74\text{E-}10$	[MPa]
	$\beta = 7.548\text{E-}9$	[MPa]
	$c = 1.17$	[-]
Da Silva Soares (2008)	$\mu_1 = 17.999$	[MPa]
	$\mu_2 = 0.17047$	[MPa]
	$a = 477.28$	[-]
Knowles (1977)	$\mu = 264.069$	[MPa]
	$b = 54.19$	[-]
	$n = 0.2554$	[-]

5.1. Simple tension

In the case of uniaxial tension of an incompressible rectangular block (Fig. 2) along the X_1 -direction, the deformation is defined by the set of equations

$$x_1 = \lambda_1 X_1 \quad x_2 = \lambda_1^{-\frac{1}{2}} X_2 \quad x_3 = \lambda_1^{-\frac{1}{2}} X_3 \quad (5.1)$$

where the stretch ratio $\lambda_1 > 1$ and $J = 1$ is assumed. It follows that

$$I_1 = \lambda_1^2 + \frac{2}{\lambda_1} \quad W = W(I_1) \quad (5.2)$$

which yields an equation for the axial component of the Lagrange stress

$$T_{11} = 2 \frac{\partial W}{\partial I_1} \left(\lambda_1 - \frac{1}{\lambda_1^2} \right) \quad (5.3)$$

The analytical Eq. (5.3) was used to verify the results of FE calculations. In numerical simulation, a 15 mm × 15 mm × 15 mm block was undergoing a uniaxial tension (Fig. 2). In the first approach, a single C3D8⁵ element was used with the material near incompressibility being enforced by using the penalty method. The penalty parameter $D_1 = 33\text{E-}9 \text{ MPa}^{-1}$. In the second approach, a hybrid element C3D8H was utilized. The comparison of the numerical results and the analytical solution for the incompressible material can be seen in Fig. 3. The FE simulations were later repeated for the block meshed with 125 elements which produced exactly the same results.

⁵Cubic, three-dimensional, 8 nodes.

Table 2. Exemplary isochoric and volumetric stored-energy functions and their derivatives

Material	Energy potential $\bar{W}(\bar{I}_1)$	1st derivative $\partial\bar{W}/\partial\bar{I}_1$	2nd derivative $\partial^2\bar{W}/\partial\bar{I}_1^2$
Jemioło (2002) – Lopez-Pamies (2010)	$\sum_{r=1}^M \frac{3^{1-\alpha_r}}{2\alpha_r} \mu_r (\bar{I}_1^{\alpha_r} - 3^{\alpha_r})$	$\sum_{r=1}^M \frac{3^{1-\alpha_r}}{2} \mu_r \bar{I}_1^{\alpha_r-1}$	$\sum_{r=1}^M \frac{3^{1-\alpha_r}}{2} \mu_r (\alpha_r - 1) \bar{I}_1^{\alpha_r-2}$
Gent (1996)	$-\frac{\mu J_m}{2} \ln\left(1 - \frac{\bar{I}_1-3}{J_m}\right)$	$\frac{\mu}{2} \left(1 - \frac{\bar{I}_1-3}{J_m}\right)^{-1}$	$\frac{\mu}{2J_m} \left(1 - \frac{\bar{I}_1-3}{J_m}\right)^{-2}$
Khajehsaeid <i>et al.</i> (2013)	$A \left[\frac{1}{a} e^{a(\bar{I}_1-3)} - \frac{1}{a} - b + b(\bar{I}_1 - 2)(1 - \ln(\bar{I}_1 - 2)) \right]$	$A [e^{a(\bar{I}_1-3)} - b \ln(\bar{I}_1 - 2)]$	$A [ae^{a(\bar{I}_1-3)} - b(\bar{I}_1 - 2)^{-1}]$
Demiray (1971)	$c \left(e^{\beta(\bar{I}_1-3)} - 1 \right)$	$c\beta e^{\beta(\bar{I}_1-3)}$	$c\beta^2 e^{\beta(\bar{I}_1-3)}$
Demiray <i>et al.</i> (1988)	$\frac{\alpha}{4} (\bar{I}_1 - 3)^2 + \frac{\beta}{4c} \left[e^{c(\bar{I}_1-3)^2} - 1 \right]$	$\frac{1}{2} (\bar{I}_1 - 3) \left[\alpha + \beta e^{c(\bar{I}_1-3)^2} \right]$	$\frac{1}{2} \left\{ \alpha + \beta e^{c(\bar{I}_1-3)^2} [1 + 2c(\bar{I}_1 - 3)^2] \right\}$
Da Silva Soares (2008)	$\mu_1 e^{-(\bar{I}_1-3)} (\bar{I}_1 - 3) + \mu_2 \ln[1 + a(\bar{I}_1 - 3)]$	$\mu_1 e^{-(\bar{I}_1-3)} (4 - \bar{I}_1) + \mu_2 a [1 + a(\bar{I}_1 - 3)]^{-1}$	$-\mu_1 e^{-(\bar{I}_1-3)} (5 - \bar{I}_1) - \mu_2 a^2 [1 + a(\bar{I}_1 - 3)]^{-2}$
Knowles (1977)	$\frac{\mu}{2b} \left\{ \left[1 + \frac{b}{n} (\bar{I}_1 - 3) \right]^n - 1 \right\}$	$\frac{\mu}{2} \left[1 + \frac{b}{n} (\bar{I}_1 - 3) \right]^{n-1}$	$\frac{\mu b(n-1)}{2n} \left[1 + \frac{b}{n} (\bar{I}_1 - 3) \right]^{n-2}$
Material	Energy potential $U(J)$	1st derivative $\partial U/\partial J$	2nd derivative $\partial^2 U/\partial J^2$
Sussman and Bathe (1987)	$\frac{1}{D_1} (J - 1)^2$	$\frac{2}{D_1} (J - 1)$	$\frac{2}{D_1}$
Simo and Taylor (1982)	$\frac{1}{D_1} [(J - 1)^2 + (\ln J)^2]$	$\frac{2}{D_1} \left(J + \frac{\ln J}{J} - 1 \right)$	$\frac{2}{D_1} \left[1 + \frac{1}{J^2} (1 - \ln J) \right]$

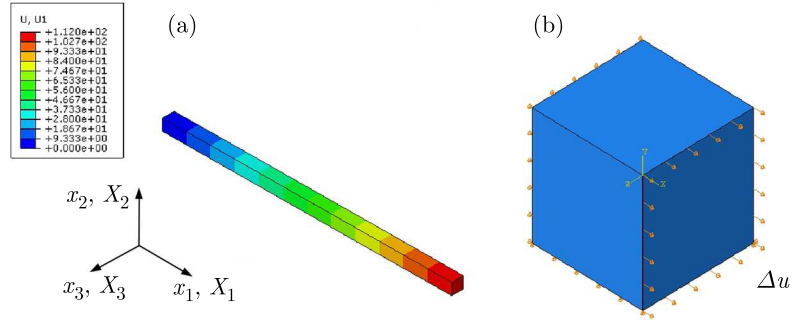


Fig. 2. Uniaxial deformation of a single element: (a) distribution of the displacement, (b) boundary conditions

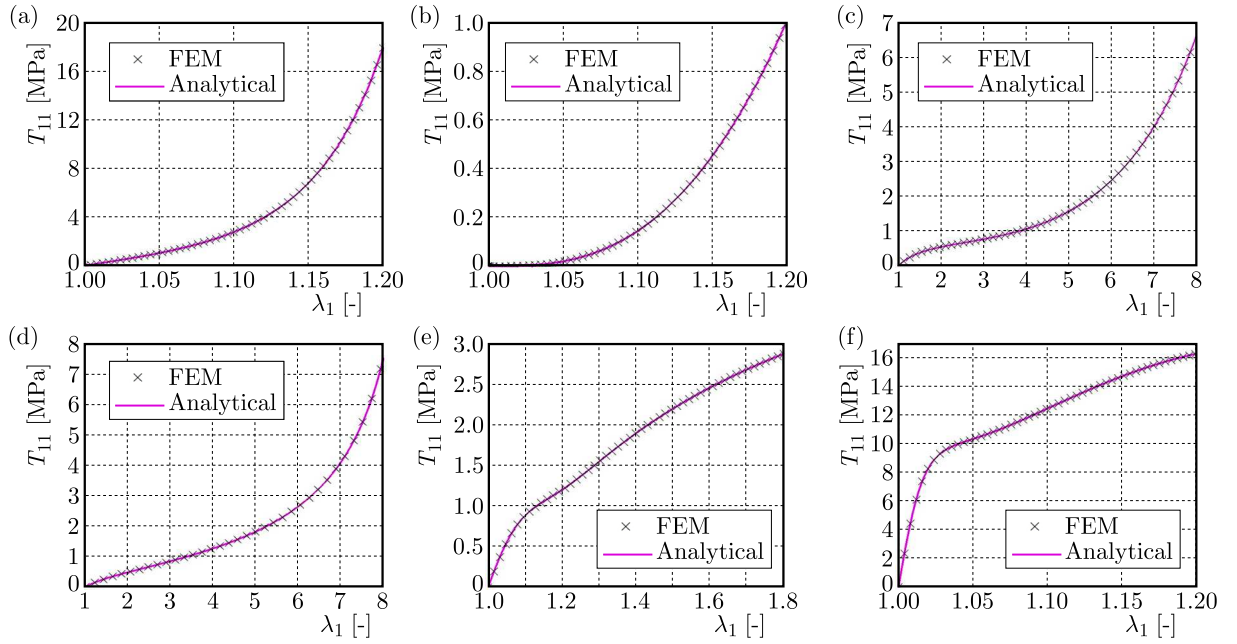


Fig. 3. Uniaxial tension for various hyperelastic models; comparison of analytical and FE results: (a) Demiray (1972), (b) Demiray *et al.* (1988), (c) Exp-Ln, (d) Gent, (e) Jemioło-Lopez-Pamies, (f) Da Silva Soares

5.2. Simple shear

In the case of simple shear of an incompressible rectangular block in the $X_1 - X_2$ plane (Fig. 4), the deformation is defined by the set of equations

$$x_1 = X_1 + \gamma X_2 \quad x_2 = X_2 \quad x_3 = X_3 \quad (5.4)$$

where $\gamma > 0$. The first invariant of the right C-G tensor is given as

$$I_1 = \gamma^2 + 3 \quad (5.5)$$

which yields the following components of the Lagrange stress tensor

$$\mathbf{T}_{3 \times 3} = \frac{2}{3} \frac{\partial W}{\partial I_1} \begin{bmatrix} -\gamma^2 & 3\gamma & 0 \\ \gamma(\gamma^2 + 3) & -\gamma^2 & 0 \\ 0 & 0 & -\gamma^2 \end{bmatrix} \quad (5.6)$$

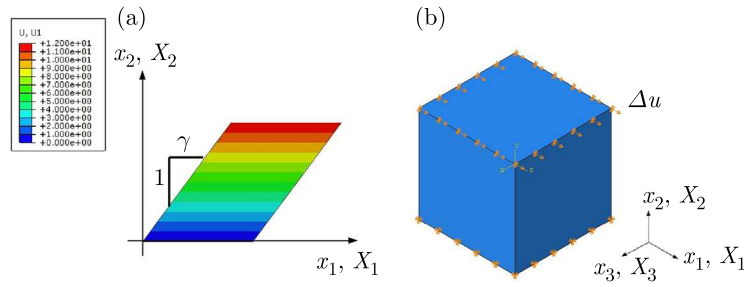


Fig. 4. Shear deformation of a single element: (a) distribution of the displacement, (b) boundary conditions

The analytical formula for T_{12} given by Eq. (5.6) was utilized to verify the results of FE calculations. In numerical simulation, a $15\text{ mm} \times 15\text{ mm} \times 15\text{ mm}$ block was undergoing a simple shear (Fig. 4). Again, the analysis was carried out using the penalty method with a single C3D8 element ($D_1 = 33\text{E-9 MPa}^{-1}$) and was subsequently repeated for a hybrid element C3D8H. The comparison of the numerical results and the analytical solution for the incompressible material can be seen in Fig. 5. The FE simulations were later performed for the block meshed with 125 elements with exactly the same results.

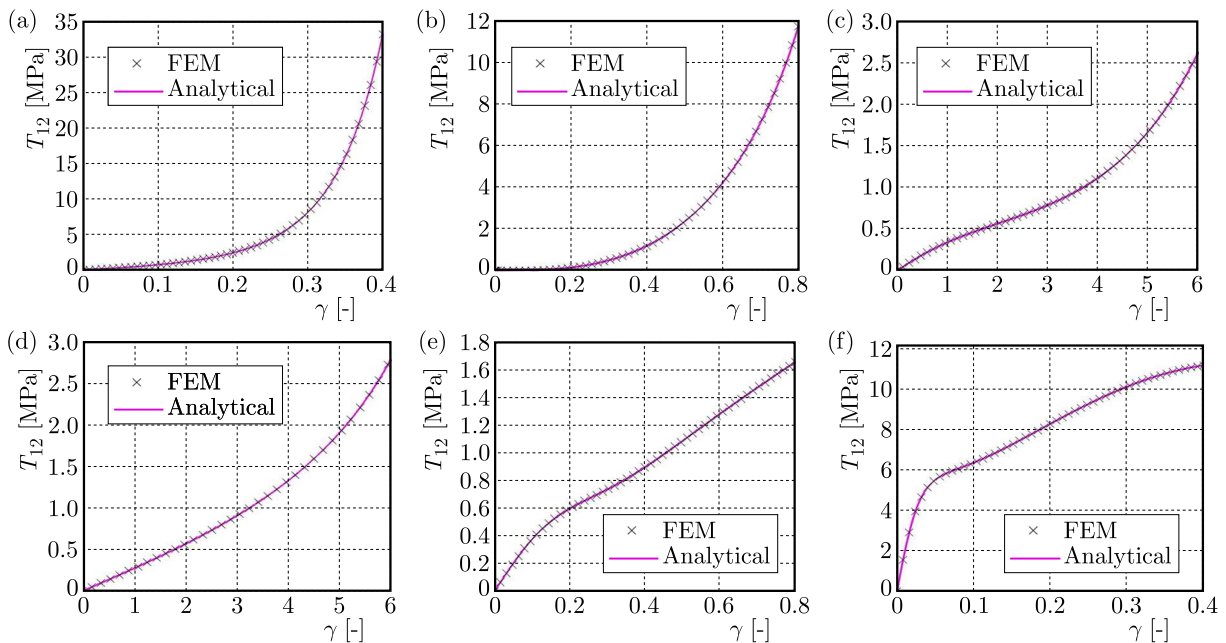


Fig. 5. Simple shear for various hyperelastic models; comparison of analytical and FE results: (a) Demiray (1972), (b) Demiray *et al.* (1988), (c) Exp-Ln, (d) Gent, (e) Jemioło-Lopez-Pamies, (f) Da Silva Soares

6. Conclusions

In this paper, the FE implementation of slightly compressible, first invariant-based, isotropic hyperelastic constitutive equations is discussed. Special attention is paid to the newly developed models for polymers and some of the stored energy functions used in the soft tissue biomechanics. A user subroutine UMAT code is attached, which enables the implementation of the aforementioned models into Abaqus and Salome-Meca FE packages. The performance of this code has been verified using some exemplary problems and an excellent agreement was found with

the analytical solutions. It should be emphasized that the stress-stretch (or stress-amount of shear) relation which yields from the potential function developed by Demiray *et al.* (1988) is characterized by a very flat slope in the small strain domain (cf. Figs. 3b and 5b). Thus, for this particular model, a considerably small strain increment should be used initially in order to avoid convergence problems. The presented UMAT code can be further modified in order to define any constitutive theory that would be an extension of the slightly compressible, first invariant-based hyperelasticity.

References

1. DA SILVA SOARES J.F., 2008, Constitutive modeling for biodegradable polymers for application in endovascular stents, PhD thesis, Texas A&M University
2. DEMIRAY H., 1972, A note on the elasticity of soft biological tissues, *Journal of Biomechanics*, **5**, 3, 309-311
3. DEMIRAY H., WEIZSÄCKER H.W., PASCALE K., ERBAY H.A., 1988, A stress-strain relation for a rat abdominal aorta, *Journal of Biomechanics*, **21**, 5, 369-374
4. GENT A.N., 1996, A new constitutive relation for rubber, *Rubber Chemistry and Technology*, **69**, 59-61
5. HIBBIT B., KARLSSON B., SORENSEN P., 2008, *ABAQUS Theory Manual*, Hibbit, Karlsson & Sorensen Inc.
6. JEMIOŁO S., 2002, A study on the hyperelastic properties of isotropic materials (in Polish), *Scientific Surveys of Warsaw University of Technology*, **140**, Warsaw University of Technology Publishing House, Warsaw
7. JEMIOŁO S., 2016, Constitutive relations of hyperelasticity (in Polish), *Studies in the Field of Engineering*, **94**, The Committee on Civil Engineering and Hydroengineering of the Polish Academy of Sciences, Warsaw
8. JEMIOŁO S., GAJEWSKI M., 2014, Hyperelastoplasticity (in Polish), *Monographs of the Department of Strength of Materials, Theory of Elasticity and Plasticity*, **4**, Warsaw University of Technology Publishing House, Warsaw
9. KHAJEHSAEID H., ARGHAVANI J., NAGHDABADI R., 2013, A hyperelastic constitutive model for rubber-like materials, *European Journal of Mechanics A/Solids*, **38**, 2, 144-151
10. KNOWLES J.K., 1977, The finite anti-plane shear field near the tip of a crack for a class of incompressible elastic solids, *International Journal of Fracture*, **13**, 5, 611-639
11. LIU C.H., HOFSTETTER G., MANG H.A., 1994, 3D finite element analysis of rubber-like materials at finite strains, *Engineering Computations*, **11**, 111-128
12. LOPEZ-PAMIES O., 2010, A new I_1 -based hyperelastic model for rubber elastic materials, *Comptes Rendus Mecanique*, **338**, 1, 3-11
13. SIMO J.C., TAYLOR R.L., 1982, Penalty function formulations for incompressible nonlinear elastostatics, *Computer Methods in Applied Mechanics and Engineering*, **35**, 107-118
14. STEIN E., SAGAR G., 2008, Convergence behavior of 3D finite elements for neo-Hookean material, *Engineering Computations: International Journal for Computer-Aided Engineering and Software*, **25**, 3, 220-232
15. SUCHOCKI C., 2011, A finite element implementation of Knowles stored-energy function: theory, coding and applications, *Archive of Mechanical Engineering*, **58**, 3, 319-346
16. SUCHOCKI C., 2013, A quasi-linear viscoelastic rheological model for thermoplastics and resins, *Journal of Theoretical and Applied Mechanics*, **51**, 1, 117-129

17. SUSSMAN T., BATHE K.J., 1987, A finite element formulation for nonlinear incompressible hyper-elastic and inelastic analysis, *Computers and Structures*, **26**, 357-409
18. YOUNG J.M., YAO J., RAMASUBRAMANIAN A., TABER L.A., PERUCCHIO R., 2010, Automatic generation of user material subroutines for biomechanical growth analysis, *Journal of Biomechanical Engineering*, **132**, 10, doi: 10.1115/1.4002375

Manuscript received April 13, 2016; accepted for print January 16, 2017

SURFACE-TO-AIR MISSILE PATH PLANNING USING GENETIC AND PSO ALGORITHMS

SEID MIAD ZANDAVI

Department of Engineering, Payam Noor University, Tehran, Iran
e-mail: zandavi@alum.sharif.edu

Optimization algorithms use various mathematical and logical methods to find optimal points. Given the complexity of models and design levels, this paper proposes a heuristic optimization model for surface-to-air missile path planning in order to achieve the maximum range and optimal height based on 3DOF simulation. The proposed optimization model involves design variables based on the pitch programming and initial pitch angle (boost angle). In this optimization model, we used genetic and particle swarm optimization (PSO) algorithms. Simulation results indicated that the genetic algorithm was closer to reality but took longer computation time. PSO algorithm offered acceptable results and shorter computation time, so it was found to be more efficient in the surface-to-air missile path planning.

Keywords: path planning, genetic algorithm, PSO algorithm, surface-to-air missile, 3DOF simulation

1. Introduction

System optimization means minimizing or maximizing system functions to improve its efficiency. Several approaches have been proposed for designing acceptable answers under time limitation. These approaches involve some algorithms which do not guarantee an optimal answer but offer the best combination of quality and time based on evidences and records. These algorithms are called heuristic algorithms (Puchinger and Raidl, 2005). Normally, the air defense missile guidance system consists of three phases: boost phase, midcourse and terminal phase. The midcourse is the longest phase of the flight and aims to direct the missile towards the target and to move it through an optimal path in order to save energy and prevent it from being seen by the enemy. This paper aims to design the midcourse of a surface-to-air missile using genetic and PSO algorithms in order to achieve the maximum range for the missile. To do so, we have to determine the initial boost angle and pitch angle over the path in the vertical sheet. This is normally a difficult job and entails real-time trial and error, which in turn imposes heavy cost, long time and real-time modeling. Path planning using heuristic algorithms helps to achieve the maximum height and range.

In 2001, a study was conducted under the title of “designing guidable interceptor missile using genetic algorithm” with a view to minimizing the contact error, interception time and takeoff weight (Anderson *et al.*, 2001). In 2004, a research was conducted under the title of “finding path for tactical missiles using genetic algorithm”, in which the application of genetic algorithm in path planning was investigated. The objectives were to increase speed, range and flight time (Cribbs, 2004). In 2006, a research was conducted under the title of “path optimization using genetic algorithm simulation”, in which path data used in optimization process were produced by simulation of the equation of motion. This paper examines a moving hypersonic missile using a path optimization technique (Farooq and Limebeer, 2002). The results indicated that the genetic algorithm was an efficient method in path planning. In 2007, a study was conducted

under the title of “path planning, optimization and guidance of boost vehicles in terminal phase of flight”. That PhD thesis proposed a method for path planning, optimization and guidance using 3DOF simulation, evaluated the paths planned for the terminal phase, and used them for the development of the guidance program (Chartres, 2007). Zhao and Fan (2009) dealt with optimal path planning for an anti-ship missile using MAKLINK graph method. In this method, genetic algorithm was used to find optimal points with an emphasis on the points which satisfied all problem constraints. Shu *et al.* (2010) optimized path height for cruise missile using the improved PSO algorithm and simulated the annealing algorithm. Peibei and Jun (2010) compared the Voronoi algorithm, grid method and visual graph for multi missile path planning. Wang *et al.* (2011) proposed a real-time path planning for UAV (Unmanned Air Vehicle) based on PSO algorithm improved by modification of inertia weight and self-adaption. Huang *et al.* (2012) proposed a method for cruise missile path planning based on the voronoi diagram and biogeography-based optimization. Liu *et al.* (2015) proposed an algorithm for path planning based on a series of geometrical constraints and rules using multi-attribute fuzzy optimization (MAFO), which produced successful results for real-time functions.

Some of the above-mentioned papers focused only on the optimization method and solved the problems using heuristic methods to increase convergence speed, reduce the number of assessments, reduce optimization time, reduce computation volume, and combine the optimization methods. They have also compared their methods with other optimization methods. Others focused on optimization results and interpreted them based on bird dynamics and the objective function by changing design variables and comparing the results with empirical methods. This paper deals with surface-to-air missile path planning based on pitch programming in order to achieve the maximum range and optimal height. In this optimization model, we used genetic and PSO algorithms and compared them in a specific problem.

2. Exploration algorithm

Generally, heuristic algorithms can be divided into three groups:

- Algorithms which focus on structural features of the problem to define a producer algorithm or local search.
- Algorithms which focus on heuristic guidance of a producer algorithm or local search so that the algorithm can overcome sensitive conditions (e.g. optimal local escape).
- Algorithms which focus on a heuristic framework or concept using mathematical programming (usually by precise methods).

The first group may perform the job very well (sometimes in optimal level) but is trapped in low quality answers. These algorithms were improved by new approaches, including algorithms which explicitly or implicitly managed the relationship between search diversity (where there are symptoms that the search is going towards bad regions of search space) and search intensification (with a view to find the best answer in the studied region). Among such algorithms, we can mention simulated annealing, particle swarm optimization, and colony optimization and neural network. The most famous and efficient algorithms are those which provide problem solving models using genetic evolution patterns. These algorithms develop an effective search method in large spaces which finally lead to finding the optimal answers. In this part, we first introduce the heuristic algorithms and then explain how to find the answer (Puchinger and Raidl, 2005).

2.1. Genetic algorithm

The idea of evolutionary algorithms was coined by Richtenberg in 1960. According to Darwin's Theory of Evolution, those natural traits which adapt more to natural laws have more chance of

survival. Based on the natural selection law, those species of a population which possess the best traits continue their generation and those which lack such traits are gradually destroyed over time. Therefore, natural selection may be considered as a competition for preserving superior traits. Genetic algorithms are evolutionary algorithms inspired by biological sciences such as genetics, mutation, natural selection and combination.

Important parameters in a genetic algorithm are encoding, population size, initial population, chromosome rating (fitness function scale), parent selection mechanism, crossover rate, genetic operators, replacement, and algorithm stoppage parameters (Holland, 1975).

Evolution begins from the initial population and is repeated in the next generations. Figure 1 illustrates the steps of a genetic algorithm. The important point in a genetic algorithm is to select the most appropriate members of each generation, not the best ones (Puchinger and Raidl, 2005; Jarvis and Goodacre, 2005).

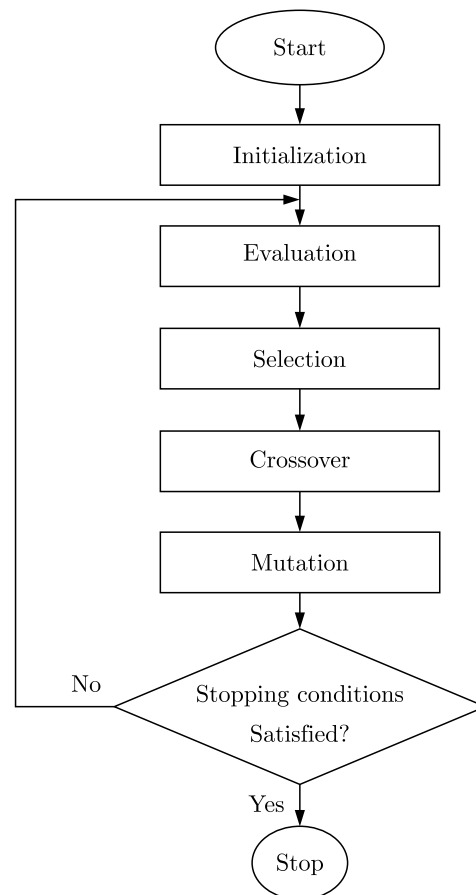


Fig. 1. Genetic algorithm

2.2. Particle swarm optimization algorithm

Birds show certain social behaviors. To better understand this technique, we will explain a scenario in the next paragraphs.

A group of birds are randomly seeking food in a specific area. In this area, only a piece of food exists and the birds are unaware of its exact location. However, they know their distance from the food in any moment. In such circumstances, a good strategy to find the exact location of food is to follow the bird that is closest to the food.

In fact, each bird in PSO algorithm is a solution to the problem. Every answer has a fitness value which is obtained from the fitness function of the problem. This technique aims to find the

location with the best fitness value in the problem space. The fitness value directly affects the direction and speed of bird movement (problem answers) towards food location (optimal answer). This algorithm starts to work with a number of initial answers and searches for the optimal answer by moving the answers during frequent repetitions. In each repetition, the location of best fitness value for each particle (pBest) and the location of the best particle in the current population (gBest) are specified (Fan and Shi, 2001). Figure 2 illustrates the steps of PSO algorithm.

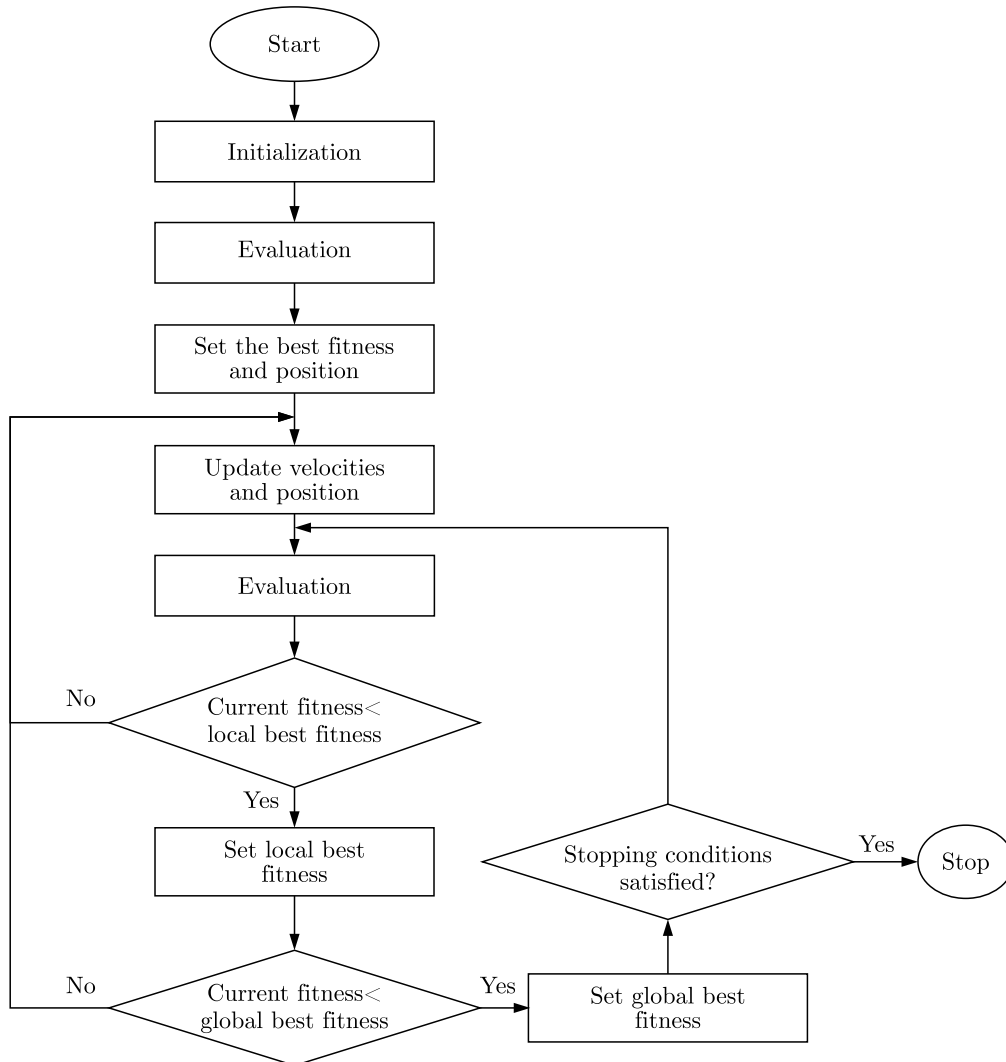


Fig. 2. Particle swarm optimization algorithm

3. 3DOF simulation

Designing and testing guidance and control systems of aerospace vehicles requires path simulation based on the system model. The advances in computer science, the increased processing power, and the efforts to model subsystems and other associated items have led to the improved planning process. On the other hand, special attention has been paid to the application of simulation in multithreaded optimization, and efforts have been made to perform simulation with high accuracy and speed. Generally, simulation of flight dynamics is divided into five parts:

1. Simplification
2. Selection of reference coordinates

3. Extraction of subsystem equations and modeling
4. Simulation of motion equations in a computer program
5. Authentication of the simulation

The simplification refers to the assumptions used to simplify the study of vehicle dynamics. Since the mass center path of the vehicle is more important than its rotation, 3DOF simulation greatly contributes to the estimation of vehicle performance and investigation of the path. In contrast to 6DOF simulation, 3DOF simulation does not use Euler laws and does not need to compute body rates, so there is no need to aerodynamic and propulsion moments. One of the subjects in each simulation is the selection and conversion of coordinates. In many parts of the simulation, we need to convert coordinates of the parameters so that we can use their values in other coordinates (Zipfel, 2007).

Body coordinates (Fig. 3) are one of the most important coordinates because they make many measurements and computations. For example, accelerations are measured by accelerometers installed in body coordinates.

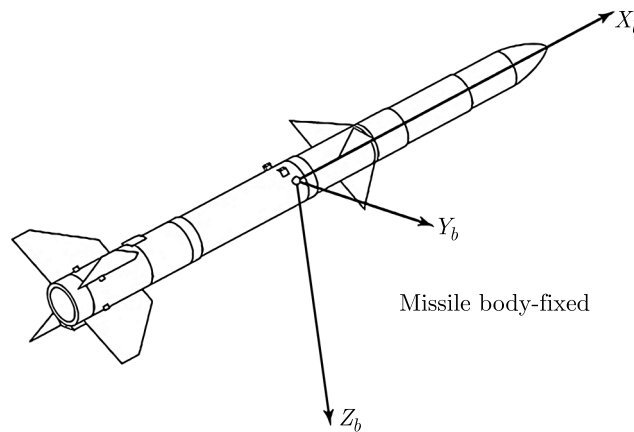


Fig. 3. Body coordinates

In missiles, all X_b and Y_b directions are the main axes due to rotational symmetry, so geometrical signs are used to locate unit vectors. As one can see, the origin of coordinates is on the boost point of the ground, the axis x is in the boost direction, the axis z is perpendicular to the ground (towards the ground), and the axis y makes the coordinate (Zipfel, 2007), see Fig. 4.

If Missile DATCOM (MD) software is used in simulation to compute aerodynamic coefficients, it is necessary to pay attention to the body coordinate and the positive directions of its axis in the software (Fig. 5).

3.1. Gravity model

In any simulation, a gravity model must be selected with the required accuracy. Distribution of non-spherical mass of the Earth affects the size and direction of gravity on the missile, but these components are so small that they are omitted in surface-to-air missile programs. According to equation (3.1), gravity acceleration depends on vehicle height in each moment and decreases with the increased height (Tewari, 2007)

$$g = g_0 \left(\frac{R_e}{R_e + H} \right)^2 \quad (3.1)$$

where g is gravity acceleration, H is height, R_e is ground radius (6378140 m), and gravity acceleration at sea level is 9.80665 m/s².

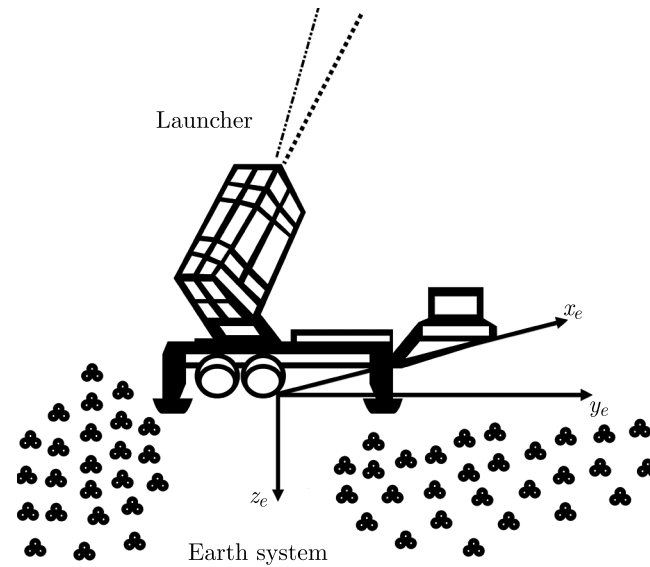


Fig. 4. Ground coordinates

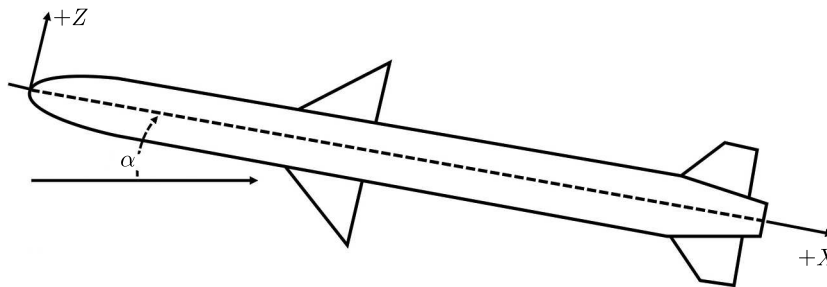


Fig. 5. MD software coordinates

3.2. Standard atmosphere model

Investigation of aerospace vehicle flight has two parts: atmosphere flight mechanics and space flight mechanics. The standard atmosphere is modeled in the form of frequent layers with different temperature rates based on height $T(h)$. The objective is to provide and develop a 21-layer standard atmosphere model for the ground to be used in simulation of atmosphere paths and in determination of dimensionless aerodynamic parameters for aerodynamic force modeling. To do so, two standard atmosphere models of 1976 and 1962 are used. These two models have negligible difference until the height of $0 \leq h \leq 86$, but the difference becomes noticeable in the exosphere layer (Tewari, 2007).

3.3. Point mass 3DOF equations

The most important step before modeling is the selection of inertia reference coordinates. For example, in aerospace vehicles flying near the Earth (such as the satellites rotating in lower orbits), circular or elliptical inertia reference is used. This may be accompanied with circular or elliptical models. The flat ground model is used for airplanes and tactical missiles. First, using Newton's second law, we write transmission equations for an aerospace vehicle exposed to aerodynamic forces and gravity

$$\begin{aligned}
\dot{v}_{x_{body}} &= \left(\frac{1}{M}\right)(T + F_{x_{aero}} + F_{x_{gravity_{body}}}) - (qv_{z_{body}} - rv_{y_{body}}) \\
\dot{v}_{y_{body}} &= \left(\frac{1}{M}\right)(F_{y_{aero}} + F_{y_{gravity_{body}}}) - (rv_{x_{body}} - pv_{z_{body}}) \\
\dot{v}_{z_{body}} &= \left(\frac{1}{M}\right)(F_{z_{aero}} + F_{z_{gravity_{body}}}) - (pv_{y_{body}} - qv_{x_{body}})
\end{aligned} \tag{3.2}$$

where M is vehicle mass and $\mathbf{v}_{body} = [v_{x_{body}}, v_{y_{body}}, v_{z_{body}}]$ is body mass center speed of the vehicle. T describes the force produced by thrust. $\mathbf{F}_{aero} = [F_{x_{aero}}, F_{y_{aero}}, F_{z_{aero}}]$ and $\mathbf{F}_{gravity} = [F_{x_{gravity_{body}}}, F_{y_{gravity_{body}}}, F_{z_{gravity_{body}}}]$ denote the aerodynamic force and gravity force, respectively. p , q and r denote the angular velocity about X_B , Y_B and Z_B directions in the body coordinates. The left side of the above equations can be easily computed in body coordinates, through which vehicle acceleration components in body coordinates will be determined. By integration of the above equations based on initial zero conditions, speed components in body coordinate will be determined (Handbook MIL, 1995).

3.4. Aerodynamic forces and torques

Atmosphere path of aerospace vehicles is under the influence of aerodynamic forces and moments. Aerodynamic forces are developed by the interaction between particles and vehicle body during movement in atmosphere. An influential factor in vehicle aerodynamics is the general configuration of the vehicle. On the other hand, the constituent parts of these forces and torques include aerodynamic factors. Identification of importance and accuracy of these factors has a determining role in the design, control and planning the path and in the analysis of vehicle stability. Assuming that wind speed is zero and angular speed of the missile is negligible, aerodynamic forces and moments relate only to dimensions, geometry, speed and parameters of atmosphere.

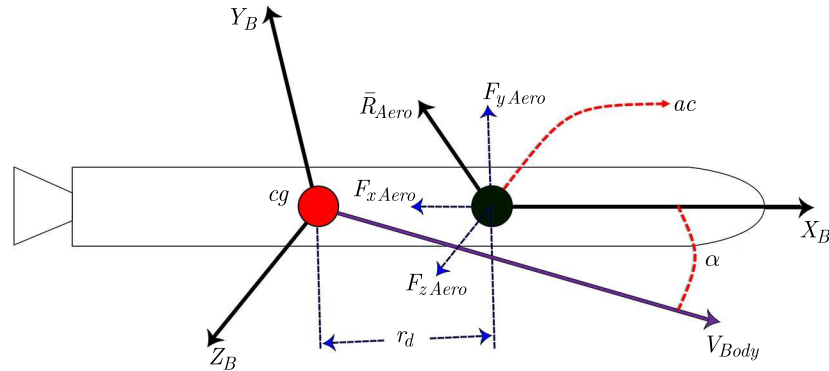


Fig. 6. Aerodynamic forces on missile

According to Fig. 6, the aerodynamic forces are determined by

$$F_{x_{aero}} = \frac{1}{2}\rho V^2 S C_A \quad F_{y_{aero}} = \frac{1}{2}\rho V^2 S C_y \quad F_{z_{aero}} = \frac{1}{2}\rho V^2 S C_N \tag{3.3}$$

where S is surface, ρ is density, C_A , C_y and C_N are coefficients of axial, lateral and normal forces, respectively, and V is mass center speed of the vehicle in the body coordinates (Tewari, 2007).

4. Numerical results

To achieve optimal planning, a code has been codified in MATLAB environment for genetic and PSO algorithms. In this program which is connected to MATLAB Simulink, first the parame-

ters of each algorithm are adjusted by the user. The cost function is optimized according to the adjusted parameters and simulation results (which exist in the algorithm). In this specific case, the optimization problem includes the cost function in the form of equation (4.1) for the achievement of optimal height and the desired maximum

$$f = (H - H_t)^2 + (R^2 - R_t)^2 \quad (4.1)$$

where H and R are height and range requested by the designer, H_t and R_t are height and range of the vehicle in each moment of flight. Tables 1 and 2 contain the parameters of genetic and PSO algorithms.

Table 1. Parameters of genetic algorithm

Parameter	Value
Generation number	100
Population number	50
Mutation rate	0.1
Selection rate	0.5

Table 2. Parameters of PSO algorithm

Parameter	Value
Particle number	100
Local optimal coefficient	2
Comprehensive optimal coefficient	2
Speed contraction coefficient	0.5

Table 3 represents the system parameters needed for 3DOF simulation of a surface-to-air missile.

Table 3. System parameters needed for simulation

Parameter	Value
Total mass in boost time	237.777 kg
Total mass of booster	45 kg
Main engine trust	35585.766 N
Booster trust	60453 N
Main engine burn time	2.9 s
Booster burn time	2 s
Pressure behind the nozzle	70000 Pa

To guide the vehicle, we used pitch programming in the simulation problem. For this purpose, we designed a boost angle and angular rate schedule and used them as the simulation input. The preset pitch rate command is generated by

$$\dot{\theta} = \begin{cases} 0 & \text{for } t < t_1 \\ \frac{a(t - t_1)}{t_2 - t_1} & \text{for } t_1 \leq t < t_2 \\ a & \text{for } t_2 \leq t < t_3 \\ ae^{b(t-t_3)} & \text{for } t \geq t_3 \end{cases} \quad (4.2)$$

where $\dot{\theta}$ is the pitch rate command used as pitch programming in the simulation problem, a and b schedule the angular rate, t denotes the simulation time, t_1 defines the engine start time, t_2 and t_3 are 0.1 s and 0.3 s after starting main engine, respectively.

Geometrical parameters of the vehicle, aerodynamic coefficients tables and angular schedule were recalled by the input file at the beginning of the program, and the related parameters were initialized.

To evaluate the vehicle performance, we had to determine the range that the vehicle would achieve if it reached the intended height. To do so, we planned the path in two scenarios: 1) the ability to achieve flight height of 10 000 m, and 2) reaching the height of 6000 m as the most common altitude in the path planning strategies. These two scenarios were investigated to reach maximum range as well as achieving altitudes in the two case studies. Optimization results of the algorithms will be represented in the following Sections.

According to the boost conditions, optimization algorithms modified speed, acceleration and height. These modifications affected aerodynamic coefficients and dynamic pressure. For this reason, the force coefficients are calculated for seven particular Mach numbers ranging from 0.3 to 3, at five angles of attack α for each Mach number in the range of 0° to $+15^\circ$. The outputs of Missile DATCOM are shown in Figs. 7 and 8. These results are set as a lookup table in SIMULINK and the interpolated based Mach number, altitude and angle of attack in the flight simulation process.

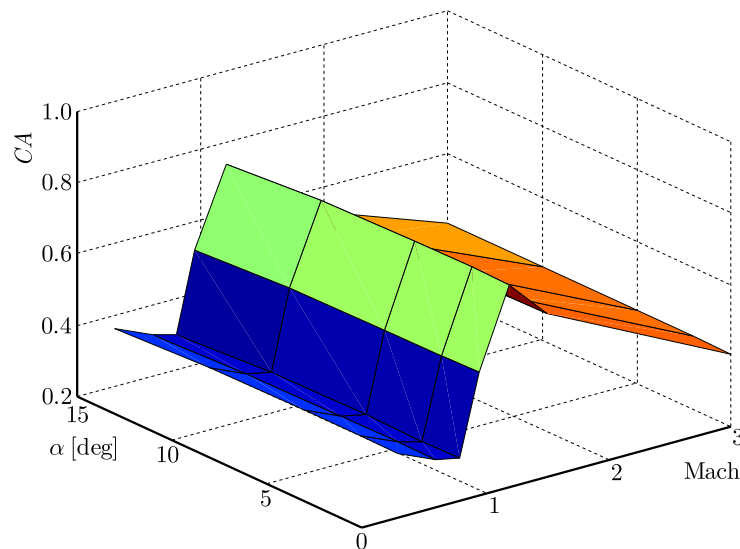


Fig. 7. Axial force coefficient with respect to Mach number and angle of attack

The average execution time of both algorithms is measured and given in Table 4, using a specific computer, characterized by Intel(R) Core(TM) i3 CPU M370 at 240GH. Given the performance of optimization algorithms in this specific problem, we found that the genetic algorithm had a relatively good performance and its optimal solutions were closer to reality. However, it had higher computation cost.

Table 4. Average execution time of PSO and GA in the path planning problem

Algorithm	Average execution time [s]	
	First scenario	Second scenario
PSO	510.2672	305.7908
GA	785.2714	486.6852

Figures 9 and 10 illustrate some of these modifications for both scenarios.

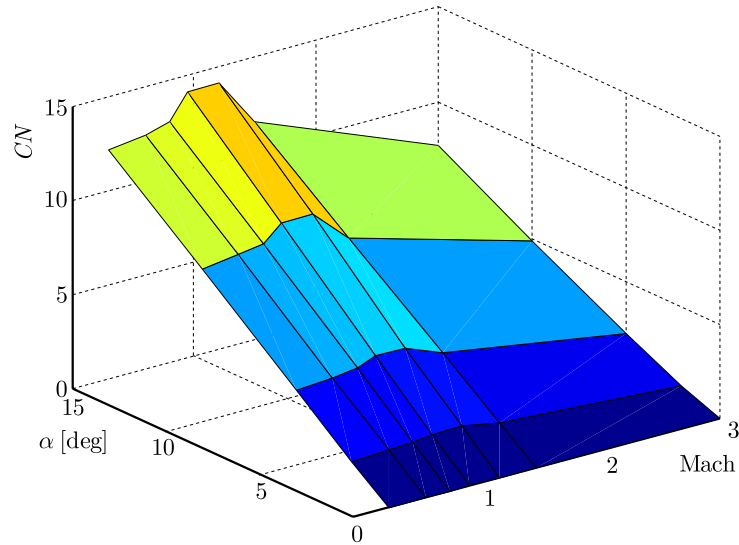


Fig. 8. Normal force coefficient with respect to Mach number and angle of attack

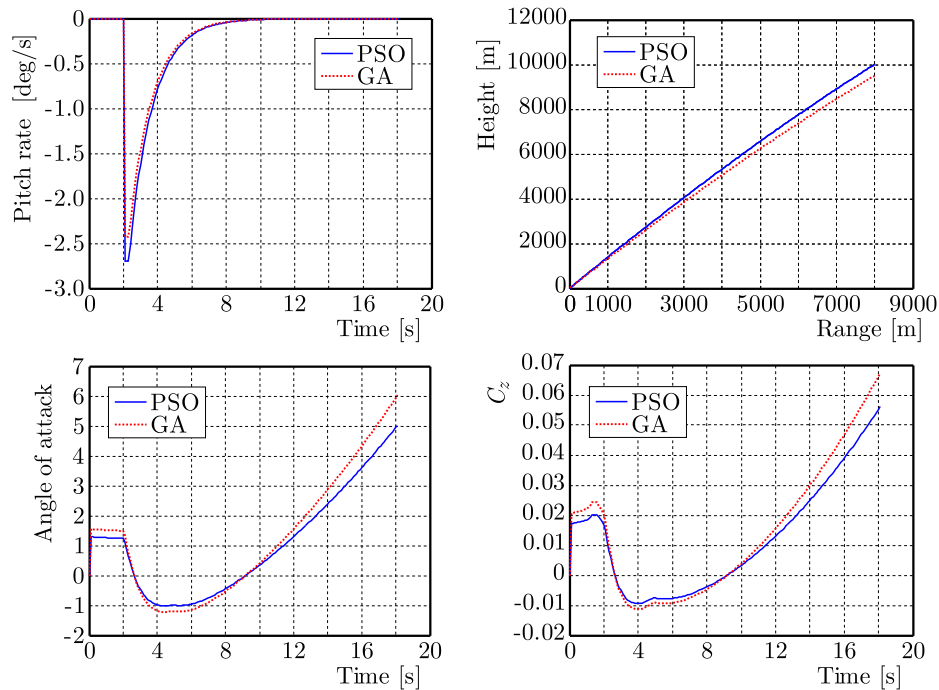


Fig. 9. Functional changes of the vehicle in the first scenario

As you can see in Figs. 9 and 10, vehicle performance in reaching the specified height is similar in both scenarios. Therefore, the changes have similar functional parameters but varied in numerical values. Tables 5 and 6 summarize the optimization results.

5. Conclusion

In this paper, we optimized a surface-to-air missile path using genetic and PSO algorithms in order to achieve the maximum range and optimal height based on 3DOF simulation. In this optimization model, design variables are based on the pitch programming, initial pitch angle and pitch variations rate slope. According to 3DOF simulation results, vehicle performance

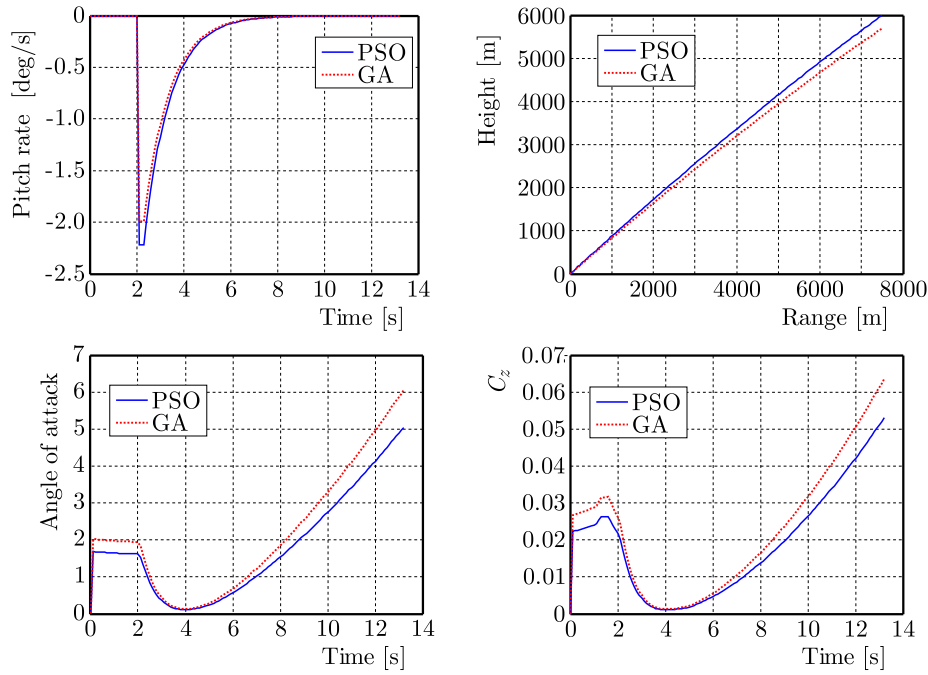


Fig. 10. Functional changes of the vehicle in the second scenario

Table 5. Comparison of algorithms for the height of 10 000 m

Parameter	Algorithm	
	PSO	GA
Initial boost angle [deg]	55.3114	53.4212
a	-0.0492	-0.0558
b	-0.7135	-0.8228
Operating range [m]	8250	8125

Table 6. Comparison of algorithms for the height of 6000 m

Parameter	Algorithm	
	PSO	GA
Initial boost angle [deg]	43.8424	42.4933
a	-0.0784	-0.0622
b	-0.3855	-0.4295
Operating range [m]	7500	7225

did not differ in the mentioned optimization algorithms. The difference lied only in the type of algorithm. In this specific case, the genetic algorithm was closer to reality but took longer computation time. PSO algorithm offered acceptable results and shorter computation time, so it was found to be more efficient in the surface-to-air missile path planning.

References

1. ANDERSON M.B., BURKHALTER J.E., JENKINS R.M., 2001, Design of a guided missile interceptor using a genetic algorithm, *Journal of Spacecraft and Rockets*, **38**, 1, 28-35
2. CHARTRES J.T.A., 2007, Trajectory design, optimisation and guidance for reusable launch vehicles during the terminal area flight phase, Diss. Universität Stuttgart

3. CRIBBS H.B., 2004, Genetics-based trajectory discovery for tactical missiles, *AIAA 1st Intelligent Systems Technical Conference*, 1-6
4. FAN H., SHI Y., 2001, Study on V_{max} of particle swarm optimization, *Proceedings of Workshop on Particle Swarm Optimization*, Purdue School of Engineering and Technology, Indianapolis, IN, USA
5. FAROOQ A., LIMEBEER D.J.N., 2002, Trajectory optimization for air-to-surface missiles with imaging radars, *Journal of Guidance, Control and Dynamics*, **25**, 5, 876-887
6. Handbook, 1995, *Military. Missile Flight Simulation*, Part One: *Surface-to-Air Missiles*, MIL-HDBK-1211 (MI)
7. HOLLAND J.H., 1975, *Adaptation in Natural and Artificial Systems: An Introductory Analysis with Applications to Biology, Control and Artificial Intelligence*, U Michigan Press
8. HUANG N., LIU G., HE B., 2012, Path planning based on Voronoi diagram and biogeographybased optimization, *Advances in Swarm Intelligence*, Springer Berlin Heidelberg, 225-232
9. JARVIS R.M., GOODACRE R., 2005, Genetic algorithm optimization for pre-processing and variable selection of spectroscopic data, *Bioinformatics*, **21**, 860-868
10. LIU G., LAO S.-Y., HOU L.-L., LI Y., TAN D.-F., 2015, OARPER-MAFO algorithm for anti-ship missile path planning, *Aerospace Science and Technology*, **47**, 135-145
11. PEIBEI M.A., JUN J.I., 2010, Comparison of three algorithms for multi missile path planning (in Chinese), *Electronics Optics and Control*, **10**, 007.
12. PUCHINGER J., RAIDL G.R., 2005, Combining metaheuristics and exact algorithms in combinatorial optimization: A survey and classification, *International Work-Conference on the Interplay Between Natural and Artificial Computation*, Springer Berlin Heidelberg, 41-53
13. SHU J., WU J., ZHAO J., WANG X., WANG S., 2010, Cruise height optimization based on improved PSO algorithm (in Chinese), *Electronics Optics and Control*, **2**, 004
14. TEWARI A., 2007, *Atmospheric and Space Flight Dynamics*, Birkhäuser Boston
15. WANG X.-Z., ET AL., 2011, Real-time route planning for UAV based on improved PSO algorithm (in Chinese), *Microelectronics and Computer*, **4**, 023
16. ZHAO X., FAN X., 2009, A method based on genetic algorithm for anti-ship missile path planning, *IEEE, International Joint Conference on Computational Sciences and Optimization, CSO 2009*, **2**
17. ZIPFEL P.H., 2007, *Modeling and Simulation of Aerospace Vehicle Dynamics*, American Institute of Aeronautics and Astronautics, AIAA Education Series

Manuscript received November 16, 2016; accepted for print January 23, 2017

EFFECT OF THE MULTIPLE DAMAGES AND TEMPERATURE CHANGES ON THE NATURAL FREQUENCY

SATTAR MOHAMMADI ESFARJANI, MEHDI SALEHI, AAZAM GHASSEMI

Department of Mechanical Engineering, Najafabad Branch, Islamic Azad University, Najafabad, Iran

e-mail: satar.iran@gmail.com (corresponding author); mehdi.salehi@pmc.iaun.ac.ir; a_ghassemi@pmc.iaun.ac.ir

Damage detection based on structural dynamic characteristics, such as natural frequencies and mode shapes, is an important area of research. Obtaining accurate structural dynamic characteristics is perhaps the most challenging aspect. In particular, changes in environmental temperature due to seasonal weather or radiation from sunshine leads to changes in the dynamic characteristics of structures. An important conclusion is that changes in the dynamic characteristics of a structure due to damage may be smaller than changes in the dynamic characteristics due to variations in temperature. Also, damage can affect the frequency response. This is the first study of evaluation of the effect of changes in temperature and multiple damages on natural frequency at the same time. In this paper, the simultaneous effect of the multiple defects and temperature on the natural frequencies of 6063 aluminum alloy beam are assessed numerically. ABAQUS finite element software is used for the numerical analysis. The present paper aims to evaluate the temperature effect and multiple damages on vibration responses. The variations in the frequency have been analysed in simulation by using an aluminum specimen and obtaining impedance signatures at temperatures ranging from -200°C to 204°C . The results show that an increase in temperature leads to a decrease in structural frequency, and that a decrease in temperature leads to an increase in structural frequency. The evaluation of the effect of multiple defects on natural frequency shows that when damages are created in the structure, there is a significant decrease in the natural frequency responses of the 6063 aluminum alloy beam. The results show that damage causes a decrease in the natural frequency of the structure. This study highlights the importance of applying simulation methods to the evaluation of the effect of changes in environmental temperature and multiple damages on the dynamic characteristics such as natural frequencies and mode shapes, especially at the same time.

Keywords: structural health monitoring, damage detection, vibration response, temperature, natural frequency

1. Introduction

Many techniques have been proposed to detect and localize structural damage using changes in dynamic characteristics of structures such as natural frequency and mode shape (Xu and Wu, 2007). Modal parameters such as natural frequencies and mode shapes are sensitive indicators of structural damage. However, they are not only sensitive to damage, but also to environmental conditions such as humidity, wind and, most important, temperature (Meruane and Heylen, 2012). In particular, changes in environmental temperature due to seasonal weather or radiation from sunshine lead to changes in the dynamic characteristics of structures. An important conclusion is that the changes in dynamic characteristics of the structure due to damage may be smaller than changes in the dynamic characteristics due to variations in temperature (Ralbovsky *et al.*, 2014). For large structures, such as long-span bridges, damage detection is affected by environmental factors. Significant damage may cause very small changes in dynamic characteristics, and these changes may go undetected due to changes in environmental and operational

conditions. These changes have an influence on the dynamic characteristics of the structure. Damage induced dynamic characteristics may be completely masked by changes in dynamic characteristics due to changes in environmental temperature (Xu and Wu, 2007).

The effect of crack location in the modal frequency of a draft gear used in auto couplers of freight railway wagon for various orientations was investigated by Harak *et al.* (2015). They showed that the defect in consecutive pads causes more changed in frequency as compared to a single defective pad. As far as the location of the defective pad is concerned, it is seen that the draft gear frequency is more sensitive to defective pads located either near the housing base plate or top follower (Harak *et al.*, 2015). The effects of crack ratios and positions on the fundamental frequencies and buckling loads of slender cantilever Euler beams with a single-edge crack are investigated by Karaağaç *et al.* (2009). Sayman *et al.* (2013) presented the effect of interface crack on the free vibration response of a sandwich composite beam experimentally and numerically. They showed that the natural frequency of the torsional mode decreases as the crack length increases (Sayman *et al.*, 2013). The effect of temperature on damage detection results was detected early. Eigenfrequency changes caused by temperature effects on different structures were described in the works of Peeters and DeRoeck (2001), Farrar *et al.* (1997) or Ralbovsky *et al.* (2010). The effect of temperature was considered as an obstacle for damage detection. Various methods for removing that effect were proposed, for example in the works of DeRoeck *et al.* (2000), Hu *et al.* (2012) and many other scientists (Ralbovsky *et al.*, 2010). Variations in frequencies are caused mainly by a change in the modulus of a material under different temperatures. Modal frequencies of steel structures, the aluminum beam, and the RC structures decrease by about 0.02, 0.03, and 0.15%, respectively, when temperature increases by one degree Celsius, regardless of modes and structural types. Frequencies of concrete structures are more sensitive to temperature changes than metallic structures (Xia *et al.*, 2012).

The present paper aims to evaluate the temperature effect and multiple damages on vibration responses. In this study, the frequency changes of a structure caused by multiple defects and temperature changes in the 6063 aluminum alloy beam are studied. The thermally induced changes in dynamic characteristics are compared with those due to damages to the 6063 aluminum alloy beam. The changes caused by temperature have been analyzed based on the following aspects: (1) change of the passion rate of the aluminum alloy; (2) changes of the elastic modulus of the aluminum alloy. Guidelines to predict changes in the frequency and mode shape curvature due to temperature changes in the aluminum alloy have been obtained, which is useful for design purposes (Xu and Wu, 2007). The remainder of the paper is organized as follows. In Section 2, theory of the temperature effect on natural frequency is discussed. Section 3 is devoted to the process of the evolution effect of multiple defects and temperature changes on structural natural frequency responses. The verification and simulation of the method is discussed in Section 4. Numerical methods and results for evaluation of the temperature effect and multiple damages on vibration responses are presented in Section 5. The conclusion is reported in Section 6.

2. Theory

Let us consider a rectangular plate which is subjected to an exponential temperature distribution along the length, i.e. in the x -direction (Arun *et al.*, 2014)

$$T = T_0 \frac{e - e^x}{e - 1} \quad (2.1)$$

where T denotes the temperature excess above the reference temperature at any point at the distance $X = x/a$ and T_0 denotes the temperature excess above the reference temperature at

the end, i.e. $x = a$ or $X = 1$. The temperature dependence of the modulus of elasticity for most of engineering materials is given by Nowacki (1962), (Arun *et al.*, 2014)

$$E(T) = E_0(1 - \gamma T) \quad (2.2)$$

where E_0 is the value of Young's modulus at the reference temperature, i.e. $T = 0$, and γ is the slope of variation of E with T (Arun *et al.*, 2014). Taking as the reference temperature, the temperature at the end of the plate, i.e. at $X = 1$, the modulus variation in view of (2.1) and (2.2) becomes (Arun *et al.*, 2014)

$$E(X) = E_0 \left(1 - \alpha \frac{e - e^X}{e - 1} \right) \quad (2.3)$$

where $\alpha = \gamma T_0$ ($0 - \alpha < 1$) is a constant known as the temperature constant. In the above literature, most studies show that an increase in temperature leads to a decrease in structural frequencies, while magnitude varies depending on structures, materials, and temperature range. Variations in natural frequencies of structures with temperature are caused by changes in material properties, in particular, the modulus of elasticity. To quantify the effect of temperature on natural frequencies, a single-span or multi-span prismatic beam made of an isotropic material is used as an example. Its undamped flexural vibration frequency of the order n is (Xia *et al.*, 2012; Blevins, 1979)

$$f_n = \frac{\lambda_n^2}{2\pi l^2} \sqrt{\frac{EI}{\mu}} \quad (2.4)$$

where λ_n is a dimensionless parameter and is a function of boundary conditions, l is length of the beam, μ is mass per unit length, E is the modulus of elasticity, and I is the moment of inertia of cross-sectional area. It is assumed that variations in temperature do not affect mass and boundary conditions, but only geometry of the structure and mechanical properties of the material.

3. Description of the process of the evolution effect of multiple defects and temperature changes on structural natural frequency responses

In recent years, the use of simulation models to develop vibration based damage detection techniques has become very popular, because it is a less expensive and time-consuming procedure than investigation of real structures or experimental models. Also, an experimental setup is also a fairly difficult process. Since the Finite Element (FE) method has been widely accepted as an analysis tool in Structural Health Monitoring (SHM), the above mentioned constraints can be overcome by using a validated FE model to simulate the real structure (Moragasipitiya *et al.*, 2013). In this Section, a FE modeling method is used to obtain natural frequencies of the structure. FE models of the sample are developed utilizing the commercial FE package ABAQUS. As shown in Fig. 1, natural frequency responses of the structure are obtained from FE modeling of the intact and damaged structure. Then, the natural frequency responses of the structure are obtained for varying temperatures from -200°C to 204°C . This is illustrated in Fig. 2.

4. Numerical simulation

In this Section, evaluation of the effect of multiple defects on natural frequencies of the 6063 aluminum alloy beam is discussed. Then, the effect of temperature changes on the natural frequencies of the 6063 aluminum alloy beam is investigated as well.

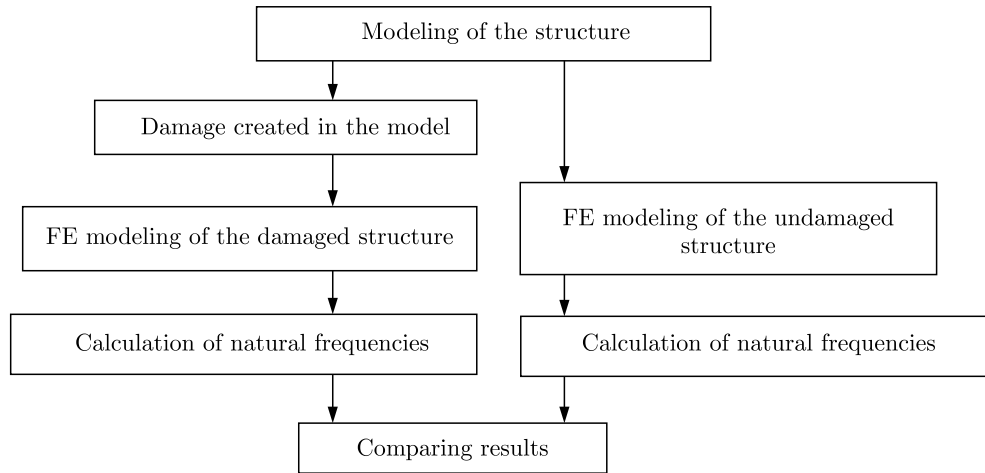


Fig. 1. Flowchart of the evolution effect of multiple defects on the natural frequency responses

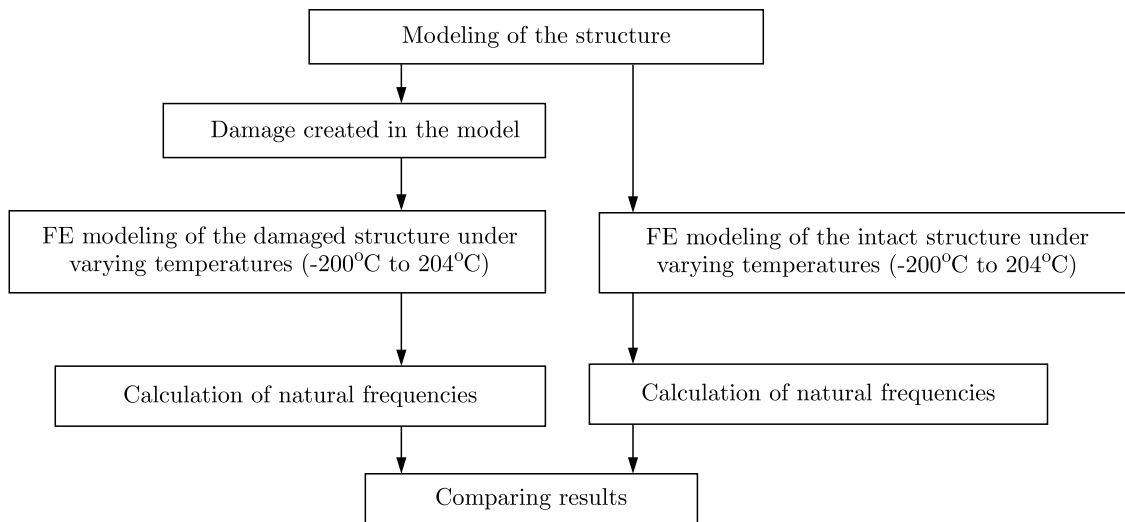


Fig. 2. Flowchart of the evolution effect of temperature changes on the natural frequency responses of the undamaged structure

4.1. Evaluation of the effect of multiple defects on natural frequencies

A 3-D FE model of the 6063 aluminum alloy beam has been created using ABAQUS (see Fig. 3). The overall dimensions of the beam are $400\text{ mm} \times 40\text{ mm} \times 0.16\text{ mm}$. The material properties are listed in Table 1. The clamped end of the beam has no rotation or displacement in any direction (see Fig. 4). Finally, the model is analysed with a frequency step, and the natural frequency responses for 10 modes are obtained from the results. As shown in Fig. 5, in order to investigate the effect of multiple defects on natural frequencies, several damage scenarios are simulated. Two types of damages are simulated (Table 2) and each is introduced using different extents to investigate the effect of multiple defects on natural frequencies. Free meshing is more suitable on the damaged section, thus free meshing with triangular and tetrahedral elements is utilized (see Fig. 6). The elements type, the total number of elements and nodes for the undamaged model and damage scenarios that are created in the model are shown in Table 3. In each step, the damaged model is analysed with a frequency step of the natural frequency responses

for 10 modes obtained from the results. Figure 7 shows the results of calculating the structural response to various damage cases to investigate the effect of multiple defects on natural frequencies. As shown in Fig. 7, when damages are created in the structure, the natural frequency responses of the 6063 aluminum alloy beam significantly decrease. The results show that the damage decreases the natural frequency of the structure.

Table 1. Material properties of the 6063 aluminum alloy beam

Density ρ [g/cc]	Poisson's ratio ν [-]	Modulus of elasticity E [GPa]
2.7	0.33	68.9

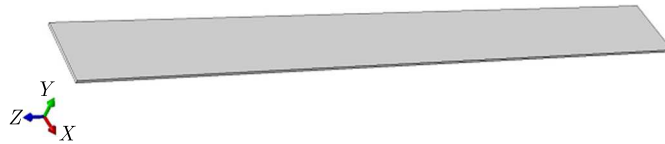


Fig. 3. A FE model of the beam created using ABAQUS



Fig. 4. Boundary conditions

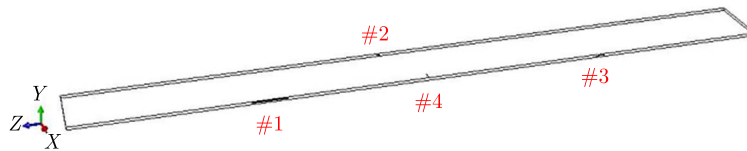


Fig. 5. Location of damages in the model



Fig. 6. Free meshing technique with linear tetrahedral and hexahedral elements

Table 2. Introduced damage types to investigate the effect of multiple defects on the natural frequency

Damage	Description	Dimensions [mm]	Location [mm]
#1	delamination in the beam	$20 \times 0.06 \times 1$	100-120
#2	delamination in the beam	$2 \times 0.02 \times 0.5$	180-182
#3	delamination in the beam	$5 \times 0.02 \times 0.077$	300-305
#4	transverse crack in the beam	$0.02 \times 0.17 \times 5$	200-200.02

Table 3. The type of elements, the total number of elements and nodes for undamaged model and damage scenarios that were created in the model

Structure status	Total number of nodes	Total number of elements	Type of elements
Undamaged model	49323	32000	linear hexahedral elements of type C3D8R
Damage scenario #1	49838	195122	linear tetrahedral elements of type C3D4
Damage scenario #2	98536	383130	linear tetrahedral elements of type C3D4
Damage scenario #3	147420	572781	linear tetrahedral elements of type C3D4
Damage scenario #4	196712	763944	linear tetrahedral elements of type C3D4

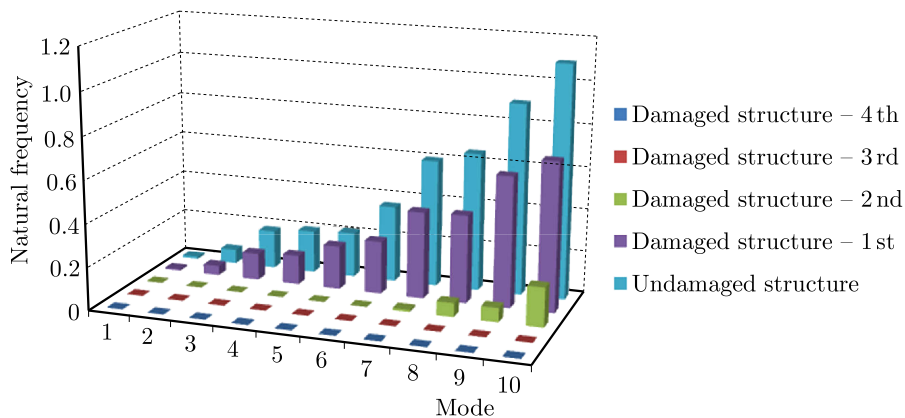


Fig. 7. Effect of multiple defects on natural frequency responses of the 6063 aluminum alloy beam

4.2. Investigation of the effect of temperature changes on natural frequencies

The investigation of the effect of temperature changes on natural frequencies is presented in this Section. For the purpose of this investigation, two types of scenarios are simulated to identify the effect of temperature changes on the natural frequencies (Table 4). The first type of scenario,

Table 4. Introduced damage types to investigate the effect of temperature changes on the natural frequency

Structure status	Description
First type of scenario: undamaged model #1	intact structure, investigate at -200°C to 204°C
Second type of scenario: damaged model #2	damaged structure with transverse crack, investigate at -200°C to 204°C

the intact model, is analysed with some frequency step, and the natural frequency responses for 10 modes are obtained. For the second type of scenario, a transverse crack is created on the model (see Fig. 8). The size of the transverse crack is $5\text{ mm}\times 0.17\text{ mm}\times 0.02\text{ mm}$, and is located at a distance of 200 mm to 200.02 mm from the fixed end. Then, the damaged model is analysed and the natural frequency responses for 10 modes are obtained. Tables 5 and 6 show respectively the

results of calculation of the undamaged and damaged structural response to various temperature cases presenting the effect of temperature on the natural frequency. Figures 9 and 10 respectively show the effect of temperature changes on natural frequency responses pertaining to undamaged and damaged structures. The results show that as temperature of the structure increases, the natural frequencies responses of the structure decrease.

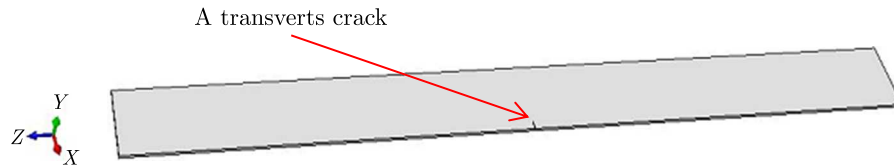


Fig. 8. Transverse crack created in the model

Table 5. Effect of temperature changes on the natural frequency responses of the undamaged structure

Mode	Natural frequencies ω [rad/s] and corresponding temperatures t [°C]						
	-200°C	-129°C	-73°C	21°C	93°C	149°C	204°C
	ω [rad/s]	ω [rad/s]	ω [rad/s]	ω [rad/s]	ω [rad/s]	ω [rad/s]	ω [rad/s]
1	0.00747343	0.00742029	0.00731643	0.00719205	0.0069961	0.00684871	0.00665982
2	0.0468166	0.0464838	0.0458331	0.045054	0.0438264	0.042903	0.0417199
3	0.131184	0.130251	0.128428	0.126245	0.122805	0.120218	0.116903
4	0.143114	0.142097	0.140108	0.137726	0.133974	0.131151	0.127534
5	0.212142	0.210634	0.207686	0.204156	0.198593	0.194408	0.189047
6	0.257473	0.255643	0.252064	0.247780	0.241028	0.235950	0.229443
7	0.426512	0.423480	0.417552	0.410455	0.399271	0.390858	0.380080
8	0.431727	0.428658	0.422657	0.415473	0.404153	0.395637	0.384727
9	0.638622	0.634082	0.625206	0.614579	0.597833	0.585236	0.569098
10	0.727410	0.722239	0.712130	0.700025	0.680951	0.666603	0.648221

Table 6. Effect of temperature changes on the natural frequency responses of the damaged structure

Mode	Natural frequencies ω [rad/s] and corresponding temperatures t [°C]						
	-200°C	-129°C	-73°C	21°C	93°C	149°C	204°C
	ω [rad/s]	ω [rad/s]	ω [rad/s]	ω [rad/s]	ω [rad/s]	ω [rad/s]	ω [rad/s]
1	0.0111536	0.0110743	0.0109193	0.0107337	0.0104412	0.0102212	0.00993934
2	0.0699099	0.0694129	0.0684413	0.0672779	0.0654448	0.0640658	0.0622991
3	0.195750	0.194358	0.191637	0.188380	0.183247	0.179386	0.174439
4	0.212484	0.210973	0.208020	0.204484	0.198912	0.194721	0.189352
5	0.224307	0.222713	0.219595	0.215862	0.209981	0.205556	0.199888
6	0.383982	0.381252	0.375916	0.369526	0.359457	0.351883	0.342180
7	0.634711	0.630199	0.621377	0.610815	0.594172	0.581652	0.565613
8	0.676172	0.671365	0.661967	0.650715	0.632985	0.619647	0.602560
9	0.948804	0.942059	0.928872	0.913084	0.888204	0.869489	0.845512
10	1.13783	1.12974	1.11393	1.09499	1.06516	1.04271	1.01396

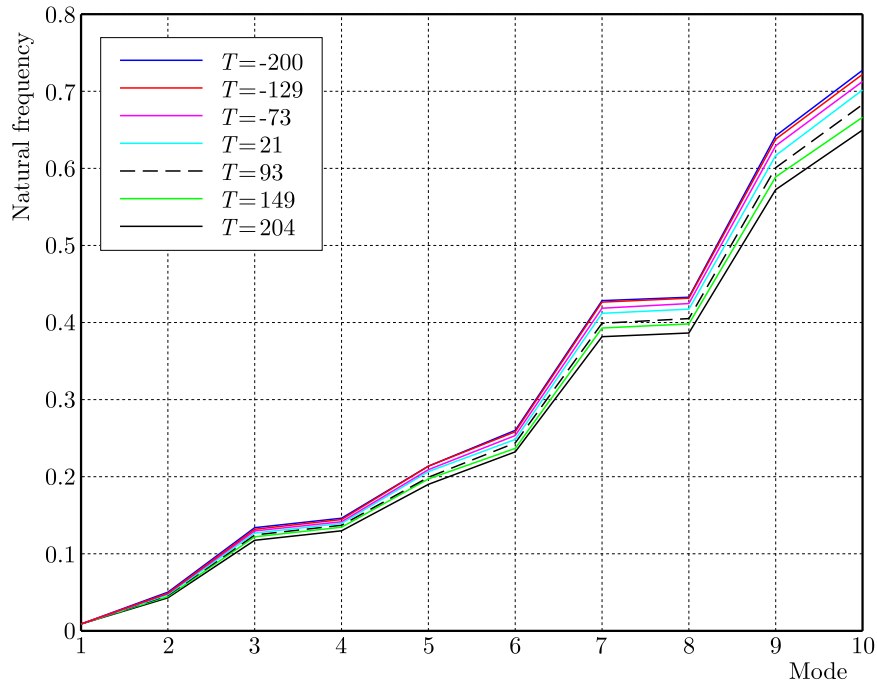


Fig. 9. Effect of temperature changes on the natural frequency for the undamaged structure

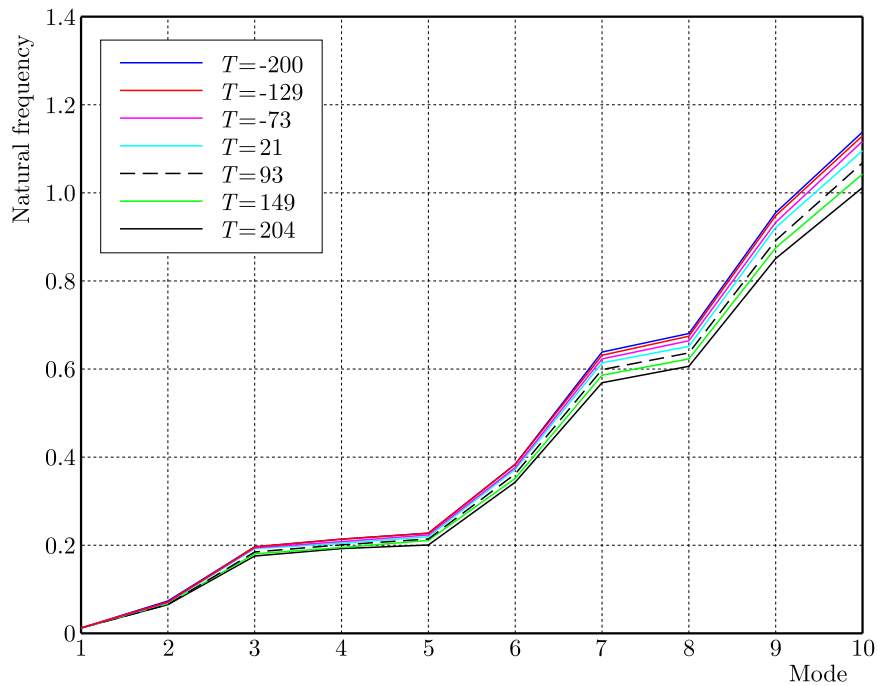


Fig. 10. Effect of temperature changes on the natural frequency for the damaged structure

5. Conclusion

This paper reviews multiple defects and the temperature effect on variations in modal properties of the structure. This is the first study of evaluation of the effect of temperature changes and multiple damages on the natural frequency at the same time. The variations in the frequency are analysed in simulation by using an aluminum specimen obtaining impedance signatures at temperatures ranging from -200°C to 204°C . The results show that an increase in temperature

leads to a decrease in the structural frequency, and that a decrease in temperature leads to an increase in the structural frequency. Therefore, temperature effects are a critical problem for structural health monitoring based on vibration responses, especially in detecting low damage levels. Efficient compensatory methods for temperature effects remain to be developed. The evaluation of the effect of multiple defects on the natural frequency shows that when damages are created in the structure, there is a significant decrease in natural frequency responses of the 6063 aluminum alloy beam. The results show that damage causes a decrease in the natural frequency of the structure. This study highlights the importance of application of simulation methods to the evaluation the effect of changes in environmental temperature and multiple damages on dynamic characteristics, such as natural frequencies and mode shapes, especially taking place at the same time.

References

1. ARUN K., GUPTA, MAMTA J., 2014, Exponential temperature effect on frequencies of a rectangular plate of non-linear varying thickness: a quintic spline technique, *Journal of Theoretical and Applied Mechanics*, **52**, 1, 15-24
2. BLEVINS R.D., 1979, *Formulas for Natural Frequency and Mode Shape*, Van Nostrand Reinhold, New York
3. DEROECK G., PEETERS B., MAECK J., 2000, Dynamic monitoring of civil engineering structures. Computational methods for shell and spatial structures, *IASS-IACM*, Athens, Greece
4. FARRAR C.R., DOEBLING S.W., CORNWELL P.J., STRASER E.G., 1997, Variability of modal parameters measured on the Alamosa Canyon Bridge, *Proceedings of 15th International Modal Analysis Conference*, Orlando, USA, 1997, 257-263
5. HARAK S.S, SHARMA S.C., SHUKLA S., GUPTA P., KUMAR S., HARSHA S.P., 2015, Effect of multiple location defects on the dynamics of draft gear used in freight railway wagon, *International Journal of Vehicle Structures and Systems*, **7**, 3, 107-113
6. HU W.H., MOUTINHO C., DE SA CAETANO E., MAGALHÃES F., CUNHA A.A.M.F, 2012, Continuous dynamic monitoring of a lively footbridge for serviceability assessment and damage detection, *Mechanical Systems and Signal Processing*, **33**, 38-55
7. KARAAĞAÇ C., ÖZTURK H., SABUNCU M., 2009, Free vibration and lateral buckling of a cantilever slender beam with an edge crack: experimental and numerical studies, *Journal of Sound and Vibration*, **326**, 235-250
8. MERUANE V., HEYLEN W., 2012, Structural damage assessment under varying temperature conditions, *Structural Health Monitoring*, **11**, 3, 345-357
9. MORAGASPITIYA P.H.N., THAMBIRATNAM D.P., PERERA N.J., CHAN T.H.T., 2013, Development of a vibration based method to update axial shortening of vertical load bearing elements in reinforced concrete buildings, *Engineering Structures*, **46**, 49-61
10. PEETERS B., DEROECK G., 2001, One-year monitoring of the Z24-Bridge: environmental effects versus damage events, *Earthquake Engineering and Structural Dynamics*, **30**, 149-171
11. RALBOVSKY M., DEIX S., FLESCH R., 2010, Frequency changes in frequency-based damage identification, *Structure and Infrastructure Engineering*, **6**, 611-619
12. RALBOVSKY M., SANTOS J., KWAPISZ M., DALLINGER S., CATARINO J.M., 2014, Damage detection based on structural response to temperature changes and model updating, *7th European Workshop on Structural Health Monitoring*, July 8-11, La Cité, Nantes, France
13. SAYMAN O.M., TOYGAR E., KIRAL Z., KIRAL B.G., 2013, Effect of the root crack on natural frequency of sandwich composite beams, *Pamukkale Üniversitesi Mühendislik Bilimleri Dergisi*, **19**, 7, 298-302

14. XIA Y., CHEN B., WENG S., NI Y.-Q., XU Y.-L., 2012, Temperature effect on vibration properties of civil structures: a literature review and case studies, *Journal of Civil Structural Health Monitoring*, **2**, 29-46
15. XU Z.-D., WU Z., 2007, Simulation of the effect of temperature variation on damage detection in a long-span cable-stayed bridge, *Structural Health Monitoring*, **6**, 177-189, DOI: 10.1177/1475921707081107

Manuscript received November 3, 2016; accepted for print January 18, 2017

LINEAR FREE VIBRATION OF GRAPHENE SHEETS WITH NANOPORE VIA AIFANTIS THEORY AND RITZ METHOD

SIMA ZIAEE

Yasouj University, Mechanical Engineering Department, Yasouj, Iran
e-mail: ziaee@yu.ac.ir

This article aims to study the natural frequency of defective graphene sheets since the existence of cut-outs in plates may be essential on the basis of their desired functionality. A combination of the Aifantis theory and Kirchhoff thin plate hypothesis is used to derive governing equations of motion. The Ritz method is employed to derive discrete equations of motion. The molecular structural mechanics method is also employed to specify the effective length scale parameter. In the ‘numerical results’ Section, the effects of different parameters such as boundary conditions and diameter of the hole-to-side length ratio on the fundamental frequency of graphene sheets are studied.

Keywords: free vibration, defective graphene sheet, Aifantis theory, molecular structural mechanics

1. Introduction

Graphene sheets, the two-dimensional carbon nanostructure, amazingly exhibit the electrical, mechanical, thermal and optical properties (Jomehzadeh *et al.*, 2015) that have been considered as a promising material for a wide range of applications (Lebedeva *et al.*, 2012) such as composites, chemical sensors, ultra capacitors, transparent electrodes, photovoltaic cells, bio-devices (Zandiatashbar *et al.*, 2014) and the gigahertz oscillator suggested based on the telescopic oscillation of graphene layers (Lebedeva *et al.*, 2012). It is of great importance to simulate mechanical behavior of single/multi-layered graphene sheets accurately due to this wide scope of applications. One important topic which has recently received great attention is the study of free and forced vibration of graphene sheets used in nano-scale devices which may experience vibration.

Among different theoretical modelings used to simulate carbon nano-structures, continuum mechanics modeling and molecular structural mechanics (MSM) methods are the most popular ones employed to study the mechanical behavior of carbon nanostructures because their computational tasks are much more time-effective than different atomistic modeling such as classical molecular dynamics, tight-binding molecular dynamics and density functional theory (Li and Chou, 2003; Hu *et al.*, 2007). The linear vibration of zigzag and armchair single-layered graphene sheets (SLGS) was studied by Sakhaee-Pour *et al.* (2008) via the MSM approach. They obtained fundamental frequencies and corresponding mode shapes for different boundary conditions and showed that the natural frequencies of SLGS are independent of chirality and aspect ratio (Sakhaee-Pour *et al.*, 2008), while the Hashemnia *et al.* study (2009) indicated that the fundamental frequency of SLGS with fixed-fixed or fixed-free end conditions decreased as the aspect ratio increased. They proposed the use of graphene sheets with a lower aspect ratio to prevent resonance and dynamic damage (Hashemnia *et al.*, 2009). Gupta and Batra (2010) implemented MSM simulation to investigate the effect of pretention on the natural frequencies of SLGS. The comparison between the results obtained by the MSM method and those predicted by an equivalent linear elastic isotropic continuum model showed that there was a noticeable

difference between the mode shapes corresponding to the several lowest frequencies of the SLGS and those of an equivalent linear elastic isotropic continuum model (Gupta and Batra, 2010). Sadeghi and Naghdabadi (2010) introduced a hybrid atomistic structural element to model the nonlinear behavior of SLGS. Their results verified with experimental observations demonstrated that natural frequencies predicted by nonlinear analysis were far higher than those obtained by the linear approach. Wang *et al.* (2013) proposed a pseudo beam model with 3-node beam element to simulate the modal behavior of the wrinkled SLGS by using the MSM method. They not only obtained the features of formation and evolution of wrinkles but also offered a prediction model to estimate the natural frequency of wrinkle SLGS (Wang *et al.*, 2013).

The importance of incorporating the size effect into continuum mechanics, in order to investigate the mechanical behavior of micro- or nano-scale devices, is well known and higher-order continuum theories containing additional material constants have been developed to this end (Askes and Aifantis, 2011). Mindlin (1964) developed a theory of elasticity with microstructure in which strain energy was considered as a function of macroscopic strain, the difference between macroscopic and microscopic deformation and the gradient of the microscopic deformation. In this theory, the strain energy contained 16 constitutive coefficients in addition to Lamé's constants. Mindlin wrote the kinetic energy density in terms of quantities at microscale and macroscale as well (Askes and Aifantis, 2011). Mindlin also simplified this theory and introduced three new versions which differed in the assumed relation between the microscopic deformation gradient and the macroscopic displacement (Mindlin, 1964; Askes and Aifantis, 2011). The Mindlin simplified theory in which strain energy is only a function of first-order gradient of strain tensor contains five new constants as well as Lamé's constants for an isotropic linear elastic material (Mindlin, 1964; Askes and Aifantis, 2011). It can be shown that these five new constants can be grouped in two new constants (Askes and Aifantis, 2011). In this way, the number of new material constants is reduced from 5 down to 2 (Askes and Aifantis, 2011). A simplified kinetic energy whose constitutive equation consists of velocity and velocity gradient was also suggested by Mindlin (1964). Therefore, Mindlin's simplified theory contains one additional inertia parameter as well as two additional elastic parameters (Askes and Aifantis, 2011).

Lam *et al.* (2003) proposed a modified strain gradient theory in which three new length scale parameters were introduced into isotropic linear elastic materials. In this theory, the total deformation energy density is independent of the anti-symmetric rotation gradient tensor and it is only a function of the symmetric strain tensor, the dilatation gradient vector, the deviatoric stretch gradient tensor and the symmetric rotation gradient tensor (Lam *et al.*, 2003).

The other well-known higher-order continuum theories are classical couple stress theory (Mindlin and Tiersten, 1962) with two material length scale parameters for an isotropic elastic material, and the modified couple stress theory (Yang *et al.*, 2002) whose modified constitutive equation contains only a new length scale parameter. It can be shown that the modified couple stress theory is a special case of the modified strain gradient elasticity theory if two of the three material length scale parameters of the modified strain gradient theory are taken to be equal to zero (Ashoori Movassagh and Mahmoodi, 2013).

On the basis of Aifantis' studies in plasticity and nonlinear elasticity, Aifantis and his coworkers proposed another gradient elasticity theory, the constitutive equation of which is a function of strain and Laplacian of strain with one internal length (Aifantis, 1992; Altan and Aifantis, 1997). It can be shown that the associated equilibrium equations obtained by simplified Mindlin's theory can be converted to those obtained by the Aifantis gradient elasticity theory if two new elastic parameters of simplified Mindlin's theory are taken to be equal to each other (Askes and Aifantis, 2011).

Another powerful gradient elasticity theory proposed to simulate dynamical behavior of micro/nano structures is achieved by combining stable strain gradients with acceleration (inertia) gradients (Askes and Aifantis, 2011) such as Mindlin's simplify theory. Metrikine and Askes

(2002, 2006) derived such a theory from a discrete lattice. It is worth mentioning that these theories known as dynamically consistent models (Askes and Aifantis, 2011), incorporate at least two length scales: one of them related to strain gradients and another related to acceleration (inertia) gradients.

The nonlocal strain gradient theory is another Laplacian based gradient elasticity whose constitutive equation is a function of strain, stress, Laplacian of strain and Laplacian of stress (Askes and Aifantis, 2011; Aifantis, 2011).

Many researchers employed different gradient elasticity theories mentioned above in conjunction with different classical continuum mechanic theories to study the mechanical behavior of size-dependent micro/nanostructures so far (Ansari *et al.*, 2011, 2013; Reddy, 2011; Rahmani and Pedram, 2014; Akgöz and Civalek, 2012, 2014, 2015; Gholami *et al.*, 2016; Binglei *et al.* 2011, 2016; Askes and Aifantis, 2009; Şimşek, 2016; Ebrahimi *et al.*, 2016; Li and Hu, 2016).

On the basis of the strain gradient Timoshenko beam theory, the free vibration characteristics of functionally graded microbeams were investigated by Ansari *et al.* (2011). Ansari *et al.* (2013) also combined the most general strain gradient elasticity theory containing five additional material length scale parameters with the classical Timoshenko beam theory to investigate bending and buckling of functionally graded microbeams. Akgöz and Civalek (2014) proposed a new size-dependent trigonometric beam model based on the strain gradient theory. They (Akgöz and Civalek, 2014) employed their new model to estimate load-bearing capacity of microbeams. A new size-dependent sinusoidal plate model to predict mechanical behavior of thin, moderately thick and thick microplate was suggested by Akgöz and Civalek (2015) as well. They employed a modified strain gradient elasticity hypothesis to incorporate the size effect into the classical continuum plate theory. In an earlier work, Akgöz and Civalek (2012) estimated vibratory behavior of single-layered graphene sheets embedded in an elastic matrix. To this end, they used the Kirchhoff plate hypothesis in conjunction with the modified couple stress theory to develop governing equations of motion (Akgöz and Civalek, 2012).

Gholami *et al.* (2016) combined Mindlin's simplified theory hypothesis with first-order shear deformation shell theory to investigate free vibration and axial buckling of circular cylindrical micro-/nano-shells. They ignored the effects of inertia gradients in their model and derived the kinetic energy in terms of macroscopic kinematic quantities. They compared three different size-dependent shell models on the basis of strain gradient theory, modified strain gradient theory, and modified couple stress theory in predicting the natural frequency and load-bearing capacity of microshells as well. They showed that the values of natural frequency and the critical buckling force predicted by the strain gradient theory are higher than those predicted by the modified strain gradient theory because of inducing a higher stiffness. Binglei *et al.* (2011) simulated static bending, static instability and vibratory behavior of a simply-supported micro-plate via the modified strain gradient theory and the modified couple stress theory. Their results clearly show that the strain gradient theory induces a higher stiffness than the modified couple stress theory. They (Binglei *et al.*, 2016) re-derived the governing equation of the nonclassical Kirchhoff micro-plate as well as the general boundary conditions based on the strain gradient elasticity to simulate mechanical behavior of a micro-plate with any reasonable boundary conditions.

Askes and Aifantis (2009) employed a dynamically consistent model with two length scales to simulate flexural wave dispersion in carbon nanotubes. They verified validity of the proposed model by comparing their findings with those obtained via molecular dynamics simulation and/or Eringen's nonlocal elasticity theory.

Using nonlocal strain gradient elasticity, Li and Hu (2016) developed a model to analyze wave propagation in fluid-conveying carbon nanotubes. They investigated the effects of different parameters such as nonlocal parameter, small scale parameter, damping coefficient and flow velocity on wave propagation properties of fluid-conveying carbon nanotubes.

The other well-known gradient theory is Eringen's nonlocal elasticity theory in which there is only one length scale parameter and its constitutive equation is expressed based on the nonlocal stress tensor and Laplacian stress tensor (Askes and Aifantis, 2011). Eringen's nonlocal elasticity is widely employed to simulate mechanical behavior of carbon nano-structures because of being a good agreement between obtained results via Eringen's theory and molecular dynamics simulation. Murmu and Pradhana (2009) employed a nonlocal elasticity theory to investigate the vibrational behavior of SLGS. Numerical results clearly revealed that the small scale value could affect the fundamental frequencies of SLGS significantly (Murmu and Pradhana, 2009). Shen *et al.* (2010) employed a nonlocal orthotropic plate model which contained small scale effects to simulate nonlinear vibration behavior of SLGS in thermal environment. They used temperature-dependent material properties obtained by molecular dynamic simulation. To estimate the value of the small-scale parameter, they reconciled the natural frequencies of graphene sheets obtained via molecular dynamics (MD) simulation with those predicted by the nonlocal plate model (Shen *et al.*, 2010). Their results clearly showed the significant impact of vibration amplitude and temperature change on the nonlinear vibration response of both armchair and zigzag graphene sheets (Shen *et al.*, 2010). Ansari *et al.* (2010) employed the nonclassical Mindlin plate theory to study the vibrational behavior of SLGS. To incorporate the size effect into the continuum plate model, they used Eringen's nonlocal elasticity theory. Matching the results obtained from MD simulation with those taken from the nonlocal model, they determined the proper value of the nonlocal parameter. They showed that the nonlocal parameter depends on chirality and boundary conditions. Using nonlocal elasticity, Farajpour *et al.* (2011) estimated the load-bearing capacity of circular graphene sheet subjected to uniform radial compression. To study the vibratory behavior of annular and circular graphene sheet in thermal environment, Mohammadi *et al.* (2014) employed Eringen's theory. They investigated the effect of different parameters such as elastic medium, boundary conditions and small scale parameter on the natural frequencies of circular and annular graphene sheets. Farajpour *et al.* (2012) estimated load-bearing capacity of a rectangular single-layered graphene sheet by combining the nonlocal elasticity theory with Kirchhoff's plate hypothesis as well as orthotropic material stress-strain relations.

Although there have been numerous studies carried out on the simulation of vibrational behavior of perfect graphene sheets, the notable studies shown that the effects of nanopores on linear and/or nonlinear vibration responses of graphene sheets do not exist, while the existence of nanopores in the graphene lattice can be essential based upon the desired functionality of graphene sheets in different nano-devices such as bio-devices and the DNA-decorated graphene (Zandiatashbar *et al.*, 2014). On the other hand, the production process used or environmental and operating conditions under which the graphene device operates can lead to the appearance of vacancy defects in the graphene lattice (Zandiatashbar *et al.*, 2014). Therefore, simulation of the dynamic response of graphene sheets with nanopores to determine how the size, the position and the shape of cut-outs influence the natural frequencies is important. Accordingly, the main purpose of this study is to model the dynamic response of SLGS with cut-outs. Different methods, such as Ritz, finite difference and finite element can be employed to this end. Rajamani and Prabhakaran (1977) used Lagrange's equations to obtain discrete equations of motion of a composite plate with a central cut-out. For this purpose, they employed potential energy and kinetic energy of a uniform plate and considered the cut-out as a displacement-dependent external loading on the plate (Rajamani and Prabhakaran, 1977). The finite difference method was used by Aksu and Ali (1976) to determine vibration characteristics of rectangular plates with one or two central cut-outs. To develop a simple method to study the effects of the rectangular cut-out on natural frequencies of rectangular plates, Ali and Atwal (1980) used Rayleigh's method and employed trigonometric functions to estimate the lateral deflection. They showed that this method can predict the fundamental frequency with a quite good accuracy although the accu-

racy could be increased if one added a correction function to the estimated lateral displacement function (Ali and Atwal, 1980). Lam *et al.* (1989) presented a modification of the Rayleigh-Ritz method to investigate the vibrational behavior of rectangular plates with one or two cut-outs. They used an orthogonal polynomial function generated based on the Gram-Schmidt process to estimate the lateral displacement of plate segments (Lam *et al.*, 1989). Similar methods were used by Liew *et al.* (2003) to investigate the effect of different boundary conditions on vibrational behavior of a rectangular plate with the central rectangular cut-out. The negative stiffness method was applied to analyze free vibration and buckling of plates with cut-outs by Tham *et al.* (1986).

One of the popular variational methods employed to derive discrete equations of motion is the Ritz method because the displacement field is approximated by a linear combination of shape functions which are only satisfied by essential boundary conditions. On the other hand, it is shown that one can reduce the complexity of the mechanical behavior modelling of structures with cut-outs by combining the construction of energy functional with the Ritz method (Malekzadeh *et al.*, 2013). Therefore, in this study, the Ritz method is employed to derive discrete equations of motion which yield the eigenvalue problem. Because Eringen's nonlocal elasticity theory does not allow the construction of energy functional (Reddy, 2011), the dynamic consistent model is used to simulate vibrational behavior of the graphene sheet with a nanopore. To this end, Aifantis' theory, as well as inertia gradients is combined with Kirchhoff's thin plate hypothesis to construct the energy functional and incorporate the size effect into the classical continuum plate model. Also, the length scales related to strain gradients and inertia gradients are set equal to each other. The molecular structural mechanics method is also used to simulate vibrational behavior of defective SLGS to estimate the length scale parameter which must be used in the proposed nonclassical plate model.

2. Governing equation

2.1. Nonclassical thin plate theory

According to Hamilton's principle, one can formulate discretized free vibration equations of a nano-plate with free edges cut-out via the Ritz method. The Aifantis theory in conjunction with inertia gradients is also used to incorporate the size effect into the equation governing natural frequencies of the nano-plate with the cut-out. For this reason, the variation of strain energy and kinetic energy can be written as

$$\begin{aligned} \delta PE &= \int_{V_I} (\sigma_{ij} \delta \varepsilon_{ij}^L) dV - \int_{V_{II}} (\sigma_{ij} \delta \varepsilon_{ij}^L) dV \\ \delta KE &= \int_{V_I} [\rho \dot{u} \delta \dot{u} + \rho \dot{v} \delta \dot{v} + \rho \dot{w} \delta \dot{w} + \rho l_1^2 (\dot{u}_{,i} \delta \dot{u}_{,i} + \dot{v}_{,i} \delta \dot{v}_{,i} + \dot{w}_{,i} \delta \dot{w}_{,i})] dV \\ &\quad - \int_{V_{II}} [\rho \dot{u} \delta \dot{u} + \rho \dot{v} \delta \dot{v} + \rho \dot{w} \delta \dot{w} + \rho l_1^2 (\dot{u}_{,i} \delta \dot{u}_{,i} + \dot{v}_{,i} \delta \dot{v}_{,i} + \dot{w}_{,i} \delta \dot{w}_{,i})] dV \end{aligned} \quad (2.1)$$

where σ_{ij} , ε_{ij}^L and l_1 are components of the stress tensor, linear strain tensor and length scale related to inertia gradients, respectively. V_i ($i = I, II$) is the volume of i -th segment of the plate. The displacement field is shown by u , v and w . ρ is the specific mass density of the plate material and the time derivative of displacements are shown by overhead dot. According to the classical plate theory hypothesis, if the xy -plane of the Cartesian coordinate system (x, y, z) coincides with the geometrical mid-plane of the undeformed rectangular micro-/nano-plate, the displacement field can be expressed as (Reddy, 1999)

$$\begin{aligned} u(x, y, z, t) &= u_0(x, y, t) - z \frac{\partial w(x, y, t)}{\partial x} & v(x, y, z, t) &= v_0(x, y, t) - z \frac{\partial w(x, y, t)}{\partial y} \\ w(x, y, z, t) &= w(x, y, t) \end{aligned} \quad (2.2)$$

where u_0 and v_0 are the x - and y -components of the displacement vector of a point in the mid-plane of the plate at time t , respectively.

According to the classical plate theory hypothesis, the linear components of the strain tensor can be found on the basis of Eqs. (2.2) (Reddy, 1999)

$$\begin{aligned} \varepsilon_{xx}^L &= \frac{\partial u_0}{\partial x} - z \frac{\partial^2 w}{\partial x^2} & \varepsilon_{yy}^L &= \frac{\partial v_0}{\partial y} - z \frac{\partial^2 w}{\partial y^2} \\ \varepsilon_{xy}^L &= \varepsilon_{yx}^L = \frac{1}{2} \left(\frac{\partial v_0}{\partial x} + \frac{\partial u_0}{\partial y} - 2z \frac{\partial^2 w}{\partial x \partial y} \right) \end{aligned} \quad (2.3)$$

According to Aifantis' theory, the stress tensor components are related to the linear strain tensor components as (more details can be found in Aifantis (1992, 2011), Askes and Aifantis (2011), Gitman *et al.* (2005))

$$\sigma_{ij} = C_{ijkl}(\varepsilon_{kl} - l^2 \varepsilon_{kl,mm}) \quad (2.4)$$

which can be obtained on the basis of the implicit gradient elasticity model given by

$$\text{tr}(\alpha_1 \boldsymbol{\varepsilon} + \alpha_2 \boldsymbol{\sigma}) \mathbf{1} + \alpha_3 \boldsymbol{\varepsilon} + \alpha_4 \boldsymbol{\sigma} + \nabla^2 [\text{tr}(\alpha_5 \boldsymbol{\varepsilon} + \alpha_6 \boldsymbol{\sigma}) \mathbf{1} + \alpha_7 \boldsymbol{\varepsilon} + \alpha_8 \boldsymbol{\sigma}] = 0$$

through a proper choice of the constants $\alpha_1, \dots, \alpha_8$ (Aifantis, 2011). \mathbf{C} can be defined based on the classical plate theory hypothesis as

$$\mathbf{C} = \begin{bmatrix} \frac{E}{1-\nu^2} & \frac{E\nu}{1-\nu^2} & 0 \\ \frac{E\nu}{1-\nu^2} & \frac{E}{1-\nu^2} & 0 \\ 0 & 0 & G \end{bmatrix} \quad (2.5)$$

where E , G and ν are the modulus of elasticity, modulus of rigidity and Poisson's ratio, respectively. l is the length scale parameter related to strain gradients.

By substituting Eqs. (2.2) to (2.5) into Eqs. (2.1), one can find the variation of strain energy and kinetic energy on the basis of the displacement field. By using the appropriate approximation of dependent unknowns (u_0, v_0, w) satisfying the essential boundary conditions and employing Hamilton's principle, one can find the following system of ordinary differential equations governing the lateral vibration of the plate. It is completely independent of the other two equations governing in-plane motion of the plate

$$(M_{mnpq}^I - M_{mnpq}^{II}) \ddot{W}_{pq} + (K_{mnpq}^I - K_{mnpq}^{II}) W_{pq} = 0 \quad (2.6)$$

in which

$$\begin{aligned} M_{mnpq}^{I,II} &= \int_{V_I, V_{II}} \left[\frac{-1}{12} \rho h^3 \left(\frac{\partial \phi_p}{\partial x} \frac{\partial \phi_m}{\partial x} \varphi_q \varphi_n + \frac{\partial \varphi_q}{\partial y} \frac{\partial \varphi_n}{\partial y} \phi_p \phi_m \right) - \rho h \phi_p \varphi_q \phi_m \varphi_n \right] dx dy \\ &- l_1^2 \int_{V_I, V_{II}} 2\rho h \left(\frac{\partial \phi_p}{\partial x} \frac{\partial \phi_m}{\partial x} \varphi_q \varphi_n + \frac{\partial \varphi_q}{\partial y} \frac{\partial \varphi_n}{\partial y} \phi_p \phi_m \right) dx dy \\ &- l_1^2 \int_{V_I, V_{II}} \frac{1}{12} \rho h^3 \left(\frac{\partial^2 \phi_p}{\partial x^2} \frac{\partial^2 \phi_m}{\partial x^2} \varphi_q \varphi_n + \frac{\partial^2 \varphi_q}{\partial y^2} \frac{\partial^2 \varphi_n}{\partial y^2} \phi_p \phi_m + 2 \frac{\partial \phi_p}{\partial x} \frac{\partial \phi_m}{\partial x} \frac{\partial \varphi_q}{\partial y} \frac{\partial \varphi_n}{\partial y} \right) dx dy \end{aligned} \quad (2.7)$$

and

$$\begin{aligned}
 K_{mnpq}^{I,II} = & \int_{V_I, V_{II}} \left[-D \left(\frac{\partial^2 \phi_p}{\partial x^2} \varphi_q + \nu \frac{\partial^2 \varphi_q}{\partial y^2} \phi_p \right) \frac{\partial^2 \phi_m}{\partial x^2} \varphi_n \right. \\
 & - D \left(\frac{\partial^2 \varphi_q}{\partial y^2} \phi_p + \nu \frac{\partial^2 \phi_p}{\partial x^2} \varphi_q \right) \frac{\partial^2 \varphi_n}{\partial y^2} \phi_m - [2D(1 - \nu)] \frac{\partial^2 (\phi_p \varphi_q)}{\partial x \partial y} \frac{\partial^2 (\phi_m \varphi_n)}{\partial x \partial y} \left. \right] dx dy \\
 & - l^2 \int_{V_I, V_{II}} \left[-D \left(\frac{\partial^4 \phi_p}{\partial x^4} \varphi_q + (1 + \nu) \frac{\partial^2 \varphi_q}{\partial y^2} \frac{\partial^2 \phi_p}{\partial x^2} + \nu \frac{\partial^4 \varphi_q}{\partial y^4} \phi_p \right) \frac{\partial^2 \phi_m}{\partial x^2} \varphi_n \right. \\
 & - D \left(\frac{\partial^4 \varphi_q}{\partial y^4} \phi_p + (1 + \nu) \frac{\partial^2 \phi_p}{\partial x^2} \frac{\partial^2 \varphi_q}{\partial y^2} + \nu \frac{\partial^4 \phi_p}{\partial x^4} \varphi_q \right) \frac{\partial^2 \varphi_n}{\partial y^2} \phi_m \\
 & \left. - [2D(1 - \nu)] \left(\frac{\partial^4 (\phi_p \varphi_q)}{\partial x^3 \partial y} + \frac{\partial^4 (\phi_p \varphi_q)}{\partial x \partial y^3} \right) \frac{\partial^2 (\phi_m \varphi_n)}{\partial x \partial y} \right] dx dy
 \end{aligned} \tag{2.8}$$

where $D = Eh^3/[12(1 - \nu^2)]$ and h is thickness of the plate. The Gram-Schmidt process is used to generate the polynomial functions $\varphi_n(y)$ ($\varphi_q(y)$) and $\phi_m(x)$ ($\phi_p(x)$) as well.

Equation (2.6) can be solved on the basis of the eigen-value problem to find the natural frequencies corresponding to lateral vibration of the nano-plate.

2.2. Molecular structural mechanics

The molecular structural mechanics approach has been built on the basis of some similarities between the molecular model of carbon nanostructures (nanotube and graphene sheet) and the structure of a space frame building (Li and Chou, 2003; Hu *et al.*, 2007; Sakhaee-Pour *et al.*, 2008; Hashemnia *et al.*, 2009; Gupta and Batra, 2010, Sadeghi and Naghdabadi, 2010; Wang *et al.*, 2013). In this method, the atomic lattice of carbon nanostructures is rebuilt by beams and point masses replacing C-C covalent bonds and carbon atoms, respectively (Li and Chou, 2003; Hu *et al.*, 2007; Sakhaee-Pour *et al.*, 2008; Hashemnia *et al.*, 2009; Gupta and Batra, 2010; Sadeghi and Naghdabadi, 2010; Wang *et al.*, 2013). To determine stiffness parameters of the equivalent beam, i.e., tensile stiffness (EA), bending stiffness (EI) and torsional rigidity (GJ), one can use the concepts of energy equivalence between the total potential energies in computational chemistry (Eq. (2.9)) and the total elemental strain energies in structural mechanics (Eq. (2.10)) (Li and Chou, 2003; Hu *et al.*, 2007; Sakhaee-Pour *et al.*, 2008; Hashemnia *et al.*, 2009; Gupta and Batra, 2010; Sadeghi and Naghdabadi, 2010; Wang *et al.*, 2013).

The total potential function among carbon atoms due to bonded and nonbonded interactions are (Li and Chou, 2003; Hu *et al.*, 2007; Sakhaee-Pour *et al.*, 2008; Hashemnia *et al.*, 2009; Gupta and Batra, 2010; Sadeghi and Naghdabadi, 2010; Wang *et al.*, 2013)

$$U_P = \sum U_r + \sum U_\theta + \sum (U_\varphi + U_\omega) + \sum U_{vdw} \tag{2.9}$$

in which U_r is the bond stretching, U_θ is the bond angle bending, U_φ is the dihedral angle torsion, U_ω is the out of plane torsion, U_{vdw} is the nonbonded van der Waals interaction and U_e is the nonbonded electrostatic interactions. On the other hand, the total strain energy for a beam element is (Li and Chou, 2003; Hu *et al.*, 2007; Sakhaee-Pour *et al.*, 2008; Hashemnia *et al.*, 2009; Gupta and Batra, 2010; Sadeghi and Naghdabadi, 2010; Wang *et al.*, 2013)

$$U_{SE} = \sum U_A + \sum U_M + \sum U_T + \sum U_V \tag{2.10}$$

where U_A is the strain energy of axial tension, U_M is the strain energy of bending, U_T is the strain energy of torsion and U_v is the strain energy of the shear force. One can obtain a relationship between the molecular mechanics force field constants and the structural mechanics parameters

by using the energy equivalence between Eq. (2.9) and Eq. (2.10) (Li and Chou, 2003; Hu *et al.*, 2007; Sakhaee-Pour *et al.*, 2008; Hashemnia *et al.*, 2009; Gupta and Batra, 2010; Sadeghi and Naghdabadi, 2010; Wang *et al.*, 2013) as follows

$$\frac{EA}{L} = k_r \quad \frac{EI}{L} = k_\theta \quad \frac{GJ}{L} = k_\tau \quad (2.11)$$

where k_r , k_θ and k_τ are force field constants in molecular mechanics.

On the basis of the previous research (Li and Chou, 2003; Hu *et al.*, 2007; Sakhaee-Pour *et al.*, 2008; Hashemnia *et al.*, 2009; Gupta and Batra, 2010; Sadeghi and Naghdabadi, 2010; Wang *et al.*, 2013), the following numerical values of the force field constants used in this research are selected

$$k_r = 65.2 \text{ nN}\text{\AA}^{-1} \quad k_\theta = 2.78 \text{ nN}\text{\AA}\text{rad}^{-2} \quad k_\tau = 2.78 \text{ nN}\text{\AA}\text{rad}^{-2} \quad (2.12)$$

Then, the diameter-to-length ratio of the beam element estimated by Eq. (2.11) shows that this element is too thick and must be modeled based on shear deformation beam theories.

Wang *et al.* (2013) used the study of Scarpa *et al.* (2009) who considered the C-C bond as a Timoshenko beam, to obtain the mechanical properties and optimized cross-section diameter of the equivalent beam element via the following relationships (Wang *et al.*, 2013)

$$d < 2\sqrt{6\frac{k_\theta}{k_r}} \quad E = \frac{k_r^2 L}{4\pi k_\theta} \quad G = \frac{k_\tau}{2k_\theta} \quad (2.13)$$

where k_θ is expressed as

$$k_\theta = \frac{k_r d^2}{16} \frac{4C_1 + C_2}{C_1 + C_2} \quad (2.14)$$

and (Wang *et al.*, 2013)

$$C_1 = 112L^2 k_\tau + 192L^2 k_\tau \nu + 64L^2 k_\tau \nu^2 \quad C_2 = 9k_r d^4 + 18k_r d^4 \nu + 9k_r d^4 \nu^2 \quad (2.15)$$

and L is length of the C-C bond. They obtained the diameter-to-length ratio of the equivalent Timoshenko beam around 0.704 (Wang *et al.*, 2013), which is used in this study.

Based on the finite element method and using modal analysis concepts, one can find the natural frequencies of this space frame-like structure constructed by Timoshenko beam elements and point masses.

3. Verification

3.1. Non-classical thin plate theory

Based on the best knowledge of the author, it is the first attempt to analyze the vibrational behavior of graphene sheets with nanopores via Aifantis' theory combined with acceleration (inertia) gradients and the Ritz method. Then, to verify the correctness of the presented model, the author first compares the obtained natural frequencies of classical thin plates with central holes with those obtained based on the finite element method (Table 1). To this end, the value of length scale parameters (l and l_1) is taken equal to zero.

According to Table 1, although natural frequencies of perfect plates can be accurately predicted by the present model, those of the defective plate are overestimated. However, the calculated percentage error (lower than 4% and 3% for the simply supported and clamped plate, respectively) shows that there is an acceptable agreement between the results.

Table 1. Comparisons of the first dimensionless natural frequencies $\Omega = (\omega a^2/\pi^2)\sqrt{\rho h/D}$ for the fully simply supported (SSSS) and fully clamped (CCCC) plate ($a/b = 1, a/h = 29.4, d$ – the diameter of the central hole)

d/a	SSSS		CCCC	
	Present	FEM	Present	FEM
0	1.9986	1.9986	3.6445	3.6445
0.1	2.0021	1.9913	3.6907	3.6533
0.2	2.0304	1.9950	3.8482	3.7644
0.3	2.0918	2.0454	4.1673	4.0898
0.4	2.1979	2.1727	4.7690	4.7286
0.5	2.4988	2.4106	5.8615	5.8571

Next, after setting the length scale parameters to be equal to each other (i.e. $l = l_1$), the effects of an increase in the length scale parameter on the variation of the first natural frequency of perfect graphene sheets by increasing the side-length of nano-plate is compared with the data available in Ansari *et al.* (2010), showing the influence of the small scale parameter on the natural frequency of perfect graphene sheets by using Eringen’s nonlocal elasticity theory. Figure 1 shows that, regardless of the boundary conditions, the first natural frequency of perfect graphene sheets decreases with an increase in the length scale parameter, although a rise in the side-length of the nano-plate reduces the importance of the length scale value, so that the non-classical natural frequencies tend to the classical ones. The observed behavior is completely in agreement with that reported in Ansari *et al.* (2010).

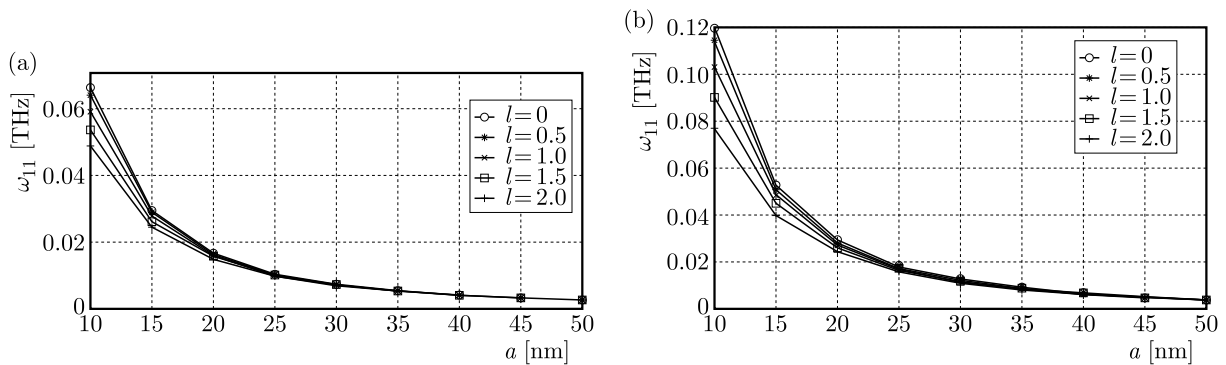


Fig. 1. The effects of the length scale value on the natural frequency of perfect graphene sheets; (a) fully simply supported nano-plates, (b) fully clamped nano-plates ($l = l_1$)

3.2. Molecular structural mechanics method

To verify the accuracy of predicted natural frequencies of graphene sheets obtained via molecular structural mechanics (MSM), the estimated first natural frequency of fully simply supported and fully clamped single-layered graphene sheets are compared with those obtained by the molecular dynamics method and are available in Ansari *et al.* (2010), see Table 2. As it is seen, there is a quite good agreement between the results.

4. Numerical results

In this Section, first, the effects of different parameters such as length scale and diameter of the central hole to the side length ratio, which is not more than the half of side length of nano-plate, on the dimensionless natural frequency of graphene nano-sheet with a central pore are

Table 2. Comparison of the first natural frequency of a square single-layered graphene sheet

Side-length a [nm]	SSSS		CCCC	
	MSM	MD	MSM	MD
10	0.0576347	0.0587725	0.1148990	0.1146223
15	0.0292556	0.0273881	0.0523147	0.0517078
20	0.0167249	0.0157524	0.0310192	0.0306219
25	0.0118420	0.0099840	0.0182260	0.0179975

investigated (see Fig. 2). Then, the variation of dimensionless natural frequencies of the graphene nano-sheet with the pore diameter to side length ratio equal to 0.5 versus the length scale and side length is studied. Finally, it is tried to estimate the effective length scale of the defective graphene sheet via matching the results obtained from the non-classical plate theory with those found on the basis of molecular structural mechanics. It should be mentioned that the length scales related to strain gradients and inertia gradients are set equal to each other (i.e. $l = l_1$) in this Section.

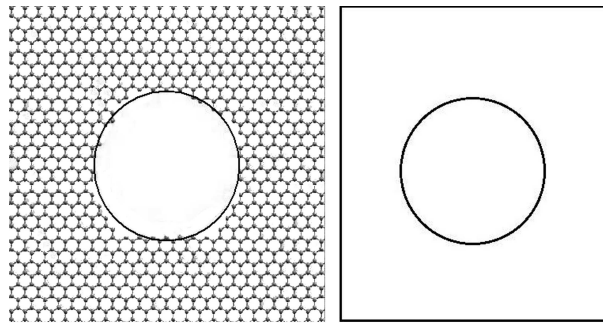


Fig. 2. Defective monolayer graphene sheet modeled with a plate with a circular hole

In Fig. 3, the effects of the length scale and diameter of the central hole to the side length ratio on the dimensionless natural frequency of the graphene nano-sheet with a central pore for two different boundary conditions are investigated. Regardless of boundary conditions, for a small value of the length scale parameter, the first natural frequency of defective graphene sheets rises as diameter of the central hole to the side length ratio increases, while with a rise in the length scale, the rate of increase of the first natural frequency with pore diameter decreases. For a larger value of the length scale, a decrease in the first natural frequency may be seen by increasing the pore diameter (Figs. 3a and 3d). Generally, however, the sensitivity of simply supported graphene sheets to the existence of the central hole is less than in the fully clamped nano-sheets. The sensitivity of the second and third natural frequency of a fully clamped graphene sheet to an increase in pore diameter is less than the first one, although the length scale value can change the increasing or decreasing trend of the curves.

The impact of side length on frequencies can be seen in Fig. 4 for fully clamped and simply supported graphene sheets. It is assumed that graphene has a central hole the diameter of which is half of the side length of the sheet.

It is clearly seen that the importance of the length scale role in decreasing the natural frequencies reduces with an increase in the side length of the defective sheet. It can be concluded that the influence of the length scale on higher order frequencies is more than the first natural frequency as well. As expected, the natural frequencies of simply-supported sheets are less than the fully clamped ones.

In order to show if the existence of vacancy defects makes a difference to the effective length scale used in the non-classical plate theory, the results obtained from the molecular structural

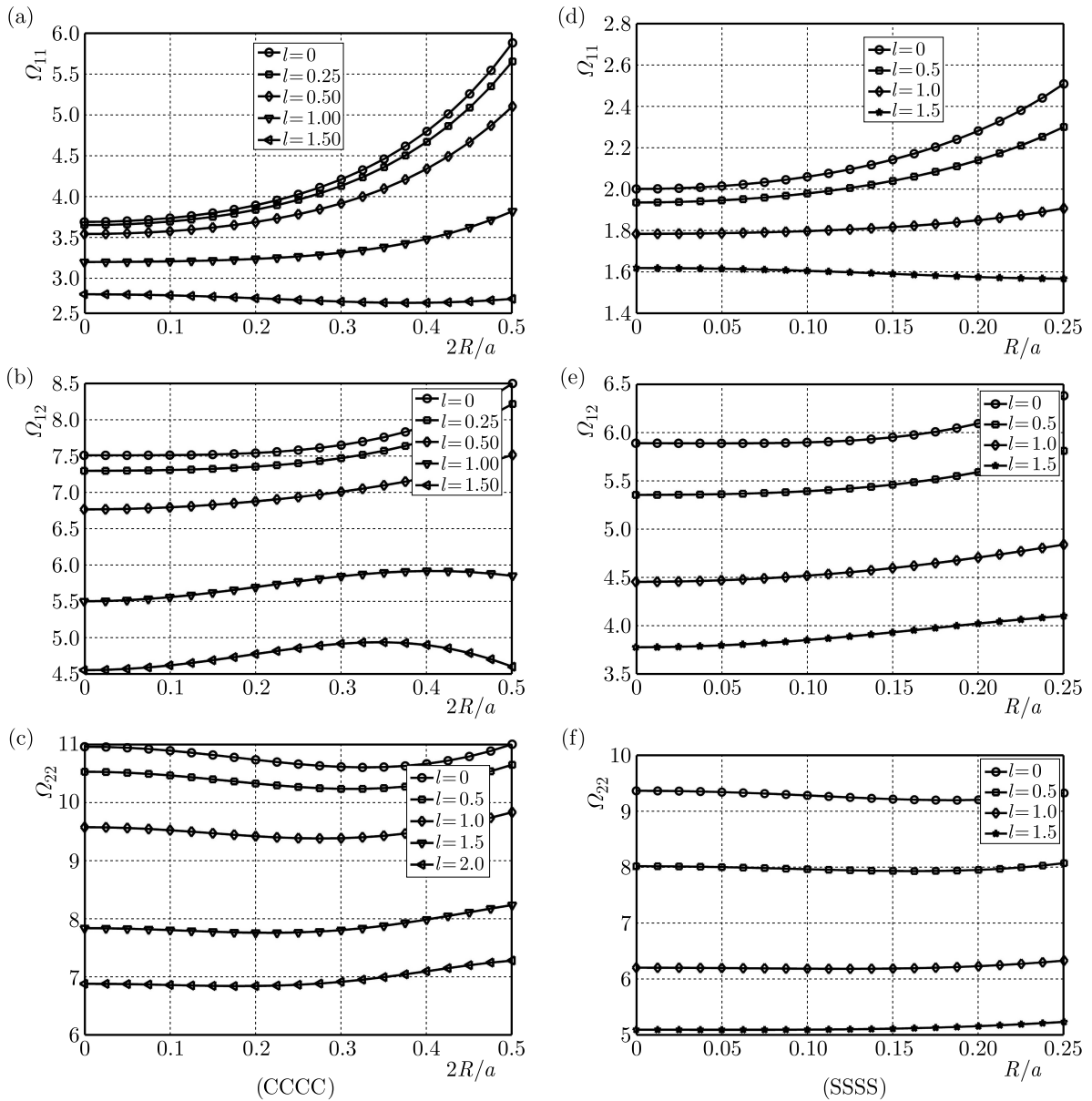


Fig. 3. The effects of the length scale and diameter of the hole to side length of plate ratio on the first three dimensionless natural frequencies of fully clamped graphene sheets (a), (b) and (c) and fully simply-supported graphene sheets (d), (e) and (f) ($l = l_1$)

mechanics are used. First, the effective length scale for perfect square graphene nano-sheets the side length of which is 10 nm is obtained by matching the first natural frequencies predicted by the molecular structural mechanics with the non-classical plate model. They are around 1.15 nm and 0.5 nm for simply supported and fully clamped nano-sheets, respectively. According to these effective length scales, the first three natural frequencies of nano-sheets are 0.0578181, 0.133181 and 0.193658 THz, 0.1150115, 0.2230178 and 0.3152479 THz for simply supported and fully clamped nano-plates, respectively. The comparison of these results with those determined by molecular structural mechanics (0.05763, 0.12857 and 0.18252 THz for simply supported sheet and 0.11490, 0.23047 and 0.34411 for clamped sheet) shows that the percentage error in higher order frequencies is more than that of the first natural frequencies. Similar results can be seen in Table 3 and 4 in which the same method is used to estimate the effective length scale of the defective sheet. It can be concluded that the effective length scale may vary with an increase

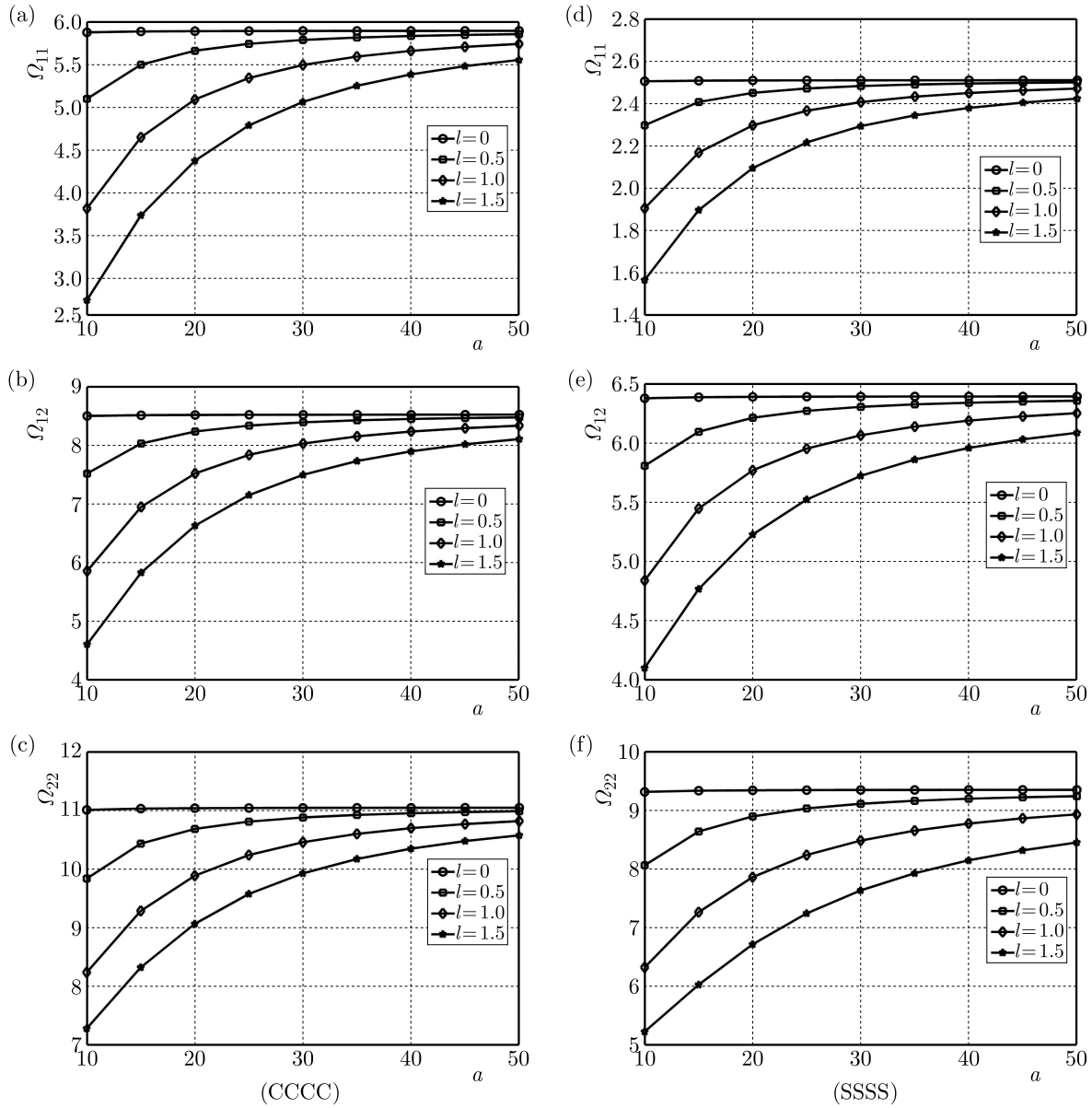


Fig. 4. The effect of the length scale and side length on the first three dimensionless natural frequencies of the fully clamped graphene sheet (a), (b) and (c) and fully simply-supported graphene sheet (d), (e) and (f) with a central hole the diameter to side length ratio of which is 0.5 ($l = l_1$)

in diameter of the vacancy defect as well. It seems that the dependency of the effective length scale on diameter of the vacancy defect changes with boundary conditions. The effective length scale of a clamped defective graphene is more sensitive to diameter of the vacancy than that of the simply supported one.

5. Conclusion

This article attempts to study the natural frequency of defective graphene sheets because the existence of cut-outs in plates may be essential on the basis of their desired functionality. In this study, Aifantis' theory in conjunction with inertia gradients is combined with Kirchhoff's thin plate hypothesis to incorporate the size effect into the classical continuum plate theory because Eringen's nonlocal elasticity theory does not allow the construction of an energy functional.

Table 3. The estimated length-scale parameter of simply supported defective graphene sheets on the basis of matching natural frequencies obtained from the present method against MSM results

No. of lost atoms	Mode No.	MSM [THz]	Present method [THz]	Length scale parameter $l = l_1$ [nm]
6	ω_{11}	0.057446	0.05738	1.2
	ω_{12}	0.12840	0.14056	
	ω_{22}	0.18224	0.19349	
24	ω_{11}	0.057170	0.05711	1.145
	ω_{12}	0.12797	0.13944	
	ω_{22}	0.18157	0.19140	
54	ω_{11}	0.057008	0.05706	1.155
	ω_{12}	0.12718	0.13934	
	ω_{22}	0.18049	0.19096	

Table 4. The estimated length-scale parameter of fully clamped defective graphene sheets on the basis of matching natural frequencies obtained from the present method against MSM results

No. of lost atoms	Mode No.	MSM [THz]	Present method [THz]	Length scale parameter $l = l_1$ [nm]
6	ω_{11}	0.11444	0.11439	0.55
	ω_{12}	0.23712	0.21931	
	ω_{13}	0.34343	0.30796	
24	ω_{11}	0.11381	0.11383	0.61
	ω_{12}	0.23650	0.21525	
	ω_{13}	0.34196	0.29900	
54	ω_{11}	0.11356	0.11355	0.71
	ω_{12}	0.23650	0.21236	
	ω_{13}	0.34196	0.29157	

The Ritz method is employed to derive discrete equations of motion which yield the eigenvalue problem. The molecular structural mechanics method is also employed to specify the effective length scale parameter. In the ‘numerical results’ Section, the effects of different boundary conditions, length scale, diameter of hole to side length ratio and side length of nano-sheets on the fundamental frequency of graphene sheets are studied. The results demonstrate that:

- Regardless of boundary conditions, for a small value of the length scale parameter, the first natural frequency of defective graphene sheets rises as diameter of the central hole to the side length ratio increases, while with a rise in the length scale, the rate of increase of the first natural frequency with pore diameter decreases.
- For larger values of the length scale, by increasing pore diameter, a decrease in the first natural frequency may be seen.
- The sensitivity of simply supported graphene sheets to the existence of the central hole is less than that of the fully clamped nano-sheets.
- The importance of the length scale role in decreasing the natural frequencies reduces with an increase in the side length of the defective sheet.

- The influence of the length scale on higher order frequencies is stronger than that on the first natural frequencies.
- Although the dependency of the effective length scale on diameter of the vacancy defect changes with boundary conditions, the effective length scale does not vary with an increase in diameter of the vacancy defect significantly.

Acknowledgements

The author gratefully acknowledges the support of Yasouj University under Grant No. Gryu-89111109.

References

1. AIFANTIS E.C., 1992, On the role of gradients in the localization of deformation and fracture, *International Journal of Engineering Science*, **30**, 1279-1299
2. AIFANTIS E.C., 2011, On the gradient approach-relation to Eringen's nonlocal theory, *International Journal of Engineering Science*, **49**, 1367-1377
3. AKGÖZ B., CIVALEK Ö., 2012, Free vibration analysis for single-layered graphene sheets in an elastic matrix via modified couple stress theory, *Materials and Design*, **42**, 167-171
4. AKGÖZ B., CIVALEK Ö., 2014, A new trigonometric beam model for buckling of strain gradient microbeams, *International Journal of Mechanical Sciences*, **81**, 88-94
5. AKGÖZ B., CIVALEK Ö., 2015, A microstructure-dependent sinusoidal plate model based on the strain gradient elasticity theory, *Acta Mechanica*, **226**, 2277-2294
6. AKSU G., ALI R., 1976, Determination of dynamic characteristics of rectangular plates with cutouts using a finite difference formulation, *Journal of Sound and Vibration*, **44**, 147-158
7. ALI R., ATWAL S.J., 1980, Prediction of natural frequencies of vibration of rectangular plates with rectangular cutouts, *Composite Structures*, **12**, 819-823
8. ALTAN B., AIFANTIS E.C., 1997, On some aspects in the special theory of gradient elasticity, *Journal of Mechanical Behavior of Material*, **8**, 231-282
9. ANSARI R., GHOLAMI R., FAGHIIH SHOJAEI M., MOHAMMADI V., SAHMANI S., 2013, Size-dependent bending, buckling and free vibration of functionally graded Timoshenko microbeams based on the most general strain gradient theory, *Composite Structures*, **100**, 385-397
10. ANSARI R., GHOLAMI R., SAHMANI S., 2011, Free vibration analysis of size-dependent functionally graded microbeams based on the strain gradient Timoshenko beam theory, *Composite Structures*, **94**, 221-228
11. ANSARI R., SAHMANI S., ARASH B., 2010, Nonlocal plate model for free vibration of single-layered graphene sheets, *Physics Letters A*, **375**, 53-62
12. ASHOORI MOVASSAGH A., MAHMOODI A.M.J., 2013, A micro-scale modeling of Kirchhoff plate based on modified strain-gradient elasticity theory, *European Journal of Mechanics A/Solids*, **40**, 50-59
13. ASKES H., AIFANTIS E.C., 2009, Gradient elasticity and flexural wave dispersion in carbon nanotubes, *Physical Review*, **B80**, 195412
14. ASKES H., AIFANTIS E.C., 2011, Gradient elasticity in statics and dynamics: An overview of formulations, length scale identification procedures, finite element implementations and new results, *International Journal of Solids and Structures*, **48**, 1962-1990
15. BINGLEI W., SHENGHUA H., JUNFENG Z., SHENJIE Z., 2016, Reconsiderations on boundary conditions of Kirchhoff micro-plate model based on a strain gradient elasticity theory, *Applied Mathematical Modelling*, **40**, 7303-7317

16. BINGLEI W., SHENJIE Z., JUNFENG Z., XI C., 2011, A size-dependent Kirchhoff micro-plate model based on strain gradient elasticity theory, *European Journal of Mechanics A/Solids*, **30**, 517-524
17. EBRAHIMI F., BARATI M.R., DABBAGH A., 2016, A nonlocal strain gradient theory for wave propagation analysis in temperature-dependent inhomogeneous nanoplates, *International Journal of Engineering Science*, **107**, 169-182
18. FARAJPOUR A., MOHAMMADI M., SHAHIDI A.R., MAHZOON M., 2011, Axisymmetric buckling of the circular graphene sheets with the nonlocal continuum plate model, *Physica E*, **43**, 1820-1825
19. FARAJPOUR A., SHAHIDI A.R., MOHAMMADI M., MAHZOON M., 2012, Buckling of orthotropic micro/nanoscale plates under linearly varying in-plane load via nonlocal continuum mechanics, *Composite Structures*, **94**, 1605-1615
20. GHOLAMI R., DARVIZEH A., ANSARI R., SADEGHI F., 2016, Vibration and buckling of first-order shear deformable circular cylindrical micro-/nano-shells based on Mindlin's strain gradient elasticity theory, *European Journal of Mechanics A/Solids*, **58**, 76-88
21. GITMAN I.M., ASKES H., AIFANTIS E.C., 2005, The representative volume size in static and dynamic micro-macro transitions, *International Journal of Fracture*, **135**, L3-L9
22. GUPTA S.S., BATRA R.C., 2010, Elastic properties and frequencies of free vibrations of single-layered graphene sheets, *Journal of Computational and Theoretical Nanoscience*, **10**, 2151-2164
23. HASHEMNIA K., FARID M., VATANKHAH R., 2009, Vibrational analysis of carbon nanotubes and graphene sheets using molecular structural mechanics approach, *Computational Materials Science*, **47**, 79-85
24. HU N., NUNOYA K., PAN D., OKABE T., FUKUNAGA H., 2007, Prediction of buckling characteristics of carbon nanotubes, *International Journal of Solids and Structures*, **44**, 6535-6550
25. JOMEHZADEH E., SAIDI A.R., JOMEHZADEH Z., BONACCORSO F., PALERMO V., GALIOTIS C., PUGNO N.M., 2015, Nonlinear subharmonic oscillation of orthotropic graphene-matrix composite, *Computational Materials Science*, **99**, 164-172
26. LAM D.C.C., YANG F., CHONG A.C.M., WANG J., TONG P., 2003, Experiments and theory in strain gradient elasticity, *Journal of the Mechanics and Physics of Solids*, **51**, 1477-1508
27. LAM K.Y., HUNG K.C., CHOW S.T., 1989, Vibration analysis of plates with cutouts by the modified Rayleigh-Ritz method, *Applied Acoustics*, **28**, 49-60
28. LEBEDEVA I.V., KNIZHNIK A.A., POPOV A.M., LOZOVIK YU. E., POTAPKIN B.V., 2012, Modeling of graphene-based NEMS, *Physica E*, **44**, 949-954
29. LI C., CHOU T.-W., 2003, A structural mechanics approach for the analysis of carbon nanotubes, *International Journal of Solids and Structures*, **40**, 2487-2499
30. LI L., HU Y., 2016, Wave propagation in fluid-conveying viscoelastic carbon nanotubes based on nonlocal strain gradient theory, *Computational Materials Science*, **112**, 282-288
31. LIEW K.M., KITIPORNCHAI S., LEUNG A.Y.T., LIM C.W., 2003, Analysis of the free vibration of rectangular plates with central cut-outs using the discrete Ritz method, *International Journal of Mechanical Sciences*, **45**, 941-959
32. MALEKZADEH P., BAHRANIFARD F., ZIAEE S., 2013, Three-dimensional free vibration analysis of functionally graded cylindrical panels with cut-out using Chebyshev-Ritz method, *Composite Structures*, **105**, 1-13
33. METRIKINE A.V., ASKES H., 2002, One-dimensional dynamically consistent gradient elasticity models derived from a discrete microstructure. Part 1: Generic formulation, *European Journal of Mechanics A/Solids*, **21**, 555-572
34. METRIKINE A.V., ASKES H., 2006, An isotropic dynamically consistent gradient elasticity model derived from a 2D lattice, *Philosophical Magazine*, **86**, 3259-3286

35. MINDLIN R., 1964, Micro-structure in linear elasticity, *Archive for Rational Mechanics and Analysis*, **16**, 52-78
36. MINDLIN R.D., TIERSTEN H.F., 1962, Effects of couple-stresses in linear elasticity, *Archive for Rational Mechanics and Analysis*, **11**, 415-448
37. MOHAMMADI M., FARAJPOUR A., GOODARZI, DINARI F., 2014, Thermo-mechanical vibration analysis of annular and circular graphene sheet embedded in an elastic medium, *Latin American Journal of Solids and Structures*, **11**, 659-682
38. MURMU T., PRADHANA S.C., 2009, Vibration analysis of nano-single-layered graphene sheets embedded in elastic medium based on nonlocal elasticity theory, *Journal of Applied Physics*, **105**, 064319
39. RAHMANI O., PEDRAM O., 2014, Analysis and modeling the size effect on vibration of functionally graded nano-beams based on nonlocal Timoshenko beam theory, *International Journal of Engineering Science*, **77**, 55-70
40. RAJAMANI A., PRABHAKARAN R., 1977, Dynamic response of composite plates with cut-outs. Part 1: Simply-supported plates, *Journal of Sound and Vibration*, **54**, 549-564
41. REDDY J.N., 1999, *Theory and Analysis of Elastic Plates*, Taylor and Francis, USA
42. REDDY J.N., 2011, Microstructure-dependent couple stress theories of functionally graded beams, *Journal of Mechanics and Physics of Solids*, **59**, 2382-2399
43. SADEGHI M., NAGHDABADI R., 2010, Nonlinear vibrational analysis of single-layered graphene sheets, *Nanotechnology*, **21**, 105705-105710
44. SAKHAEI-POUR A., AHMADIAN M.T., NAGHDABADI R., 2008, Vibrational analysis of single-layered graphene sheets, *Nanotechnology*, **19**, 85702-85707
45. SCARPA F., ADHIKARI S., PHANI A.S., 2009, Effective elastic mechanical properties of single layer graphene sheets, *Nanotechnology*, **20**, 065709
46. SHEN L., SHEN H.-S., ZHANG C.-L., 2010, Nonlocal plate model for nonlinear vibration of single layer graphene sheets in thermal environments, *Computational Materials Science*, **48**, 680-685
47. ŞİMŞEK M., 2016, Nonlinear free vibration of a functionally graded nanobeam using nonlocal strain gradient theory and a novel Hamiltonian approach, *International Journal of Engineering Science*, **105**, 12-27
48. THAM L.G., CHAN A.H.C., CHEUNG Y.K., 1986, Free vibration and buckling analysis of plates by negative stiffness method, *Composite Structures*, **22**, 687-692
49. WANG C.G., LAN L., LIU Y.P., TAN H.F., HE X.D., 2013, Vibration characteristics of wrinkled single-layered graphene sheets, *International Journal of Solids and Structures*, **50**, 1812-1823
50. YANG F., CHONG A.C., LAM D.C.C., TONG P., 2002, Couple stress based strain gradient theory for elasticity, *International Journal of Solids and Structures*, **39**, 2731-2743
51. ZANDIATASHBAR A., LEE G.-H., AN S.J., LEE S., MATHEW N., TERRONES M., HAYASHI T., PICU C.R., HONE J., KORATKAR N., 2014, Effect of defects on the intrinsic strength and stiffness of graphene, *Nature Communications*, **5**, 3186, DOI: 10.1038/ncomms4186

APPLICATION OF THE ALTERNATING DIRECTION IMPLICIT METHOD FOR NUMERICAL SOLUTION OF THE DUAL PHASE LAG EQUATION

MARIUSZ CIESIELSKI

Czestochowa University of Technology, Institute of Computer and Information Sciences, Czestochowa, Poland
e-mail: mariusz.ciesielski@icis.pcz.pl

The problem discussed in the paper concerns the numerical modeling of thermal processes proceeding in micro-scale described using the Dual Phase Lag Model (DPLM) in which the relaxation and thermalization time appear. The cylindrical domain of a thin metal film subjected to a strong laser pulse beam is considered. The laser action is taken into account by the introduction of an internal heat source in the energy equation. At the stage of numerical modeling, the Control Volume Method is used and adapted to resolve the hyperbolic partial differential equation. In particular, the Alternating Direction Implicit (ADI) method for DPLM is presented and discussed. The examples of computations are also presented.

Keywords: micro-scale heat transfer, dual phase lag model, control volume method, alternating direction implicit method, numerical simulation

1. Introduction

Thermal processes proceeding in the microscale are characterized, as a rule, by an extremely short duration, extreme temperature gradients and very small geometrical dimensions of the domain considered. It is a reason that typical mathematical models basing on the macroscopic Fourier-type equations are not suitable for the analysis of this type problems. In the recent years, the problem of heat transfer through domains subjected to an strong external heat source (e.g. an ultrafast laser pulse) has been of vital importance in microtechnology applications, and it is a reason that the problems connected with fast heating of solids has become a very active research area (Tzou, 2015; Zhang, 2007; Chen *et al.*, 2004).

From the mathematical point of view, nowadays there exist different models describing the mechanism of the process discussed. In this group, the microscopic two-temperature parabolic or hyperbolic models (belonging to a group of continuum models) should be mentioned (Chen and Beraun, 2001; Kaba and Dai, 2005; Lin and Zhigilei, 2008; Majchrzak, 2012; Majchrzak and Dziatkiewicz, 2015). The two-step parabolic and hyperbolic models involve two energy equations determining the thermal processes in the electron gas and the metal lattice. The coupling factor combining these equations is introduced. Depending on the variant of the model, parabolic or hyperbolic PDEs are considered. Assuming certain simplifications, the two-temperature model can be transformed into a single equation containing the second order time derivative and higher order mixed derivative in both time and space (known as the dual phase lag model (DPLM)). In this equation, two positive constants τ_q , τ_T appear and they correspond to the relaxation time, which is the mean time for electrons to change their energy states and the thermalization time, which is the mean time required for electrons and lattice to reach equilibrium (Orlande *et al.*, 1995).

The Cattaneo-Vernotte and the dual phase lag models belong also to the group of continuum ones. They result from the generalization of the well-known Fourier law. To take into account the finite velocity of a thermal wave the lag time between the heat flux and temperature gradient

has been introduced (Cattaneo, 1958). The Cattaneo-Vernotte hyperbolic equation (CVE) can be treated as a certain microscale heat transfer model, but for this purpose is rarely used. The model discussed often finds application in the case of bioheat transfer problems, e.g. (Ciesielski *et al.*, 2016). In fact, according to literature, e.g. (Mitra *et al.*, 1995) the lag time (relaxation time) for processed meat is of the order of several seconds.

Introduction of two lag times in the generalized form of the Fourier law (relaxation and thermalization ones) leads, after relatively simple mathematical manipulations, to the dual phase lag equation. At present, in literature one can find big number of analytical and (first of all) numerical solutions of various thermal problems described by this model. The majority of the solutions presented in the literature concerns the 1D problems. Such an assumption is often fully acceptable. For example, considering the laser pulse interactions with thin metal films it is reasonable to treat the interactions as a one-dimensional heat transfer process (Chen and Beraun, 2001). In this paper, the axially-symmetrical problem is analyzed.

Most of the works in this field concerns direct problems. Homogeneous and also heterogeneous domains are considered. The problem of the single layer heating was discussed, among others, by Tang and Araki (1999), Kaba and Dai (2005), Mochnacki and Ciesielski (2012), Majchrzak and Turchan (2016). In the subject of non-homogeneous micro-domains, one can mention the paper presented by Dai and Nassar (2000), in which the heat transfer in a double layered gold-chromium film is analyzed, and the papers prepared by Majchrzak *et al.* (2009a,b) concerning a multi-layered film subjected to ultrafast laser heating.

Both in the case of the CVE and DPLE, the typical boundary conditions appearing in heat transfer problems should be modified in a adequate way.

In literature, one can find works devoted to sensitivity of the transient temperature field in microdomains with respect to the dual phase lag model parameters (Majchrzak, and Mochnacki, 2014). The issue of the inverse problems was also developed, e.g. by Mochnacki and Paruch (2013), Dziatkiewicz *et al.* (2014), Mochnacki and Ciesielski (2015).

A next group of microscale heat transfer models is based on the Boltzmann transport equation (BTE). It is a conservation equation where the conserved quantity is the number of particles (Tian and Yang, 2008). The general form of BTE is rather complex, but it can be modified to analyze special tasks, for instance systems created by phonons, electrons, etc. In this field, deserving special attention is repeatedly cited paper presented by Escobar *et al.* (2006). One can also mention the work by Belhayat-Piasecka and Korczak (2016) in which the microscale heat transport was analyzed using the interval lattice Boltzmann method.

Microscale heat transfer processes can be also considered using the molecular approaches (Smith and Norris, 2003; Theodosiou and Saravanos, 2007; Chen *et al.*, 2007; Liu and Tsai, 2009).

2. Governing equations

Let us consider the diffusion equation in the domain Ω

$$(r, z) \in \Omega \quad c \frac{\partial T(r, z, t)}{\partial t} = -\nabla \cdot \mathbf{q}(r, z, t) + Q(r, z, t) \quad (2.1)$$

where $c = c(T)$ is the volumetric specific heat, $\mathbf{q}(r, z, t)$ is the heat flux vector, $Q(r, z, t)$ is the capacity of internal heat sources, r, z, t are the geometrical co-ordinates and time.

The value of heat flux is determined by Tzou's dual-phase-lag theory (Tzou, 2015), as the generalization of the Fourier law, in particular

$$\mathbf{q}(r, z, t + \tau_q) = -\lambda \nabla T(r, z, t + \tau_T) \quad (2.2)$$

where τ_q is called the relaxation time, while τ_T is the thermalization time, $\lambda = \lambda(T)$ is the thermal conductivity, $\nabla T(r, z, t)$ is the temperature gradient. For $\tau_T = 0$, this model leads to the Cattaneo-Vernotte equation, while for $\tau_T = 0$ and $\tau_q = 0$ it corresponds to the Fourier law.

The Taylor series expansions of equation (2.2) is the following

$$\mathbf{q}(r, z, t) + \tau_q \frac{\partial \mathbf{q}(r, z, t)}{\partial t} = -\lambda \left[\nabla T(r, z, t) + \tau_T \frac{\partial \nabla T(r, z, t)}{\partial t} \right] \quad (2.3)$$

Introducing formula (2.3) into equation (2.1) one obtains

$$c \left[\frac{\partial T(r, z, t)}{\partial t} + \tau_q \frac{\partial^2 T(r, z, t)}{\partial t^2} \right] = \nabla \cdot [\lambda \nabla T(r, z, t)] + \tau_T \frac{\partial \nabla \cdot [\lambda \nabla T(r, z, t)]}{\partial t} + Q(r, z, t) + \tau_q \frac{\partial Q(r, z, t)}{\partial t} \quad (2.4)$$

In the case of the axially-symmetrical task discussed in this work, the component $\nabla \cdot [\lambda \nabla T(r, z, t)]$ is the following

$$\nabla \cdot [\lambda \nabla T(r, z, t)] = \frac{1}{r} \frac{\partial}{\partial r} \left[r \lambda \frac{\partial T(r, z, t)}{\partial r} \right] + \frac{\partial}{\partial z} \left[\lambda \frac{\partial T(r, z, t)}{\partial z} \right] \quad (2.5)$$

It should be pointed out that the boundary conditions (which appear in the typical Fourier heat conduction models) for the DPL should be transformed to the form

$$(r, z) \in \Gamma : \quad q_b(r, z, t) + \tau_q \frac{\partial q_b(r, z, t)}{\partial t} = -\lambda \left[\mathbf{n} \cdot \nabla T(r, z, t) + \tau_T \frac{\partial [\mathbf{n} \cdot \nabla T(r, z, t)]}{\partial t} \right] \quad (2.6)$$

In Fig. 1, the domain considered (limited by the planes $z = 0$, $z = Z$ and surface $r = R$) is shown.

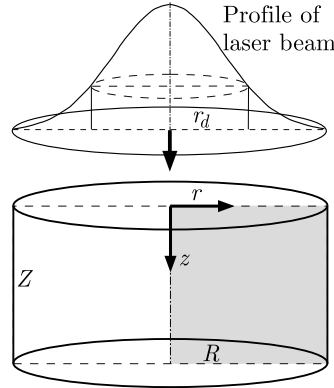


Fig. 1. Cylindrical micro-domain

The effects of femtosecond laser pulse irradiation on the upper surface limiting the system causes that the energy is delivered to metal and its absorption occurs. The internal heat source $Q(r, z, t)$ generated inside metal is related with action of the laser beam (Chen and Beraun, 2001)

$$Q(r, z, t) = \sqrt{\frac{\beta}{\pi}} \frac{1 - R_f}{t_p \delta} I_0 \exp\left(-\frac{z}{\delta}\right) \exp\left(-\frac{r^2}{r_d^2}\right) \exp\left(-\beta \left(\frac{t - 2t_p}{t_p}\right)^2\right) = I_\Omega(r, z) I_t(t) \quad (2.7)$$

where

$$I_\Omega(r, z) = I_0 \frac{1 - R_f}{\delta} \exp\left(-\frac{r^2}{r_d^2}\right) \exp\left(-\frac{z}{\delta}\right) \quad I_t(t) = \frac{\sqrt{\beta}}{t_p \sqrt{\pi}} \exp\left(-\beta \left(\frac{t - 2t_p}{t_p}\right)^2\right) \quad (2.8)$$

and I_0 is laser intensity, R_f is reflectivity of the irradiated surface, δ is optical penetration depth, r_d is characteristic radius of Gaussian laser beam, $\beta = 4 \ln 2$ and t_p is characteristic time of the laser pulse. Here, it is assumed that the total time of the laser action beam on the surface is equal to $4t_p$.

So, action of the laser beam is taken into account by introduction of the internal heat source $Q(r, z, t)$. At the same time the dimensions Z and R are large enough that on the appropriate boundaries adiabatic conditions $q_b(r, z, t) = 0$ can be assumed. In the case of the problem considered (see: Eq. (2.6)) one has

$$(r, z) \in \Gamma : \quad -\lambda \left[\mathbf{n} \cdot \nabla T(r, z, t) + \tau_T \frac{\partial [\mathbf{n} \cdot \nabla T(r, z, t)]}{\partial t} \right] = 0 \quad (2.9)$$

The initial conditions (the initial temperature of domain $T_0(r, z)$ and the initial heating rate $v_0(r, z)$) are also given

$$t = 0 : \quad T(r, z, 0) = T_0(r, z) \quad \left. \frac{\partial T(r, z, t)}{\partial t} \right|_{t=0} = v_0(r, z) \quad (2.10)$$

3. Numerical solution using the Control Volume Method

To solve the problem presented in the previous Section, the control volume method (CVM) is used. This method constitutes a very effective tool for numerical modeling of heat transfer processes described by the Fourier-type equations. In the case of numerical simulation of microscale heat transfer and the models based on the DPL equation, this method has so far been applied only to the numerical solution using an ‘explicit’ scheme (Mochnecki and Ciesielski, 2015).

The first stage of the method application is the division of the domain considered into small cells (known as the control volumes CV). In this work, the shape of control volumes is regular one (it corresponds to the rings of a rectangular cross-section). The more complex discretization using e.g. the Voronoi polygons can be also taken into account (Ciesielski and Mochnecki, 2014).

In Fig. 2, the domain discretization is presented, while in Fig. 3 the selected internal and boundary (top) control volumes are shown.

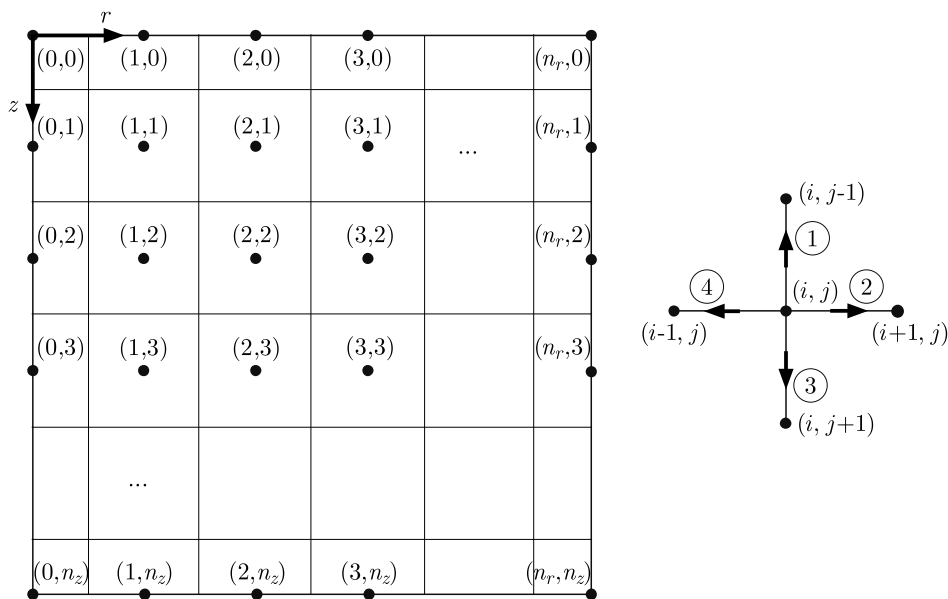


Fig. 2. Discretization of the domain

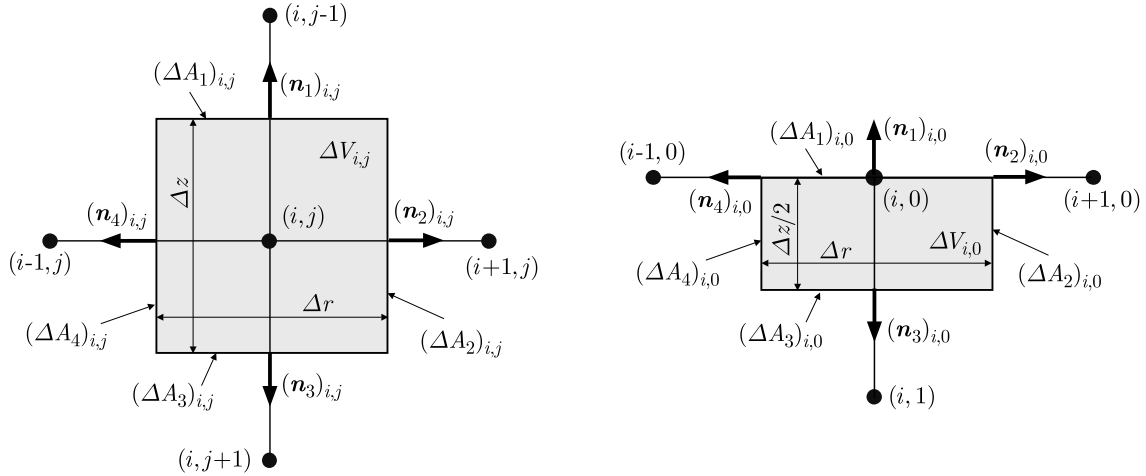


Fig. 3. The internal and boundary control volumes

On the basis of simple geometrical considerations, one can determine values of the successive volumes $\Delta V_{i,j}$ and surfaces $(\Delta A_k)_{i,j}$ limiting $\Delta V_{i,j}$ in each k -direction. Numerical modelling of transient problems requires introduction of the time grid, too: $0 = t^0 < t^1 < \dots < t^f < \dots < t^F$, $t^f = f \Delta t$.

The aim of the CVM is to find the transient temperature field at the set of control volumes. The thermal capacities are concentrated at the elements, whereas the thermal resistances are concentrated on the sectors connecting nodes of the control volumes. The average temperatures in all control volumes can be found on the basis of energy balances for the successive volumes. The energy balances corresponding to the heat exchange between the analyzed control volume and adjacent control volumes results from integration of the energy equation with respect to volume and time.

3.1. Integration of the energy equation with respect to volume

Integration of Eq. (2.4) over the control volume $\Omega_{i,j}$ leads to

$$\int_{\Omega_{i,j}} c \left(\frac{\partial T(r, z, t)}{\partial t} + \tau_q \frac{\partial^2 T(r, z, t)}{\partial t^2} \right) d\Omega = \int_{\Omega_{i,j}} \left(\nabla \cdot [\lambda \nabla T(r, z, t)] + \tau_T \frac{\partial \nabla \cdot [\lambda \nabla T(r, z, t)]}{\partial t} \right) d\Omega + \int_{\Omega_{i,j}} \left(Q(r, z, t) + \tau_q \frac{\partial Q(r, z, t)}{\partial t} \right) d\Omega \quad (3.1)$$

The integral occurring on the left-hand side of equation (3.1) can be approximated in the form

$$\int_{\Omega_{i,j}} c \left(\frac{\partial T(r, z, t)}{\partial t} + \tau_q \frac{\partial^2 T(r, z, t)}{\partial t^2} \right) d\Omega \cong c_{i,j} \left(\frac{\partial T(r, z, t)}{\partial t} \Big|_{\substack{r=r_i \\ z=z_j}} + \tau_q \frac{\partial^2 T(r, z, t)}{\partial t^2} \Big|_{\substack{r=r_i \\ z=z_j}} \right) \Delta V_{i,j} = c_{i,j} \left(\frac{dT_{i,j}}{dt} + \tau_q \frac{d^2 T_{i,j}}{dt^2} \right) \Delta V_{i,j} \quad (3.2)$$

where $T_{i,j} = T(r_i, z_j, t)$, while $c_{i,j} = c(T_{i,j})$ is the integral mean of thermal capacity in the volume $\Omega_{i,j}$. In a similar way, the numerical approximation of the source term in Eq. (3.1) can be found

$$\int_{\Omega_{i,j}} \left(Q(r, z, t) + \tau_q \frac{\partial Q(r, z, t)}{\partial t} \right) d\Omega \cong \left(Q_{i,j} + \tau_q \frac{dQ_{i,j}}{dt} \right) \Delta V_{i,j} \quad (3.3)$$

where $Q_{i,j}$ is determined as the integral mean of the heat source in the volume $\Omega_{i,j}$

$$\begin{aligned} Q_{i,j} &\equiv Q_{i,j}(t) \cong \frac{1}{\Delta V_{i,j}} \int_{\Omega_{i,j}} Q(r, z, t) d\Omega = I_t(t) \frac{1}{\Delta V_{i,j}} \int_{\Omega_{i,j}} I_\Omega(r, z) d\Omega \\ &= I_t(t) \frac{I_0 \pi (1 - R_f) r_d^2}{\Delta V_{i,j}} \left[\exp\left(-\frac{\bar{r}_1^2}{r_d^2}\right) - \exp\left(-\frac{\bar{r}_2^2}{r_d^2}\right) \right] \left[\exp\left(-\frac{\bar{z}_1}{\delta}\right) - \exp\left(-\frac{\bar{z}_2}{\delta}\right) \right] \end{aligned} \quad (3.4)$$

and $\bar{r}_1, \bar{r}_2, \bar{z}_1, \bar{z}_2$ are the limits of the control volume $\Omega_{i,j} = \{(r_i, z_i) | \bar{r}_1 \leq r_i \leq \bar{r}_2, \bar{z}_1 \leq z_i \leq \bar{z}_2\}$. In the case of a more complex form of the function Q , one can compute $Q_{i,j}(t) = Q(r_i, z_j, t)$, but this estimation is less accurate.

Applying the divergence theorem to the term determining heat conduction (right hand side of Eq. (3.1)) between the volume $\Omega_{i,j}$ bounded by the surfaces $\Delta A_{i,j}$ and its neighbourhoods, one obtains

$$\begin{aligned} &\int_{\Omega_{i,j}} \left(\nabla \cdot [\lambda \nabla T(r, z, t)] + \tau_T \frac{\partial \nabla \cdot [\lambda \nabla T(r, z, t)]}{\partial t} \right) d\Omega \\ &= \int_{\Omega_{i,j}} \nabla \cdot \lambda \left(\nabla T(r, z, t) + \tau_T \frac{\partial \nabla T(r, z, t)}{\partial t} \right) d\Omega \\ &= \int_{A_{i,j}} \left[\mathbf{n} \cdot \lambda \left(\nabla T(r, z, t) + \tau_T \frac{\partial \nabla T(r, z, t)}{\partial t} \right) \right] dA \end{aligned} \quad (3.5)$$

and then this term can be written in the form

$$\begin{aligned} &\int_{A_{i,j}} \left[\mathbf{n} \cdot \lambda \left(\nabla T(r, z, t) + \tau_T \frac{\partial \nabla T(r, z, t)}{\partial t} \right) \right] dA \\ &= \sum_{k=1}^4 \int_{(A_k)_{i,j}} \left[(\mathbf{n}_k)_{i,j} \cdot (\lambda_k)_{i,j} \left(\nabla T(r, z, t)|_k + \tau_T \frac{\partial \nabla T(r, z, t)}{\partial t} \Big|_k \right) \right]_{i,j} dA_k \\ &\cong \sum_{k=1}^4 (\mathbf{n}_k)_{i,j} \cdot (\lambda_k)_{i,j} \left(\nabla T(r, z, t)|_k + \tau_T \frac{\partial \nabla T(r, z, t)}{\partial t} \Big|_k \right)_{i,j} (\Delta A_k)_{i,j} = \sum_{k=1}^4 (q_k)_{i,j} (\Delta A_k)_{i,j} \end{aligned} \quad (3.6)$$

where $(q_k)_{i,j}$ is approximated by the following finite differences (taking into account also the adiabatic boundary conditions (2.9) on the boundary surfaces)

$$(q_1)_{i,j} = \begin{cases} (\lambda_1)_{i,j} \left[\frac{T_{i,j-1} - T_{i,j}}{\Delta z} + \tau_T \frac{d}{dt} \left(\frac{T_{i,j-1} - T_{i,j}}{\Delta z} \right) \right] & \text{if } j > 0 \\ 0 & \text{if } j = 0 \end{cases} \quad (3.7)$$

$$(q_2)_{i,j} = \begin{cases} (\lambda_2)_{i,j} \left[\frac{T_{i+1,j} - T_{i,j}}{\Delta r} + \tau_T \frac{d}{dt} \left(\frac{T_{i+1,j} - T_{i,j}}{\Delta r} \right) \right] & \text{if } i < n_r \\ 0 & \text{if } i = n_r \end{cases} \quad (3.8)$$

$$(q_3)_{i,j} = \begin{cases} (\lambda_3)_{i,j} \left[\frac{T_{i,j+1} - T_{i,j}}{\Delta z} + \tau_T \frac{d}{dt} \left(\frac{T_{i,j+1} - T_{i,j}}{\Delta z} \right) \right] & \text{if } j < n_z \\ 0 & \text{if } j = n_z \end{cases} \quad (3.9)$$

$$(q_4)_{i,j} = \begin{cases} (\lambda_4)_{i,j} \left[\frac{T_{i-1,j} - T_{i,j}}{\Delta r} + \tau_T \frac{d}{dt} \left(\frac{T_{i-1,j} - T_{i,j}}{\Delta r} \right) \right] & \text{if } i > 0 \\ 0 & \text{if } i = 0 \end{cases} \quad (3.10)$$

and $(\lambda_k)_{i,j}$ are harmonic mean thermal conductivities between two central points of adjoining control volumes

$$\begin{aligned}
 (\lambda_1)_{i,j} &= \frac{2\lambda_{i,j}\lambda_{i,j-1}}{\lambda_{i,j} + \lambda_{i,j-1}} & (\lambda_2)_{i,j} &= \frac{2\lambda_{i,j}\lambda_{i+1,j}}{\lambda_{i,j} + \lambda_{i+1,j}} \\
 (\lambda_3)_{i,j} &= \frac{2\lambda_{i,j}\lambda_{i,j+1}}{\lambda_{i,j} + \lambda_{i,j+1}} & (\lambda_4)_{i,j} &= \frac{2\lambda_{i,j}\lambda_{i-1,j}}{\lambda_{i,j} + \lambda_{i-1,j}}
 \end{aligned}
 \tag{3.11}$$

and next, the thermal resistances are defined as follows

$$(R_1)_{i,j} = \frac{\Delta z}{(\lambda_1)_{i,j}} \quad (R_2)_{i,j} = \frac{\Delta r}{(\lambda_2)_{i,j}} \quad (R_3)_{i,j} = \frac{\Delta z}{(\lambda_3)_{i,j}} \quad (R_4)_{i,j} = \frac{\Delta r}{(\lambda_4)_{i,j}}
 \tag{3.12}$$

Then, Eq. (3.6) takes the form

$$\int_{A_{i,j}} \left[\mathbf{n} \cdot \lambda \left(\nabla T(r, z, t) + \tau_T \frac{\partial \nabla T(r, z, t)}{\partial t} \right) \right] dA \cong \sum_{k=1}^4 \frac{(\theta_k)_{i,j}}{(R_k)_{i,j}} (\Delta A_k)_{i,j}
 \tag{3.13}$$

where

$$\begin{aligned}
 (\theta_1)_{i,j} &= \left(T_{i,j-1} - T_{i,j} + \tau_T \frac{d(T_{i,j-1} - T_{i,j})}{dt} \right) \Big|_{\text{if } j>0} \\
 (\theta_2)_{i,j} &= \left(T_{i+1,j} - T_{i,j} + \tau_T \frac{d(T_{i+1,j} - T_{i,j})}{dt} \right) \Big|_{\text{if } i<n_r} \\
 (\theta_3)_{i,j} &= \left(T_{i,j+1} - T_{i,j} + \tau_T \frac{d(T_{i,j+1} - T_{i,j})}{dt} \right) \Big|_{\text{if } j<n_z} \\
 (\theta_4)_{i,j} &= \left(T_{i-1,j} - T_{i,j} + \tau_T \frac{d(T_{i-1,j} - T_{i,j})}{dt} \right) \Big|_{\text{if } i>0}
 \end{aligned}
 \tag{3.14}$$

while the notation $expression \Big|_{\text{if condition}}$ introduced above, means

$$expression \Big|_{\text{if condition}} = \begin{cases} expression & \text{if condition} = true \\ 0 & \text{otherwise} \end{cases}
 \tag{3.15}$$

After the introduction of all discrete terms into equation (3.1), one obtains

$$c_{i,j} \left(\frac{dT_{i,j}}{dt} + \tau_q \frac{d^2 T_{i,j}}{dt^2} \right) \Delta V_{i,j} = \sum_{k=1}^4 \frac{(\theta_k)_{i,j}}{(R_k)_{i,j}} (\Delta A_k)_{i,j} + \left(Q_{i,j} + \tau_q \frac{dQ_{i,j}}{dt} \right) \Delta V_{i,j}
 \tag{3.16}$$

or

$$c_{i,j} \left(\frac{dT_{i,j}}{dt} + \tau_q \frac{d^2 T_{i,j}}{dt^2} \right) = \sum_{k=1}^4 \frac{(\theta_k)_{i,j}}{(R_k)_{i,j}} (\Phi_k)_{i,j} + Q_{i,j} + \tau_q \frac{dQ_{i,j}}{dt}
 \tag{3.17}$$

where $(\Phi_k)_{i,j} = (\Delta A_k)_{i,j} / \Delta V_{i,j}$.

3.2. Integration of the equation with respect to time

The second stage of CVM is integration of equation (3.17) with respect to time. The same effect can be obtained introducing the approximation of time derivatives occurring in (3.17) by appropriate finite differences.

The idea of the ADI method is to split the time step $\Delta t = t^{f+1} - t^f$ into two half-steps and apply two different finite difference schemes for each half time step. In the first half time step, a simple implicit scheme for directions (d_1, d_2) is used and simultaneously an explicit scheme for directions (d_3, d_4) is applied. Next, in the second half time step, the difference schemas are written by reversing the directions of the explicit and implicit schemes. The notation $'(d_1, d_2)-(d_3, d_4)'$, where the indexes d_i indicate directions of the neighbouring CV (see Fig. 1), is introduced.

For passing: $t^f \rightarrow t^{f+0.5} \rightarrow t^{f+1}$, $f = 1, \dots, F$, and using the variant of ADI: (1,2)-(3,4), the following differential schemas are proposed

$$\begin{aligned}
 c_{i,j}^f & \left(\frac{T_{i,j}^{f+0.5} - T_{i,j}^f}{0.5\Delta t} + \tau_q \frac{T_{i,j}^{f+0.5} - 2T_{i,j}^f + T_{i,j}^{f-0.5}}{(0.5\Delta t)^2} \right) \\
 & = \sum_{k=1,2} \frac{(\theta_k)_{i,j}^{f+0.5}}{(R_k)_{i,j}^f} (\Phi_k)_{i,j} + \sum_{k=3,4} \frac{(\theta_k)_{i,j}^f}{(R_k)_{i,j}^f} (\Phi_k)_{i,j} + Q_{i,j}^{f+0.5} + \tau_q \frac{Q_{i,j}^{f+0.5} - Q_{i,j}^f}{0.5\Delta t}
 \end{aligned} \tag{3.18}$$

and

$$\begin{aligned}
 c_{i,j}^{f+0.5} & \left(\frac{T_{i,j}^{f+1} - T_{i,j}^{f+0.5}}{0.5\Delta t} + \tau_q \frac{T_{i,j}^{f+1} - 2T_{i,j}^{f+0.5} + T_{i,j}^f}{(0.5\Delta t)^2} \right) \\
 & = \sum_{k=1,2} \frac{(\theta_k)_{i,j}^{f+0.5}}{(R_k)_{i,j}^{f+0.5}} (\Phi_k)_{i,j} + \sum_{k=3,4} \frac{(\theta_k)_{i,j}^{f+1}}{(R_k)_{i,j}^{f+0.5}} (\Phi_k)_{i,j} + Q_{i,j}^{f+1} + \tau_q \frac{Q_{i,j}^{f+1} - Q_{i,j}^{f+0.5}}{0.5\Delta t}
 \end{aligned} \tag{3.19}$$

and $(\theta_k)_{i,j}^s$ for $s \in \{f, f + 0.5, f + 1\}$ for this method are approximated in the following way

$$\begin{aligned}
 (\theta_1)_{i,j}^s & = \left[T_{i,j-1}^s - T_{i,j}^s + \tau_T \left(\frac{T_{i,j-1}^{s-0.5} - T_{i,j-1}^s}{0.5\Delta t} - \frac{T_{i,j}^{s-0.5} - T_{i,j}^s}{0.5\Delta t} \right) \right] \Big|_{\text{if } j > 0} \\
 (\theta_2)_{i,j}^s & = \left[T_{i+1,j}^s - T_{i,j}^s + \tau_T \left(\frac{T_{i+1,j}^{s-0.5} - T_{i+1,j}^s}{0.5\Delta t} - \frac{T_{i,j}^{s-0.5} - T_{i,j}^s}{0.5\Delta t} \right) \right] \Big|_{\text{if } i < n_r} \\
 (\theta_3)_{i,j}^s & = \left[T_{i,j+1}^s - T_{i,j}^s + \tau_T \left(\frac{T_{i,j+1}^{s-0.5} - T_{i,j+1}^s}{0.5\Delta t} - \frac{T_{i,j}^{s-0.5} - T_{i,j}^s}{0.5\Delta t} \right) \right] \Big|_{\text{if } j < n_z} \\
 (\theta_4)_{i,j}^s & = \left[T_{i-1,j}^s - T_{i,j}^s + \tau_T \left(\frac{T_{i-1,j}^{s-0.5} - T_{i-1,j}^s}{0.5\Delta t} - \frac{T_{i,j}^{s-0.5} - T_{i,j}^s}{0.5\Delta t} \right) \right] \Big|_{\text{if } i > 0}
 \end{aligned} \tag{3.20}$$

After transformations, the first system of equations (3.18) can be written in the final form as

$$(A_0)_{i,j}^f T_{i,j}^{f+0.5} + (A_1)_{i,j}^f T_{i,j-1}^{f+0.5} \Big|_{\text{if } j > 0} + (A_2)_{i,j}^f T_{i+1,j}^{f+0.5} \Big|_{\text{if } i < n_r} = (D')_{i,j}^f \tag{3.21}$$

where

$$\begin{aligned}
(A'_k)_{i,j}^f &= -(1 + 2\mu_T) \frac{(\Phi_k)_{i,j}}{(R_k)_{i,j}^f} \quad k = 1, 2 \\
(A'_0)_{i,j}^f &= 2c_{i,j}^f \frac{1 + 2\mu_q}{\Delta t} - \left((A'_1)_{i,j}^f \Big|_{\text{if } j > 0} + (A'_2)_{i,j}^f \Big|_{\text{if } i < n_r} \right) \\
(D')_{i,j}^f &= 2\mu_T (T_{i,j}^f - T_{i,j-1}^f) \frac{(\Phi_1)_{i,j}}{(R_1)_{i,j}^f} \Big|_{\text{if } j > 0} + 2\mu_T (T_{i,j}^f - T_{i+1,j}^f) \frac{(\Phi_2)_{i,j}}{(R_2)_{i,j}^f} \Big|_{\text{if } i < n_r} \\
&\quad + \left[-(1 + 2\mu_T)(T_{i,j}^f - T_{i,j+1}^f) + 2\mu_T (T_{i,j}^{f-0.5} - T_{i,j+1}^{f-0.5}) \right] \frac{(\Phi_3)_{i,j}}{(R_3)_{i,j}^f} \Big|_{\text{if } j < n_z} \\
&\quad + \left[-(1 + 2\mu_T)(T_{i,j}^f - T_{i-1,j}^f) + 2\mu_T (T_{i,j}^{f-0.5} - T_{i-1,j}^{f-0.5}) \right] \frac{(\Phi_4)_{i,j}}{(R_4)_{i,j}^f} \Big|_{\text{if } i > 0} \\
&\quad + 2c_{i,j}^f \frac{(1 + 4\mu_q)T_{i,j}^f - 2\mu_q T_{i,j}^{f-0.5}}{\Delta t} + (1 + 2\mu_q)Q_{i,j}^{f+0.5} - 2\mu_q Q_{i,j}^f
\end{aligned} \tag{3.22}$$

while the second system of equations (3.19) – in the following form

$$(A''_0)_{i,j}^{f+0.5} T_{i,j}^{f+1} + (A''_3)_{i,j}^{f+0.5} T_{i,j+1}^{f+1} \Big|_{\text{if } j < n_z} + (A''_4)_{i,j}^{f+0.5} T_{i-1,j}^{f+1} \Big|_{\text{if } i > 0} = (D'')_{i,j}^{f+0.5} \tag{3.23}$$

where

$$\begin{aligned}
(A''_k)_{i,j}^{f+0.5} &= -(1 + 2\mu_T) \frac{(\Phi_k)_{i,j}}{(R_k)_{i,j}^{f+0.5}} \quad k = 3, 4 \\
(A''_0)_{i,j}^{f+0.5} &= 2c_{i,j}^{f+0.5} \frac{1 + 2\mu_q}{\Delta t} - \left((A''_3)_{i,j}^{f+0.5} \Big|_{\text{if } j < n_z} + (A''_4)_{i,j}^{f+0.5} \Big|_{\text{if } i > 0} \right) \\
(D'')_{i,j}^{f+0.5} &= 2\mu_T (T_{i,j}^{f+0.5} - T_{i,j+1}^{f+0.5}) \frac{(\Phi_3)_{i,j}}{(R_3)_{i,j}^{f+0.5}} \Big|_{\text{if } j < n_z} + 2\mu_T (T_{i,j}^{f+0.5} - T_{i-1,j}^{f+0.5}) \frac{(\Phi_4)_{i,j}}{(R_4)_{i,j}^{f+0.5}} \Big|_{\text{if } i > 0} \\
&\quad + \left[-(1 + 2\mu_T)(T_{i,j}^{f+0.5} - T_{i,j-1}^{f+0.5}) + 2\mu_T (T_{i,j}^f - T_{i,j-1}^f) \right] \frac{(\Phi_1)_{i,j}}{(R_1)_{i,j}^{f+0.5}} \Big|_{\text{if } j > 0} \\
&\quad + \left[-(1 + 2\mu_T)(T_{i,j}^{f+0.5} - T_{i+1,j}^{f+0.5}) + 2\mu_T (T_{i,j}^f - T_{i+1,j}^f) \right] \frac{(\Phi_2)_{i,j}}{(R_2)_{i,j}^{f+0.5}} \Big|_{\text{if } i < n_r} \\
&\quad + 2c_{i,j}^{f+0.5} \frac{(1 + 4\mu_q)T_{i,j}^{f+0.5} - 2\mu_q T_{i,j}^f}{\Delta t} + (1 + 2\mu_q)Q_{i,j}^{f+1} - 2\mu_q Q_{i,j}^{f+0.5}
\end{aligned} \tag{3.24}$$

The initial conditions (1.10) are implemented as

$$T_{i,j}^0 = T_0(r_i, z_j) \quad T_{i,j}^{0.5} = T_{i,j}^0 + 0.5\Delta t v_0(r_i, z_j) \tag{3.25}$$

In a similar way, one can obtain the other variants of ADI, e.g. (1,3)-(2,4), (2,4)-(1,3), etc, by replacing the indexes of directions in the sums in Eqs. (3.18) and (3.19).

Both systems of equations lead to systems with three-diagonal matrices.

4. Results

Numerical simulations of the thermal process in a thin film (chromium) subjected to the short-pulse laser heating have been done. Thermophysical parameters of chromium are the following:

$\lambda = 93 \text{ W}/(\text{mK})$, $c = 3.2148 \cdot 10^6 \text{ J}/(\text{m}^3\text{K})$, $\tau_q = 0.136 \cdot 10^{-12} \text{ s}$, $\tau_T = 7.86 \cdot 10^{-12} \text{ s}$ (Tang and Araki, 1999). The cylindrical domain with dimensions $Z = 100 \cdot 10^{-9} \text{ m}$, $R = 100 \cdot 10^{-9} \text{ m}$ is considered. The parameters of the Gaussian-shaped pulse are equal to: $r_d = 50 \cdot 10^{-9} \text{ m}$, $I_0 = 13.7 \text{ W}/\text{m}^2$, $R_f = 0.93$, $\delta = 15.3 \cdot 10^{-12} \text{ m}$, $t_p = 100 \cdot 10^{-15} \text{ s}$. The initial temperature and the initial heating rate of the metal are equal to: $T_0(r, z) = 20^\circ\text{C}$ and $v_0(r, z) = 0 \text{ K}/\text{s}$. Different mesh steps: Δz , Δr and different time step Δt are tested in this example.

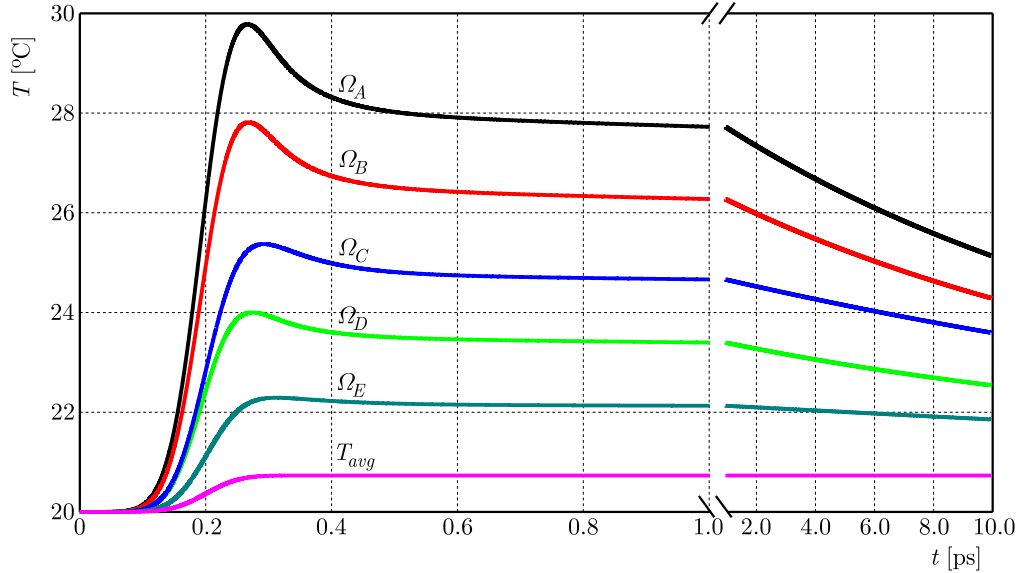


Fig. 4. Heating curves at the selected control volumes Ω_k and the average temperature of the domain

In Fig. 4, the temperature histories (calculated as the average temperature) at five selected control volumes of the domain

$$\begin{aligned}
 \Omega_A &= \left\{ (r, z) \mid 0 \leq r \leq \frac{\Delta r}{2}, 0 \leq z \leq \frac{\Delta z}{2} \right\} \\
 \Omega_B &= \left\{ (r, z) \mid \frac{R}{4} - \frac{\Delta r}{2} \leq r \leq \frac{R}{4} + \frac{\Delta r}{2}, 0 \leq z \leq \frac{\Delta z}{2} \right\} \\
 \Omega_C &= \left\{ (r, z) \mid \frac{R}{2} - \frac{\Delta r}{2} \leq r \leq \frac{R}{2} + \frac{\Delta r}{2}, 0 \leq z \leq \frac{\Delta z}{2} \right\} \\
 \Omega_D &= \left\{ (r, z) \mid 0 \leq r \leq \frac{\Delta r}{2}, \frac{Z}{5} - \frac{\Delta z}{2} \leq z \leq \frac{Z}{5} + \frac{\Delta z}{2} \right\} \\
 \Omega_E &= \left\{ (r, z) \mid \frac{R}{2} - \frac{\Delta r}{2} \leq r \leq \frac{R}{2} + \frac{\Delta r}{2}, \frac{Z}{5} - \frac{\Delta z}{2} \leq z \leq \frac{Z}{5} + \frac{\Delta z}{2} \right\}
 \end{aligned} \tag{4.1}$$

are shown. In this figure, the course of the average temperature T_{avg} of the whole cylindrical domain is also presented. Here, the calculations are performed using the ADI variant: (1,2)-(3,4) for the following parameters of meshes: $\Delta z = 10^{-9} \text{ m}$, $\Delta r = 10^{-9} \text{ m}$, $\Delta t = 10^{-16} \text{ s}$.

The courses of isotherms for the selected moments of time: 0.3, 0.5, 1 and 10 ps are presented in Fig. 5.

Next, the comparison of different variants of the ADI method (here: schemas (1,2)-(3,4) and (1,3)-(2,4) are chosen) for different sizes of meshes is studied. Adequate numerical simulations have been performed. The differences in the numerical solutions are hard to see in the graphs. So, the numerical results (as the average temperature at the selected control volumes (4.1) at time $t = 0.3 \text{ ps}$) for different sizes of meshes are collected in Table 1. The analytical solution of the problem considered is so far unknown in literature and, hence, it is difficult to estimate which numerical scheme is the best.

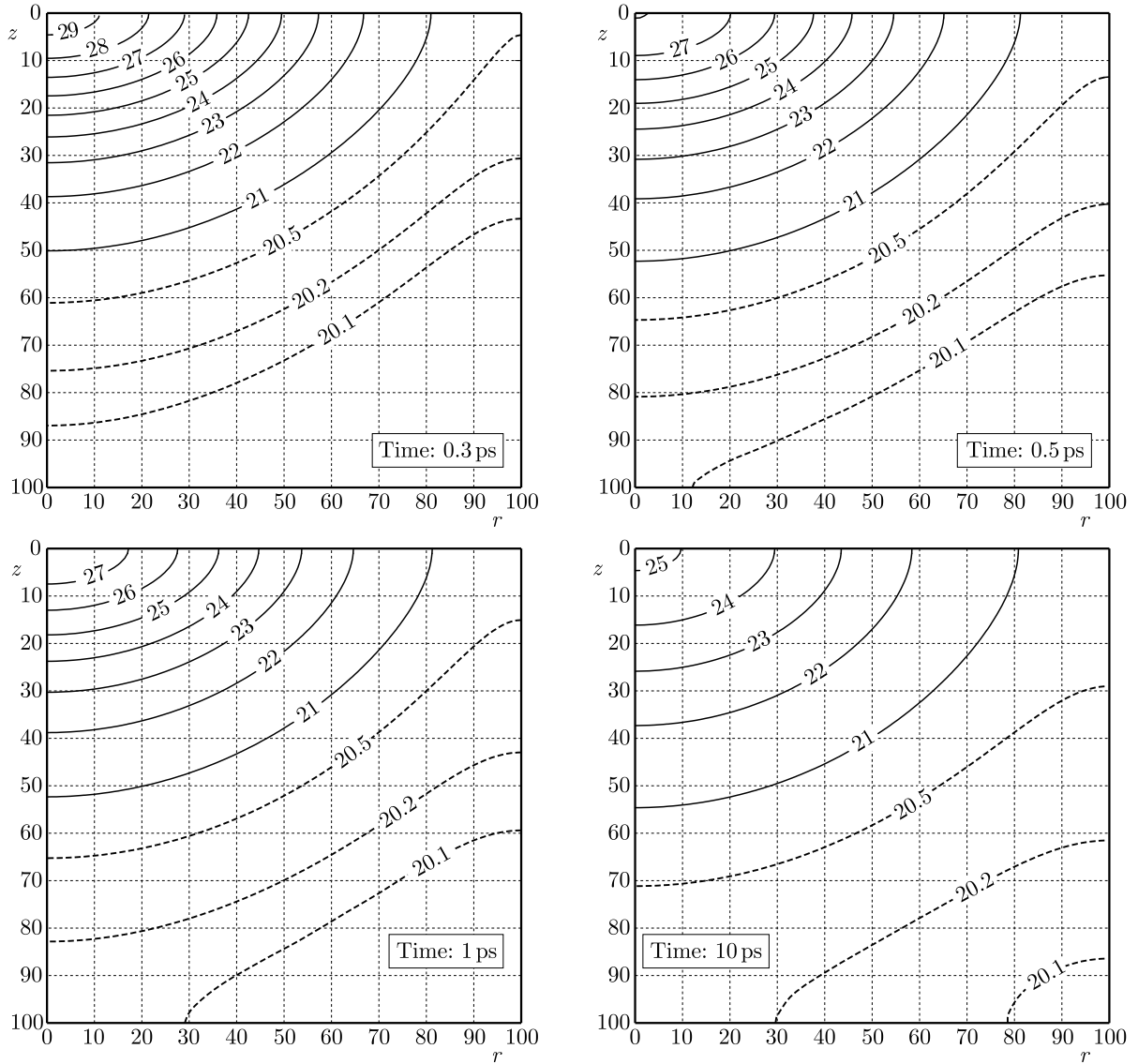


Fig. 5. Courses of isotherms in the cross-section of the domain for different times

Table 1. Numerical results (temperature) for different sizes of meshes

$\Delta r = \Delta z$ [m]	Δt [s]	Method	Average temperature at time $t = 0.3$ ps at selected CV [°C]				
			Ω_A	Ω_B	Ω_C	Ω_D	Ω_E
10^{-8} ($n_r = n_z = 10$)	10^{-15}	(1,2)-(3,4)	29.407462	28.175041	23.939626	25.296615	22.257754
		(1,3)-(2,4)	29.407477	28.175054	23.939633	25.296637	22.257766
	10^{-16}	(1,2)-(3,4)	29.423528	28.188169	23.943812	25.297708	22.256563
		(1,3)-(2,4)	29.423528	28.188169	23.943812	25.297709	22.256563
	10^{-17}	(1,2)-(3,4)	29.425095	28.189446	23.944210	25.297781	22.256427
		(1,3)-(2,4)	29.425095	28.189446	23.944210	25.297781	22.256427
10^{-9} ($n_r = n_z = 100$)	10^{-15}	(1,2)-(3,4)	29.385557	27.542517	23.924927	25.361719	22.284553
		(1,3)-(2,4)	29.387539	27.544204	23.926049	25.365099	22.286141
	10^{-16}	(1,2)-(3,4)	29.403565	27.555886	23.930159	25.366322	22.284954
		(1,3)-(2,4)	29.403585	27.555903	23.930170	25.366356	22.284970
	10^{-17}	(1,2)-(3,4)	29.405160	27.557048	23.930567	25.366453	22.284839
		(1,3)-(2,4)	29.405159	27.557046	23.930567	25.366452	22.284839

The total energy (ΔQ [J]) applied to the considered domain during one laser pulse is equal to

$$\begin{aligned} \Delta Q &= \int_0^{4t_p} \int_0^Z \int_0^R \int_0^{2\pi} Q(r, z, t) r \, d\Phi \, dr \, dz \, dt \\ &= I_0(1 - R_f)\pi \frac{r_d^2}{2} \left[1 - \exp\left(-\frac{R^2}{r_d^2}\right) \right] \left[1 - \exp\left(-\frac{Z}{\delta}\right) \right] [\operatorname{erf}(2\beta) - \operatorname{erf}(-2\beta)] \end{aligned} \quad (4.2)$$

The laser energy causes a rise in temperature equal to ΔT [°C] in the domain (assuming adiabatic conditions at all boundaries)

$$\Delta T = \frac{\Delta Q}{cV} \quad (4.3)$$

where $V = \pi R^2 Z$ [m³] is the volume of the whole domain. For the above mentioned values of parameters, the temperature increases by $\Delta T = 0.731048^\circ\text{C}$ after one laser pulse. This value is used, among others, to compare the correctness of the numerical results. It should be pointed out that the analytical value and numerical values are practically the same (the errors are of the order 0.00001°C).

5. Conclusion

The dual phase lag model seems to be adequate for mathematical description of microscale heat transfer. In many situations when analytical solutions are not known, the numerical solutions are desired to be found. To obtain an effective solution to the considered problem, the algorithm based on the control volume method is presented. The DPLM consists of the partial differential equation of a hyperbolic type, and thus the more complex numerical schemes should be developed, of course. In this paper, the Alternating Direction Implicit scheme is constructed. This scheme can be easily implemented in computer programs. In opposite to other schemes, such as the Crank-Nicolson scheme, where it is necessary to solve the system of equations characterized by a 5-band matrix, the ADI method requires double solving of the systems with 3-band matrices. From the computational point of view, the solution of the system of equations with the 3-band matrix is efficient and fast. The numerical scheme allows one to use the thermophysical parameters of the material (i.e. thermal conductivity and volumetric specific heat) as the temperature-dependent (in this paper these parameters are assumed to be constant values). The results (see: the temperatures presented in Table 1) obtained by application of the two types of numerical schemes are very similar, especially the results obtained for the same set of the parameters of meshes: $\{\Delta z, \Delta r, \Delta t\}$ are practically identical.

Acknowledgement

The paper is a part of research project 2015/19/B/ST8/01101 sponsored by NSC (Poland).

References

1. BELKHAYAT-PIASECKA A., KORCZAK A., 2016, Modeling of transient heat transport in metal films using the interval lattice Boltzmann method, *Bulletin of the Polish Academy of Sciences – Technical Sciences*, **64**, 3, 599-505
2. CATTANEO C., 1958, A form of heat conduction equation which eliminates the paradox of instantaneous propagation, *Compte Rendus*, **27**, 431-433

3. CHEN G., BORCA-TASCIUC D., YANG R.G., 2004, Nanoscale heat transfer, [In:] *Encyclopedia of Nanoscience and Nanotechnology*, Nalwa H.S. (Edit.), Vol. X, 1-30, <http://www.aspbs.com/enn.html>
4. CHEN J.K., BERAUN J.E., 2001, Numerical study of ultrashort laser pulse interactions with metal films, *Numerical Heat Transfer, Part A*, **40**, 1-20
5. CHEN W.H., CHENG H.C., HSU Y.C., 2007, Mechanical properties of carbon nanotubes using molecular dynamics simulations with the inlayer van der Waals interactions, *CMES: Computer Modeling in Engineering and Sciences*, **20**, 2, 123-145
6. CIESIELSKI M., DUDA M., MOCHNACKI B., 2016, Comparison of bio-heat transfer numerical models based on the Pennes and Cattaneo-Vernotte equations, *Journal of Applied Mathematics and Computational Mechanics*, **15**, 4, 33-38
7. CIESIELSKI M., MOCHNACKI B., 2014, Application of the control volume method using the Voronoi polygons for numerical modeling of bio-heat transfer processes, *Journal of Theoretical and Applied Mechanics*, **52**, 4, 927-935
8. DAI W., NASSAR R., 2000, A domain decomposition method for solving three-dimensional heat transport equations in a double-layered thin film with microscale thickness. *Numerical Heat Transfer, Part A*, **38**, 243-255
9. DZIATKIEWICZ J., KUŚ W., MAJCHRZAK E., BURCZYŃSKI T., TURCHAN L., 2014, Bioinspired identification of parameters in microscale heat transfer, *International Journal for Multiscale Computational Engineering*, **12**, 1, 79-89
10. ESCOBAR R.A., GHAI S.S., JHON M.S., AMON C.H., 2006, Multi-length and time scale thermal transport using the lattice Boltzmann method with application to electronics cooling, *International Journal of Heat and Mass Transfer*, **49**, 97-107
11. KABA I.K., DAI W., 2005, A stable three-level finite difference scheme for solving the parabolic two-step model in a 3D micro-sphere heated by ultrashort-pulsed lasers, *Journal of Computational and Applied Mathematics*, **181**, 125-147
12. LIN Z., ZHIGILEI L.V., 2008, Electron-phonon coupling and electron heat capacity of metals under conditions of strong electron-phonon nonequilibrium, *Physical Review, B*, **77**, 075133-1-075133-17
13. LIU D.S., TSAI C.Y., 2009, Estimation of thermo-elasto-plastic properties of thin-film mechanical properties using MD nanoindentation simulations and an inverse FEM/ANN computational scheme, *CMES: Computer Modeling in Engineering and Sciences*, **39**, 1, 29-47
14. MAJCHRZAK E., 2012, Parabolic and hyperbolic two-temperature models of microscopic heat transfer. Comparison of numerical solutions, *Materials Science Forum*, **706-709**, 1454-1459
15. MAJCHRZAK E., DZIATKIEWICZ J., 2015, Analysis of ultrashort laser pulse interactions with metal films using a two-temperature model, *Journal of Applied Mathematics and Computational Mechanics*, **14**, 2, 31-39
16. MAJCHRZAK E., MOCHNACKI B., 2014, Sensitivity analysis of transient temperature field in microdomains with respect to the dual phase lag model parameters, *International Journal for Multiscale Computational Engineering*, **12**, 1, 65-77
17. MAJCHRZAK E., MOCHNACKI B., GREER A.L., SUCHY J.S., 2009a, Numerical modeling of short pulse laser interactions with multi-layered thin metal films, *CMES: Computer Modeling in Engineering and Sciences*, **41**, 2, 131-146
18. MAJCHRZAK E., MOCHNACKI B., SUCHY J.S., 2009b, Numerical simulation of thermal processes proceeding in a multi-layered film subjected to ultrafast laser heating, *Journal of Theoretical and Applied Mechanics*, **47**, 2, 383-396
19. MAJCHRZAK E., TURCHAN L., 2016, Modeling of phase changes in the metal micro-domains subjected to ultrafast laser heating using dual-phase lag equation, *Materialwissenschaft und Werkstofftechnik*, **47**, 5/6, 409-418

20. MITRA K., KUMAR S., VEDAVARZ A., MOALLEMI M.K., 1995, Experimental evidence of hyperbolic heat conduction in processed meat, *ASME Journal of Heat Transfer*, **17**, 568-573
21. MOCHNACKI B., CIESIELSKI M., 2012, Numerical model of thermal processes in domain of thin film subjected to a cyclic external heat flux, *Materials Science Forum*, **706-709**, 1460-1465
22. MOCHNACKI B., CIESIELSKI M., 2015, Micro-scale heat transfer. Algorithm basing on the control volume method and the identification of relaxation and thermalization times using the search method, *Computer Methods in Materials Science*, **15**, 2, 353-361
23. MOCHNACKI B., PARUCH M., 2013, Estimation of relaxation and thermalization times in micro-scale heat transfer, *Journal of Theoretical and Applied Mechanics*, **51**, 4, 837-845
24. ORLANDE H.R.B., ÖZİŞİK M.N., TZOU D.Y., 1995, Inverse analysis for estimating the electron-phonon coupling factor in thin metal films, *Journal of Applied Physics*, **78**, 3, 1843-1849
25. SMITH A.N., NORRIS P.M., 2003, *Microscale Heat Transfer*, Chapter 18 in: *Heat Transfer Handbook*, John Wiley & Sons
26. TANG D.W., ARAKI N., 1999, Wavy, wavelike, diffusive thermal responses of finite rigid slabs to high-speed heating of laser-pulses, *International Journal of Heat and Mass Transfer*, **42**, 855-860
27. THEODOSIOU T.C., SARAVANOS D.A., 2007, Molecular mechanics based finite element for carbon nanotube modeling, *CMES: Computer Modeling in Engineering and Sciences*, **19**, 121-134
28. TIAN W., YANG R., 2008, Phonon transport and thermal conductivity percolation in random nanoparticle composites, *CMES: Computer Modeling in Engineering and Sciences*, **24**, 123-142
29. TZOU D.Y., 2015, *Macro- to Microscale Heat Transfer: The Lagging Behavior*, John Wiley & Sons, Ltd.
30. ZHANG Z.M., 2007, *Nano/microscale Heat Transfer*, McGraw-Hill, New York

Manuscript received January 25, 2017; accepted for print February 16, 2017

**BENDING, BUCKLING, AND FORCED VIBRATION ANALYSES OF
NONLOCAL NANOCOMPOSITE MICROPLATE USING TSDT
CONSIDERING MEE PROPERTIES DEPENDENT TO VARIOUS VOLUME
FRACTIONS OF $\text{CoFe}_2\text{O}_4\text{-BaTiO}_3$**

MEHDI MOHAMMADIMEHR, RASOUL ROSTAMI

*University of Kashan, Department of Solid Mechanics, Faculty of Mechanical Engineering, Kashan, Iran
e-mail: mmohammadimehr@kashanu.ac.ir; r_rostami@grad.kashanu.ac.ir*

In this article, the bending, buckling, free and forced vibration behavior of a nonlocal nano-composite microplate using the third order shear deformation theory (TSDT) is presented. The magneto-electro-elastic (MEE) properties are dependent on various volume fractions of $\text{CoFe}_2\text{O}_4\text{-BaTiO}_3$. According to Maxwell's equations and Hamilton's principle, the governing differential equations are derived. These equations are discretized by using Navier's method for an MEE nanocomposite Reddy plate. The numerical results show the influences of elastic foundation parameters such as aspect ratio, length to thickness ratio, electric and magnetic fields and various volume fractions of $\text{CoFe}_2\text{O}_4\text{-BaTiO}_3$ on deflection, critical buckling load and natural frequency. The natural frequency and critical buckling load increases with the increasing volume fraction of $\text{CoFe}_2\text{O}_4\text{-BaTiO}_3$, also the amplitude vibration decreases with an increase in the volume fraction. This model can be used for various nanocomposite structures. Also, a series of new experiments are recommended for future work.

Keywords: bending and buckling analysis, free and forced vibration analysis, nonlocal nano-composite microplate, various volume fractions of $\text{CoFe}_2\text{O}_4\text{-BaTiO}_3$

1. Introduction

In the recent years, the use of nano-technology is a subject of the main discussion in the world of engineering sciences. Nano-technology is science in which the design and application of nanostructures relates different properties at the nanoscale. The size of nanoparticles and their dispersion in a matrix composite is one of the ways to achieve desired properties of nanocomposites. According to the nanometer-scale, the reinforcement particles in nanocomposites, intermolecular forces between the matrix and reinforcing is much greater than in ordinary composites, which improves properties of the nanocomposites. The reinforcing phase in terms of the material can be used as polymeric, metal and ceramic, which, according to different properties of each, have different applications. Because of their magnetoelectric coupling effects, magneto-electric-elastic (MEE) materials have been widely employed in many technological fields, such as sensor and actuator applications, robotics, medical instruments, structural health monitoring, energy harvesting. Many researchers have carried out static, buckling, and free vibration analysis of nanocomposites, see Sih and Yu (2005) who analyzed the volume fraction effect of a MEE composite on enhancement and impediment of crack growth. Their results showed that with the increasing electric field to normal stress ratio and the volume fraction effect of the MEE composite, the crack growth increased and decreased, respectively. Ke and Wang (2014) examined free vibration of size-dependent magneto-electro-elastic nanobeams based on the nonlocal elasticity theory. By using the Hamilton principle, the governing equations and boundary conditions were derived and discretized by using the differential quadrature method (DQM) to determine natural frequencies. Their results showed that with the increasing magnetic and electric potential, the

natural frequencies of nanobeams increased. Shokrani *et al.* (2016) employed the generalized differential quadrature method (GDQM) to the buckling analysis of double orthotropic nanoplates (DONP) embedded in elastic media under biaxial, uniaxial and shear loadings. Their results showed that for higher values of the non-local parameter, the shear buckling was not dependent on the van der Waals and Winkler moduli. Lang and Xuewu (2013) studied the buckling and vibration of functionally graded magneto-electro-thermo-elastic circular cylindrical shells. Based on using the third order shear theory (TSDT), they employed Hamilton's principle to obtain equations of motion and numerical solutions to find the natural frequencies. Ghorbanpour Arani *et al.* (2012) investigated the effect of the CNT volume fraction on the magneto-thermo-electro-mechanical behavior of a smart nanocomposite cylinder. Their results indicated that the influence of internal pressure on the radial stress was larger than thermal, magnetic and electric fields. Also, their results are very useful for the optimization of nano-composite structures. Xin and Hu (2015) analyzed free vibration of multilayered magneto-electro-elastic plates based on the state space approach (SSA) and the discrete singular convolution (DSC) algorithm. The results showed that the piezoelectric effect had a tendency to increase the stiffness of the plate, and vice versa for the magnetostrictive effect. Karimi *et al.* (2015a) investigated surface effects and non-local two variable refined plate theories that were combined on the shear/biaxial buckling and vibration of rectangular nanoplates. Their results showed that by increasing the non-local parameter, the effects of surface on the buckling and vibration increased. Shooshtari and Razavi (2015) studied nonlinear free vibration behavior of a symmetrically laminated MEE doubly-curved thin shell resting on an elastic foundation. By introducing a force function and using the Galerkin method, the nonlinear partial differential equations of motion were reduced to a single nonlinear ordinary differential equation. That equation was solved analytically by the Lindstedt-Poincaré perturbation method. Their results showed that the shear constant coefficient of the foundation had much greater effect on the natural frequency when compared with the spring constant coefficient, and both of those coefficients increased the fundamental natural frequency. Ebrahimi and Nasirzadeh (2016) analyzed free vibration of thick nanobeams based on Eringen nonlocal elasticity theory and Timoshenko beam theory. Chen *et al.* (2014) studied free vibration of multilayered MEE plates under combined clamped/free lateral boundary conditions. Using semi-analytical solution, they obtained the natural frequency. Their results illustrated the effect of stacking sequences and magneto-electric coupling on natural frequencies and mode shapes. Karimi *et al.* (2015c) analyzed size-dependent free vibration characteristics of rectangular nanoplates considering surface stress effects. Numerical results demonstrated that the obtained natural frequency by considering the surface effects was lower than that without considering the surface properties. Razavi and Shooshtari (2015) employed nonlinear free vibration of symmetric MEE laminated rectangular plates with simply supported boundary conditions. Their results for the nonlinear natural frequency ratio were compared with the available results for isotropic, laminated layers and piezo-layers and laminated MEE plates. Their results depicted that the foundation parameters, negative electric potential and positive magnetic potential increased the equivalent stiffness of the system. Using Bert's model, Khan *et al.* (2014) studied free and forced vibration characteristics of bimodular composite laminated circular cylindrical shells. The results indicated that the relative difference of positive and negative half cycle frequencies was considerably less for single layer orthotropic shells, and it was significant for cross-ply shells with the axisymmetric mode of vibration. Du *et al.* (2014) illustrated nonlinear forced vibration analysis of infinitely long functionally graded cylindrical shells using the Lagrangian theory and the multiple scale method. Their results found that the power-law exponent had not any influence on the qualitative behavior of FG cylindrical shells, but it would change the amplitude in a complex nonlinear way. Hasani Baferani *et al.* (2011) presented free vibration analysis of FG thick rectangular plates resting on an elastic foundation. They obtained governing equations of motion using the third order shear deformation plate theory and Hamilton's

principle. Their results showed that the Pasternak elastic foundation drastically changed the natural frequency. Also some boundary conditions and in-plane displacements had significant effects on the natural frequency of FG thick plates. Arefi (2015) analyzed free vibration of a FG solid and annular circular plates with two functionally graded piezoelectric layers at the top and bottom subjected to an electric field. Sobhy (2013) investigated buckling and free vibration of exponentially graded sandwich plates resting on elastic foundations under various boundary conditions. The governing equations of plates were derived by using various shear deformation plate theories. They showed influence of the inhomogeneity parameter, aspect ratio, thickness ratio and foundation parameters on natural frequencies and critical buckling loads. Zidour *et al.* (2014) illustrated buckling of chiral single-walled carbon nanotubes by using the nonlocal Timoshenko beam theory. Their results showed influence of a nonlocal small-scale coefficient and the vibration mode number on the nonlocal critical buckling loads. Karimi *et al.* (2015b) studied influence of the nonlocal parameter, van der Waals, Winkler, shear modulus on shear vibration and buckling of double-layer orthotropic nanoplates resting on an elastic foundation.

In this article, bending, buckling, free and forced vibration of a magneto-electro-elastic (MEE) microplate based on the third order shear deformation theory (TSDT) is presented. According to Maxwell's equations and Hamilton's principle, the governing differential equation is obtained. These equations discretized by using Navier's method for a MEE microplate with all edges simply supported boundary enabled determination of the deflection, critical buckling load, natural frequency, response of the system as well as the electric and magnetic intensity of the microplate. The numerical results show the influence of elastic foundation parameters, aspect ratio l/b , length to thickness ratio l/h , volume fraction, normal pressure on the deflection, critical buckling load, natural frequency, response of the system and the electric and magnetic intensity.

2. Nonlocal theory of the MEE

The non-local modulus of elasticity was presented by Eringen (1983). This model states that the stress of a point in the micro and nano dimension is dependent on the strain in all parts of the model. The fundamental equations of a homogeneous and isotropic non-local elastic solid are given by Eringen (2002)

$$\sigma_{ij}^{nl}(x) = \int_V \alpha(|x - x'|, \tau) \sigma'_{ij} dV(x') \quad \forall x \in V \tag{2.1}$$

For the MEE solid, the nonlocal fundamental equations for magnetic induction and electric displacement can be obtained as follows

$$\begin{aligned} D_{ij}^{nl}(x) &= \int_V \alpha(|x - x'|, \tau) D'_{ij} dV(x') & \forall x \in V \\ B_{ij}^{nl}(x) &= \int_V \alpha(|x - x'|, \tau) B'_{ij} dV(x') & \forall x \in V \end{aligned} \tag{2.2}$$

where σ_{ij}^{nl} , σ'_{ij} , D_{ij}^{nl} , D'_{ij} , B_{ij}^{nl} and B'_{ij} are the nonlocal and local stress tensor, components of the nonlocal and local electric displacements, components of the nonlocal and local magnetic inductions, respectively. $\alpha(|x - x'|, \tau)$ is the nonlocal modulus, $|x - x'|$ is the Euclidean distance, $\tau = e_0 a/l$ is defined as the small scale parameter.

According to Eringen (1983, 2002), the nonlocal elasticity theory can be simplified to partial differential equations. Thus we have

$$[1 - (e_0 a)^2 \nabla^2] \sigma_{ij}^{nl} = \sigma'_{ij} \quad [1 - (e_0 a)^2 \nabla^2] D_{ij}^{nl} = D'_{ij} \quad [1 - (e_0 a)^2 \nabla^2] B_{ij}^{nl} = B'_{ij} \tag{2.3}$$

3. Constitutive equations of the MEE nanocomposite microplate

Consider an MEE nanocomposite microplate with length l , width b and thickness h , resting on an elastic foundation as shown in Fig. 1. A Cartesian coordinate system (x, y, z) is considered such that the z direction denotes thickness of the nanocomposite microplate.

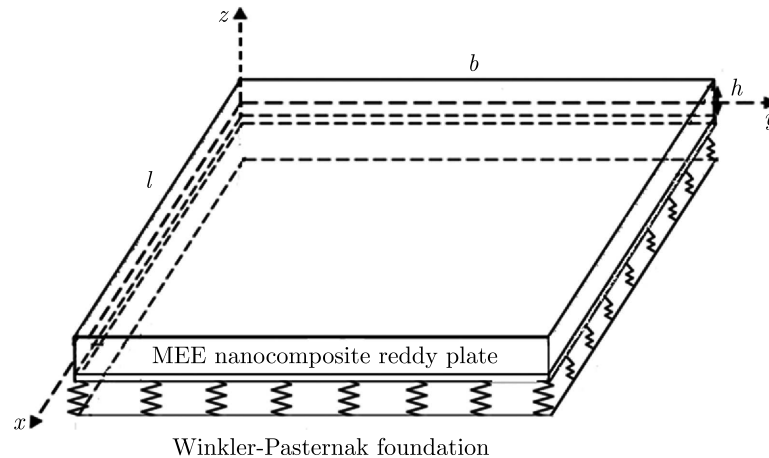


Fig. 1. Schematic of an MEE nanocomposite microplate on the elastic foundation

Based on the third-order shear deformation theory (TSDT) for a nanocomposite plate, the displacements of an arbitrary point in the beam along the x , y and z axes are denoted by $u_1(x, y, z, t)$, $u_2(x, y, z, t)$ and $u_3(x, y, z, t)$, respectively. They are written as follows

$$\begin{aligned} u_1(x, y, z, t) &= u(x, y, t) + z \left[\psi_x(x, y, t) - \frac{4}{3} \left(\frac{z}{h} \right)^2 [\psi_x(x, y, t) + w(x, y, t),_x] \right] \\ u_2(x, y, z, t) &= v(x, y, t) + z \left[\psi_y(x, y, t) - \frac{4}{3} \left(\frac{z}{h} \right)^2 [\psi_y(x, y, t) + w(x, y, t),_y] \right] \\ u_3(x, y, z, t) &= w(x, y, t) \end{aligned} \quad (3.1)$$

where u , v , w are the mid-plane displacements of the MEE rectangular nanocomposite microplate along the (x, y, z) coordinate directions, respectively, ψ_x , ψ_y denote rotations of the plate cross-section and t is time.

The linear constitutive equations for the MEE nanocomposite microplate in the plane stress state are expressed in the following form (Mohammadimehr *et al.*, 2016a,b, 2017; Ghorbanpour Arani *et al.*, 2016)

$$\begin{aligned} \begin{Bmatrix} \sigma_{11} \\ \sigma_{22} \\ \tau_{12} \\ \tau_{13} \\ \tau_{23} \end{Bmatrix} &= \frac{1}{1 - (e_0 a)^2 \nabla^2} \begin{bmatrix} C_{11} & C_{12} & 0 & 0 & 0 \\ C_{12} & C_{22} & 0 & 0 & 0 \\ 0 & 0 & C_{44} & 0 & 0 \\ 0 & 0 & 0 & C_{44} & 0 \\ 0 & 0 & 0 & 0 & C_{55} \end{bmatrix} \begin{Bmatrix} \varepsilon_{11} \\ \varepsilon_{22} \\ \gamma_{12} \\ \gamma_{13} \\ \gamma_{23} \end{Bmatrix} \\ &- \begin{bmatrix} 0 & 0 & e_{31} \\ 0 & 0 & e_{31} \\ 0 & e_{24} & 0 \\ e_{15} & 0 & 0 \\ 0 & 0 & 0 \end{bmatrix} \begin{Bmatrix} E_x \\ E_y \\ E_z \end{Bmatrix} - \begin{bmatrix} 0 & 0 & f_{31} \\ 0 & 0 & f_{31} \\ 0 & f_{24} & 0 \\ f_{15} & 0 & 0 \\ 0 & 0 & 0 \end{bmatrix} \begin{Bmatrix} H_x \\ H_y \\ H_z \end{Bmatrix} \end{aligned}$$

$$\begin{aligned}
 \begin{Bmatrix} D_x \\ D_y \\ D_z \end{Bmatrix} &= \frac{1}{1 - (e_0 a)^2 \nabla^2} \begin{pmatrix} 0 & 0 & 0 & e_{15} & 0 \\ 0 & 0 & e_{24} & 0 & 0 \\ e_{31} & e_{31} & 0 & 0 & 0 \end{pmatrix} \begin{Bmatrix} \varepsilon_{11} \\ \varepsilon_{22} \\ \gamma_{12} \\ \gamma_{13} \\ \gamma_{23} \end{Bmatrix} \\
 &+ \begin{bmatrix} h_{11} & 0 & 0 \\ 0 & h_{22} & 0 \\ 0 & 0 & h_{33} \end{bmatrix} \begin{Bmatrix} E_x \\ E_y \\ E_z \end{Bmatrix} + \begin{bmatrix} g_{11} & 0 & 0 \\ 0 & g_{22} & 0 \\ 0 & 0 & g_{33} \end{bmatrix} \begin{Bmatrix} H_x \\ H_y \\ H_z \end{Bmatrix} \\
 \begin{Bmatrix} B_x \\ B_y \\ B_z \end{Bmatrix} &= \frac{1}{1 - (e_0 a)^2 \nabla^2} \begin{pmatrix} 0 & 0 & 0 & f_{15} & 0 \\ 0 & 0 & f_{24} & 0 & 0 \\ f_{31} & f_{31} & 0 & 0 & 0 \end{pmatrix} \begin{Bmatrix} \varepsilon_{11} \\ \varepsilon_{22} \\ \gamma_{12} \\ \gamma_{13} \\ \gamma_{23} \end{Bmatrix} \\
 &+ \begin{bmatrix} g_{11} & 0 & 0 \\ 0 & g_{22} & 0 \\ 0 & 0 & g_{33} \end{bmatrix} \begin{Bmatrix} E_x \\ E_y \\ E_z \end{Bmatrix} + \begin{bmatrix} \mu_{11} & 0 & 0 \\ 0 & \mu_{22} & 0 \\ 0 & 0 & \mu_{33} \end{bmatrix} \begin{Bmatrix} H_x \\ H_y \\ H_z \end{Bmatrix}
 \end{aligned} \tag{3.2}$$

where σ_{11} , σ_{22} and ε_{11} , ε_{22} are the normal stresses and strains, respectively. τ_{12} , τ_{13} , τ_{23} and γ_{12} , γ_{13} , γ_{23} denote the shear stresses and strains, respectively. C_{ij} , e_{ij} , f_{ij} and g_{ij} denote elastic, piezoelectric, piezomagnetic and magnetoelectric constants, respectively; h_{ij} and μ_{ij} are dielectric and magnetic permeability coefficients, respectively. E_{ij} and H_{ij} are the electric magnetic field intensity, respectively.

The electric and magnetic fields are considered in terms of electric and magnetic potentials ϕ and φ , respectively, which are defined as follows

$$E_i = -\phi_{,i} \quad H_i = -\varphi_{,i} \quad i = 1, 2, 3 \tag{3.3}$$

4. The governing equations of motion for the MEE nanocomposite microplate

The governing differential equations of motion for the MEE nanocomposite microplate are derived using Hamilton's principle which is given by (Mohammadimehr and Mostafavifar, 2016)

$$\int_0^t (\delta T - \delta U - \delta W) dt = 0 \tag{4.1}$$

where δT , δU and δW are the variations of kinetic energy and strain energy, the work done by external applied forces, respectively.

Variations of the kinetic energy for a sandwich plate can be described as follows (Ghorbanpour and Haghparast, 2017)

$$\delta T = \int_V \rho_i \frac{\partial u_i}{\partial t} \delta \left(\frac{\partial u_i}{\partial t} \right) dV = \int_A \int_{-\frac{h}{2}}^{\frac{h}{2}} \rho_i (\dot{u}_1 \delta \dot{u}_1 + \dot{u}_2 \delta \dot{u}_2 + \dot{u}_3 \delta \dot{u}_3) dz dA \tag{4.2}$$

where

$$I_i = \int_{-h}^h \rho z^i dz \quad (i = 1, 2, 3, 4, 6) \quad C_1 = \frac{4}{3h^2}$$

Variations of the strain energy for the MEE nanocomposite microplate can be expressed as

$$\begin{aligned}
\delta U &= \int_V (\sigma_{ij} \delta \varepsilon_{ij} - D_i \delta E_i - B_i H_i) dV \\
&= \int_V [(\sigma_{11} \delta \varepsilon_{11} + \sigma_{22} \delta \varepsilon_{22} + \sigma_{33} \delta \varepsilon_{33} + \tau_{12} \delta \gamma_{12} + \tau_{13} \delta \gamma_{13} + \tau_{23} \delta \gamma_{23}) \\
&\quad - (D_x \delta E_x + D_y \delta E_y + D_z \delta E_z) - (B_x \delta H_x + B_y \delta H_y + B_z \delta H_z)] dV
\end{aligned} \tag{4.3}$$

Variations of the work can be considered as follows

$$\delta W = - \int P(x, y) \delta w \, dx + \int (k_w w - k_G \nabla^2 w) \delta w \, dx \tag{4.4}$$

where K_w and K_G are the transverse and shear coefficients of elastic medium, respectively.

By substituting Eqs. (4.2)-(4.4) into Eq. (4.1), the equilibrium equations of the MEE nano-composite microplate resting on an elastic foundation can be obtained in the following form

$$\begin{aligned}
\delta u : \quad N_{1,x} + N_{6,y} &= I_0 \ddot{u} + I_1 \ddot{\psi}_x - C_1 I_3 \left(\ddot{\psi}_x + \frac{\partial \ddot{w}}{\partial x} \right) \\
\delta v : \quad N_{2,y} + N_{6,x} &= I_0 \ddot{v} + I_1 \ddot{\psi}_y - C_1 I_3 \left(\ddot{\psi}_y + \frac{\partial \ddot{w}}{\partial y} \right) \\
\delta \psi_x : \quad M_{1,x} + M_{6,y} - Q_1 - \frac{4}{3h^2} (P_{1,x} + P_{6,y}) + \frac{4\lambda}{h^2} R_1 \\
&= I_1 \ddot{u} + I_2 \ddot{\psi}_x - C_1 \left(I_3 \ddot{u} + 2I_4 \ddot{\psi}_x + I_4 \frac{\partial \ddot{w}}{\partial x} \right) + C_1^2 I_6 \left(\ddot{\psi}_x + \frac{\partial \ddot{w}}{\partial x} \right) \\
\delta \psi_y : \quad M_{2,y} + M_{6,x} - Q_2 - \frac{4}{3h^2} (P_{2,y} + P_{6,x}) + \frac{4}{h^2} R_2 \\
&= I_1 \ddot{v} + I_2 \ddot{\psi}_y - C_1 \left(I_3 \ddot{v} + 2I_4 \ddot{\psi}_y + I_4 \frac{\partial \ddot{w}}{\partial y} \right) + C_1^2 I_6 \left(\ddot{\psi}_y + \frac{\partial \ddot{w}}{\partial y} \right) \\
\delta w : \quad Q_{1,x} + Q_{2,y} + \frac{4}{3h^2} (P_{1,xx} + P_{2,yy} + 2P_{6,xy}) - \frac{4}{h^2} (R_{2,y} + R_{1,x}) \\
&\quad + (-k_w w + k_G \nabla^2 w) + P(x, y) = C_1 I_3 \left(\frac{\partial \ddot{u}}{\partial x} + \frac{\partial \ddot{v}}{\partial y} \right) \\
&\quad + C_1 I_4 \left(\frac{\partial \ddot{\psi}_x}{\partial x} + \frac{\partial \ddot{\psi}_y}{\partial y} \right) + C_1^2 I_6 \left(\frac{\partial \ddot{\psi}_x}{\partial x} + \frac{\partial \ddot{\psi}_y}{\partial y} - \frac{\partial^2 \ddot{w}}{\partial x^2} - \frac{\partial^2 \ddot{w}}{\partial y^2} \right) + I_0 \ddot{w}
\end{aligned} \tag{4.5}$$

and

$$\frac{\partial D_z}{\partial z} = 0 \quad \frac{\partial B_z}{\partial z} = 0 \tag{4.6}$$

where N_i , M_i ($i = 1, 2, 6$) denote the resultant forces and moments, respectively. R_i , P_i are higher order resultant shear forces and moments, respectively, and Q_i are transverse shear forces which are all defined by the following expressions

$$\begin{aligned}
\left(\left\{ \begin{matrix} N_1 \\ N_2 \\ N_6 \end{matrix} \right\}, \left\{ \begin{matrix} M_1 \\ M_2 \\ M_6 \end{matrix} \right\}, \left\{ \begin{matrix} P_1 \\ P_2 \\ P_6 \end{matrix} \right\} \right) &= \int_{-\frac{h}{2}}^{\frac{h}{2}} \left\{ \begin{matrix} \sigma_{11} \\ \sigma_{22} \\ \tau_{12} \end{matrix} \right\} (1, z, z^3) \, dz \\
\left(\left\{ \begin{matrix} Q_1 \\ Q_2 \end{matrix} \right\}, \left\{ \begin{matrix} R_1 \\ R_2 \end{matrix} \right\} \right) &= \int_{-\frac{h}{2}}^{\frac{h}{2}} \left\{ \begin{matrix} \tau_{13} \\ \tau_{23} \end{matrix} \right\} (1, z^2) \, dz
\end{aligned} \tag{4.7}$$

By substituting Eqs. (3.3) into Eqs. (4.6), the electric and magnetic potential are obtained which electric and magnetic boundary conditions assumed as follows

$$\begin{aligned} \phi\left(\frac{h}{2}\right) = \phi\left(-\frac{h}{2}\right) = 0 & \quad \phi = \lambda_1 \Delta_1 \left(\frac{z^2}{2} - \frac{z^4}{3h^2} - \frac{23h^2}{192}\right) + \lambda_1 \Delta_2 \left(\frac{h^2}{192} - \frac{z^4}{3h^2}\right) \\ \varphi\left(\frac{h}{2}\right) = \varphi\left(-\frac{h}{2}\right) = 0 & \quad \varphi = \lambda_2 \Delta_1 \left(\frac{z^2}{2} - \frac{z^4}{3h^2} - \frac{23h^2}{192}\right) + \lambda_2 \Delta_2 \left(\frac{h^2}{192} - \frac{z^4}{3h^2}\right) \end{aligned} \quad (4.8)$$

where

$$\lambda_1 = \frac{e_{31} - \frac{g_{33}f_{31}}{\mu_{33}}}{h_{33} - \frac{g_{33}^2}{\mu_{33}}} \quad \lambda_2 = \frac{f_{31} - g_{33}\lambda_1}{\mu_{33}} \quad \Delta_1 = \psi_{x,x} + \psi_{y,y} \quad \Delta_2 = w_{,xx} + w_{,yy}$$

By substituting Eqs. (4.7) into Eqs. (4.5) and (4.6), the governing equations of motion for the MEE nanocomposite microplate based on TSDT are obtained as follows

$$\begin{aligned} \delta u : \quad & A_{11}u_{,xx} + (A_{12} + A_{66})v_{,xy} + A_{66}u_{,yy} = I_0\ddot{u} - e_0^2a^2I_0(\ddot{u}_{,xx} + \ddot{u}_{,yy}) + (I_1 - C_1I_3)\ddot{\psi}_x \\ & - (I_1 - C_1I_3)e_0^2a^2(\ddot{\psi}_{x,xx} + \ddot{\psi}_{x,yy}) - C_1I_3\ddot{w}_{,x} + C_1I_3e_0^2a^2(\ddot{w}_{,xxx} + \ddot{w}_{,xyy}) \end{aligned} \quad (4.9)$$

$$\begin{aligned} \delta v : \quad & A_{22}v_{,yy} + (A_{12} + A_{66})u_{,xy} + A_{66}v_{,xx} = I_0\ddot{v} - e_0^2a^2I_0(\ddot{v}_{,xx} + \ddot{v}_{,yy}) + (I_1 - C_1I_3)\ddot{\psi}_y \\ & - (I_1 - C_1I_3)e_0^2a^2(\ddot{\psi}_{y,xx} + \ddot{\psi}_{y,yy}) - C_1I_3\ddot{w}_{,y} + C_1I_3e_0^2a^2(\ddot{w}_{,yxx} + \ddot{w}_{,yyy}) \end{aligned} \quad (4.10)$$

$$\begin{aligned} \delta \psi_x : \quad & \left(B_{11} - \frac{4H_{11}}{3h^2}\right)\psi_{x,xx} + \left(F_{11} - \frac{4L_{11}}{3h^2}\right)\psi_{x,yy} + \left(\frac{4T_{22}}{3h^2} - T_{11}\right)\psi_x \\ & + \left(F_{11} + B_{12} - \frac{4H_{12}}{3h^2} - \frac{4L_{11}}{3h^2}\right)\psi_{y,xy} + \left(\frac{4K_{11}}{3h^2} - D_{11}\right)w_{,xxx} \\ & + \left(\frac{4L_{12}}{3h^2} + \frac{4K_{12}}{3h^2} - D_{12} - F_{12}\right)w_{,xyy} + \left(\frac{4T_{22}}{3h^2} - T_{11}\right)w_{,x} \\ & = (I_1 - C_1I_3)\ddot{u} - (I_1 - C_1I_3)e_0^2a^2(\ddot{u}_{,xx} + \ddot{u}_{,yy}) + (I_2 - 2C_1I_4 + C_1^2I_6)\ddot{\psi}_x \\ & + (2C_1I_4 + C_1^2I_6 - I_2)e_0^2a^2(\ddot{\psi}_{x,xx} + \ddot{\psi}_{x,yy}) + (C_1^2I_6 - C_1I_4)\ddot{w}_{,x} \\ & + (C_1I_4 - C_1^2I_6)e_0^2a^2\ddot{w}_{,xxx} + (C_1I_4 - C_1^2I_6)e_0^2a^2\ddot{w}_{,xyy} \end{aligned} \quad (4.11)$$

$$\begin{aligned} \delta \psi_y : \quad & \left(B_{22} - \frac{4H_{22}}{3h^2}\right)\psi_{y,yy} + \left(F_{11} - \frac{4L_{11}}{3h^2}\right)\psi_{y,xx} + \left(\frac{4T_{22}}{3h^2} - T_{11}\right)\psi_y \\ & + \left(F_{11} + B_{12} - \frac{4H_{12}}{3h^2} - \frac{4L_{11}}{3h^2}\right)\psi_{x,xy} + \left(\frac{4K_{22}}{3h^2} - D_{11}\right)w_{,yyy} \\ & + \left(\frac{4L_{12}}{3h^2} + \frac{4K_{12}}{3h^2} - D_{12} - F_{12}\right)w_{,xxy} + \left(\frac{4T_{22}}{3h^2} - T_{11}\right)w_{,y} \\ & = (I_1 - C_1I_3)\ddot{v} - (I_1 - C_1I_3)e_0^2a^2(\ddot{v}_{,xx} + \ddot{v}_{,yy}) + (I_2 - 2C_1I_4 + C_1^2I_6)\ddot{\psi}_y \\ & + (2C_1I_4 + C_1^2I_6 - I_2)e_0^2a^2(\ddot{\psi}_{y,xx} + \ddot{\psi}_{y,yy}) + (C_1^2I_6 - C_1I_4)\ddot{w}_{,y} \\ & + (C_1I_4 - C_1^2I_6)e_0^2a^2\ddot{w}_{,yxx} + (C_1I_4 - C_1^2I_6)e_0^2a^2\ddot{w}_{,yyy} \end{aligned} \quad (4.12)$$

$$\begin{aligned} \delta w : \quad & \left(T_{11} - \frac{4T_{22}}{h^2}\right)\psi_{x,x} + \left(T_{11} - \frac{4T_{22}}{h^2}\right)\psi_{y,y} + \frac{4H_{11}}{3h^2}\psi_{x,xxx} + \frac{4H_{22}}{3h^2}\psi_{y,yyy} \\ & + \left(\frac{4H_{12}}{3h^2} + \frac{8L_{11}}{3h^2}\right)(\psi_{x,xyy} + \psi_{y,xxy}) + \left(T_{11} - \frac{4T_{22}}{h^2} + e_0^2a^2K_w - K_G\right)(w_{,xx} + w_{,yy}) \\ & + \left(e_0^2a^2K_G - \frac{4K_{11}}{3h^2}\right)w_{,xxxx} + \left(e_0^2a^2K_G - \frac{4K_{22}}{3h^2}\right)w_{,yyyy} - \left(\frac{8K_{12}}{3h^2} + \frac{8L_{12}}{3h^2}\right)w_{,xxyy} \\ & - K_w w + P(x, y) = C_1I_3\ddot{u}_{,x} - C_1I_3e_0^2a^2(\ddot{u}_{,xxx} + \ddot{u}_{,xyy}) + C_1I_3\ddot{v}_{,x} \\ & - C_1I_3e_0^2a^2(\ddot{v}_{,xxx} + \ddot{v}_{,xyy}) + (C_1I_4 + C_1^2I_6)\ddot{\psi}_{x,x} - (C_1I_4 + C_1^2I_6)e_0^2a^2(\ddot{\psi}_{x,xxx} + \ddot{\psi}_{x,xyy}) \\ & + (C_1I_4 + C_1^2I_6)\ddot{\psi}_{y,y} - (C_1I_4 + C_1^2I_6)e_0^2a^2(\ddot{\psi}_{y,yxx} + \ddot{\psi}_{y,yyy}) - (C_1^2I_6 + e_0^2a^2)\ddot{w}_{,xx} \\ & - (C_1^2I_6 + e_0^2a^2)\ddot{w}_{,yy} + e_0^2a^2C_1I_6(\ddot{w}_{,xxxx} + \ddot{w}_{,yyyy}) + 2e_0^2a^2C_1I_6\ddot{w}_{,xxyy} + I_0\ddot{w} \end{aligned} \quad (4.13)$$

where the above coefficients are defined in Appendix A.

Substituting Eqs. (4.8) into Eq. (3.3), the electric and magnetic field is written as

$$\begin{aligned} E_z &= \lambda_1 \left(z - \frac{4z^3}{3h^2} \right) (\psi_{x,x} + \psi_{x,x}) - \frac{4z^3}{3h^2} \lambda_1 (w_{,xx} + w_{,yy}) \\ H_z &= \lambda_2 \left(z - \frac{4z^3}{3h^2} \right) (\psi_{x,x} + \psi_{x,x}) - \frac{4z^3}{3h^2} \lambda_2 (w_{,xx} + w_{,yy}) \end{aligned} \quad (4.14)$$

5. Navier's type solution for the MEE nanocomposite microplate

Analytical solutions for a simply supported rectangular MEE nanocomposite microplate are obtained using Navier's solution technique. Using Navier's solution, the displacements of the microplate can be written as follows (Mohammadimehr *et al.*, 2016a)

$$\begin{aligned} u(x, y, t) &= \sum_{m=1}^{\infty} \sum_{n=1}^{\infty} U_{mn} \cos(\alpha x) \sin(\beta y) e^{i\omega t} \\ v(x, y, t) &= \sum_{m=1}^{\infty} \sum_{n=1}^{\infty} V_{mn} \sin(\alpha x) \cos(\beta y) e^{i\omega t} \\ \psi_x(x, y, t) &= \sum_{m=1}^{\infty} \sum_{n=1}^{\infty} \Psi_{xmn} \cos(\alpha x) \sin(\beta y) e^{i\omega t} \\ \psi_y(x, y, t) &= \sum_{m=1}^{\infty} \sum_{n=1}^{\infty} \Psi_{ymn} \sin(\alpha x) \cos(\beta y) e^{i\omega t} \\ w(x, y, t) &= \sum_{m=1}^{\infty} \sum_{n=1}^{\infty} W_{mn} \sin(\alpha x) \sin(\beta y) e^{i\omega t} \end{aligned} \quad (5.1)$$

where α and β are equal to $m\pi/l$, $n\pi/b$, respectively.

5.1. Free vibration analysis of the nanocomposite microplate

The matrix form of free vibration equations of the microplate is written as

$$(\mathbf{S} - \omega^2 \mathbf{M}) \mathbf{U} = \mathbf{0} \quad (5.2)$$

where the non-zero elements of the mass and stiffness matrix are given in Appendix B.

5.2. Buckling analysis of the nanocomposite microplate

The matrix form of buckling equations for the nanocomposite microplate can be written as follows

$$\begin{bmatrix} S_{11} & S_{12} & S_{13} & S_{14} & S_{15} \\ S_{21} & S_{22} & S_{23} & S_{24} & S_{25} \\ S_{31} & S_{32} & S_{33} & S_{34} & S_{35} \\ S_{41} & S_{42} & S_{43} & S_{44} & S_{45} \\ S_{51} & S_{52} & S_{53} & S_{54} & S_{55} - N_0(\alpha^2 + k\beta^2) \end{bmatrix} \begin{Bmatrix} U_{mn} \\ V_{mn} \\ \Psi_{xmn} \\ \Psi_{ymn} \\ W_{mn} \end{Bmatrix} = \begin{Bmatrix} 0 \\ 0 \\ 0 \\ 0 \\ 0 \end{Bmatrix} \quad (5.3)$$

$$\bar{\mathbf{C}} = \begin{bmatrix} S_{11} & S_{12} & S_{13} & S_{14} \\ S_{21} & S_{22} & S_{23} & S_{24} \\ S_{31} & S_{32} & S_{33} & S_{34} \\ S_{41} & S_{42} & S_{43} & S_{44} \end{bmatrix}^{-1} \quad k = \frac{N_{xx}}{N_{yy}}$$

Using Eq. (5.3), we obtain an expression for the critical buckling load N_0 of the MEE nanocomposite microplate

$$N_0 = \frac{1}{\alpha^2 + k\beta^2} \left(S_{55} - \{S_{51} \ S_{52} \ S_{53} \ S_{54}\} \bar{\mathbf{C}} \{S_{15} \ S_{25} \ S_{35} \ S_{45}\}^T \right) \quad (5.4)$$

5.3. Forced vibration of the nanocomposite microplate

The load $P(x, y, t)$ can be expressed in the form of series

$$p(x, y, t) = \sum_{m=1}^{\infty} \sum_{n=1}^{\infty} P_0 \sin(\Omega t) \sin(\alpha x) \sin(\beta y) \quad (5.5)$$

where Ω is the frequency of forced vibration. The equation of motion for the MEE nanocomposite microplate will then include a variable, time-dependent, transverse load $p(x, y, t)$.

The matrix form of the response system equations for the MEE microplate is obtained as follows

$$\{U_m \ V_m \ \Psi_{xmn} \ \Psi_{ymn} \ W_{mn}\}^T = \frac{1}{\omega_n^2 - \Omega^2} \mathbf{M}^{-1} [0 \ 0 \ 0 \ 0 \ P_0]^T \quad (5.6)$$

5.4. Dimensionless parameter of the nanocomposite microplate

The dimensionless deflection, natural frequency and buckling load of the MEE nanocomposite microplate is written as follows

$$\bar{W} = \frac{C_{ij \ max} h^3 w}{P_0 l^4} \quad \bar{\omega} = \sqrt{\frac{\rho l^4 \omega}{C_{ij \ max} h^2}} \quad \bar{N} = \frac{l^2 N_0}{C_{ij \ max} h^3} \quad (5.7)$$

6. Numerical results and discussions

The piezoelectric and piezomagnetic properties of the BaTiO₃ (inclusion)-CoFe₂O₄ (matrix) nanocomposite microplate with different volume fractions V_f of the inclusions can be found in Sih and Sog (2002), Song and Sih (2002). They are listed in Table 1.

Numerical results for bending, buckling, free and forced vibration are presented for the MEE nanocomposite microplate resting on a two-parameter elastic foundations with all edges simply supported.

To validate the results of this research with the literature, a single-layered MEE square thick plate, with $l = b = 1$ m, $h = 0.3$ m, simply-supported boundary conditions, and material properties given by Table 2 is considered. The dimensionless fundamental frequency is calculated as $\bar{\omega} = \sqrt{\rho_{max}/C_{ij \ max} l \omega}$, where $C_{ij \ max}$ and ρ_{max} are the maximum values of the stiffness coefficient and density of the layers, respectively. The results are shown in Table 2 along with some other published results.

Table 3 indicates the dimensionless biaxial buckling load of simply-supported square nano-plates. From this Table, it is observed that the presented results are in good agreement with those reported in the literature.

Table 4 presents the dimensionless center deflections of isotropic square plates under uniform loading. They are calculated with various side-to-thickness ratios up to $a/h = 10000$, and compared to earlier studies.

The natural frequencies of the simply supported MEE nanocomposite microplate are obtained using Eq. (5.2). From Fig. 2a, it is seen that the volume fraction plays an important role for the MEE nanocomposite microplate in terms of the natural frequency, and its effects can

Table 1. Properties of the BaTiO₃, CoFe₂O₄ and BaTiO₃-CoFe₂O₄ nanocomposite microplate with different volume fractions

Properties	Piezoelectric (BaTiO ₃)	Piezomagnetic (CoFe ₂ O ₄)	V_f (volume fraction for CoFe ₂ O ₄ in BaTiO ₃ -CoFe ₂ O ₄ nanocomposite)				
			0.1	0.3	0.5	0.7	0.9
C_{11} [Gpa]	166	286	178.0	202	226	250.0	274
C_{12} [Gpa]	77	173	87.2	105.7	124	142.7	161
C_{22} [Gpa]	166	286	172.8	194.2	216	237.3	259
C_{44} [Gpa]	43	45.3	43.2	43.7	44	44.6	45
e_{31} [c/m ²]	43	45.3	-3.96	-3.08	-2.2	-1.32	-4.4
e_{33} [c/m ²]	44.5	56.5	16.74	13.02	9.3	5.58	1.86
e_{15} [c/m ²]	-4.4	0	10.44	8.12	5.8	3.48	1.16
h_{11} [$\times 10^{-10}C^2/(Nm^2)$]	0	580.3	100.9	78.6	56.4	34.2	11.9
h_{33} [$\times 10^{-10}C^2/(Nm^2)$]	-4.4	0	113.5	88.5	63.5	38.5	13.4
f_{31} [N/(Am)]	0	580.3	58.03	174.1	290.2	406.2	522.3
f_{33} [N/(Am)]	11.6	0	69.97	209.9	350.0	489.8	629.7
f_{15} [N/(Am)]	0	550	55.00	165.0	275.0	385.0	495.0
μ_{11} [$\times 10^{-6}NS^2/C^2$]	11.6	0	63.5	180.5	297.0	414.5	531.5
μ_{33} [$\times 10^{-6}NS^2/C^2$]	0	550	24.7	541.0	83.5	112.9	142.3
ρ [kg/m ³]	126	0.93	5750	5650	5550	5450	5350

Table 2. Dimensionless fundamental frequencies of MEE plates

Method	Material	
	Piezoelectric BaTiO ₃	Piezomagnetic CoFe ₂ O ₄
Wu and Lu (2009)	1.2523	1.0212
Shooshtari and Razavi (2015)	1.2426	1.1023
Present study	1.2952	1.1130

Table 3. Comparison of dimensionless biaxial buckling load ($N_{cr} = N_0a/D$, $D = Eh^3/[12(1 - \nu^2)]$) for square nanoplates with all edges simply-supported ($a = 10$ nm, $a/h = 2$)

Method	e_0a [nm]	
	0	1
Malekzadeh and Shojaee (2013)	8.5249	7.1039
Wang and Wang (2011)	8.4543	7.1533
Karimi <i>et al.</i> (2015)	8.6052	7.2204
Present study	8.5232	7.1138

not be ignored for microplate. It is shown that by increasing the volume fraction, the dimensionless natural frequency increases. The reason is that a greater volume fraction makes the microplate stiffer. Figure 2b depicts the effects of the Pasternak shear constant on the natural frequency. From this figure, it can be found that by increasing this parameter, the stiffness of the nanocomposite microplate increases and this result is similar to the dimensionless natural frequency. The effect of volume fraction on the deflection is shown in Fig. 3a. It is shown that an increase in the volume fraction will decrease the dimensionless deflection. The critical buckling loads of the MEE nanocomposite microplate are obtained using Eq. (5.4). Figure 3b depicts the variation of critical buckling load versus volume fraction. From this figure, it can be seen that with an increase in the volume fraction, the critical buckling load for all the length to width

Table 4. Comparison of dimensionless center deflection $W\left(\frac{a}{2}, \frac{b}{2}\right)D/[(P_0a^4), D = Eh^3/[12(1 - \nu^2)]]$ for simply-supported square isotropic plates under uniform loads

Method	a/h			
	10	100	1000	10000
Nguyen <i>et al.</i> (2016)	0.4272	0.4064	0.4062	0.4062
Nguyen-Xuan <i>et al.</i> (2008), MITC4	0.4273	0.4064	0.4062	0.4062
Nguyen-Xuan <i>et al.</i> (2008), MISC1	0.4273	0.4065	0.4063	0.4063
Taylor and Auricchio (1993)	0.4273	0.4064	0.4062	0.4062
Present study	0.4266	0.4055	0.4053	0.4053

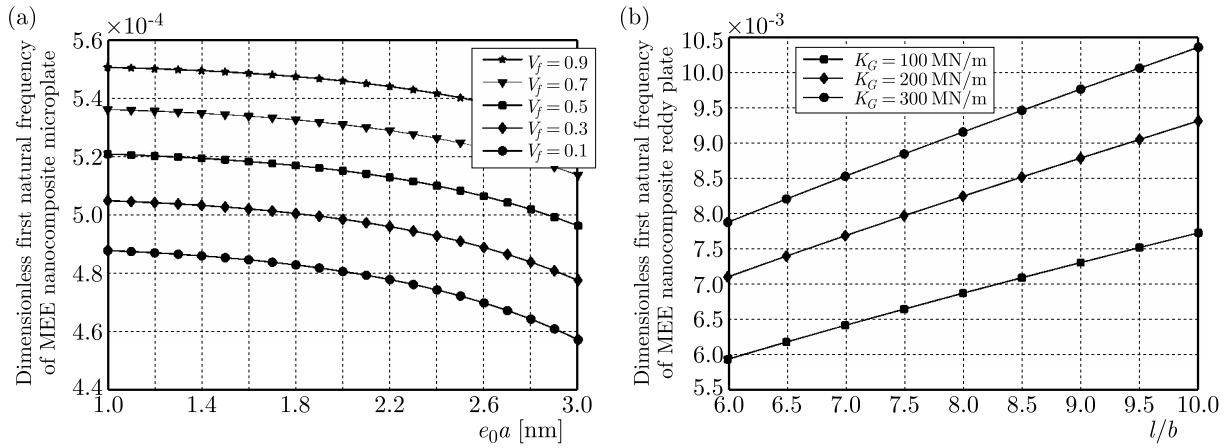


Fig. 2. (a) The effect of volume fraction on the dimensionless natural frequency: $l = 4 \mu\text{m}$, $b = 4 \mu\text{m}$, $h = 0.04 \mu\text{m}$, $K_w = 0$, $K_G = 0$. (b) The effect of the Pasternak shear constant on the dimensionless natural frequency: $l = 400 \mu\text{m}$, $h = 80 \mu\text{m}$, $V_f = 0.5$, $K_w = 0$, $e_0a = 1 \text{ nm}$

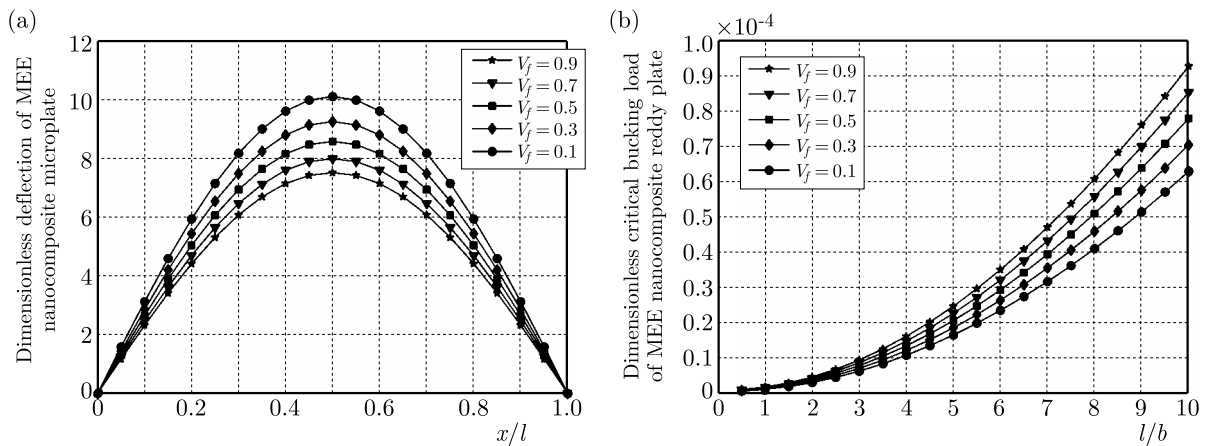


Fig. 3. (a) The effect of volume fraction on the dimensionless deflection: $l = 400 \mu\text{m}$, $b = 400 \mu\text{m}$, $h = 80 \mu\text{m}$, $K_w = 0$, $K_G = 0$, $P = 100 \text{ N/m}^2$, $e_0a = 2 \text{ nm}$. (b) The effect of volume fraction on the dimensionless critical buckling load: $l = 400 \mu\text{m}$, $h = 80 \mu\text{m}$, $K_w = 0$, $K_G = 0$, $e_0a = 1 \text{ nm}$

ratios l/b will increase. The influence of the length to thickness ratio l/h is shown in Fig. 4a. This figure shows that by increasing the length to thickness ratio l/h , the dimensionless critical buckling load decreases. The response system of the MEE nanocomposite microplate is obtained using Eq. (5.6). Figure 4b indicates the response system of the MEE nanocomposite microplate and different values of the volume fraction. It is seen from the results that by increasing the excitation frequency to the natural frequency ratio Ω/ω , the amplitude of the nanocomposite

microplate reinforced by $\text{CoFe}_2\text{O}_4\text{-BaTiO}_3$ increases. Also, by increasing the volume fraction, the deflection to thickness ratio w/h decreases. Figure 5 depicts the effects of volume fraction on the maximum deflection to thickness ratio w_{max}/h . From this figure, it can be found that by increasing the volume fraction, the maximum deflection to thickness ratio w_{max}/h decreases.

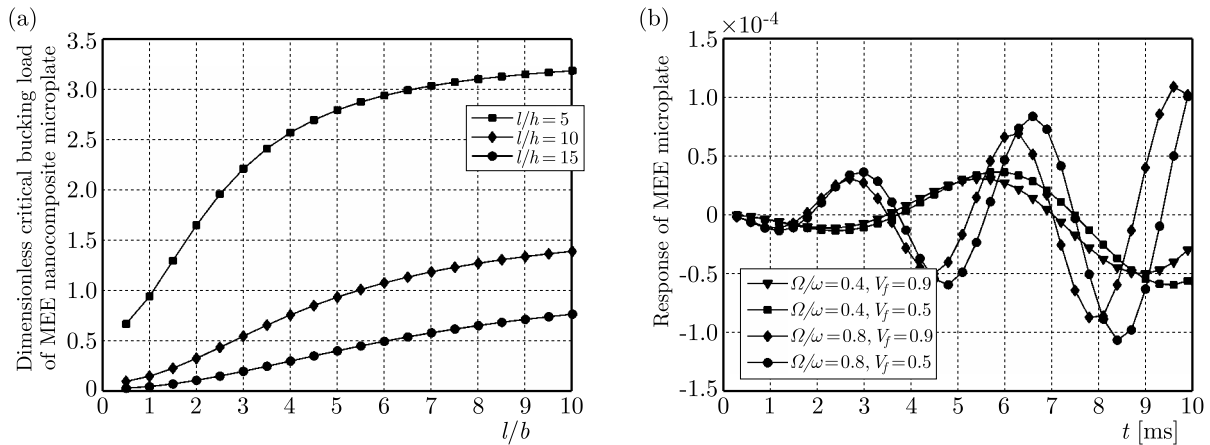


Fig. 4. (a) The effect of the length to thickness ratio l/h on the critical buckling load: $l = 400 \mu\text{m}$, $V_f = 0.5$, $K_w = 0$, $K_G = 0$, $e_0a = 1 \text{ nm}$. (b) The effect of volume fraction on the response system: $l = 400 \mu\text{m}$, $b = 400 \mu\text{m}$, $h = 20 \mu\text{m}$, $K_w = 0$, $K_G = 0$, $P_0 = 1 \text{ N/m}^2$, $e_0a = 1 \text{ nm}$

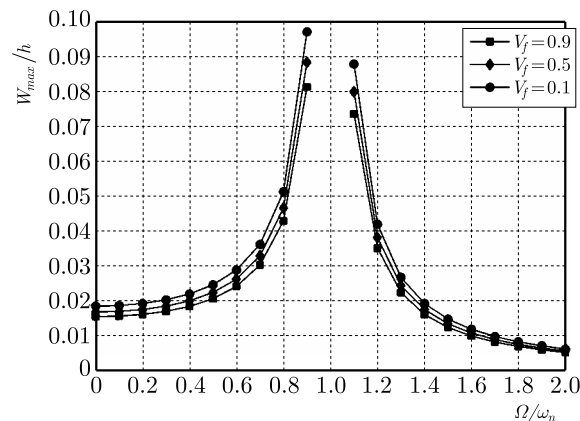


Fig. 5. The effect of volume fraction on the maximum deflection to thickness ratio W_{max}/h : $l = 4 \mu\text{m}$, $b = 4 \mu\text{m}$, $h = 0.1 \mu\text{m}$, $K_w = 0$, $K_G = 0$, $P_0 = 1 \text{ N/m}^2$, $e_0a = 1 \text{ nm}$

Figure 6a shows that by increasing the spring constant of the Winkler type, the intensity of electric field decreases. Figure 6b presents the influence of the Pasternak shear constant on the magnetic field, respectively. The results show that by increasing the elastic constant, the intensity of magnetic and electric field decreases.

7. Conclusions

A theoretical analysis on bending, buckling, free and forced vibration characteristics of an MEE nanocomposite microplate are carried out in the present work. The Hamilton principle, higher order shear deformation theory and Maxwell's equations are considered to derive the equations of motion and distribution of electrical potential, magnetic field along the thickness direction of the MEE nanocomposite microplate. Some conclusions of this research can be listed as follows:

- For the MEE nanocomposite microplate, the natural frequency and critical buckling load increases with the increasing volume fraction of $\text{CoFe}_2\text{O}_4\text{-BaTiO}_3$, because the nanocomposite microplate becomes stiffer in such a case.

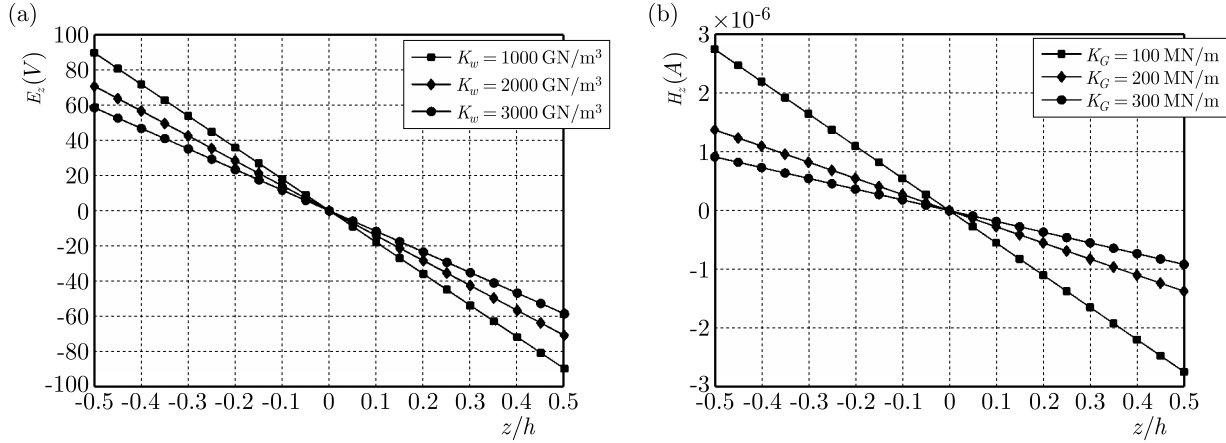


Fig. 6. (a) The effect of the Winkler spring constant on the intensity of electric field: $l = 40 \mu\text{m}$, $b = 40 \mu\text{m}$, $h = 1 \mu\text{m}$, $K_G = 0$, $P = 1 \text{ N/m}^2$, $e_0 a = 1 \text{ nm}$. (b) The effect of the Pasternak shear constant on the intensity of magnetic field : $l = 40 \mu\text{m}$, $b = 40 \mu\text{m}$, $h = 1 \mu\text{m}$, $K_w = 0$, $P = 1 \text{ N/m}^2$, $e_0 a = 1 \text{ nm}$

- The natural frequency and critical buckling load decreases, and also the maximum deflection, whereas the intensity of magnetic and electric fields increases with the decreasing Winkler and Pasternak shear constants of the MEE nanocomposite microplate.
- For the MEE nanocomposite microplate, the amplitude of vibration decreases with the increasing volume fraction.

Appendix A

$$\begin{aligned}
 A_{11} &= C_{11}h & A_{12} &= C_{12}h & A_{22} &= C_{22}h & A_{66} &= C_{66}h \\
 B_{11} &= \frac{h^3}{15}(C_{11} + e_{31}\lambda_1 + f_{31}\lambda_2) & B_{12} &= \frac{h^3}{15}(C_{12} + e_{31}\lambda_1 + f_{31}\lambda_2) \\
 B_{22} &= \frac{h^3}{15}(C_{22} + e_{31}\lambda_1 + f_{31}\lambda_2) & D_{11} &= \frac{h^3}{60}(C_{11} + e_{31}\lambda_1 + f_{31}\lambda_2) \\
 D_{12} &= \frac{h^3}{60}(C_{12} + e_{31}\lambda_1 + f_{31}\lambda_2) & D_{22} &= \frac{h^3}{60}(C_{22} + e_{31}\lambda_1 + f_{31}\lambda_2) \\
 F_{11} &= C_{66}\frac{h^3}{15} & F_{12} &= C_{66}\frac{h^3}{30} & H_{11} &= \left(\frac{h^5}{80} - \frac{h^5}{336}\right)(C_{11} + e_{31}\lambda_1 + f_{31}\lambda_2) \\
 H_{12} &= \left(\frac{h^5}{80} - \frac{h^5}{336}\right)(C_{12} + e_{31}\lambda_1 + f_{31}\lambda_2) & H_{22} &= \left(\frac{h^5}{80} - \frac{h^5}{336}\right)(C_{22} + e_{31}\lambda_1 + f_{31}\lambda_2) \\
 K_{11} &= \frac{h^5}{336}(C_{11} + e_{31}\lambda_1 + f_{31}\lambda_2) & K_{12} &= \frac{h^5}{336}(C_{12} + e_{31}\lambda_1 + f_{31}\lambda_2) \\
 K_{22} &= \frac{h^5}{336}(C_{22} + e_{31}\lambda_1 + f_{31}\lambda_2) & L_{11} &= \left(\frac{h^5}{80} - \frac{h^5}{336}\right)C_{66} & L_{12} &= \frac{h^5}{168}C_{66} \\
 T_{11} &= \frac{2h}{3}C_{44} & T_{22} &= \left(\frac{h^3}{12} - \frac{h^3}{20}\right)C_{44}
 \end{aligned}$$

Appendix B

$$\begin{aligned}
 S_{11} &= -A_{11}\alpha^2 - A_{66}\beta^2 & S_{12} &= -(A_{12} + A_{66})\alpha\beta \\
 S_{21} &= -(A_{12} + A_{66})\alpha\beta & S_{22} &= -A_{22}\beta^2 - A_{66}\alpha^2 \\
 S_{33} &= \left(B_{11} - \frac{4H_{11}}{3h^2}\right)(-\alpha^2) - \left(F_{11} - \frac{4L_{11}}{3h^2}\right)\beta^2 + \frac{4T_{22}}{3h^2} - T_{11}
 \end{aligned}$$

$$\begin{aligned}
S_{34} &= \left(B_{12} + F_{11} - \frac{4H_{12}}{3h^2} - \frac{4L_{11}}{3h^2} \right) (-\alpha\beta) \\
S_{35} &= \left(\frac{4K_{11}}{3h^2} - D_{11} \right) (-\alpha^3) - \left(\frac{4L_{12}}{3h^2} + \frac{4K_{12}}{3h^2} - D_{12} - F_{12} \right) \alpha\beta^2 + \left(\frac{4T_{22}}{3h^2} - T_{11} \right) \alpha \\
S_{43} &= - \left(B_{12} + F_{11} - \frac{4H_{12}}{3h^2} - \frac{4L_{11}}{3h^2} \right) \alpha\beta \\
S_{44} &= - \left(B_{22} - \frac{4H_{22}}{3h^2} \right) \beta^2 - \left(F_{11} - \frac{4L_{11}}{3h^2} \right) \alpha^2 + \frac{4T_{22}}{3h^2} - T_{11} \\
S_{45} &= - \left(\frac{4K_{22}}{3h^2} - D_{22} \right) \beta^3 - \left(\frac{4L_{12}}{3h^2} + \frac{4K_{12}}{3h^2} - D_{12} - F_{12} \right) \alpha^2\beta + \left(\frac{4T_{22}}{3h^2} - T_{11} \right) \beta \\
S_{53} &= \left(T_{11} - \frac{4T_{22}}{h^2} \right) (-\alpha) - \frac{4H_{11}}{3h^2} \alpha^3 + \left(\frac{4H_{12}}{3h^2} + \frac{8L_{11}}{3h^2} \right) \alpha\beta^2 \\
S_{54} &= \left(T_{11} - \frac{4T_{22}}{h^2} \right) (-\beta) - \frac{4H_{22}}{3h^2} \beta^3 + \left(\frac{4H_{12}}{3h^2} + \frac{8L_{11}}{3h^2} \right) \alpha^2\beta \\
S_{55} &= - \left(T_{11} - \frac{4T_{22}}{h^2} + e_0^2 a^2 K_w - K_G \right) (\alpha^2 + \beta^2) + \left(e_0^2 a^2 K_G - \frac{4K_{11}}{3h^2} \right) \alpha^4 \\
&\quad + \left(e_0^2 a^2 K_G - \frac{4K_{22}}{3h^2} \right) \beta^4 - \left(\frac{8K_{12}}{3h^2} + \frac{8L_{12}}{3h^2} \right) \alpha^2\beta^2 - K_w \\
m_{11} &= -I_0 - e_0^2 a^2 I_0 (\alpha^2 + \beta^2) & m_{13} &= (-I_1 - C_1 I_3) - e_0^2 a^2 (I_1 - C_1 I_3) (\alpha^2 + \beta^2) \\
m_{15} &= C_1 I_3 \alpha + C_1 I_3 e_0^2 a^2 (\alpha^3 + \alpha\beta^2) & m_{22} &= -I_0 - I_0 e_0^2 a^2 (\alpha^2 + \beta^2) \\
m_{24} &= -(I_1 - C_1 I_3) - e_0^2 a^2 (I_1 - C_1 I_3) (\alpha^2 + \beta^2) & m_{25} &= C_1 I_3 \beta + e_0^2 a^2 C_1 I_3 (\alpha^2 \beta + \beta^3) \\
m_{31} &= -(I_1 - C_1 I_3) + (C_1 I_3 - I_1) e_0^2 a^2 (\alpha^2 + \beta^2) \\
m_{33} &= -(I_2 - 2C_1 I_4 + C_1^2 I_6) + (2C_1 I_4 - C_1^2 I_6 - I_2) e_0^2 a^2 (\alpha^2 + \beta^2) \\
m_{35} &= -(C_1^2 I_6 - C_1 I_4) \alpha + (C_1 I_4 - C_1^2 I_6) e_0^2 a^2 (\alpha^3 + \alpha\beta^2) \\
m_{42} &= -(I_1 - C_1 I_3) + (C_1 I_3 - I_1) e_0^2 a^2 (\alpha^2 + \beta^2) \\
m_{44} &= -(I_2 - 2C_1 I_4 + C_1^2 I_6) + (2C_1 I_4 - C_1^2 I_6 - I_2) e_0^2 a^2 (\beta^2 + \alpha^2) \\
m_{45} &= -(C_1^2 I_6 - C_1 I_4) \beta + (C_1 I_4 - C_1^2 I_6) e_0^2 a^2 (\beta^3 + \alpha^2 \beta) \\
m_{51} &= C_1 I_3 \alpha + C_1 I_3 e_0^2 a^2 (\alpha^3 + \alpha\beta^2) & m_{52} &= C_1 I_3 \beta + C_1 I_3 e_0^2 a^2 (\beta^3 + \alpha^2 \beta) \\
m_{53} &= (C_1 I_4 + C_1^2 I_6) \alpha + (C_1 I_4 + C_1^2 I_6) e_0^2 a^2 \alpha^3 + (C_1 I_4 + C_1^2 I_6) e_0^2 a^2 \alpha\beta^2 \\
m_{54} &= (C_1 I_4 + C_1^2 I_6) \beta + (C_1 I_4 + C_1^2 I_6) e_0^2 a^2 \beta^3 + (C_1 I_4 + C_1^2 I_6) e_0^2 a^2 \alpha^2 \beta \\
m_{55} &= -(C_1^2 I_6 + e_0^2 a^2) (\alpha^2 + \beta^2) - C_1^2 I_6 e_0^2 a^2 (\alpha^4 + \beta^4) - 2C_1^2 I_6 e_0^2 a^2 \alpha^2 \beta^2 - I_0
\end{aligned}$$

Acknowledgments

The authors would like to thank the referees for their valuable comments. They are also grateful to the Iranian Nanotechnology Development Committee for their financial support and University of Kashan for supporting this work by Grant No. 463855/4.

References

1. AREFI M., 2015, The effect of different functionalities of FGM and FGPM layers on free vibration analysis of the FG circular plates integrated with piezoelectric layers, *Smart Structures and Systems*, **15**, 1345-1362
2. CHEN J.Y., HEYLIGER P.R., PAN E., 2014, Free vibration of three-dimensional multilayered magneto-electro-elastic plates under combined clamped/free boundary conditions, *Journal of Sound and Vibration*, **333**, 4017-4029
3. DU C., LI Y., JIN X., 2014, Nonlinear forced vibration of functionally graded cylindrical thin shells, *Thin-Walled Structures*, **78**, 26-36

4. EBRAHIMI F., NASIRZADEH P., 2016, A nonlocal Timoshenko beam theory for vibration analysis of thick nonobeam using differential transform method, *Journal of Theoretical and Applied Mechanics*, **53**, 1041-1053
5. ERINGEN A.C., 1983, On differential equations of nonlocal elasticity and solutions of screw dislocation and surface waves, *Journal of Applied Physics*, **54**, 4703-4710
6. ERINGEN A.C., 2002, *Nonlocal Continuum Field Theories*, Springer-Verlag, New York
7. GHORBANPOUR ARANI A., HAGHPARAST E., 2017, Vibration analysis of axially moving carbon nanotubereinforced composite plate under initial tension, *Polymer Composites*, **38**, 4, 814-822
8. GHORBANPOUR ARANI A., HAGHPARAST E., BABA AKBAR ZAREI H., 2016, Nonlocal vibration of axially moving graphene sheet resting on orthotropic visco-Pasternak foundation under longitudinal magnetic field, *Physica B: Condensed Matter*, **495**, 35-49
9. GHORBANPOUR ARANI A., RAHNAMA MOBARAKEH M., SHAMS SH., MOHAMMADIMEHR M., 2012, The effect of CNT volume fraction on the magneto-thermo-electro-mechanical behavior of smart nanocomposite cylinder, *Journal of Mechanical Science and Technology*, **26**, 2565-2572
10. HASANI BAFERANI A., SAIDI A.R., EHTESHAMI H., 2011, Accurate solution for free vibration analysis of functionally graded thick rectangular plates resting on elastic foundation, *Composite Structures*, **93**, 1842-1853
11. KARIMI M., HADDAD H.A., SHAHIDI A.R., 2015a, Combining surface effects and non-local two variable refined plate theories on the shear/biaxial buckling and vibration of silver nanoplates, *IET Micro and Nano Letters*, **10**, 276-281
12. KARIMI M., MIRDAMADI H.R., SHAHIDI A.R., 2015b, Shear vibration and buckling of double-layer orthotropic nanoplates based on RPT resting on elastic foundations by DQM including surface effects, *Microsystem Technologies*, **23**, 1-33
13. KARIMI M., SHOKRANI M.H., SHAHIDI A.R., 2015c, Size-dependent free vibration analysis of rectangular nanoplates with the consideration of surface effects using finite difference method, *Journal of Applied and Computational Mechanics*, **1**, 122-133
14. KE L.L., WANG Y.S., 2014, Free vibration of size-dependent magneto-electro-elastic nanobeams based on the nonlocal theory, *Acta Mechanical Sinica*, **63**, 52-61
15. KHAN K., PATEL B.P., NATH Y., 2014, Free and forced vibration characteristics of bimodular composite laminated circular cylindrical shells, *Composite Structures*, **126**, 386-397
16. LANG Z., XUEWU L., 2013, Buckling and vibration analysis of functionally graded magneto-electro-thermo-elastic circular cylindrical shells, *Applied Mathematical Modelling*, **37**, 2279-2292
17. MALEKZADEH P., SHOJAEI M., 2013, A two-variable first-order shear deformation theory coupled with surface and nonlocal effects for free vibration of nanoplates, *Journal of Vibration and Control*, doi: 10.1177//1077546313516667
18. MOHAMMADIMEHR M., MOHAMMADI-DEHABADI A.A., KHODDAMI MARAGHI Z., 2017, The effect of non-local higher order stress to predict the nonlinear vibration behavior of carbon nanotube conveying viscous nanoflow, *Physica B: Condensed Matter*, **510**, 48-59
19. MOHAMMADIMEHR M., MOSTAFAVIFAR M., 2017, Free vibration analysis of sandwich plate with a transversely flexible core and FG-CNTs reinforced nanocomposite face sheets subjected to magnetic field and temperature-dependent material properties using SGT, *Composites Part B: Engineering*, **94**, 253-270
20. MOHAMMADIMEHR M., ROUSTA NAVI B., GHORBANPOUR ARANI A., 2016a, Modified strain gradient Reddy rectangular plate model for biaxial buckling and bending analysis of double-coupled piezoelectric polymeric nanocomposite reinforced by FG-SWNT, *Composites Part B: Engineering*, **87**, 132-148
21. MOHAMMADIMEHR M., SALEMI M., ROUSTA NAVI B., 2016b, Bending, buckling, and free vibration analysis of MSGT microcomposite Reddy plate reinforced by FG-SWCNTs with temperature-dependent material properties under hydro-thermo-mechanical loadings using DQM, *Composite Structures*, **138**, 361-380

22. NGUYEN T., NGUYEN V., CHAU-DINH T., VO T., NGUYEN X., 2016, Static and vibration analysis of isotropic and functionally graded sandwich plates using an edge-based MITC3 finite elements, *Composites Part B*, **107**, 162-173
23. NGUYEN-XUAN H., RABCUK T., BORDAS S., DEBONGNIE J., 2008, A smoothed finite element method for plate analysis, *Computer Methods in Applied Mechanics and Engineering*, **197**, 1184-1203
24. RAZAVI S., SHOOSHTARI A., 2015, Nonlinear free vibration of magneto-electro-elastic rectangular plates, *Composite Structures*, **119**, 377-384
25. SHOKRANI M.H., KARIMI M., TEHRANI M.S., MIRDAMADI H.R., 2016, Buckling analysis of double-orthotropic nanoplates embedded in elastic media based on non-local two-variable refined plate theory using the GDQ method, *Journal Brazilian Society of Mechanical Sciences and Engineering*, **38**, 2589-2606
26. SHOOSHTARI A., RAZAVI S., 2015, Linear and nonlinear free vibration of a multilayered magneto-electro-elastic doubly curved shell on elastic foundation, *Composite Part B: Engineering*, **78**, 95-108
27. SIH G.C., SONG Z.F., 2002, Damage analysis of tetragonal perovskite structure ceramics implicated by asymptotic field solutions and boundary conditions, *Theoretical and Applied Fracture Mechanics*, **38**, 15-36
28. SIH G.C., YU H.Y., 2005, Volume fraction effect of magnetoelastic composite on enhancement and impediment of crack growth, *Composite Structures*, **68**, 1-11
29. SOBHY M., 2013, Buckling and free vibration of exponentially graded sandwich plates resting on elastic foundations under various boundary conditions, *Composite Structures*, **99**, 76-87
30. SONG Z.F., SIH G.C., 2002, Electromechanical influence of crack velocity at bifurcation for poled ferroelectric materials, *Theoretical and Applied Fracture Mechanics*, **38**, 121-139
31. TAYLOR R.L., AURICCHIO F., 1993, Linked interpolation for Reissner-Mindlin plate elements: Part II – A simple triangle, *International Journal for Numerical Methods in Engineering*, **36**, 3057-3066
32. WANG K.F., WANG B.L., 2011, Combining effects of surface energy and non-local elasticity on the buckling of nanoplates, *Micro and Nano Letters*, **6**, 941-943
33. WU C.P. LU Y.C., 2009, A modified Pagano method for the 3D dynamic responses of functionally graded magneto-electro-elastic plates, *Composite Structures*, **90**, 363-372
34. XIN L., HU Z., 2015, Free vibration of simply supported and multilayered magneto-electro-elastic plates, *Composite Structures*, **121**, 344-355
35. ZIDOUR M., DAOUADJI T.H., BENRAHOU K.H., TOUNSI A., ADDA BEDIA E.A., HADJI L., 2014, Buckling analysis of chiral single-walled carbon nanotubes by using the nonlocal Timoshenko beam theory, *Mechanics of Composite Materials*, **50**, 95-104

Manuscript received November 5, 2016; accepted for print February 16, 2017

A NEW AUTOMATED STRETCHING FINITE ELEMENT METHOD FOR 2D CRACK PROPAGATION

MOHAMMED BENTAHAR, HABIB BENZAAMA

Ecole Nationale Polytechnique, Mechanical Engineering Department, Laboratory of Applied Biomechanics and Biomaterials, ENPO, Oran, Algeria; e-mail: bentahae@yahoo.fr; habenza@yahoo.fr

MOHAMED BENTOUMI

Institute of Optics and Precision Mechanics, Ferhat Abbas University, Setif, Algeria; e-mail: hamoudi_10@yahoo.fr

MOHAMED MOKHTARI

Ecole Nationale Polytechnique, Mechanical Engineering Department, Laboratory of Applied Biomechanics and Biomaterials, ENPO, Oran, Algeria; e-mail: mokhtarimohamed44@yahoo.fr

This work presents a study of crack propagation with a new 2D finite element method with the stretching of the mesh. This method affects at each propagation step new coordinates of each element node of the mesh. The structure is divided to areas and each area has its own coordinate formulas. A program in FORTRAN allows us to create a parametric mesh, which keeps the same number of nodes and elements during different steps of crack propagation. The nodes are stretched using the criterion of maximum circumferential stress (MCS). The fracture parameters such as stress intensity factors in modes I and II and the orientation angles are calculated by solving the problem by the finite element code ABAQUS.

Keywords: 2D crack propagation, FEM, stretching finite element method (SFEM), stress intensity factor (SIF)

1. Introduction

Today, crack propagation is a large and very complex problem in the study of life of a structure. It is based on the principles of fracture mechanics, in particular, on calculation of the SIF in various modes.

Many analytical formulas exist to determine the SIF. However, these expressions are often developed for different cases of geometry and the solicitation is simple, see Tada and Irwin (1985). Others authors developed numerical methods for modeling crack propagation (Chan *et al.*, 1970; Bouchard *et al.*, 2003). They proposed a solution by the finite element method to model crack propagation problems in 2D. In the recent years, various approaches have been proposed such as the extended finite element method (XFEM), Mões *et al.* (1999), and methods of generalized finite elements (GFEM), Babuska and Banerjee (2012). Both methods are based on the partition of the unity method proposed by Babuska and Belenik (1997). In addition, the use of mesh regeneration crack schemes improved the estimate of the increment criteria. Bouchard *et al.* (2000) developed a crack propagation method using a linking technique that optimized the size and quantity of the elements, but the geometry was quite remeshed in each step.

The same method was used for several elastic and plastic examples. Bouchard *et al.* (2003), Phongthanapanich and Dechaumphai (2004) developed a method that completely reconstructed the mesh between refinement steps using the adaptive mesh and Delaunay triangulations.

Meyer *et al.* (2006) proposed a crack propagation method that combined an adaptive iterative solver, mesh refinement and mesh coarsening techniques as well as optimization of the number of nodes.

In exchange, Askes *et al.* (2001) discussed linkage strategies based on the relocation of nodes for r -adaptive and h/r -adaptive analysis of crack propagation.

Another approach is the boundary element method (Aliabadi, 1997; Portela *et al.*, 1991; Yan and Nguyen-Dang, 1995), Galerkin method (Belytschko *et al.*, 1994), meshfree element methods (Belytschko *et al.*, 1994; Yan, 2006; DufLOT and Nguyen-Dang, 2004) and the finite element method (FEM) Singh *et al.* (2012).

Numerical methods have been widely used to calculate fracture parameters, including the mechanics of linear elastic plastic-fracture (Bouchard *et al.*, 2003), mechanical dynamics and breaking (Réthoré *et al.*, 2005), tiredness (Miranda *et al.*, 2003) and the spread of quasi-static crack (Khoei *et al.*, 2008). Azocar *et al.* (2010) proposed a new method for the simulation of crack propagation in solids (LEFM) (2D). They used the Lepp-Delaunay method based on the refinement of the triangular mesh by an algorithm that allowed both generation of the first mesh and local modification of the current mesh during propagation of the crack.

This method uses a technique of displacement extrapolation to calculate K_I and K_{II} , and the maximum circumferential stress criterion to calculate the crack propagation angle. Alshoabi (2015) used the method of extrapolation of the movement to simulate crack propagation in 2D by the finite element method of a linear elastic plate. He also characterized the singularity of the crack tip, and the stress intensity factors around the crack tip. Zaleha *et al.* (2007) proposed to assess the displacement extrapolation technique (DET) for predicting the stress intensity factor.

The DET is used when the singular element is present at the tip of the crack. It uses differential movements to adjacent nodes through the crack to calculate the SIF. Cho (2015) proposed mixed modes for stress intensity factors of a 2D inclined crack and evaluated them by Petrov-Galerkin natural element method (PG-NE). Murat (2016) presented a comparative study of the finite element method (FEM) and an analytical method for the problem of a plane layered composite containing an internal perpendicular crack.

2. Law of fatigue crack propagation (Paris and Erdogan, 1963)

The simplest and the oldest law to model fatigue crack propagation in the two-dimensional case is the law proposed by Paris and Erdogan (1963). It is based on constant amplitude tests for which the propagation velocities appear as a linear function of the variation in the SIF in a log-log diagram. It takes the form

$$\frac{dA}{dN} = C(\Delta K)^m \quad (2.1)$$

where C and m are material properties, A is crack length, N is the number of loading cycles and ΔK variation of the stress intensity factor. C and m are the material constants. The crack propagation length is kept constant during propagation steps.

3. Crack propagation criteria

In order to simulate crack propagation under the linear elastic condition, the crack path direction must be determined. There are several methods used to predict the direction of the crack trajectory such as the maximum normal stress theory (or the maximum circumferential stress theory, Erdogan and Sih (1963)) and the minimum strain energy density theory (Sih, 1974).

3.1. Maximum circumferential stress criterion (MCSC)

This criterion is used for elastic materials. It states that the crack propagates in the direction for which the circumferential stress $\sigma_{\theta\theta}$ is maximum. It is a local approach since the direction of crack growth is directly determined by the local stress field along a small circle of radius r centered at the crack tip.

The kinking angle α of the propagating crack can be determined after calculating the values of the stress intensity factors K_I and K_{II} .

$$\alpha = 2 \arctan \left[\frac{1}{4} \frac{K_I}{K_{II}} \pm \frac{1}{4} \sqrt{\left(\frac{K_I}{K_{II}}\right)^2 + 8} \right] \tag{3.1}$$

where K_I and K_{II} are, respectively, the stress intensity factors corresponding to mode I and mode II loading.

4. Criterion of Richard 2D

$$K_V = \frac{K_I}{2} + \frac{1}{2} \sqrt{K_I^2 + 5.366 K_{II}^2} = K_{IC} \tag{4.1}$$

where K_V depends on the stress intensity factors K_I and K_{II} . It is noticeable that unstable crack growth occurs if K_V exceeds the fracture toughness K_{IC} .

This criterion has an excellent approximation of the fracture limit surface of the maximum tangential stress criterion (Erdogan and Sih, 1963). The crack kinking angle α can be determined by

$$\alpha = \mp \left[140^\circ \frac{|K_{II}|}{|K_I| + |K_{II}|} - 70^\circ \left(\frac{|K_{II}|}{|K_I| + |K_{II}|} \right)^2 \right] \tag{4.2}$$

whereby for $K_{II} > 0$ the kinking angle $\alpha < 0$ and vice versa while always $K_I > 0$. There are some more criteria, e.g. criterion of Nuismer (1975) or criterion of Amestoy *et al.* (1980), which are based on the energy release rate and describes the crack growth for 2D-mixed-mode-loading situations.

4.1. Field of the stresses in the vicinity of the forehead of the crack

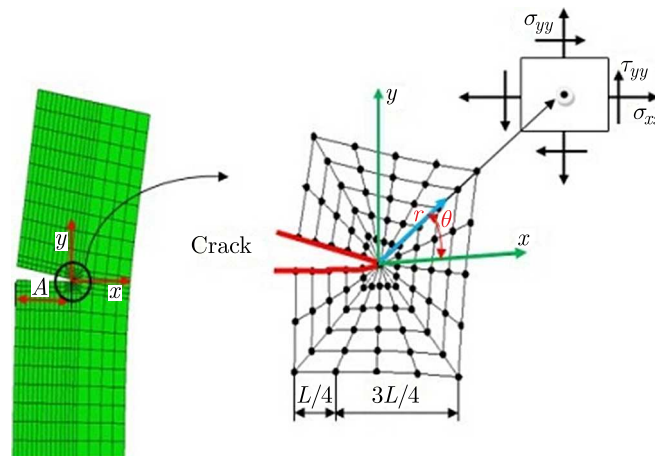


Fig. 1. Field of stresses in the vicinity of the front of the crack

The general equation of the stress field in 2D near the crack front defined by the stress intensity factor K is given by Tada *et al.* (2000)

$$\sigma_{i,j}^{I,II}(r, \theta) = \frac{K_{I,II}}{\sqrt{2\pi r}} f_{ij}(\theta) \quad (4.3)$$

$K_{I,II}$ is the SIF in mode I and II, $\sigma_{i,j}^{I,II}$ is the associated stress field with mode I.

K_I is one that contributes the most to the propagation of the fatigue cracks. Fatigue cracks tend to spread according to the perpendicular direction to the maximum tangential (Erdogan and Sih, 1962)

$$\begin{aligned} \sigma_{xx} &= \frac{K_I}{\sqrt{2\pi r}} \cos \frac{\theta}{2} \left(1 - \sin \frac{\theta}{2} \sin \frac{3\theta}{2} \right) & \sigma_{yy} &= \frac{K_I}{\sqrt{2\pi r}} \cos \frac{\theta}{2} \left(1 + \sin \frac{\theta}{2} \sin \frac{3\theta}{2} \right) \\ \tau_{xy} &= \frac{K_I}{\sqrt{2\pi r}} \sin \frac{\theta}{2} \cos \frac{\theta}{2} \cos \frac{3\theta}{2} \end{aligned} \quad (4.4)$$

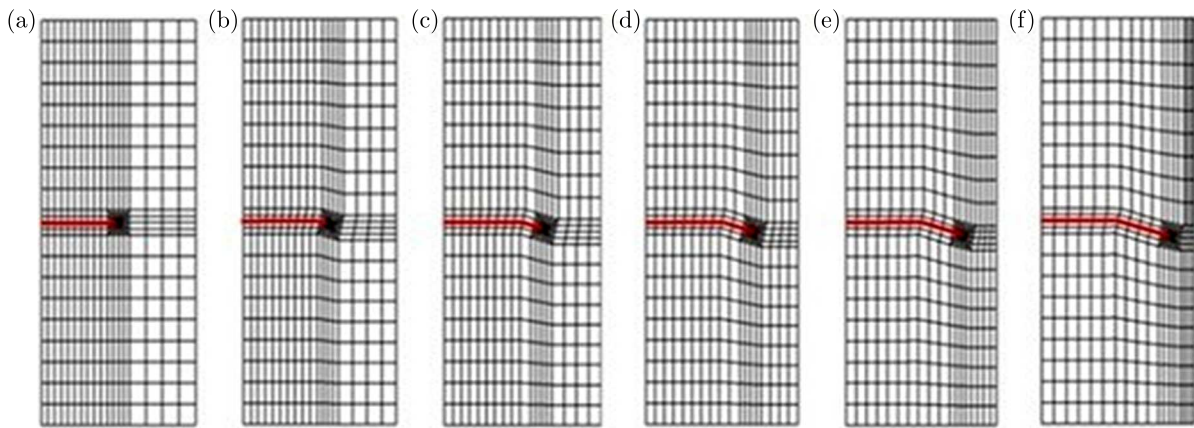


Fig. 2. Stretching finite element method for 5 crack propagation

5. Illustration of 2D SFEM crack propagation

The finite element method by the stretching of the mesh (SFEM) generates for each propagation new coordinates to each node through the following steps:

- Creation of singular elements and elements of contours of zone 5, see Fig. 3a by SFEM using the crack propagation law respecting the propagation criterion.
- The elements of zone 1 and 2 are stretched and at each propagation. Column one of these elements moves to the front of the mesh, the zones are divided in two parts, one is zone 1' and the other is area 2', Fig. 3b.
- The elements of zones 4 and 6 are compressed in each crack propagation, see Fig. 3c.

Point 1 is the center the forehead of the crack and the starting basis for creation of other nodes by this method. The coordinates of this point are given by the following relationship

$$X(1) = A \quad Y(1) = 0 \quad (5.1)$$

where A is the crack length.

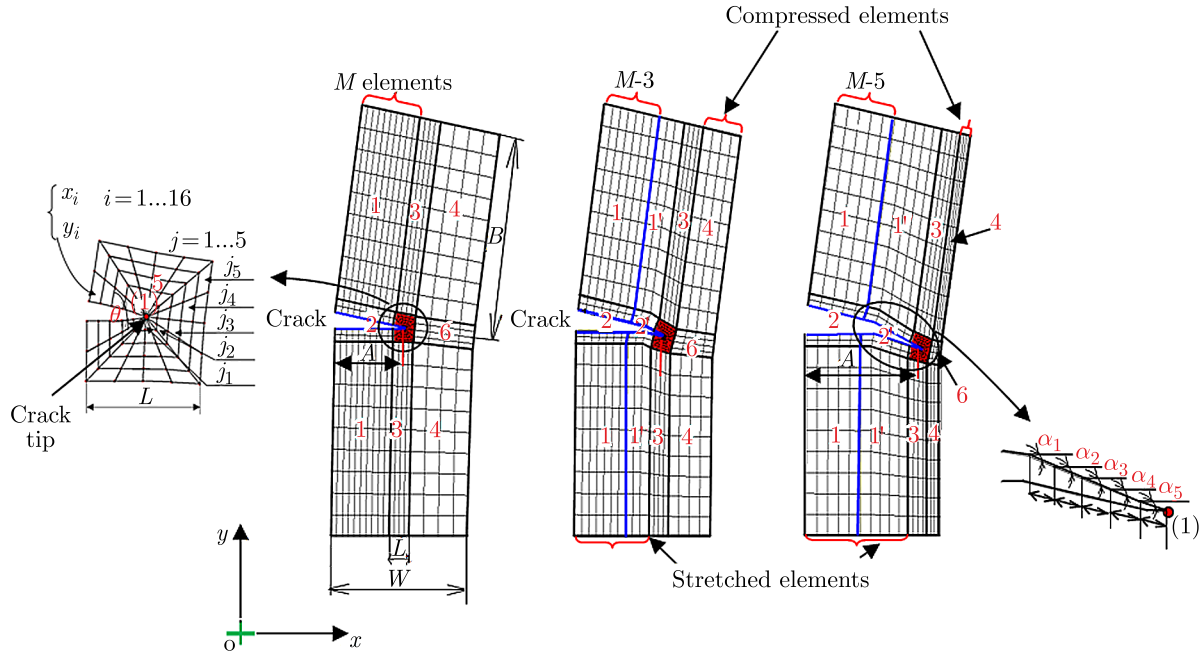


Fig. 3. Schematic illustration of SFEM method: (a) mesh without crack propagation, (b) mesh with 3 crack step propagation, (c) mesh with 5 crack propagations

Singular elements of the CPE4 type are used to determine zone 5. The following equation defines the coordinates of the element nodes in this zone

$$x_i = X(1) - j \frac{L}{t} \cos((i - 1)\theta) \quad y_i = Y(1) - j \frac{L}{t} \sin(i\theta) \quad (5.2)$$

where $j = 1, \dots, t$ is the number of contour, $i = 1, \dots, 16$ – number of elements, $\theta = \pi/16$ – angular division.

6. New coordinates of different areas for n propagations

Node 1 is the front of the crack; it is taken as the reference for all the other nodes of the mesh. The coordinates of this node for n propagation are given by the following relationship

$$X(1) = A + \frac{L}{2} \sum_{p=1}^n \left(\cos \sum_{k=1}^p \alpha_k \right) \quad Y(1) = \frac{L}{2} \sum_{p=1}^n \left(\sin \sum_{k=1}^p \alpha_k \right) \quad (6.1)$$

where α is the crack orientation angle; p is the number of total crack propagation, $p = 1, \dots, n$; L is length of the crack front.

From the first propagation, area 1 is divided into two areas: 1 and 1', see Fig. 3b. The coordinates in the second area can be given by the following formulas

$$x_i = \frac{1}{M - p} \left\{ X(1) - \left[\sum_{p=1}^n \left(\cos \sum_{k=1}^p \alpha_k \right) + S \sum_{p=1}^n \left(\sin \sum_{k=1}^p \alpha_k \right) \right] \frac{L}{2} \right\} (i - 1) \quad (6.2)$$

$$y_j = -S \frac{L}{2} + \frac{B - \frac{L}{2}}{N} (j - 1)$$

where

$$\begin{aligned} i = 1, \dots, 10 & \quad \text{and} \quad M = 10 & \quad p = 1, \dots, n \\ j = 1, \dots, 9 & \quad \text{and} \quad N = 9 & \quad k = 1, \dots, p \end{aligned}$$

and for zone 1', the node coordinates are

$$\begin{aligned}
 x_i &= X(1) - \left[\sum_{p=1}^n \left(\cos \sum_{k=1}^p \alpha_k \right) - S \sum_{p=1}^n \left(\sin \sum_{k=1}^p \alpha_k \right) \right] \frac{L}{2} \\
 &\quad + \frac{1}{M-p} \left\{ \frac{L}{2} \sum_{p=1}^n \left(\cos \sum_{k=1}^p \alpha_k \right) \right\} (i-1) \\
 y_j &= Y(1) + \left[-S \sum_{p=1}^n \left(\cos \sum_{k=1}^p \alpha_k \right) - \sum_{p=1}^n \left(\sin \sum_{k=1}^p \alpha_k \right) \right] \frac{L}{2} \\
 &\quad + \frac{1}{N} \left\{ B - \left[\sum_{p=1}^n \left(\cos \sum_{k=1}^p \alpha_k \right) + \sum_{p=1}^n \left(\sin \sum_{k=1}^p \alpha_k \right) \right] \frac{L}{2} \right\} (j-1)
 \end{aligned} \tag{6.3}$$

where

$$\begin{aligned}
 i &= 1, \dots, n & \text{and} & & M &= 4 & & p &= 1, \dots, 5 \\
 j &= 1, \dots, 9 & \text{and} & & N &= 9 & & k &= 1, \dots, 5
 \end{aligned}$$

and M is the number of vertical elements, N is the number of horizontal elements, B is height of the structure, S is sign of the exchange factor between the two zones, the top and the bottom ($S = -1$ for the top part area and $S = 1$ for the bottom part area).

The new coordinates of the elements of area 3, for n propagation can be written as

$$\begin{aligned}
 x_i &= X(1) - \left[\sum_{p=1}^n \left(\cos \sum_{k=1}^p \alpha_k \right) - S \sum_{p=1}^n \left(\sin \sum_{k=1}^p \alpha_k \right) \right] \frac{L}{2} \\
 &\quad + \frac{1}{M-p} \left\{ \frac{L}{4} \sum_{p=1}^n \left(\cos \sum_{k=1}^p \alpha_k \right) \right\} (i-1) \\
 y_j &= Y(1) - \left[S \sum_{p=1}^n \left(\cos \sum_{k=1}^p \alpha_k \right) - S \sum_{p=1}^n \left(\sin \sum_{k=1}^p \alpha_k \right) \right] \frac{L}{2} \\
 &\quad - \frac{1}{N} \left\{ SB + \left[Y(1) - S \sum_{p=1}^n \left(\cos \sum_{k=1}^p \alpha_k \right) + S \sum_{p=1}^n \left(\sin \sum_{k=1}^p \alpha_k \right) \right] \frac{L}{2} \right\} (j-1)
 \end{aligned} \tag{6.4}$$

where

$$\begin{aligned}
 i &= 1, \dots, 4 & \text{and} & & M &= 4 & & p &= 1, \dots, n \\
 j &= 1, \dots, 9 & \text{and} & & N &= 9 & & k &= 1, \dots, p
 \end{aligned}$$

The elements of area 4 are compressed as shown in Fig. 3b. The definition of coordinates of this area may be given by the following relationship:

$$\begin{aligned}
 x_i &= X(1) + \left[\sum_{p=1}^n \left(\cos \sum_{k=1}^p \alpha_k \right) + S \sum_{p=1}^n \left(\sin \sum_{k=1}^p \alpha_k \right) \right] \frac{L}{2} \\
 &\quad + \frac{1}{M-p} \left\{ W - \left[X(1) - S \sum_{p=1}^n \left(\cos \sum_{k=1}^p \alpha_k \right) + S \sum_{p=1}^n \left(\sin \sum_{k=1}^p \alpha_k \right) \right] \frac{L}{2} \right\} (i-1) \\
 y_j &= Y(1) + \left[-S \sum_{p=1}^n \left(\cos \sum_{k=1}^p \alpha_k \right) + \sum_{p=1}^n \left(\sin \sum_{k=1}^p \alpha_k \right) \right] \frac{L}{2} \\
 &\quad + \frac{1}{N} \left\{ B - \left[Y(1) - \left[\sum_{p=1}^n \left(\cos \sum_{k=1}^p \alpha_k \right) - \sum_{p=1}^n \left(\sin \sum_{k=1}^p \alpha_k \right) \right] \frac{L}{2} \right] \right\} (j-1)
 \end{aligned} \tag{6.5}$$

where

$$\begin{aligned} i &= 1, \dots, 4 & \text{and} & & M &= 4 & & p &= 1, \dots, n \\ j &= 1, \dots, 9 & \text{and} & & N &= 9 & & k &= 1, \dots, p \end{aligned}$$

and C is width of the structure.

Area 2 is an area which contains elements of singularity. During the steps of propagation, zone 2 is divided into two zones 2 and 2', see Fig. 3b. Equations (6.6) and (6.7) show the coordinates of area nodes 2 and 2', respectively

$$\begin{aligned} x_i &= \frac{1}{M-p} \left\{ X(1) - \left[\sum_{p=1}^n \left(\cos \sum_{k=1}^p \alpha_k \right) + S \sum_{p=1}^n \left(\sin \sum_{k=1}^p \alpha_k \right) \right] \frac{L}{2} \right\} (i-1) \\ y_j &= -S \frac{L}{4} + \frac{L}{2N} (j-1) \end{aligned} \tag{6.6}$$

where

$$\begin{aligned} i &= 1, \dots, 10 & \text{and} & & M &= 10 & & p &= 1, \dots, 5 \\ j &= 1, \dots, 4 & \text{and} & & N &= 4 & & k &= 1, \dots, 5 \end{aligned}$$

and

$$\begin{aligned} x_i &= X(1) - \left[\sum_{p=1}^n \left(\cos \sum_{k=1}^p \alpha_k \right) + \sum_{p=1}^n \left(\sin \sum_{k=1}^p \alpha_k \right) \right] \frac{L}{2} \\ &+ \frac{1}{M-p} \left\{ X(1) - \left[\sum_{p=1}^n \left(\cos \sum_{k=1}^p \alpha_k \right) + \sum_{p=1}^n \left(\sin \sum_{k=1}^p \alpha_k \right) \right] \frac{L}{2} \right\} (i-1) \\ y_j &= Y(1) + \left[\sum_{p=1}^n \left(\cos \sum_{k=1}^p \alpha_k \right) - \sum_{p=1}^n \left(\sin \sum_{k=1}^p \alpha_k \right) \right] \frac{L}{2} \\ &+ \frac{1}{N} \left\{ L \sum_{p=1}^n \left(\sin \sum_{k=1}^p \alpha_k \right) - \frac{L}{2} \sum_{p=1}^n \left(\sin \sum_{k=1}^p \alpha_k \right) \right\} (j-1) \end{aligned} \tag{6.7}$$

where

$$\begin{aligned} i &= 1, \dots, 4 & \text{and} & & M &= 4 & & p &= 1, \dots, n \\ j &= 1, \dots, 4 & \text{and} & & N &= 4 & & k &= 1, \dots, p \end{aligned}$$

The coordinates of the node elements of area 6 can be written as

$$\begin{aligned} x_i &= X(1) + \left[\sum_{p=1}^n \left(\cos \sum_{k=1}^p \alpha_k \right) - \sum_{p=1}^n \left(\sin \sum_{k=1}^p \alpha_k \right) \right] \frac{L}{2} \\ &+ \frac{1}{M-p} \left\{ W - \left[X(1) + \sum_{p=1}^n \left(\cos \sum_{k=1}^p \alpha_k \right) - \sum_{p=1}^n \left(\sin \sum_{k=1}^p \alpha_k \right) \right] \right. \\ &\quad \left. - L \sum_{p=1}^n \left(\sin \sum_{k=1}^p \alpha_k \right) \right\} (i-1) \\ y_j &= Y(1) + \left[\sum_{p=1}^n \left(-\cos \sum_{k=1}^p \alpha_k \right) + \sum_{p=1}^n \left(\sin \sum_{k=1}^p \alpha_k \right) \right] \frac{L}{2} \\ &+ \frac{1}{N} \left\{ B - \left[L \sin \alpha_k + Y(1) + \left[\sum_{p=1}^n \left(-\cos \sum_{k=1}^p \alpha_k \right) + \sum_{p=1}^n \left(\sin \sum_{k=1}^p \alpha_k \right) \right] \frac{L}{2} \right] \right\} (j-1) \end{aligned} \tag{6.8}$$

where

$$\begin{aligned} i &= 1, \dots, n & \text{and} & & M &= 4 & & p &= 1, \dots, n \\ j &= 1, \dots, N & \text{and} & & N &= 4 & & k &= 1, \dots, p \end{aligned}$$

7. Interface FORTRAN ABAQUS

In structure of executing the FORTRAN program in interface with the ABAQUS (FEM) is shown in Fig. 4.

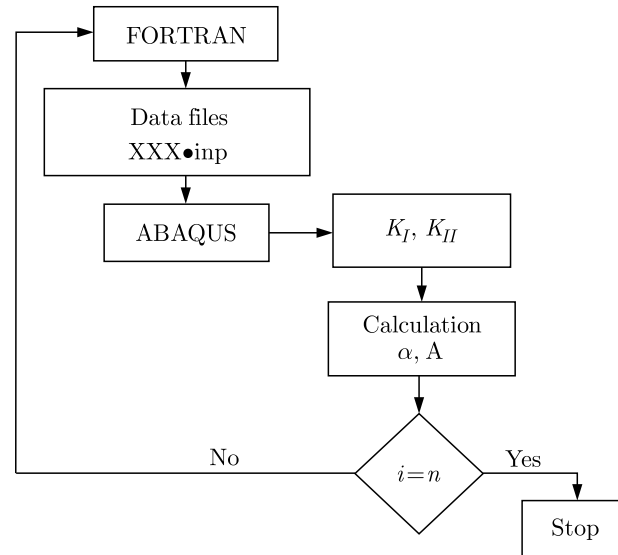


Fig. 4. The structure of the interface between FORTRAN and ABAQUS to calculate K_I , K_{II} and α

8. Numerical model (mesh)

The structure considered has length $B = 8$ mm and width $W = 7$ mm, the horizontal crack length is $A = 3.5$ mm, length of the front $L = 1$ mm. The parametric mesh consists of 478 square CPE4 type elements with four nodes.

The total number of degrees of freedom is equal to 1016. The FORTRAN program for creation of the mesh that will be analyzed by the finite element code ABAQUS has been applied. The steel structure with $E = 1 \cdot 10^7$ Pa and $\nu = 0.25$ is subjected to a uniform tensile stress $\sigma = 100$ MPa.

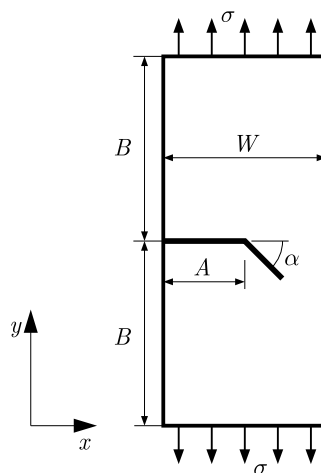


Fig. 5. The specimen with a crack

9. Analytical calculation of stress intensity factors

The analytical stress intensity factor K_I for this problem is given (Ewalds and Wanhill, 1989) as

$$K_I = F\sigma\sqrt{A\pi} \quad (9.1)$$

where F is the correction factor given by

$$F = 1.12 - 0.23\frac{A}{W} + 10.6\left(\frac{A}{W}\right)^2 - 21.7\left(\frac{A}{W}\right)^3 + 30.4\left(\frac{A}{W}\right)^4 \quad (9.2)$$

where the stress intensity factor K_{II} is calculated by the relation

$$K_I \sin \theta + K_{II} (3 \cos \theta - 1) = 0 \quad (9.3)$$

The analytical values of calculated stress intensity factors are compared with the numerical results obtained by SFEM.

Table 1. Comparison of analytical results and SFEM for stress intensity factor K_I and K_{II}

α [°]	K_I^{ANAL} [MPa√m]	K_I^{SFEM} [MPa√m]	Error [%]	K_{II}^{ANAL} [MPa√m]	K_{II}^{SFEM} [MPa√m]	Error [%]
-14.76	31.58	33.03	-4.591	4.232	4.427	-4.608
-0.643	42.90	42.84	0.139	0.2408	0.2404	0.166
0.8313	56.95	55.90	1.844	-0.4132	-0.4056	1.839
1.577	75.68	76.65	-1.282	-1.041	-1.056	-1.441
2.049	114.51	113.9	0.532	-2.049	-2.038	0.54

10. Evaluation of the SIFs as functions of area 5

Zone 5 (singular area) is the most important area, see Fig. 3a. This zone consists of singular elements and other constituent element contours. Its shape is a square of side L . This area can be parametrically varied in order to optimize the mesh.

Figures 6a and 6b show the change in crack length A depending on the size L of the front of singularity zone 5. The stress intensity factors K_I and K_{II} are compared with theoretical values for each stage of propagation of the rift. The interval optimization of zone 5 is in an interval L between $0.1 \leq L \leq 1.1$. This comparison shows a good correlation between the analytical method proposed by Ewalds and Wanhill (1989) and the method of stretching the (SFEM) mesh for the value of $L = 1.0$ mm. There is a very good correspondence between the results obtained in the case of $L = 1.0$ mm compared to other values of L .

The results given by the SFEM are close to those of the analytical solution. The results are obtained for different tilt angles for different crack ratios A/W between 0.5 and 0.8. Figure 7a, shows the evolutions between the SIF and the crack length A , and Fig. 7b depicts an increases in this ratio for which the intensity factor K_I increases and K_{II} decreases.

Figure 8 illustrates the variation of the angle of inclination α estimated at each increment of length of the crack. This comparison shows a good comparison between the two criteria, the criterion of Richard and the MCS criterion we used in our study.

For different values of SIF for the two numerical models and the analytical one, Fig. 7b shows similar values for K_I and K_{II} as functions of the crack length A . Similarly, see Fig. 7a for the ratio A/W one can observe that there is an increase in length and crack orientation angle, which

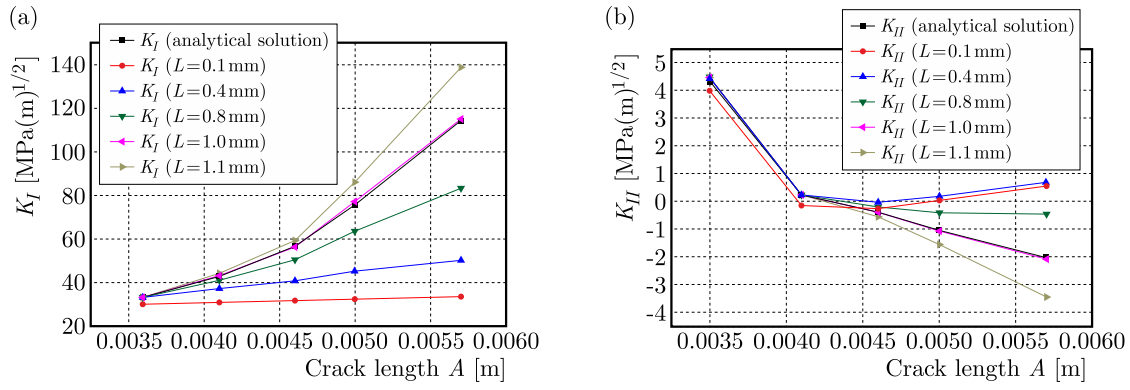


Fig. 6. Variation of SIF along crack length A for different values of L : (a) K_I , (b) K_{II}

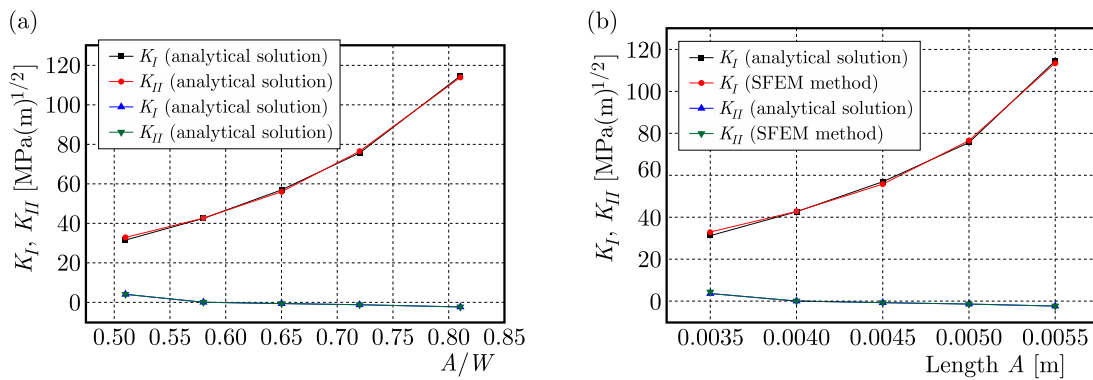


Fig. 7. Comparison of SIF between SFEM and the analytical method: (a) function of the ratio A/W , (b) function of the crack length A

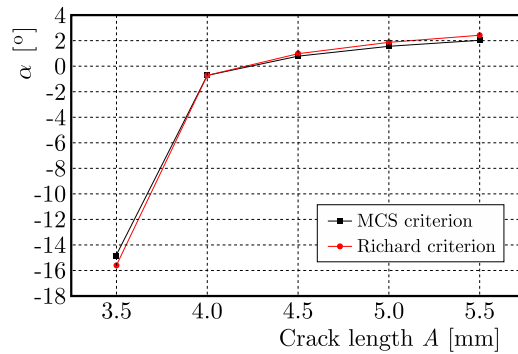


Fig. 8. Evolution of the inclination angle α during crack propagation, comparison between the MCSC and Richard criterion

causes an increase in K_I and a decrease in K_{II} . These results were obtained by Boulenouar *et al.* (2014), Ariffin (2008). The results obtained by the SFEM method and the analytical method show a good correlation between them and allow one to conclude that the numerical model is used correctly.

The values of the stress intensity factors K_I and K_{II} and the orientation angle α are well estimated. Figure 9 illustrates the variation of the estimated angle for each contour of the crack length. There is a very good correspondence between the results obtained by the two methods. In this example, the angle α varies between -14.79° and 2.049° .

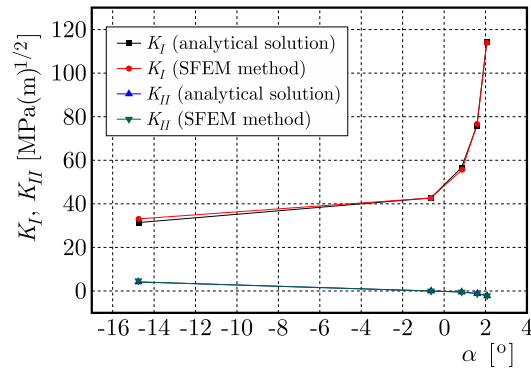


Fig. 9. Tilt angle α according to SIF (K_I , K_{II}) for the two methods: SFEM and analytical

11. Conclusion

The proposed method for the modeling of crack propagation, the stretching finite element method, allows one to get similar results to those obtained through analytical solution. This has been checked for the case in which the analytical solution is well established. The stress intensity factor is rated by the finite element method and its results are in good agreement with those from the exact solution.

Compared (in the case where $A/W = 0.5$ to 0.8) with the analytical method, the results of the present approach provide favorably comparable values and prove its effectiveness in the modeling of problems with crack propagation. The two MCS criteria and the Richard criterion used to determine the angle of crack orientation show a good correlation between them.

On the other hand the estimation of the error of the stress intensity factors for modes I and II is less than 4.591 per cent. It is assessed as an acceptable threshold. The SFEM method as another finite element method is a function of mesh density. It gives more precision if we increase the number of contours around a singularity point. We have used an example with 5 contours in this study, but our parametric mesh allows us to increase the number of contours, which can improve the results even more. The advantage of this method is keeping the same mesh with the same number of nodes and elements while analyzing crack propagation. It is the only finite element method without remeshing during crack propagation.

References

1. ALIABADI M.H., 1997, Boundary element formulations in fracture mechanics, *Applied Mechanics Reviews*, **50**, 2, 83-96
2. ALSHOAIBI M.A., 2015, Finite element modelling of mixed mode crack propagation, *International Journal of Soft Computing and Engineering (TM)*, **5**, 5, 61-66
3. AMESTOY M., BUI H.D., DANG VAN K., 1980, [In:] *International Advances in Fracture Research*, François D. et al. (Eds.), Oxford, 107-113
4. ARIFFIN A.K., 2008, Fatigue life and crack path prediction in 2G structural components using an adaptive finite element strategy, *International Journal of Mechanical and Materials Engineering (IJMME)*, **3**, 1, 97-104
5. ASKES H., SLUYS L.J., JONG B.B.C., 2001, Remeshing techniques for r -adaptive and combined h/r -adaptive analysis with application to 2D/3D crack propagation, *International Journal Structural Engineering and Mechanics*, **12**, 5, 475-490
6. AZOCAR D., ELGUETA M., RIVARA M.C., 2010, Automatic LEFM crack propagation method based on local Lepp-Delaunay mesh refinement, *Advances in Engineering Software*, **41**, 111-119

7. BABUSKA I., BANERJEE U., 2012, Stable generalized finite element method (SGFEM), *Computer Methods in Applied Mechanics and Engineering*, **201-204**, 91-111
8. BABUSKA I., BELENK J., 1997, The partition of unity method, *International Journal Numerical Methods Engineering*, **40**, 727-758
9. BELYTSCHKO T., GU L., LU Y.Y., 1994, Fracture and crack growth by element-free Galerkin methods, *Modelling and Simulation in Materials Science and Engineering*, **2**, 3A, 519-534
10. BOUCHARD P.O., BAY F., CHASTEL Y., TOVENA I., 2000, Crack propagation modelling using an advanced remeshing technique, *Computer Methods Applied Mechanics Engineering*, **189**, 3, 723-742
11. BOUCHARD P.O., BAY F., CHASTEL Y., 2003, Numerical modelling of crack propagation automatic remeshing and comparison of different criteria, *Computer Methods Applied Mechanics Engineering*, **192**, 35/36, 3887-3908
12. BOULENOUAR A., BENSEDDIQ N., MAZARI M., BENAMARA N., 2014, FE model for linear-elastic mixed mode loading: estimation of SIFs and crack propagation, *Journal of Theoretical and Applied Mechanics*, **52**, 2, 373-383
13. CHAN S.K., TUBA I.S., WILSON W.K., 1970, On the finite element method in linear fracture mechanics, *Engineering Fracture Mechanics*, **10**, 1, 1-17
14. CHO J.R., 2015, Computation of 2-D mixed-mode stress intensity factors by Petrov-Galerkin natural element method, *Structural Engineering and Mechanics*, **56**, 4, 589-603
15. DUFLOT M., NGUYEN-DANG H., 2004, Fatigue crack growth analysis by an enriched meshless method, *Journal of Computational and Applied Mathematics*, **168**, 1/2, 155-164
16. ERDOGAN F., SIH G.C., 1963, On the crack extension in plates under plane loading and shear, *Journal of Basic Engineering*, **85**, 4, 519-527
17. EWALDS H., WANHILL R., 1989, *Fracture Mechanics*, New York, Edward Arnold
18. KHOEI A.R., AZADIA H., MOSLEMIA H., 2008, Modeling of crack propagation via an automatic adaptive mesh refinement based on modified superconvergent patch recovery technique, *Engineering Fracture Mechanics*, **75**, 2921-2945
19. MEYER A., RABOLD F., SCHERZER M., 2006, Efficient finite element simulation of crack propagation using adaptive iterative solvers, *Communications in Numerical Methods in Engineering*, **22**, 2, 93-108
20. MIRANDA A.C.O., MEGGIOLARO M.A., CASTRO J.T.P., MARTHA L.F., BITTENCOURT T.N., 2003, Fatigue life and crack predictions in generic 2D structural components, *Engineering Fracture Mechanics*, **70**, 10, 1259-1279
21. MÖES N., DOLBOW J., BELYTSCHKO T., 1999, A finite element method for crack growth without remeshing, *International Journal Numerical Methods Engineering*, **46**, 1, 131-150
22. MURAT Y., 2016, The investigation crack problem through numerical analysis, *Structural Engineering and Mechanics*, **57**, 6, 1143-1156
23. NUISMER R.J., 1975, An energy release rate criterion for mixed mode fracture, *International Journal of Fracture*, **11**, 2, 245-250
24. PARIS P., ERDOGAN F., 1963, A critical analysis of crack propagation laws, *Journal of Basic Engineering, Transactions ASME*, **85**, 4, 528-534
25. PHONGTHANAPANICH S., DECHAUMPHAI P., 2004, Adaptive Delaunay triangulation with object-oriented programming for crack propagation analysis, *Finite Elements in Analysis and Design*, **40**, 13/14, 1753-1771
26. PORTELA A., ALIABADI M., ROOKE D.P., 1991, The dual boundary element method effective implementation for crack problem, *International Journal for Numerical Methods in Engineering*, **33**, 6, 1269-1287

27. RÉTHORÉ J., GRAVOUIL A., COMBESCURE A., 2005, An energy-conserving scheme for dynamic crack growth using the extended finite element method, *International Journal for Numerical Methods in Engineering*, **63**, 5, 631-659
28. SIH G.C., ERDOGAN F., 1962, On crack extension in plates (plates) under plane loading and transverse shear, *ASME Meeting WA-163*, New York, NY, United States
29. SIH G.C., 1974, Strain-energy-density factor applied to mixed mode crack problems, *International Journal of Fracture*, **10**, 3, 305-321
30. SINGH I.V., MISHRA B.K., BHATTACHARYA S., PATIL R.U., 2012, The numerical simulation of fatigue crack growth using extended finite element method, *International Journal of Fatigue*, **36**, 1, 109-119
31. TADA H.P., IRWIN G.R., 1985, *The Stress Analysis of Cracks Handbook*, Paris Productions Incorporated
32. TADA H.P., PARIS P.C., IRWIN G.R., 2000, *The Stress Analysis of Cracks Handbook*, American Society of Mechanical Engineering
33. YAN A.M., NGUYEN-DANG H., 1995, Multiple-cracked fatigue crack growth by BEM, *Computational Mechanics*, **16**, 5, 273-80
34. YAN X., 2006, A boundary element modeling of fatigue crack growth in a plane elastic plate, *Mechanics Research Communications*, **33**, 470-481
35. ZALEHA M., ARIFFIN A.K., MUCHTAR A., 2007, Prediction of crack propagation direction for holes under quasi-static loading, *Computational and Experimental Mechanics*, 141-151

Manuscript received December 28, 2016; accepted for print March 16, 2017

NONLOCAL ANALYSIS OF SINGLE AND DOUBLE-LAYERED GRAPHENE CYLINDRICAL PANELS AND NANO-TUBES UNDER INTERNAL AND EXTERNAL PRESSURES CONSIDERING THERMAL EFFECTS

SHAHRIAR DASTJERDI

*Young Researchers and Elite Club, Mashhad Branch, Islamic Azad University, Mashhad, Iran
e-mail: dastjerdi_shahriar@yahoo.com*

MASSOUMEH LOTFI, MEHRDAD JABBARZADEH

Department of Mechanical Engineering, Mashhad branch, Islamic Azad University, Mashhad, Iran

Mechanical behavior of a bilayer graphene cylindrical panel and nano-tube is studied based on nonlocal continuum mechanics with regard to this aim, von-Karman assumptions and nonlocal theory of Eringen are considered. Then, the governing equations and boundary conditions have been derived applying energy method. While analyzing the bilayer cylindrical panel, the van der Waals interaction between the layers is considered in calculations. The constitutive equations are developed for nano-tubes under internal and external pressures. In order to solve the governing equations, the semi-analytical polynomial method (SAPM), which was presented by the authors before, is utilized and bending behavior of bilayer cylindrical panels and nano-tubes is investigated. Finally, the effects of temperature, boundary conditions, elastic foundation, loading, van der Waals interaction between the layers and single layer to bilayer analyses are studied for graphene cylindrical panels and nano-tubes.

Keywords: cylindrical graphene panels, nano-tube, nonlocal elasticity theory, first-order shear deformation theory

1. Introduction

Shells and panels are the most frequently applied engineering structures and are categorized in several groups. The curvature of shells is one basis of the categorization which is most significant in geometric shapes (cylindrical, conical, and spherical, etc.) and related equations. Another basis of the categorization is thickness of the shell, which divides into two groups of low thickness (shell) and high thickness (plate), for the thickness-to-radius ratio of $(h/R)_{max} \leq 1/20$, it is assumed to be a low thickness shell. According to ever-increasing application of shells in industries, the significance of studying behavior of shell structures in different cases of loading including bending and buckling becomes more pronounced. One interesting nano structure which scientifics are devoted to is the carbon nano-tube. The tubes were discovered in 1991 (Iijima, 1991). Single wall carbon nano-tubes can be assumed as 2D single layer graphene sheets which are rolled. The extraordinary attributes of graphene sheets, carbon nano-tubes and their exclusive specifications made them a reason to progress and renovation of difference researches and nano-science (Tans *et al.*, 1997; Martel *et al.*, 1998; Postma *et al.*, 2001). Experimental tests in nano scale are difficult and expensive. Therefore, developing a suitable mathematical model for nano structures is important. Continuum mechanics model is an appropriate and a low-cost solution. Disadvantages of the continuum method is that it is not possible to estimate the exact small scale effects. When the size of structures is small, the effects of small scale on mechanical behavior are very important. To eliminate the disadvantage in the classic continuum model, Eringen and Edelen (1972) presented a nonlocal elasticity theory and modified the classical continuum mechanics to consider the effects of small size. By considering the effects of size in

related equations as material properties, the nonlocal theory of Eringen is extremely effective in presenting an exact and appropriate model of nano structures. Hence to study behavior of nano plates in many presented studies, the nonlocal theory is applied.

Murmu and Pradhan (2009) applied the theory of nonlocal elasticity to rectangular single layer graphene sheets in elastic environment. They applied both models of Winkler and Pasternak to simulate reactions of graphene sheets with their elastic environment. Reddy and Pang (2008) studied bending and buckling of carbon nano-tubes based on nonlocal theory. Aghababaei and Reddy (2009) investigated bending and free vibration equations based on the third-order shear deformation theory/ The nonlocal effects were then solved analytically for a isotropic rectangular sheet with simple boundary conditions. They concluded that two first order and third order shear deformation theories had similar results while related results from nonlocal theory of thin shell were difference. Pradhan (2009) analyzed buckling of isotropic graphene rectangular plates based on the third-order shear deformation theory and the Navier method. He concluded that by increasing the small scale effects or decreasing length of the plate, the ratio of nonlocal buckling loads to the local case would be increased. The first solution of the buckling problem of cylindrical shells under uniform lateral pressure was presented by Brush and Almroth (1975). Then many extensive researches on buckling of cylindrical shells by different materials and different boundary conditions have been done. Hoff and Soong (1965) studied buckling of a cylindrical shell under axial load in different conditions. They showed that if the ratio of shell length to its thickness was large enough, the value of stress in buckling mode would always be independent from length of the shell and the maximum critical stress would occur for simply supported boundary conditions. Linghai *et al.* (2008) considered buckling of a cylindrical panel under axial load by a differential quadrature method in which the load was perpendicular to the surface. Zhao and Liew (2009) analyzed a cylindrical panel made of a functionally graded material (FGM) under thermal and dynamic loads based on the first order nonlinear shear deformation theory by applying the free element method. Nguyen and Hoang (2010) studied stability of a cylindrical panel made of a functionally graded material under axial pressure and simple supported boundary conditions. It was found that by increasing the ratio of length to radius of the cylindrical panel, critical load always increased. Khazaeinejad *et al.* (2010) analyzed buckling of cylindrical shells made of a functionally graded material under both axial loads and internal pressure by using the first order shear deformation theory. They concluded that by decreasing the power factor of material properties, critical load increased.

Lancaster *et al.* (2004) investigated the effect of imperfections on the buckling load in the form of local initial stress, which were probably more typical in practice than in purely geometric ones. Bisagni and Cordisco (2003) experimentally studied buckling and post-buckling behavior of four unstiffened thin-walled CFRP cylindrical shells for which the test equipment allowed application of axial and torsional loadings. Their results identified the effect of laminate orientation, showed that the buckling loads were essentially independent of the load sequence and demonstrated that the shells were able to sustain load in the post-buckling field without any damage. Degenhardt *et al.* (2010) performed buckling tests and buckling simulations on CFRP cylindrical shells to investigate the imperfection sensitivity and to validate the applied simulation methodologies. Fazelzadeh and Ghavanloo (2014) pursued vibration characteristics of curved graphene ribbons (CGRs) embedded in an orthotropic elastic shell and investigated that there was significant dependence of natural frequencies on the curvature change. Biswas (2014) presented nonlinear analysis of plate and shell structures under mechanical and thermal loadings.

Ansari *et al.* (2016) studied size-dependent nonlinear mechanical behavior of third-order shear deformable functionally graded microbeams using the variational differential quadrature method. They used the gradient elasticity theory in their study. Zhang *et al.* (2016) applied FSDT element free IMLS-Ritz method to analyze free vibration of triangular CNT-reinforced composite plates subjected to in-plane stresses.

Dastjerdi *et al.* (2016a) derived constitutive equations for graphene plates in Cartesian and cylindrical coordinate systems based on the nonlocal first and higher order shear deformation theories. Zhang *et al.* (2015) presented a nonlocal continuum model for vibration of single-layered graphene sheets based on the element-free kp-Ritz method. All the mentioned solving methods are popular in analyzing the small scale effects of nano structures. Continuing, Dastjerdi *et al.* (2016b,c) worked on static analysis of single layer annular/circular graphene sheets (Dastjerdi *et al.*, 2016b) and the effect of vacant defects on bending analysis of circular graphene sheets (Dastjerdi *et al.*, 2016c) based on the nonlocal theory of Eringen. They presented a new semi-analytical polynomial method (SAPM) for solving ordinary and partial differential equations.

In this paper, for the first time, the nonlinear bending analysis of bilayer graphene cylindrical panels and nano-tubes has been studied. Nonlocal constitutive equations have been derived and solved applying SAPM (Dastjerdi *et al.*, 2016c). It has been tried to consider all effective parameters on study such as boundary conditions, nonlocal parameter, temperature, loading, elastic foundation, etc.

2. Nonlocal theory

Different non-classical theories have been presented to analyze structures in nano and micro scales such as strain-gradient theories, couples stress and the nonlocal theory of Eringen. With regard to considering the simplicity of the equations and satisfactory results of the nonlocal theory, this theory has been applied by many researchers to analysis of mechanical behavior of nano structures. In other words, this theory has been applied in the present article, considering its advantages. According to the nonlocal theory of Eringen, stress in a specified point of surface is a function of strain in all points of the surface. As below in the integral equation, it is shown as a function of local stress (Eringen and Edelen, 1972)

$$\sigma_{ij} = \int_V \alpha(|\chi' - \chi|) \sigma_{ij}^L(\chi') dV(\chi') \quad (2.1)$$

The integral must be calculated on the total surface. χ is a point whose stress can be calculated according to stress of all χ' points of the structure. The indices i, j are the same for x, y, z of the shell coordinate components. The distance between χ and χ' can be presented by $|\chi' - \chi|$ and $\alpha(|\chi' - \chi|)$, which are nonlocal weight functions. σ_{ij}^L and σ_{ij}^{NL} are local and nonlocal stresses, respectively. Finally, Eq. (2.1) can be expressed for the 2D case as

$$(1 - \mu \nabla^2) \sigma_{ij}^{NL} = \sigma_{ij}^L \quad \mu = (e_0 a)^2 \quad \nabla^2 = \frac{\partial^2}{\partial x^2} + \frac{\partial^2}{\partial y^2} \quad (2.2)$$

In the above, a is related to internal dimensions and small size, e_0 is the material coefficient which results from experimental studies. The value of the nonlocal parameter μ is not specified exactly and is dependent on boundary conditions, mode number, layer quantity and type of movement (Eringen and Edelen, 1972). Wang and Wang (2007) illustrated that the value of the nonlocal parameter ($e_0 a$) is between 0 and 2 nm. Consequently, many researchers have considered this range of the nonlocal parameter in their investigations. As a result, in this paper, the nonlocal parameter is assumed between 0 and 2 nm, too.

3. Governing equations

A bilayer graphene cylindrical panel is considered as shown in Fig. 1, resting on a Winkler-Pasternak elastic medium under uniform transverse loading q . The Winkler-Pasternak stiffness coefficients are k_w and k_p , respectively. Winkler considers the elastic foundation to be completely

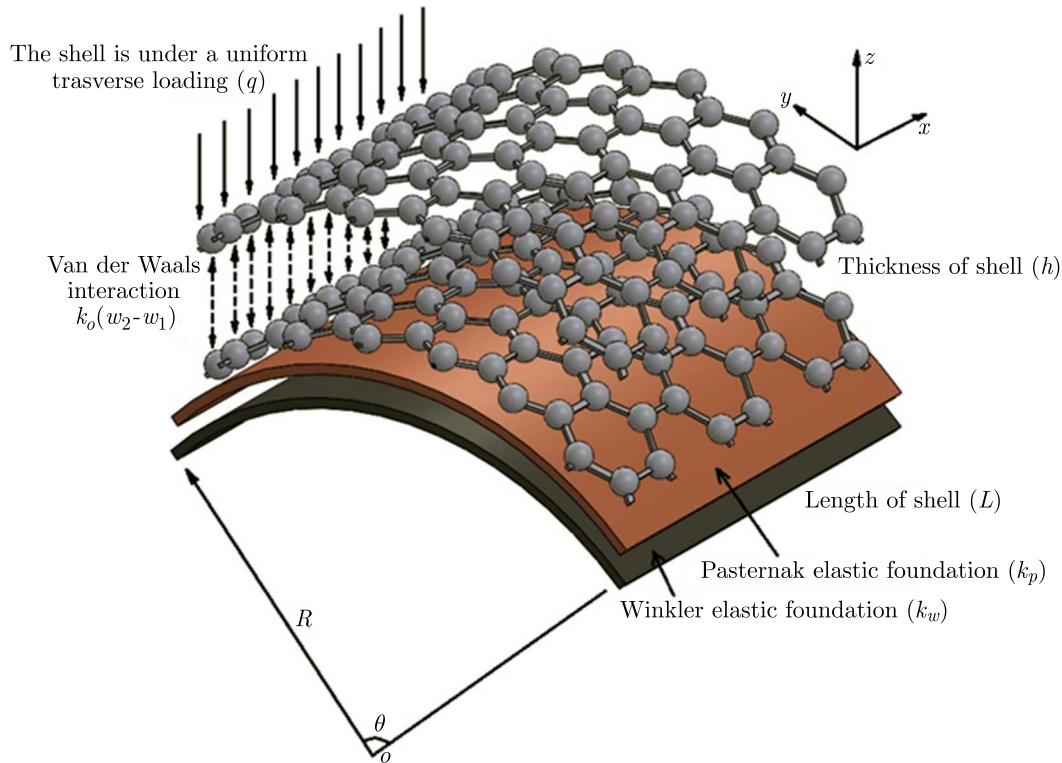


Fig. 1. Schematic view of a bilayer graphene cylindrical panel rested on Winkler-Pasternak elastic foundation

made of linear springs ($P = k_w w$). If the mentioned foundation is affected by a transverse loading q , the springs would not be influenced beyond the loaded domain.

In the Pasternak elastic matrix, the effect of shear force among the spring elements is considered, which is completed by connecting the ends of the springs to the plate that only undergoes transverse shear deformation. The relationship between the load and deflection is obtained by assuming the vertical equilibrium of a shear layer ($P = k_w w + k_p \nabla^2 w$). The amount of van der Waals interaction depends on the distance between the layers. k_o and k_o^* can be introduced as a stiffness of spring force (van der Waals interaction) as $k_o(w_2 - w_1) + k_o^*(w_2 - w_1)^3$ in which w_1 represents deflection of the upper layer and w_2 - the bottom layer. In practical investigations, the values of w_1 and w_2 are close to each other. So, the term $(w_2 - w_1)^3$ is extremely insignificant. As a result, the non-linear term can be neglected for simplicity of calculations, and the van der Waals interaction can be considered linear as $k_o(w_2 - w_1)$.

In this study, the constitutive equations are derived based on the first-order shear deformation theory (FSDT) in which the neglected assumptions in the classical plate theory are considered with more accuracy. According to the first-order shear deformation theory, the displacement field can be written as follows

$$U_i = u_i + z\varphi_i \quad V_i = v_i + z\psi_i \quad W_i = w_i \quad (3.1)$$

where u_i , v_i and w_i are the displacement components of the mid-plane along the x , y and z directions, respectively. φ_i and ψ_i refer to the rotation functions of the transverse normal to y and x directions. The index $i = 1, 2$ refers to the upper and bottom layers, respectively. The strain field is then as below

$$\begin{aligned}
 \varepsilon i_x &= \frac{\partial w_i}{\partial x} + \frac{1}{2} \left(\frac{\partial w_i}{\partial x} \right)^2 + z \frac{\partial \varphi_i}{\partial x} - \alpha \Delta T \\
 \varepsilon i_y &= \frac{w_i}{R} + \frac{\partial v_i}{\partial y} + \frac{1}{2} \left(\frac{\partial w_i}{\partial y} \right)^2 + z \frac{\partial \psi_i}{\partial y} - \alpha \Delta T \\
 \gamma i_{xy} &= \frac{\partial v_i}{\partial x} + \frac{\partial w_i}{\partial y} + \left(\frac{\partial w_i}{\partial x} \frac{\partial w_i}{\partial y} \right) + z \left(\frac{\partial \varphi_i}{\partial y} + \frac{\partial \psi_i}{\partial x} \right) \\
 \gamma i_{xz} &= \varphi_i + \frac{\partial w_i}{\partial x} \quad \gamma i_{yz} = \psi_i + \frac{\partial w_i}{\partial y} - \frac{v_i}{R}
 \end{aligned}
 \tag{3.2}$$

Now to obtain equilibrium equations, an energy method is applied in which variation of potential energy for external loads and strain energy must be zero

$$\delta \pi = \delta U + \delta V = 0 \quad \delta V = \iint_A (q - k_w w_0) \delta w_0 \, dA
 \tag{3.3}$$

and

$$\delta U = \iiint_A (\sigma_{ij} \delta \varepsilon_{ij}) \, dv
 \tag{3.4}$$

Equation (3.4) describes the strain energy which can be expanded as follows

$$\delta U = \iiint_A (\sigma i_x \delta \varepsilon i_x + \sigma i_y \delta \varepsilon i_y + \sigma i_{xy} \delta \varepsilon i_{xy} + \sigma i_{yz} \delta \gamma i_{yz} + \sigma i_{xz} \delta \gamma i_{xz}) \, dv \quad i = 1, 2
 \tag{3.5}$$

The stress and moment resultants are specified as follows

$$\begin{aligned}
 [N i_x, N i_y, N i_{xy}]^{NL} &= \int_{-h/2}^{h/2} [\sigma i_x, \sigma i_y, \sigma i_{xy}]^{NL} \, dz \\
 [M i_x, M i_y, M i_{xy}]^{NL} &= \int_{-h/2}^{h/2} [\sigma i_x, \sigma i_y, \sigma i_{xy}]^{NL} z \, dz \\
 [Q i_y, Q i_x]^{NL} &= k_s \int_{-h/2}^{h/2} [\sigma i_{yz}, \sigma i_{xz}]^{NL} \, dz
 \end{aligned}
 \tag{3.6}$$

where k_s is the shear factor correction coefficient for the first-order shear deformation theory, which is taken 5/6. Now by substituting Eqs. (3.6) into Eq. (3.3) and integrating with respect to z , Eq. (3.3) can be developed. The obtained total energy equation must be equal to zero. The equilibrium equations are based on the nonlocal theory of Eringen. Applying Eq. (2.2) into the resultants (Eqs. (3.3)) and then substituting into the nonlocal governing equations, the constitutive equations can be obtained in the local form of the resultants considering the effects of the nonlocal parameter. Dastjerdi *et al.* (2016a) explained the process of obtaining the local form of governing equations from nonlocal ones. Finally, the nonlocal constitutive equations for the bilayer graphene cylindrical panel can be expressed as follows (some inconsiderable terms are neglected)

$$\begin{aligned}
 \frac{\partial N i_x^L}{\partial x} + \frac{\partial N i_{xy}^L}{\partial y} &= 0 & \frac{\partial N i_y^L}{\partial y} + \frac{Q i_y^L}{R} + \frac{\partial N i_{xy}^L}{\partial x} &= 0 \\
 \frac{\partial M i_x^L}{\partial x} + \frac{\partial M i_{xy}^L}{\partial y} - Q i_x^L &= 0 & \frac{\partial M i_y^L}{\partial y} + \frac{\partial M i_{xy}^L}{\partial x} - Q i_y^L &= 0
 \end{aligned}
 \tag{3.7}$$

— upper layer

$$-\frac{N1_y^L}{R} + \frac{\partial Q1_y^L}{\partial y} + \frac{\partial Q1_x^L}{\partial x} + (1 - \mu\nabla^2) \left[N1_x^L \frac{\partial^2 w1}{\partial x^2} + 2N1_{xy}^L \frac{\partial^2 w1}{\partial x \partial y} + N1_y^L \frac{\partial^2 w1}{\partial y^2} + q - k_o(w2 - w1) \right] = 0 \quad (3.8)$$

— bottom layer

$$-\frac{N2_y^L}{R} + \frac{\partial Q2_y^L}{\partial y} + \frac{\partial Q2_x^L}{\partial x} + (1 - \mu\nabla^2) \left[N2_x^L \frac{\partial^2 w2}{\partial x^2} + 2N2_{xy}^L \frac{\partial^2 w2}{\partial x \partial y} + N2_y^L \frac{\partial^2 w2}{\partial y^2} + k_o(w2 - w1) + (-k_w w2 + k_p \nabla^2 w2) \right] = 0 \quad (3.9)$$

4. Boundary conditions

All possible boundary conditions have been assumed as simply supported (S), clamped (C) and free (F) edges, which can be written as follows (for the first line $0 < x < L_x$ and for the second line $0 < y < L_y$)

$$\begin{aligned} S : \quad & u_i = v_i = w_i = \psi_i = M_{i_x} = 0 & C : \quad & u_i = v_i = w_i = \varphi_i = \psi_i = 0 \\ & u_i = v_i = w_i = \varphi_i = M_{i_y} = 0 & & u_i = v_i = w_i = \varphi_i = \psi_i = 0 \\ F : \quad & N_{i_x} = N_{i_{xy}} = Q_{i_x} = M_{i_x} = M_{i_{xy}} = 0 & & \\ & N_{i_x} = N_{i_{xy}} = Q_{i_y} = M_{i_y} = M_{i_{xy}} = 0 & & \end{aligned} \quad (4.1)$$

5. Solution

Taking a look on the governing equations, it is clear that a system of nonlinear partial differential equations has been obtained whose solution is not possible to be determined by common analytical methods. In the paper, a new semi-analytical polynomial method (SAPM) is applied, which was presented before by the authors (Dastjerdi *et al.*, 2016c). The SAPM formulation is extremely simple and its accuracy was proved before (Dastjerdi *et al.*, 2016c). According to the mentioned explanations for SAPM, to achieve a solution to the governing equations, the below displacements and rotations can be introduced (Dastjerdi *et al.*, 2016c) ($i = 1, 2$ for the upper and bottom layers)

$$\begin{aligned} u_i &= \sum_{k=1}^N \sum_{t=1}^M a_{i\{k+t-[1-(k-1)(M-1)]\}} x^{(k-1)} y^{(t-1)} \\ v_i &= \sum_{k=1}^N \sum_{t=1}^M a_{i\{k+t-[1-(k-1)(M-1)]+MN\}} x^{(k-1)} y^{(t-1)} \\ w_i &= \sum_{k=1}^N \sum_{t=1}^M a_{i\{k+t-[1-(k-1)(M-1)]+2MN\}} x^{(k-1)} y^{(t-1)} \\ \varphi_i &= \sum_{k=1}^N \sum_{t=1}^M a_{i\{k+t-[1-(k-1)(M-1)]+3MN\}} x^{(k-1)} y^{(t-1)} \\ \psi_i &= \sum_{k=1}^N \sum_{t=1}^M a_{i\{k+t-[1-(k-1)(M-1)]+4MN\}} x^{(k-1)} y^{(t-1)} \end{aligned} \quad (5.1)$$

By considering Eqs. (5.1) in constitutive equations (3.7)-(3.9), the partial differential equations will be transformed into algebraic equations. The obtained equations can be solved by considering boundary conditions.

6. Numerical results and discussion

The curvature radius of the graphene panel has been assumed to tend to infinity in order to obtain a rectangular plate. Then, the results are compared with those by Dastjerdi and Jabbarzadeh (2016). According to Fig. 2, it can be seen that the results are close to each other. The small differences occurred because of tending the radius of the cylindrical panel to infinity. Also, it can be concluded that the differences increase for more flexible boundary conditions. However, the maximum difference is about 2.5%, which is insignificant. Consequently, the obtained results of DQM (Dastjerdi and Jabbarzadeh, 2016) are in compliance with the results of SAPM in this paper.

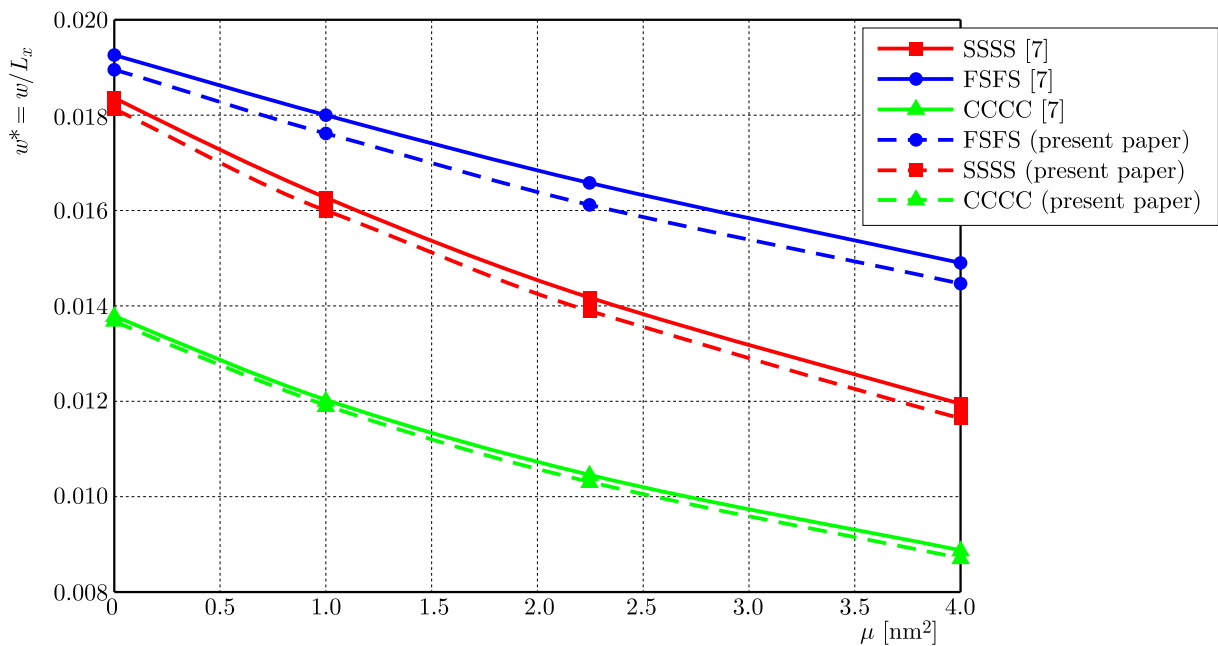


Fig. 2. Comparison between the results of the present paper and Dastjerdi and Jabbarzadeh (2016)

Table 1 indicates the effect of temperature on the results for different types of boundary conditions. It is observed that in higher temperature, the maximum deflection increases. The variations are approximately linear and there is not a considerable difference between CCC and SSSS boundary conditions. The variations are the same. Also, it is observed that by increasing the nonlocal coefficient, the deflection decreases and the rate of variations remains constant. In CCC boundary conditions, by increasing the nonlocal effect, the deflection decreases faster, but in SSSS boundary conditions, the variations are small. For example, deflections for $e_0a = 1$ nm and $e_0a = 2$ nm are not considerably different, but in CCC boundary condition, they are different. It may result that in SSSS boundary conditions, due to its more flexibility, temperature raise versus an increase in the small-scale effects is more than in CCC boundary conditions, and by increasing e_0a , the deflection has a less descending rate. The properties of the panel are presented below

$$\begin{aligned}
 L_x &= 5 \text{ nm} & \theta &= \pi & h &= 0.34 \text{ nm} & R &= 5 \text{ nm} \\
 E_x &= E_y = 1.06 \text{ TPa} & \nu_{xy} &= \nu_{yx} = 0.3 & q &= 0.5 \text{ GPa} & & \\
 k_w &= 1.13 \text{ GPa/nm} & k_p &= 1.13 \text{ Pa m} & \alpha &= 2.02 \cdot 10^{-6} \text{ C}^{o-1} & &
 \end{aligned}
 \tag{6.1}$$

Table 1. Effect of temperature on nonlocal analysis

ΔT [C°]	w [nm]					
	$e_0a = 0$ nm	$e_0a = 1$ nm	$e_0a = 2$ nm	$R_m = \frac{w_{e_0a=1nm}^*}{w_{e_0a=0nm}^*}$	$R_m = \frac{w_{e_0a=2nm}^*}{w_{e_0a=0nm}^*}$	
0	0.0307	0.0294	0.0249	0.9557	0.8086	CCCC
100	0.0321	0.0307	0.0262	0.9576	0.8156	
500	0.0374	0.0362	0.0316	0.9653	0.8441	
1000	0.0443	0.0432	0.0390	0.9746	0.8800	
0	0.0326	0.0318	0.0311	0.9769	0.9560	SSSS
100	0.0340	0.0332	0.0325	0.9782	0.9572	
500	0.0396	0.0389	0.0381	0.9822	0.9616	
1000	0.0466	0.0461	0.0451	0.9873	0.9657	

To survey the effect of Winkler-Pasternak elastic foundation, Tables 2 and 3 present different types of boundary conditions. In both tables, higher values of elastic the foundation stiffness lead to smaller deflections. As mentioned before, SSSS boundary conditions have more effects on the results, as seen in Table 1. For example, in Table 2, it is considered that by increasing e_0a in CCCC boundary conditions, the normal falling rate is available, but in SSSS boundary conditions, the falling rate is smaller. The mentioned variations can be observed in Table 3, too, but it seems that the effect of Pasternak elastic foundation is more evident. Basically, Winkler and Pasternak elastic foundations have a fairly important role in the analysis. It is due to the direct effect of the nonlocal coefficient on the elasticity of Winkler and Pasternak foundations in Eq. (3.9). Consequently, the availability and their values are important in the small scale effect when the nonlocal elasticity theory is applied.

Table 2. Effect of Winkler elastic foundation on the results

k_w [GPa/nm]	w [nm]					
	$e_0a = 0$ nm	$e_0a = 1$ nm	$e_0a = 2$ nm	$R_m = \frac{w_{e_0a=1nm}^*}{w_{e_0a=0nm}^*}$	$R_m = \frac{w_{e_0a=2nm}^*}{w_{e_0a=0nm}^*}$	
0	0.0335	0.0336	0.0330	1.0020	0.9850	CCCC
1	0.0316	0.0311	0.0288	0.9841	0.9114	
5	0.0259	0.0238	0.0188	0.9189	0.7259	
10	0.0210	0.0183	0.0131	0.8714	0.6238	
0	0.0354	0.0363	0.0377	1.0254	1.0649	SSSS
1	0.0333	0.0335	0.0325	1.0060	0.9759	
5	0.0268	0.0255	0.0209	0.9514	0.7798	
10	0.0214	0.0195	0.0144	0.9112	0.6729	

The van der Waals force is a kind of force which depends on the distance between the layers (Dastjerdi and Jabbarzadeh, 2016). As the distance between two layers decreases, the van der Waals force increases. Figure 3a is drawn for CCCC boundary conditions, and Fig. 3b for SSSS boundary conditions. According to the figures, it is observed that by increasing k_0 , the deflections of two layers approach each other, and after a specified value, an increase in k_0 has no impact on the results. In both Figs. 3a and 3b, also it is observed that by increasing the nonlocal parameter, the deflections of both layers approach each other faster than before. Therefore, increasing the nonlocal effect results in an increase in van der Waals interaction between the layers. In Fig. 3b, it can be concluded that by increasing small-scale effects, more variation results rather than in CCCC boundary conditions. However, the variations are approximately similar and no considerable change is observed. In this case, the elastic foundation is available and the variations in both cases of CCCC and SSSS boundary conditions are approximately similar.

Table 3. Effect of Pasternak elastic foundation on the results

k_p [Pa m]	w [nm]					
	$e_0a = 0$ nm	$e_0a = 1$ nm	$e_0a = 2$ nm	$R_m = \frac{w_{e_0a=1nm}^*}{w_{e_0a=0nm}^*}$	$R_m = \frac{w_{e_0a=2nm}^*}{w_{e_0a=0nm}^*}$	
0	0.0335	0.0336	0.0330	1.0029	0.9851	CCCC
1	0.0328	0.0321	0.0289	0.9786	0.8811	
5	0.0302	0.0266	0.0182	0.8808	0.6026	
10	0.0273	0.0216	0.0122	0.7912	0.4469	
0	0.0354	0.0363	0.0377	1.0254	1.0650	SSSS
1	0.0349	0.0360	0.0367	1.0315	1.0516	
2	0.0345	0.0355	0.0347	1.0289	1.0058	
10	0.0302	0.0299	0.0251	0.9900	0.8311	

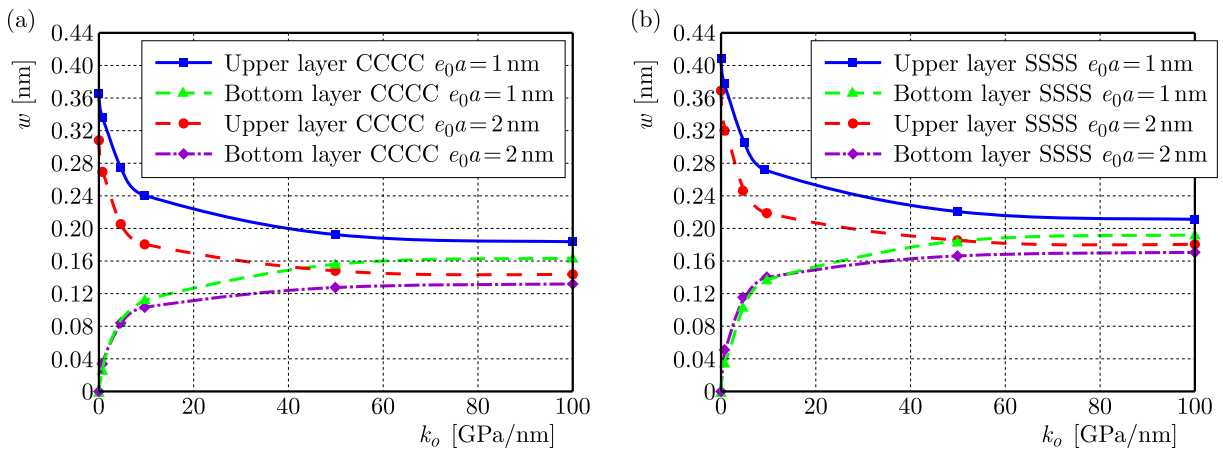


Fig. 3. Variation of deflection versus van der Waals interaction between the layers for (a) CCCC, (b) SSSS boundary conditions

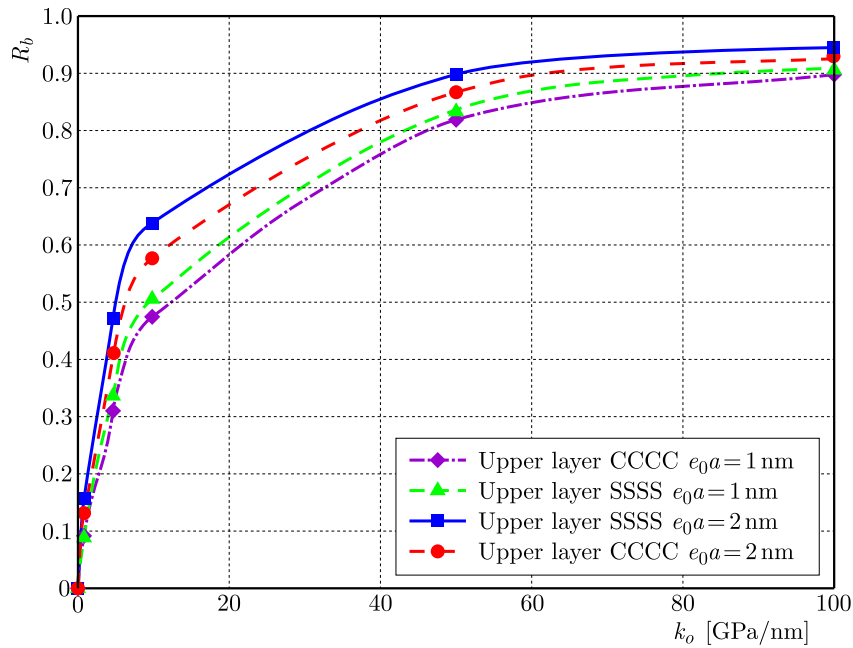


Fig. 4. The effect of van der Waals interaction on the ratio R_b

For better perception, Fig. 4 shows variation of the ratio between the deflections of the bottom layer to the upper layer R_b versus an increase in the van der Waals force. It is clearly observed that at the beginning of rising k_0 , the rate of variations is elevated, and in the following, it decreases. Totally, variations in SSSS boundary conditions are greater than in CCCC boundary conditions. This observation results from Figs. 3a and 3b too. Also, by increasing the nonlocal effects, R_b becomes greater. In one specified k_0 , which in this case is about 10 GPa/nm, R_b has the maximum distance from other ones in four cases of boundary conditions and nonlocal coefficients.

An increase in radius of the nano graphene shell (R) makes curvature lower and the cylindrical shell transforms into a flat rectangular sheet. Figure 5 shows the effects of increasing R on the results. By increasing R , the deflection grows and the rate of variation is high. Continuing, the rate becomes less and remains constant. An infinite value of R means that the cylindrical shell is transformed into a flat rectangular plate. Therefore, by bending the rectangular plate, its deflection subsequently decreases. In SSSS boundary conditions, due to its flexibility, the deflection variations due to R are slow. Also the effect of nonlocal analysis in CCCC boundary conditions is greater than in SSSS boundary conditions. According to Fig. 5, it is observed that when R rises, the value of R_m in CCCC boundary conditions decreases more. In this case, the nonlocal effects on the results are more evident (the specifications of panel are similar to Eq. (6.1), only $L_y = 5$ nm and $\Delta T = 0$).

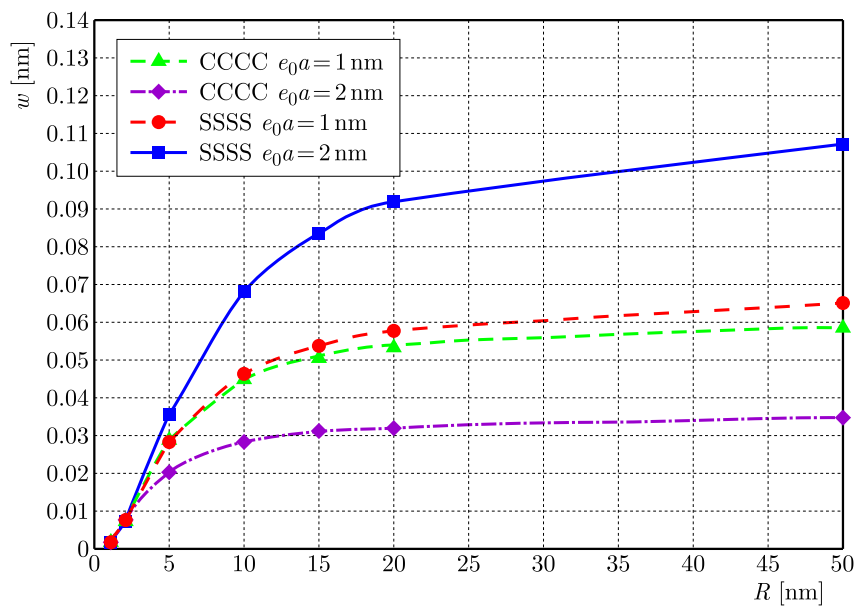


Fig. 5. Deflection due to the increase of radius R of the cylindrical panel

As told before, the nonlocal analysis is more effective in small scales. In this regard, Fig. 6a and 6b are drawn. It is observed that by increasing length of the graphene shell, the deflection increases too, and then, the rate of ascending becomes less and remains fixed at one specified value whose further increase in size has no any considerable impact on the results. It is observed that the increasing length results in smaller nonlocal effects, and the effects become greater by decreasing the size. Increasing the size leads to a rise in the ascending rate of reduction of the nonlocal effect, and this conclusion is clearly obvious for higher values of e_0a . Generally, in small sizes, the nonlocal effects are considerable and nonlocal analysis must be applied. But in larger sizes, the classical theory gives acceptable results by considering a suitable approximation. So, the classical theory is applied for the sizes greater than the nano scale.

Now a nano-tube under internal pressure is studied. This case could be assumed as a shell with radius R whose curvature between both ending edges is 2π in θ direction, so that the

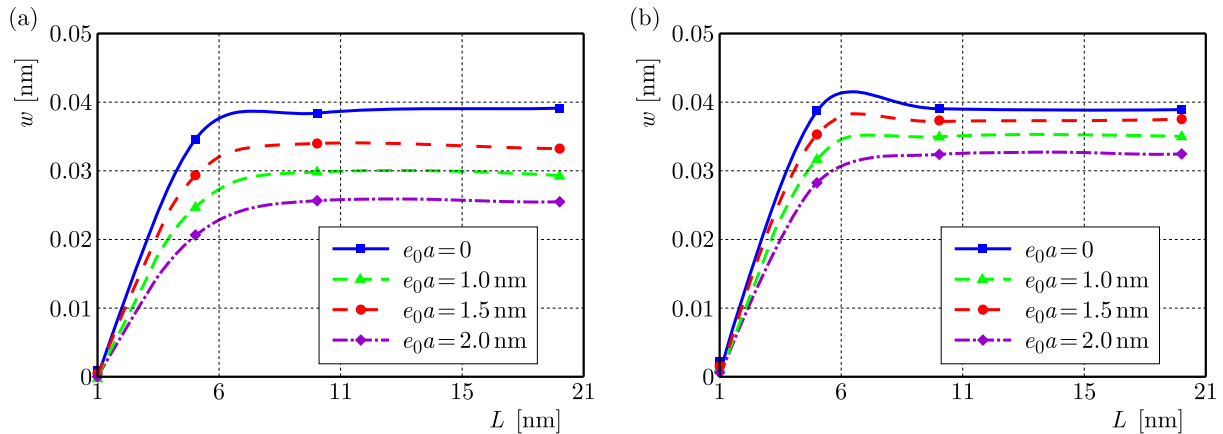


Fig. 6. Variations of deflection versus of the length shell L_x for (a) CCCC, (b) SSSS boundary conditions

edges are connected to each other. Nano-tubes can be used widely. For example, to transfer fluid through nano-tubes, the related mechanical properties must be specified. These nano-tubes can be applied in medical purposes such as nano vessels. In this study, the value of expansion and contraction of a nano graphene tube under internal and external pressure are surveyed. At first, a bi-layer nano-tube is studied, whose layers are connected to each other by van der Waals interaction. The ratio of deflection of the bottom layer to the upper layer is defined as R_b . Now, a bilayer nano-tube is assumed with the specifications given below ($R_b = w_{bottom\ layer}/w_{upper\ layer}$)

$$\begin{aligned}
 L_x &= 15 \text{ nm} & h &= 0.34 \text{ nm} & E_x &= E_y = 1.06 \text{ TPa} \\
 \nu_{xy} &= \nu_{yx} = 0.3 & q &= 0.5 \text{ GPa} & k_w &= 1.13 \text{ GPa/nm} \\
 p &= 1.13 \text{ Pa m} & \Delta T &= 0 & e_0 a &= 1 \text{ nm}
 \end{aligned}
 \tag{6.2}$$

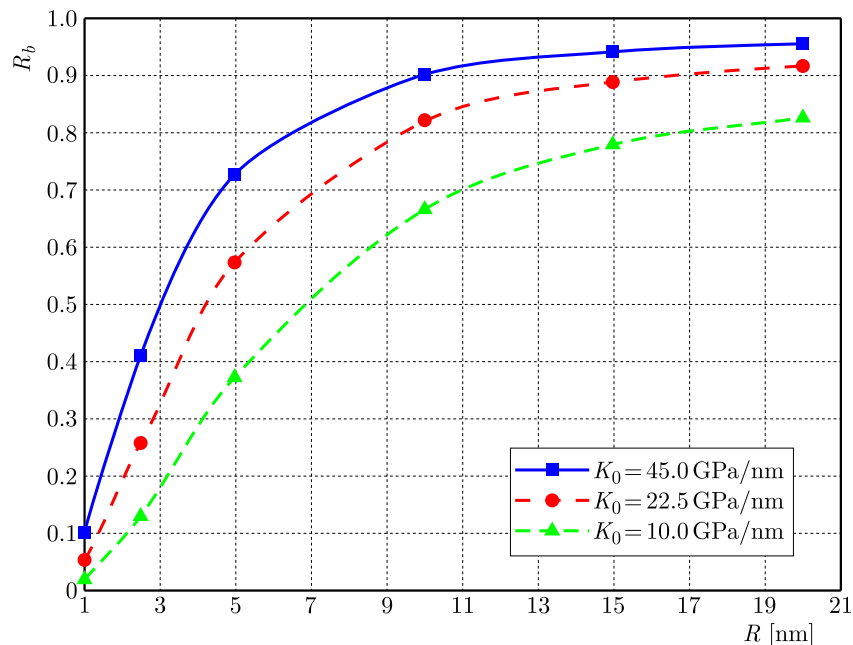


Fig. 7. Variation of nano-tube radius on R_b for different van der Waals interactions

Figure 7 shows the effect of increasing radius of the nano-tube on its expansion R_b for different values of van der Waals forces. It is observed that by increasing the value of R , it leads to an increase in R_b too, and in the following, its raising rate lowers and, finally, an increase

in R , does not have any considerable effect on variation of R_b any longer. The obtained results are similar with the related results for the shell type studied in Fig. 5. As it is expected, an increase in the van der Waals force has direct effect on the deflection of two bottom and upper layers. By increasing the van der Waals force, these deflections approach each other faster.

To reinforce single layer nano-tubes, bilayer nano-tubes can be applied. To survey the effect of being bilayer nano-tubes on the results, Fig. 8 is presented ($R_{bs} = w_{bilayer}/w_{single\ layer}$). Figure 8 shows variation of R_{bs} versus nano-tube radius. As it is observed, by increasing radius R , the deflections of both bilayer and single layer nano-tubes approach each other, but for small values of radius R , the deflection of the bilayer sheet is considerably less than the single layer one. In this case, strength of the bilayer sheet is greater than the single layer one, but for a larger radius, the strength becomes smaller and the deflection of the bilayer sheet approaches the single layer sheet. Therefore, a single layer nano-tube can be used instead of nano-tube with R radius. Figure 8 is very useful for selection a nano-tube based on the single layer or bilayer one. The figure could be drawn for different conditions, and according to the requirements of the problem, the design must be chosen ($k_o = 45\text{ GPa/nm}$)

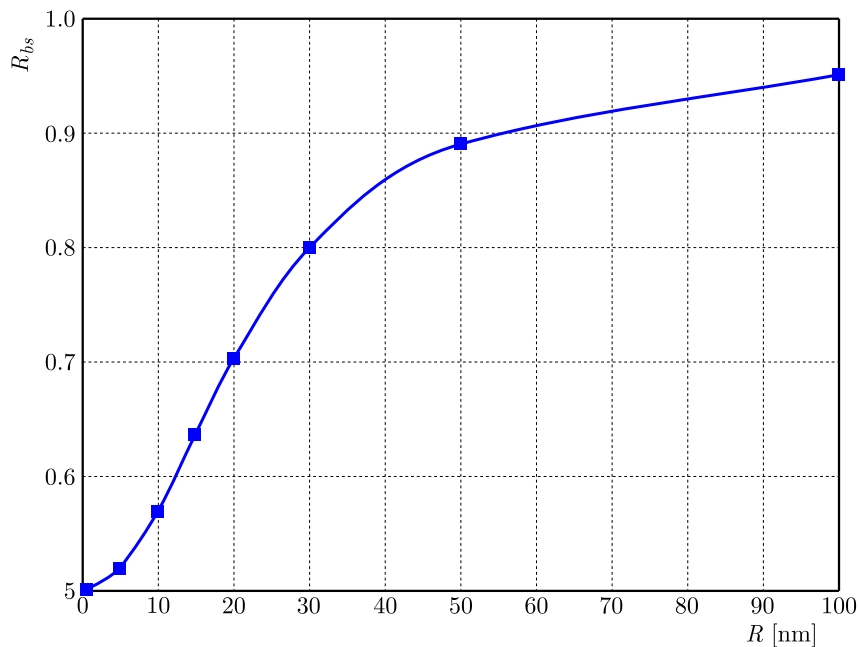


Fig. 8. Single layer to bilayer R_{bs} versus variations of nano-tube radius

7. Conclusions

In this paper, for the first time, the mechanical behavior of a graphene cylindrical panel and nano-tube under internal and external pressure is studied. The system is embedded in an elastic matrix and the effect of thermal conduction has been taken into account too. Remarkable conclusions can be listed as follows:

- An increase in the nonlocal effect results in an increase in van der Waals interaction between the layers.
- The small scale effect decreases along the increase of temperature.
- By increasing nonlocal effects, the deflections of the upper and bottom layers approach each other.
- Whatever radius R of the shell is smaller, the nonlocal decrease effects. So, the maximum nonlocal effects occur for rectangular plates (when radius R tends to infinity).

- An increase in size leads to a rise in the ascending rate of reduction of the nonlocal effect.
- Whatever the radius of nano-tube R rises, the deflection of two layers approach each other.
- The strength of the bilayer nano-tube decreases due to an increase in radius. Consequently, for a high range of radius R , a single layer nano-tube can be applied instead of a bilayer one.

Acknowledgement

I want to dedicate this paper to dr. Jabbarzadeh for his help and my father Reza Dastjerdi who has supported me in every second of my life.

References

1. AGHABABAEI R., REDDY J.N., 2009, Nonlocal third-order shear deformation plate theory with application to bending and vibration of plates, *Journal of Sound and Vibration*, **326**, 277-289
2. ANSARI R., FAGHIH SHOJAEI M., GHOLAMI R., 2016, Size-dependent nonlinear mechanical behavior of third-order shear deformable functionally graded microbeams using the variational differential quadrature method, *Composite Structures*, **136**, 669-683
3. BISAGNI CH., CORDISCO P., 2003, An experimental investigation into the buckling and post-buckling of CFRP shells under combined axial and torsion loading, *Composite Structures*, **60**, 391-402
4. BISWAS P., 2014, Thermal stresses, deformations and vibrations of plates and shells – a nonlinear approach, *Procedia Engineering*, **144**, 1023-1030
5. BRUSH D.O., ALMROTH B.O., 1975, *Buckling of Bars, Plate and Shells*, McGraw hill, New York
6. DASTJERDI SH., ALIABADI SH., JABBARZADEH M., 2016a, Decoupling of constitutive equations for multi-layered nano-plates embedded in elastic matrix based on non-local elasticity theory using first and higher order shear deformation theories, *Journal of Mechanical Science and Technology*, **30**, 1253-1264
7. DASTJERDI SH., JABBARZADEH M., 2016, Nonlinear bending analysis of bilayer orthotropic graphene sheet resting on Winkler-Pasternak elastic foundation based on non-local continuum mechanics, *Composites Part B*, **87**, 161-175
8. DASTJERDI SH., JABBARZADEH M., ALIABADI SH., 2016b, Nonlinear static analysis of single layer annular/circular graphene sheets embedded in Winkler-Pasternak elastic matrix based on non-local theory of Eringen, *Ain Shams Engineering Journal*, **7**, 873-884
9. DASTJERDI SH., LOTFI M., JABBARZADEH M., 2016c, The effect of vacant defect on bending analysis of graphene sheets based on the Mindlin nonlocal elasticity theory, *Composites Part B*, **98**, 78-87
10. DEGENHARDT R., KLING A., BETHGE A., ORF J., KARGER L., ROHWER K., CALVI A., 2010, Rolf Zimmermann Investigations on imperfection sensitivity and deduction of improved knock-down factors for unstiffened CFRP cylindrical shells, *Composite Structures*, **92**, 1939-1946
11. ERINGEN A.C., EDELEN D.G.B., 1972, On nonlocal elasticity, *International Journal of Engineering Science*, **10**, 233-248
12. FAZELZADEH S.A., GHAVANLOO E., 2014, Vibration analysis of curved graphene ribbons based on an elastic shell model, *Mechanics Research Communications*, **56**, 61-68
13. HOFF N.J., TSAI-CHEN S., 1965, Buckling of circular cylindrical shells in axial compression, *International Journal of Mechanical Science*, **7**, 489-520
14. IJIMA S., 1991, Helical microtubules of graphitic carbon, *Nature*, **354**, 56-58

15. KHAZAEINEJAD P., NAJAFIZADE M.M., JENABI J., 2010, On the buckling of functionally graded cylindrical shells under combined external pressure and axial compression, *Journal of Pressure Vessel Technology ASME*, 132-136
16. LANCASTER E.R., CALLADINE C.R., PALMER S.C., 2004, Paradoxical buckling behaviour of a thin cylindrical shell under axial compression, *International Journal of Mechanical Science*, **42**, 843-865
17. LINGHAI J., YONGLIANG W., XINWEI W., 2008, Buckling analysis of stiffened circular cylindrical panels using DQ method, *Thin Walled Structures*, **46**, 390-398
18. MARTEL R., SCHMIDT T., SHEA H.R., HERTEL T., AVOURIS P., 1998, Single and multi-wall carbon nanotube field-effect transistors, *Applied Physics Letter*, **73**, 2447
19. MURMU T., PRADHAN S.C., 2009, Vibration analysis of nano-single-layered graphene sheets embedded in elastic medium based on nonlocal elasticity theory, *Journal of Applied Physics*, **105**, 064319
20. NGUYEN D., HOANG VAN T., 2010, Nonlinear analysis of stability for functionally graded cylindrical panels under axial compression, *Computational Materials Science*, **49**, S313-S316
21. POSTMA H.W.C., TEEPEN T., YAO Z., GRIFONI M., DEKKER C., 2001, Carbon nanotube single-electron transistors at room temperature, *Science*, **293**, 76
22. PRADHAN S.C., 2009, Buckling of single layer graphene sheet based on nonlocal elasticity and higher order shear deformation theory, *Physics Letters A*, **373**, 4182-4188
23. REDDY J.N., PANG S.D., 2008, Nonlocal continuum theories of beams for the analysis of carbon nanotubes, *Journal of Applied Physics*, **103**, 023511
24. TANS S.J., DEVORET M.H., DAI H., THESS A., SMALLEY R.E., GEERLIGS L.J., DEKKER C., 1997, Individual single-wall carbon nanotubes as quantum wires, *Nature*, **386**, 474-477
25. WANG Q., WANG C.M., 2007, The constitutive relation and small scale parameter of nonlocal continuum mechanics for modeling carbon nanotube, *Nanotechnology*, **18**, 1-10
26. ZHANG L.W., ZHANG Y., ZOU G.L., LIEW K.M., 2016, Free vibration analysis of triangular CNT-reinforced composite plates subjected to in-plane stresses using FSDT element-free method, *Composite structures*, **149**, 247-260
27. ZHANG Y., LEI Z.X., ZHANG L.W., LIEW K.M., YU J.L., 2015, Nonlocal continuum model for vibration of single-layered graphene sheets based on the element-free kp-Ritz method, *Engineering Analysis with Boundary Elements*, **56**, 90-97
28. ZHAO X., LIEW K.M., 2009, Geometrically nonlinear analysis of functionally graded shells, *International Journal of Mechanical Science*, **51**, 131-144

Manuscript received August 30, 2016; accepted for print March 21, 2017

MODELING AND SIMULATIONS FOR QUASISTATIC FRICTIONAL CONTACT OF A LINEAR 2D BAR

MIKAEL BARBOTEU, NACERA DJEHAF

Laboratoire de Mathématiques et Physique, University of Perpignan Via Domitia, Perpignan, France
e-mail: barboteu@univ-perp.fr; nacera.djehaf@univ-perp.fr

MEIR SHILLOR

Department of Mathematics and Statistics, Rochester, MI, USA; e-mail: shillor@oakland.edu

MIRCEA SOFONEA

Laboratoire de Mathématiques et Physique, University of Perpignan Via Domitia, Perpignan, France
e-mail: sofonea@univ-perp.fr

This work considers a mathematical model that describes quasistatic evolution of an elastic 2D bar that may come in frictional contact with a deformable foundation. We present the model and some of its underlying assumptions. In particular, the novelty in the model is that both vertical and horizontal motions are taken into account, which makes it especially useful when frictional contact is concerned. Contact is described with the normal compliance condition and friction with the Coulomb law of dry friction. We introduce a hybrid variational formulation of the problem and a numerical discretization based on a uniform time step and the finite element method in space. The numerical algorithm has been implemented, and we present computer simulations that illustrate the mechanical behavior of the system with emphasis on frictional aspects of the problem.

Keywords: new 2D bar, contact, friction, computational results, finite element discretization

1. Introduction

A considerable progress has been achieved in the last two decades in the modeling, mathematical analysis and numerical simulations of various processes involved in the mechanical contact of solids. As a result, Mathematical Theory of Contact Mechanics (MTCM) has been reaching a state of maturity. The theory is concerned with mathematical structures that underly the modeling of general contact processes with different constitutive laws, i.e., different materials, different possible geometries and different contact conditions, see for instance (Eck *et al.*, 2005; Han and Sofonea, 2002; Migórski *et al.*, 2013; Panagiotopoulos, 1993; Shillor *et al.*, 2004; Sofonea and Matei, 2012) and the many references therein. MTCM aims to provide a sound, clear and rigorous framework to construct models for processes involved in contact, and necessary tools and ideas to prove the existence, possible uniqueness and regularity results for the solutions of these models. Moreover, the variational formulation of these models leads directly and naturally to sophisticated numerical methods for computer approximations of the solutions.

The interest in contact problems involving thin structures such as bars, rods, beams and plates lies in the fact that their mathematical analysis is simpler as it avoids some of the complications arising in 3D settings and often provide considerable insight into the possible types of behavior of the solutions, i.e., behavior of such structures. Often, there is decoupling of some of the equations, which simplifies the analysis and computer simulations. Moreover, one may use such models as tests and benchmarks for computer schemes meant for simulations of more complicated multidimensional contact problems. Models, analysis and computer simulations of

various contact problems for rods and beams can be found in (Ahn *et al.*, 2012; Andrews *et al.*, 2012; Kuttler *et al.*, 2001; Shillor *et al.*, 2001) and the references therein. A mathematical model that describes unilateral contact of a beam between two deformable obstacles was studied in (Barboteu *et al.*, 2012b).

In this paper, we introduce a new mathematical model that describes quasistatic frictional contact between a 2D bar and a foundation. The full model derivation and analysis can be found in (Sofonea and Shillor, 2017). We assume that the foundation is deformable and we model the contact with the normal compliance contact condition, and friction is described by the associated Coulomb law. The model is two-dimensional and its main unknowns are vertical and horizontal displacement fields, both defined on an arbitrary section of the bar. We state the variational formulation of the model, which includes a set-inclusion related to the friction condition, then present a numerical approach. Finally, we provide numerical simulations that illustrate the mechanical behavior of the solution of the quasistatic frictional contact model. In particular, we study the behavior of the numerical solution with respect to the stiffness coefficient of the normal compliance law. This study clearly shows that the problem with a unilateral constraint, in which the obstacle is assumed to be completely rigid, may be approached as closely as one wishes by the solution to the contact problem with normal compliance, with a sufficiently large stiffness coefficient.

The rest of paper is structured as follows. In Section 2, we describe our model. Section 3 introduces the variational formulation of the problem, and a fully discrete variational approximation by considering a hybrid formulation. Section 4 describes a special 2D finite rectangular element used in the discretization of the 2D bar. In Section 5, we present numerical results on the contact of the bar with a planar or circular foundation. Finally, in Section 6, we provide a very short summary and mention some further topic for study.

2. The model

We consider an elastic 3D rectangular domain \mathcal{B} identified with a region in \mathbb{R}^3 that is the undeformed reference configuration of the body. We denote by (x, y, z) the coordinates and we assume that \mathcal{B} is sufficiently long in the direction Oz so that the end effects in this direction are negligible. Thus, $\mathcal{B} = (0, L) \times (-h, h) \times (-\infty, +\infty)$. Since \mathcal{B} is a 3D body, which is infinite in the z direction, we refer to \mathcal{B} as a plate, and L and $2h$ represent its length and its thickness, respectively. We denote in what follows by $\Omega = (0, L) \times (-h, h)$ the cross section of the plate and, therefore, $\mathcal{B} = \Omega \times (-\infty, +\infty)$. Moreover, when $h \ll L$ we refer to Ω as a 2D bar, which is the topic of this paper.

Let $\Gamma_D = 0 \times (-h, h)$, $\Gamma_N = (0, L) \times \{h\}$, $\Gamma_F = L \times (-h, h)$ and $\Gamma_C = (0, L) \times \{-h\}$. The plate is clamped on $\Gamma_D \times (-\infty, +\infty)$ so the displacement field vanishes there. It is free on $\Gamma_F \times (-\infty, +\infty)$. On the top, $\Gamma_N \times (-\infty, +\infty)$, it is being acted upon by distributed surface tractions of density \mathbf{p} . On the bottom, $\Gamma_C \times (-\infty, +\infty)$, the plate may come in frictional contact with a foundation or obstacle described by the function $y = \Psi(x)$, which for the sake of simplicity is assumed to be time independent. The physical setting (the cross section of the plate) is depicted in Fig. 1. Contact is described with the normal compliance condition (in the vertical direction) and friction with the Coulomb law of dry friction (in the horizontal direction). It is assumed that the forces and tractions vary sufficiently slowly so that the quasistatic approximation is valid. In addition, for the sake of simplicity, body forces are neglected.

We denote by ν the unit normal vector on the surface of \mathcal{B} and we use the subscripts ν and τ to represent normal and tangential components, respectively, of vectors and tensors. The time interval of interest is $[0, T]$ ($T > 0$) and a dot above a variable represents its partial time derivative. We denote by \mathcal{S}^3 the linear space of the second order symmetric tensors in \mathbb{R}^3 or,

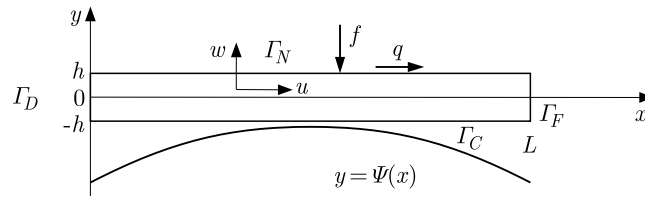


Fig. 1. The setting of the problem; Γ_C is the potential contact surface and Ψ describes the obstacle or foundation

equivalently, the space of symmetric matrices of the order three, while “ \cdot ” and $\|\cdot\|$ represent the inner products and the Euclidean norms on \mathbb{R}^3 and \mathcal{S}^3 .

The mathematical model for the quasistatic evolution of the state of the elastic plate, on the assumptions described above, is the following (Sofonea and Shillor, 2017).

Problem \mathcal{P}_{3D} . Find a displacement field $\mathbf{u} : \Omega \times (-\infty, +\infty) \times (0, T) \rightarrow \mathbb{R}^3$ and a stress field $\boldsymbol{\sigma} : \Omega \times (-\infty, +\infty) \times (0, T) \rightarrow \mathcal{S}^3$ such that:

$$\boldsymbol{\sigma} = \lambda(\operatorname{tr} \boldsymbol{\varepsilon}(\mathbf{u}))\mathbf{I}_3 + 2\delta\boldsymbol{\varepsilon}(\mathbf{u}) \quad \text{in } \Omega \times (-\infty, +\infty) \times (0, T) \quad (2.1)$$

$$\operatorname{Div} \boldsymbol{\sigma} = \mathbf{0} \quad \text{in } \Omega \times (-\infty, +\infty) \times (0, T) \quad (2.2)$$

$$\mathbf{u} = \mathbf{0} \quad \text{on } \Gamma_D \times (-\infty, +\infty) \times (0, T) \quad (2.3)$$

$$\boldsymbol{\sigma}\boldsymbol{\nu} = \mathbf{0} \quad \text{on } \Gamma_F \times (-\infty, +\infty) \times (0, T) \quad (2.4)$$

$$\boldsymbol{\sigma}\boldsymbol{\nu} = \mathbf{p} \quad \text{on } \Gamma_N \times (-\infty, +\infty) \times (0, T) \quad (2.5)$$

$$-\sigma_\nu = \lambda_{nc}(u_\nu - g)_+ \quad \text{on } \Gamma_C \times (-\infty, +\infty) \times (0, T) \quad (2.6)$$

$$\left. \begin{array}{l} \|\boldsymbol{\sigma}_\tau\| \leq \mu|\sigma_\nu| \\ -\boldsymbol{\sigma}_\tau = \mu|\sigma_\nu| \frac{\dot{\mathbf{u}}_\tau}{\|\dot{\mathbf{u}}_\tau\|} \quad \text{if } \dot{\mathbf{u}}_\tau \neq \mathbf{0} \end{array} \right\} \quad \text{on } \Gamma_C \times (-\infty, +\infty) \times (0, T) \quad (2.7)$$

$$\mathbf{u}(0) = \mathbf{u}_0 \quad \text{in } \Omega \times (-\infty, +\infty) \quad (2.8)$$

We turn to a short description of equations and conditions (2.1)-(2.8). First, equation (2.1) represents the linear elastic constitutive law in which λ and δ are the material Lamé coefficients, $\boldsymbol{\varepsilon}(\mathbf{u})$ is the linearized strain tensor associated with the displacement field $\mathbf{u} = (u, w, v)$, $\operatorname{tr} \boldsymbol{\varepsilon}(\mathbf{u})$ denotes its trace and \mathbf{I}_3 represents the identity tensor or matrix in \mathcal{S}^3 . Equation (2.2) represents the balance of the forces. We use it in this simplified version since we assume that the process is quasistatic and we neglect any body forces. Here, $\operatorname{Div} \boldsymbol{\sigma}$ represents divergence of the stress field $\boldsymbol{\sigma}$. Condition (2.3) describes the clamping on Γ_D , and conditions (2.4) and (2.5) represent the traction conditions, described above.

Next, we describe the contact conditions. Equality (2.6) represents the so called *normal compliance* condition in which $g = -h - \Psi$ denotes the gap between the lower surface at $-h$ and the obstacle, measured in the direction of the outward normal, λ_{nc} is the normal compliance stiffness coefficient of the foundation and $r_+ = \max\{0, r\}$. The normal compliance condition was introduced in (Martins and Oden, 1987) and was studied extensively, see, e.g., Han and Sofonea (2002), Klarbring *et al.* (1988, 1989), Shillor *et al.* (2004) and the many references therein, where more general normal compliance conditions can also be found. Condition (2.7) represents Coulomb’s law of dry friction in which μ is the coefficient of friction, assumed to be a positive constant. We refer to references (Eck *et al.*, 2005; Han and Sofonea, 2002; Shillor *et al.*, 2004; Sofonea and Matei, 2012), among the many others for explanation of this condition and related generalizations.

Finally, the problem is quasistatic since Coulomb's condition contains the tangential speed $\|\dot{\mathbf{u}}_\tau\|$, therefore, we need to provide initial condition (2.8), in which \mathbf{u}_0 denotes the given initial displacement.

Next, we follow (Gao, 1998; Gao and Russell, 1994) and introduce additional assumptions that allow us to derive a simplified two-dimensional model associated with Problem \mathcal{P}_{3D} . We assume that

$$\mathbf{p} = [q, f, 0] \quad \text{with} \quad f = f(x, t) \quad \text{and} \quad q = q(x, t) \quad (2.9)$$

In other words, we assume that on the top $y = h$ the plate is subjected to a distributed vertical load f and tangential traction q , which do not depend on z . Also, we assume that the initial displacement is such that

$$\mathbf{u}_0 = [u_0, w_0, 0] \quad \text{with} \quad u_0 = u_0(x, y) \quad \text{and} \quad w_0 = w_0(x) \quad (2.10)$$

Load (2.9) and initial data (2.10), because of the symmetry, cause deformations of the elastic plate with a displacement field \mathbf{u} that is independent of z in the form

$$\mathbf{u} = [u, w, 0] \quad \text{with} \quad u = u(x, y, t) \quad \text{and} \quad w = w(x, t) \quad (2.11)$$

Here, u is the horizontal displacement, w is the vertical one, and the displacement in the z -direction vanishes. We note that w does not depend on y , which is also an interesting part of the model.

It follows that the components of the stress field do not depend on z . Therefore, we are in the situation when both the data and the unknown of this problem do not depend on z . Thus, the simplified problem with symmetry is two-dimensional and can be formulated in the domain Ω as follows

Problem \mathcal{P}_{2D} . *Under assumptions (2.9) and (2.10), find a displacement field $\mathbf{u} = (u, w) : \Omega \times (0, T) \rightarrow \mathbb{R}^2$ and a stress field $\boldsymbol{\sigma} : \Omega \times (0, T) \rightarrow \mathcal{S}^3$ such that (2.1) and (2.2) hold in $\Omega \times (0, T)$, (2.3)-(2.5) hold in $\Gamma_D \times (0, T)$, $\Gamma_F \times (0, T)$ and $\Gamma_N \times (0, T)$, respectively, (2.6) and (2.7) hold in $\Gamma_C \times (0, T)$ and, finally, (2.8) holds in Ω .*

A detailed description of Problem \mathcal{P}_{2D} , together with its variational analysis, including the existence and uniqueness results, can be found in our recent paper (Sofonea and Shillor, 2017). We also refer to Sofonea and Bartosz (2017) where the analysis of a dynamic contact problem for viscoelastic plates was provided. There, the model considered was two-dimensional and was derived from the full three-dimensional problem by using very similar arguments.

3. Variational form and its approximation

In this Section, we present a hybrid variational formulation of Problem \mathcal{P}_{2D} and then its approximation that leads to our algorithm for its numerical solutions. The method is based on a combination of the penalty method for normal compliance condition (2.6) and the augmented Lagrangian method for the numerical treatment of friction conditions (2.7). The Lagrange multiplier is associated with the tangential frictional traction. Then, we present the approximation of the problem by using a uniform discretization of the time interval and the finite element method in the plane. We use arguments similar to those used in Barboteu *et al.* (2012a, 2014, 2016) and, for this reason, we skip many of the details.

3.1. A hybrid variational formulation

To introduce the hybrid variational problem, we need the following function spaces. We note that $u = u(x, y, t)$ is defined on $\overline{\Omega} \times [0, T]$ while $w = w(x, t)$ is defined on $[0, L] \times [0, T]$, which is the peculiarity of our problem, hence we seek the displacement field in the spaces

$$V = \{u \in H^1(\Omega) : u(0, \cdot) = 0\} \quad W = \{w \in H^1(0, L) : w(0) = 0\} \quad X = V \times W$$

These are real Hilbert spaces with inner products defined by

$$\begin{aligned} (u, \psi)_V &= \iint_{\Omega} (uw + u_x\psi_x + u_y\psi_y) \, dx \, dy & \psi &\in V \\ (w, \varphi)_W &= \int_0^L (w\psi + w_x\psi_x) \, dx & w, \varphi &\in W \\ (\mathbf{u}, \mathbf{v})_X &= (u, \psi)_V + (w, \varphi)_W & \mathbf{u} = [u, w], \mathbf{v} = [\psi, \varphi] &\in X \end{aligned}$$

We seek for the stress field in the space

$$Q = \left\{ \boldsymbol{\sigma} = (\sigma_{ij}) : \sigma_{ij} = \sigma_{ji} \in L^2(\Omega) \right\}$$

endowed with its canonical inner product. Also, we consider the function $\mathbf{f} : [0, T] \rightarrow X$ given by

$$(\mathbf{f}(t), \mathbf{v})_X = \int_0^L q(x, t)\psi(x, h) \, dx + \int_0^L f(x, t)\varphi(x) \, dx$$

for all $\mathbf{u} = [u, w], \mathbf{v} = [\psi, \varphi] \in X$ and $t \in [0, T]$. Note that the definition of \mathbf{f} is based on Riesz's representation theorem, under appropriate regularity assumptions on q and f .

To deal with the Lagrange multiplier, we introduce the space $X_\tau = \{\psi(x, -h) : \psi \in V\}$, equipped with its usual norm and denote by X'_τ its dual. Then, we introduce a function $\mathcal{I}_\tau : X_\tau \rightarrow (-\infty, +\infty]$ by

$$\mathcal{I}_\tau(\psi) = \int_0^L |\psi(x, -h)| \, dx \quad \psi \in X_\tau$$

Next, we note that for all $t \in (0, T)$, friction condition (2.7) is equivalent to the subdifferential inclusion

$$-\xi_\tau(t) \in -\mu\lambda_{nc}(-w(t) - g)_+ \partial\mathcal{I}_\tau(\dot{u}(t)) \quad \text{in } X'_\tau \tag{3.1}$$

where $\partial\mathcal{I}_\tau$ denotes the subdifferential of \mathcal{I}_τ in the sense of the convex analysis. Inclusion (3.1) leads us to consider the Lagrange multiplier that is related to the friction traction and is considered as an additional unknown. Then, the hybrid variational formulation of the contact problem \mathcal{P}_{2D} , obtained by multiplying the equations with the relevant test functions and performing integration by parts, is as follows.

Problem \mathcal{P}_{2D}^V . Given $\mathbf{u}_0 \in X$, find a displacement field $\mathbf{u} = [u, w] : [0, T] \rightarrow X$, a stress field $\boldsymbol{\sigma} : [0, T] \rightarrow Q$ and a Lagrange multiplier $\xi_\tau : [0, T] \rightarrow X'_\tau$ such that for all $t \in [0, T]$

$$\boldsymbol{\sigma}(t) = \lambda(\operatorname{tr} \boldsymbol{\varepsilon}(\mathbf{u}(t)))\mathbf{I}_2 + 2\delta\boldsymbol{\varepsilon}(\mathbf{u}(t)) \quad \text{in } \Omega \tag{3.2}$$

$$\iint_{\Omega} \boldsymbol{\sigma}(t) \cdot \boldsymbol{\varepsilon}(\mathbf{v}) \, dx - \int_0^L \lambda_{nc}(-w(t) - g)_+ \varphi \, dx \tag{3.3}$$

$$- \int_0^L \xi_{\tau}(t)\psi(x, -h) \, dx = (\mathbf{f}(t), \mathbf{v})_X \quad \mathbf{v} = [\varphi, \psi] \in X$$

$$-\xi_{\tau}(t) \in -\mu\lambda_{nc}(-w(t) - g)\partial\mathcal{I}_{\tau}(\dot{u}(t)) \quad \text{in } X'_{\nu} \tag{3.4}$$

$$\mathbf{u}(0) = \mathbf{u}_0 \quad \text{in } \Omega \tag{3.5}$$

3.2. Numerical approximation

We turn to the numerical approximation of Problem \mathcal{P}_{2D}^V . We use the finite element method for spatial discretization of the domain Ω by introducing a specific finite rectangle element and a uniform discretization of the time interval $[0, T]$. Since Ω is a rectangular domain, we denote by $\{\mathcal{T}^h\}$ a regular family of rectangular finite element partitions of $\overline{\Omega}$ that are compatible with the boundary decomposition $\Gamma = \overline{\Gamma}_D \cup \overline{\Gamma}_N \cup \overline{\Gamma}_F \cup \overline{\Gamma}_C$. Here and below, h represents the spatial discretization parameter. In the numerical examples presented in the next Section, we approximate the space X by the finite dimensional space of continuous piecewise affine functions, denoted X^h . The space Q is approximated by the finite element space of piecewise constants, denoted Q^h . For the discretization of the Lagrange multiplier ξ_{τ} , we consider a discrete space $Y_{\tau}^h \subset X'_{\tau} \cap L^2(\Gamma_C)$. For the time discretization, we use a collection of discrete times $\{t_n\}_{n=0}^N$ which define a uniform partition of the time interval $[0, T] = \bigcup_{n=1}^N [t_{n-1}, t_n]$ with $t_0 = 0$, $t_n = t_{n-1} + k$ and $t_N = T$, where $N > 0$ is an integer and $k = T/N$ is the time step size. We use the notation $g_j = f(t_j)$, $0 \leq j \leq N$, for a continuous function $g(t)$ with values in a function space. Additional details about the discretization can be found in (Khenous, 2006a,b).

Let $\mathbf{u}_0^h \in X^h$ be a finite element approximation of \mathbf{u}_0 . Then, using the previous notations and an implicit Euler scheme $\delta u_n^h = (u_n^h - u_{n-1}^h)/k$ for the approximation of the time derivative $\dot{u}(x, -h)$, the fully discrete approximation of Problem \mathcal{P}_{2D}^{Vh} at the time t_n is the following.

Problem \mathcal{P}_{2D}^{Vh} . Find a discrete displacement field $\mathbf{u}^{hk} = \{\mathbf{u}_n^{hk}\}_{n=0}^N \subset X^h$, a discrete stress field $\boldsymbol{\sigma}^{hk} = \{\boldsymbol{\sigma}_n^{hk}\}_{n=0}^N \subset Q^h$ and a discrete tangential traction $\xi_{\tau}^{hk} = \{\xi_{\tau_n}^{hk}\}_{n=0}^N \subset Y_{\tau}^h$ such that, for all $n = 1, \dots, N$

$$\boldsymbol{\sigma}_n^{hk} = \lambda(\operatorname{tr} \boldsymbol{\varepsilon}(\mathbf{u}_n^{hk}))\mathbf{I}_2 + 2\delta\boldsymbol{\varepsilon}(\mathbf{u}_n^{hk}) \tag{3.6}$$

$$\iint_{\Omega} \boldsymbol{\sigma}_n^{hk} \cdot \boldsymbol{\varepsilon}(\mathbf{v}^h) \, dx - \int_0^L \lambda_{nc}(-w_n^{hk} - g)_+ \varphi^h \, dx \tag{3.7}$$

$$- \int_0^L \xi_{\tau_n}^{hk}\psi^h(x, -h) \, dx = (\mathbf{f}_n^{hk}, \mathbf{v}^h)_X \quad \forall \mathbf{v}^h = (\varphi^h, \psi^h) \in X^h$$

$$-\xi_{\tau_n}^{hk} \in -\mu\lambda_{nc}(-w_n^{hk} - g)_+\partial\mathcal{I}_{\tau}(\delta u_n^{hk}) \tag{3.8}$$

$$\mathbf{u}_0^{hk} = \mathbf{u}_0^h \tag{3.9}$$

Concerning the numerical solution of hybrid variational Problem \mathcal{P}_{2D}^{Vh} , we have the following comments: The numerical treatment of condition (3.8) is based on a combination of the penalty method for the normal compliance condition, with an augmented Lagrangian method for the

friction condition. Then, the numerical approximation of Problem $\mathcal{P}_{2D}^{V^h}$ leads at each time step to the solution of a system of nonlinear equations. Next, the unknown pair (\mathbf{u}, ξ_τ) of this nonlinear system is computed by using a generalized Newton method which leads, at each iteration, to the solution of a linear non-symmetric system. Details on this method can be found in (Laursen, 2002). Finally, the successive linear non-symmetric systems are solved by using a Conjugate Gradient Squared Method (CGS) with Incomplete LU factorization preconditioners. We note that the contact and friction terms lead to poor conditioning of the non-symmetric system matrix that is overcome by using an element-by-element factorization, see Alart *et al.* (1997) for details.

4. A specific finite rectangular element

In this Section, we focus on the presentation of a 2D finite rectangular element used in the discretization of the 2D linear elastic bar considered in this work. Since the domain Ω is rectangular, we consider finite rectangular elements Ω^e for the spatial discretization of Ω . Due to the fact that the horizontal displacement u depends on x and y , and the vertical displacement w depends only on x , the use of the usual isoparametric formulation is not possible. Therefore, in each element we introduce the following displacement interpolations for $u(x, y)$ and $w(x)$, respectively (see Fig. 2).

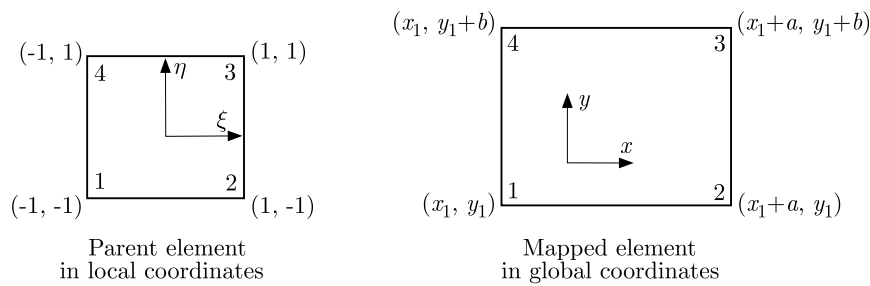


Fig. 2. 2D finite rectangular element

We write

$$u(\xi, \eta) = \mathbf{N}(\xi, \eta)\mathbf{u}^e \quad w(\xi) = \mathbf{M}(\xi)\mathbf{w}^e \tag{4.1}$$

where the shape functions \mathbf{N} and \mathbf{M} are defined in the local coordinate system (ξ, η) by

$$\mathbf{N}(\xi, \eta) = \frac{1}{4} \begin{bmatrix} (1 - \xi)(1 - \eta) \\ (1 + \xi)(1 - \eta) \\ (1 + \xi)(1 + \eta) \\ (1 - \xi)(1 + \eta) \end{bmatrix}^T \quad \mathbf{M}(\xi) = \frac{1}{2} \begin{bmatrix} 1 - \xi \\ 1 + \xi \end{bmatrix}^T \tag{4.2}$$

In (4.1), we use \mathbf{u}^e and \mathbf{w}^e to denote the vectors of displacements at the local nodes of the finite rectangular element, that is

$$\mathbf{u}^e = \begin{bmatrix} u_1 \\ u_2 \\ u_3 \\ u_4 \end{bmatrix} \quad \mathbf{w}^e = \begin{bmatrix} w_1 \\ w_2 \end{bmatrix} = \begin{bmatrix} w_3 \\ w_4 \end{bmatrix} \tag{4.3}$$

We note that in contrast with the displacement interpolations used in the literature, the required mapping from the local coordinate system (ξ, η) to the global coordinate system (x, y)

is based on the same shape function \mathbf{N} , both for x and y . Then, the finite element mapping can be defined by

$$x = \mathbf{N}(\xi, \eta)\mathbf{x}^e \quad y = \mathbf{N}(\xi, \eta)\mathbf{y}^e \quad (4.4)$$

Here, the local vectors \mathbf{x}^e and \mathbf{y}^e contain the value of the local coordinates at the nodes of the rectangle, that is

$$\mathbf{x}^e = [x_1 \quad x_2 \quad x_3 \quad x_4]^T = [x_1 \quad x_1 + a \quad x_1 + a \quad x_1]^T$$

$$\mathbf{y}^e = [y_1 \quad y_2 \quad y_3 \quad y_4]^T = [y_1 \quad y_1 \quad y_1 + b \quad y_1 + b]^T$$

where a and b are real positive numbers that represent the width and height of the rectangle, respectively.

Based on (4.1) and (4.4), we construct in what follows the element stiffness matrix \mathbf{K}^e arising from the elementary discretization of the first term in (3.3). To this end, we consider a special finite rectangular element oriented with its sides parallel to the x, y axes. Then, the Jacobian mapping matrix \mathbf{J} is defined by

$$\mathbf{J}(\xi, \eta) = \begin{bmatrix} \frac{\partial x}{\partial \xi} & \frac{\partial y}{\partial \xi} \\ \frac{\partial x}{\partial \eta} & \frac{\partial y}{\partial \eta} \end{bmatrix} = \begin{bmatrix} \frac{\partial N_1}{\partial \xi} & \frac{\partial N_2}{\partial \xi} & \frac{\partial N_3}{\partial \xi} & \frac{\partial N_4}{\partial \xi} \\ \frac{\partial N_1}{\partial \eta} & \frac{\partial N_2}{\partial \eta} & \frac{\partial N_3}{\partial \eta} & \frac{\partial N_4}{\partial \eta} \end{bmatrix} \begin{bmatrix} x_1 & y_1 \\ x_2 & y_2 \\ x_3 & y_3 \\ x_4 & y_4 \end{bmatrix}$$

In our special case, by using the shape function N given in (4.2), we obtain

$$\mathbf{J}(\xi, \eta) = \frac{1}{4} \begin{bmatrix} -1 + \eta & 1 - \eta & 1 + \eta & -1 - \eta \\ -1 + \xi & -1 - \xi & 1 + \xi & 1 - \xi \end{bmatrix} \begin{bmatrix} x_1 & y_1 \\ x_1 + a & y_1 \\ x_1 + a & y_1 + b \\ x_1 & y_1 + b \end{bmatrix}$$

As is customary in the finite element method, we use a vectorial notation for the components of both the strain tensor $\boldsymbol{\varepsilon}$ and the stress tensor $\boldsymbol{\sigma}$, i.e.

$$\boldsymbol{\varepsilon} = \begin{bmatrix} \varepsilon_{xx} \\ \varepsilon_{yy} \\ 2\varepsilon_{xy} \end{bmatrix} = \begin{bmatrix} u_x \\ w_y \\ u_y + w_x \end{bmatrix} = \begin{bmatrix} \frac{\partial}{\partial x} & 0 \\ 0 & \frac{\partial}{\partial y} \\ \frac{\partial}{\partial y} & \frac{\partial}{\partial x} \end{bmatrix} \begin{bmatrix} u(x, y) \\ w(x) \end{bmatrix} \quad (4.5)$$

and

$$\boldsymbol{\sigma} = \begin{bmatrix} \sigma_{xx} \\ \sigma_{yy} \\ 2\sigma_{xy} \end{bmatrix} = \mathbf{E}\boldsymbol{\varepsilon} \quad (4.6)$$

Here, the matrix \mathbf{E} takes into account the linear elastic constitutive behavior given in (3.2) and is defined by

$$\mathbf{E} = \begin{bmatrix} \lambda + 2\delta & \lambda & 0 \\ \lambda & \lambda + 2\delta & 0 \\ 0 & 0 & \delta \end{bmatrix} = \begin{bmatrix} E_1 & E_2 & 0 \\ E_2 & E_3 & 0 \\ 0 & 0 & E_6 \end{bmatrix}$$

Using (4.1) and (4.2), equalities (4.5) and (4.6) yield

$$\boldsymbol{\varepsilon} = \mathbf{B}(\xi, \eta) \cdot \mathbf{d}^e \quad \boldsymbol{\sigma} = \mathbf{EB}(\xi, \eta) \cdot \mathbf{d}^e \quad (4.7)$$

where $\mathbf{d}^e = [u^e, w^e]^T$ is the vector of nodal variables and $\mathbf{B}(\xi, \eta)$ is the deformation strain-displacement matrix given by

$$\mathbf{B}(\xi, \eta) = \begin{bmatrix} \frac{\partial N_1}{\partial x} & \frac{\partial N_2}{\partial x} & \frac{\partial N_3}{\partial x} & \frac{\partial N_4}{\partial x} & 0 & 0 \\ 0 & 0 & 0 & 0 & 0 & 0 \\ \frac{\partial N_1}{\partial y} & \frac{\partial N_2}{\partial y} & \frac{\partial N_3}{\partial y} & \frac{\partial N_4}{\partial y} & \frac{\partial M_1}{\partial x} & \frac{\partial M_2}{\partial x} \end{bmatrix} \quad (4.8)$$

It follows from forms (4.2) of the shape functions \mathbf{N} and \mathbf{M} that

$$\mathbf{B}(\xi, \eta) = \begin{bmatrix} -\frac{1}{2a}(1-\eta) & \frac{1}{2a}(1-\eta) & \frac{1}{2a}(1+\eta) & -\frac{1}{2a}(1+\eta) & 0 & 0 \\ 0 & 0 & 0 & 0 & 0 & 0 \\ -\frac{1}{2b}(1-\xi) & -\frac{1}{2b}(1+\xi) & \frac{1}{2b}(1+\xi) & \frac{1}{2b}(1-\xi) & -\frac{1}{a} & \frac{1}{a} \end{bmatrix}$$

Using now (4.7), the element stiffness matrix \mathbf{K}^e of our 2D linear elastic bar can be written as

$$\mathbf{K}^e = \int_{\Omega^e} \mathbf{B}^T \mathbf{EB} \, d\Omega = \sum_{i=1}^4 \frac{1}{4} [\mathbf{B}(\xi_i, \eta_i)]^T \mathbf{E} [\mathbf{B}(\xi_i, \eta_i)] |J| \omega_i.$$

Then, after some algebra, we derive the following element stiffness matrix

$$\mathbf{K}^e = \frac{ab}{16} \begin{bmatrix} 2\left(\frac{E_1}{a^2} + \frac{E_6}{b^2}\right) & -2\frac{E_1}{a^2} & 0 & -2\frac{E_6}{b^2} & 2\frac{E_6}{ab} & -2\frac{E_6}{ab} \\ -2\frac{E_1}{a^2} & 2\left(\frac{E_1}{a^2} + \frac{E_6}{b^2}\right) & -2\frac{E_6}{b^2} & 0 & 2\frac{E_6}{ab} & -2\frac{E_6}{ab} \\ 0 & -2\frac{E_6}{b^2} & 2\left(\frac{E_1}{a^2} + \frac{E_6}{b^2}\right) & -2\frac{E_1}{a^2} & -2\frac{E_6}{ab} & 2\frac{E_6}{ab} \\ -2\frac{E_6}{b^2} & 0 & -2\frac{E_1}{a^2} & 2\left(\frac{E_1}{a^2} + \frac{E_6}{b^2}\right) & -2\frac{E_6}{ab} & 2\frac{E_6}{ab} \\ 2\frac{E_6}{ab} & 2\frac{E_6}{ab} & -2\frac{E_6}{ab} & -2\frac{E_6}{ab} & -4\frac{E_6}{a^2} & 4\frac{E_6}{a^2} \\ -2\frac{E_6}{ab} & -2\frac{E_6}{ab} & 2\frac{E_6}{ab} & 2\frac{E_6}{ab} & -4\frac{E_6}{a^2} & 4\frac{E_6}{a^2} \end{bmatrix} \quad (4.9)$$

This form, (4.9), of the element stiffness matrix is the starting point in the construction of the global stiffness matrix of the system to be solved.

5. Numerical simulations

The method described in the previous Section has been implemented and a number of computer solutions for the contact problem obtained. Here, we present numerical simulations of two settings in which the foundation is either planar or curved. In the first case, the foundation is defined by the function $\Psi(x) = -0.1$. In the second case, it is a circular arc lying on the circle defined by the function $y = \Psi(x)$ that is given by $(x - 0.5)^2 + (y + 1)^2 = 0.9^2$.

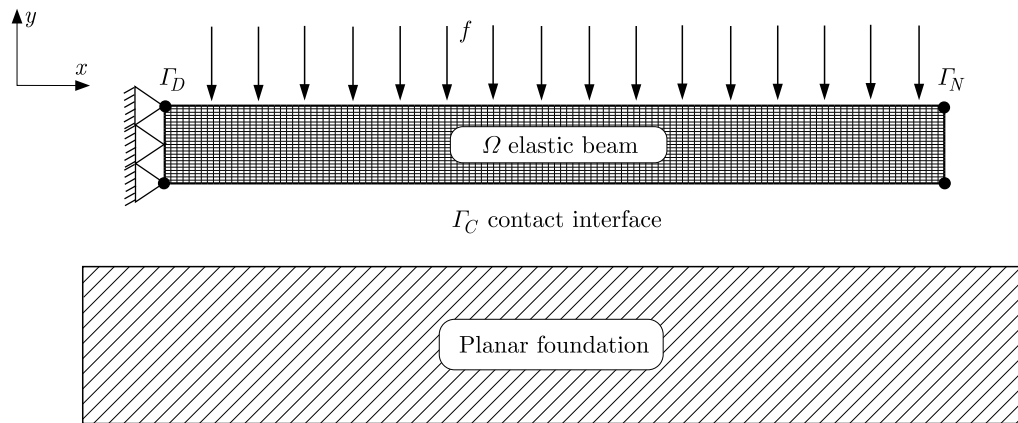


Fig. 3. The bar in potential contact with a planar obstacle

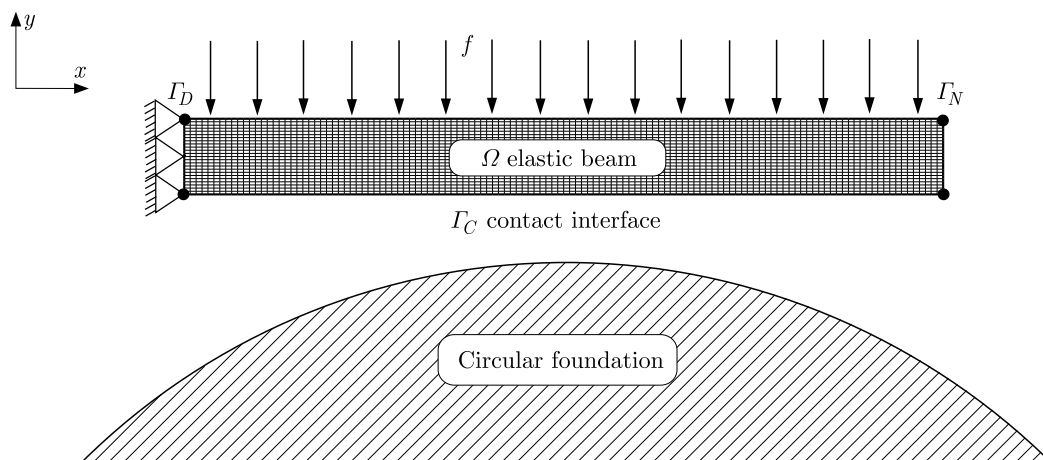


Fig. 4. The bar in potential contact with a circular obstacle

The physical settings of these two configurations are depicted in Figs. 3 and 4. We pay particular attention to the mechanical aspects of the frictional contact conditions (2.6) and (2.7) and we provide a study of the dependence of the numerical solution with respect to the stiffness coefficient of the normal compliance law.

In the computations, we use a rectangular mesh composed of a uniform partition of finite rectangular elements introduced in the previous Section. The spatial discretization parameters in both the x and y directions are $h_x = 1/128$ and $h_y = 1/240$, respectively. The rest of the data are the following: $L = 1$ m, $h = 0.05$ m, $E = 1000$ N/m², $G = 0.3$, $T = 1.1$ s, $N = 11$, $k = 0.1$ s, $\mathbf{f} = [0, -20]$ N/m² on Γ_N , $\mu = 0.4$ (friction) and $\mu = 0$ (frictionless), $\mathbf{u}_0 = [0, 0]$ m in Ω .

Our numerical simulations are presented in Figs. 5-10 below in which the deformed configuration of the bar, at the end of the time interval, is depicted. The arrows in the figures that originate on the contact surface represent the frictional contact interface tractions exerted by the bar on the foundation. Moreover, for the simulations presented in Figs. 5-8, we use $\lambda_{nc} = 100$ N/m². A detailed description of our numerical results is the following.

We observe in Fig. 5 that in the case of a planar obstacle, the contact takes place on a large fraction of the contact nodes on the contacting surface $y = -h$ and so the interface tractions are nonzero there. Here, we chose the friction coefficient to be $\mu = 0.4$, which is rather large, to make the effects more noticeable. Moreover, it is seen that the nodes that are on the right side of the contact region are in a *stick* state, a state in which $\dot{\mathbf{u}} = 0$. The other nodes that are in active contact are in a *slip* state. This is a state in which $\dot{\mathbf{u}} \neq 0$ and the friction bound has been reached by the friction traction. In the frictionless case, depicted in Fig. 6, when $\mu = 0$, we note

that the contact forces are vertical and all the nodes that are in active contact are in the slip state (since the friction bound vanishes).

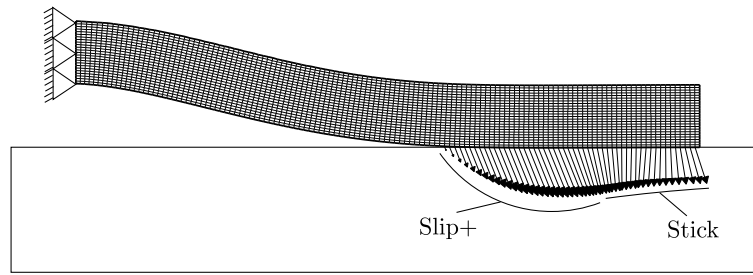


Fig. 5. Deformed mesh and interface tractions in the frictional case, $\mu = 0.4$

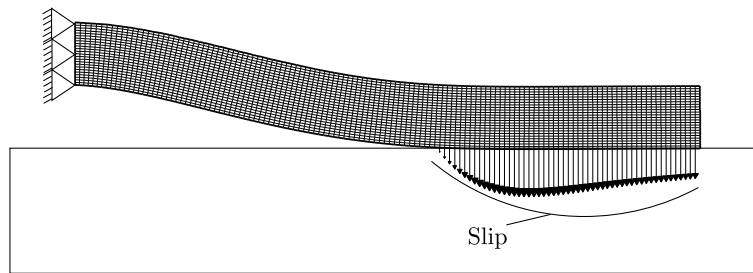


Fig. 6. Deformed mesh and interface tractions in the frictionless case, $\mu = 0$

We turn to describe the second case of contact with a circular obstacle, see Fig. 7. In contrast to the first case, here active contact arises in fewer nodes on the contact boundary and the rest of the boundary is in state of separation where the interface tractions vanish. We note that most of the nodes in contact are in the slip state, and only a few nodes are in the stick state. In the frictionless case, Fig. 8, all the contact nodes are in the slip state and the contact tractions are oriented in the normal direction of the foundation.

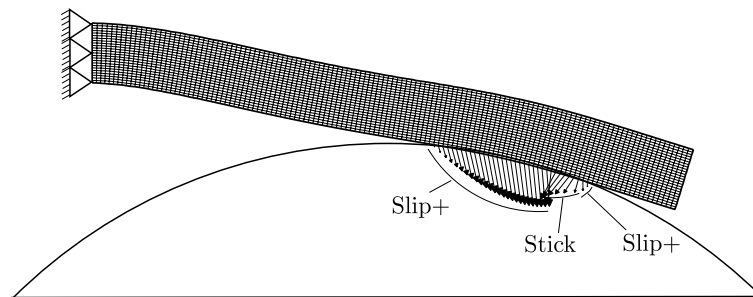


Fig. 7. Deformed mesh and interface tractions in the case with friction

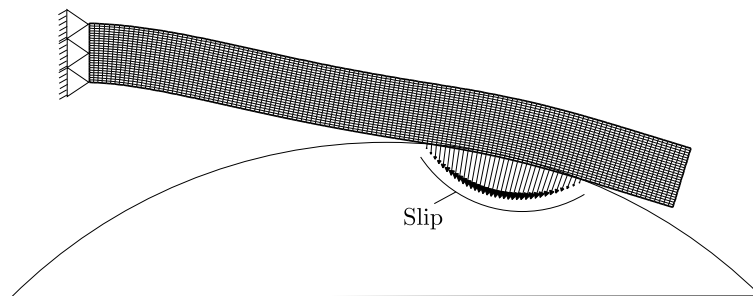


Fig. 8. Deformed mesh and interface tractions in the frictionless case

We next describe our numerical experiments concerning the normal compliance stiffness coefficient λ_{nc} , since we expect the solutions to the problem with the normal compliance condition to converge, as $\lambda_{nc} \rightarrow \infty$, to the solutions of the problem with the Signorini nonpenetration contact condition. The latter describes a perfectly rigid foundation. We present results obtained in the case of the planar obstacle in Fig. 9, for four different values of λ_{nc} . We plot the deformed configurations as well as the frictional contact interface tractions for $\lambda_{nc} = 1 \text{ N/m}^2$, 10 N/m^2 , 100 N/m^2 and $\lambda_{nc} = 1000 \text{ N/m}^2$. We note that for $\lambda_{nc} = 1 \text{ N/m}^2$, a large proportion of the contact nodes are in relatively large penetration into the foundation since, in this case, the foundation is soft and so easily deformable. As the stiffness coefficient λ_{nc} becomes larger, the penetration of the bar into the foundation decreases. For $\lambda_{nc} = 1000 \text{ N/m}^2$, we observe that the penetration is negligible. This behavior of the numerical solution shows that for a large stiffness coefficient λ_{nc} , the foundation behaves like a rigid one, and shows that we may use the normal compliance as an approximation for very stiff foundations.

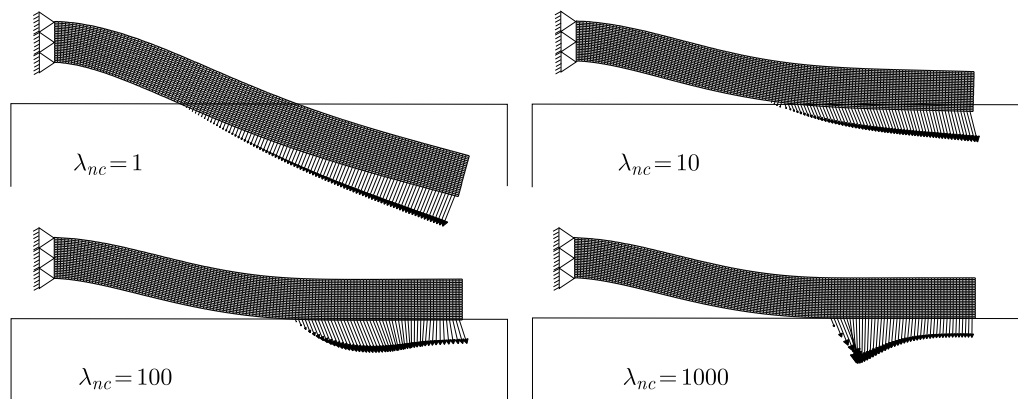


Fig. 9. Deformed mesh and interface tractions for various values of λ_{nc}

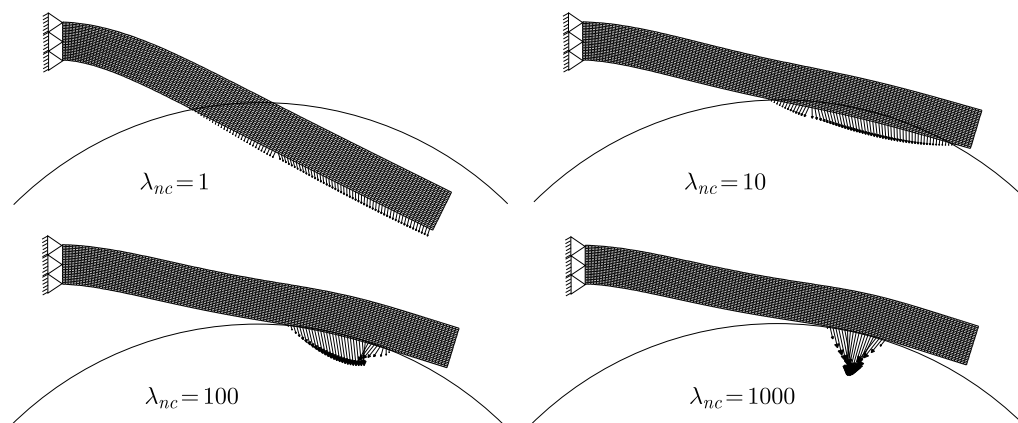


Fig. 10. Deformed mesh and interface tractions for various values of λ_{nc}

Finally, in Fig. 10, we present similar results for the case of the circular obstacle. These results provide the same conclusion: the contact problem with unilateral constraint may be approached by a contact problem with normal compliance, with a sufficiently large stiffness coefficient. Our numerical results are summarized in Table 1.

Table 1

	$\lambda_{nc} = 1$	$\lambda_{nc} = 10$	$\lambda_{nc} = 100$	$\lambda_{nc} = 1000$	$\lambda_{nc} = 10000$
max. penetration (planar obstacle)	0.242322	0.0285327	0.003274	0.000418	0.000438
max. penetration (circular obstacle)	0.188659	0.032852	0.005161	0.000984	0.000101

6. Conclusions and comments

This work presents a two-dimensional model for a long thin bar. It is simpler than a 2D model of an elastic long object in which the vertical displacement depends only on x . This makes the model easier to analyze and computationally simulate. The numerical simulations show that the model is especially useful in dealing with frictional contact.

The extension of the model to include dynamic effects is straightforward. It may be of interest to extend the model and set it as an optimal control problem by introducing the traction on the top surface as the control. Finally, more numerical simulations with different friction coefficients may be of interest (see, e.g., Barboteu *et al.*, 2012b; Gao and Russell, 1994).

References

- ALART P., BARBOTEU B., LEBON F., 1997, Solutions of frictional contact problems using an *EBE* preconditioner, *Computational Mechanics*, **30**, 370-379
- AHN J., KUTTLER K.L., SHILLOR M., 2012, Dynamic contact of two Gao beams, *Electronic Journal of Differential Equation*, **194**, 1-42
- ANDREWS K.T., DUMONT Y., M'BENGUE M.F., PURCELL J., SHILLOR M., 2012, Analysis and simulations of a nonlinear dynamic beam, *Journal of Applied Mathematics and Physics*, **63**, 1005-1019
- BARBOTEU M., BARTOSZ K., KALITA P., RAMADAN A., 2014, Analysis of a contact problem with normal compliance, finite penetration and nonmonotone slip dependent friction, *Communications in Contemporary Mathematics*, **16**, 1, DOI 10.1142/S0219199713500168
- BARBOTEU M., CHENG X.-L., SOFONEA M., 2016, Analysis of a contact problem with unilateral constraint and slip-dependent friction, *Mathematics and Mechanics of Solids*, **21**, 791-811
- BARBOTEU M., MATEI A., SOFONEA, M., 2012a, Analysis of quasistatic viscoplastic contact problems with normal compliance, *Quarterly Journal of Mechanics and Applied Mathematics*, **65**, 555-579
- BARBOTEU M., SOFONEA M., TIBA D., 2012b, The control variational method for beams in contact with deformable obstacles, *Zeitschrift für Angewandte Mathematik und Mechanik*, **92**, 25-40
- ECK C., JARUŠEK J., KRBEČ M., 2005, *Unilateral Contact Problems: Variational Methods and Existence Theorems*, Pure and Applied Mathematics, **270**, Chapman/CRC Press, New York
- GAO D.Y., 1998, Bi-complementarity and duality: A framework in nonlinear equilibria with applications to the contact problems of elastoplastic beam theory, *Journal of Mathematical Analysis and Applications*, **221**, 672-697
- GAO D.Y., RUSSELL D.L., 1994, A finite element approach to optimal control of a 'smart' beam, [In:] *International Conference of Computational Methods in Structural and Geotechnical Engineering*, P.K.K. Lee, L.G. Tham and Y.K. Cheung (Edit.), Hong Kong, 135-140

11. HAN W., SOFONEA M., 2002, *Quasistatic Contact Problems in Viscoelasticity and Viscoplasticity*, Studies in Advanced Mathematics, **30**, American Mathematical Society, Providence, RI, International Press, Somerville, MA
12. KHENOUS H.B., LABORDE P., RENARD Y., 2006a, On the discretization of contact problems in elastodynamics, *Lecture Notes in Applied and Computational Mechanics*, **27**, 31-38
13. KHENOUS H.B., POMMIER J., RENARD Y., 2006, Hybrid discretization of the Signorini problem with Coulomb friction. Theoretical aspects and comparison of some numerical solvers, *Applied Numerical Mathematics*, **56**, 163-192
14. KUTTLER K.L., PARK A., SHILLOR M., ZHANG W., 2001, Unilateral dynamic contact of two beams, *Mathematical and Computer Modelling*, **34**, 365-384
15. KUTTLER K.L., PURCELL J., SHILLOR M., 2012, Analysis and simulations of a contact problem for a nonlinear dynamic beam with a crack, *Quarterly Journal of Mechanics and Applied Mathematics*, **65**, 1-25
16. KLARBRING A., MIKELIC A., SHILLOR M., 1988, Frictional contact problems with normal compliance, *International Journal of Engineering Science*, **26**, 811-832
17. KLARBRING A., MIKELIC A., SHILLOR M., 1989, On friction problems with normal compliance, *Nonlinear Analysis*, **13**, 935-955
18. LAURSEN T., 2002, *Computational Contact and Impact Mechanics*, Springer, Berlin
19. MARTINS J.A.C., ODEN J.T., 1987, Existence and uniqueness results for dynamic contact problems with nonlinear normal and friction interface laws, *Nonlinear Analysis TMA*, **11**, 407-428
20. MIGÓRSKI S., OCHAL A., SOFONEA M., 2013, *Nonlinear Inclusions and Hemivariational Inequalities. Models and Analysis of Contact Problems*, Advances in Mechanics and Mathematics, **26**, Springer, New York
21. PANAGIOTOPOULOS P.D., 1993, *Hemivariational Inequalities, Applications in Mechanics and Engineering*, Springer-Verlag, Berlin
22. SHILLOR M., SOFONEA M., TELEGA J.J., 2004, *Models and Analysis of Quasistatic Contact*, Lecture Notes in Physics, **655**, Springer, Berlin
23. SHILLOR M., SOFONEA M., TOUZANI R., 2001, Quasistatic frictional contact and wear of a beam, *Dynamics of Continuous, Discrete and Impulsive Systems*, **8**, 201-218
24. SOFONEA M., BARTOSZ K., 2017, A Dynamic contact model for viscoelastic plates, *Quarterly Journal of Mechanics and Applied Mathematics*, **70**, 1, 1-19, DOI:10.1093/qjmam/hbw013
25. SOFONEA M., MATEI A., 2012, *Mathematical Models in Contact Mechanics*, London Mathematical Society Lecture Note Series, **398**, Cambridge University Press, Cambridge
26. SOFONEA M., SHILLOR M., 2017, Modelling and analysis of a frictional contact problem for elastic bars, submitted to *Electronic Journal of Differential Equations*

Manuscript received January 16, 2017; accepted for print March 31, 2017

THERMAL MODELLING, SIMULATION AND EXPERIMENTAL VALIDATION OF HEAT ACCUMULATION IN A FRAMED GLASS CABIN

TARUN K. BERA, SUSHANK DIXIT

Mechanical Engineering Department, Thapar University, Patiala, India
e-mail: tarunkumarbera@gmail.com

ANIRBAN BHATTACHARYA

Mechanical Engineering Department, Indian Institute of Technology (IIT) Patna, India

DEVENDER KUMAR

Mechanical Engineering Department, Thapar University, Patiala, India

ARUN K. SAMANTARAY

Mechanical Engineering Department, Indian Institute of Technology (IIT) Kharagpur, India

The present work concerns prediction of the amount of heat accumulation within the interior of a framed glass cabin and proposes some remedial measures to reduce temperature in the cabin. Various configurations such as double layer glass box filled with static air, static argon gas and flowing argon gas within the space between the two glass-layers are considered to conduct the experiments. Multi-physics bond graph models for these configurations are developed considering thermo-fluidic aspects. The experimental results are compared with the simulations using bond graph models. Though, direct application to a vehicle is not made, without loss of generality, the modelling and experimental procedure can be extended to analyze the heat accumulation inside a vehicle cabin when the vehicle is parked under direct sunlight.

Keywords: car cabin, experimental thermal analysis, bond graph modelling, double layer glass window

1. Introduction

During summer season, the environmental temperature generally varies between 40°C-50°C in southern Asia. The interior of a vehicle heats up significantly when parked in an open environment under direct sunlight in such conditions. As the heat wave passes through the glass, the wavelength of the electromagnetic wave increases, and higher wavelength electromagnetic waves cannot escape outside the car compartment. Thus, the heat entrapment expedites interior temperature of the car by nearly 20°C to 30°C above the surrounding atmosphere (Dadour *et al.*, 2011).

As a solution to the problems, vanadium dioxide coating for window glasses has been proposed (Chen *et al.*, 2012). This multilayer coating structure is transparent to visible light and is opaque to infrared light at high temperature. A mathematical study was done in (Xamána *et al.*, 2014) on two layer windows with a solar control film. It was shown therein that the use of the solar control film along with the double pane window reduces the heat flow from inside to outside by up to 52%. Transmittance of solar radiation through the glazed window can be reduced by using two glass panes without any air space between these panes (Mazzoni, 1977). The effect of solar radiation over the air flow and temperature distribution in the compartment of a car was studied (Lee *et al.*, 2014). The thermal modelling of the car cabin and controlling the temperature by means of a fuzzy logic controller were developed in (Sanaye *et al.*, 2012).

A comprehensive review of different models developed to predict thermal comfort of vehicular cabins in addition to different experimental techniques was provided in (Alahmer *et al.*, 2011). In (Al-Kayiem *et al.*, 2010), experiments were performed by parking a salon car in direct sunlight and in an un-shaded area. Temperatures at 12 different locations were measured and then those values were used in 3-D CFD simulation performed with FLUENT software.

The bond graph is a multi-energy domain modelling tool (Merzouki *et al.*, 2012). It was used therein to model the heat transfer from the external environment to the inside of a building. Many authors have worked on the bond graph modelling of thermo-fluidic systems: general modelling framework development, thermo-fluid library for process engineering systems (Samantharay *et al.*, 2004), multi-phase systems (Brown, 2002) and applications to steam generators (Ould Bouamama *et al.*, 2006).

The usual control of cabin temperature is based on the feed-back principle. However, when a vehicle moves from a shaded zone to a sunny area or vice-versa, the feed-back control is usually too slow to timely react due to the inherently slow dynamics of thermal systems. Therefore, it is preferable to use feed-forward control strategies with estimation of the cabin temperature change profile based on environmental temperature, air-conditioning load (number of passengers and interior furniture), and exposure to sunlight and its intensity. It is further useful to combine both feedback and feed-forward controls in a cascaded loop. However, such control laws require a well-developed and validated thermal model of the system. In the present work, bond graph models for such systems are developed and validated through experiments. The bond graph model of a double layer toughened glass with air (stagnant) and argon (stagnant and flowing) in between the two glasses is developed and experimentally validated.

2. Thermal model of the system through the bond graph method

A wooden frame structure with toughened glass windows each having a dimension of $548\text{ mm} \times 310\text{ mm} \times 5\text{ mm}$ is constructed (shown in Fig. 1a) and exposed to direct sunlight for experimentations. This assembly of wooden frame and the glass is assumed to be equivalent to the internal compartment of a car. The glass is properly sealed with sealant (clay based) so that no air can escape from the assembly. The frame is insulated with expanded polystyrene sheets at the top and the bottom panels so that no heat or little heat could escape from those sides.

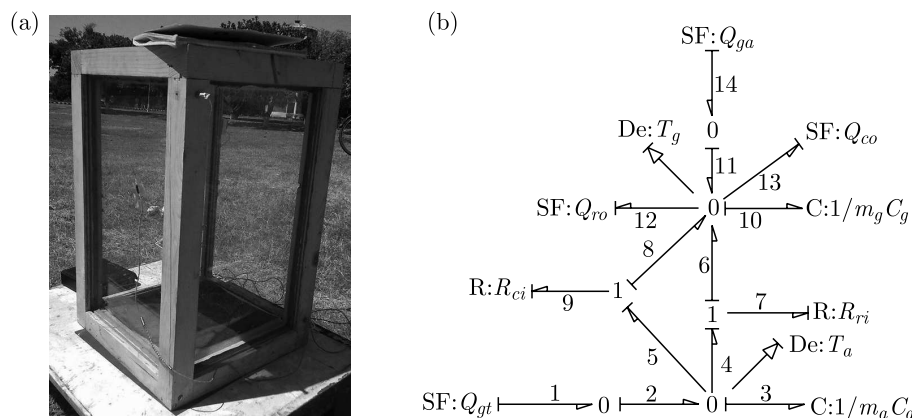


Fig. 1. (a) Cabin with single glass windows and (b) its bond graph model

2.1. Thermal modelling of the cabin system with single layer glass panel windows

The system made of single glass windows is modelled with the help of the bond graph so that the results can be validated experimentally. The bond graph model of the system is given in

Fig. 1b. Note that the pseudo-bond graph formalism is adopted here for simplicity of formulation without unnecessarily bringing entropy into the picture.

The heat flux on the glass surface is absorbed, reflected or transmitted. An effort sensor or detector (De) measures the temperature T_g of the glass. The stiffness $K10$ of the $C10$ element is given by

$$K10 = \frac{1}{m_g C_g} \quad (2.1)$$

where m_g and C_g are mass and specific heat of the glass panel, respectively.

As shown in Fig. 1b, SF14 represents the amount of heat absorbed by the glass surface Q_{ga} , and this is given by

$$Q_{ga} = I_r A_g a_g \quad (2.2)$$

where I_r , A_g and a_g are the irradiance, area and absorptivity of glass, respectively. The amount of heat radiated by the glass surface into the surroundings Q_{ro} is modelled by SF12 element, and is given by

$$Q_{ro} = e_g \sigma A_g (T_g^4 - T_s^4) \quad (2.3)$$

where e_g , σ , T_g and T_s are the emissivity of glass, Stefan-Boltzmann constant, glass temperature and space temperature, respectively.

Some of the heat from the glass surface is taken away by the surrounding air through convection. Q_{co} is the heat flow by convection into the surroundings (modelled by SF13 in Fig. 1b), and is given by

$$Q_{co} = h_{ao} A_g (T_g - T_{ao}) \quad (2.4)$$

where h_{ao} and T_{ao} are the convective heat transfer coefficient of the outside air and atmospheric temperature, respectively. R_{ci} (modelled as R9 in the bond graph model) is the convective thermal resistance to the heat transfer between the inside air and the inner surface of the glass. The general heat transfer equation can be written as

$$Q_{ci} = Ah_{ai} \Delta T \quad Q_{ci} = \frac{\Delta T}{R_{ci}} \quad (2.5)$$

Thus, the convective thermal resistance R_{ci} is given by

$$R_{ci} = \frac{1}{Ah_{ai}} \quad (2.6)$$

where h_{ai} is the convective heat transfer coefficient of the fixed (inner) air.

Similarly, R_{ri} is the radiative thermal resistance (denoted by the resistive element R7 in the bond graph model) to the radiative heat flow from the inside air to the surface of the glass. This heat flow can be obtained as

$$T_{ac} - T_g = \frac{Q_{ri}}{A_g e_a \sigma (T_{ac}^2 + T_g^2) (T_{ac} + T_g)} \quad (2.7)$$

Defining the above in terms of resistance as $Q_{ri} = \Delta T / R_{ri}$, the radiative thermal resistance R_{ri} can be obtained as

$$R_{ri} = \frac{1}{A_g e_a \sigma (T_{ac}^2 + T_g^2) (T_{ac} + T_g)} \quad (2.8)$$

where T_{ac} is the air temperature of the cabin. SF1 element represents the heat transmitted by the glass, and this heat is absorbed by the air of the cabin. Thus, the amount of heat transmitted Q_{gt} by the glass is given by

$$Q_{gt} = I_r A_g t_g \quad (2.9)$$

where t_g is the transmissivity of glass. The element C3 models the heat stored by the inside air and in the given integral causality, it outputs the effort information (temperature of the air of the cabin). Its stiffness is defined as

$$K3 = \frac{1}{m_a C_a} \quad (2.10)$$

where m_a and C_a are mass and specific heat of the inside air. The effort detector (De) is used to measure the temperature of the air inside the glass compartment. In the bond graph model given in Fig. 1b, all other parameters except R_{ri} and the flow sources are constant values which depend upon material properties and geometric dimensions. The parameter values used in the simulation of the bond graph model shown in Fig. 1b are given in Table 1. The heat flux obtained from the experiment has been used as the input to the bond graph model of a single layer of the glass. The results obtained from the simulation of the bond graph model of the single glass layer configuration are shown in Fig. 2a. It is seen from Fig. 2a that the central cabin temperature increases very fast during the first half an hour and, after that, the rate of increase of temperature slows down. The maximum temperature reached after 2.5 h is about 59.4°C and, after that, the temperature becomes steady. The temperature of the glass also increases in the similar fashion as the cabin air; however, its value remains between temperatures of the cabin air and the atmospheric air. After almost 2 h, the difference between temperatures of the central cabin and the atmosphere becomes almost steady at 20.3°C. This simulation indicates that the temperature inside a closed car parked in direct sunlight increases rapidly.

Table 1. Parameter values of the single layer glass cabin

Parameter	Value	Description
a_g	0.25	Absorptivity of glass
A_g	0.68 m ²	Total area of all four glasses
C_a	919 kJ/(kg K)	Specific heat of air
C_g	720 kJ/(kg K)	Specific heat of glass
e_a	0.01	Emissivity of air
e_g	0.9	Emissivity of glass
h_{ai}	8 W/m ² K	Convective heat transfer coefficient of fixed air
h_{ao}	10 W/m ² K	Heat transfer coefficient of outside air with speed of 14 km/h
I_r	110 W/m ²	Heat flux
m_a	0.063 kg	Mass of air inside cabin
m_g	23.4 kg	Mass of glass
t_g	0.5	Transmissivity of glass
T_s	12 K	Temperature of space
σ	5.67 · 10 ⁻⁸	Boltzmann constant

2.2. Thermal modelling of the cabin system with air-trapped two-layer glass panel windows

In the second phase of the experiment and simulation, two layers of toughened glass having dimensions of 548 mm × 310 mm × 5 mm are used in each window panel. These two layers are

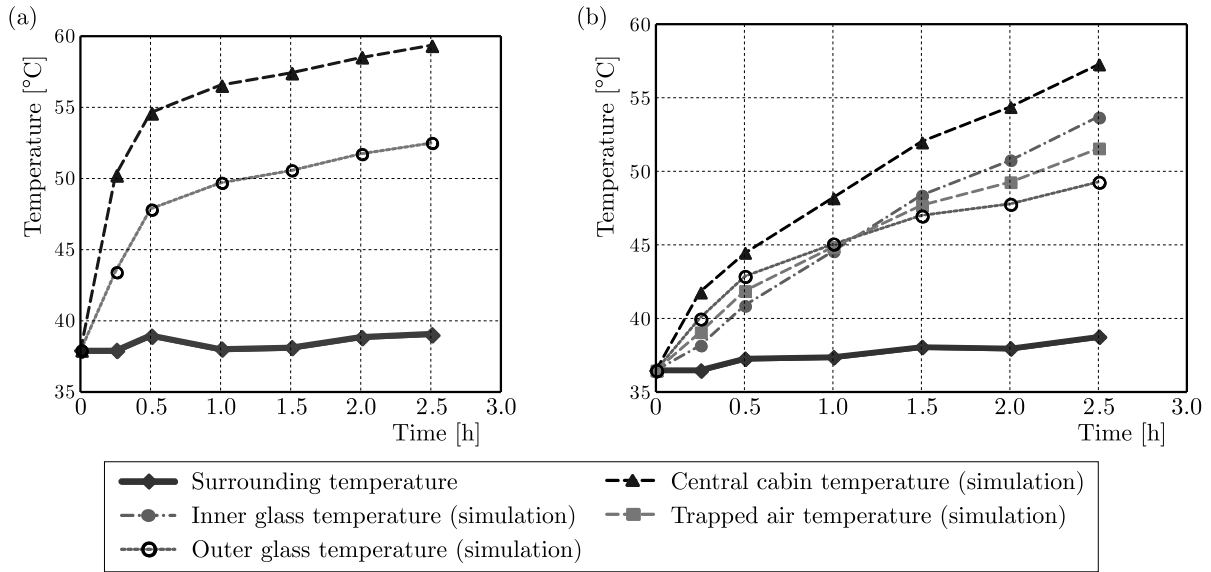


Fig. 2. Simulation results of (a) single layer glass and (b) double layer glass with entrapped air

assembled together in such a way that there is a fixed gap of 10 mm in between them. For this purpose, some separators are used. This entire setup is placed in an open environment under direct sunlight. The bond graph model of this modified system is shown in Fig. 3a. A part of the heat flux falling on the outer glass is absorbed by the glass; a part is reflected back and the remaining part is transmitted. The heat absorbed by the outer glass is represented by Q_{ga2} and is modelled by the SF14 element. As there are two layers of glasses separated by the air gap of 10 mm, the trapped air absorbs some part of the heat transmitted by the outer glass. The remaining transmitted heat after getting absorbed by the air is reflected by the inner glass. From this reflected heat, again a part of the heat is absorbed by the air present in between the two glasses. The rest of the reflected heat after getting absorbed by the air in between the two glasses is further absorbed by the outer glass. So, the total heat absorbed (Q_{ga2}) by the outer glass is

$$Q_{ga2} = I_r A_g a_g + I_r A_g t_g (1 - a_a) r_g (1 - a_a) a_g \quad (2.11)$$

where a_a and r_g are absorptivity of air and reflectivity of glass, respectively. The heat radiated and convected from the outer glass are expressed by (2.3) and (2.4), respectively. The radiative thermal resistance is obtained by replacing T_{ac} and T_g by T_{a2} (temperature of the atmospheric air present in between two glasses) and T_{ga2} (temperature at the outer glass) in (2.8). The total amount of heat Q_{aa2} absorbed by the air in between the two glasses is given by

$$Q_{aa2} = I_r A_g t_g a_a + I_r A_g t_g (1 - a_a) r_g a_a \quad (2.12)$$

The temperature of the inner glass is detected by the effort detector (De) connected to 0_{g1} -junction. The heat absorbed Q_{ga1} by the inner glass is given by

$$Q_{ga1} = I_r A_g t_g (1 - a_a) a_g \quad (2.13)$$

The transmitted heat Q_{gt1} that directly enters into the cabin is given by

$$Q_{gt1} = I_r A_g t_g (1 - a_a) t_g \quad (2.14)$$

The parameter values in the earlier simulations are given in Table 1, and the additional parameters related to the double layer configuration are given in Table 2.

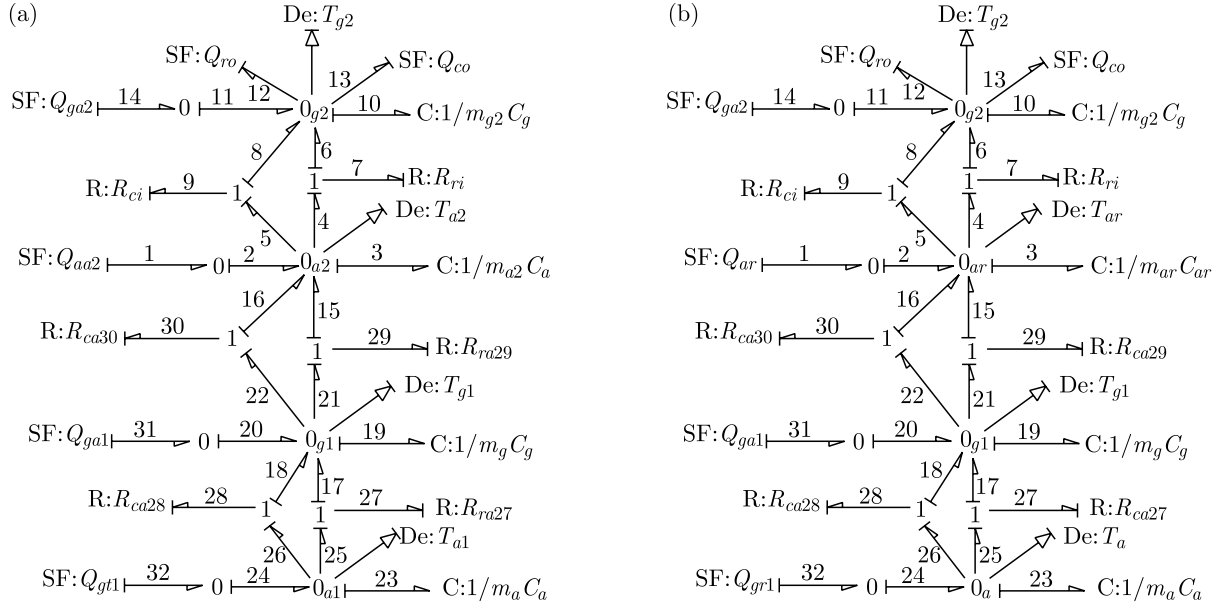


Fig. 3. Bond graph model of (a) double glass cabin with trapped air and (b) double layer glass cabin with entrapped argon

Table 2. Parameter values of the double layer glass cabin with entrapped air

Parameter	Value	Description	Parameter	Value	Description
a_a	0.01	Absorptivity of air	m_{g1}	23.4 kg	Mass of outer glass
I_r	118 W/m ²	Heat flux	m_{g2}	23.4 kg	Mass of inner glass
m_{a2}	0.00806 kg	Mass of air present between two glasses	r_g	0.25	Reflectivity of glass

The results obtained from simulations performed are shown in Fig. 2b. The initial temperature of atmosphere is 36.5°C. The temperature of the central cabin after 2.5 h becomes 57.3°C, whereas for the single glass this temperature is 59.4°C although the heat flux in the double glass layer configuration (118 W/m²) is greater than that in the single glass configuration (110 W/m²). Note that the environmental conditions for both simulations are different as they have been conducted in different times. The maximum rise of the cabin temperature with the double glass layer configuration is found to be 18.6°C. The inner glass temperature is less than the outer glass temperature for up to 1 h duration after exposure to direct sunlight. However, after the initial 1 h duration, the inner glass temperature exceeds the out glass temperature. Another important observation is that the cabin air temperatures increases faster than the entrapped air.

2.3. Thermal modelling of the cabin system with argon-trapped two-layer glass panel windows

The experiments for this configuration are performed in a similar manner to that performed for the double glass layers with argon entrapped in between the glasses. The bond graph model is given in Fig. 3b, which is similar to Fig. 3a in its structure. The total heat Q_{ga2} absorbed by the outer glass is given by

$$Q_{ga2} = I_r A_g a_g + I_r A_g t_g (1 - a_{ar}) r_g (1 - a_{ar}) a_g \quad (2.15)$$

where a_{ar} is the absorptivity of argon. The total heat Q_{ar} absorbed by the argon gas is given by

$$Q_{ar} = I_r A_g t_g a_{ar} + I_r A_g t_g (1 - a_{ar}) r_g a_{ar} \quad (2.16)$$

where R_{ca30} ($1/(Ah_{ar})$) and the R_{ra29} are convective and the radiative thermal resistances, respectively, for argon present between the outer and inner glass. The heat absorbed by the inner glass is given as

$$Q_{ga1} = I_r A_g t_g (1 - a_{ar}) a_g \quad (2.17)$$

Out of the total heat transmitted by the outer glass, some of the heat is absorbed by the argon gas and the inner glass. The remaining heat is transmitted through the inner glass into the internal chamber of the closed cabin. This transmitted heat Q_{gt1} is given by

$$Q_{gt1} = I_r A_g t_g (1 - a_{ar}) t_g \quad (2.18)$$

Most of the parameter values used in the simulation of the bond graph model developed in Fig. 3b are given Table 1 and Table 2. The values of the modified and additional parameters are listed in Table 3.

Table 3. Parameter values for the double layer glass cabin with entrapped argon

Parameter	Value	Description	Parameter	Value	Description
a_{ar}	0.1	Absorptivity of argon	h_{ar}	5.3 W/(m ² K)	Heat transfer coeff. of argon
C_{ar}	520 kJ/(kg K)	Specific heat of argon	I_r	100 W/m ²	Heat flux
e_{ar}	0.05	Emissivity of argon	m_{ar}	0.01209 kg	Mass of argon

The simulation results for the double layer glass cabin with entrapped argon are shown in Fig. 4a. The initial temperature of the surrounding is 36°C. The temperature of the central cabin after 2.5 h is 57.08°C, whereas for the double glass with air, this temperature is 7.3°C. The temperature differences between the central cabin and the atmosphere are 16.7°C and 18.6°C, respectively, for the double layer glass with argon and air insulation between the glass layers. So, as expected, the use of the argon gas between the glass layers yields better thermal insulation.

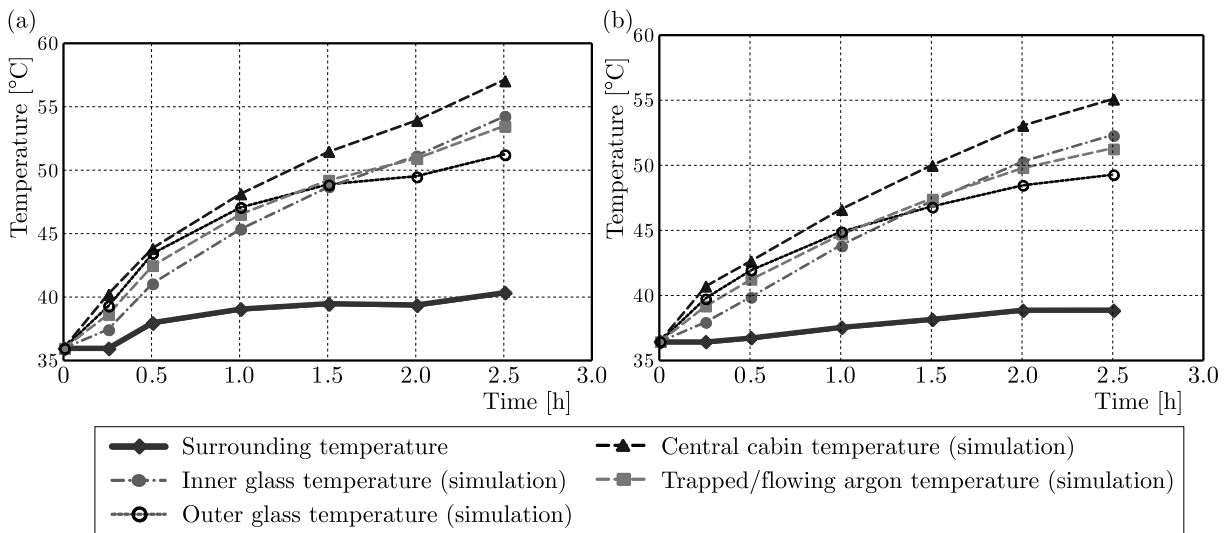


Fig. 4. Simulation results of the double layer glass with (a) entrapped and (b) flowing argon

2.4. Thermal modelling of the cabin system with flowing argon between two-layer glass panel windows

This configuration is intended for the double layer glass with the argon gas continuously flowing through the system with a flow rate of 0.403182 g/s. The bond graph model of the

system is similar to that for the earlier case. However, the heat transfer coefficient for flowing argon is different. The parameter values for the simulation are given Tables 1, 2 and 3. The convective heat transfer coefficient h_{ar} of argon is considered as $7 \text{ W}/(\text{m}^2\text{K})$ for the flow rate of 0.403182 g/s . The simulation results for the double layer glass with flowing argon are shown in Fig. 4b. The initial temperature of the surrounding is 36.5°C . The temperature of the central cabin after 2.5 h is 55.07°C whereas for the double glass with static argon, this temperature is 57.08°C . The steady-state temperature difference between the central cabin and the atmosphere is 16.7°C and 16.1°C for the double glass layer configuration with static argon and with flowing argon, respectively. So, flowing argon between the two glass layers is preferable.

3. Experimental validation

3.1. Selection of the material and sensors

The materials and sensors used for the development of the experimental setup are wooden frame, toughened glass, separator, air-oxygen separator, thermocouple, digital thermometer, argon cylinder, pipe and T-connectors as shown in Fig. 5. The dimension of the frame has been selected according to size of the toughened glass. The dimensions of the wooden frame are $411.6 \text{ mm} \times 411.6 \text{ mm} \times 649.6 \text{ mm}$. Laminated glass and toughened glass are widely used in vehicles due to its non-breaking tendency. The size of the toughened glass used is $310 \text{ mm} \times 548 \text{ mm} \times 5 \text{ mm}$. A solar power meter is used to measure the solar heat intensity x , and this value is used to calculate the solar heat flux Y as obtained after calibrating with a pyranometer ($R^2 = 0.99$)

$$Y = 0.745x + 1.839 \quad (3.1)$$



Fig. 5. Experimental accessories (a) glass supporting structure, (b) digital thermometer, (c) argon cylinder, (d) separator, (e) solar power meter and (f) argon-oxygen separator

3.2. Experimentation on the cabin system with single layer glass panel windows

It is the first phase of the experiment; toughened glass having dimensions $548\text{ mm} \times 310\text{ mm} \times 5\text{ mm}$ is fitted into the wooden frame. The glass is properly sealed with the sealant (clay) so that no air can escape from the assembly. The frame is insulated with expanded polystyrene from the top and the bottom so that very little heat could escape. The entire setup is exposed to direct solar heat waves. The heat starts to accumulate in the interior of the cabin by means of conduction, convection and radiation. Most of the accumulated heat is due to the radiation. Two digital thermometers are used to measure cabin temperature and atmospheric temperature. A solar power meter is used to measure the solar light intensity which eventually gives the value of the solar heat flux. The experiment starts at 11 am on a hot sunny day of summer and readings are taken at an interval of 15 minutes for the first half hour and then onwards at 30 minute intervals. Initially, the temperature difference between the atmosphere and the cabin compartment is less, but as the time passes, this temperature difference goes on increasing. The results obtained by the experiment are compared with the results from the bond graph modelling, and these are shown in Fig. 6a. As shown in Fig. 6a, the simulated results for the central cabin temperature are very close to those obtained from the experiment.

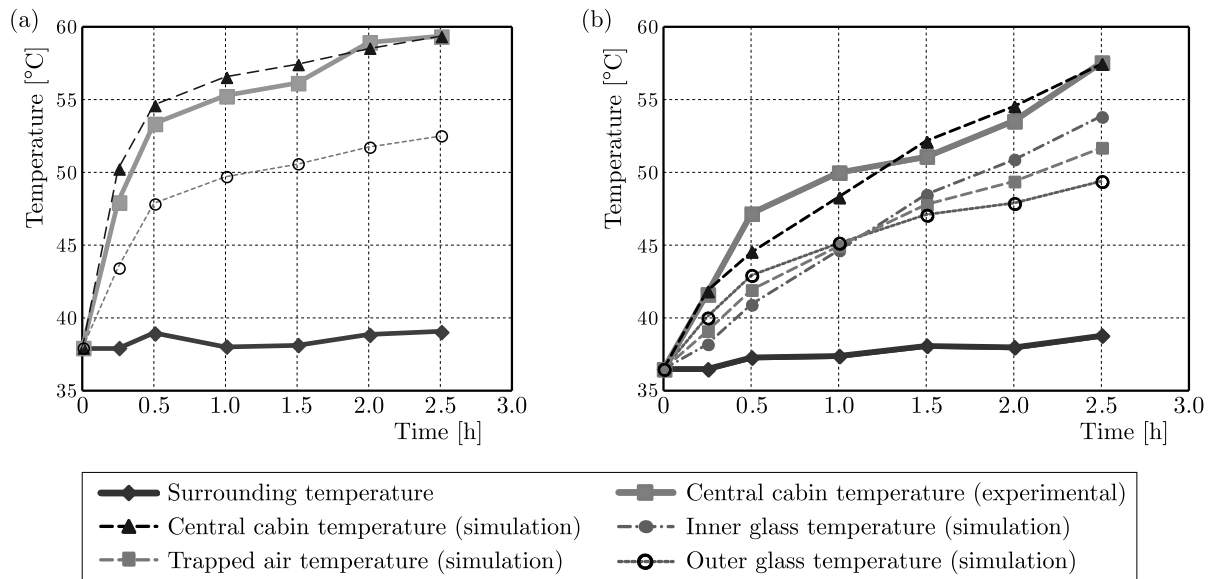


Fig. 6. Experimental vs simulation results for (a) single layer glass and (b) double layer glass with entrapped air

3.3. Experiments on the cabin system with air-trapped double layer glass panel windows

The top and the bottom portion of the cabin prepared with the double layer glass panel are covered by expanded polystyrene sheets so that little heat could get escape through them. Two digital thermometers are used to measure the temperature inside and outside the cabin. The basic principle of such a type of arrangement is to form a barrier for the heat flow. The toughened glass and trapped air inside the two layers of glasses have low thermal conductivity and thus inhibit heat transfer. The experimental and simulation results for this configuration are shown in Fig. 6b where the atmospheric temperature (an input to the simulation model) has a variation of about $2^{\circ}\text{--}3^{\circ}\text{C}$. Although there is not much variation in the atmospheric temperature, the central cabin temperature goes on increasing. Initially, the temperature difference between the central cabin temperature and the atmospheric temperature is less, but with time, this temperature difference increases. When compared to Fig. 6a, i.e. the experiment performed on the single

layer glass, the temperature difference obtained in the double layer glass panel configuration is quite less.

3.4. Experiments on the cabin system with argon-trapped double layer glass panel windows

The experiments are performed on the double glass with argon entrapped in between the glasses. A hole of 3 mm is drilled through the separator. A pipe of 3 mm diameter is inserted through the hole of the separator and this pipe is further connected to the argon gas cylinder. This assembly is prepared so as to fill the gap with argon (stored in the cylinder) and prevent any leakage. A constant flow of the argon gas is maintained in all four double layer glass assemblies so that atmospheric air is displaced by the pressurized argon gas. The constant flow is checked by counting the bubbles coming out from the outlet pipe which is dipped in water. When the bubble count per time unit is stabilized, the argon gas flow is stopped. The displacement of the atmospheric air by the pressurized argon gas is also verified by a parallel arrangement installed during the experiment. In this arrangement, the outlet line is made to pass through a closed chamber (Fig. 5f) having a burning candle inside it. The candle stops burning as soon as there is no oxygen available in the outlet pipe coming out from the double layered glass assemblies. When the pressure at the supply and at the outlet of the assembly of the glasses becomes equal, it indicates that the argon gas has been completely filled in the gap of the two glasses. Then the entire setup is exposed to the sunlight at the scheduled time.

The experimental and simulation results for this case are shown in Fig. 7a. During this experiment, the atmospheric temperature ranges between 36°-40.4°C and the rise in temperature of the central cabin is 16.7°C. Compared to the results obtained for the single glass panel cabin (20.3°C) and the double layer glass panel cabin with air insulation (18.6°C), the rise in the cabin temperature is less for the double layer glass panel cabin with argon gas insulation between the glass layers. The cabin temperature has fallen by nearly 3.6°C from the single layer glass panel configuration.

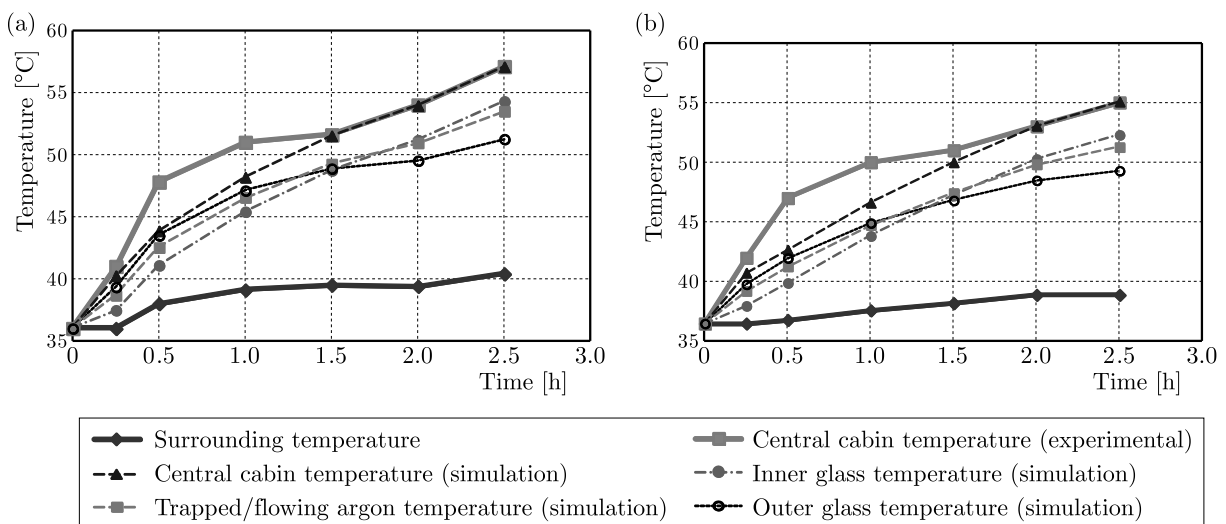


Fig. 7. Experimental vs simulation results for the double layer glass with (a) entrapped argon and (b) flowing argon

3.5. Experiments on the cabin system with two-layer glass panel windows and argon flowing between the glass layers

Experiments were further conducted using the same setup with argon flowing at a rate of 0.403 g/s through the gap between the two glass layers. The simulation and experimental results

for this configuration are shown in Fig. 7b. The temperature difference (16.1°C) between the central cabin temperature and atmospheric temperature is lower than that for the single glass layer (20.3°C) and the double glass with the entrapped air (18.6°C), but nearly the same as that of the double glass with entrapped argon (16.7°C). The continuous flow of argon helps carrying away the heat outside the cabin and, therefore, reduces a rise in the cabin temperature. This reduction could be more effective if the argon flow rate is increased. In addition, while the sealed glass panels with permanently entrapped air or argon can be easily fabricated as a unit, the flowing argon configuration requires additional components like air/argon pump, pipes, etc. due to which the manufacturing and maintenance problems encountered far outweigh the minor performance gain.

4. Conclusions

Experiments have been conducted in a closed cabin of toughened glass to understand the heat accumulation in the interior of a vehicle when it is exposed to direct sunlight. A bond graph model of the setup has been developed to perform simulation studies. The simulations and the experiments give an idea about the rate at which heat gets accumulated in the cabin. Replacing the single layer toughened glass panels with double layer toughened glass panels with static air trapped between the two glass layers, a reduction in the rate of increase of the cabin temperature has been observed. When the argon gas was trapped between the two glass layers, further reduction in temperature of the cabin air was observed. Moreover, when the argon gas was allowed to flow continuously at a slow flow rate, the rate of heat accumulation inside the cabin reduced further. The bond graph models developed for all these different configurations give very good predictions of the rate of heat accumulation or temperature of the cabin air. Such models can be used to develop predictive feed-forward or cascaded feedback and feed-forward control systems for cabin temperature regulation in the place of purely feedback controllers used in contemporary vehicles. This research work will be pursued further to deal with the heat transfer and storage through/in the roof and interior materials of a vehicle with aim to develop an optimized model-based control system of the cabin temperature.

References

1. ALAHMER A., MAYYAS O.A., SHAN D., 2011, Vehicular thermal comfort models; a comprehensive review, *Applied Thermal Engineering*, **31**, 995-1002
2. AL-KAYIEM H.H., FIRDAUS BIN M., SIDIK M. MUNUSAMMY Y.R.A.L., 2010, Study on the thermal accumulation and distribution inside a parked car cabin, *American Journal of Applied Sciences*, **7**, 6, 784-789
3. BROWN F.T., 2002, Non-iterative evaluation of multiphase thermal compliances in bond graphs, *Journal of Systems and Control Engineering*, **216**, 1, 13-19
4. CHEN X., LV Q., YI X., 2012, Smart window coating based on nanostructured VO_2 thin film, *International Journal for Light and Electron Optics*, **123**, 13, 1187-1189
5. DADOUR I.R., ALMANJAHIE I., FOWKES N.D., KEADY G., VIJAYAN K., 2011, Temperature variations in a parked vehicle, *Forensic Science International*, **207**, 205-211
6. LEE J.W., JANG E.Y., LEE S.H., RYOU H.S., CHOI S., KIM Y., 2014, Influence of the spectral solar radiation on the air flow and temperature distributions in a passenger compartment, *International Journal of Thermal Sciences*, **75**, 36-44
7. MAZZONI, 1977, Reducing solar radiation transmittance of installed glazing, US Patent, Application No. 710031, 4,041663

8. MERZOUKI R., SAMANTARAY A.K., PATHAK P.M., OULD BOUAMAMA B., 2012, *Intelligent Mechatronic Systems*, London, Springer
9. OULD BOUAMAMA B., MEDJAHER K., SAMANTARAY A.K., STAROSWIECKI M., 2006, Supervision of an industrial steam generator. Part I: Bond graph modeling, *Control Engineering Practice*, **14**, 1, 71-83
10. SAMANTARAY A.K., MEDJAHER K., OULD BOUAMAMA B., STAROSWIECKI M., DAUPHIN-TANGUY G., 2004, Component-based modelling of thermofluid systems for sensor placement and fault detection, *Simulation*, **80**, 7/8, 381-398
11. SANAYE S., DEGHANDOKHT M., FARTAJ A., 2012, Temperature control of a cabin in an automobile using thermal modelling and fuzzy controller, *Applied Energy*, **97**, 860-868
12. XAMÁNA J., PÉREZ-NUCAMENDIA C., ARCE J., HINOJOSA J.F., DEL SOCORRO ÁLVAREZ-GARCA G., ZAVALA-GUILLÉN I., 2014, Thermal analysis for a double pane window with a solar control film for using in cold and warm climate, *Energy and Buildings*, **76**, 429-439

Manuscript received April 5, 2016; accepted for print March 31, 2017

STUDY OF THE INFLUENCE OF COLD WORKING ON MECHANICAL BEHAVIOR AND DUCTILE FRACTURE OF 5754 ALUMINUM ALLOY: EXPERIMENTAL AND NUMERICAL SIMULATIONS

WAFATAKTAK

*Laboratoire des Systemes Electro-mecaniques (LASEM), National School of Engineers of Sfax, Tunisia
e-mail: wafa.taktak@yahoo.fr*

RIM TAKTAK, NADDER HADDAR

Laboratoire Genie des Materiaux et Environnement (LGME), National School of Engineers of Sfax, Tunisia

RIADH ELLEUCH

Laboratoire des Systemes Electro-mecaniques (LASEM), National School of Engineers of Sfax, Tunisia

The ductile damage of automotive aluminum sheet alloy AA5754-H111 is investigated by experiments and numerical simulation using the Gurson-Tvergaard-Needleman (GTN) model. The GTN parameters were determined by a uni-axial tensile test and the inverse finite element method. The same parameters were employed to provide the ductile damage behavior of central cracked panel (CCP) specimens. A good prediction can be established among the numerical simulation and experimental data in from of the force opening displacement. As an application, the identified GTN model is used to predict the influence of cold working on deformation and ductile damage. The numerical simulation results obtained are assimilated with experimental data.

Keywords: GTN model, ductile fracture, AA5754-H111, cold working

1. Introduction

In automotive applications, the aluminum alloys are extensively used for obtaining light mass and high strength structures. Aluminum-Magnesium (Al-Mg) aluminum alloys, indicated by 5xxx series, have a very good formability but a relativity low strength. This series of alloys strengthen only by work hardening (Burger *et al.*, 1995). The results of investigation of mechanical damage of 5754-H111 aluminum alloy has indicated that damage and fracture are mostly results of nucleating, growing and coalescing of micro cavities or micro voids. In order to predict the ductile fracture process, several theoretical models using local approaches have been presented in the literature (Betegon *et al.*, 1997; Corigliano *et al.*, 2000; Imad *et al.*, 2003; Achouri *et al.*, 2012). So, the selection of an adapted micromechanical model allows understanding of the fracture mechanism of 5457-H111 aluminum alloy. The basic research was started by McClintock (1968) and afterwards by Rice and Tracey (1969) who investigated the growth of cylindrical and spherical voids in ductile solids. Founded on theses analysis, Gurson (1977) proposed a micromechanical approach model. Later, the Gurson model was modified by Tvergaard and Needleman (1984) by introducing parameters q_1 and q_2 . They founded the void fusion equation f^* to describe ductile failure by nucleation, growth and coalescence of spherical micro voids. Generally, the modified Gurson model is named the GTN model. Many researchers have used the GTN model to provide ductile porous materials. Benseddiq and Imad (2007) used the GTN damage model to investigate ductile tearing of 2024-T351 aluminum alloy. Oh *et al.* (2007) proposed a phenomenological model of ductile fracture for API X65 using the GTN model. Yan *et al.* (2013) employed the GTN damage model to study the initiation and propagation of the crack near the edge under

rolling condition. Guo *et al.* (2013), Zhang *et al.* (2000), Huang *et al.* (2007) and Hu *et al.* (2014) used numerical results and experimental data to obtain parts of the GTN parameters. Unknown parameters of the model were obtained by using the inverse finite element method.

In the present research, ductile tearing of 5754 aluminum alloy has been analyzed by using the GTN model. The GTN parameters are identified by combining uni-axial tensile tests and detailed finite element analyses. The identified parameters have been employed to predict ductile failure of central cracked panel specimens. A good agreements can be established between the numerical and experimental results in form of the force versus displacement curves. As an application, the calibrated model is used to measure the cold working influence on deformation and fracture of 5754 aluminum alloy. The theoretical results are compared with experimental ones in the case of cold worked tensile and central cracked panels (CCP).

2. The GTN model

Gurson (1977) proposed a model to describe damage of ductile materials based on a micro-mechanical approach to porous plastic solids. This model takes into account degradation of the load carrying capacity due to the presence of porosity in isotropic materials. The original Gurson model was modified by Tvergaard and Needleman (1984) who relied on the coalescence of voids. The yield surface is presented by

$$\Phi(\sigma_y, \sigma_{eq}, f) = \frac{\sigma_{eq}^2}{\sigma_y^2} + 2f^* q_1 \cosh\left(\frac{3}{2} q_2 \frac{\sigma_m}{\sigma_y}\right) - [1 + q_3 (f^*)^2] = 0 \quad (2.1)$$

where q_1 , q_2 and $q_3 = (q_1)^2$ are the constitutive parameters incorporated by Tvergaard (1981) to amplify the hydrostatic stress effect for all strain levels. σ_{eq} is the conventional von Mises equivalent stress defined by: $\sigma_{eq} = \sqrt{\frac{3}{2} S_{ij} S_{ij}}$ (S_{ij} is the stress deviator) and σ_y is the yield stress of the undamaged matrix material.

For good prediction of the effect of void coalescence, Tvergaard and Needleman (1984) introduced the damage function f^* defined as follows

$$f^*(f) = \begin{cases} f & \text{for } f < f_c \\ f_c + \delta(f - f_c) & \text{for } f_c \leq f \leq f_F \\ f_u^* & \text{for } f \geq f_F \end{cases} \quad (2.2)$$

where $\delta = (f_u^* - f_c)/(f_F - f_c)$ is the void growth acceleration factor, f_c is the critical value of the void volume fraction corresponding to the beginning of the void coalescence, $f_u^* = 1/q_1$ is the ultimate value of the void volume fraction when the material load capacity is reduced to zero, f_F is the final void volume fraction.

The evolution of the void volume fraction f during plastic deformation is assumed to be a result of both the void growth and new voids nucleation given by

$$\dot{f} = f_{nucleation} + f_{growth} \quad (2.3)$$

Nucleation is considered to depend exclusively on the effective strain of the matrix material and can be estimated by the following equation

$$f_{nucleation} = A \dot{\epsilon}_{eq}^p \quad (2.4)$$

where $\dot{\epsilon}_{eq}^p$ is the equivalent plastic strain rate.

The parameter A is defined as a function of the matrix equivalent plastic strain

$$A = \frac{f_n}{S_n \sqrt{2\pi}} \exp\left(-\frac{1}{2}\left(\frac{\varepsilon^p - \varepsilon_n}{S_n}\right)^2\right) \quad (2.5)$$

where f_n is the volume fraction of void nucleating particles, ε_n is the mean void nucleation strain, S_n is the corresponding standard deviation and ε_p is the effective plastic strain.

The void growth is a function of the plastic strain rate, such that

$$\dot{f}_{growth} = (1 - f)\dot{\varepsilon}_{kk}^p \quad (2.6)$$

where $\dot{\varepsilon}_{kk}^p$ is the plastic part of the strain rate tensor.

3. Experimental results

In the present investigation, 2.45 mm in thickness 5754 aluminium alloy sheets have been used. The chemical composition of this alloy is given in Table 1.

Table 1. Chemical composition of the studied 5754-H111 aluminum alloy (wt%, rest: Al)

Si	Fe	Cu	Mn	Mg	Cr	Zn	Ti
0.40	0.40	0.1	0.5	2.6-3.6	0.3	0.2	0.15

Tensile testing has been performed at room temperature using a 50KN LLOYD universal test machine (Fig. 1). The tensile specimens have been stretched in the rolling direction (RD), the transversal direction (TD) and the diagonal direction (DD 45° between RD and TD) of the sheets. For each condition, three specimens have been tested at a constant speed of 1 mm/min. During testing, the axial displacement was monitored using an axial extensometer with length of 25 mm. The geometry and dimensions of the employed specimen work are presented in Fig. 2a.

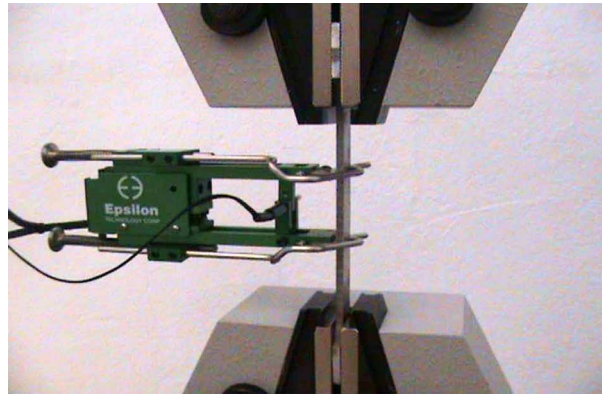


Fig. 1. Configuration of tensile tests

The uniaxial plastic flow behavior has been assumed to follow the Ramberg-Osgood stress-strain law presented as follows

$$\varepsilon = \varepsilon_e + \varepsilon_p \quad \sigma = \begin{cases} E\varepsilon_e & \text{if } \sigma \leq \sigma_y \\ \sigma_y + k\varepsilon_p^n & \text{if } \sigma > \sigma_y \end{cases} \quad (3.1)$$

with the hardening exponent n and ductility coefficient k .

The mechanical proprieties of 5457-H111 aluminum alloy are summarized in Table 2.

As shown in Fig. 3, the true stress-strain results of 5457-H111 aluminum alloy are similar in the three directions.

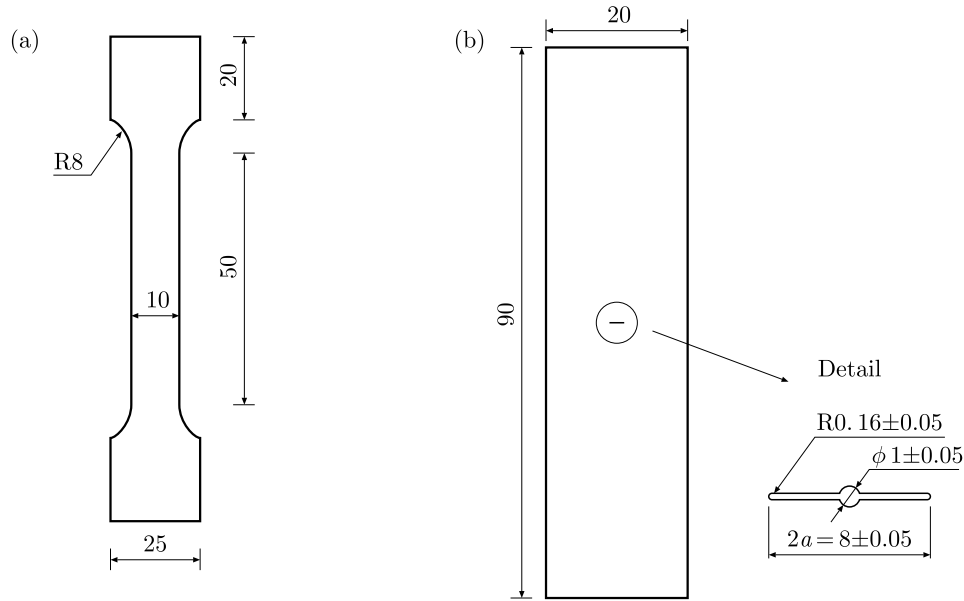


Fig. 2. (a) Geometry of the tensile specimen (in mm), (b) dimensions of the CCP specimens (in mm)

Table 2. Mechanical proprieties of 5457-H111 aluminum alloy in three directions: E – Young’s modulus, σ_y – yield stress, σ_u – ultimate stress, $A\%$ – elongation, n – hardening exponent and k – ductility coefficient

	E [MPa]	σ_y [MPa]	σ_u [MPa]	δ [%]	n	K [MPa]
RD	70612	100	270	15.28	0.586	575.554
TD	70134	99	265	14.89	0.589	599.659
DD	69978	98	259	15.13	0.580	590.034

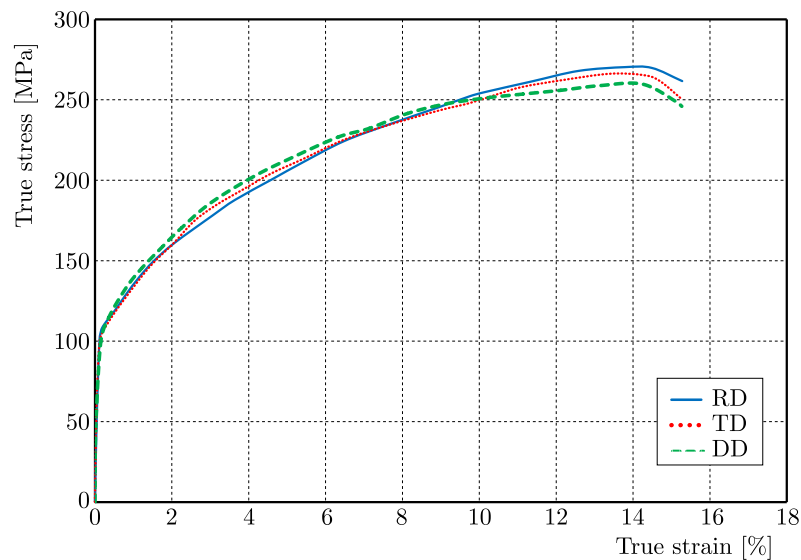


Fig. 3. Strain-stress curves of 5754-H111 aluminum alloy in the rolling direction (RD), transverse direction (TD) and diagonal direction (DD)

Ductile tearing tests were carried out on central cracked panels (CCP) at a constant displacement rate of 1 mm/min. The specimen geometry is presented in Fig. 2b. The ductile tearing specimens were manufactured in the rolling direction (RD) and transverse direction (TD) of the plates. In order to obtain a normalized crack length ratio a/w equal to 0.36, the specimens

were pre-cracked by the fatigue test. These tests were achieved using the single specimen method (Taktak *et al.*, 2009). Three specimens were operated at a constant cross-head speed of 1 mm/min.

The experimental load versus displacement curves of 5754-H111 aluminum alloy are exposed in Fig. 4. It is noted that these curves show a low experimental dispersion.

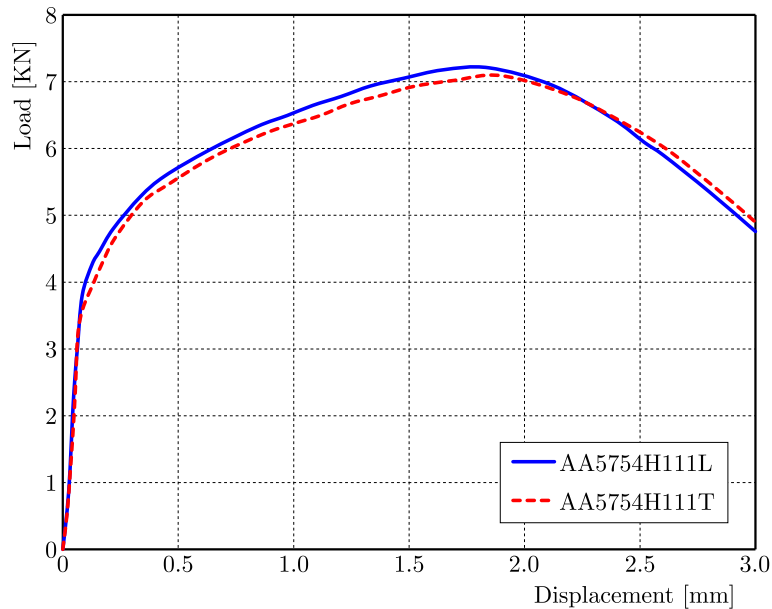


Fig. 4. Load versus displacement curves of 5754 aluminum alloy in the rolling direction (RD) and transverse direction (TD)

Also the fractographic examinations of 5754 aluminum alloy were performed on the fracture surfaces of the broken specimens from tensile testing by employing a scanning electron microscope (SEM). The SEM fractographs for 5754 aluminum alloy indicate the significant presence of ductile dimples (large voids beside smaller voids), which show the characteristic micro-void coalescence mechanism of ductile fracture (Fig. 5a-5d).

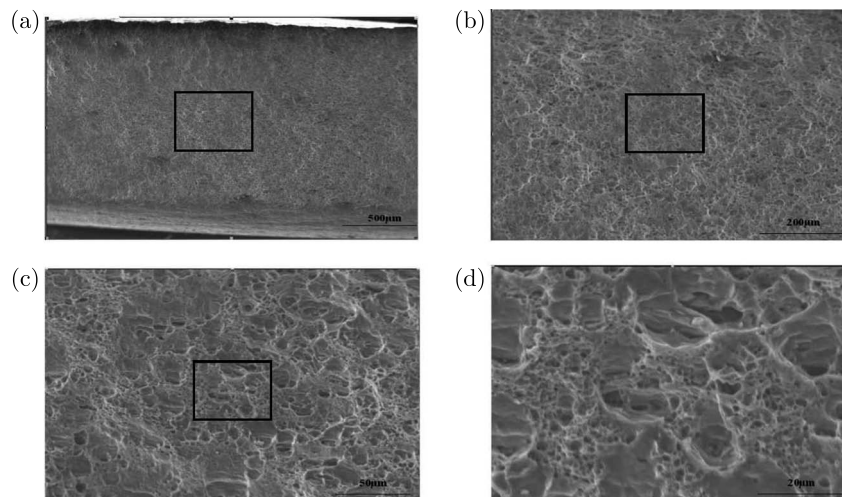


Fig. 5. SEM fractographs of the fracture surface for a tensile specimen abstracted from 5754 aluminum alloys under different magnifications: *a* overview morphology; *b* extended image of indicated region of the picture (a), *c* extended image of the indicated region of the picture (b), and *d* extracted image of the indicated region of the picture (c)

4. Numerical analysis

4.1. The meshing and boundary conditions

To obtain the theoretical force versus displacement curves, three-dimensional computation was performed using the finite element program ANSYS. In this study, the material is supposed to be elastoplastic, homogeneous and exhibit isotropic hardening. Two forms have been studied: the tensile specimen (Fig. 1a) and the CCP specimen (Fig. 1b). The meshing corresponding to each specimen using SOLID 185 finite element of ANSYS is presented in Fig. 6. The meshing near the crack tip consists of square mesh with 0.2 mm size (Taktak *et al.*, 2008). All the nodes on the ligament in front of the crack tip are fully constrained to have a zero displacement in the y -direction normal to the plane of the crack. Due to symmetry, only a quarter of the tensile specimen (Fig. 6a) and CCP specimen (Fig. 6b) are modeled.

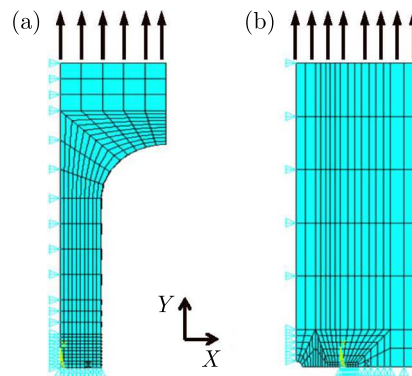


Fig. 6. (a) Meshing of a quarter of tensile specimen, (b) meshing of a quarter of the CCP specimen

4.2. Identification of damage parameters

The (GTN) ductile damage model has 9 necessary parameters: Three constitutive parameters related to the refined yield locus, q_1 , q_2 and q_3 , three void nucleation parameters ϵ_n , S_n and f_n and three parameters for void growth and coalescence f_0 , f_c and f_F . In the present investigation, seven parameters are determined by typical values proposed in literature (Tvergaard and Needleman, 1984; Lievers *et al.*, 2004): $\epsilon_n = 0.65$, $S_n = 0.03$, $f_n = 0.00035$, $q_1 = 1.5$, $q_2 = 1$, $q_3 = q_1^2 = 2.25$ and $f_f = 0.25$. In accordance with the discussion in (Zhang *et al.*, 2000; Rousselier, 2001), the critical void volume fraction f_c can be chosen as 0.15 for aluminum alloys. Thus, only the initial volume fraction f_0 needs to be determined. Generally, in aluminum alloys, the void is made up of a fragile intermetallic phase (Ghahremaninezhad and Ravi-Chandar, 2012). The evaluation of the initial void volume fraction f_0 is obtained by metallographic examination on a polished surface of undamaged materials. Also, f_0 is very little for this kinds of alloy. The initial void volume fraction f_0 can be estimated by the inverse finite element method using the finite element modeling and experiments. Guo *et al.* (2013) identified this parameter using the original Rousselier model to obtain three values of f_0 0.0001, 0.001, 0.005, respectively. By comparison with experimental results, he found a good agreement with $f_0 = 0.0001$ for AA5052. Hu *et al.* (2014) identified the parameter f_0 by an inverse method using experimental results. The simulations were done by setting the value of f_0 from 0.001 to 0.03. The initial void volume fraction f_0 for AA 6016 equal 0.001 improved the good agreement between the simulation and experimental results.

In this work, to estimate the parameter f_0 , an inverse method is used based on the FE method presented in this Section and the experimental results presented in Section 2. Six analyses have been made using the GTN model and the following initial void volume fraction f_0 : 0.00001, 0.0001, 0.001, 0.01, 0.05 and 0.1, respectively.

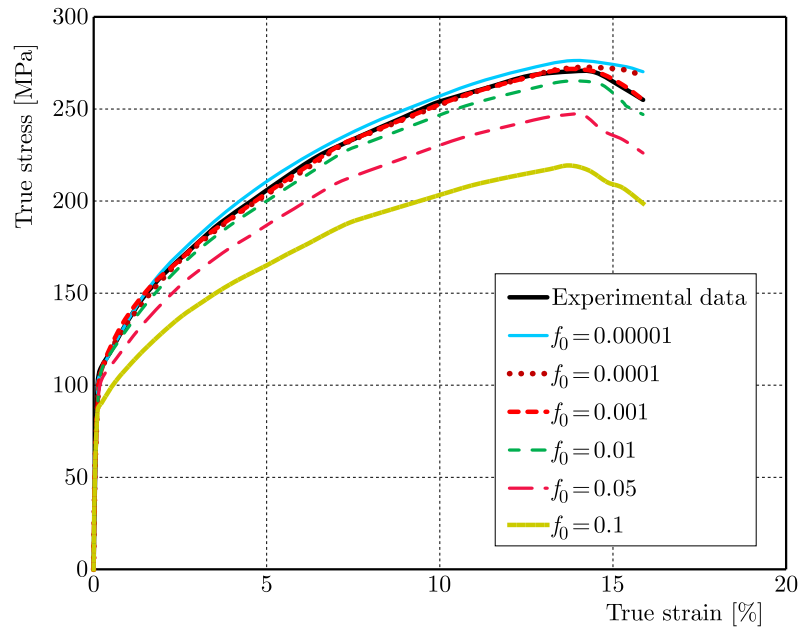


Fig. 7. The true stress-strain curves with different initial void volume fractions f_0 obtained by FE using the GTN model

The true stress-strain curves made by simulations with different f_0 are shown in Fig. 7. It can also be shown that, for $f_0 = 0.001$, the difference between the simulation and experiment results is admissible. So, the initial void volume fraction f_0 was identified as 0.001 for this material. The whole GTN parameters of the material are now presented in Table 3.

Table 3. Calibrated parameters of the GTN model for the 5754-H111 aluminum alloy

q_1	q_2	q_3	f_0	f_n	ε_n	S_n	f_c	f_f
1.5	1	2.25	0.001	0.00035	0.65	0.03	0.15	0.25

To validate the identified parameters listed in Table 3, the experimental load versus displacement curve issued from tearing tests on the CCP specimen are compared with the simulated ones using these parameters in Fig. 8. A good agreement is observed between the experimental results and those predicted by the finite element method. This shows that the GTN parameters identified in this work are acceptable.

5. Application to cold working effects

In the preceding Sections, the ductile fracture model based on the GTN model has been found for 5754-H111 aluminum alloy. This model has many potential application domains: it can be used for predicting not only the failure behavior of ductile tearing tests specimens but also for predicting size effects of ductile tearing tests specimens. The application of 5754-H111 aluminum alloy in automotive industry needs a high strength/weight ratio (Burger *et al.*, 1995). So, it is possible to carry out the strain hardening in the rolling direction. In the literature, many experimental investigations have been published on quantification of the strain hardening impact on mechanical cold working fracture properties for aluminum alloys. Our essential interest in this Section is the application and validation of the identified GTN model to measure cold working effects on numerical simulation. Tests were carried to measure the cold working effects on tensile and ductile tearing proprieties of 5754-H111 aluminum alloy. In these tests, the used material was

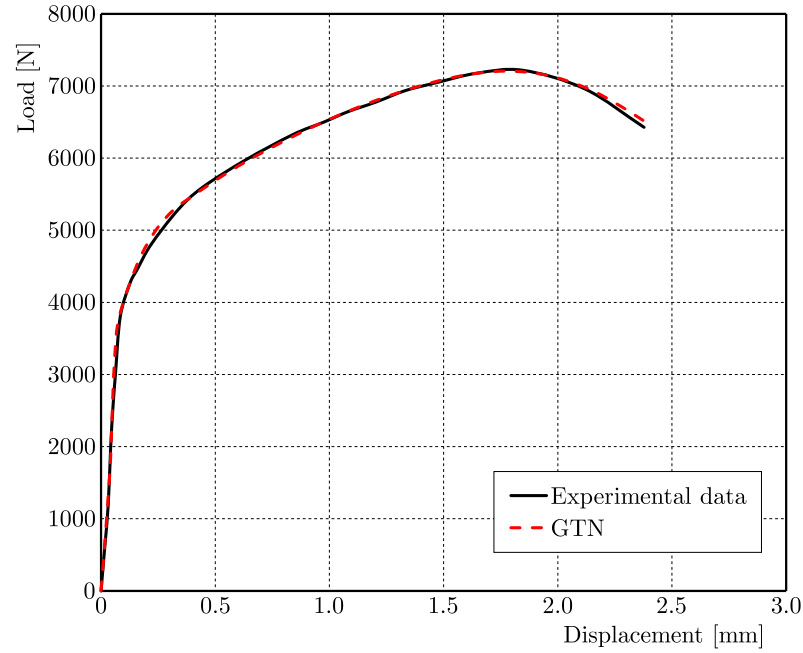


Fig. 8. Load versus displacement. Comparison between the experiment and FE simulation for the GTN model

similar condition to the one used in the previous Sections. A plate of the alloy (with thickness of 2.45 mm, width 150 mm and length of 150 mm) was cold rolled by a laboratory rolling mill to the reduction of 25% and 50% in area ($CW = 25\%$ and $CW = 50\%$).

Both the tensile and CCP specimens were abstracted from the plate in the longitudinal direction. The experimental conditions and geometry of the tensioned specimen and ductile tearing tests were same as those in the previous Sections. The tensile properties of the material subjected to different cold working rates are summarized in Table 4. It shows that the yield and tensile strength increase with the increasing percent of cold working, but the ductility decreases (Cosham, 2001; Mansourinejad and Mirzakhani, 2012). The strengthening of the material can be described by the increase of dislocation density with plastic deformation. The average distance between dislocations decreases and the dislocations start blocking motion of each other (Hajizadeh *et al.*, 2014).

It is widely acknowledged that the cold working effect on tensile curves can be quantified simply by shifting the true strain-stress curve by an increase of cold working (Ainsworth, 1986; Cosham, 2001), which is carried out by analyzing the present experimental results, as shown in Fig. 9.

Table 4. Main mechanical characteristics for different cold working rates: E – Young’s modulus, σ_y – yield stress, σ_u – ultimate stress, $A\%$ – elongation

CW	E [MPa]	σ_y [MPa]	σ_u [MPa]	A [%]
0%	70612	100	270	15.28
25%	71334	168	278	7.50
50%	69789	190	307	5.29

As shown in Fig. 10, the values of the hardening exponent n and ductility coefficient k are similar in the two directions. For this reason, we can consider that the behavior of these work-hardened materials is isotropic.

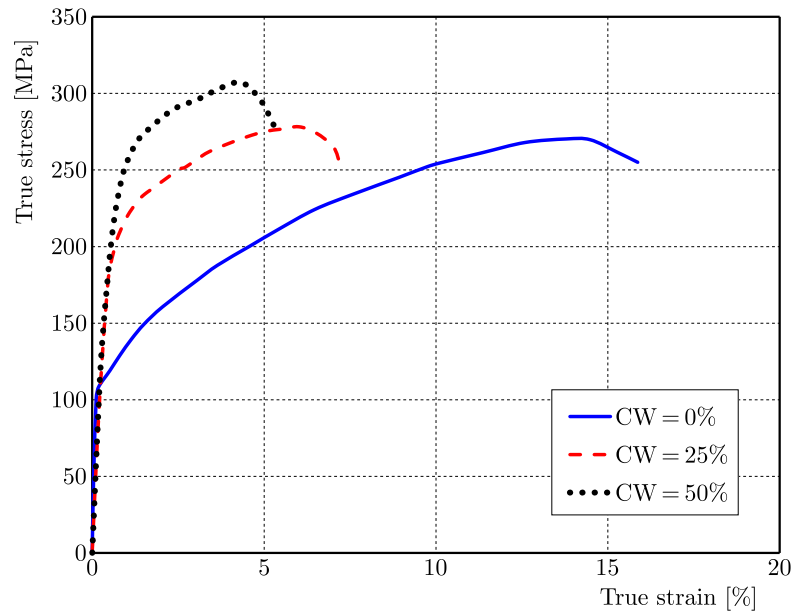


Fig. 9. Experimental results of the cold working effect on tensile curves

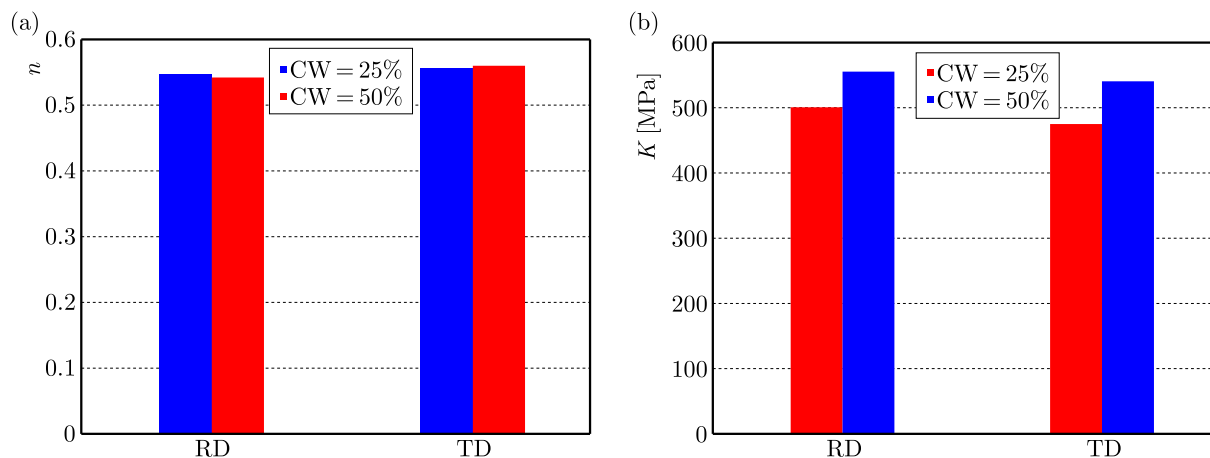


Fig. 10. Values of the hardening exponent n and ductility coefficient k in the rolling direction (RD), transverse direction (TD)

The SEM pictures of the cold worked specimens indicated a fine network of dimples (elongated voids with the fibrous structure) and little quasi-cleavage parts corresponding to the ductile fragile failure mechanism when the percentage of cold working increases (shown in Fig. 11). Generally, in FCC metals like 5457-H111 aluminum alloys, even at low temperature, the dislocation of leavings is important and the material rests ductile enough.

Thus, the morphology of fracture ought to be fundamentally fibrous plus some cleavage, reflecting the fragile failure behavior of the alloys when the percentage of cold working high.

The experimental load-displacement curves are summarized in Fig. 12. It indicates that the maximum loads for cold working are lower than those for without cold working.

Using the overhead information, finite element damage analyses based on the GTN model are used for simulating tensile tests and ductile tearing using ANSYS. To incorporate cold working into finite element damage analyses, two modifications are added. First, the true stress-strain curve is modified according to cold working. Secondly, the value of the initial void volume fraction f_0 is changed (Oh *et al.*, 2007). As noted, the value of the initial void volume fraction f_0 increases when the cold working rate increases (Oh *et al.*, 2007).

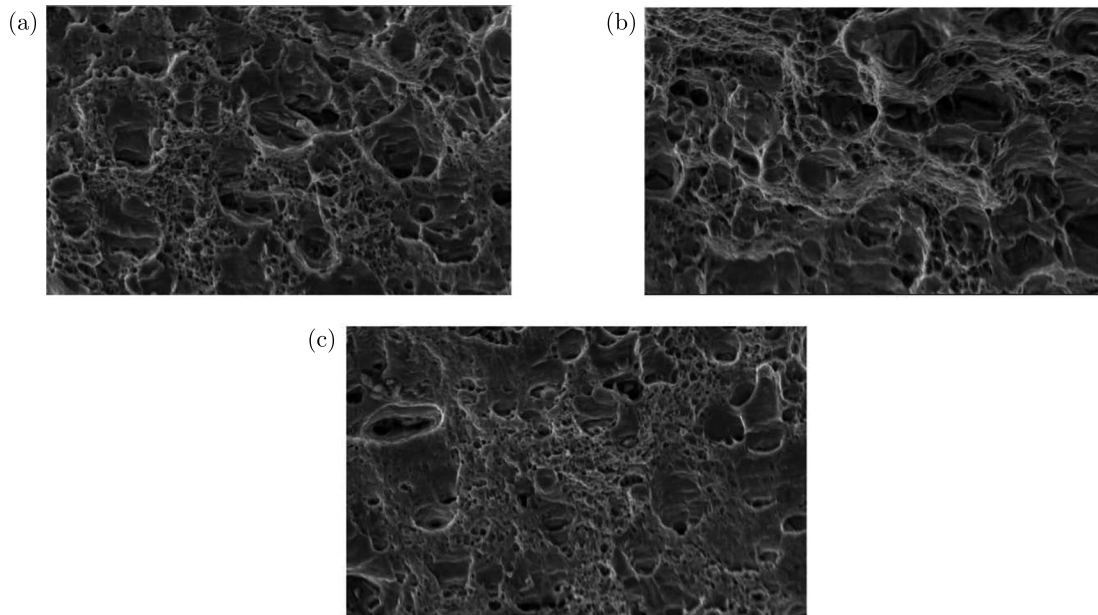


Fig. 11. SEM fractographs of 5457 aluminum alloy at different percentage of cold working: (a) 0%, (b) 25% and (c) 50%

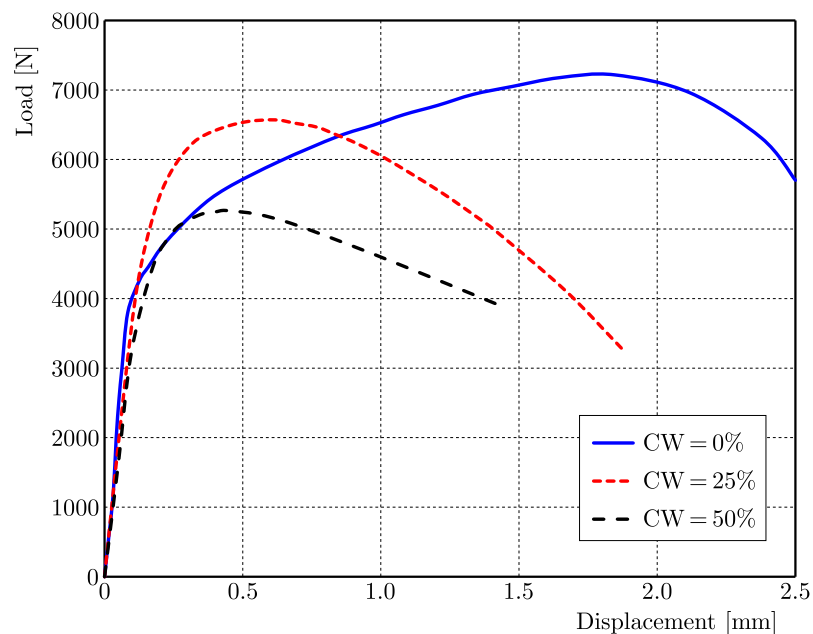


Fig. 12. Experimental results of cold working effects on load versus displacement curves

Figure 13 compares the experimental true stress-strain results with the numerical ones from finite element damage analyses based on the GTN model for different choices of f_0 for selected cases (CW = 25% and 50%).

From Figs. 13a and 13b, it can be seen that the choice of $f_0 = 0.006$ and $f_0 = 0.009$ for the cold working rate 25% and 50%, respectively, enables achieving the best agreement between the (FE) damage analyses and experimental results.

For validation, the results from finite element damage analyses for cold working rates 25% and 50% are compared with the experimental load-displacement curves, and reasonably good comparisons are found. It is shown in Fig. 14.

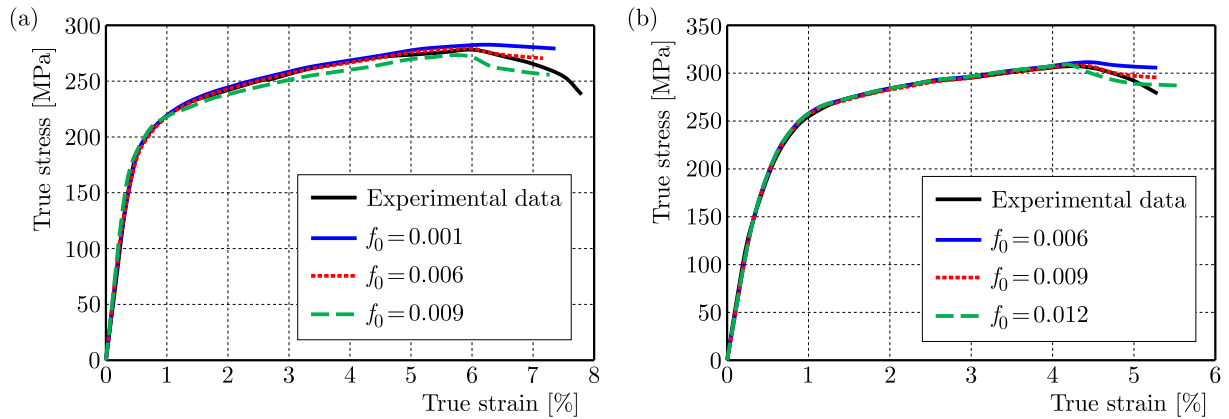


Fig. 13. True stress-strain curves with different initial void volume fractions f_0 obtained by FE using the GTN model. (a) The initial void volume fraction f_0 is calibrated as 0.006 for CW = 25%. (b) The initial void volume fraction f_0 is calibrated as 0.009 for CW = 50%

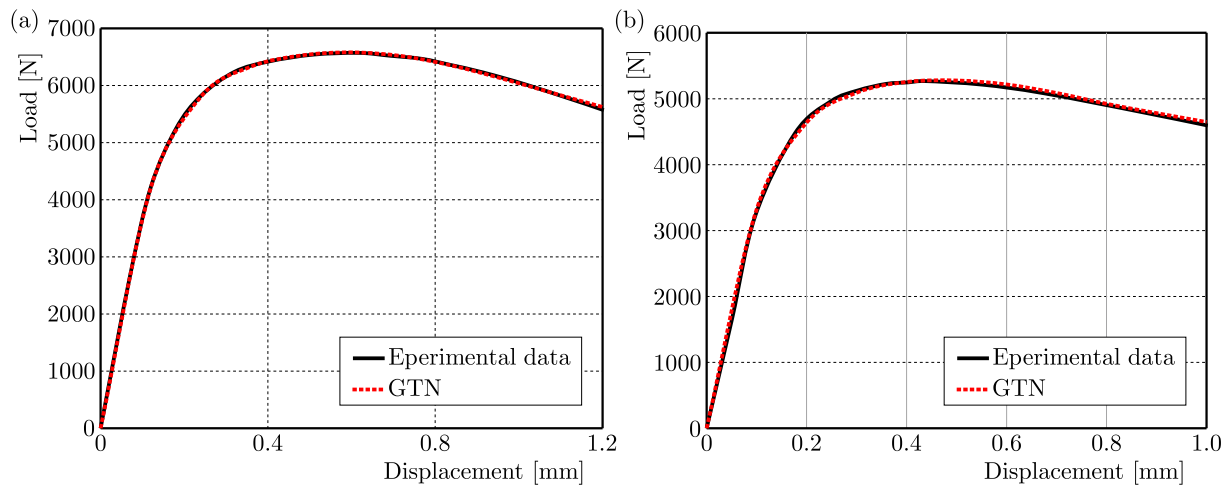


Fig. 14. Comparisons of FE simulations with experiments for the load versus displacement curves (a) CW = 25%, (b) CW = 50%

The results show that the experimental tensile tests and load versus displacement have been successfully predicted by the GTN model, and can take into account the cold working effect not only on plastic deformation but also on ductile fracture.

6. Summary and conclusions

- The continuum damage mechanics model (GTN) has been used to simulate the ductile tearing behavior of 5754-H111 aluminum alloy sheet metal.
- The parameters of the GTN model have been identified by an experimental tensile test (true stress versus true strain) and the inverse finite element method.
- The validity of the proposed parameters has been investigated by comparing the simulated results with the experimental ones from the tensile and ductile tearing tests (load versus displacement).
- The determined GTN model has been applied to predict the cold working influence on deformation and fracture. Comparison of experimental data of cold working, tensile tests and ductile tearing tests with finite element damage analyses have shown good agreements.

References

1. ACHOURI M., GERMAIN G., DAL SANTO P., SAIDANE D., 2012, Implementation and validation of a Gurson damage model modified for shear loading: effect of void growth rate and mesh size on the predicted behavior, *Key Engineering Materials*, **504**, 691-696
2. AINSWORTH R.A., 1986, An assessment of the effects of prestrain on upper shelf fracture toughness, *The Journal of Strain Analysis for Engineering Design*, **21**, 219-224
3. BENSEDIDIQ N., IMAD A., 2007, A ductile fracture analysis using a local damage model, *International Journal of Pressure Vessels and Piping*, **85**, 219-227
4. BETEGON C., RODRIGUEZ C., BELZUNCE F.J., 1997, Analysis and modelisation of short crack growth by ductile fracture micromechanisms, *Fatigue and Fracture of Engineering Material and Structures*, **20**, 633-644
5. BURGER G.B., GUPTA A.K., JEFFREY P.W., LLOYD D.J., 1995, Microstructural control of aluminum sheet used in automotive applications, *Materials Characterization*, **35**, 23-39
6. COSHAM A., 2001, A model of pre-strain effects on fracture toughness, *Journal of Offshore Mechanics and Arctic Engineering*, **123**, 182-190
7. CORIGLIANO A., MARIANI S., ORSATTI B., 2000, Identification of Gurson-Tvergaard material model parameters via Kalman filtering technique. I. Theory, *International Journal of Fracture*, **104**, 349-373
8. GHAHREMANINEZHAD A., RAVI-CHANDAR K., 2012, Ductile failure behavior of polycrystalline Al 6061-T6, *International Journal of Fracture*, **174**, 177-202
9. GUO J., ZHAO S., MURAKAMI R.I., ZANG S., 2013, Experimental and numerical investigation for ductile fracture of Al-alloy 5052 using modified Rousselier model, *Computational Materials Science*, **71**, 115-123
10. GURSON A.L., 1977, Continuum theory of ductile rupture by void nucleation and growth: Part I – Yield criteria and flow rules for porous ductile media, *Journal of Engineering Materials and Technology*, **99**, 2-15
11. HAJIZADEH K., TAJALL M., EMADODDIN E., BORHANI E., 2014, Study of texture, anisotropy and formability of cartridge brass sheets, *Journal of Alloys and Compounds*, **588**, 690-696
12. HU Y.M., CHEN M.Z., XIAO Y., XIAO J., TAN X., TANG Q., CUI T.S., 2014, Parameters determination of GTN model and damage analysis of aluminum alloy 6016 sheet, *International Conference on Material Science and Applications (ICMSA-15)*, Atlantis Press
13. HUANG X.-C., CHEN Y.-Z., CHEN Y.-M., NIU W., 2007, Identification of mesodamage parameters of 2169 steel, *Journal of Materials Engineering*, **4**, 50-52
14. IMAD A., WILSIUS J., ABDELAZIZ M.N., MESMACQUE G., 2003, Experiments and numerical approaches to ductile tearing in an 2024-T351 aluminium alloy, *International Journal of Mechanical Sciences*, **45**, 1849-1861
15. LIEVERS W.B., PILKEY A.K., LLOYD D.J., 2004, Using incremental forming to calibrate a void nucleation model for automotive aluminum sheet alloys, *Acta Materialia*, **52**, 3001-3007
16. MANSOURINEJAD M., MIRZAKHANI B., 2012, Influence of sequence of cold working and aging treatment on mechanical behaviour of 6061 aluminum alloy, *Transactions of Nonferrous Metals Society of China*, **22**, 2072-2079
17. MCCLINTOCK F.A., 1968, A criterion for ductile fracture by the growth of holes, *Journal of Applied Mechanics*, **35**, 363-371
18. OH C.K., KIM Y.J., BAEK J.H., KIM Y.P., 2007, A phenomenological model of ductile fracture for API X65 steel, *International Journal of Mechanical Sciences*, **49**, 1399-1412
19. RICE J.R., TRACEY D.M., 1969, On the ductile enlargement of voids in triaxial stress fields, *Journal of the Mechanics and Physics of Solids*, **17**, 201-217

20. ROUSSELIER G., 2001, The Rousselier model for porous metal plasticity and ductile fracture, *Handbook of Materials Behavior Models*, **2**, 436-445
21. TAKTAK R., BENSEDDIQ N., IMAD A., 2009, Analysis of ductile tearing using a local approach to fracture, *Fatigue and Fracture of Engineering Materials and Structures*, **32**, 525-530
22. TVERGAARD V., 1981, Influence of voids on shear band instabilities under plane strain conditions, *International Journal of Fracture*, **17**, 389-407
23. TVERGAARD V., NEEDLEMAN A., 1984, Analysis of the cup-cone fracture in a round tensile bar, *Acta Metallurgica*, **32**, 157-169
24. YAN Y., SUN Q., CHEN J., PAN H., 2013, The initiation and propagation of edge cracks of silicon steel during tandem cold rolling process based on the Gurson-Tvergaard-Needleman damage model, *Journal of Materials Processing Technology*, **213**, 598-605
25. ZHANG Z.L., THAULOW C., ODEGARD, 2000, A complete Gurson model approach for ductile fracture, *Engineering Fracture Mechanics*, **67**, 155-168

Manuscript received October 14, 2016; accepted for print March 31, 2017

THERMOELASTIC RESPONSE OF NANOBEAM RESONATORS SUBJECTED TO EXPONENTIAL DECAYING TIME VARYING LOAD

AHMED E. ABOUELREGAL

Mansoura University, Faculty of Science, Department of Mathematics, Mansoura, Egypt
e-mail: ahabogal@gmail.com

ASHRAF M. ZENKOUR

King Abdulaziz University, Faculty of Science, Department of Mathematics, Jeddah, Saudi Arabia and
Kafrelsheikh University, Faculty of Science, Department of Mathematics, Kafrelsheikh, Egypt
e-mail: zenkour@kau.edu.sa; zenkour@sci.kfs.edu.eg

This work investigates the vibrational response of thermoelastic nanobeam resonators induced by ramp-type heating and subjected to exponential decaying time varying load via Euler-Bernoulli beam theory. Governing equations are derived in the context of nonlocal generalized thermoelasticity theory with dual phase lags. The nonlocal nanobeam theory incorporates a nonlocal parameter to capture the small scale effect. Using the Laplace transform technique, an analytical solution has been attained. and inversions of the transformed solutions have been carried out by means of calculus of residues. The effects of nonlocal, point load and ramping-time parameters on all studied fields of the nanobeam are investigated and discussed.

Keywords: thermoelasticity, nonlocal nanobeam, varying load, ramp-type heating

1. Introduction

The fields of micro-, electro-, and mechanical systems (MEMS) have become quickly and gone into many resistances and correspondence technologies. Advanced applications for fabricating a variety of MEMS gadgets have been created to deal with all requirements for industries. It is known that all MEMS systems have mechanical flexible components. Microscales of cantilevers, bridges and membranes with various geometrical measurements and arrangements that often carry load are considered as MEMS systems (Younis, 2011). For MEMS designers, it is essential to understand mechanical properties of flexible micro-devices keeping in mind the end goal to predict the amount of transverse displacement from a distributed load and the other way around to forestall cracking-fracture, improve performance and to increase lifetime of MEMS gadgets (Allameh, 2003).

Both investigational and atomistic reproduction computations have demonstrated a significant dimension influence in mechanical properties when the sizes of such structures become very small. For this purpose, the size influence has a crucial role in dynamic and static behavior of micro-/nano-structures and cannot be neglected. It is famous that classical continuum mechanics does not represent such dimension influences in microscale and nanoscale structures. It is well known in the classical (local) elasticity theory that the stress at a point depends just on the strain at the same point. That is not the same in nonlocal elasticity theory, in which the stress at a point may be a function of strains at all points in the solid.

The nonlocal elasticity theory of Eringen (1983, 2002) has been increasingly used to deal with nanostructures as a reliable and quick technique. Nonlocal elasticity has been applied to micro- and nanomaterials and it recently received much attention among nanotechnology. The

basic difference between both classical and nonlocal elasticity theories is based on the definition of stress. Eringen's nonlocal theory includes more information about long range forces about atoms and, thus, internal scale length is introduced (Arefi and Zenkour, 2016; Zenkour, 2016a,c; Zenkour and Abouelregal, 2014a,b, 2015, 2016).

Lord and Shulman (LS) (1967) presented generalized theory of thermoelasticity with first relaxation time for isotropic homogeneous materials, in which an altered law of heat conduction that incorporates both time derivative of the heat flux and the heat flux itself, replaces Fourier's law conventional. The heat equation associated with LS theory is of hyperbolic type and consequently eliminates the paradox of infinite velocity of propagation inherent in both coupled (CTE) and uncoupled theories of thermoelasticity. Tzou (1995, 1997) presented another alteration with Fourier's law to investigate two time lags (see also Abbas and Zenkour, 2014; Abouelregal, 2011; Abouelregal and Abo-Dahab, 2012; Zenkur, 2016b; Zenkour *et al.*, 2013).

The objective of this paper is to derive governing equations of motion for free vibration of nonlocal Euler-Bernoulli nanobeams subjected to time-varying transverse load. In this work, a thermoelastic model based on the dual-phase-lag modification (DPL) heat conduction equation is used. The Laplace transform method and its inversion is used in the derivation. The effects due to nonlocal, point load and ramping time parameters will be studied. The current model may be used in micro-electro-mechanical applications such as frequency filters, relay switches, accelerometers, mass flow sensors and resonators.

2. Mathematical model and problem formulation

A schematic diagram of a thin elastic nanobeam is illustrated in Fig. 1 in which geometrical parameters of length ($0 \leq x \leq L$), width b ($-b/2 \leq y \leq b/2$) and uniform thickness h ($-h/2 \leq z \leq h/2$) are also indicated. We take x -axis along the axis of the nanobeam and y - and z -axes correspond to width and thickness, respectively. The nanobeam is considered to be unstrained, unstressed and at environment temperature T_0 in equilibrium.

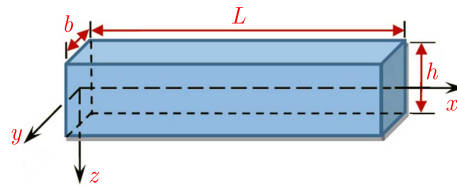


Fig. 1. Schematic diagram of the nanobeam

The linear Euler-Bernoulli theory is used to investigate bending vibration of the nanobeam. Any plane cross-section in the beginning perpendicular to the axis of the nanobeam remains plane and perpendicular to the neutral surface through bending. Hence, displacements of any point of the nanobeam can be written as

$$u = -z \frac{\partial w}{\partial x} \quad v = 0 \quad w = w(x, t) \quad (2.1)$$

in which w represents the lateral transverse deflection.

According to Eringen's nonlocal theory of elasticity (Eringen, 1983), with the aid of Eq. (2.1), the one-dimensional constitutive relation can be simplified to

$$\sigma_x - \xi \frac{\partial^2 \sigma_x}{\partial x^2} = -E \left(z \frac{\partial^2 w}{\partial x^2} + \alpha_T \theta \right) \quad (2.2)$$

where σ_x is the nonlocal axial stress, $\alpha_T = \alpha_t / (1 - 2\nu)$ in which α_t is the thermal expansion coefficient and ν is Poisson's ratio, $\xi = (e_0 a)^2$ represents the nonlocal parameter in which

a is internal characteristic length and e_0 is a constant appropriate to each material and being determined by experiment. It can be observed that when the parameter a is ignored, i.e., the elements of a medium are considered to be continuously distributed, then $\xi = 0$, and then Eq. (2.2) may be reduced to be the constitutive equation of the classical case. Then, the bending moment of cross-section may be represented as

$$M(x, t) = \int_{-h/2}^{h/2} z \sigma_x dz \quad (2.3)$$

Upon using Eqs. (2.2) and (2.3), we obtain

$$M(x, t) - \xi \frac{\partial^2 M}{\partial x^2} = -EI \left(\frac{\partial^2 w}{\partial x^2} + \alpha_T M_T \right) \quad (2.4)$$

in which $I = bh^3/12$ represents inertia moment of the nanobeam cross-section, EI represents flexural rigidity and M_T is the moment of the beam due to presence of thermal effects, which is given by

$$M_T = \frac{12}{h^3} \int_{-h/2}^{h/2} \theta(x, z, t) z dz \quad (2.5)$$

If the nanobeam is subjected to a distributed transverse load $q(x, t)$, the equation of transverse motion will be in the following form (Zhang *et al.*, 2005)

$$\frac{\partial^2 M}{\partial x^2} = -q(x, t) + \rho A \frac{\partial^2 w}{\partial t^2} \quad (2.6)$$

in which $A = bh$ represents the area of nanobeam cross section. The flexure moment can be determined from Eqs. (2.4) and (2.6) as

$$M(x, t) = \xi \left(\rho A \frac{\partial^2 w}{\partial t^2} - q \right) - EI \left(\frac{\partial^2 w}{\partial x^2} + \alpha_T M_T \right) \quad (2.7)$$

Eliminating the moment M from Eq. (2.6) with the aid of Eq. (2.7), we get the equation of motion of the nanobeam as

$$\left[\frac{\partial^4}{\partial x^4} + \frac{\rho A}{EI} \frac{\partial^2}{\partial t^2} \left(1 - \xi \frac{\partial^2}{\partial x^2} \right) \right] w - \frac{1}{EI} \left(1 - \xi \frac{\partial^2}{\partial x^2} \right) q + \alpha_T \frac{\partial^2 M_T}{\partial x^2} = 0 \quad (2.8)$$

The generalized heat conduction equation in terms of the constitutive relations in the context of Tzou theory (Tzou, 1995, 1997) of generalized (non-Fourier) thermoelasticity is given by

$$\left(1 + \tau_\theta \frac{\partial}{\partial t} \right) (K \theta_{,i})_{,i} + \left(1 + \tau_q \frac{\partial}{\partial t} \right) (\rho Q) = \left(1 + \tau_q \frac{\partial}{\partial t} \right) \frac{\partial}{\partial t} (\rho C_E \theta + \gamma T_0 e) \quad (2.9)$$

where K denotes the thermal conductivity, C_E represents specific heat per unit mass at uniform strain, Q is heat source, $\theta = T - T_0$ is the excess temperature distribution, in which T_0 denotes environmental temperature, τ_q denotes the phase-lag of heat flux, and τ_θ denotes the phase-lag of gradient of temperature, and $e = \frac{\partial u}{\partial x} + \frac{\partial w}{\partial z}$ is volumetric strain. Substituting Eq. (2.1) into heat equation Eq. (2.9), without considering heat source ($Q = 0$), gives

$$K \left(1 + \tau_\theta \frac{\partial}{\partial t} \right) \left(\frac{\partial^2}{\partial x^2} + \frac{\partial^2}{\partial z^2} \right) \theta = \left(1 + \tau_q \frac{\partial}{\partial t} \right) \frac{\partial}{\partial t} \left(\rho C_E \theta - \gamma T_0 z \frac{\partial^2 w}{\partial x^2} \right) \quad (2.10)$$

Equations (2.8) and (2.10) describe the nonlocal thermoelasticity theory with phase lags. The classical thermoelasticity theory may be recovered by putting $\xi = 0$ in the above equations. For $\tau_\theta = 0$ and $\tau_q > 0$, one obtains the Lord and Shulman model (LS), and the classical coupled theory (CTE) is also obtained when $\tau_q = \tau_\theta = 0$.

3. General solution along the direction of thickness

Let the temperature increment vary sinusoidally through-the-thickness of the nanobeam as

$$\theta(x, z, t) = \Theta(x, t) \sin\left(\frac{\pi}{h}z\right) \quad (3.1)$$

Using Eq. (3.1) in governing equations (2.7), (2.8) and (2.10), we obtain

$$\begin{aligned} M(x, t) &= \xi\left(\rho A \frac{\partial^2 w}{\partial t^2} - q\right) - EI\left(\frac{\partial^2 w}{\partial x^2} + \frac{24T_0\alpha_T}{\pi^2 h}\Theta\right) \\ \left[\frac{\partial^4}{\partial x^4} + \frac{\rho A}{EI} \frac{\partial^2}{\partial t^2}\left(1 - \xi \frac{\partial^2}{\partial x^2}\right)\right]w - \frac{1}{EI}\left(1 - \xi \frac{\partial^2}{\partial x^2}\right)q + \frac{24\alpha_T}{\pi^2 h} \frac{\partial^2 \Theta}{\partial x^2} &= 0 \\ \left(1 + \tau_\theta \frac{\partial}{\partial t}\right)\left(\frac{\partial^2 \Theta}{\partial x^2} - \frac{\pi^2}{h^2}\Theta\right) &= \left(1 + \tau_q \frac{\partial}{\partial t}\right) \frac{\partial}{\partial t} \left(\frac{\rho C_E}{K}\Theta - \frac{\gamma T_0 \pi^2 h}{24K} \frac{\partial^2 w}{\partial x^2}\right) \end{aligned} \quad (3.2)$$

For convenience, one can present the following dimensionless variables

$$\{u', w', x', z', L', b', h'\} = \eta c \{u, w, x, z, L, b, h\} \quad \{t', \tau'_q, \tau'_\theta\} = \eta c^2 \{t, \tau_q, \tau_\theta\} \quad (3.3)$$

and

$$\begin{aligned} \Theta' &= \frac{1}{T_0}\Theta & \xi' &= \eta^2 c^2 \xi & M &= \frac{1}{\eta c EI} M \\ q' &= \frac{A}{EI} q & c^2 &= \frac{E}{\rho} & \eta &= \frac{\rho C_E}{K} \end{aligned} \quad (3.4)$$

Upon introducing the above dimensionless quantities into the governing equations, we can obtain (dropping the primes for convenience)

$$\begin{aligned} M(x, t) &= \frac{12\xi}{h^2} \frac{\partial^2 w}{\partial t^2} - \xi q - \frac{\partial^2 w}{\partial x^2} - \frac{24T_0\alpha_T}{\pi^2 h}\Theta \\ \left[\frac{\partial^4}{\partial x^4} + \frac{12}{h^2} \frac{\partial^2}{\partial t^2}\left(1 - \xi \frac{\partial^2}{\partial x^2}\right)\right]w - \left(1 - \xi \frac{\partial^2}{\partial x^2}\right)q + \frac{24T_0\alpha_T}{\pi^2 h} \frac{\partial^2 \Theta}{\partial x^2} &= 0 \\ \left(1 + \tau_\theta \frac{\partial}{\partial t}\right)\left(\frac{\partial^2 \Theta}{\partial x^2} - \frac{\pi^2}{h^2}\Theta\right) &= \left(1 + \tau_q \frac{\partial}{\partial t}\right) \frac{\partial}{\partial t} \left(\Theta - \frac{\gamma \pi^2 h}{24K\eta} \frac{\partial^2 w}{\partial x^2}\right) \end{aligned} \quad (3.5)$$

Now, we consider an exponentially decaying time varying load in the form

$$q(x, t) = -q_0(1 - \delta e^{-\Omega t}) \quad (3.6)$$

where q_0 is the dimensionless magnitude of the point load and Ω represents the dimensionless frequency of the applied load, respectively ($\delta = 0$ for the uniformly distributed load).

Initially, the considered nanobeam has been assumed to be homogeneous, at rest, undeformed and at uniform temperature T_0 . So, the dimensionless initial conditions of the problem may be reconsidered as

$$w(x, t)|_{t=0} = \frac{\partial w(x, t)}{\partial t} \Big|_{t=0} = 0 \quad \Theta(x, t)|_{t=0} = \frac{\partial \Theta(x, t)}{\partial t} \Big|_{t=0} = 0 \quad (3.7)$$

The above conditions can be completed by adding other conditions at the ends of the nanobeam. Let these ends satisfy the following simply-supported boundary conditions

$$w(x, t)|_{x=0, L} = 0 \quad \frac{\partial^2 w(x, t)}{\partial x^2} \Big|_{x=0, L} = 0 \quad (3.8)$$

Let us also consider that the nanobeam is thermally loaded on the boundary $x = 0$. Then, according to Eq. (3.1), we can put

$$\Theta = \theta_0 f(x, t) \quad \text{on} \quad x = 0 \tag{3.9}$$

in which θ_0 is a constant and $f(x, t)$ is a varying ramp-type function with time described mathematically as follows

$$f(x, t)|_{x=0} = \begin{cases} 0 & \text{for } t \leq 0 \\ \frac{t}{t_0} & \text{for } 0 \leq t \leq t_0 \\ 1 & \text{for } t > t_0 \end{cases} \tag{3.10}$$

in which t_0 represents a positive constant called the ramp-type parameter of the same dimensionless as time t . Also, the temperature at the edge of the nanobeam satisfies the relation

$$\left. \frac{\partial \Theta}{\partial x} \right|_{x=L} = 0 \tag{3.11}$$

4. Laplace transform space solution

If we apply the Laplace transform method to both sides of Eqs. (3.5), we can get

$$\begin{aligned} \overline{M}(x, s) &= -\left(\frac{d^2}{dx^2} - A_3 s^2\right)\overline{w} - A_2 \overline{\Theta} + \xi \overline{g}(s) \\ \left[\frac{d^4}{dx^4} - A_3 s^2 \frac{d^2}{dx^2} + A_1 s^2\right]\overline{w} &= -A_2 \frac{d^2 \overline{\Theta}}{dx^2} - \overline{g}(s) \\ \left(\frac{d^2}{dx^2} - B_1\right)\overline{\Theta} &= -B_2 \frac{d^2 \overline{w}}{dx^2} \end{aligned} \tag{4.1}$$

where

$$\begin{aligned} A_1 &= \frac{12}{h^2} & A_2 &= \frac{24T_0 \alpha_T}{\pi h} & A_3 &= \xi A_1 & A_4 &= \frac{\pi^2}{h^2} & A_5 &= \frac{\gamma \pi^2 h}{24K\eta} \\ B_1 &= A_4 + \frac{s(1 + \tau_q s)}{1 + \tau_\theta s} & B_2 &= \frac{s(1 + \tau_q s)}{1 + \tau_\theta s} A_5 & \overline{g}(s) &= q_0 \left(\frac{1}{s} - \frac{\delta}{\Omega + s}\right) \end{aligned} \tag{4.2}$$

Eliminating the function $\overline{\Theta}$ from Eqs. (4.1)₂ and (4.1)₃, we get the six-order differential equation for \overline{w} in the form

$$\left[\frac{d^6}{dx^6} - A \frac{d^4}{dx^4} + B \frac{d^2}{dx^2} - C\right]\overline{w} = 0 \tag{4.3}$$

where

$$A = B_1 + A_2 B_2 + A_3 s^2 \quad B = s^2(A_1 + A_3 B_1) \quad C = A_1 B_1 s^2 \tag{4.4}$$

The general solution of \overline{w} can be obtained as

$$\overline{w}(x, s) = \sum_{j=1}^3 (C_j e^{-m_j x} + C_{j+3} e^{m_j x}) \tag{4.5}$$

where m_1^2 , m_2^2 and m_3^2 represent roots of the characteristic equation

$$m^6 - Am^4 + Bm^2 - C = 0 \tag{4.6}$$

Substituting Eq. (4.1)₃ into Eq. (4.1)₂, leads to

$$\bar{\Theta}(x, s) = -\frac{1}{A_2B_1} \left[\frac{d^4\bar{w}}{dx^4} - (A_2B_2 + A_3s^2) \frac{d^2\bar{w}}{dx^2} + A_1s^2\bar{w} + \bar{g}(s) \right] \tag{4.7}$$

The general solution to Eq. (4.7) with the help of Eq. (4.5) can be simplified as

$$\bar{\Theta}(x, s) = \sum_{j=1}^3 H_j (C_j e^{-m_j x} + C_{j+3} e^{m_j x}) - H_4 \tag{4.8}$$

where

$$H_j = -\frac{1}{A_2B_1} [m_j^4 - (A_2B_2 + A_3s^2)m_j^2 + A_1s^2] \quad H_4 = \frac{\bar{g}(s)}{A_2B_1} \tag{4.9}$$

Substituting the expressions of \bar{w} and $\bar{\Theta}$ from Eqs. (4.5) and (4.8) into Eq. (4.1)₁, we get the solution for the bending moment \bar{M} as

$$\bar{M}(x, s) = -\sum_{j=1}^3 (m_j^2 - A_3s^2 + A_2H_j) (C_j e^{-m_j x} + C_{j+3} e^{m_j x}) + A_2H_4 + \xi\bar{g}(s) \tag{4.10}$$

In addition, the axial displacement \bar{u} after using the deflection $\bar{w}(x, s)$ appearing in Eq. (4.5) can be expressed as

$$\bar{u} = -z \frac{d\bar{w}}{dx} = z \sum_{j=1}^3 m_j (C_j e^{-m_j x} - C_{j+3} e^{m_j x}) \tag{4.11}$$

Finally, the boundary conditions in Eqs. (3.8), (3.9) and (3.11) in the Laplace transform domain are reduced to

$$\begin{aligned} \bar{w}(x, s)|_{x=0,L} = 0 \quad \left. \frac{d^2\bar{w}(x, s)}{dx^2} \right|_{x=0,L} = 0 \\ \bar{\Theta}(x, s)|_{x=0} = \theta_0 \left(\frac{1 - e^{-t_0s}}{t_0s^2} \right) = \bar{G}(s) \quad \left. \frac{d\bar{\Theta}}{dx} \right|_{x=L} = 0 \end{aligned} \tag{4.12}$$

The above boundary conditions are applied to Eqs. (4.5) and (4.8) to determine the unknown parameters C_j and C_{j+3} as

$$\begin{aligned} \begin{bmatrix} 1 & 1 & 1 & 1 & 11 & \\ e^{-m_1L} & e^{-m_2L} & e^{-m_3L} & e^{m_1L} & e^{m_2L} & e^{m_3L} \\ m_1^2 & m_2^2 & m_3^2 & m_1^2 & m_2^2 & m_3^2 \\ m_1^2 e^{-m_1L} & m_2^2 e^{-m_2L} & m_3^2 e^{-m_3L} & k_1 e^{m_1L} & m_2^2 e^{m_2L} & m_3^2 e^{m_3L} \\ H_1 & H_2 & H_3 & H_1 & H_2 & H_3 \\ -m_1 H_1 e^{-m_1L} & -m_2 H_2 e^{-m_2L} & -m_3 H_3 e^{-m_3L} & m_1 H_1 e^{m_1L} & m_2 H_2 e^{m_2L} & m_3 H_3 e^{m_3L} \end{bmatrix} \\ \cdot \begin{bmatrix} C_1 \\ C_2 \\ C_3 \\ C_4 \\ C_5 \\ C_6 \end{bmatrix} = \begin{bmatrix} 0 \\ 0 \\ 0 \\ 0 \\ \bar{G}(s) + H_4 \\ 0 \end{bmatrix} \end{aligned} \tag{4.13}$$

It is difficult to get an inversion to the Laplace transform of the complicated solutions for the lateral vibration, displacement, thermodynamic temperature, stress and strain in the Laplace transform space. Therefore, the results will be analyzed numerically using a method based on the Fourier series expansion technique.

5. Numerical results

This Section is devoted to investigate some numerical examples of field quantities using material properties of *silicon* as

$$\begin{aligned} E &= 169 \text{ GPa} & \rho &= 2330 \text{ kg/m}^3 & C_E &= 713 \text{ J/(kg K)} \\ \alpha_T &= 2.59 \cdot 10^{-9} \text{ (1/K)} & \nu &= 0.22 & K &= 156 \text{ W/(m K)} \end{aligned} \quad (5.1)$$

The environment temperature of the nanobeam is considered as $T_0 = 293 \text{ K}$. In addition, some parameters like the length-to-thickness (L/h) ratio, width-to-thickness (b/h) ratio, magnitude (q_0), frequency (Ω) of the applied load and the dimensionless nonlocal parameter $\bar{\xi}$ are fixed to be

$$\frac{L}{h} = 10 \quad \frac{b}{h} = \frac{1}{2} \quad q_0 = 1 \cdot 10^{-8} \quad \Omega = 0.1076 \quad \bar{\xi} = 10^6 \xi \quad (5.2)$$

Also, Figures 2-5 are plotted by considering the non-dimensional forms appearing in Eqs. (3.3) and (3.4) for a wide range of nanobeam length taken into account that

$$L = 1 \quad t = 0.1 \quad z = \frac{h}{3} \quad (5.3)$$

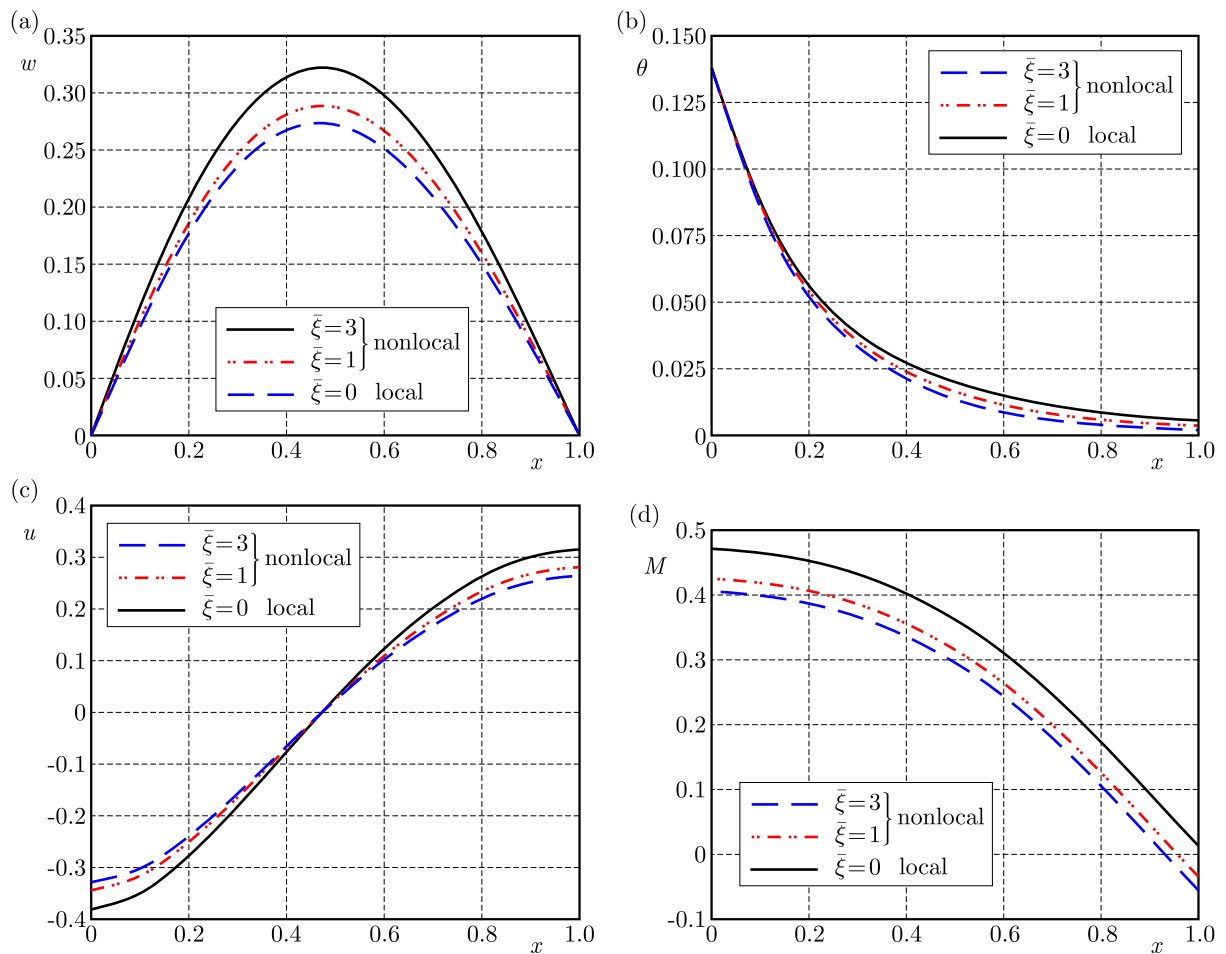


Fig. 2. The transverse deflection, temperature, displacement and bending moment distributions of the nanobeam for different values of the nonlocal thermoelastic parameters $\bar{\xi}$: (a) transverse deflection w versus x , (b) temperature θ versus x , (c) displacement u versus x , (d) bending moment M versus x

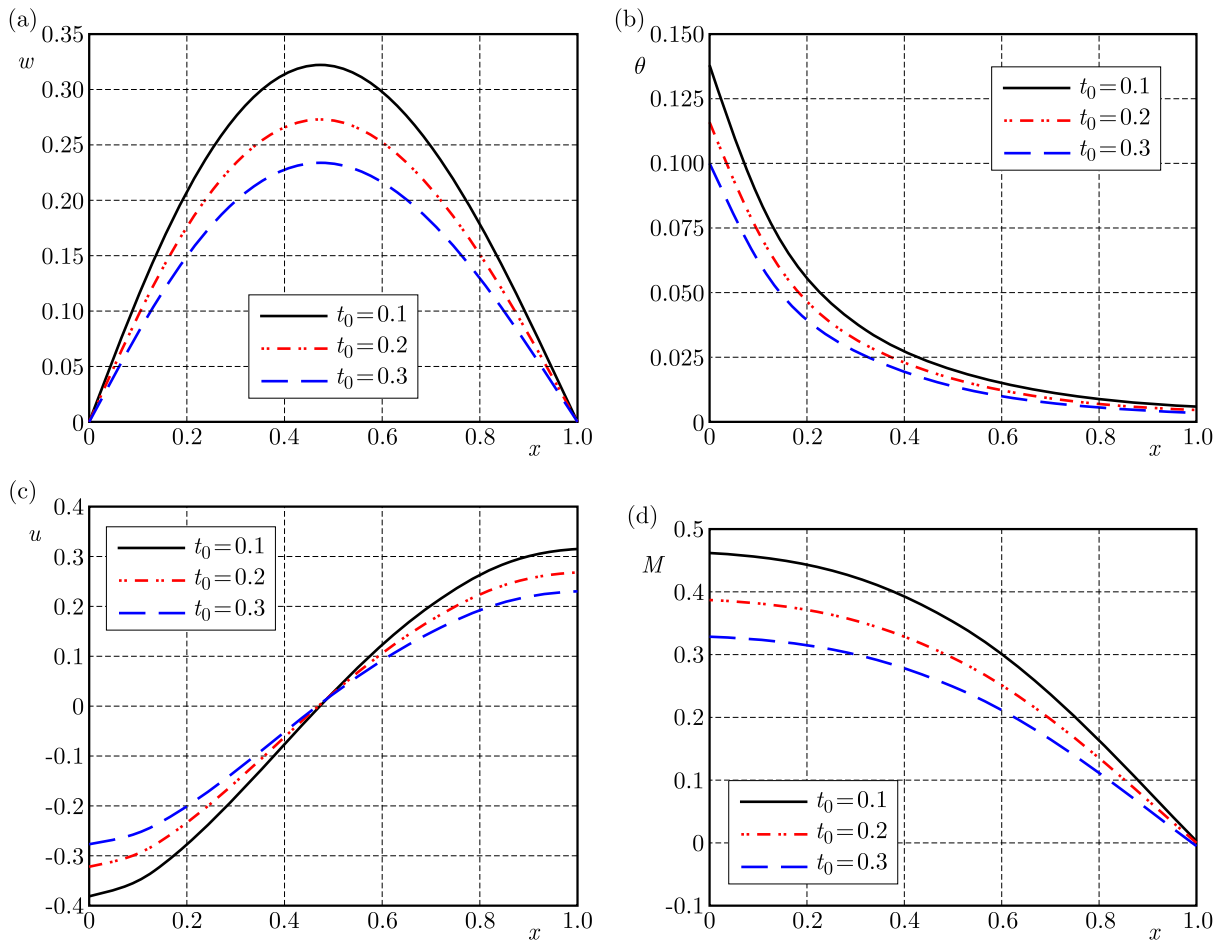


Fig. 3. The transverse deflection, temperature, displacement and bending moment distributions of the nanobeam for different values of the ramping time parameter t_0 : (a) transverse deflection w versus x , (b) temperature θ versus x , (c) displacement u versus x , (d) bending moment M versus x

The first example discussed here is to investigate the dimensionless forms of lateral vibration (deflection), temperature, axial displacement and bending moment with different dimensionless nonlocal parameters $\bar{\xi}$. In this example, one considers the ramping time parameter $t_0 = 0.1$ and phase-lags τ_q and τ_θ remaining constants ($\tau_q = 0.02$, $\tau_\theta = 0.01$). It is clear that the case of $\bar{\xi} = 0$ indicates the local thermoelasticity theory. However, the values $\bar{\xi} = 1$ and $\bar{\xi} = 3$ indicate the nonlocal thermoelasticity theory. The effect of $\bar{\xi}$ on vibration characteristics along the axial direction of the nanobeam is shown in Figs. 2a-2d. From these figures, we can see that:

- 1) The deflection w is no longer increasing and vanishes again at the boundaries. Its maximum values occur near the center of the nanobeam.
- 2) The lateral vibration w decreases as the nonlocal parameter $\bar{\xi}$ increases.
- 3) The nanobeam exhibits the maximum deflection near the mid-point of the nanobeam at all times and irrespective of the value of $\bar{\xi}$.
- 4) The thermal temperature θ is decreasing as the distance x increases and it is moving in the direction of wave propagation.
- 5) As $\bar{\xi}$ increases, the temperature θ decreases.
- 6) Distribution of the axial displacement u starts increasing with the nonlocal parameter $\bar{\xi}$ in the interval $0 \leq x \leq 0.45$, thereafter it increases up to maximum amplitudes in the interval $0.45 \leq x \leq 1$.

- 7) The bending moment M is decreasing with the increasing distance x . Also, we observe that an increase in $\bar{\xi}$ leads to growth of the distribution of M .
- 8) All plots show that this parameter has a significant effect on the field quantities.
- 9) It is obvious that according to the value of $\bar{\xi}$, the difference between the local and nonlocal generalized thermoelasticity theory is evident.

The second example discussed here is to investigate the variation of dimensionless lateral vibration, temperature, displacement and bending moment versus the ramping time parameter t_0 when the phase-lags τ_q and τ_θ and nonlocal parameter $\bar{\xi}$ remain fixed. The plots of this example are illustrated in Figs. 3a-3d. It is concluded in this case that:

- 1) Values of the deflection, temperature and bending moment are increasing as the ramping time parameter t_0 is decreasing.
- 2) As t_0 increases, the displacement u increases in the interval $0 \leq x < 0.48$ and decreases in the interval $0.48 < x \leq 1$. The axial displacement u increases along the axial direction.
- 3) The distribution of all variables is very sensitive to the variation of the ramping time parameter t_0 .

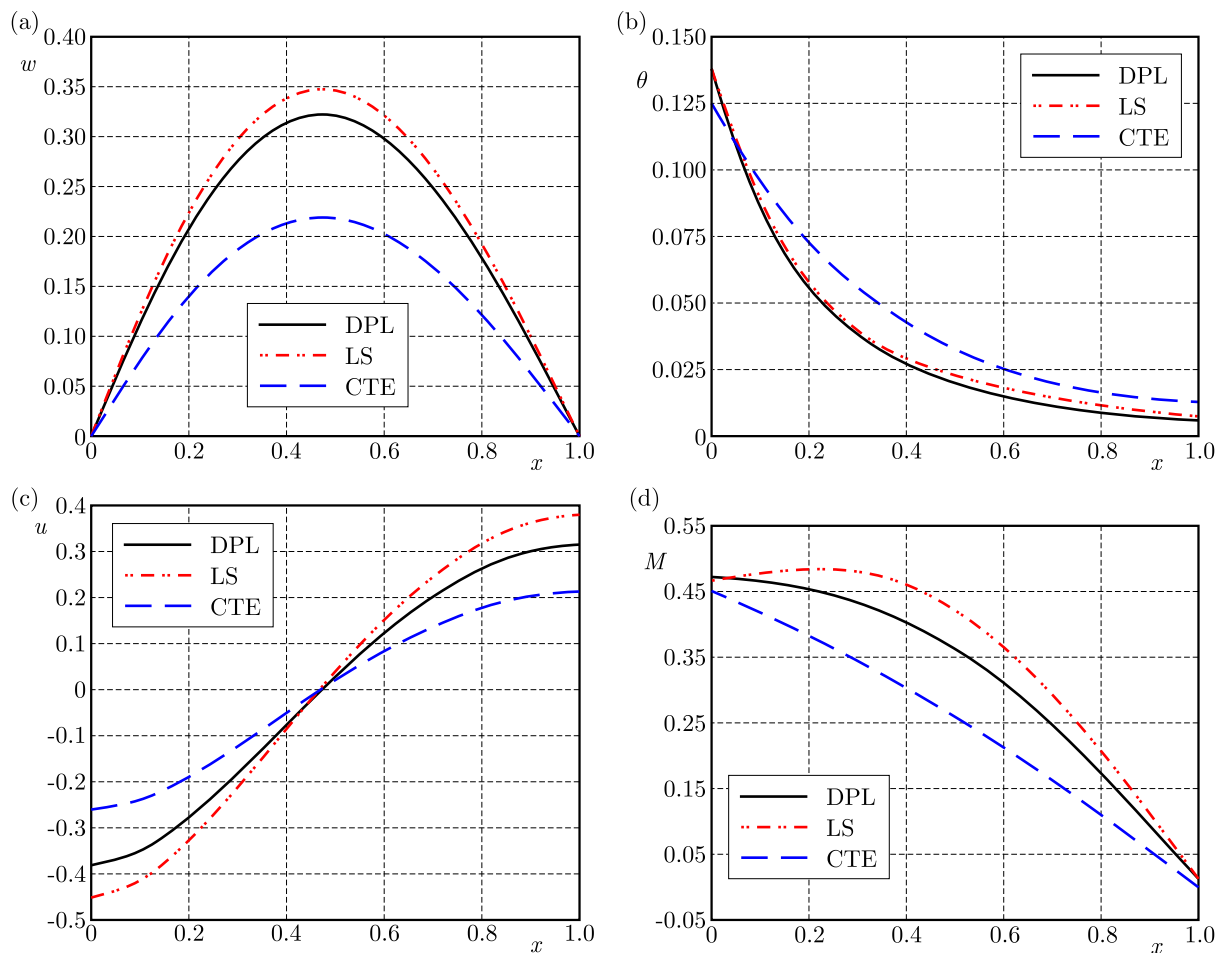


Fig. 4. The transverse deflection, temperature, displacement and bending moment distributions of the nanobeam for different values of the phase lags τ_q and τ_θ : (a) transverse deflection w versus x , (b) temperature θ versus x , (c) displacement u versus x , (d) bending moment M versus x

In the third example, Figs. 4a-4d are plotted to give a comparison of the results obtained for dimensionless lateral vibration, temperature, displacement and bending moment distributions

for different values of τ_q and τ_θ at $t_0 = 0.2$ and $\bar{\xi} = 2$. The graphs in Figs. 4a-4d represent four curves predicted by two thermoelasticity theories, the coupled theory (CTE) and the Lord-Shulman theory (LS), obtained as special cases of the dual-phase-lag model. The computations have been performed for one value of time, namely for $t = 0.12$ and various values of the parameters τ_q and τ_θ . The coupled theory (CTE) is given by setting ($\tau_\theta = \tau_q = 0$), the Lord-Shulman theory (LS) is given by putting ($\tau_\theta = 0$ and $\tau_q = \tau_0 > 0$) and the DPL is given by setting $\tau_q > 0$ and $\tau_\theta > 0$. It can be found from Figs. 4a-4d that the distribution in LS model is near to that in DPL theory, whereas the distributions in CTE theory are different from that in DPL theory. Also, values of τ_q and τ_θ can judge whether the wavelike behavior in the phase-lag heat conduction is dominant or not.

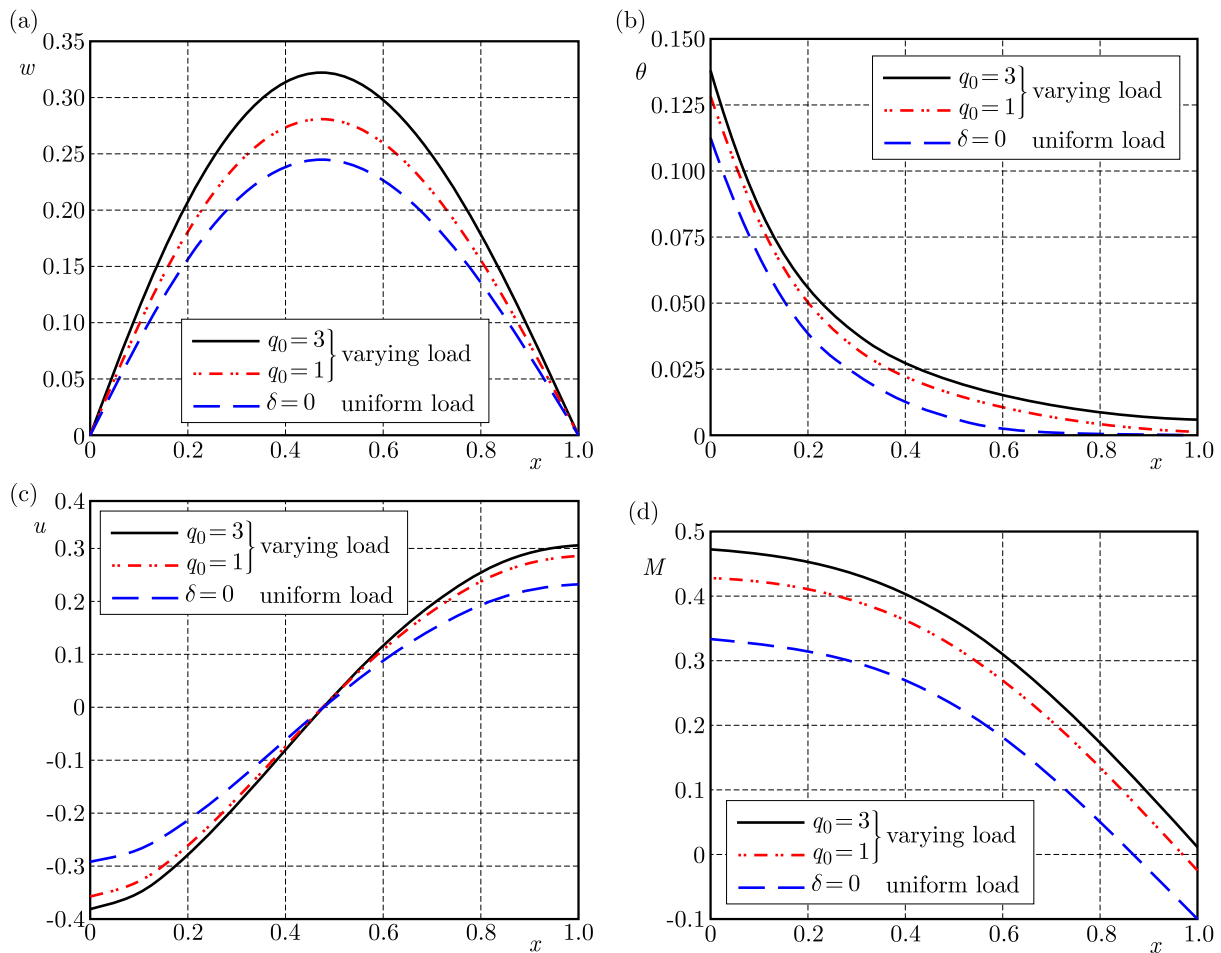


Fig. 5. The transverse deflection, temperature, displacement and bending moment distributions of the nanobeam for different values of the point load q_0 : (a) transverse deflection w versus x , (b) temperature θ versus x , (c) displacement u versus x , (d) bending moment M versus x

In the last example, three different values of the dimensionless magnitude of the point load q_0 are considered. For a uniformly distributed load, we put $\delta = 0$, and for an exponential decaying time varying load, we take $\delta = 1$. We found from Figs. 5a-5d that, as the point load q_0 increases, the values of lateral vibration, temperature, moment fields are also increasing. Once again, the displacement u increases in the interval $0 \leq x < 0.48$ and decreases in the interval $0.48 < x \leq 1$. Finally, all variables are very sensitive to the variation of the point load q_0 .

6. Conclusions

In this work, a mathematical model that governs the nonlocal generalized theory of thermoelasticity with phase lags for nanobeams subjected to dynamical transverse loads is established. The first boundary of the nanobeam is subjected to a ramp-type heating. The Laplace transformation numerical technique has been used. The effects of dynamic loads q_0 , nonlocal parameter $\bar{\xi}$ and ramping time parameter t_0 on all quantities are investigated and illustrated graphically. One can conclude, according to the numerical results shown in all figures, that:

- The nonlocal $\bar{\xi}$ and ramping time t_0 parameters have significant effects on all quantities.
- Some quantities like thermoelastic moment, displacement and temperature are strongly dependent on the ramping time parameter t_0 .
- A phenomenon of finite speeds of propagation is observed in all depicted figures. This is predictable since the thermal wave travels with a finite speed.
- The effects of dynamic loads on all the studied fields are very significant.
- Significant differences in the physical quantities are observed between the exponential decaying time varying load and the uniformly distributed load.
- Vibration of nanotubes is an important subject in the study of nanotechnology since it relates to electronic and optical properties of multiwall carbon nanotubes.
- This study is required for researchers and designers to be applied in the design and development of different devices, especially those being under environmental loads, like resonators.

References

1. ABBAS I.A., ZENKOUR A.M., 2014, Dual-phase-lag model on thermoelastic interactions in a semi-infinite medium subjected to a ramp-type heating, *Journal of Computational and Theoretical Nanoscience*, **11**, 3, 642-645
2. ABOUELREGAL A.E., 2011, Generalized thermoelasticity for an isotropic solid sphere in dual-phase-lag of heat transfer with surface heat flux, *International Journal for Computational Methods in Engineering Science and Mechanics*, **12**, 96-105
3. ABOUELREGAL A.E., ABO-DAHAB S.M., 2012, Dual phase lag model on magneto-thermoelasticity infinite non-homogeneous solid having a spherical cavity, *Journal of Thermal Stresses*, **35**, 820-841
4. ALLAMEH S.M., 2003, An introduction to mechanical-properties-related issues in MEMS structures, *Journal of Materials Science*, **38**, 4115-4123
5. AREFI M., ZENKOUR A.M., 2016, A simplified shear and normal deformations nonlocal theory for bending of functionally graded piezomagnetic sandwich nanobeams in magneto-thermo-electric environment, *Journal of Sandwich Structures and Materials*, **18**, 5, 624-651
6. ERINGEN A.C., 1983, On differential equations of nonlocal elasticity and solutions of screw dislocation and surface waves, *Journal of Applied Physics*, **54**, 4703-4710
7. ERINGEN A.C., 2002, *Nonlocal Continuum Field Theories*, New York: Springer Verlag
8. LORD H.W., SHULMAN Y., A generalized dynamical theory of thermoelasticity, *Journal of the Mechanics and Physics of Solids*, **15**, 299-309
9. TZOU D.Y., 1995, A unified approach for heat conduction from macro- to micro-scales, *Journal of Heat Transfer*, **117**, 8-16
10. TZOU D.Y., 1997, *Macro-to-Micro Scale Heat Transfer: the Lagging Behavior*, Taylor and Francis, Washington (DC)

11. YOUNIS M.I., 2011, *MEMS Linear and Non-linear Statics and Dynamics*, Springer, New York, USA, 2011
12. ZENKOUR A.M., 2016a, Nonlocal transient thermal analysis of a single-layered graphene sheet embedded in viscoelastic medium, *Physica E*, **79**, 87-97
13. ZENKOUR A.M., 2016b, Two-dimensional coupled solution for thermoelastic beams via generalized dual-phase-lags model, *Mathematical Modelling and Analysis*, **21**, 3, 319-335
14. ZENKOUR A.M., 2016c, Vibration analysis of a single-layered graphene sheet embedded in visco-Pasternak's medium using nonlocal elasticity theory, *Journal of Vibroengineering*, **18**, 4, 2319-2330
15. ZENKOUR A.M., ABOUELREGAL A.E., 2014a, Nonlocal thermoelastic vibrations for variable thermal conductivity nanobeams due to harmonically varying heat, *Journal of Vibroengineering*, **16**, 8, 3665-3678
16. ZENKOUR A.M., ABOUELREGAL A.E., 2014b, Vibration of FG nanobeams induced by sinusoidal pulse-heating via a nonlocal thermoelastic model, *Acta Mechanica*, **225**, 12, 3409-3421
17. ZENKOUR A.M., ABOUELREGAL A.E., 2015, Nonlocal thermoelastic nanobeam subjected to a sinusoidal pulse heating and temperature-dependent physical properties, *Microsystem Technologies*, **21**, 8, 1767-1776
18. ZENKOUR A.M. AND ABOUELREGAL A.E., 2016, Nonlinear effects of thermo-sensitive nanobeams via a nonlocal thermoelasticity model with relaxation time, *Microsystem Technologies*, **22**, 10, 2407-2415
19. ZENKOUR A.M., MASHAT D.S., ABOUELREGAL A.E., 2013, The effect of dual-phase-lag model on reflection of thermoelastic waves in a solid half space with variable material properties, *Acta Mechanica Solida Sinica*, **26**, 6, 659-670
20. ZHANG Y.Q., LIU G.R., XIE X.Y., 2005, Free transverse vibrations of double-walled carbon nanotubes using a theory of nonlocal elasticity, *Physical Review B*, **71**, 195 404, 2005.

Manuscript received November 24, 2016; accepted for print March 31, 2017

SOLUTIONS OF VIBRATION PROBLEMS FOR THIN INFINITE PLATES SUBJECTED TO HARMONIC LOADS

MICHAEL KLANNER, KATRIN ELLERMANN

Graz University of Technology, Institute of Mechanics, Graz, Austria

e-mail: michael.klanner@tugraz.at

New closed form solutions for harmonic vibrations of infinite Kirchhoff plates subjected to a constant harmonic ring load, a constant harmonic circular load and an alternating harmonic circular load are derived. Two different approaches are used to define the closed form solutions. The first approach uses the integration of the harmonic point force and the addition theorem for Bessel functions, while the second approach applies the Hankel transform to solve the inhomogeneous partial differential equation of the Kirchhoff plate theory. The new closed form particular solutions can especially be used in Trefftz like methods and extend their field of application.

Keyword: Kirchhoff plate theory, infinite plate, ring load, circular load, Hankel transform

1. Introduction

The simulation of vibrations and emitted sound of plates is an important step in the development of new products, since the noise and vibration characteristics have to be considered in an early design phase. The most common method to simulate vibrations of plates is the Finite Element Method (FEM) (Bathe, 2006), which is especially well applicable for low frequency vibrations. In the recent years, several methods which use the concept presented by Trefftz in 1926 (Trefftz, 1926), have been developed to calculate vibrations of plates more efficiently for higher frequencies. Among these methods one can mention the Wave Based Method (Vanmaele *et al.*, 2007; Klanner and Ellermann, 2015) and the Variational Theory of Complex Rays (VTCR) (Rouch and Ladevèze, 2003; Riou *et al.*, 2013). In general, the so-called indirect Trefftz methods require a particular solution of the inhomogeneous partial differential equation to be applied efficiently. This is the motivation to develop new closed form solutions for the vibrations of Kirchhoff plates in this paper.

To the authors knowledge, closed form particular solutions for infinite Kirchhoff plates only exist in literature for undamped plates excited by a concentrated point force, which can be found in e.g. (Junger and Feit, 1986).

The Kirchhoff plate theory was introduced by Kirchhoff in 1850 (Kirchhoff, 1850) and neglects rotatory inertia and shear deformation. Therefore, it is only applicable if the ratio of the plate thickness to the lesser of the other two dimensions is smaller than 1 : 20 (Chandrashekara, 2001) and the ratio of the plate thickness to the bending wave length is smaller than 1 : 6 (Cremer *et al.*, 2005). In many practical problems, these limits are fulfilled and the Kirchhoff plate model can be used very sufficiently compared to a full 3D model.

The paper is structured in Sections as follows: The particular solution of an infinite Kirchhoff plate excited by a concentrated point force in the case of a damped plate is derived in Section 2. In Section 3, other axisymmetric load cases, the constant ring load and the constant circular load, are considered and two different approaches are shown to determine the closed form solutions. In Section 4, a non-axisymmetric load is considered, which represents an alternating circular

load. The vibrations in the case of an undamped plate are derived in Section 5. The responses to the mentioned excitations are plotted in Section 6 for an aluminum plate. Finally, a conclusion is given and further research topics are discussed.

2. Point force excitation

In this Section, the governing equation of the Kirchhoff plate theory is stated and the governing equation in the special case of an axisymmetric vibration is shown. The Hankel transform of the order zero is briefly presented and the closed form solution for the Kirchhoff plate under harmonic point force excitation is derived.

2.1. Governing equation for time harmonic problems

The governing equation of the Kirchhoff plate theory for time harmonic vibrations in Cartesian coordinates is given by (Rao, 2007)

$$\nabla^4 w(x, y) - k_b^4 w(x, y) = \frac{q(x, y)}{D} \quad (2.1)$$

where $\nabla^4 = \frac{\partial^4}{\partial x^4} + 2\frac{\partial^4}{\partial x^2 \partial y^2} + \frac{\partial^4}{\partial y^4}$, the bending wavenumber $k_b^4 = \rho h \omega^2 / D$ and the plate bending stiffness $D = Eh^3 / [12(1 - \nu^2)]$, E is Young's modulus, h – plate thickness, ρ – plate density, ν – Poisson's ratio, ω – angular frequency and $q(x, y)$ – external force distribution. For axisymmetric problems, e.g. the point force excitation, the governing equation in polar coordinates

$$\left(\frac{d^2}{dr^2} + \frac{1}{r} \frac{d}{dr} \right)^2 w(r) - k_b^4 w(r) = \frac{q(r)}{D} \quad (2.2)$$

depends only on the radius r . Using a complex elastic modulus introduces damping of the plate, and the plate parameters become complex

$$E \rightarrow \tilde{E} = E(1 + i\eta) \quad D \rightarrow \tilde{D} = D(1 + i\eta) \quad k_b^4 \rightarrow \tilde{k}_b^4 = \frac{k_b^4}{1 + i\eta} = k_{bd}^4 e^{-i\Phi} \quad (2.3)$$

with

$$k_{bd}^4 = \frac{k_b^4}{\sqrt{1 + \eta^2}} \quad k_{bd}^4 \in \mathbb{R}^+ \quad \Phi = \arctan \eta \quad 0 < \Phi < \frac{\pi}{2} \quad (2.4)$$

and $\eta > 0$ the material loss factor.

2.2. Hankel transform of the order zero

The Hankel transform of the order zero is defined by (Debnath and Bhatta, 2014)

$$\tilde{f}(k_r) = \int_0^\infty f(r) r J_0(k_r r) dr \quad \text{and} \quad f(r) = \int_0^\infty \tilde{f}(k_r) k_r J_0(k_r r) dk_r \quad (2.5)$$

with the operational property for the axisymmetric Laplace operator (Debnath and Bhatta, 2014)

$$\left(\frac{d^2}{dr^2} + \frac{1}{r} \frac{d}{dr} \right) f(r) \mapsto -k_r^2 \tilde{f}(k_r) \quad (2.6)$$

In the case of axisymmetric vibrations, the governing equation of the Kirchhoff plate (Eq. (2.2)) transforms to

$$\tilde{w}(k_r) = \frac{1}{\tilde{D} k_r^4 - \tilde{k}_b^4} \tilde{q}(k_r) \quad (2.7)$$

2.3. Point load at the origin of the coordinate system

A point load at the origin of the coordinate system ($x = 0$, $y = 0$ or $r = 0$) is given by

$$q_{point}(x, y) = q_0 \delta(x) \delta(y) \Rightarrow q_{point}(r) = \frac{q_0 \delta(r)}{2\pi r} \mapsto \tilde{q}_{point}(k_r) = \frac{q_0}{2\pi} \quad (2.8)$$

with q_0 being the amplitude of the harmonic point load. The inverse Hankel transform leads to the solution for the out-of-plane displacement in an integral form

$$w_{point}(r) = \frac{q_0}{2\pi \tilde{D}} \int_0^\infty \frac{k_r}{k_r^4 - \tilde{k}_b^4} J_0(k_r r) dk_r \quad (2.9)$$

To obtain a closed form solution, the integral representation of the Bessel function of the first kind (Watson, 1944)

$$J_0(k_r r) = \frac{2}{\pi} \int_0^\infty \sin(k_r r \cosh u) du \quad (2.10)$$

is used in Eq. (2.9). Interchanging the order of integration leads to

$$w_{point}(r) = \frac{q_0}{\pi^2 \tilde{D}} \int_0^\infty \left(\int_0^\infty \frac{k_r}{k_r^4 - \tilde{k}_b^4} \sin(k_r r \cosh u) dk_r \right) du \quad (2.11)$$

The integral is symmetric with respect to k_r and, therefore, can be written as

$$w_{point}(r) = \frac{i q_0}{2\pi^2 \tilde{D}} \int_0^\infty \left(\int_{-\infty}^\infty \frac{k_r}{k_r^4 - \tilde{k}_b^4} e^{-i k_r r \cosh u} dk_r \right) du \quad (2.12)$$

since the integral of an odd function over a symmetric interval vanishes. The integral with respect to k_r can be performed using the residue theorem and Jordan's lemma (Mitrinović and Kečkić, 1984). The integrand in Eq. (2.12) has first order poles, if $k_r^4 - \tilde{k}_b^4 = 0$, which leads to the four poles

$$\begin{aligned} k_{r1} &= k_{bd} e^{-i\frac{\phi}{4}} && \text{with } \text{Im}(k_{r1}) < 0 \\ k_{r2} &= -k_{bd} e^{-i\frac{\phi}{4}} && \text{with } \text{Im}(k_{r2}) > 0 \\ k_{r3} &= i k_{bd} e^{-i\frac{\phi}{4}} && \text{with } \text{Im}(k_{r3}) > 0 \\ k_{r4} &= -i k_{bd} e^{-i\frac{\phi}{4}} && \text{with } \text{Im}(k_{r4}) < 0 \end{aligned} \quad (2.13)$$

with

$$k_{bd} = \sqrt[4]{\frac{k_b^4}{\sqrt{1 + \eta^2}}} \quad (2.14)$$

According to the residue theorem and Jordan's lemma (Mitrinović and Kečkić, 1984)

$$\int_{-\infty}^\infty f(x) e^{iax} dx = \begin{cases} 2\pi i \sum_{k=1}^{s^+} \text{Res} [f(z) e^{iaz}] + \pi i \sum_{k=1}^m \text{Res} [f(z) e^{iaz}] & \text{for } a > 0 \\ -2\pi i \sum_{k=1}^{s^-} \text{Res} [f(z) e^{iaz}] - \pi i \sum_{k=1}^m \text{Res} [f(z) e^{iaz}] & \text{for } a < 0 \end{cases} \quad (2.15)$$

with z_k^+ poles in the upper half plane, z_k^- poles in the lower half plane, p_k poles on the real axis and $\text{Res}[\cdot]$ for the residue at the pole. The residue for simple poles is given by (Mitrinović and Kečkić, 1984)

$$\text{Res}_{z=z_k} [f(z)e^{iaz}] = \lim_{z \rightarrow z_k} (z - z_k) f(z) e^{iaz} \tag{2.16}$$

In the integral of Eq. (2.12) the function $f(z) = z/(z^4 - \tilde{k}_b^4)$ and the parameter $a = -r \cosh u < 0$ and, therefore, according to Eq. (2.15)₂, only the poles k_{r1} and k_{r4} with the negative imaginary part contribute to the integral. The residues for these two poles are

$$\text{Res}_{z=k_{r1}} [f(z)e^{iaz}] = \frac{e^{-ir \cosh(u)\tilde{k}_b}}{4\tilde{k}_b^2} \quad \text{Res}_{z=k_{r4}} [f(z)e^{iaz}] = -\frac{e^{-r \cosh(u)\tilde{k}_b}}{4\tilde{k}_b^2} \tag{2.17}$$

with

$$\tilde{k}_b^2 = k_{bd}^2 e^{-i\frac{\varphi}{2}} \quad \tilde{k}_b = k_{bd} e^{-i\frac{\varphi}{4}} \tag{2.18}$$

Using Heine’s formulas for the integral representation of the Hankel functions (Magnus *et al.*, 1966)

$$\begin{aligned} H_0^{(1)}(z) &= -\frac{2i}{\pi} \int_0^\infty e^{iz \cosh u} du & 0 < \arg(z) < \pi \\ H_0^{(2)}(z) &= \frac{2i}{\pi} \int_0^\infty e^{-iz \cosh u} du & -\pi < \arg(z) < 0 \end{aligned} \tag{2.19}$$

leads to the final result

$$w_{point}(r) = \frac{iq_0}{8\tilde{D}\tilde{k}_b^2} \left(H_0^{(1)}(-r\tilde{k}_b) + H_0^{(2)}(-ir\tilde{k}_b) \right) \tag{2.20}$$

The result in Eq. (2.20) can be given in different forms using the relations (Abramowitz and Stegun, 1972)

$$\begin{aligned} K_0(z) &= \frac{1}{2}\pi i H_0^{(1)}(iz) & -\pi < \arg(z) \leq \frac{1}{2}\pi \\ K_0(z) &= -\frac{1}{2}\pi i H_0^{(2)}(-iz) & -\frac{1}{2}\pi < \arg(z) \leq \pi \\ H_0^{(1)}(iz) &= -H_0^{(2)}(-iz) & -\frac{1}{2}\pi < \arg(z) \leq \frac{1}{2}\pi \end{aligned} \tag{2.21}$$

which leads to

$$w_{point}(r) = \frac{q_0}{4\pi\tilde{D}\tilde{k}_b^2} \left(K_0(ir\tilde{k}_b) - K_0(r\tilde{k}_b) \right) = \frac{iq_0}{8\tilde{D}\tilde{k}_b^2} \left(H_0^{(2)}(-ir\tilde{k}_b) - H_0^{(2)}(r\tilde{k}_b) \right) \tag{2.22}$$

The displacement at $r = 0$ can be computed with the limiting case $r \rightarrow 0$

$$w_{point}(0) = \lim_{r \rightarrow 0} w_{point}(r) = -\frac{iq_0}{8\tilde{D}\tilde{k}_b^2} \tag{2.23}$$

2.4. Point load at an arbitrary point of the coordinate system

The out-of-plane displacement w_{point} depends only on the distance between the response point (x, y) and the point of excitation (\bar{x}, \bar{y}) , which is given by $r = \sqrt{(x - \bar{x})^2 + (y - \bar{y})^2}$. The out-of-plane displacement of the plate subject to a point force at the drive point (\bar{x}, \bar{y}) is, therefore, given by

$$w_{point}(x, y) = \frac{iq_0}{8\tilde{D}\tilde{k}_b^2} \left(H_0^{(1)}\left(-\sqrt{(x - \bar{x})^2 + (y - \bar{y})^2}\tilde{k}_b\right) + H_0^{(2)}\left(-i\sqrt{(x - \bar{x})^2 + (y - \bar{y})^2}\tilde{k}_b\right) \right) \quad (2.24)$$

Using a coordinate transformation to polar coordinates with

$$x = r \cos \varphi \quad y = r \sin \varphi \quad \bar{x} = \bar{r} \cos \bar{\varphi} \quad \bar{y} = \bar{r} \sin \bar{\varphi} \quad (2.25)$$

leads to

$$w_{point}(r, \varphi) = \frac{iq_0}{8\tilde{D}\tilde{k}_b^2} \left(H_0^{(1)}\left(-\sqrt{r^2 + \bar{r}^2 - 2r\bar{r}\cos(\varphi - \bar{\varphi})}\tilde{k}_b\right) + H_0^{(2)}\left(-i\sqrt{r^2 + \bar{r}^2 - 2r\bar{r}\cos(\varphi - \bar{\varphi})}\tilde{k}_b\right) \right) \quad (2.26)$$

3. Other axisymmetric loadings

In this Section, the solutions for a constant ring load and a constant circular load, shown in Figs. 1a and 1b, are derived. Two different solution techniques are shown. The first technique uses the integration of the point force response given in Eq. (2.26), which was also used in (Matrinček, 1994) for the dynamic response of pavement structures. The second approach uses the Hankel transform defined in Eqs. (2.5) to obtain the results.

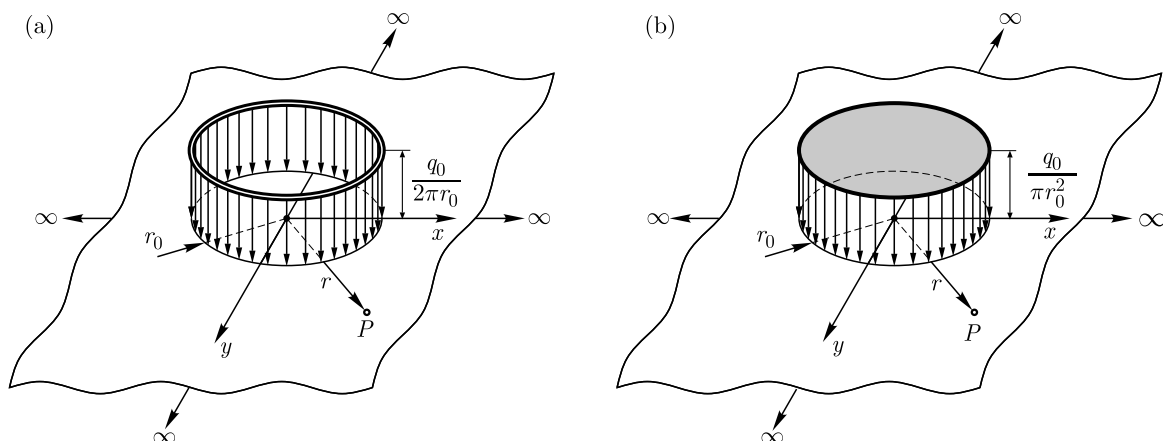


Fig. 1. Other axisymmetric load cases: (a) constant ring load, (b) constant circular load

3.1. Constant ring load

The constant ring load in Fig. 1a is given by

$$q_{ring}(r) = \frac{q_0}{2\pi r} \delta(r - r_0) \quad (3.1)$$

with $\delta(\cdot)$ being the Dirac delta function, r_0 – radius of the ring load and q_0 – total external force. According to the theory of linear partial differential equations, the response to an arbitrary load can be found by integration of the point force solution (harmonic Green’s function). This leads to

$$\begin{aligned}
 w_{ring}(r, \varphi) &= \int_0^\infty \left(\int_0^{2\pi} q_{ring}(\bar{r}) w_{point}(r, \varphi, \bar{r}, \bar{\varphi}) \bar{r} \, d\bar{\varphi} \right) d\bar{r} \\
 &= \frac{iq_0}{16\pi \tilde{D} \tilde{k}_b^2} \int_0^\infty \left(\int_0^{2\pi} \frac{\delta(\bar{r} - r_0)}{\bar{r}} \left(H_0^{(1)}(-a\tilde{k}_b) + H_0^{(2)}(-ia\tilde{k}_b) \right) \bar{r} \, d\bar{\varphi} \right) d\bar{r}
 \end{aligned} \tag{3.2}$$

with $a = \sqrt{r^2 + \bar{r}^2 - 2r\bar{r} \cos(\varphi - \bar{\varphi})}$. The integration with respect to $\bar{\varphi}$ can be carried out using the addition theorem for Bessel functions (Magnus *et al.*, 1966)

$$H_0^{(n)}(\gamma z) = J_0(\gamma\rho)H_0^{(n)}(\gamma\bar{\rho}) + 2 \sum_{m=1}^\infty J_m(\gamma\rho)H_m^{(n)}(\gamma\bar{\rho}) \cos(m\psi) \quad \begin{matrix} n = 1, 2 \\ \bar{\rho} > \rho \end{matrix} \tag{3.3}$$

with $z = \sqrt{\rho^2 + \bar{\rho}^2 - 2\rho\bar{\rho} \cos\psi}$. Using that the integral

$$\int_0^{2\pi} \cos(m(\varphi - \bar{\varphi})) \, d\bar{\varphi} = 0 \quad \text{for } m = 1, 2, \dots \tag{3.4}$$

leads to

$$w_{ring}(r) = \begin{cases} \frac{iq_0}{8\tilde{D}\tilde{k}_b^2} \int_0^\infty \delta(\bar{r} - r_0) \left(J_0(-\tilde{k}_b\bar{r})H_0^{(1)}(-\tilde{k}_br) + J_0(-i\tilde{k}_b\bar{r})H_0^{(2)}(-i\tilde{k}_br) \right) d\bar{r} & r > \bar{r} \\ \frac{iq_0}{8\tilde{D}\tilde{k}_b^2} \int_0^\infty \delta(\bar{r} - r_0) \left(J_0(-\tilde{k}_br)H_0^{(1)}(-\tilde{k}_b\bar{r}) + J_0(-i\tilde{k}_br)H_0^{(2)}(-i\tilde{k}_b\bar{r}) \right) d\bar{r} & r < \bar{r} \end{cases} \tag{3.5}$$

Using the integral property of the dirac delta function gives the final result

$$w_{ring}(r) = \begin{cases} \frac{iq_0}{8\tilde{D}\tilde{k}_b^2} \left(J_0(-\tilde{k}_br_0)H_0^{(1)}(-\tilde{k}_br) + J_0(-i\tilde{k}_br_0)H_0^{(2)}(-i\tilde{k}_br) \right) & r > r_0 \\ \frac{iq_0}{8\tilde{D}\tilde{k}_b^2} \left(J_0(-\tilde{k}_br)H_0^{(1)}(-\tilde{k}_br_0) + J_0(-i\tilde{k}_br)H_0^{(2)}(-i\tilde{k}_br_0) \right) & r < r_0 \end{cases} \tag{3.6}$$

The function depends only on r , and it is obvious that the function is continuous at $r = r_0$.

Another possibility to get the result is the Hankel transform. The Hankel transform of the constant ring load is given by

$$q_{ring}(r) = \frac{q_0}{2\pi r} \delta(r - r_0) \mapsto \tilde{q}_{ring}(k_r) = \frac{q_0}{2\pi} J_0(k_r r_0) \tag{3.7}$$

and combined with the transformed governing equation (Eq. (2.7)), the result in an integral form is given by

$$w_{ring}(r) = \frac{q_0}{2\pi \tilde{D}} \int_0^\infty \frac{k_r}{k_r^4 - \tilde{k}_b^4} J_0(k_r r_0) J_0(k_r r) \, dk_r \tag{3.8}$$

The result of this integral can be found by the general formula for integrals involving products of two Bessel functions (Lin, 2014)

$$\int_0^{\infty} \frac{x^{\mu-\nu+2\ell+1}}{x^2+a^2} J_{\mu}(px) J_{\nu}(qx) dx = (-1)^{\ell} a^{\mu-\nu+2\ell} K_{\mu}(pa) I_{\nu}(qa) \quad \ell \in \mathbb{N}_0 \quad (3.9)$$

with the restrictions

$$-(\ell+1) < \operatorname{Re}(\mu) < \operatorname{Re}(\nu) - 2\ell + 2 \quad \text{and} \quad p > q \quad \text{and} \quad -\frac{\pi}{2} < \arg(a) < \frac{\pi}{2} \quad (3.10)$$

Choosing $\mu = 0$, $\nu = 0$ and $\ell = 0$ and the partial fraction decomposition

$$\frac{k_r}{k_r^4 - \tilde{k}_b^4} = \frac{1}{2\tilde{k}_b^2} \left(\frac{k_r}{k_r^2 + (-\tilde{k}_b^2)} - \frac{k_r}{k_r^2 + \tilde{k}_b^2} \right) \quad (3.11)$$

leads to the final result

$$w_{ring}(r) = \begin{cases} \frac{q_0}{4\pi \tilde{D} \tilde{k}_b^2} \left(K_0(i\tilde{k}_b r) I_0(i\tilde{k}_b r_0) - K_0(\tilde{k}_b r) I_0(\tilde{k}_b r_0) \right) & r > r_0 \\ \frac{q_0}{4\pi \tilde{D} \tilde{k}_b^2} \left(K_0(i\tilde{k}_b r_0) I_0(i\tilde{k}_b r) - K_0(\tilde{k}_b r_0) I_0(\tilde{k}_b r) \right) & r < r_0 \end{cases} \quad (3.12)$$

Using the relations in Eqs. (2.21) and the relation (Abramowitz and Stegun, 1972)

$$I_0(z) = J_0(iz) \quad -\pi < \arg(z) \leq \frac{1}{2}\pi \quad (3.13)$$

the results in Eqs. (3.6) become equivalent to Eqs. (3.12).

3.2. Constant circular load

The constant circular load in Fig. 1b is given by

$$q_{circ}(r) = \frac{q_0}{r_0^2 \pi} H(r_0 - r) \quad (3.14)$$

where $H(\cdot)$ is the Heaviside step function, r_0 – radius of the circular load and q_0 – total external force. The integration of the point load response leads to

$$\begin{aligned} w_{circ}(r, \varphi) &= \int_0^{\infty} \int_0^{2\pi} q_{circ}(\bar{r}) w_{point}(r, \varphi, \bar{r}, \bar{\varphi}) \bar{r} d\bar{\varphi} d\bar{r} \\ &= \frac{iq_0}{8\pi r_0^2 \tilde{D} \tilde{k}_b^2} \int_0^{\infty} \int_0^{2\pi} H(r_0 - \bar{r}) \left(H_0^{(1)}(-a\tilde{k}_b) + H_0^{(2)}(-ia\tilde{k}_b) \right) \bar{r} d\bar{\varphi} d\bar{r} \end{aligned} \quad (3.15)$$

The integration with respect to $\bar{\varphi}$ is equivalent to integration from Eq. (3.2) to Eqs. (3.5). Using the property of the Heaviside step function and distinguishing between the case $r > r_0$ and $r < r_0$ leads to

$$w_{circ}(r) = \begin{cases} \frac{iq_0}{4r_0^2 \tilde{D} \tilde{k}_b^2} \int_0^{r_0} \left(J_0(-\tilde{k}_b \bar{r}) H_0^{(1)}(-\tilde{k}_b r) + J_0(-i\tilde{k}_b \bar{r}) H_0^{(2)}(-i\tilde{k}_b r) \right) \bar{r} d\bar{r} & r > r_0 \\ \frac{iq_0}{4r_0^2 \tilde{D} \tilde{k}_b^2} \left(\int_0^r \left(J_0(-\tilde{k}_b \bar{r}) H_0^{(1)}(-\tilde{k}_b r) + J_0(-i\tilde{k}_b \bar{r}) H_0^{(2)}(-i\tilde{k}_b r) \right) \bar{r} d\bar{r} \right. \\ \quad \left. + \int_r^{r_0} \left(J_0(-\tilde{k}_b r) H_0^{(1)}(-\tilde{k}_b \bar{r}) + J_0(-i\tilde{k}_b r) H_0^{(2)}(-i\tilde{k}_b \bar{r}) \right) \bar{r} d\bar{r} \right) & r < r_0 \end{cases} \quad (3.16)$$

The recurrence formulas for Bessel and Hankel functions are given by (Watson, 1944)

$$\begin{aligned} \frac{d}{dz} (zJ_1(z)) &= zJ_0(z) \quad \rightarrow \quad zJ_1(z) = \int zJ_0(z) dz \\ \frac{d}{dz} (zH_1^{(n)}(z)) &= zH_0^{(n)}(z) \quad \rightarrow \quad zH_1^{(n)}(z) = \int zH_0^{(n)}(z) dz \quad n = 1, 2 \end{aligned} \tag{3.17}$$

which allows the evaluation of the integrals in Eqs. (3.16). The final results are given by

$$w_{circ}(r) = \begin{cases} \frac{-iq_0}{4r_0 \tilde{D} \tilde{k}_b^2} \left(\frac{1}{\tilde{k}_b} J_1(-\tilde{k}_b r_0) H_0^{(1)}(-\tilde{k}_b r) + \frac{1}{i\tilde{k}_b} J_1(-i\tilde{k}_b r_0) H_0^{(2)}(-i\tilde{k}_b r) \right) & r > r_0 \\ \frac{-iq_0}{4r_0^2 \tilde{D} \tilde{k}_b^2} \left(\frac{4}{i\pi \tilde{k}_b^2} + \frac{r_0}{\tilde{k}_b} J_0(-\tilde{k}_b r) H_1^{(1)}(-\tilde{k}_b r_0) + \frac{r_0}{i\tilde{k}_b} J_0(-i\tilde{k}_b r) H_1^{(2)}(-i\tilde{k}_b r_0) \right) & r < r_0 \end{cases} \tag{3.18}$$

In the computation of Eq. (3.18)₂, the formulas for Wronskian determinants of Bessel functions (Magnus *et al.*, 1966)

$$\begin{aligned} J_1(z)H_0^{(1)}(z) - J_0(z)H_1^{(1)}(z) &= \frac{2}{i\pi z} \\ J_1(z)H_0^{(2)}(z) - J_0(z)H_1^{(2)}(z) &= -\frac{2}{i\pi z} \end{aligned} \tag{3.19}$$

are used.

The response of the plate to a constant circular load can also be derived using the Hankel transform. Inserting the Hankel transform of a constant circular load

$$q_{circ}(r) = \frac{q_0}{r_0^2 \pi} H(r_0 - r) \mapsto \tilde{q}_{circ}(k_r) = \frac{q_0}{r_0 \pi k_r} J_1(k_r r_0) \tag{3.20}$$

in transformed governing equation (Eq. (2.7)) leads to

$$w_{circ}(r) = \frac{q_0}{r_0 \pi \tilde{D}} \int_0^\infty \frac{1}{k_r^4 - \tilde{k}_b^4} J_1(k_r r_0) J_0(k_r r) dk_r \tag{3.21}$$

The integral in Eq. (3.21) can be evaluated using the general formula from Eq. (3.9). The partial fraction decomposition

$$\frac{1}{k_r^4 - \tilde{k}_b^4} = \frac{1}{2\tilde{k}_b^2} \left(\frac{1}{k_r^2 + (-\tilde{k}_b^2)} - \frac{1}{k_r^2 + \tilde{k}_b^2} \right) \tag{3.22}$$

and the parameters $\mu = 0, \nu = 1$ and $l = 0$ lead to the result for $r > r_0$. The result for $r < r_0$ can be found by expanding the partial fraction decomposition in Eq. (3.22) to

$$\frac{1}{2\tilde{k}_b^2} \left(\frac{1}{k_r^2 + (-\tilde{k}_b^2)} - \frac{1}{k_r^2 + \tilde{k}_b^2} \right) = \frac{1}{2\tilde{k}_b^4} \left(-2 + \frac{k_r^2}{k_r^2 + (-\tilde{k}_b^2)} + \frac{k_r^2}{k_r^2 + \tilde{k}_b^2} \right) \tag{3.23}$$

The integrals involving the rational functions can be evaluated using Eq. (3.9) with the parameters $\mu = 1, \nu = 0$ and $l = 0$, while the integral with the constant factor is a discontinuous Weber-Schafheitlin integral (Watson, 1944)

$$\int_0^\infty J_0(at)J_1(bt) dt = \begin{cases} 0 & b < a \\ \frac{1}{b} & b > a \end{cases} \tag{3.24}$$

The final results are

$$w_{circ}(r) = \begin{cases} \frac{-q_0}{2r_0\pi\tilde{D}\tilde{k}_b^2} \left(\frac{1}{\tilde{k}_b} I_1(\tilde{k}_b r_0) K_0(\tilde{k}_b r) - \frac{1}{i\tilde{k}_b} I_1(i\tilde{k}_b r_0) K_0(i\tilde{k}_b r) \right) & r > r_0 \\ \frac{-q_0}{2r_0^2\pi\tilde{D}\tilde{k}_b^2} \left(\frac{2}{\tilde{k}_b^2} - \frac{r_0}{\tilde{k}_b} I_0(\tilde{k}_b r) K_1(\tilde{k}_b r_0) + \frac{r_0}{i\tilde{k}_b} I_0(i\tilde{k}_b r) K_1(i\tilde{k}_b r_0) \right) & r < r_0 \end{cases} \quad (3.25)$$

Using the relations between the Bessel functions, the results become equivalent to the results in Eqs. (3.18).

4. Non-axisymmetric loading

A closed-form solution for the out-of-plane displacement of a plate can also be calculated for certain types of non-axisymmetric loading by the integration of the point force response. Especially, the loading shown in Fig. 2 has a practical value, since it appears when a circular cylinder is mounted to a plate and loaded with a harmonic horizontal force (Korenev, 2002).

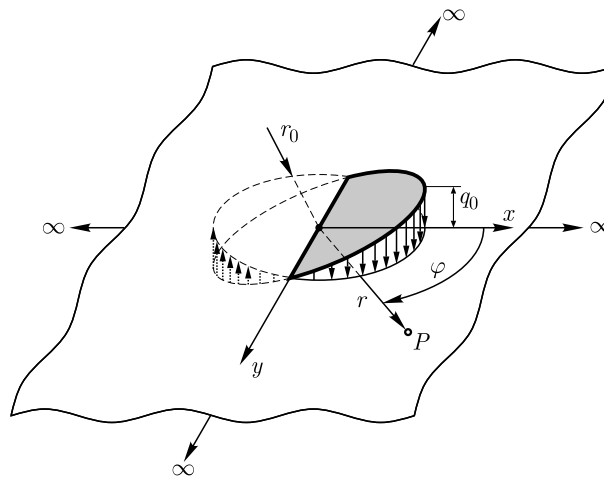


Fig. 2. Alternating circular load

The load shown in Fig. 2 is given in the polar coordinates by

$$q_{nonaxi}(r, \varphi) = \frac{q_0 r}{r_0} H(r_0 - r) \cos \varphi. \quad (4.1)$$

Integrating the point load response leads to

$$\begin{aligned} w_{nonaxi}(r, \varphi) &= \int_0^\infty \left(\int_0^{2\pi} q_{nonaxi}(\bar{r}, \bar{\varphi}) w_{point}(r, \varphi, \bar{r}, \bar{\varphi}) \bar{r} d\bar{\varphi} \right) d\bar{r} \\ &= \frac{iq_0}{8r_0\tilde{D}\tilde{k}_b^2} \int_0^\infty \left(\int_0^{2\pi} H(r_0 - \bar{r}) \left(H_0^{(1)}(-a\tilde{k}_b) + H_0^{(2)}(-ia\tilde{k}_b) \right) \bar{r}^2 \cos \bar{\varphi} d\bar{\varphi} \right) d\bar{r} \end{aligned} \quad (4.2)$$

The integration with respect to $\bar{\varphi}$ can be carried out using the addition theorem for Bessel functions, given in Eq. (3.3) and the integral

$$\int_0^{2\pi} \cos \bar{\varphi} \cos(n(\varphi - \bar{\varphi})) d\bar{\varphi} = \begin{cases} \pi \cos \varphi & n = 1 \\ 0 & n \in \mathbb{N}_0 | n \neq 1 \end{cases} \quad (4.3)$$

Using the property of the Heaviside step function and distinguishing between the case $r > r_0$ and $r < r_0$, the integrals with respect to \bar{r} are given by

$$w_{nonaxi}(r, \varphi) = \begin{cases} \frac{iq_0\pi \cos \varphi}{4r_0\tilde{D}\tilde{k}_b^2} \int_0^{r_0} \left(J_1(-\tilde{k}_b\bar{r})H_1^{(1)}(-\tilde{k}_br) + J_1(-i\tilde{k}_b\bar{r})H_1^{(2)}(-i\tilde{k}_br) \right) \bar{r}^2 d\bar{r} & r > r_0 \\ \frac{iq_0\pi \cos \varphi}{4r_0\tilde{D}\tilde{k}_b^2} \left(\int_0^r \left(J_1(-\tilde{k}_b\bar{r})H_1^{(1)}(-\tilde{k}_br) + J_1(-i\tilde{k}_b\bar{r})H_1^{(2)}(-i\tilde{k}_br) \right) \bar{r}^2 d\bar{r} \right. \\ \quad \left. + \int_r^{r_0} \left(J_1(-\tilde{k}_b\bar{r})H_1^{(1)}(-\tilde{k}_b\bar{r}) + J_1(-i\tilde{k}_b\bar{r})H_1^{(2)}(-i\tilde{k}_b\bar{r}) \right) \bar{r}^2 d\bar{r} \right) & r < r_0 \end{cases} \quad (4.4)$$

Using the recurrence formulas for Bessel and Hankel functions (Watson, 1944)

$$\begin{aligned} \frac{d}{dz} \left(z^2 J_2(z) \right) &= z^2 J_1(z) \quad \rightarrow \quad z^2 J_2(z) = \int z^2 J_1(z) dz \\ \frac{d}{dz} \left(z^2 H_2^{(n)}(z) \right) &= z^2 H_1^{(n)}(z) \quad \rightarrow \quad z^2 H_2^{(n)}(z) = \int z^2 H_1^{(n)}(z) dz \quad n = 1, 2 \end{aligned} \quad (4.5)$$

and the formulas for Wronskian determinants of the Bessel functions given in Eqs. (3.19), the integration with respect to \bar{r} leads to the final result

$$w_{nonaxi}(r) = \begin{cases} \frac{-iq_0\pi r_0 \cos \varphi}{4\tilde{D}\tilde{k}_b^2} \left(\frac{1}{\tilde{k}_b} J_2(-\tilde{k}_br_0)H_1^{(1)}(-\tilde{k}_br) \right. \\ \quad \left. + \frac{1}{i\tilde{k}_b} J_2(-i\tilde{k}_br_0)H_1^{(2)}(-i\tilde{k}_br) \right) & r > r_0 \\ \frac{-iq_0\pi \cos \varphi}{4\tilde{D}\tilde{k}_b^2} \left(\frac{4r}{ir_0\tilde{k}_b^2\pi} + \frac{r_0}{\tilde{k}_b} J_1(-\tilde{k}_br)H_2^{(1)}(-\tilde{k}_br_0) \right. \\ \quad \left. + \frac{r_0}{i\tilde{k}_b} J_1(-i\tilde{k}_br)H_2^{(2)}(-i\tilde{k}_br_0) \right) & r < r_0 \end{cases} \quad (4.6)$$

5. Limit absorption principle – the undamped plate

The limit absorption principle states that a purely elastic solid is an idealization of a weakly absorbing material and, therefore, the solution of the undamped plate can be found by the limiting case $\eta \rightarrow 0$ and $\Phi \rightarrow 0$ (Filippi, 2010). Replacing $\tilde{D} \rightarrow D$ and $\tilde{k}_b \rightarrow k_b$ in Eqs. (2.20), (3.6), (3.18) and (4.6) gives the resulting displacement of the undamped plate. The solution for the point force excitation in Eq. (2.20) becomes identical to the solutions, which can be found in the literature, e.g. (Vanmaele *et al.*, 2007) for the undamped plate.

6. Numerical example

In this Section, the harmonic response of an infinite aluminium plate with a Young’s modulus $E = 7 \cdot 10^{10} \text{ N/m}^2$, Poisson’s ratio $\nu = 0.3$, density $\rho = 2790 \text{ kg/m}^3$, material loss factor $\eta = 0.001$ and thickness $h = 0.002 \text{ m}$ is shown. For all load cases, the excitation frequency is $f = 50 \text{ Hz}$.

The real and imaginary part of the out-of-plane displacement w of the plate excited by a harmonic point force ($q_0 = 1 \text{ N}$), harmonic constant ring load ($q_0 = 1 \text{ N}$, $r_0 = 2.5 \text{ m}$), harmonic constant circular load ($q_0 = 1 \text{ N}$, $r_0 = 2.5 \text{ m}$) and a harmonic alternating circular load ($q_0 = 1 \text{ N}$, $r_0 = 2.5 \text{ m}$) is shown in Figs. 3-6. The point load solution shows the highest displacement amplitude at the center of the excitation ($r = 0$).

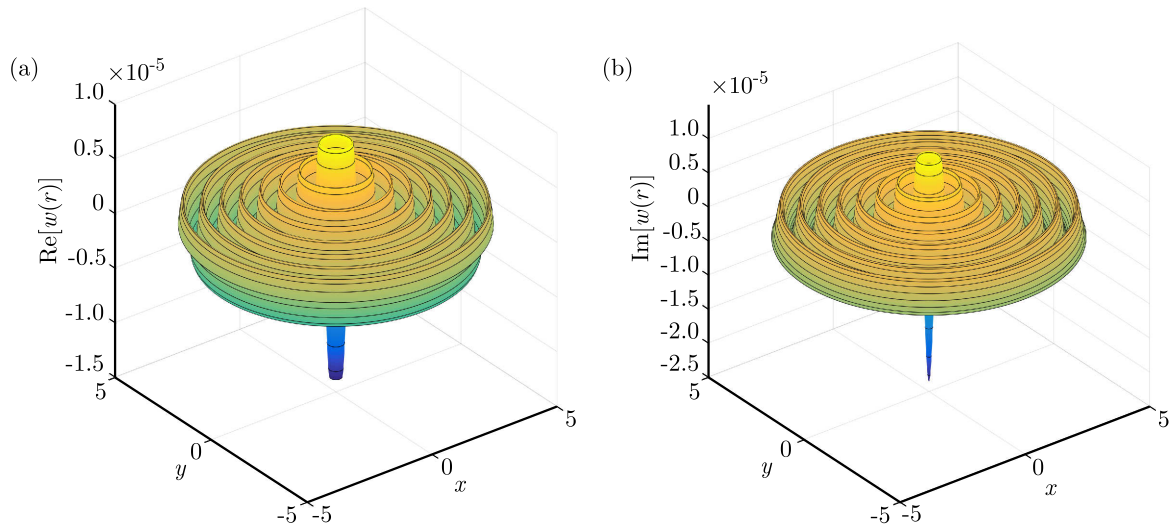


Fig. 3. Plate response to a harmonic point load: (a) real part of $w(r)$, (b) imaginary part of $w(r)$

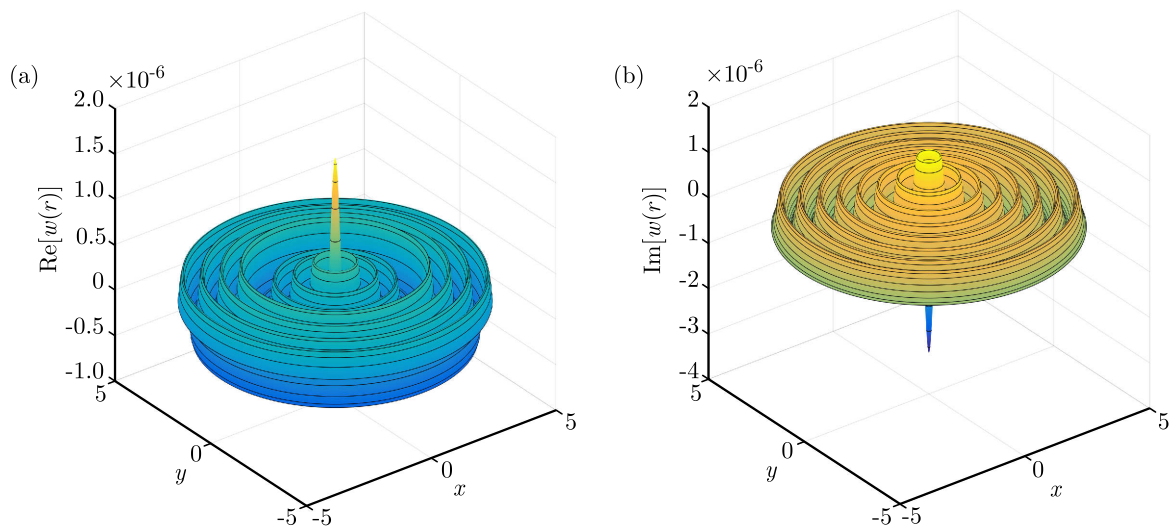


Fig. 4. Plate response to a harmonic ring load: (a) real part of $w(r)$, (b) imaginary part of $w(r)$

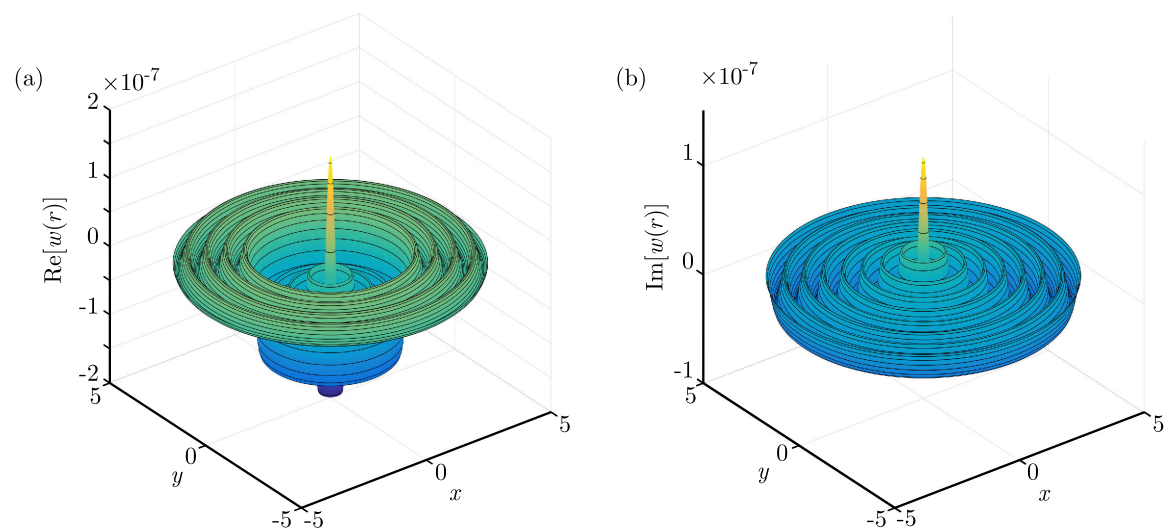


Fig. 5. Plate response to a harmonic circular load: (a) real part of $w(r)$, (b) imaginary part of $w(r)$

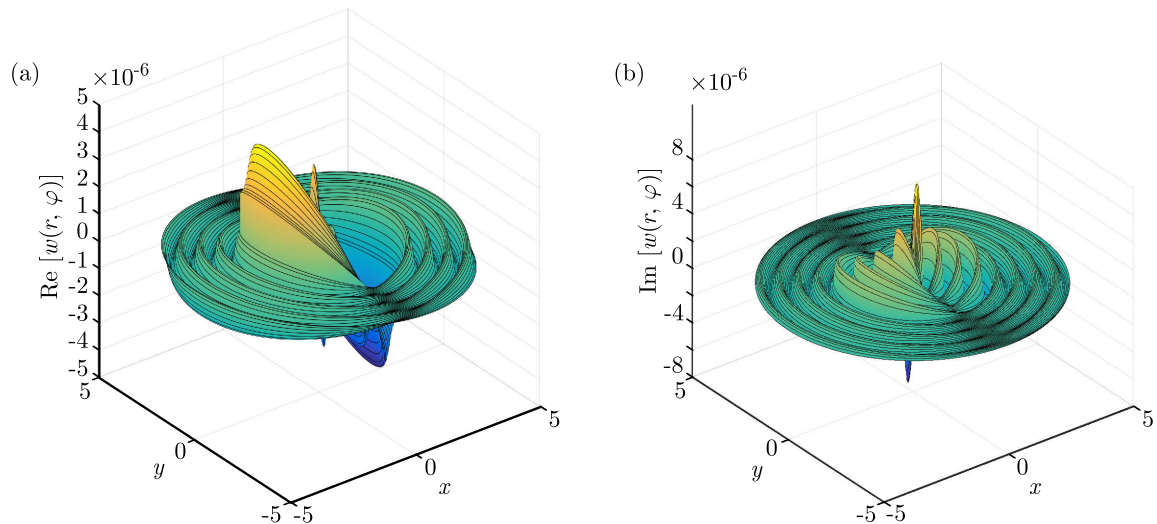


Fig. 6. Plate response to a harmonic alternating circular load: (a) real part of $w(r, \varphi)$, (b) imaginary part of $w(r, \varphi)$

7. Conclusion and future research topics

New closed-form solutions for the harmonic vibrations of infinite Kirchhoff plates have been developed for different load cases. The response to a harmonic point load has been reviewed and two different techniques, the Hankel transform and the integration of the point load solution, have been used to calculate the response to a harmonic ring load, harmonic circular load and a harmonic alternating circular load. The new particular solutions can be used to extend the applicability of indirect Trefftz methods for the analysis of forced Kirchhoff plate vibrations.

References

1. ABRAMOWITZ M., STEGUN I., 1972, *Handbook of Mathematical Functions: with Formulas, Graphs, and Mathematical Tables*, New York, Dover Publications
2. BATHE K., 2006, *Finite Element Procedures*, New Jersey, Prentice Hall
3. CHANDRASHEKHARA K., 2001, *Theory of Plates*, Hyderabad, Universities Press
4. CREMER L., HECKL M., PETERSSON B., 2005, *Structure-Born Sound*, Berlin, Springer Verlag
5. DEBNATH L., BHATTA D., 2014, *Integral Transforms and Their Applications*, Boca Raton, CRC Press
6. FILIPPI P.J.T., 2010, *Vibrations and Acoustic Radiation of Thin Structures: Physical Basis, Theoretical Analysis and Numerical Methods*, Hoboken, Wiley
7. JUNGER M.C., FEIT D., 1986, *Sound, Structures, and their Interaction*, Massachusetts, MIT Press
8. KIRCHHOFF B., 1850, Über das Gleichgewicht und die Bewegung einer elastischen Scheibe, *Journal für die reine und angewandte Mathematik*, **40**, 51-88
9. KLANNER M., ELLERMANN K., 2015, Wave Based Method for the steady-state vibrations of thick plates, *Journal of Sound and Vibration*, **345**, 146-161
10. KORENEV B., 2002, *Bessel Functions and their Applications*, London, Taylor & Francis
11. LIN Q.-G., 2014, Infinite integrals involving Bessel functions by an improved approach of contour integration and the residue theorem, *The Ramanujan Journal*, **35**, 3, 443-466

12. MAGNUS W., OBERHETTINGER F., SONI R., 1966, *Formulas and Theorems for the Special Functions of Mathematical Physics*, Berlin, Springer Verlag
13. MARTINČEK G., 1994, *Dynamics of Pavement Structures*, London, Taylor & Francis
14. MITRINOVIĆ D., KEČKIĆ J., 1984, *The Cauchy Method of Residues*, Dordrecht, D. Reidel Publishing Company
15. RAO S. 2007, *Vibration of Continuous Systems*, New Jersey, Wiley
16. RIOU H., LADEVÈZE P., KOVALEVSKY L., 2013, The variational theory of complex rays: An answer to the resolution of mid-frequency 3D engineering problems, *Journal of Sound and Vibration*, **332**, 1947-1960
17. ROUCH P., LADEVÈZE P., 2003, The variational theory of complex rays: A predictive tool for medium-frequency vibrations, *Computer Methods in Applied Mechanics and Engineering*, **192**, 28/30, 3301-3315
18. TREFFTZ E., 1926, Ein Gegenstück zum Ritzschen Verfahren, *Proceedings of the 2nd International Congress of Applied Mechanics*, Zurich, Orell Fussli Verlag, 131-137
19. VANMAELE C., VANDEPITTE D., DESMET W., 2007, An efficient wave based prediction technique for plate bending vibrations, *Computer Methods in Applied Mechanics and Engineering*, **196**, 3178-3189
20. WATSON G., 1944, *A Treatise on the Theory of Bessel Functions*, London, Cambridge University Press

Manuscript received November 1, 2016; accepted for print April 5, 2017

INFLUENCE OF FLIGHT CONTROL LAW ON SPIN DYNAMICS OF AERODYNAMICALLY ASYMMETRIC AIRCRAFT

BILAL MALIK

*Avionics Department, Institute of Avionics and Aeronautics, Air University, Islamabad, Pakistan
e-mail: ahmedbilal786@yahoo.com*

SUHAIL AKHTAR

Department of Avionics Engineering, CAE, NUST, Rislapur, Pakistan; e-mail: suhail@cae.nust.edu.pk

JAHANZEB MASOOD

*Mechanical Engineering Department, Institute of Avionics and Aeronautics, Air University, Islamabad, Pakistan
e-mail: jehanzeb.masud@mail.au.edu.pk*

In this paper, we analyze the spin dynamics of an aerodynamically asymmetric aircraft in open-loop configuration and also evaluate the performance of gain scheduled flight control law in improving dynamic characteristics of aircraft spin. A look-up tables based aerodynamic model is developed from static, coning and oscillatory coning rotary balance wind tunnel test data. As a starting point, all possible steady spin modes are identified by solving the aircraft dynamic model comprising moment equations. The influence of high-alpha yawing moment asymmetry on predicted right and left spin modes is discussed. Six degree of freedom simulations of left and right flat spins are performed in open-loop and closed-loop configurations with the flight control law. Our studies reveal that large amplitude oscillations in the angle of attack and sideslip observed in the open-loop configuration are significantly damped by the control law. The control law reduces the recovery time of the left flat spin. However, the aircraft natural tendency to rotate rightwards due to yawing moment asymmetry at high angles of attack renders flight control law ineffective in aiding the recovery of the right flat spin.

Keywords: aerodynamic model, steady spin modes, unsteady effects, simulations

Nomenclature

α, β	–	angle-of-attack; sideslip angle, [deg]
ϕ, θ, ψ	–	roll, pitch, yaw Euler angles, [deg]
p, q, r	–	roll, pitch, yaw rates in body axes, [deg/s]
v	–	velocity, [m/s]
Ω	–	wind axis rotation rate, [deg/s]
Ω^*	–	non-dimensional wind axis rotation rate, $\Omega b/(2v)$ [rad]
h	–	altitude, [m]
$\delta_a, \delta_e, \delta_r$	–	aileron, elevator and rudder deflections, [deg]
C_A, C_Y, C_N	–	axial, side and normal force coefficients in body axes
C_l, C_m, C_n	–	rolling, pitching and yawing moment coefficients in body axes
C_L, C_D	–	coefficient of lift and drag in wind axes
I_x, I_y, I_z	–	moments of inertia about X , Y and Z body axis respectively, [kg m ²]
m	–	mass, [kg]
S_w, b	–	wing area, [m ²] and b wing span, [m], respectively
c	–	mean aerodynamic chord, [m]
ρ	–	air density, [kg/m ³]
Δ	–	increment

1. Introduction

Good high angle of attack characteristics are required for modern fighter aircraft to enhance maneuverability during actual combat and tactical training missions. While performing high-alpha maneuvers, fighter aircraft become susceptible to loss of controlled flight due to significant degradation in stability and control characteristics. Moreover, fighter configurations featuring long pointed nose and slender fuselage may also experience large asymmetric yawing moments at high angles of attack that result in loss of directional stability (Cobleigh, 1994). This phenomenon may cause yaw divergence and subsequent entry into spin, in the direction depending upon orientation of yawing moment asymmetry. Past statistics show that such inadvertent loss of control caused numerous stall/spin related accidents resulting in loss of aircraft/aircrew or both. As a result, prediction and analysis of post stall maneuvers using wind tunnel data and computer techniques in the early design/production stage of aircraft has received enormous attention from aeronautical engineering community.

A detailed account of evolution of aircraft spin and corresponding research to meet the challenges, since early years of aviation, was given by Abzug and Larrabee (2005). Aerodynamic models developed around the 1930's for studying aircraft spin were based on Bryan and Hartley (1911), which assumed that instantaneous values of aerodynamic coefficients depended only on instantaneous values of flight parameters and also that those coefficients varied linearly with those parameters. Such aerodynamic models, though suited for analyzing low angle of attack flights, proved inaccurate and inadequate for predicting and analyzing aircraft spin characteristics, because such high-alpha maneuvers involve aerodynamic loads that are highly nonlinear and show time lag with respect to flight parameters. Considerable efforts have, therefore, been put in by various countries in design and development of dynamic wind tunnel test facilities like rotary balance apparatus, forced oscillation motion rigs, oscillatory coning motion rigs, etc., that can emulate aircraft motion in post stall maneuvers (Bergmann, 2009; Jin *et al.*, 2015; Zhang *et al.*, 2015). Aerodynamic data from such dynamic wind tunnel test setups has been used effectively in identifying aircraft steady spin modes and simulation of post stall maneuvers (Bihrlé, 1990; Murch and Foster, 2007; Khrabrov *et al.*, 2013; Paul and Gopalathnam, 2012).

Traditionally, a spin maneuver consists of three phases; incipient, fully developed spin and recovery phase. During incipient phase, aircraft transients from an aggravated stall to auto-rotation and flight path changes from horizontal to vertical. In the fully developed or steady spin phase, equilibrium is attained between inertia and aerodynamic forces and moments, and the aircraft descends downwards in a spiral trajectory about the vertical spin axis. The steady spin phase is extremely critical because if requisite anti-spin controls are not applied promptly, the spin may continue until the aircraft hits the ground. In the spin recovery phase, normally initiated by control inputs, the rotation rate decreases, aircraft nose attitude steepens, airspeed builds up and aircraft returns to the low-alpha flight regime. Bifurcation analysis and numerical continuation algorithms were used in the past to predict characteristics of steady spin such as flat or steep, stable or unstable, left or right, erect or inverted, steady or oscillatory, etc. (Paranjape and Ananthkrishnan, 2010). However, such methods present only a quasi-static state of the aircraft dynamics, and do not provide any details about transient motion (Raghavendra *et al.*, 2005). Numerical continuation methods also require smooth functional representation of aerodynamic loads; as a result they are not suitable for look-up tables based aerodynamic models (Kolesnikov and Goman, 2012).

This paper addresses the problem of analyzing spin dynamics of a fighter aircraft cosponsored by China and Pakistan (Hewson, 2005). As a starting point, all possible steady spin modes are identified by numerically solving the aircraft dynamic model comprising moment equations. Influence of high-alpha yawing moment asymmetry on identified left and right spin modes is illustrated with a steady spin modes location diagram. Flight parameters corresponding to the spin

modes are used as initial conditions for six degree-of-freedom simulations of the aircraft spin. For this purpose, the flight dynamic model of the aircraft is developed in MATLAB/SIMULINK environment that can accurately simulate post-stall maneuvers. Six degree of freedom simulations of the aircraft spin are performed in open-loop configuration to study spin dynamic characteristics. Simulations in closed-loop configuration are also performed to evaluate the performance of the gain scheduled flight control law in improving aircraft spin dynamic characteristics and aiding spin recovery.

The past spin research focused on general aviation and fighter configurations that either did not experience aerodynamic asymmetries at high angles of attack or influence of such aerodynamic asymmetries on dynamic characteristics of spin are not addressed explicitly (Tischler and Barlow, 1981; Sibilski and Wróblewski, 2012). The work presented in this paper is, therefore, aimed at providing better physical insight into the effect of high-alpha yawing moment asymmetry on spin dynamics and recovery characteristics by performing computer simulations of left and right flat spins. Our results show that computer simulations can be effectively used in predicting and analyzing the key dynamic characteristics of aircraft spin like dynamic stability, rotation rate about spin axis, number of rotations before recovery, altitude loss during spin recovery, and contribution of the control law in aiding spin recovery, etc.

2. Aircraft flight dynamics model

The aircraft flight dynamical model is based on full six degree of freedom nonlinear equations of motion and utilizes the aerodynamic model stored in the form of look-up tables. The model also incorporates the actuator dynamics with range saturations and rate limitations, sensor dynamics and engine dynamics.

2.1. Development of aerodynamic model

A high fidelity aerodynamical model, in the form of look-up tables, is developed using experimental data from static, rotary balance coning motion and oscillatory coning motion tests. Broadly, each aerodynamic coefficient in the system of body axes can be represented as the sum of three components: the static aerodynamic component, increment due to steady rotations and increment due to unsteady aerodynamic effects

$$C_i = C_{i,static} + \Delta C_{i,steady} + \Delta C_{i,unsteady} \quad (2.1)$$

where $C_i = C_A, C_Y, C_N, C_l, C_m, C_n$.

The static component $C_{i,static}$ is measured from static wind tunnel tests for the angle of attack range $-45^\circ < \alpha < 90^\circ$ and sideslip angles $-15^\circ < \beta < 15^\circ$. The static aerodynamic component is modeled as

$$C_{i,static} = C_i(\alpha, \beta, \delta = 0) + \Delta C_i(\alpha, \delta_a) + \Delta C_i(\alpha, \delta_e) + \Delta C_i(\alpha, \delta_r) + \Delta C_i(\alpha, \delta_e, \delta_r) + \Delta C_i(\alpha, \beta, \delta_r) \quad (2.2)$$

The first term on the right-hand side of equation (2.2) represents the static effect for different angles of attack and sideslips, with all control surfaces set at the neutral position. The 2-nd to 4-th terms represent increments due to deflections of the aileron, elevator and rudder, respectively. The last two terms are aerodynamic increments due to rudder-horizontal tail and rudder-sideslip couplings.

The steady aerodynamic component $\Delta C_{i,steady}$ is measured from rotary balance coning motion tests carried out on an aircraft model over the same range of aerodynamic angles as static tests and rotation rates between $-700^\circ/\text{s}$ and $700^\circ/\text{s}$. The steady aerodynamic component is modeled as

$$\Delta C_{i,steady} = C_i(\alpha, \beta, \Omega, \delta_{a,e,r} = 0) + \Delta C_i(\alpha, \Omega, \delta_a) + \Delta C_i(\alpha, \Omega, \delta_e) + \Delta C_i(\alpha, \Omega, \delta_r) \quad (2.3)$$

The first term on the right hand side of equation (2.3) represents the rotational effects with aerodynamic controls at the neutral position; whereas the last three terms represent the aerodynamic increment due to the ailerons, elevator and rudder deflections, respectively. Each individual term in equations (2.2) and (2.3) represent an n -dimensional lookup table, where n is the number of independent variables. Values of the coefficients are obtained by linear interpolation between the table nodes.

In coning motion dynamic wind tunnel tests, the aircraft model emulates a steady spin flight and, hence, the data from these tests is used to predict steady spin modes of the aircraft (Bihle, 1990). During post stall maneuvers like oscillatory spins, incipient spins, spin recovery, etc., aerodynamic effects are highly nonlinear and time dependent (Bergmann, 2009). Accurate modeling of these unsteady aerodynamic effects is essential for correct simulations of the aircraft flight during such post stall maneuvers.

2.2. Modeling of unsteady aerodynamic effects

Generally, two approaches are followed to address the problem of modeling unsteady aerodynamic effects; computational fluid dynamics (CFD) (Luchtenburg *et al.*, 2015; Ghoreyshi *et al.*, 2014) and an experimental approach where the data from wind tunnel tests is used in conjunction with the system identification (SID) to obtain an adequate mathematical model from the data, such as a differential equation model (Abramov *et al.*, 2004), neural network model (Ignatyev and Khrabrov, 2015), support vector machine (Wang *et al.*, 2015), etc. Modeling of unsteady aerodynamic effects using CFD have shown very promising results, however its use in aircraft simulation applications remains limited because simultaneous solution of equations of fluid dynamics in conjunction with integration of aircraft equations of motion become extremely resource consuming. In the present work, a differential equation based model of the following form is used for the modeling of unsteady aerodynamic effects

$$\tau_i(\alpha) \frac{d\Delta C_{i,unsteady}}{dt} + \Delta C_{i,unsteady} = k_i(\alpha) \dot{\alpha} \quad (2.4)$$

The coefficient k represents the instantaneous response, whereas the time constant τ corresponds to the time lag response. The values of τ and k are computed from oscillatory coning motion test data using the least squares method. In Fig. 1, the model for the unsteady aerodynamic effect in the normal force coefficient is plotted with oscillatory coning data, whereas Fig. 2 shows the same plot for the pitching moment coefficient. The modeling is done for three different mean angles of attack $\alpha_0 = 35^\circ, 40^\circ, 50^\circ$. It is observed that the proposed model response in the two cases is reasonably close to the experimental data. The unsteady aerodynamic models are integrated with the overall aircraft dynamic model for simulation of flat oscillatory spins.

2.3. High angle of attack aerodynamics

Wind tunnel tests carried out on an aircraft model reveal two aerodynamic phenomena in the high angle of attack regime: strong aerodynamic asymmetry in the yawing moment and ineffectiveness of the rudder at high angles of attack. Variation of the static yawing moment coefficient C_n with the angle of attack is illustrated in Fig. 3 for three rudder settings.

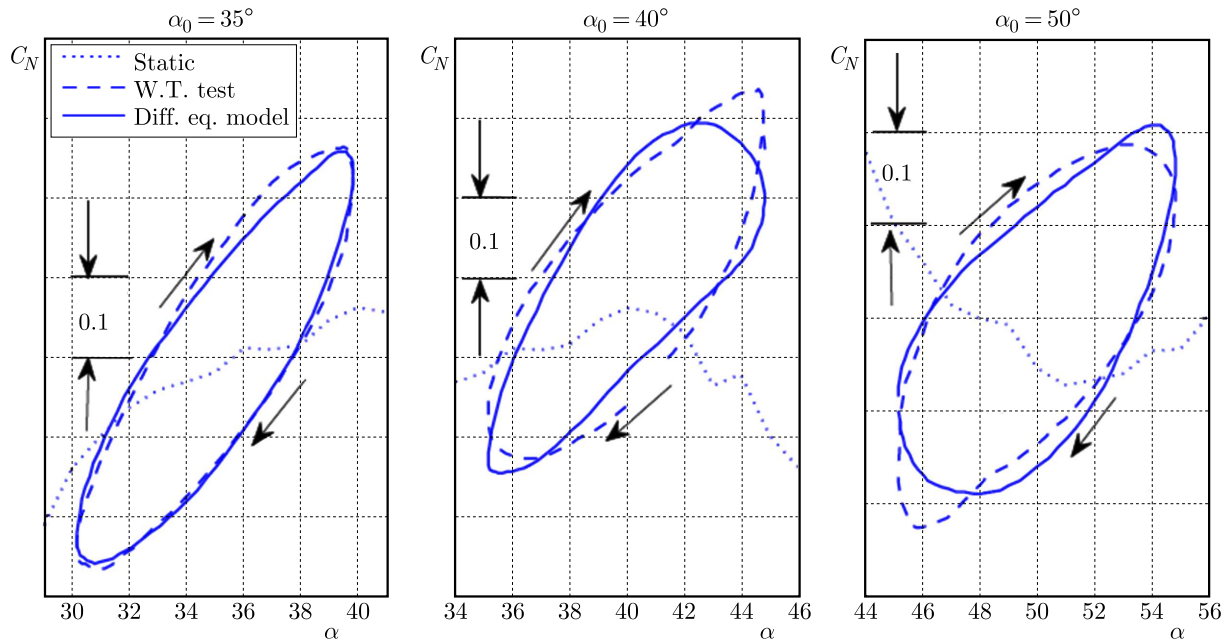


Fig. 1. Unsteady aerodynamic model response compared with test data: normal force C_N

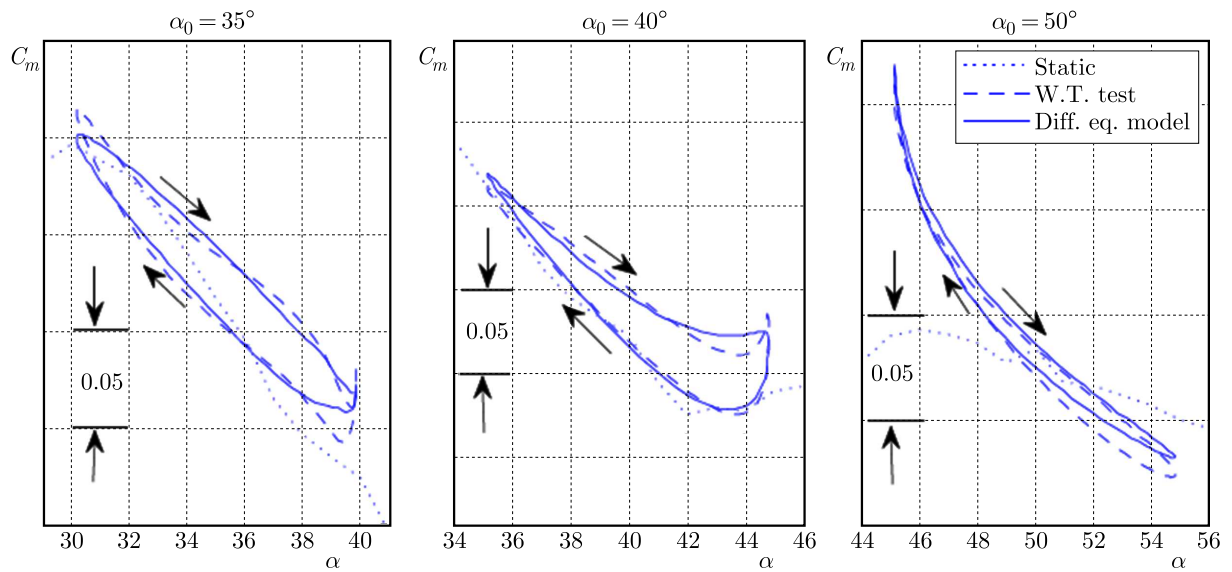


Fig. 2. Unsteady aerodynamic model response compared with test data: pitching moment C_m

As seen in Fig. 3, the yawing moment coefficient C_n remains symmetric below 40° angles of attack region, which is expected. However, as the angle of attack increases beyond 40° , strong asymmetry in the yawing moment is observed. Since the yawing moment coefficient C_n is seen to remain positive in the region of asymmetry, the aircraft has inherent tendency to yaw towards right thus promoting departure and spin entry in the same direction. The exact reason of the observed high angle of attack yawing moment asymmetry is under investigation by conducting further wind tunnel tests and extended CFD simulations. Moreover, for angles of attack below 40° , the rudder is observed to be effective. As the angle of attack exceeds 40° , the rudder deflection does not produce a corresponding change in yawing moment, thus rendering the rudder ineffective at high angles of attack. This inefficiency of the rudder is due to influence of the wing and fuselage wake on the vertical tail surface.

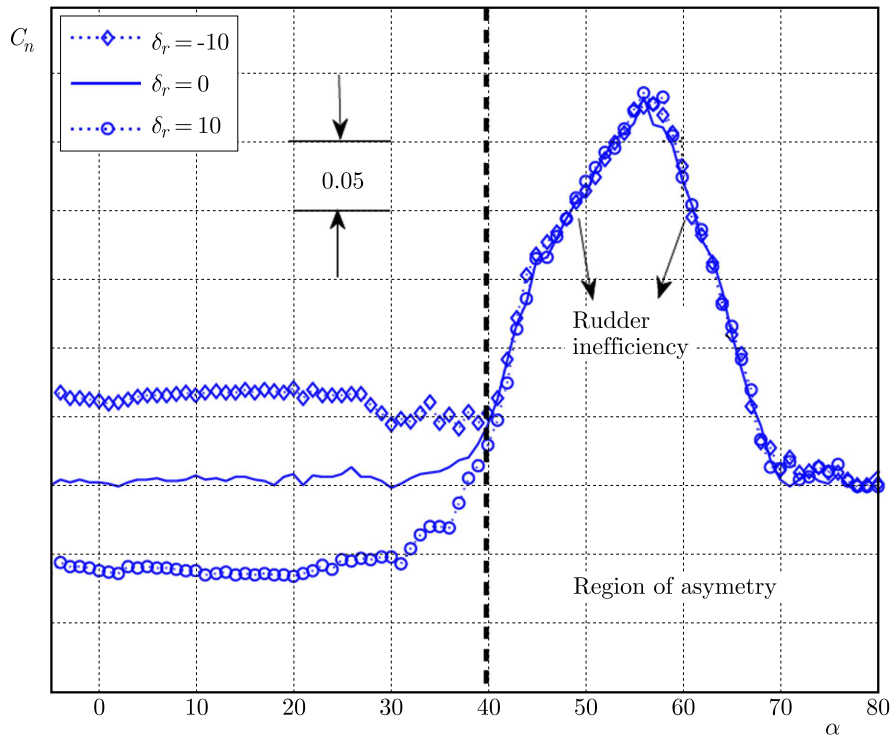


Fig. 3. Variation of yawing moment coefficient C_n with angle of attack

2.4. Control law architecture

Flight control systems of modern fighter aircraft are designed to attain benefits like stabilization and control of a relatively unstable airframe, enhanced maneuverability at high angles of attack, automatic departure/spin prevention, enhanced safety and reduced pilot workload. This section presents high level description of the gain-scheduled flight control law selected for studying closed-loop spin dynamics. Conceptually, the control law can be divided into two main sections: longitudinal control law and lateral/directional control law. Functional block diagrams of longitudinal and lateral/directional control laws are illustrated in Figs. 4 and 5, respectively.

Each main section of the control law comprises of three main functional units: a command shaping module, feed-forward path and feedback path. The control law accepts pilot pitch, roll and yaw commands through longitudinal, lateral stick deflections and rudder pedals, respectively. These pilot inputs are fed to the command shaping modules where they are processed by a stick gradient, command limiter and command filter sub-modules to provide desired command augmentation properties. The outputs of the command shaping modules are then summed with the feedback signals to form command error signals ep , er and ey . The pitch error signal ep is multiplied with the main gain of the longitudinal flight control path Kp to form the feedforward command which after passing through a proportional plus integral compensation filter is sent to the horizontal tail actuator. The roll error signal er after multiplication with the main gain of the roll control law Kr and passing through the proportional compensation filter is sent to the aileron actuator. Similarly, the yaw error signal ey is multiplied with the main gain of the yaw control law Ky which after passing through the proportional compensation filter is sent to the rudder actuator.

The dynamic feedback compensation module contains lead-lag filters and washout filters for achieving requisite gain and phase margins and improving the damping response, respectively. The notch filters in the feedback path attenuate the aircraft structural modes. The alpha-limiting

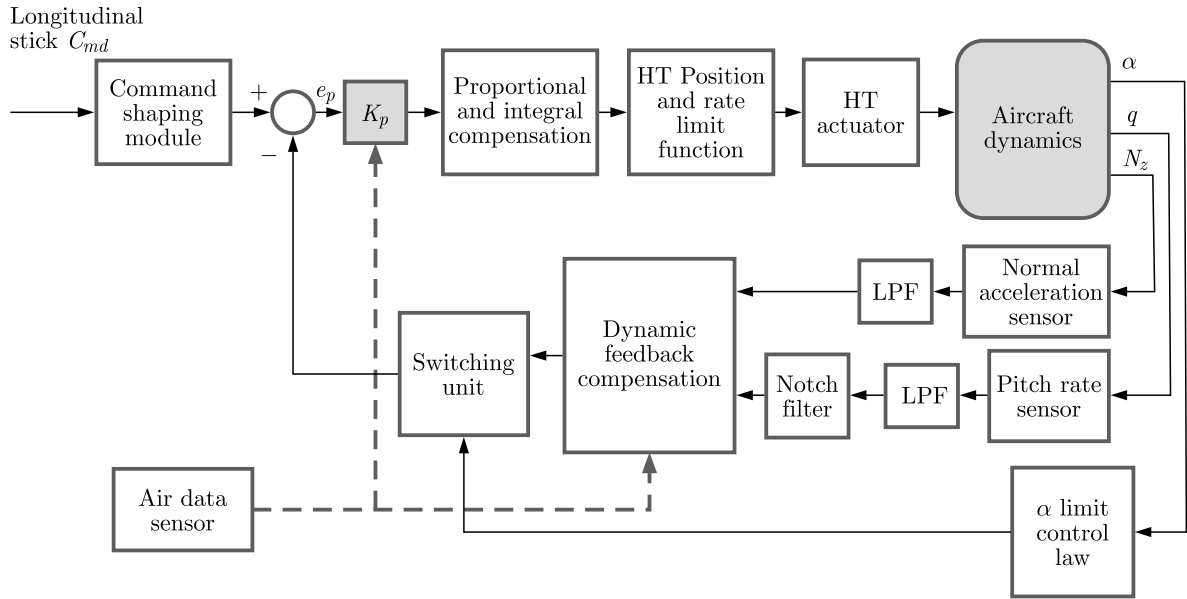


Fig. 4. Longitudinal control law: block diagram

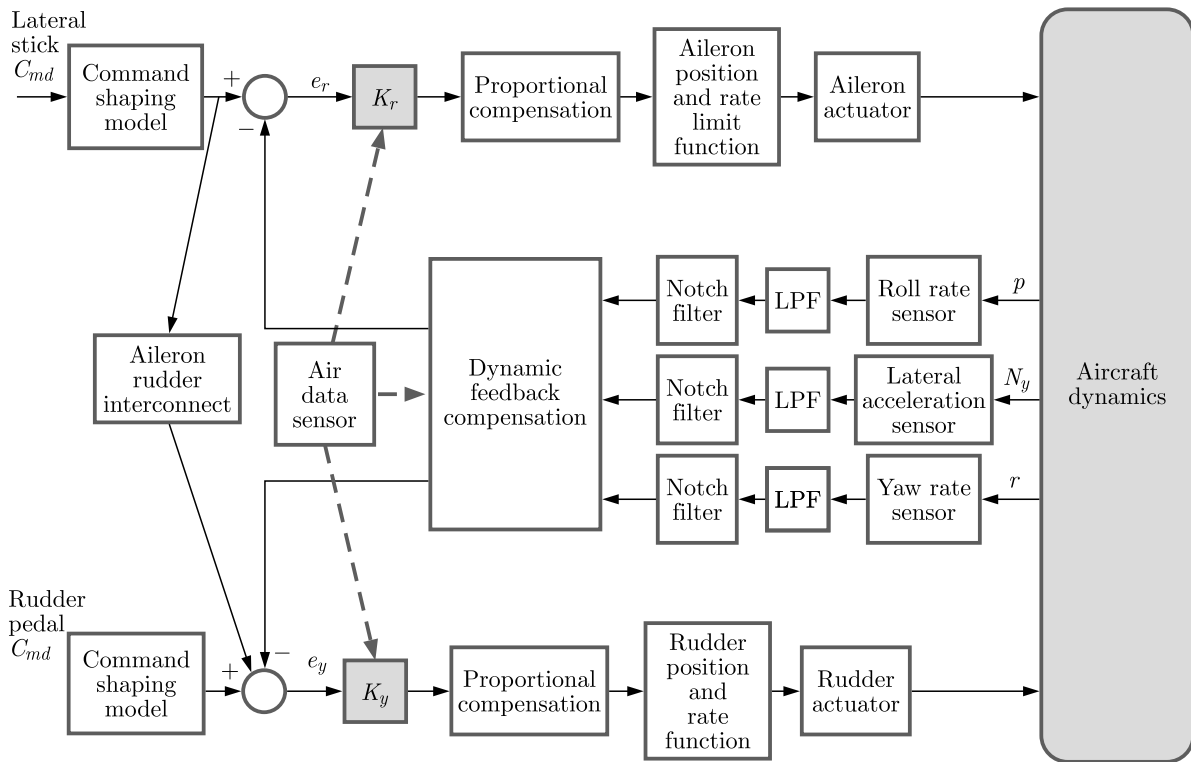


Fig. 5. Lateral-directional control law: block diagram

control law in the longitudinal feedback prevents aircraft excursions beyond the requisite angle of attack limits. The Aileron Rudder Interconnect (ARI) is provided to mitigate some of the adverse yaw effects encountered in fighter aircraft by aileron deflection, particularly at high angles of attack.

3. Identification of steady spin modes

The first step in the prediction of aircraft spin characteristics is the identification of all possible steady spin modes and their sensitivity to aerodynamic control settings. The aircraft equations of motion in the steady spin phase were derived in detail by Pamadi (2004). In the steady spin phase, all accelerations along and about the aircraft body axes system are zero. Figure 6 illustrates forces acting on the aircraft in the steady spin. The resultant aerodynamic force acts normal to the wing chord line and the side-force is negligibly small. The resultant aerodynamic force is decomposed into two components: the lift (L) acting in the horizontal direction and the drag (D) in the vertical plane. The force equilibrium condition is satisfied when the drag balances aircraft weight (W) and the lift balances the centrifugal force acting on the aircraft

$$D = \frac{1}{2}\rho v^2 S_w C_D = W \quad L = \frac{1}{2}\rho v^2 S_w C_L = mr\Omega^2 \quad (3.1)$$

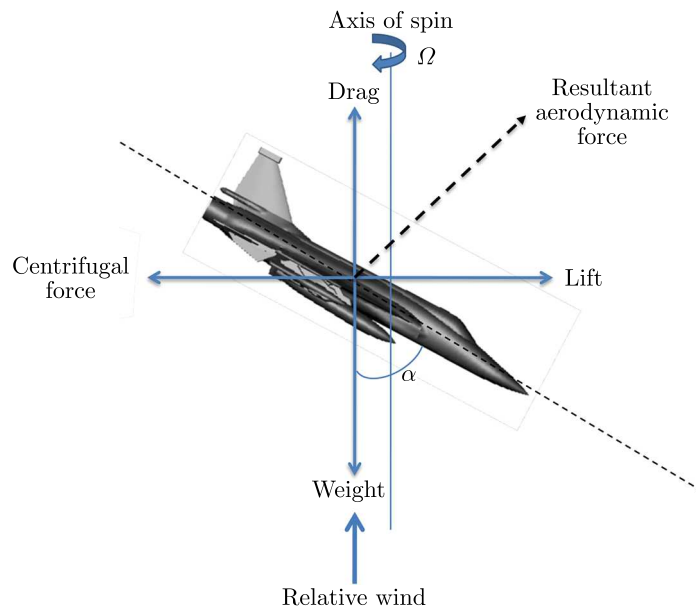


Fig. 6. Aircraft in steady spin

With the above stated flight conditions, the force equations are decoupled from the aircraft moment equations. Since force equilibrium can be attained at any attitude and spin rate by adjusting the spin radius and rate of descent, it is the balance of inertial and aerodynamic moment terms in the following moment equations that must be satisfied to ensure the steady spin condition

$$\begin{aligned} \frac{4(I_y - I_z)}{\rho S_w b^3} \Omega^{*2} \sin \alpha \sin(2\beta) + C_l(\alpha, \beta, \Omega^*) &= f_1(\mathbf{X}, \mathbf{U}) \\ \frac{4(I_z - I_x)}{\rho S_w \bar{c} b^2} \Omega^{*2} \sin(2\alpha) \cos^2 \beta + C_m(\alpha, \beta, \Omega^*) &= f_2(\mathbf{X}, \mathbf{U}) \\ \frac{4(I_x - I_y)}{\rho S_w b^3} \Omega^{*2} \cos \alpha \sin(2\beta) + C_n(\alpha, \beta, \Omega^*) &= f_3(\mathbf{X}, \mathbf{U}) \end{aligned} \quad (3.2)$$

where $\mathbf{X} = [\alpha, \beta, \Omega^*]$ represents the state vector and $\mathbf{U} = [\delta_a, \delta_e, \delta_r, h, m]$ the control input. Equilibrium is reached when the inertial terms (first terms on the left hand side of equations (3.2)) balance the aerodynamic terms (second terms on the left-hand side of the same equations). Since the inertial as well as aerodynamic terms are functions of \mathbf{X} , the steady spin modes are

computed by simultaneous solution of the moment equations for the unknown state vector \mathbf{X} at a specific control input \mathbf{U} . Locations of the computed left and right spin modes in terms of the angle of attack, for the complete range of aileron deflections and for all elevator settings, are illustrated in Fig. 7. As seen, the right spin modes are significantly higher than the left spin modes. This correlates well with fact that high-alpha yawing moment asymmetry results in natural tendency of the aircraft to yaw toward right thus promoting departure and spin entry in the same direction.

Locations of the spin modes in Fig. 7 provide insight into their recoverability characteristics. As highlighted by Bihrlé and Barnhart (1983), if the spin mode exists for pro-spin control settings and none for recovery or neutral control settings, the recovery is assisted by setting controls at positions where the spin mode does not exist. As seen in Figs. 7a and 7b, the left flat spin modes exist for elevator settings at 0° and -30° and for the aileron deflection range $\delta_a < 0^\circ$. No left flat spin modes exist for the elevator settings at 15° (Fig. 7c). Hence, the recovery of left flat spins seems to be aided if the elevator is fully pitched down, i.e. $\delta_e = 15^\circ$ and the aileron set to $\delta_a \geq 0^\circ$. However, for the right flat spins, which exist for all elevator settings and across the complete range of aileron deflections, the recovery through control surfaces input is seen to be problematic.

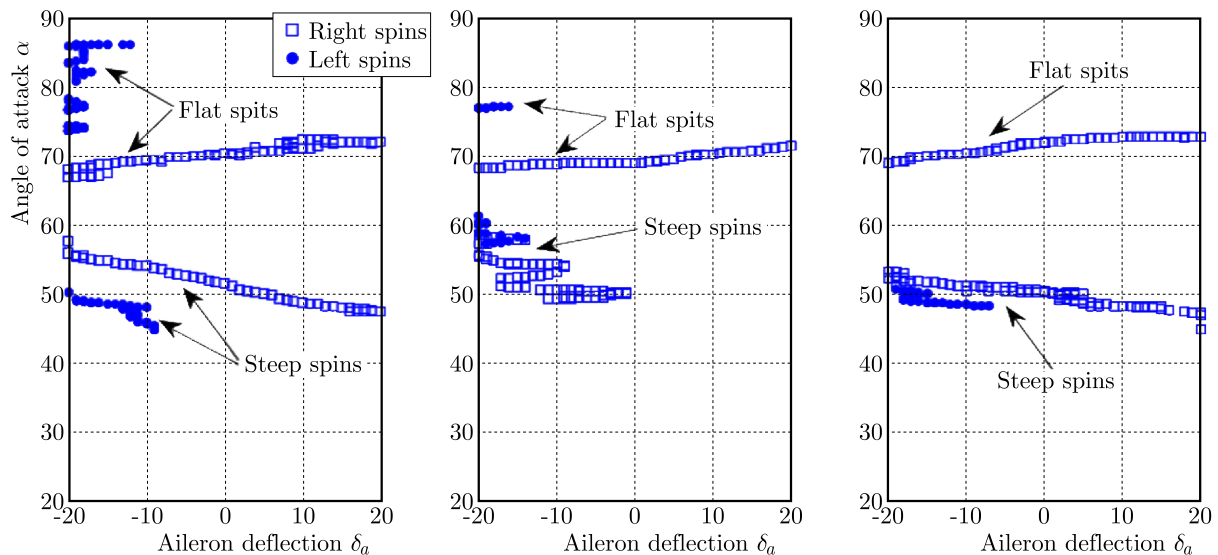


Fig. 7. Locations of steady spin modes for various elevator settings: (a) $\delta_e = 0^\circ$, (b) $\delta_e = -30^\circ$, (c) $\delta_e = 15^\circ$

4. Time history simulations

Time history simulations provide clear understanding on dynamic stability of identified spins, their oscillatory characteristics and effectiveness of flight control law in aiding the spin recovery. Simulations are carried out in MATLAB/SIMULINK environment, by integrating the full set of aircraft non-linear equations using the fourth-order Runge-Kutta routine. The force equations are taken in the aircraft wind axis and the moment equations are taken in the body axis system. Time history simulations are initialized with flight parameters corresponding to the aircraft steady spin and the results are demonstrated for two flat spins, left and right, listed in Table 1. The aircraft is said to be recovered from spin when the angle of attack reduces to 20° , which is safely below the stall region, and attain full effectiveness of control surfaces.

Table 1. Right and left flat spins: initial conditions

	Spin type													
	α	β	Ω^*	v	ϕ	θ	ψ	p	q	r	z	δ_a	δ_e	δ_r
Right flat spin	72.1	-3.1	0.08	59.3	0	-11.9	0	28.3	-5.2	88.3	3000	10	0	0
Left flat spin	78.2	2.8	-0.11	58.8	0	-17.8	0	-25.3	-5.8	-120	3000	-20	0	0

4.1. Dynamic characteristics of right flat spin

Time histories of the right flat spin in closed-loop configuration (solid curves) are plotted in Fig. 8 and compared with spin simulations in open-loop configuration (dashed curves). The right flat spin is oscillatory in nature, since the angle of attack (Fig. 8d) and sideslip (Fig. 8e) exhibit oscillations about the steady spin equilibrium point. Natural spin recovery is seen to occur because as the time passes, the aircraft descends downwards (Fig. 8f), airspeed increases (Fig. 8g), rotation rate about the spin axis decreases (Fig. 8j), angle of attack decreases well below the stalling angle and the aircraft enters the low alpha flight regime (Fig. 8d), where the aerodynamic controls become fully effective to attain low alpha steady flight conditions. Since the aircraft recovers naturally from the steady spin state, the right flat spin is unstable or divergent. It takes about 2.5 rotations for the aircraft to recover naturally from spin (Fig. 8h).

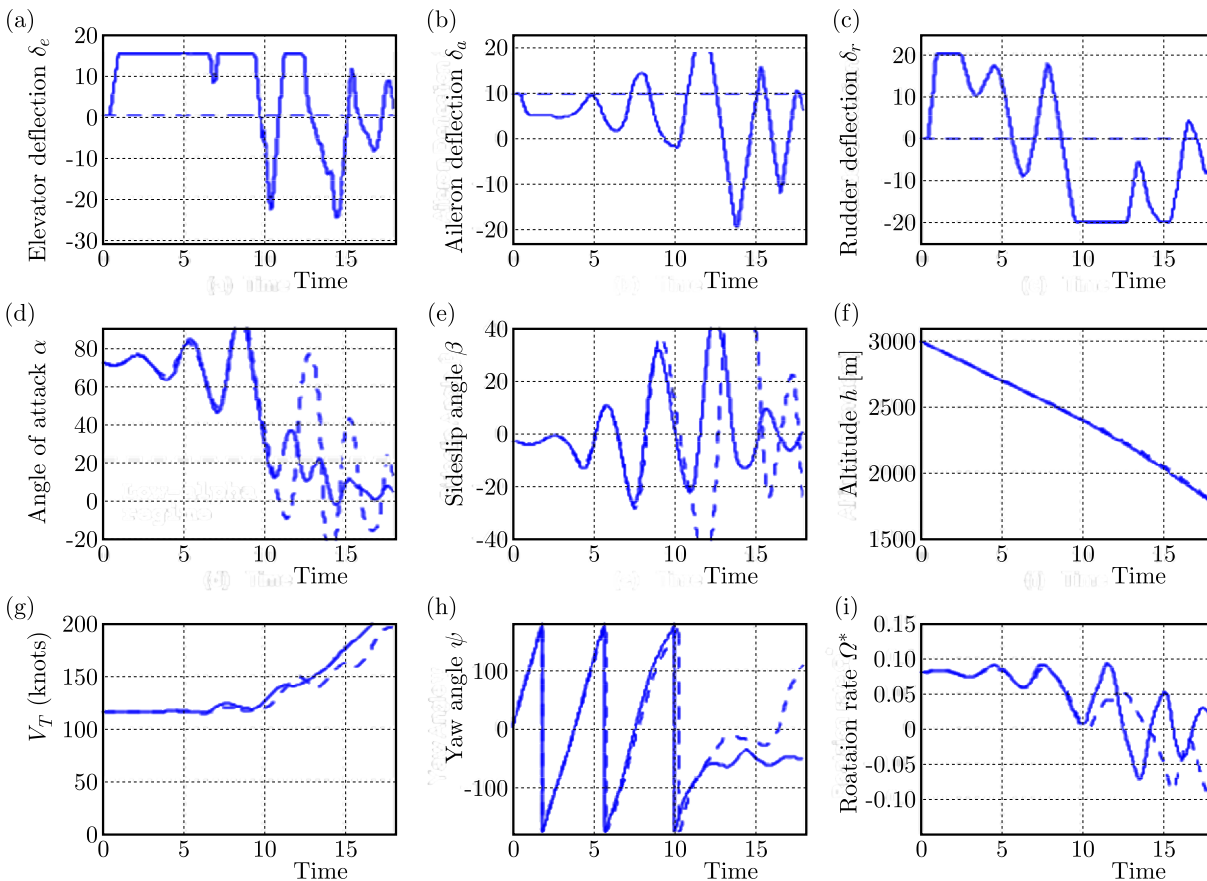


Fig. 8. Comparison of open loop (dashed) and closed loop (solid) time history simulations: right flat spin

It is seen from Fig. 8d that the gain scheduled flight control law does not reduce the recovery time of the right flat spin, since the aircraft enters the low-alpha flight regime at the same time in both cases, i.e. open-loop and closed loop configurations. The aircraft natural tendency to yaw rightwards due to high-alpha yawing moment asymmetry and existence of right steady

spin modes across the entire aileron deflection range and elevator settings renders the control law ineffective in aiding the spin recovery. However, large amplitude oscillations in the angle of attack and sideslip (Fig. 8d and 8e), observed in the open loop spin dynamics, are significantly damped by the flight control law.

4.2. Dynamic characteristics of left flat spin

Time histories of the left flat spin in closed-loop configuration (solid curves) are plotted in Fig. 9 and compared with spin simulations in open-loop configuration (dashed curves). As observed from the time histories, the left flat spin is also oscillatory and divergent. As the spin gets flatter with the increasing angle of attack, the rotation rate about the spin axis increases and the recovery becomes difficult or may take a longer time (Pamadi, 2004). This phenomenon is observed in the case of the left flat spin, which is more flat ($\alpha = 78.2^\circ$) as compared to the right flat spin ($\alpha = 72.1^\circ$). The left flat spin in open-loop configuration is seen to have a high rotation rate and takes almost 17.5 seconds (Fig. 9d) and five turns (Fig. 9h) to transit from the steady spin flight phase to the low alpha-flight regime. It is observed that the gain scheduled flight control law is effective in reducing the recovery time of the left flat spin (Fig. 9d), and also damping of large amplitude oscillations in the angle of attack and sideslip observed in open-loop spin dynamics (Figs. 9d and 9e).

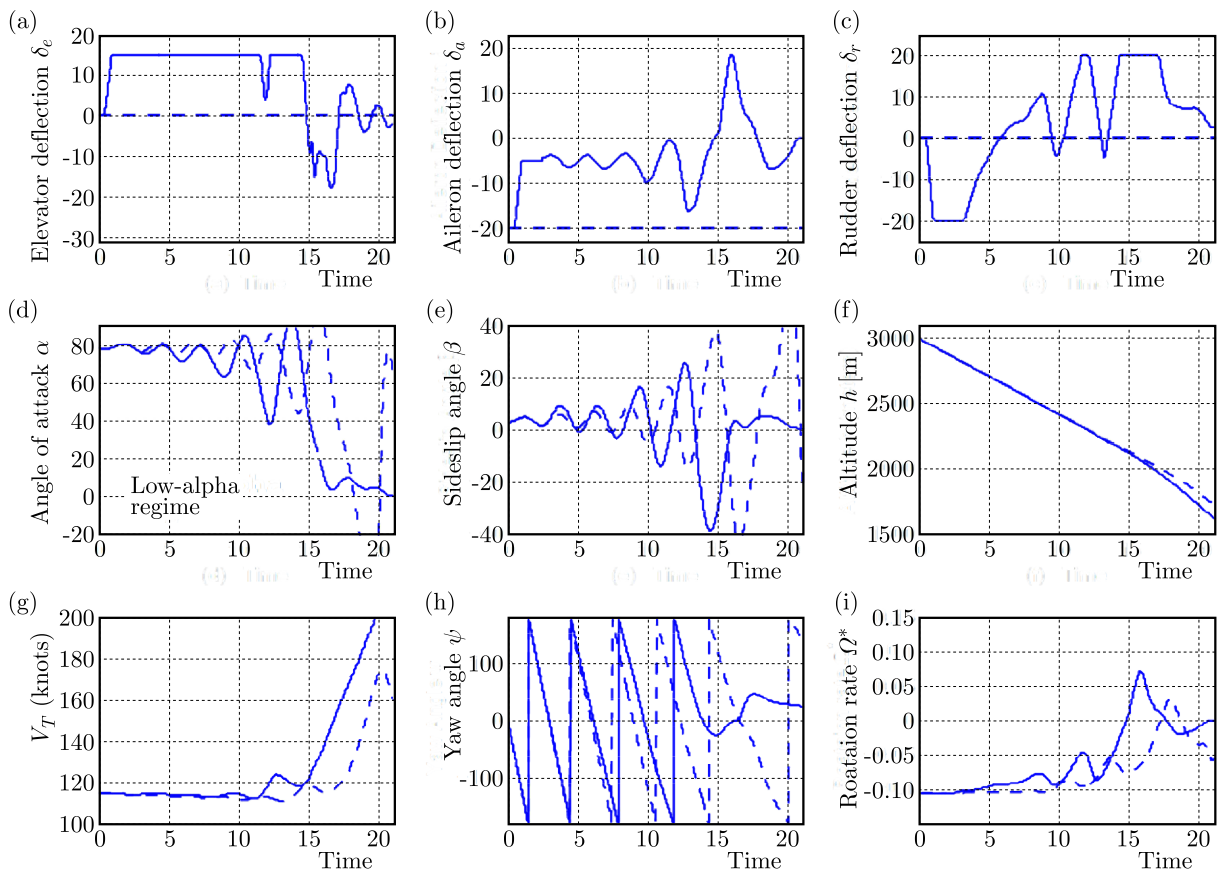


Fig. 9. Comparison of open loop (dashed) and closed loop (solid) time history simulations: left flat spin

The gain scheduled approach to designing of the flight controller has limitation since the controllers are designed only at equilibrium operating points within the prescribed flight envelope and therefore, may not cope with highly nonlinear aerodynamic effects encountered in the post stall flight regime. Moreover, problems may also be faced when scheduling with respect to rapidly changing state variables (Gill *et al.*, 2015). To overcome such limitations, nonlinear control

law designs such as dynamic inversion (Slotine and Li, 1991) and various adaptive techniques (Crespo *et al.*, 2012) may be tested with the aircraft flight simulation model for obtaining further improvements in dynamical characteristics of the aircraft spin.

5. Conclusion

The results presented in this paper demonstrate that computer simulations are an effective tool for prediction and analysis of dynamic characteristics of aircraft post-stall and spin maneuvers. For correct simulation of high alpha maneuvers, an accurate aerodynamic model which incorporates non-linear and unsteady aerodynamic effects encountered in such maneuvers is required. Whilst the dynamical system theory based approach facilitates understanding of asymptotic characteristics of the aircraft dynamics, time history simulations are vital to investigate dynamic effects in transitory flights such as dynamic stability of developed spins, ease or difficulty with which aircraft enters or recovers from a spin etc.

The spin dynamics of fighter configuration with high-alpha yawing moment asymmetry is analyzed in open loop and closed loop configurations, and the performance of the gain scheduled flight control law in improving recovery and oscillatory characteristics of fully developed spins is evaluated. The aircraft natural tendency to rotate towards right due to high alpha yawing moment asymmetry has strong influence on the predicted spin modes. The right flat spins are found to exist across the entire aileron deflections and for all elevator settings. The right and left flat spins are oscillatory and unstable. The left spin being more flat than the right one, takes longer to recover and has a higher rotation rate. The control law is effective in reducing the recovery time for left spins; however fails to do the same for right flat spins as they exist across the full range of ailerons deflections and all elevator settings. Moreover, the control law effectively damps large amplitude oscillations observed in the left and right flat spins in open loop configuration.

References

1. ABRAMOV N., GOMAN M., KHRABROV A.N., 2004, Aircraft dynamics at high incidence flight with account of unsteady aerodynamic effects, *AIAA Atmospheric Flight Mechanics Conference and Exhibit*, Rhode Island
2. ABZUG M.J., LARRABEE E.E., 2005, *Airplane Stability and Control: a History of the Technologies that Made Aviation Possible*, Cambridge University Press, England
3. BERGMANN A., 2009, Modern wind tunnel techniques for unsteady testing—development of dynamic test rigs, [In:] *Hermann Schlichting – 100 Years*, R. Radespiel, C.-C. Rossow, B.W. Brinkmann (Edit.), Springer Berlin Heidelberg, 59-77
4. BIHRLE W., 1990, Use of rotary balance data in the prediction of aircraft dynamics, AGARD Advisory Report, No. 265, 188-208
5. BIHRLE W., BARNHART B., 1983, Spin prediction techniques, *Journal of Aircraft*, **2**, 97-101
6. BRYAN, HARTLEY G., 1911, *Stability in Aviation: An Introduction to Dynamical Stability as Applied to the Motions of Aeroplanes*, Macmillan and Co. Limited
7. COBLEIGH B.R., 1994, High angle of attack yawing moment asymmetry of the X-31 aircraft from flight test, NASA Contractor Report 186030, 1-36
8. CRESPO L.G., MATSUTANI M., ANNASWAMY A.M., 2012, Design of an adaptive controller for a remotely operated air vehicle, *Journal of Guidance, Control, and Dynamics*, **2**, 406-422

9. GHOREYSHI M., JIRASEK A., CUMMINGS R.M., 2014, Reduced order unsteady aerodynamic modeling for stability and control analysis using computational fluid dynamics, *Progress in Aerospace Sciences*, **71**, 167-217
10. GILL S.J., LOWENBERG M.H., NEILD S.A., CRESPO L.G., KRAUSKOPF B., PUYOU G., 2015, Nonlinear dynamics of aircraft controller characteristics outside the standard flight envelope, *Journal of Guidance, Control, and Dynamics*, **12**, 2301-2308
11. HEWSOM R., 2005, Sino-Pakistani fighter improved, *Jane's Defense Weekly*, 99-100
12. IGNATYEV D.I., KHRABROV A.N., 2015, Neural network modeling of unsteady aerodynamic characteristics at high angles of attack, *Aerospace Science and Technology*, **41**, 106-115
13. JIN L., NONG C., YUHUI S., JING H., KE X., 2015, New dynamic stability rig for tri-sonic wind-tunnel, *Procedia Engineering*, **99**, 1591-1596
14. KHRABROV A., SIDORYUK M., GOMAN M., 2013, Aerodynamic model development and simulation of airliner spin for upset recovery, *Progress in Flight Physics*, **5**, 621-636
15. KOLESNIKOV E., GOMAN M., 2012, Analysis of aircraft nonlinear dynamics using non-gradient based numerical methods and attainable equilibrium sets, *AIAA Atmospheric Flight Mechanics Conference*, Minnesota
16. LUCHTENBURG D.M., ROWLEY C.W., LOHRY M.W., MARTINELLI L., STENGEL R.F., 2015, Unsteady high-angle-of-attack aerodynamic models of a generic jet transport, *Journal of Aircraft*, **3**, 890-895
17. MURCH A.M., FOSTER J.V., 2007, Recent NASA research on aerodynamic modeling of post-stall and spin dynamics of large transport airplanes, *45th AIAA Aerospace Sciences Meeting and Exhibit*, Nevada
18. PAMADI B.N., 2004, *Performance, Stability, Dynamics, and Control of Airplanes*, AIAA Education Series, USA
19. PARANJAPE A.A., ANANTHKRISHNAN N., 2010, Analytical criterion for aircraft spin susceptibility, *Journal of Aircraft*, **5**, 1804-1807
20. PAUL R., GOPALARATHNAM A., 2012, Simulation of flight dynamics with an improved post-stall aerodynamics model, *AIAA Atmospheric Flight Mechanics Conference*, Minnesota
21. RAGHAVENDRA P.K., SAHAI T., KUMAR P.A., CHAUHAN M., ANANTHKRISHNAN N., 2005, Aircraft spin recovery, with and without thrust vectoring, using nonlinear dynamic inversion, *Journal of Aircraft*, **6**, 1492-1503
22. SIBILSKI K., WRÓBLEWSKI W., 2012, Prediction of aircraft spin characteristics by continuation and bifurcation methods, *AIAA Atmospheric Flight Mechanics Conference*, Minnesota
23. SLOTINE J.J., LI W., 1991, *Applied Nonlinear Control*, Prentice Hall, Engle-wood Cliffs, New Jersey
24. TISCHLER M.B., BARLOW J.B., 1981, Determination of the spin and recovery characteristics of a general aviation design, *Journal of Aircraft*, **4**, 238-244
25. WANG Q., QIAN W., HE K., 2015, Unsteady aerodynamic modeling at high angles of attack using support vector machines, *Chinese Journal of Aeronautics*, **3**, 659-668
26. ZHANG J., TANG Y.K., SUN H.S., LIU Z.T., 2015, Dynamic test experiment system of single degree of freedom of Ø3.2m wind tunnel, *Proceedings of the Institution of Mechanical Engineers, Part G: Journal of Aerospace Engineering*, **7**, 1300-1309

VOLUMETRIC LOCKING SUPPRESSION METHOD FOR NEARLY INCOMPRESSIBLE NONLINEAR ELASTIC MULTI-LAYER BEAMS USING ANCF ELEMENTS

GRZEGORZ ORZECZOWSKI, JANUSZ FRĄCZEK

Warsaw University of Technology, Institute of Aeronautics and Applied Mechanics, Warsaw, Poland

e-mail: gorzech@meil.pw.edu.pl

The analysis and solution of many modern flexible multibody dynamic problems require formulations that are able to effectively model bodies with nonlinear materials undergoing large displacements and deformations. The absolute nodal coordinate formulation (ANCF) in connection with a continuum-based approach is one way to deal with these systems. The main objective of this work is to extend an existent approach for the modelling of slender structures within the ANCF framework with nonlinear, nearly incompressible materials using the volumetric energy penalty technique. The main part of the study is devoted to the evaluation of multi-layer beam models and simplifications in the locking suppression method based on F -bar projection. The results present significantly better agreement with the reference solution for multi-layer structures built with the standard ANCF beam element as compared with the earlier implementation.

Keywords: multibody dynamics, ANCF, incompressibility, locking phenomena, multi-layer beams

1. Introduction

The dynamic analysis of bodies that undergo large deformations and are built with complex and nonlinear materials is a vital part of the modern computer-aided design and modelling techniques. Therefore, such features should be included in a reliable manner in the advanced multibody system (MBS) simulation software. In flexible multibody dynamics, the most frequently used method is the floating frame of reference formulation (Shabana, 1997b) that is usually limited to linear-elastic deformations. The geometrical and material nonlinearities can be included within the finite element analysis (FEA) (Bathe, 1996), however, the FEA is not perfectly compatible with the MBS (Wasfy and Noor, 2003).

The absolute nodal coordinate formulation (ANCF) proposed by Shabana (1997a) can be efficiently used within the flexible multibody dynamics. The unique characteristics of this method allow straightforward modelling of beam and plate elements using nonlinear material models. ANCF employs the slope coordinates rather than rotations to describe local orientation, which enables, among other things, representation of complicated shapes using just a few elements. Flexible ANCF bodies can exactly represent rigid body modes, including large rotations, and model large body deformations. Additionally, the ANCF beam elements may employ general constitutive formulations (in addition to the classical beam theories) for a variety of nonlinear material models, including incompressible ones. All these features cause that the ANCF is well suited for the dynamic analysis of highly flexible beam structures using nonlinear material models within the MBS framework (Shabana, 2008).

Incompressible rubber-like materials are used in many engineering and industrial applications like defence, automotive, safety and others. Consequently, reliable and effective application of the incompressible nonlinear materials in many biomechanical and engineering models is one of the

key goals. However, commercial FEA packages restrict the work with incompressible materials to shell and solid elements (ANSYS® Academic Research, 2010), also when slender structures are considered that are otherwise modelled with beam elements. One can overcome this limitation in the mentioned kind of common applications by applying fully parameterized ANCF beam elements (Shabana, 2008; Orzechowski and Frączek, 2015).

Most investigations devoted to the ANCF framework assume a linear-elastic material model. Compressible and incompressible hyperelastic and isotropic material models were firstly used within the ANCF by Maqueda and Shabana (2007). Furthermore, Maqueda *et al.* (2010) presented the application of the ANCF beams with incompressible materials to rubber chains systems. Moreover, the validation of the ANCF model based on the experiment that captured motion of the rubber-like beam was presented in (Jung *et al.*, 2011). Nonetheless, none of the above works have stressed the importance of using the locking alleviation techniques. It is worth to point out that many issues that are actively researched in the ANCF field have already been studied for nonlinear finite elements.

The main objective of this paper is to recall and extend the volumetric locking elimination techniques for nonlinear, hyperelastic, nearly incompressible material models applied to the ANCF beams. The previous paper by Orzechowski and Frączek (2015) showed an importance of volumetric locking elimination techniques in typical applications, however, only higher-order elements, like those presented in Orzechowski and Shabana (2016), which were also numerically expensive due to the high number of coordinates and integration points, provided a reasonable results. Therefore, exemplary techniques that may reduce the computational cost are introduced and validated with several numerical examples. Strictly speaking, the implementation of multi-layer beam models with appropriate continuity between layers make it possible to use the lower-order ANCF beam element, while the use of lower-order projection basis with the F -bar projection technique simplifies this locking suppression formulation. Therefore, in the current study, the standard three-dimensional fully parameterized element is used (Shabana and Yakoub, 2001; Yakoub and Shabana, 2001) together with two simple incompressible material models: one-parameter Neo-Hookean and two-parameter Mooney-Rivlin (Shabana, 2008). Incompressibility of the materials is ensured by the penalty method, which is chosen due to its simple form and common use, and two methods of the locking suppression are applied. Due to introduced multi-layer structures, the results of numerical tests are in significantly better agreement with the reference for models built with the standard ANCF beam element as compared with the earlier implementation.

2. Kinematics and dynamics of deformable bodies

The nodal coordinates of the ANCF elements are prescribed with respect to the global reference frame and they include translational and slope coordinates. Consequently, no rotational coordinates are used to identify the element orientation. Thus, the independent rotation field interpolation is not required and only the displacement field is interpolated (Sugiyama *et al.*, 2006).

In this investigation, the fully parameterized ANCF beam element with twenty-four nodal coordinates is used (Shabana and Yakoub, 2001; Yakoub and Shabana, 2001). Twelve nodal parameters of this beam are $\mathbf{e}^{iT} = [\mathbf{r}^{iT} \quad \mathbf{r}_{,x}^{iT} \quad \mathbf{r}_{,y}^{iT} \quad \mathbf{r}_{,z}^{iT}]$, where \mathbf{e}^i is the vector of nodal coordinates of the i -th node, \mathbf{r}^i is the vector of the i -th node global position, while $\mathbf{r}_{,k}^i = \partial \mathbf{r}^i / \partial k$ for $k = x, y, z$ are vectors of the slope coordinates of the i -th node. The beam element used in the study consists of two nodes, therefore, the vector of the nodal coordinates for a single-beam element is given by $\mathbf{e}^T = [\mathbf{e}^{AT} \quad \mathbf{e}^{BT}]$, where A and B indicate nodes at the beam ends. The position of an arbitrary point on the ANCF element can be obtained as follows

$$\mathbf{r}(\mathbf{x}, t) = \mathbf{S}(\mathbf{x})\mathbf{e}(t) \quad (2.1)$$

where $\mathbf{x} = [x \ y \ z]^T$, $\mathbf{S}(\mathbf{x}) = [s_1\mathbf{I} \ s_2\mathbf{I} \ \cdots \ s_8\mathbf{I}]$ is the element shape function matrix, \mathbf{I} is a 3×3 identity matrix, and

$$\begin{aligned} s_1 &= 1 - 3\xi^2 + 2\xi^3 & s_3 &= l(\eta - \xi\eta) & s_5 &= 3\xi^2 - 2\xi^3 & s_7 &= l\xi\eta \\ s_2 &= l(\xi - 2\xi^2 + \xi^3) & s_4 &= l(\zeta - \xi\zeta) & s_6 &= l(-\xi^2 + \xi^3) & s_8 &= l\xi\zeta \end{aligned} \quad (2.2)$$

where l is length of the element in the undeformed state while $\xi = x/l$, $\eta = y/l$ and $\zeta = z/l$ are element dimensionless coordinates. It can be shown that the shape function matrix \mathbf{S} can describe arbitrary rigid body motion (Yakoub and Shabana, 2001).

The mass matrix \mathbf{M} of the element can be written as $\mathbf{M} = \int_V \rho \mathbf{S}^T \mathbf{S} dV$, where ρ and V are, respectively, density and volume of the element. In the ANCF, the mass matrix is constant. In addition, the forces resulting from differentiation of kinetic energy, like Coriolis, tangential, centrifugal and others, are equal to zero. Therefore, the only nonzero quantities in the system equations of motion are the vectors of the elastic and external forces.

To derive the vector of the external forces, which comprise, for example, the gravitational forces, the principle of virtual work can be used in the form $\delta W_e = \mathbf{F}_e^T \delta \mathbf{r} = \mathbf{F}_e^T \mathbf{S} \delta \mathbf{e} = \mathbf{Q}_e^T \delta \mathbf{e}$, where δW_e is the virtual work of the external force \mathbf{F}_e and \mathbf{Q}_e is the vector of the generalized external forces. For example, the nodal force vector due to gravity can be obtained as $\mathbf{Q}_{eg}^T = \int_V \mathbf{F}_{eg}^T \mathbf{S} dV$, where $\mathbf{F}_{eg}^T = [0 \ -mg \ 0]$ is the gravity force vector acting along the vertical axis, m is total mass of an element and g is the gravitational constant.

The position vector gradient of the fully parameterized ANCF element may be expressed by $\mathbf{F} = \partial \mathbf{r} / \partial \mathbf{X}$ where \mathbf{r} is given by Eq. (2.1) and $\mathbf{X} = [X \ Y \ Z]^T$. Using directly the expression of the tensor \mathbf{F} , one can evaluate the value of the strain energy for an element. In the case of the linear-elastic material model, the strain energy can be written as $U_s = \frac{1}{2} \int_V \boldsymbol{\varepsilon}^T \mathbf{E} \boldsymbol{\varepsilon} dV$, where $\boldsymbol{\varepsilon}$ is the strain vector associated with the Green-Lagrange strain tensor and \mathbf{E} is the matrix of elastic coefficients (Sopanen and Mikkola, 2003). The vector of the elastic forces for an element can be defined using the strain energy U_s as follows

$$\mathbf{Q}_s = \left(\frac{\partial U_s}{\partial \mathbf{e}} \right)^T \quad (2.3)$$

The present study is mainly devoted to isotropic, hyperelastic, nonlinear, and nearly incompressible material models, and the proper value of the strain energy density function for these materials is presented in the next Section of the paper.

The mass matrices and vectors of external and elastic forces of the elements follow the standard finite element assembly procedure for each flexible body. In the case of the ANCF, usually all the position and slope coordinates are shared between the elements. Finally, one can write dynamic equations of motion of the constrained flexible multibody system in the general form (Shabana, 2013)

$$\overline{\mathbf{M}} \ddot{\mathbf{e}} + \overline{\mathbf{Q}}_s + \boldsymbol{\Phi}_e^T \boldsymbol{\lambda} = \overline{\mathbf{Q}}_e \quad \boldsymbol{\Phi} = \mathbf{0} \quad (2.4)$$

where $\overline{\mathbf{M}}$, $\overline{\mathbf{Q}}_s$ and $\overline{\mathbf{Q}}_e$ are, respectively, the mass matrix, the vector of elastic forces and the vector of external forces of the system, $\ddot{\mathbf{e}}$ is the acceleration vector of the system, $\boldsymbol{\Phi}$ represents the vector of constraint equations (Sugiyama *et al.*, 2003), $\boldsymbol{\Phi}_e = \partial \boldsymbol{\Phi} / \partial \overline{\mathbf{e}}$ is the Jacobian matrix of constraints and $\boldsymbol{\lambda}$ is the vector of Lagrange multipliers. Equations of motion (2.4) form a set of differential-algebraic equations with the differential index equal to 3. Finding the solution to these equations is usually a more demanding task than for the solution to ordinary differential equations (Brenan *et al.*, 1996). Moreover, differential-algebraic equations require special numerical techniques, as denoted by Hairer and Wanner (1996). For a review of the

methods used to solve Eq. (2.4), see e.g. García de Jalón and Bayo (1994). However, the most common methods for solving differential-algebraic equations are the direct integration with, e.g., implicit Runge-Kutta schemes (Hairer and Wanner, 1996), integration of the transformed system with a lower index and stabilization (Gear *et al.*, 1985) or the generalized coordinate partitioning scheme (Wehage and Haug, 1982). In the present work, a Fortran-based research code is used and the implicit Runge-Kutta Radau IIA scheme is utilized. It is worth noting that if all the constrained equations were linear and time independent, system (2.4) would come down to a set of ordinary differential equations $\widehat{\mathbf{M}}\ddot{\mathbf{e}} + \widehat{\mathbf{Q}}_s = \widehat{\mathbf{Q}}_e$ where the vectors and matrices with hat are obtained after linear transformation due to constraint elimination (Garcia-Vallejo *et al.*, 2003).

2.1. Multi-layer beam models

Figure 1 presents a two-layer beam model. Two beams, *I* and *II* with local coordinate systems $x_I y_I z_I$ and $x_{II} y_{II} z_{II}$ (for clarity local z axes are omitted) are connected across their height. Each

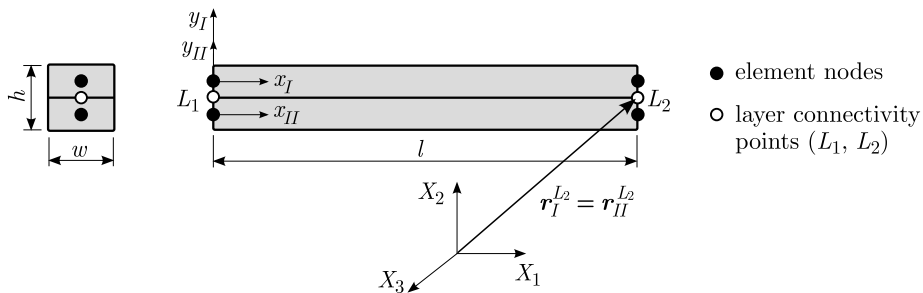


Fig. 1. Two-layer beam model

beam has length l , width w and height $h/2$, therefore, the two-beam model has height equal to h . The nodes are marked as black dots and they are shared between the elements in each layer, i.e., they follow the standard assembly procedure. The white dots (denoted as L_1 and L_2) represent the layer connectivity points at which one can impose linear constraint equations between two adjacent elements. $X_1 X_2 X_3$ is the global reference frame, while the position vectors $\mathbf{r}_I^{L_2}$ and $\mathbf{r}_{II}^{L_2}$ points to the L_2 using the parameters, respectively, of element *I* and *II*. The layer connectivity constraints can be enforced at the position and slope level, thus the required continuity might be achieved. For example $\Phi^T = [(\mathbf{r}_I^{L_1} - \mathbf{r}_{II}^{L_1})^T \quad (\mathbf{r}_I^{L_2} - \mathbf{r}_{II}^{L_2})^T]$ enforces the continuity at the position level only, while constraints $\Phi^T = [(\mathbf{r}_I^{L_1} - \mathbf{r}_{II}^{L_1})^T \quad (\mathbf{r}_{I,x}^{L_1} - \mathbf{r}_{II,x}^{L_1})^T \quad (\mathbf{r}_I^{L_2} - \mathbf{r}_{II}^{L_2})^T \quad (\mathbf{r}_{I,x}^{L_2} - \mathbf{r}_{II,x}^{L_2})^T]$, which are used in the numerical examples Section, impose additional constraints on the slope along the local x axis. The total constraint vector should consist of constraints for each layer connectivity point. This approach might be used to build a beam structures with more than two layers across the height or to create a model with layers in both transversal directions. In addition, the use of multi-layer structures further enables the modelling of complex systems like vehicle tires (Patel *et al.*, 2016). As will be shown later in the paper, the multi-layer beam model may ensure a better convergence when the nearly incompressible materials are used. It is worth noting that the approach for modelling a multi-layer beam used by Patel *et al.* (2016) and introduced in (Liu *et al.*, 2011) is based on subdomains with different material properties created within a single element and cannot be easily adopted for hyperelastic and nonlinear material models.

3. Nearly incompressible polynomial material models

The hyperelastic material models, which are shown in this Section, are in the well-known form of the Mooney-Rivlin models (Bonet and Wood, 1997; Orzechowski and Frączek, 2015). These models are commonly used to represent incompressible rubber-like materials. To fulfil the incompressibility condition, the penalty technique is employed, due to its efficiency and simplicity. Therefore, any member of the Mooney-Rivlin models family can be adopted. Herein, two simplest incompressible models are used and mentioned, namely the Neo-Hookean and two-parameter Mooney-Rivlin.

The strain-energy density function can be written for isotropic materials as a function of the invariants of the deviatoric part of the right Cauchy-Green deformation tensor $\mathbf{C}_r = \mathbf{F}^T \mathbf{F}$, defined as $\bar{I}_1 = J^{-2/3} I_1$ and $\bar{I}_2 = J^{-4/3} I_2$, where $J = \det(\mathbf{F})$ and the invariants of the tensor \mathbf{C}_r itself are $I_1 = \text{tr}(\mathbf{C}_r)$ and $I_2 = \frac{1}{2}[\text{tr}(\mathbf{C}_r)^2 - \text{tr}(\mathbf{C}_r^2)]$. In addition, the constraint $J = 1$ must be ensured through the body in order to account for the material incompressibility. The strain energy density function in the form of the Mooney-Rivlin models is the following

$$U_s = \sum_{i+j=1}^K \mu_{ij} (\bar{I}_1 - 3)^i (\bar{I}_2 - 3)^j \quad (3.1)$$

where μ_{ij} are material coefficients, usually determined from an experiment. K may be an arbitrarily large number, but in practice values of $K > 2$ are rarely used. In the present paper, only material models with $K = 1$ are considered.

The material models from Eq. (3.1) implicitly assume that the incompressibility is ensured by setting J equal to one. This condition is fulfilled by the penalty method (Maqueda and Shabana, 2007; Orzechowski and Frączek, 2015). In this technique, the volumetric energy penalty function U_p is added to the expression of the strain energy function. This term can be expressed as

$$U_p = \frac{1}{2} k (J - 1)^2 \quad (3.2)$$

where k is the penalty coefficient that represent the bulk modulus, a real material property (Bonet and Wood, 1997). In practice, k should be selected sufficiently large to assure incompressibility, but also not too large to avoid numerical complications. The use of energy function from Eq. (3.2) with a finite coefficient k causes that the material can be considered as nearly incompressible only.

Finally, one can combine Eqs (3.1) and (3.2) as

$$U_{sic} = U_s + U_p \quad (3.3)$$

To obtain the vector of the elastic forces \mathbf{Q}_s , the above expression should be integrated over the flexible body volume and inserted into Eq. (2.3). Below, two models based on that representation are shown.

3.0.1. Incompressible Neo-Hookean material

The incompressible Neo-Hookean is the simplest member of the Mooney-Rivlin models family, which depends on only one elastic coefficient μ_{10} . Therefore, the expression for the strain energy function can be written as $U_s^{nh} = \mu_{10}(\bar{I}_1 - 3)$, and μ_{10} is initially equal to one-half of the shear modulus.

3.0.2. Incompressible Mooney-Rivlin material

A two-parameter incompressible Mooney-Rivlin material is another widely used and simple material model which is obtained by assuming that two elastic parameters, μ_{10} and μ_{01} , are not equal to zero. Therefore, the strain energy density function takes the form $U_s^{mr} = \mu_{10}(\bar{I}_1 - 3) + \mu_{01}(\bar{I}_2 - 3)$. It can be shown that in the case of small strains, Young's modulus is $E = 6(\mu_{10} + \mu_{01})$ and the shear modulus is equal to $\mu = 2(\mu_{10} + \mu_{01})$ (Bathe, 1996).

4. Locking elimination techniques for nearly incompressible materials

The locking phenomena can be noticed in the case of many ANCF elements both for linear-elastic (Gerstmayr and Shabana, 2006) and nonlinear (Orzechowski and Frączek, 2015) material models. Its occurrence often causes an erroneously stiff bending characteristic, and is especially noticeable for approaches that directly employ the continuum mechanics. Moreover, a far greater impact of the locking is observed in the case of an incompressible material than in the case of compressible models. The paper presents shortly two methods that can be used for locking suppression for incompressible material models. Both methods were introduced in the previous work (Orzechowski and Frączek, 2015). In addition, simplifications of the projection space of the F -bar method are introduced.

4.1. Selective reduced integration

This locking alleviation technique is commonly used to prevent Poisson's locking in many FEA elements (Zienkiewicz and Taylor, 2005) as well as in continuum-based ANCF elements with a linear material model (Gerstmayr *et al.*, 2008). In this method, the integral of the strain energy function is split into two parts that are treated differently. In the first part, which is fully integrated in the total element volume, one does not consider the Poisson effect, while in the second part, which is integrated only along the beam centerline or plate midplane, i.e. uses a reduced integration scheme, one takes the Poisson effect into account. Adequately, the expression of the strain energy density function given by Eq. (3.1) can also be split. The first part of the Mooney-Rivlin material model, denoted as U_s , can be fully integrated as it does not consider the volumetric effect. However, the volumetric energy penalty function U_p should be considered only at the beam axis, as it accounts for the volumetric behaviour. Therefore, the following formula is used

$$U_{sic}^{sri} = \int_V U_s dV + A \int_l U_p dl \quad (4.1)$$

where l is length of the element, A denotes cross-section area and the index *sri* designates the selective reduced integration technique.

4.2. F -bar projection method

The F -bar projection method involves product decomposition of the position vector gradient into volumetric and deviatoric parts (Bonet and Wood, 1997; Elguedj *et al.*, 2008) and is especially convenient to use when the split of the energy density function into deviatoric and volumetric parts is not straightforward and the use of the selective reduced integration might be troublesome. This method is a generalization of the strain projection B -bar technique to finite-strain analysis which is considered as an extension of the selective and reduced integration approaches (Hughes, 1987).

The gradient tensor \mathbf{F} may be split as $\mathbf{F} = \mathbf{F}^{dil}\mathbf{F}^{dev}$ where $\mathbf{F}^{dev} = J^{-1/3}\mathbf{F}$ is the deviatoric (volume preserving) part and $\mathbf{F}^{dil} = J^{1/3}\mathbf{I}$ is the volumetric-dilatational part, and \mathbf{I} is the identity matrix. One can notice that $\det(\mathbf{F}^{dev}) = 1$ and $\det(\mathbf{F}^{dil}) = J$. Now, the tensor \mathbf{F} can be modified by the use of the modified dilatational part as $\overline{\mathbf{F}}^{dil} = \overline{J^{1/3}}\mathbf{I}$, where

$$\overline{J^{1/3}} = \pi(J^{1/3}) \tag{4.2}$$

and π is the linear projection operator presented in details below. Consequently, one can write

$$\overline{\mathbf{F}} = \overline{\mathbf{F}}^{dil}\mathbf{F}^{dev} = \frac{\overline{J^{1/3}}}{J^{1/3}}\mathbf{F} \tag{4.3}$$

The modified tensor $\overline{\mathbf{F}}$ can be directly employed to calculate the energy density function given by Eq. (3.1). However, because U_s is volume preserving, only the penalty function U_p can be affected.

4.2.1. Projection operator π

Studies performed for the isogeometric analysis beam by Elguedj *et al.* (2008) and further carried out in the ANCF framework by Orzechowski and Frączek (2015) show that the L^2 projection of strains is a good candidate for the projection space. Whilst the associated space on which this projection is performed, it should have a constant value in the transversal directions. Therefore, in the previous work (Orzechowski and Frączek, 2015), the following lower-order basis was employed

$$\tilde{\mathbf{S}}_4 = \begin{bmatrix} 1 - 3\xi^2 + 2\xi^3 & l(\xi - 2\xi^2 + \xi^3) & 3\xi^2 - 2\xi^3 & l(-\xi^2 + \xi^3) \end{bmatrix} \tag{4.4}$$

where $\tilde{\mathbf{S}}_4$ denotes a lower order cubic basis with four components. However, even a lower order basis may be introduced as constant, linear or quadratic (with one, two and three components, respectively) in the longitudinal direction

$$\begin{aligned} \tilde{\mathbf{S}}_1 &= [1] & \tilde{\mathbf{S}}_2 &= [1 - \xi \quad \xi] \\ \tilde{\mathbf{S}}_3 &= [2\xi^2 - 3\xi + 1 \quad 4\xi - 4\xi^2 \quad 2\xi^2 - \xi] \end{aligned} \tag{4.5}$$

Next, Eq. (4.2) may be written in the new space (using any basis from Eqs (4.4) and (4.5)) as $\overline{J^{1/3}} = \tilde{\mathbf{S}}\tilde{\mathbf{J}}^{1/3}$ (Elguedj *et al.*, 2008; Hughes, 1987) where

$$\tilde{\mathbf{J}}^{1/3} = \left[\int_V \tilde{\mathbf{S}}^T \tilde{\mathbf{S}} dV \right]^{-1} \int_V \tilde{\mathbf{S}}^T J^{1/3} dV \tag{4.6}$$

The presented procedure corresponds to L^2 projection of $J^{1/3}$ into the $\tilde{\mathbf{S}}$ basis. Next, the newly calculated value of $\overline{J^{1/3}}$ may be substituted into Eq. (3.2) to obtain a modified volumetric penalty function as

$$\overline{U}_p = \frac{1}{2}k \left[(\overline{J^{1/3}})^3 - 1 \right]^2 \tag{4.7}$$

Finally, the strain energy density function for the F -bar strain projection method is expressed as follows

$$U_{sic}^{F\text{-bar}} = \int_V U_s dV + A \int_l \overline{U}_p dl \tag{4.8}$$

where \overline{U}_p can be calculated only at the element centerline, as the value of $\overline{J^{1/3}}$ depends only on the longitudinal coordinate.

5. Numerical examples

Exemplary numerical calculations are carried out with the fully parameterized three-dimensional ANCF beam element with twelve nodal coordinates at each of its two nodes. In order to effectively model bodies with nearly incompressible materials, the techniques of alleviating the volumetric locking presented in Section 4 are applied. In addition, to assembly multi-layer beam structures, the procedure described in Section 2.1 is used. In this study, three simple models of highly deformable clamped beams and physical pendulums are shown. All examples use the standard, spatial, two-node ANCF beam element with twenty-four coordinates (Shabana and Yakoub, 2001; Yakoub and Shabana, 2001).

5.1. Physical pendulum

A dynamical analysis of a flexible beam attached at one end to the ground by a spherical joint and falling under the gravity forces is carried out for the purpose of numerical verification. A similar pendulum was examined by Maqueda and Shabana (2007). In the undeformed state, the beam has 1 m in length, a square cross-section of dimension 20 mm, and a material density of 7200 kg/m³. In this example, the elastic coefficient for the incompressible Neo-Hookean model is $\mu_{10} = 1$ MPa, while in the case of the two-parameter Mooney-Rivlin material, the values of its coefficients are $\mu_{10} = 0.8$ MPa and $\mu_{01} = 0.2$ MPa. The material properties allow large deformations of the body. To ensure incompressibility, the penalty term is assumed to be $k = 10^3$ MPa. The pendulum model is shown in Fig. 2. To increase body deformations, the base of the pendulum is subjected to prescribed motion. The constraint equations for this model can be written as $\Phi^T = [r_1^N + 0.02 \sin(2\pi t) \quad r_2^N \quad r_3^N]$, where r_i^N for $i = 1, 2, 3$ denotes the component of the position vector of the node N (in meters), and t is time expressed in seconds.

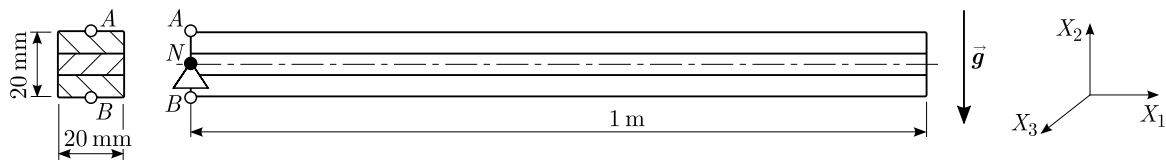


Fig. 2. Very flexible physical pendulum, three-layer model

The pendulum body is built of four beam elements along its length. Figures 3a and 3b show displacements of the pendulum free end tip resulting from performed dynamical simulations for three types of models: without the locking suppression method, with the F -bar projection and the three-layer model with the F -bar projection. Figure 3a presents results for the Neo-Hookean material, while in Fig. 3b results for the Mooney-Rivlin material are shown. Despite the differences in materials, the results in both figures are very similar. The models without the locking suppression method show very small deformations as they behave almost like a rigid body, despite very low elastic coefficients and large pendulum density. On the other hand, all models that employ the locking elimination by the F -bar projection show reasonable deformations. The lack of the over-stiff response in the incompressible models during bending indicates that the influence of the volumetric locking has been suppressed (Orzechowski and Frączek, 2015). Therefore, it can be concluded that the influence of the volumetric locking on the results of hyperelastic nearly incompressible material models might be enormous, and that the multi-layer beam model produces acceptable results, comparable with those of the standard beam model. The results for the selective reduced integration exhibit very similar behaviour.

Figures 4a and 4b show how well the incompressibility condition is preserved by the analysed models by plotting the value of the determinant of the deformation gradient tensor $J = \det(\mathbf{F})$. Figure 4a presents the value of J as a function of time at the point A of the body (see Fig. 2).

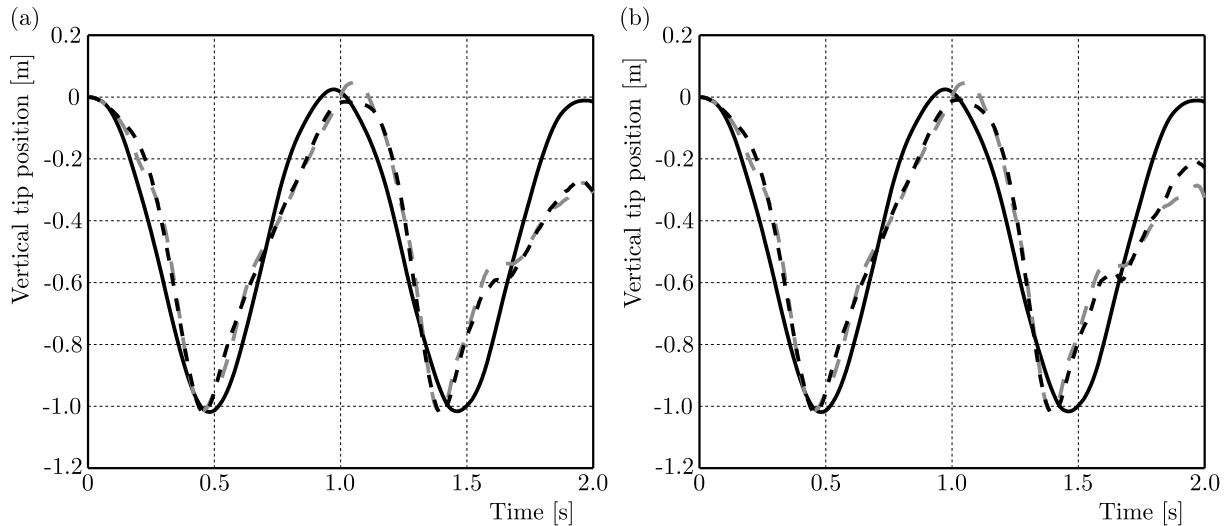


Fig. 3. Vertical position of the beam free end tip for (a) incompressible Neo-Hookean and (b) incompressible Mooney-Rivlin material: (—) without the locking suppression method, (---) with the F -bar projection, (-.-) with the F -bar projection, three-layer model

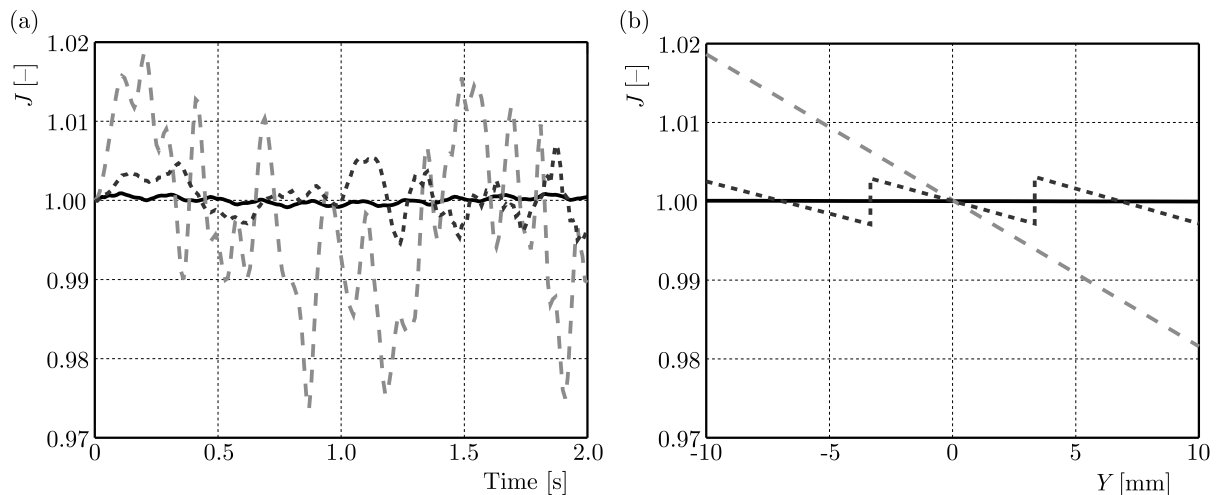


Fig. 4. Value of $J = \det(\mathbf{F})$ (a) in time and (b) along beam thickness for incompressible Neo-Hookean material: (—) without the locking suppression method, (---) with the F -bar projection, (-.-) with the F -bar projection, three-layer model

Likewise, Fig. 4b presents the value of J along the line connecting points A and B of the body (shown in Fig. 2) for a specific time instant (at $t = 0.2$ s). It can be clearly seen that the incompressibility condition for the whole body volume is preserved only for the formulation that does not use any locking alleviation technique.

For beams using the F -bar strain projection method, the value of J is changing noticeably, however, in the case of the three-layer model this violation is significantly smaller than for the one-layer beam as the region of constraint violation is bounded to the beam boundaries. Since the lack of continuity of the J value between the beam layers is crucial for preventing the locking behaviour (continuous J would result in its constant value equal to one), it must be ensured that the continuity does not occur on the gradient perpendicular to the layer boundary.

5.2. Cantilever beam

In this example, static simulation of the cantilever beam, similar to that shown in Figure 5, is employed. The beam is clamped at one end with the help of a linear constraint equation in

the form of $\Phi = \mathbf{e}^N$. The gravitational force is the only external force that acts on the system. The material and geometrical properties of the flexible body are the same as in the previous example, except for the size of the cross section that is increased to 40 mm for both height and width. For a verification purpose, the ANCF models with one, two and three layers are examined and the results of simulations are compared with the solution of an analogous model obtained with a commercial FEA package (ANSYS® Academic Research, 2010).

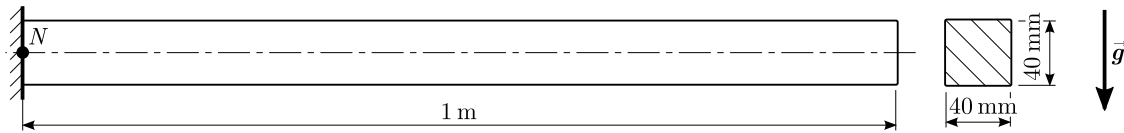


Fig. 5. Very flexible cantilever beam under gravity forces

The main purpose of this example is to assess the impact of the new modelling techniques, like the use of the multi-layer beams and the low order projection basis, on the obtained solution. The results are shown for both presented locking elimination techniques, the F -bar strain projection and the selective reduced integration as well as for both material models, the incompressible Neo-Hookean and two-parameter Mooney-Rivlin. For the F -bar method, four different projection bases are employed as has been proposed in Section 4.2. The results are compared against the FEA package solution. For this reason, we applied a very fine mesh in the FEA package consisting of 1600 higher-order solid elements (SOLID186).

In Table 1, the results of static ANCF analysis are presented for the models with one, two and three layers across thickness, together with reference FEA results. The results show for both locking elimination procedures, the SRI and F -bar, the convergence to nearly the same solution for a given number of layers and irrespective of the employed projection basis.

Table 1. Deformation of the free end tip of the clamped beam for models with 48 elements in each layer (NoL – number of layers, ICNH – incompressible Neo-Hookean, ICMR – incompressible Mooney-Rivlin, SRI – selective reduced integration). Results for one-layer models for SRI and cubic F -bar locking suppression methods are taken from (Orzechowski and Frączek, 2015)

Method	NoL	ICNH analysis		ICMR analysis	
		X [m]	Y [m]	X [m]	Y [m]
FEA	–	–0.828	–0.940	–0.828	–0.941
ANCF SRI	1	–0.894	–0.965	–0.893	–0.964
	2	–0.838	–0.941	–0.838	–0.941
	3	–0.829	–0.938	–0.830	–0.938
ANCF F -bar constant projection basis	1	–0.894	–0.965	–0.893	–0.965
	2	–0.840	–0.943	–0.840	–0.943
	3	–0.832	–0.940	–0.832	–0.941
ANCF F -bar linear projection basis	1	–0.894	–0.965	–0.893	–0.965
	2	–0.837	–0.941	–0.838	–0.941
	3	–0.829	–0.938	–0.830	–0.939
ANCF F -bar quadratic projection basis	1	–0.892	–0.963	–0.891	–0.962
	2	–0.837	–0.941	–0.838	–0.941
	3	–0.829	–0.938	–0.830	–0.938
ANCF F -bar cubic projection basis	1	–0.891	–0.962	–0.890	–0.962
	2	–0.837	–0.941	–0.838	–0.941
	3	–0.829	–0.938	–0.830	–0.938

The results presented in Table 1 show that the convergent solutions given by ANCF are noticeably different when different numbers of layers are used. For the one-layer model, the ANCF results are significantly different from the reference. The noticeable discrepancy between the reference FEA results and the ANCF models is mainly due to violation of the incompressibility assumption at the beam surface. Nevertheless, this behaviour is consistent with the characteristics of the finite element analysis, where incompressibility is ensured only on the average (Adler *et al.*, 2014). The standard approach to deal with such a problem is to employ a larger number of elements across thickness, and the results in Table 1 show that the beam models with two and three layers conform much better to the reference. Therefore, when the incompressible material model employs the locking elimination technique based on reduced integration, it is crucial to apply more elements across the transversal direction in order to obtain reasonable results. In addition, in the case of the F -bar method, the simplest constant projection basis is able to reproduce a proper solution that is only slightly different than the reference one, while offering the smallest computational complexity.

5.3. Cantilever rubber-like beam

The last example is the dynamic analysis of the clamped beam model, wherein the constraint equations are identical as those in the previous Section. The system is similar to the model shown by Jung *et al.* (2011). The body undergoes the gravitational force, and is made of a rubber-like material having density of 2150 kg/m^3 , Kirchhoff's modulus of 1.91 MPa and the penalty term of 10^3 MPa . The beam has a rectangular cross section of 7 mm width and 5 mm height, and 0.35 m in length. The models use thirty fully parameterized ANCF beam elements for each layer, whilst one- and three-layer models are compared. Such a large number of elements is needed to obtain a converged solution for both locking elimination procedures. The results of ANCF simulations are compared with the results obtained with the FEA package. The beam elements from the classic FEA package cannot be used with nonlinear incompressible material models. Therefore, SOLID185 (ANSYS® Academic Research, 2010) elements with reduced integration are used. To obtain a convergent solution, the use of 336 solids is sufficient. In this example, the only considered material model is the incompressible Neo-Hookean.

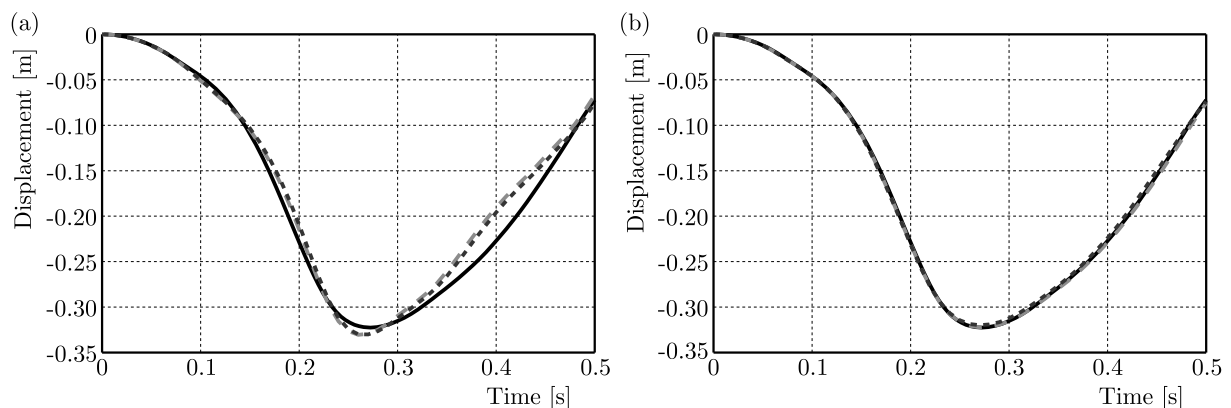


Fig. 6. Beam end tip displacements, (a) one-layer model, (b) three-layer model: (—) reference FEA, (---) ANCF with selective reduced integration, (· · ·) ANCF full integration with $\bar{\mathbf{F}}$

Figure 6a shows the results for two ANCF models with different locking suppression methods and for the reference FEA solution (Orzechowski and Frączek, 2015). The results are recalled here for easier comparison with the three-layer model. Both ANCF models provide almost the same results, and for the one-layer model a reasonably good agreement with the reference can be observed. However, the results in Fig. 6b show a large improvement for the three-layer model, irrespective of the employed projection basis. The results for the SRI present a similar advance.

One can conclude that the alleviation of the volumetric locking effect and introduction of the multi-layer structures leads to a substantial improvement as compared with the one-layer model and ensures the quality of the results obtained using higher-order beam elements with forty-two nodal parameters as shown by Orzechowski and Frączek (2015). In addition, in comparison with the FEA solid model, the number of parameters involved is, in the given application, more than four times less in the ANCF one-layer beam model, and two times less in the case of the three-layer model.

6. Conclusions

The ANCF is used successfully in the analysis of flexible bodies undergoing large deformations. The current study presents that nonlinear and nearly incompressible material models can be included in the ANCF in a straightforward way. The implementation of nonlinear incompressible materials and locking elimination techniques within the ANCF framework presented so far in the literature exhibit inaccurate behaviour in bending-dominated examples for a standard twenty-four parameter three-dimensional beam element.

In order to carry out accurate and efficient model simulations with incompressibility, two locking elimination techniques are presented – the F -bar strain projection method and the selective reduced integration. Both methods are implemented in the ANCF framework and tested with multi-layer beam structures. In addition, for the F -bar method, different projection spaces are investigated. Numerical tests show that the locking influence for an incompressible material models is enormous. The results of ANCF simulations are compared with a commercial FEA package and a very good agreement is found, especially for three-layer models. In the case of the F -bar method, the order of the projection space has a minor influence on the quality of the solution.

In the classical FEA, solid elements must be used when the materials with a nonlinear characteristic are used to model slender structures. In contrast, in the ANCF, fully parameterized beam elements can be employed in such systems, the result of which are models with much less parameters than for the FEA. However, the application of ANCF beams modelled with nonlinear materials to complex cross-sectional shapes might require further investigations (Orzechowski, 2012; Orzechowski and Shabana, 2016).

A desirable direction for future research is the development of alternative methods that would enable efficient locking elimination. In addition, it is indicated in the literature that, applying the systems which use incompressible material models, one may obtain solutions that are highly imprecise in stresses, although a proper solution exist for displacements (Bathe, 1996). Hence, the distribution of stresses in such models should also be taken into account as an essential research topic.

Acknowledgements

This work has been supported under grant No. DEC-2012/07/B/ST8/03993 by the National Science Centre.

References

1. ADLER J.H., DORFMANN L., HAN D., MACLACHLAN S., PAETSCH C., 2014, Mathematical and computational models of incompressible materials subject to shear, *IMA Journal of Applied Mathematics*, **79**, 5, 889-914
2. ANSYS®ACADEMIC RESEARCH, 2010, *ANSYS Mechanical APDL Documentation*, ANSYS Inc., release 13.0

3. BATHE K.J., 1996, *Finite Element Procedures*, Prentice Hall, New Jersey
4. BONET J., WOOD R.D., 1997, *Nonlinear Continuum Mechanics for Finite Element Analysis*, Cambridge University Press, Cambridge; New York, NY, USA
5. BRENNAN K.E., CAMPBELL S.L., PETZOLD L.R., 1996, *Numerical Solution of Initial-Value Problems in Differential-Algebraic Equations*, SIAM, Philadelphia
6. ELGUEDJ T., BAZILEVYS Y., CALO V.M., HUGHES T.J., 2008, B-bar and F-bar projection methods for nearly incompressible linear and non-linear elasticity and plasticity using higher-order NURBS elements, *Computer Methods in Applied Mechanics and Engineering*, **197**, 33-40, 2732-2762
7. GARCÍA DE JALÓN J., BAYO E., 1994, *Kinematic and Dynamic Simulation of Multibody Systems. The Real-Time Challenge*, Springer, New York
8. GARCIA-VALLEJO D., ESCALONA J.L., MAYO J., DOMÍNGUEZ J., 2003, Describing rigid-flexible multibody systems using absolute coordinates, *Nonlinear Dynamics*, **34**, 1-2, 75-94
9. GEAR C.W., LEIMKUHNER B., GUPTA G.K., 1985, Automatic integration of Euler-Lagrange equations with constraints, *Journal of Computational and Applied Mathematics*, **12-13**, 77-90
10. GERSTMAYR J., MATIKAINEN M.K., MIKKOLA A.M., 2008, A geometrically exact beam element based on the absolute nodal coordinate formulation, *Multibody System Dynamics*, **20**, 4, 359-384
11. GERSTMAYR J., SHABANA A.A., 2006, Analysis of thin beams and cables using the absolute nodal co-ordinate formulation, *Nonlinear Dynamics*, **45**, 1, 109-130
12. HAIRER E., WANNER G., 1996, *Solving Ordinary Differential Equations II. Stiff and Differential-Algebraic Problems*, Springer, Berlin, 2nd edition
13. HUGHES T.J.R., 1987, *The Finite Element Method. Linear Static and Dynamic Finite Element Analysis*, Prentice Hall, New Jersey
14. JUNG S., PARK T., CHUNG W., 2011, Dynamic analysis of rubber-like material using absolute nodal coordinate formulation based on the non-linear constitutive law, *Nonlinear Dynamics*, **63**, 1, 149-157
15. LIU C., TIAN Q., HU H., 2011, Dynamics of a large scale rigid-flexible multibody system composed of composite laminated plates, *Multibody System Dynamics*, **26**, 3, 283-305
16. MAQUEDA L.G., MOHAMED A.N.A., SHABANA A.A., 2010, Use of general nonlinear material models in beam problems: Application to belts and rubber chains, *Journal of Computational and Nonlinear Dynamics*, **5**, 2, 021003, 10 pages
17. MAQUEDA L.G., SHABANA A.A., 2007, Poisson modes and general nonlinear constitutive models in the large displacement analysis of beams, *Multibody System Dynamics*, **18**, 3, 375-396
18. ORZECOWSKI G., 2012, Analysis of beam elements of circular cross section using the absolute nodal coordinate formulation, *Archive of Mechanical Engineering*, **LIX**, 3, 283-296
19. ORZECOWSKI G., FRĄCZEK J., 2015, Nearly incompressible nonlinear material models in the large deformation analysis of beams using ANCF, *Nonlinear Dynamics*, **82**, 1, 451-464
20. ORZECOWSKI G., SHABANA A.A., 2016, Analysis of warping deformation modes using higher order ANCF beam element, *Journal of Sound and Vibration*, **363**, 428-445
21. PATEL M., ORZECOWSKI G., TIAN Q., SHABANA A.A., 2016, A new multibody system approach for tire modeling using ANCF finite elements, *Proceedings of the Institution of Mechanical Engineers, Part K: Journal of Multi-body Dynamics*, **230**, 1, 69-84
22. SHABANA A.A., 1997a, Definition of the slopes and the finite element absolute nodal coordinate formulation, *Multibody System Dynamics*, **1**, 3, 339-348
23. SHABANA A.A., 1997b, Flexible multibody dynamics: review of past and recent developments, *Multibody System Dynamics*, **1**, 2, 189-222
24. SHABANA A.A., 2008, *Computational Continuum Mechanics*, Cambridge University Press, Cambridge, first edition

25. SHABANA A.A., 2013, *Dynamics of Multibody Systems*, Cambridge University Press, 4th edition
26. SHABANA A.A., YAKOUB R.Y., 2001, Three dimensional absolute nodal coordinate formulation for beam elements: theory, *Journal of Mechanical Design*, **123**, 4, 606-613
27. SOPANEN J.T., MIKKOLA A.M., 2003, Description of elastic forces in absolute nodal coordinate formulation, *Nonlinear Dynamics*, **34**, 1, 53-74
28. SUGIYAMA H., ESCALONA J.L., SHABANA A.A., 2003, Formulation of three-dimensional joint constraints using the absolute nodal coordinates, *Nonlinear Dynamics*, **31**, 2, 167-195
29. SUGIYAMA H., GERSTMAYR J., SHABANA A.A., 2006, Deformation modes in the finite element absolute nodal coordinate formulation, *Journal of Sound and Vibration*, **298**, 4-5, 1129-1149
30. WASFY T.M., NOOR A.K., 2003, Computational strategies for flexible multibody systems, *Applied Mechanics Reviews*, **56**, 6, 553-613
31. WEHAGE R.A., HAUG E.J., 1982, Generalized coordinate partitioning for dimension reduction in analysis of constrained dynamic systems, *Journal of Mechanical Design*, **104**, 1, 247-255
32. YAKOUB R.Y., SHABANA A.A., 2001, Three dimensional absolute nodal coordinate formulation for beam elements: implementation and applications, *Journal of Mechanical Design*, **123**, 4, 614-621
33. ZIENKIEWICZ O.C., TAYLOR R.L., 2005, *The Finite Element Method for Solid and Structural Mechanics*, Butterworth-Heinemann, Oxford, 6th edition

Manuscript received September 19, 2016; accepted for print April 5, 2017

THE SPECIFIC DYNAMIC CAPACITY OF A PLANETARY ROLLER SCREW WITH RANDOM DEVIATIONS OF THE THREAD PITCH

FILIP LISOWSKI

Cracow University of Technology, Institute of Machine Design, Cracow, Poland
e-mail: ftisow@mech.pk.edu.pl

The paper presents an analysis of the specific dynamic capacity of a planetary roller screw including random deviations of the thread pitch. Results are based on a statistical analysis of loads between the screw and the roller obtained for the accepted bar model to determine the load distribution. Furthermore, the finite element analysis has been applied to determine stiffness coefficients of the screw-roller and the roller-nut cooperation. The purpose of the following considerations is to assess a decrease in the specific dynamic capacity of the planetary roller screw depending on random deviations of the thread pitch.

Key words: planetary roller screw, specific dynamic capacity, random deviations

1. Introduction

The planetary roller screw (PRS) is a highly efficient mechanical actuator for demanding applications (Fig. 1). The mechanism is used to convert rotational motion into linear motion or in the other way round. The main advantage of PRS is very high load capacity while maintaining high speed of operation and high positioning accuracy.

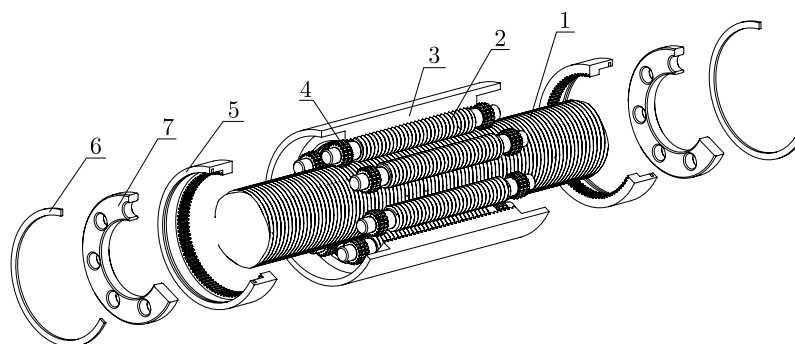


Fig. 1. Structure of the planetary roller screw (exploded view); 1 – screw, 2 – roller, 3 – nut, 4 – satellite gear, 5 – ring gear, 6 – retainer ring, 7 – annular hoop

One of the major problems concerning planetary roller screws is the carrying capacity related to the load distribution between cooperating elements. Theoretical load characteristics provide information about the most loaded regions of threads and enable determination of the equivalent load. Several authors of previous publications related to the planetary roller screw considered models for determination of the load distribution. Ma *et al.* (2012) adopted a model developed for ball screws given by Xuesong *et al.* (2003) to determine the static load distribution. The rollers were assumed as rigid bodies and only contact deformations of threads were involved in calculations based on the Hertzian theory. Ryś and Lisowski (2014) presented an analytical model for determination of the load distribution between cooperating elements for an arbitrary number of rollers. The idea of the model was to consider deformations of engaged elements as

deformations of rectangular volumes subjected to shear stresses. Contact deformations of threads and deformations of the screw and nut cores were taken into account by a properly chosen shear modulus. However, the model was intended only for the preliminary design. Lisowski (2014) proposed a model to determine the load distribution between the roller and the screw as well as between the roller and the nut, which allowed one to take into account contact deformations of threads and deformations of the screw and nut cores. Also, the various thread profiles were considered.

Lastly, Jones and Velinsky (2014) used the direct stiffness method to construct a model which considered the roller screw mechanism as a large spring system composed of individual springs referred to various elements. The authors used their method to calculate the axial stiffness of PRS and the load distribution between particular elements. In an earlier article, Velinsky *et al.* (2009) analysed kinematics, efficiency and the load carrying capacity. The load carrying capacity was derived based on geometric conditions and equilibrium of forces.

Recently, Abevi *et al.* (2015) presented a method to compute the static load distribution in any type of planetary roller screw based on a hybrid model including one-dimensional finite elements and non-linear springs.

However, apart from theoretical load distributions determined for nominal dimensions of cooperating threads, it is also essential to take into account the impact of manufacturing deviations. Deviations of the thread pitch affect theoretical load distributions between cooperating elements and, therefore, they impact the specific dynamic capacity of the planetary roller screw.

Although some authors have mentioned the importance of the impact of random deviations on the load distribution, the problem related to PRS has not been analysed in publications yet. In turn, a similar problem but related to helical gears was analysed by Ryś (1990). The author studied the impact of random deviations of the gears pitch on static and dynamic loads. Owing to dynamic overload, mostly the problem of start-up was analysed.

This paper presents an analysis of the impact of random deviations of the thread pitch on the specific dynamic capacity of the planetary roller screw mechanism. The results are based on a statistical analysis of the loads on threads, obtained based on the bar model.

2. The load distribution between cooperating elements – bar model

In order to determine the load distribution between cooperating elements of the planetary roller screw, a bar model proposed by Lisowski (2014), has been accepted. This model is preferable as it enables taking into account random deviations of the thread pitch for particular pairs of threads. However, determining the stiffness of a single pair of cooperating threads of the screw and the roller as well as the roller and the nut requires doing an additional finite element analysis.

The model refers to the section of PRS including one roller cooperating with the screw and the nut as shown in Fig. 2. The number of cooperating threads is arbitrary. Also, various thread profiles can be accepted by assuming proper stiffness parameters obtained from FEA.

For further considerations, the following assumptions have been made: the core of the roller is non-deformable; cores of the screw and the nut are deformable; threads of the roller, screw and the nut are deformable; stiffness of the screw core is close to stiffness of the nut core; forces in the screw and nut cores change in steps. Due to the small helix angle, the forces q_{s_j} and q_{n_j} belong to the same plane; the external force Q is distributed proportionally into the rollers.

The axial forces in the screw and nut cores can be consistent or opposite. The system of forces shown in Fig. 2 which refers to the case when both the screw and the nut are compressed (a) or the screw is compressed while the nut is tensioned (b). However, depending on locations where the forces are applied, it is also possible to obtain two other cases in which both the screw and the nut are tensioned or the screw is tensioned while the nut is compressed. In further

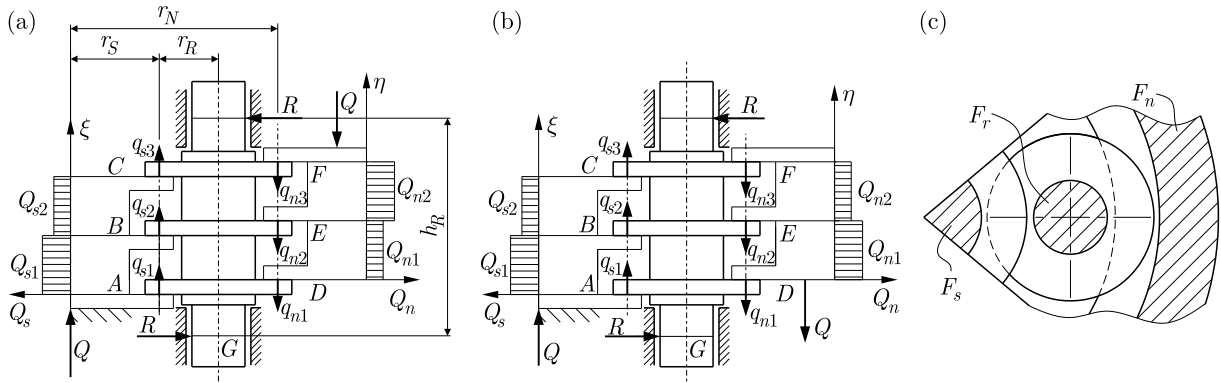


Fig. 2. Dimensions and the system of forces of the bar model: (a) screw and nut compressed, (b) screw compressed, nut tensioned, (c) cross-sections of cooperating elements

considerations, the cases of consistent and opposite loads in the screw and in the nut (Fig. 2a,b) will be considered as an example.

Under the load Q , the cores of the screw and the nut undergo axial displacements Δ_{si} and Δ_{ni} . At the same time, the thread displacements occur: δ_{sj} at the screw-roller thread interface and δ_{nj} at the nut-roller threads interface. These displacements include contact deformations as well as shear strains. The displacements of cooperating elements and dimensional chains are shown in Fig. 3.

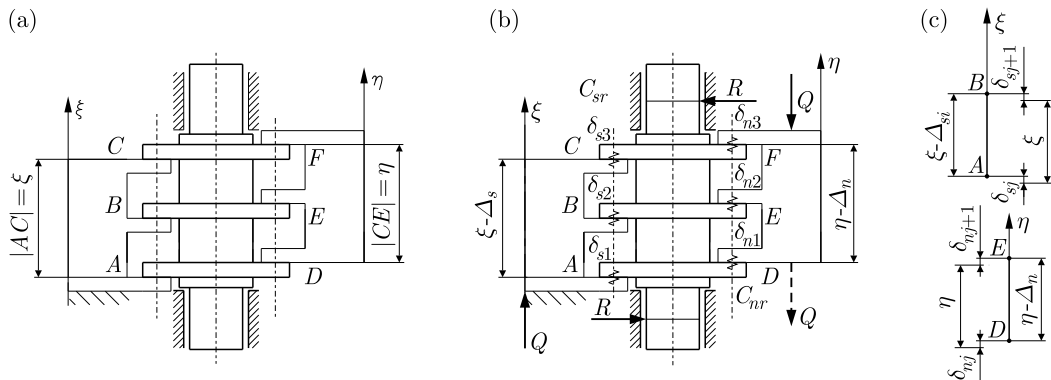


Fig. 3. Deformations of planetary roller screw elements: (a) unloaded model, (b) loaded model, (c) dimensional chains

According to Hooke's law, assuming that stress in cross-sections of the screw and nut cores is distributed uniformly, the axial displacements of the screw core for any value of $\xi < |AC|$ and, respectively, the axial displacement of the nut core for any value of $\eta < |DF|$ are obtained from the following equation

$$\Delta_s = \int_0^{\xi_a} \frac{\sigma_s(\xi)}{E_s} d\xi = \int_0^{\xi_a} \frac{Q_s(\xi)}{E_s F_s} d\xi \quad \Delta_n = \int_0^{\eta_a} \frac{\sigma_n(\eta)}{E_n} d\eta = \int_0^{\eta_a} \frac{Q_n(\eta)}{E_n F_n} d\eta \quad (2.1)$$

where $\sigma_s(\xi)$, $\sigma_n(\eta)$ are normal stresses in cross-sections of the screw and nut cores; $Q_s(\xi)$, $Q_n(\eta)$ – axial forces in the screw and in the nut; E_s , E_n – Young's modules of the screw and the nut; F_s , F_n – cross-sectional areas of the screw and nut cores.

Assuming a step change of forces in cross-sections of the screw and nut cores (wherein the step is equal to the thread pitch) and accepting n intervals of force variation, Eq. (2.1) takes the form

$$\Delta_s = \sum_{i=1}^n \Delta_{s_i} = \sum_{i=1}^n \frac{Q_{s_i} p}{E_s F_s} \quad \Delta_n = \sum_{i=1}^n \Delta_{n_i} = \sum_{i=1}^n \frac{Q_{n_i} p}{E_n F_n} \tag{2.2}$$

where $\Delta_{s_i}, \Delta_{n_i}$ are axial displacements of cross-sections of the screw and nut cores; Q_{s_i}, Q_{n_i} – axial forces in the screw and in the nut for the i -th interval ($i = 1, \dots, n, n$ – number of intervals of force variation); p – thread pitch.

Axial displacements at the interfaces of the screw-roller and roller-nut threads, which include contact deformations as well as shear strains, can be determined as

$$\delta_{s_j} = \frac{q_{s_j}}{C_{sr}} \quad \delta_{n_j} = \frac{q_{n_j}}{C_{nr}} \tag{2.3}$$

where C_{sr}, C_{nr} are stiffness coefficients of the screw-roller and the roller-nut cooperation; q_{s_j}, q_{n_j} – axial forces at the interfaces of the screw-roller and the roller-nut threads ($j = 1, \dots, m, m$ – number of threads). Considering the system of forces shown in Fig. 2a, the axial forces in the screw and in the nut in the case of consistent loads can be determined using Eqs. (2.4). Consequently, for the opposite loads in the screw and in the nut (Fig. 2b), Eqs. (2.5) can be used. The axial load is a sum of forces on threads as given by Eqs. (2.6)

$$\begin{cases} Q_{s_1} = Q - q_{s_1} \\ Q_{s_2} = Q - q_{s_1} - q_{s_2} \end{cases} \quad \begin{cases} Q_{n_1} = Q - q_{n_3} - q_{n_2} \\ Q_{n_2} = Q - q_{n_3} \end{cases} \tag{2.4}$$

$$\begin{cases} Q_{s_1} = Q - q_{s_1} \\ Q_{s_2} = Q - q_{s_1} - q_{s_2} \end{cases} \quad \begin{cases} Q_{n_1} = Q - q_{n_1} \\ Q_{n_2} = Q - q_{n_1} - q_{n_2} \end{cases} \tag{2.5}$$

$$Q = q_{s_1} + q_{s_2} + q_{s_3} \quad Q = q_{n_1} + q_{n_2} + q_{n_3} \tag{2.6}$$

Considering the dimensional chains obtained for the loaded model (Fig. 3b,c), the displacement equilibrium equations take the following form

$$\begin{aligned} \Delta_{S1} &= \delta_{S1} - \delta_{S2} & \Delta_{N1} &= \delta_{N2} - \delta_{N1} \\ \Delta_{S2} &= \delta_{S2} - \delta_{S3} & \Delta_{N2} &= \delta_{N3} - \delta_{N2} \end{aligned} \tag{2.7}$$

Taking into account Eqs. (2.2)-(2.7), the system of equations for determination of the load distribution are obtained. Equations (2.8) refer to the case of the consistent load in the screw and the nut while Eqs. (2.9) refer to the case of the opposite load in the screw and the nut. In both cases, the sum of loads on threads is equal to the axial load as given by Eq. (2.10)

$$\frac{p}{E_s F_s} \left(Q - \sum_{j=1}^i q_{s_j} \right) = (C_{sr})^{-1} (q_{s_i} - q_{s_{i+1}}) \quad (n \text{ equations}) \tag{2.8}$$

$$\frac{p}{E_n F_n} \left(Q - \sum_{j=i+1}^m q_{n_j} \right) = (C_{nr})^{-1} (q_{n_i} - q_{n_{i+1}}) \quad (n \text{ equations})$$

$$\frac{p}{E_s F_s} \left(Q - \sum_{j=1}^i q_{s_j} \right) = (C_{sr})^{-1} (q_{s_i} - q_{s_{i+1}}) \quad (n \text{ equations}) \tag{2.9}$$

$$\frac{p}{E_n F_n} \left(Q - \sum_{j=1}^i q_{n_j} \right) = (C_{nr})^{-1} (q_{n_{i+1}} + q_{n_i}) \quad (n \text{ equations})$$

$$Q = \sum_{j=1}^m q_{s_j} \quad Q = \sum_{j=1}^m q_{n_j} \tag{2.10}$$

$j = 1, \dots, m, m$ – number of threads; $i = 1, \dots, n, n$ – number of intervals of force variation.

2.1. Determination of the stiffness coefficients

Stiffness coefficients of the screw-roller thread pair (C_{sr}) as well as the nut-roller thread pair (C_{nr}) can be determined using FE analysis. The finite element models including sections of cooperating pairs of threads and the accepted boundary conditions are shown in Fig. 4. A triangular thread profile with the pressure angle $\alpha_0 = 45^\circ$ has been accepted. The helix angle has been omitted.

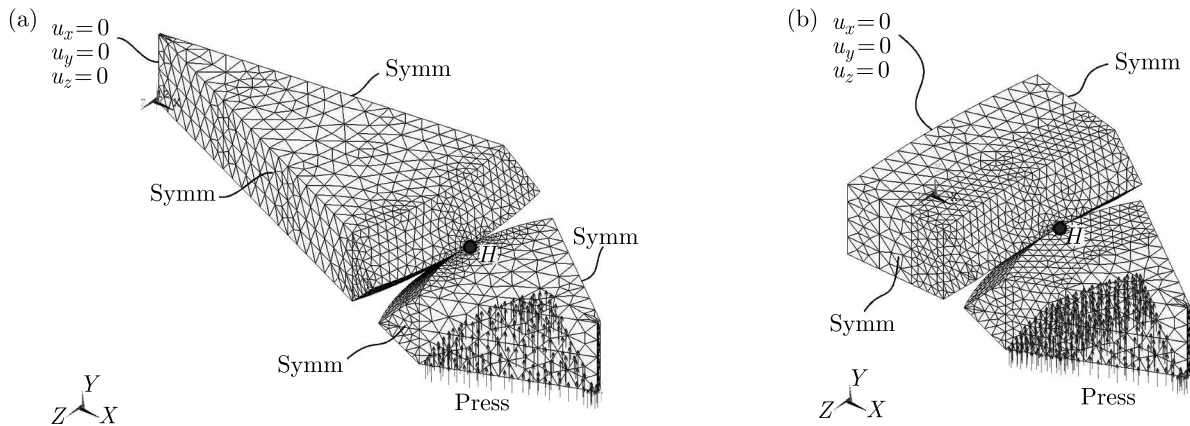


Fig. 4. Finite element models of the screw-roller, nut-roller sections with boundary conditions

The load is applied to the roller core as a normal pressure. The axial displacement u_y is measured in the point H . The stiffness coefficients are determined using the following equations

$$C_{sr} = \frac{P_H}{u_y} \quad C_{nr} = \frac{P_H}{u_y} \quad P_H = \frac{P_n x_c}{r_r - h_z/2} \quad (2.11)$$

where P_n is the normal load on the roller core surface (axial load per single pair of cooperating threads), P_H – normal load on the roller core surface reduced to the point H , x_c – distance between the gravity centre of the roller core cross-section and the roller axis, h_z – height of the thread profile, r_r – pitch diameter of the roller.

Stiffness coefficients for various load levels and for a series of pitch diameter combinations referred to the triangular thread profile, can also be assumed using the graphs presented by Lisowski (2015).

2.2. Load distribution based on the bar model

Examples of theoretical load distributions obtained for the bar model are shown in Figs. 5a and 5b. The accepted parameters of the planetary roller screw and load conditions are presented in Table 1. The stiffness coefficients of the screw-roller thread pair and the nut-roller thread pair have been determined as has been stated in the previous Section.

3. Specific dynamic capacity of the planetary roller screw

Taking into account a formula for the rolling contact life, the specific dynamic capacity of the planetary roller screw depends on the equivalent load transferred by the mechanism, as given by

$$N = \left(\frac{C}{P}\right)^3 N_0 \quad (3.1)$$

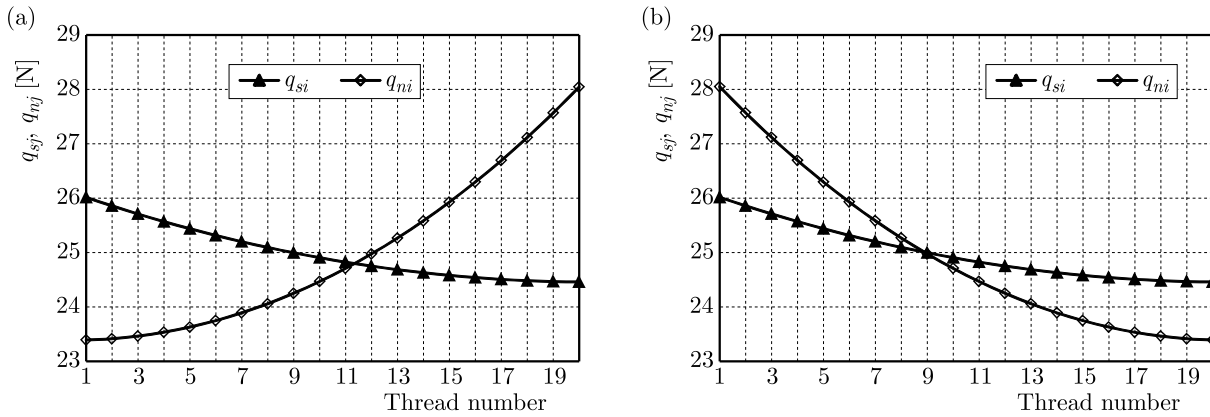


Fig. 5. Load distribution on the screw (q_{si}) and nut (q_{ni}) threads – (a) consistent and (b) opposite loads in the screw and the nut; $r_s = 15$ mm, $r_r = 5$ mm, $r_n = 25$ mm, $p = 2$ mm, $m = 5$, $P_n = 25$ N

Table 1. Planetary roller screw parameters

Pitch radius of screw	$r_s = 15$ mm
Pitch radius of roller	$r_r = 5$ mm
Pitch radius of nut	$r_n = 25$ mm
Lead	$p = 2$ mm
Pressure angle	$\alpha_0 = 45^\circ$
Number of intervals of force variation	$n = 19$
Number of threads	$m = 20$
Axial load per one roller	$Q = 500$ N
Axial load per single pair of cooperating threads	$P_n = 25$ N
Stiffness coefficient of screw-roller thread pair	$C_{sr} = 2505$ N/mm
Stiffness coefficient of nut-roller thread pair	$C_{nr} = 7482$ N/mm

where N is life in million cycles, N_0 – life equal to 1 million cycles, C – specific dynamic capacity, P – equivalent load. According to Lisowski (2015), limitation of the planetary roller screw capacity is related to the permissible contact pressure between threads of the screw and the roller. Therefore, the analysis of PRS capacity is referred to cooperation of the screw and the roller. Considering the screw-roller cooperation, the equivalent load can be accepted as the average load on all threads.

However, the actual dimensions of threads would be subjected to random deviations. Distributions of the deviations are very diverse and usually have an irregular form. They can be determined based on the results of measurements of a large batch of machined parts under stated conditions, for example by building a histogram of deviations. However, in many cases, a theoretical distribution determined empirically can be accepted. Referring to (Białas, 1986), if many independent factors affect manufacturing deviations, the normal distribution, defined by the density function of deviations, is obtained.

Taking into account the random deviations of the thread pitch, the load density distribution related to the average load of threads ($x = P_i/P_{ave}$) is a normal distribution given by

$$\psi(x) = \frac{1}{\sigma\sqrt{2\pi}} \exp\left(\frac{-(x - \mu)}{2\sigma^2}\right) \tag{3.2}$$

where σ is the standard deviation, μ – expected value.

Assuming that the PRS life $N = N_0 = 1$ million cycles, the specific dynamic capacity is proportional to the equivalent load. Consequently, the same relation is obtained when the random deviations of the thread pitch are taken into account

$$C = P \quad C_{dev} = P_{dev} \tag{3.3}$$

Since in Eq. (3.1) the relation between the specific dynamic capacity and the equivalent force is to the third power, the function given by Eq. (3.4)₁ is accepted. The integral of this function, which can be expressed as a sum, is given by Eq. (3.4)₂

$$\eta(x) = [\psi(x)]^3 \quad \eta_1 = \int_0^x [\psi(x)]^3 dx = \frac{1}{n_i} \sum \left(\frac{P_i}{P_{ave}}\right)^3 \quad n_i = n_t + n_d \tag{3.4}$$

where P_i are axial forces on particular threads in the case with random deviations of the thread pitch, P_{ave} – average load of all threads, n_i – number of forces including the number of cooperating threads and the number of intervals of deviation variation, n_t – number of cooperating threads, n_d – number of intervals of deviation variation.

The equivalent force as well as the specific dynamic capacity, including random deviations of the thread pitch, can be determined using Eqs. (3.5)_{1,2}. The decrease of the specific dynamic capacity caused by the occurrence of random deviations can be estimated as

$$P_{dev} = P_{ave} \sqrt[3]{\frac{1}{n_i} \sum \left(\frac{P_i}{P_{ave}}\right)^3} \quad C_{dev} = C \sqrt[3]{\frac{1}{n_i} \sum \left(\frac{P_i}{P_{ave}}\right)^3} \tag{3.5}$$

$$\Delta_{dev} = \left| \frac{C_{dev}}{C} - 1 \right|$$

where P_{dev} is the equivalent load including random deviations of the thread pitch C – specific dynamic capacity of PRS excluding random deviations of the thread pitch, C_{dev} – specific dynamic capacity including random deviations of the thread pitch, Δ_{dev} – decrease of the specific dynamic capacity caused by the random deviations of the thread pitch.

3.1. The impact of random deviations of the thread pitch on the decrease of the specific dynamic capacity of PRS

A series of calculations using the bar model to determine the load distribution has been conducted in order to obtain load distributions including random deviations of the thread pitch. Those load distributions are analysed to assess how the magnitude of random deviations of the thread pitch affects the specific dynamic capacity of the planetary roller screw. The load case, in which the screw is compressed, is considered. In that case, the load distribution between the screw and the roller, including random deviations of the thread pitch, can be obtained by introducing an additional displacement δ_i^{sr} into Eq. (2.8)₁. This displacement represents the value of the random deviation of the thread pitch. As a result, a system of equations Eq. (3.6)₁ is obtained, wherein the sum of loads on particular threads is equal to the axial load as given by Eq. (3.6)₂

$$\frac{p}{E_s F_1} \left(Q - \sum_{j=1}^i qS_j \right) + \delta_i^{sr} = (C_{S-R})^{-1} (qS_i - qS_{i+1}) \quad (n \text{ equations}) \tag{3.6}$$

$$Q = \sum_{j=1}^m qS_j$$

$j = 1, \dots, m$, m – number of threads; $i = 1, \dots, n$, n – number of intervals of force variation.

One thousand load distributions including random deviations of the thread pitch has been assumed for the particular case of analysis. The random deviations have been generated using a random number generator implemented in MATLAB. For each pair of cooperating threads of the screw and the roller, one thousand random deviations has been generated. Due to the lack

of information about results of measurements of a large batch of machined PRS parts under the stated conditions, the probability density function of normal (Gaussian) distribution with a mean of $\mu = 0$ and standard deviation $\sigma = 2$ has been assumed (Fig. 6). The random deviations in μm generated for the desired parameters of normal distribution are presented in Table 2 and as a surface graph in Fig. 7.

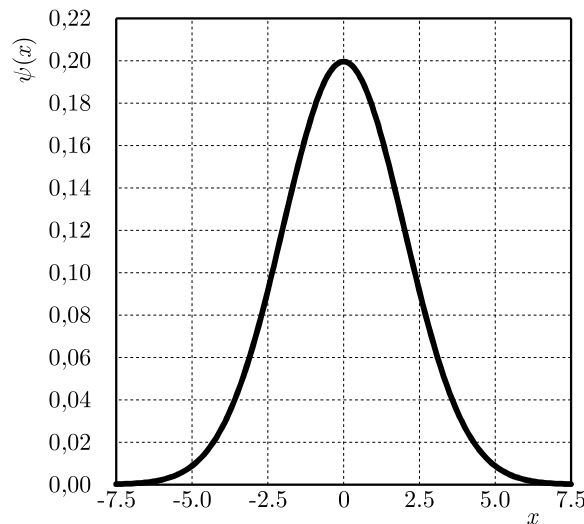


Fig. 6. Gaussian density distribution of random deviations ($\mu = 0, \sigma = 2$)

Table 2. Random deviations in μm ($\mu = 0, \sigma = 2$)

		Thread number											
		1	2	3	4	5	6	7	8	9	10	...	20
Sampling number	1	2.611	-0.855	-0.983	-2.884	-1.291	-2.100	-3.837	-0.277	2.282	0.328	2.221	2.221
	2	1.968	-1.159	1.315	-1.920	-0.578	0.937	-0.262	0.864	1.866	-1.414	...	1.427
	3	-2.503	1.852	2.872	0.695	2.001	0.566	-1.537	4.506	-1.041	4.593	...	-1.292
	4	-0.360	0.011	-3.070	-0.206	-1.176	2.682	4.780	-0.919	-1.179	0.855	...	1.753
	5	-1.487	-1.269	3.506	1.321	3.115	0.761	0.154	0.181	2.763	3.224	...	0.171
	6	0.466	1.717	2.566	2.314	-2.723	2.871	0.751	5.216	-0.609	-1.302	...	-0.121
	7	4.203	-0.962	0.187	-1.839	3.800	1.599	0.791	-2.074	0.391	-1.907	...	-0.790
	8	-1.753	2.979	3.160	-1.941	0.356	3.257	-0.225	0.506	2.318	-2.077	...	-2.759
	9	3.898	-1.259	0.490	0.912	-4.333	0.258	-3.658	-0.533	0.066	1.107	...	-1.033
	10	-0.931	-1.188	-2.041	-0.242	1.414	-4.170	4.183	2.635	-1.910	0.974	...	-1.021

1000	2.706	-0.844	0.652	-2.440	-2.416	0.206	-2.889	-2.219	-0.382	0.445	...	3.456	

In order to assess the impact of magnitude of the random deviations of the thread pitch on the decrease of the specific dynamic capacity of PRS, the decreasing coefficient f , defined by Eq. (3.7), has been accepted. This coefficient refers to the average axial displacement of all threads in the case without random deviations of the thread pitch. Therefore, the impact of the load level is included as

$$f = \frac{\kappa_{dev} u_0}{\delta_{max}} \tag{3.7}$$

where δ_{max} is the maximum value of random deviations, u_0 – average axial displacement of all threads in the case without random deviations of the thread pitch, κ_{dev} – factor determining the relation between the maximum random deviation δ_{max} and the average axial displacement u_0 , wherein $\kappa_{dev} = \{10, 20, 40\}\%$.

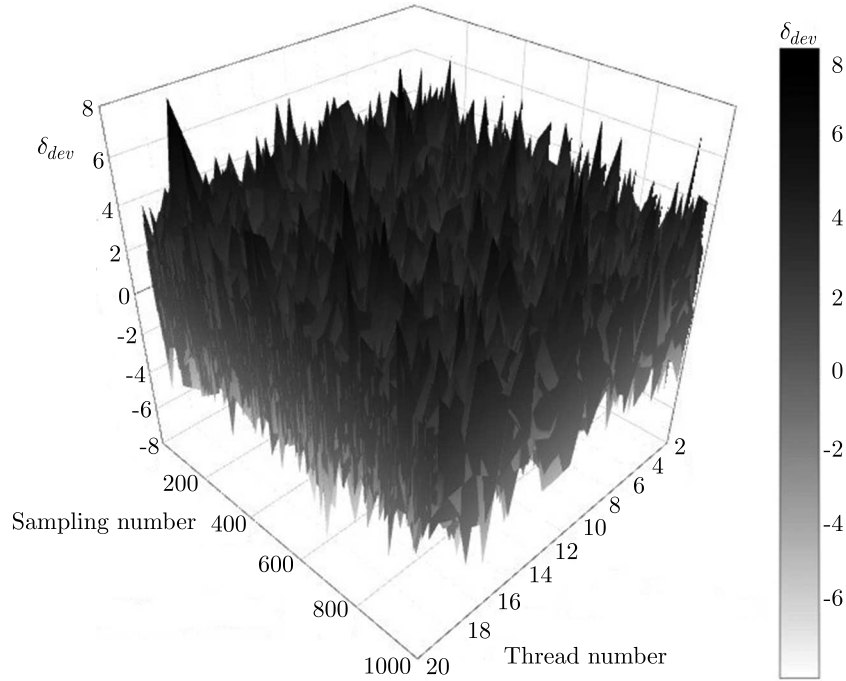


Fig. 7. Surface plot of 20 000 random deviations of the thread pitch

For the considered geometry of PRS, the average axial displacement of all threads in the case without random deviations of the thread pitch is $u_0 = 19.973 \mu\text{m}$. The maximum drawn deviation, obtained among 20 000 values, is $\delta_{max} = 8.184$. Accordingly, the decreasing coefficients, listed in Table 3, have been accepted.

Table 3. Decreasing coefficients and maximum random deviations

κ_{dev}	f	$\delta_{max} [\mu\text{m}]$
10%	0.244	1.997
20%	0.488	3.977
40%	0.976	7.990

Tables of random deviations for three considered values of κ_{dev} have been obtained by multiplying the values of random deviations in Table 2 by the consecutive f coefficients. Table 4, referring to the case of $\kappa_{dev} = 10\%$, presents exemplary results. In the same case, one thousand load distributions between the screw and the roller including random deviations of thread pitch are presented in a surface plot in Fig. 8.

Using Eq. (3.5)₃, the decrease of the specific dynamic capacity related to particular threads and to all cooperating threads of the screw and the roller have been determined. The results of calculations are presented in Figs. 9a and 9b.

4. Conclusions

The decrease of the specific dynamic capacity related to particular threads is the greatest in the end parts of the roller. The largest decrease occurs on the first engaged threads, which are in fact the most loaded ones. Concerning the cooperation of all engaged threads, it has been shown that the decrease of the specific dynamic capacity increases with an increase in the random deviations of the thread pitch. In the case in which the maximum deviation of the thread pitch

Table 4. Random deviations in μm ($\mu = 0, \sigma = 2$); $\kappa_{dev} = 10\%$, $f = 0.244$

		Thread number											
		1	2	3	4	5	6	7	8	9	10	...	20
Sampling number	1	0.637	-0.209	-0.240	-0.704	-0.315	-0.512	-0.936	-0.068	0.557	0.080	0.542	0.542
	2	0.480	-0.283	0.321	-0.469	-0.141	0.229	-0.064	0.211	0.455	-0.345	...	0.348
	3	-0.611	0.452	0.701	0.170	0.488	0.138	-0.375	1.099	-0.254	1.121	...	-0.315
	4	-0.088	0.003	-0.749	-0.050	-0.287	0.655	1.166	-0.224	-0.288	0.209	...	0.428
	5	-0.363	-0.310	0.855	0.322	0.760	0.186	0.038	0.044	0.674	0.787	...	0.042
	6	0.114	0.419	0.626	0.565	-0.664	0.700	0.183	1.273	-0.149	-0.318	...	-0.030
	7	1.025	-0.235	0.046	-0.449	0.927	0.390	0.193	-0.506	0.095	-0.465	...	-0.193
	8	-0.428	0.727	0.771	-0.474	0.087	0.795	-0.055	0.124	0.566	-0.507	...	-0.673
	9	0.951	-0.307	0.119	0.223	-1.057	0.063	-0.893	-0.130	0.016	0.270	...	-0.252
	10	-0.227	-0.290	-0.498	-0.059	0.345	-1.017	1.021	0.643	-0.466	0.238	...	-0.249

1000	0.660	-0.206	0.159	-0.595	-0.589	0.050	-0.705	-0.541	-0.093	0.109	...	0.843	

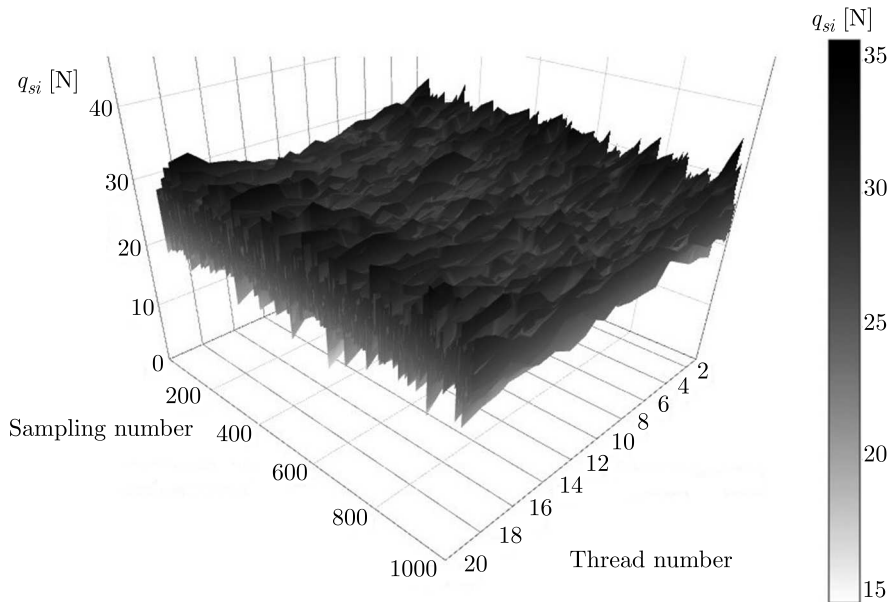


Fig. 8. Surface plot of one thousand load distributions between the screw and the roller including random deviations of the thread pitch ($f = 0.244, \kappa_{dev} = 10\%$)

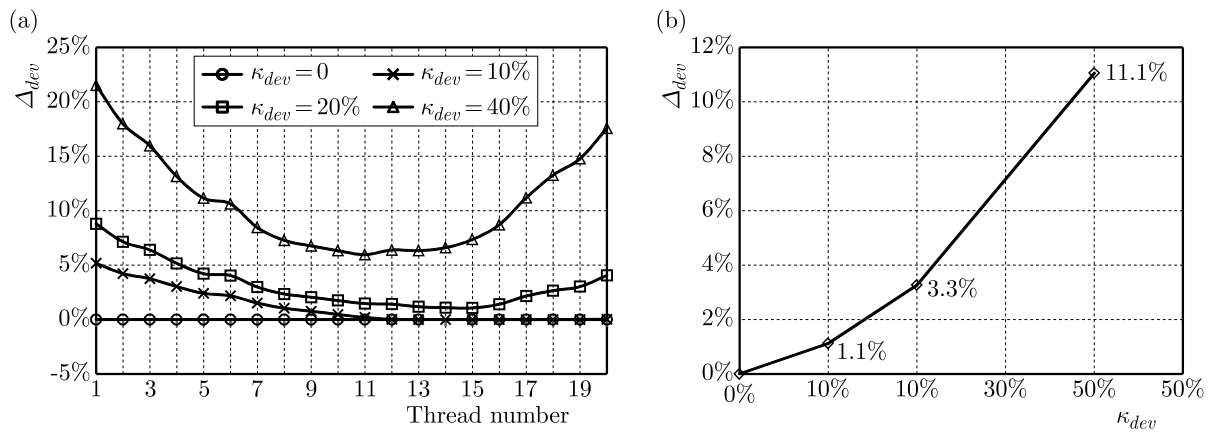


Fig. 9. Decrease of the specific dynamic capacity for: (a) particular screw-roller threads pair, (b) all cooperating threads

does not exceed 20% of the average axial displacement of all the threads, the maximum decrease in the specific dynamic capacity of PRS is small and equals 3.3%. On the other hand, in the case where the maximum deviation of the thread pitch is 40% of the average axial displacement of all the threads, the decrease of the specific dynamic capacity is up to 11.1%. Based on the analysis, it can be concluded that the maximum deviation of the thread pitch, which does not significantly affect the reduction of the specific dynamic capacity of the planetary roller screw under the nominal load, should not exceed 20% of the average axial displacement of all the threads.

Similar results can be expected for different dimensions of the planetary roller screw. This is due to taking into account the relation between the random deviations of the thread pitch and the average displacement of all the threads for the accepted load level.

While considering the essence of cooperation of the PRS elements, we deal with a multipoint support. Therefore, the specific dynamic capacity does not depend on the capacity of the most loaded pair of threads. Even if the carrying capacity of this pair is exhausted, the other threads take over the load. The specific dynamic capacity of a significant number of thread pairs has to be exhausted, to exhaust the carrying capacity of the planetary rollers screw.

Accordingly, the decrease of the specific dynamic capacity of all the cooperating threads, presented in Fig. 9b, is the conclusive parameter.

A similar procedure of assessing the impact of random deviations of the thread pitch on the specific dynamic capacity can be also carried out in the case of non-Gaussian distributions of random deviations.

References

1. ABEVI F.K., DAIDIÉ A., CHAUSSUMIER M., SARTOR M., 2015, Static load distribution and axial stiffness in a planetary roller screw mechanism, *Journal of Mechanical Design*, doi: 10.1115/1.4031859
2. BIAŁAS S., 1986, *Tolerancje geometryczne*, PWN, Warszawa
3. JONES M.H., VELINSKY A., 2014, Stiffness of the roller screw mechanism by the direct method, *Mechanics Based Design of Structures and Machines: An International Journal*, **42**, 17-34, doi: 10.1080/15397734.2013.839385
4. LISOWSKI F., 2014, The Analysis of displacements and the load distribution between elements in a Planetary Roller Screw, *Applied Mechanics and Materials*, **680**, 361-364
5. LISOWSKI F., 2015, *Load analysis and optimization design of selected planetary roller screws* (in Polish), Wydawnictwo Politechniki Krakowskiej, ISBN 978-83-7242-865-3
6. MA S., LIU G., TONG R., ZHANG X., 2012, A new study on the parameter relationships of planetary roller screws, *Mathematical Problems in Engineering*, Article ID 340437, doi: 10.1155/2012/340437
7. MEI X., TSUTSUMI M., TAO T., SUN N., 2003, Study on the load distribution of ball screws with errors, *Mechanism and Machine Theory*, **38**, 1257-1269
8. RYŚ J., 1990, Transient and steady vibration of helical gears, *Journal of Theoretical and Applied Mechanics*, **28**, 1/2, 207-216
9. RYŚ J., LISOWSKI F., 2014, The computational model of the load distribution between elements in planetary roller screw, *Journal of Theoretical and Applied Mechanics*, **52**, 3, 699-705
10. VELINSKY A., CHU B., LASKY T.A., 2009, Kinematics and efficiency analysis of the planetary roller screw mechanism, *Journal of Mechanical Design*, **131**, doi: 10.1115/1.3042158.

INVESTIGATION OF BOUNDARY CONDITION EFFECTS ON THE STABILITY OF FGP BEAMS IN THERMAL ENVIRONMENT

REZA NASIRZADEH, BASHIR BEHJAT, MAHSA KHARAZI, ATA KHABAZAGHDAM

Mechanical Engineering Faculty, Sahand University of Technology, Tabriz, Iran

e-mail: behjat@sut.ac.ir

In this paper, stability and instability of Functionally Graded Piezoelectric (FGP) beams is investigated based on the Timoshenko beam theory. The material properties of the beam are considered to change gradually through thickness of the beam by a simple power law. By using the principle of minimum total potential energy, governing equations of the beam are derived. Stability behavior of the beam is predicted by solving the governing equations of the FGP beam. The results show that the homogeneity of boundary conditions plays a critical role in the stability of the FGP beam. While non-homogeneous boundary conditions lead to stable behavior of the FGP beam; homogeneous boundary conditions cause instability in the beam. By solving the eigenvalue equation of the FGP beam, the buckling load of the beam is obtained for the beams that have unstable behavior. Finally, the effects of various parameters on the buckling load of the unstable beam, such as power law index, temperature, applied voltage and aspect ratio are investigated, and the results are compared with the Euler-Bernoulli beam theory.

Keywords: FGP beam, stability, instability, buckling load, Timoshenko beam theory, non-homogeneous and homogeneous boundary conditions

1. Introduction

Piezoelectric materials have been commonly used in various types of structures. Recently, a new kind of materials called the FGP materials, have been developed to improve the reliability and effectiveness of piezoelectric structures by extending the concept of well-known Functionally Graded Materials (FGM) to piezoelectric materials. The emergence of FGP materials has demonstrated that they have the potential to reduce stress concentration and provide improved residual stress distribution, enhanced thermal properties, and higher fracture toughness. Beam-like FGP structures are commonly used as sensors and actuators in a variety of mechanical, civil, and structural applications at various scales (Qin, 2013; Yang, 2005). Li *et al.* (2006) studied thermal post-buckling of Functionally Graded (FG) beams based on Timoshenko beam theory. They extracted nonlinear governing equations of the beam under non-uniform thermal and mechanical loads. Then, they evaluated thermal post-buckling of fixed-fixed beams by using a shooting method. Ying *et al.* (2008) studied bending and free vibration of an FG beam, which was located on the Winkler-Pasternak elastic substrate, using an analytical method. They investigated the effect of various parameters such as the power law index and aspect ratio on the response of the FG beam. Pradhan and Murmu (2009) explored vibration of the FG beam located on the Winkler elastic substrate by using a modified DQ (differential quadrature) method. Kiani and Eslami (2010) accomplished an analytical research into thermal buckling of FG beams, assuming that material properties changed according to the power law. They utilized the Euler-Bernoulli beam theory with consideration of nonlinear terms of strain in the formulation. In that paper, the critical temperature was obtained for three types of uniform, linear and nonlinear thermal loadings through the thickness direction of the beam. Doroushi *et al.* (2011)

reported the dynamic response of FGPM beams based on the third-order shear deformation theory of a simple higher-order theory by using the finite element method. Fallah and Aghdam (2011) used the Euler-Bernoulli beam theory to study free vibration and post-buckling of the FG beams which were supported by a nonlinear elastic substrate. Furthermore, they assumed the von Kármán nonlinear strains in the formulation and solved the obtained governing equations of the beam by He's variational method. Wattanasakulpong *et al.* (2011) studied buckling and vibration of FG beams based on the third order shear deformation beam theory by using the power law model to define material properties through the thickness direction. They solved the eigenvalue problem by the Ritz method. Davoodinik and Rahimi (2011) investigated large deformation of tapered FG beams using a semi-analytical method. Li and Batra (2013) studied the buckling load of functionally graded Timoshenko and Euler-Bernoulli beams. They used the equilibrium method to derive governing equations of the FG beam and solved the obtained equations for different boundary conditions except a clamped-simply supported (C-S) beam. For C-S beams, they used a transcendental equation to find the critical buckling load. Zhang (2013) analyzed nonlinear bending of FGM beams based on the physical neutral surface and higher order shear deformation theory. He considered material properties to be temperature-dependent and variable in the thickness direction. Esfahani *et al.* (2013) studied non-linear thermal stability of temperature dependent FGM beams supported on non-linear hardening elastic foundations. They utilized a modified DQ method to solve the governing equations. They also explored some kinds of boundary conditions and thermal loading in analysis of the stability of FGM beams. Fu *et al.* (2012) investigated buckling, free vibration and dynamic stability of FGP beams in thermal environment by using nonlinear analysis. To perform thermal-electrical buckling solutions, they used the Euler-Bernoulli beam theory and Galerkin method. Komijani *et al.* (2013a) studied non-linear thermo-electrical stability of FGP beams based on the Timoshenko beam theory. They utilized the finite element method to analyze nonlinear behavior of beams in different boundary conditions. In an other work, Komijani *et al.* (2013b) investigated nonlinear stability and vibration of pre and post-buckled FGPM microstructures.

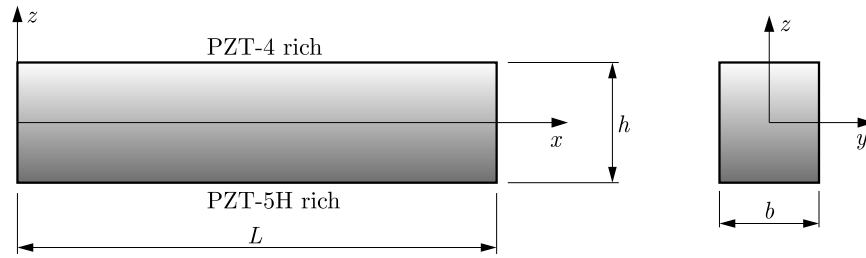
In this paper, thermal, mechanical and electrical loads are considered. A modified coupled stress theory and the von Kármán strains are utilized to obtain governing equations of the beam. Nasirzadeh *et al.* (2014) studied stability of FGP beams under thermal, electrical and mechanical loadings, and showed that thermal loading had a greater effect on the buckling point of the FGP beam in comparison with the electrical loading.

In this paper, stability and instability of FGP beams are investigated under thermal and electrical loadings. Material properties are considered to change gradually according to the power law. The governing equations are derived based on the Timoshenko beam theory. The FGP beam is under electrical, thermal and mechanical loadings. The temperature field is assumed to change uniformly and linearly in the thickness direction of the beam. The governing equation of the FGP beam is derived using the minimum potential theory and then the governing equation is solved by using an analytical method. Stability of the beam is investigated in the presence of thermal and electrical fields. The influence of effective parameters on the buckling load of the FGP beam such as: power law index, temperature field, applied voltage and aspect ratio is investigated.

2. Theoretical formulation

2.1. Governing equations

Figure 1 shows the proposed FGP beam of length L and a rectangular cross section with thickness h and width b that is subjected to an axial compression load P . The coordinate axes are shown in Fig. 1.

Fig. 1. FGP beam of length L and rectangular cross section

The smooth and continuous distribution of material properties along thickness of the FGP beam, composed of two piezoelectric materials, follows a simple power law as (Komijani *et al.*, 2013a)

$$P(z) = P_L + P_{UL} \left(\frac{1}{2} + \frac{z}{h} \right)^k \quad (2.1)$$

in which $P_{UL} = P_U - P_L$, where P_L and P_U are the material properties of lower and upper surfaces of the beam, respectively.

By applying a constant voltage to the FGP beam, an electric field is produced which can be defined as (Kiani and Eslami, 2010)

$$E_z = -\frac{V_0}{h} \quad (2.2)$$

In this paper, the governing equation is derived based on the Timoshenko beam theory. The displacements of an arbitrary point along the z - and x -axes are denoted by $\tilde{w}(x, z)$ and $\tilde{u}(x, z)$, respectively. These displacements are formulated clearly as (Komijani *et al.*, 2013b)

$$\tilde{u}(x, z) = u(x) - z\phi(x) \quad \tilde{w}(x, z) = w(x) \quad (2.3)$$

where $u(x)$ and $w(x)$ are displacements components in the mid-plane of the beam in the z and x direction, and ϕ is the rotation of plane of cross section.

From equations (2.3), the von Kármán type strains can be calculated as

$$\varepsilon_x = u_{,x} + \frac{1}{2}(w_{,x})^2 - z\phi_{,x} \quad \gamma_{xz} = \phi + w_{,x} \quad (2.4)$$

The constitutive equations of the FGP beam are derived considering the thermal and electrical fields as follows (Komijani *et al.*, 2013a)

$$\begin{aligned} \sigma_x &= Q_{11}(z)(\varepsilon_x - \alpha(z)\Delta\theta) - e_{31}(z)E_z & \tau_{xz} &= Q_{55}(z)\gamma_{xz} \\ D_z &= e_{31}(z)\varepsilon_x + k_{33}(z)E_z + p_3\Delta\theta & D_x &= e_{15}(z)\gamma_{xz} \end{aligned} \quad (2.5)$$

in which σ_x , τ_{xz} , ε_x , γ_{xz} , D_i and E_z are the axial stress, shear stress, axial strain, shear strain, electrical displacement and electrical field, respectively. Moreover, Q_{ij} , α_{ij} , e_{ij} , k_{ij} , p_3 and $\Delta\theta$ are the elastic stiffness coefficient, thermal expansion coefficient, piezoelectric coefficient, dielectric coefficient, pyroelectric coefficient and temperature rise, respectively. In the current paper, the governing equations of the FGP beam subjected to mechanical, electrical and thermal loads are derived using the principle of minimum potential energy. Based on this principle, the equilibrium equations are derived when the following equation is satisfied (Komijani *et al.*, 2013a)

$$\delta\Pi = \delta H + \delta W_{ext} = 0 \quad (2.6)$$

in which H is the electrical enthalpy and W_{ext} is the virtual work of external forces imposed on the beam. The variation of electrical enthalpy for the FGP beam can be derived as (Kiani and Eslami, 2010)

$$\delta H = \iiint_V [\sigma_x \delta \varepsilon_x + K_s \tau_{xz} \delta y_{xz} - D_z \delta E_z] dV \quad (2.7)$$

where K_s is the shear correction coefficient and is equal here to 5/6 (Bathe, 1996). It should be noted that since the electrical field is not varied, E_z is constant, so δE_z is equals to zero. The virtual work done by external forces can be calculated as (Ballas, 2007)

$$\delta W_{ext} = - \int_0^L q \delta w dx - \bar{P} \delta u - \bar{M} \delta w_{,x} - \bar{R} \delta w \quad (2.8)$$

The parameters, \bar{R} , \bar{P} , \bar{M} are the axial resultant reaction force, supports external resultant reactions and external moment resultant reactions applied at the ends of the beam, respectively. Also, q is the transversally distributed applied load. Based on Timoshenko beam theory, the stress resultant forces of the beam are derived using equations (2.7) and (2.8) as

$$\begin{aligned} N_x &= A_{11} u_{,x} - B_{11} w_{,xx} - N_x^T - N_x^e \\ M_x &= B_{11} u_{,x} - D_{11} w_{,xx} - M_x^T - M_x^e \\ Q_x &= K_s A_{55} (\phi + w_{,x}) \end{aligned} \quad (2.9)$$

where N_x^T and M_x^T are the corresponding thermal force and moment. Furthermore, D_{11} , B_{11} , A_{11} are tension stiffness, tension bending and bending coefficients, which are defined as

$$(A_{11}, B_{11}, D_{11}) = \int_{-h/2}^{h/2} Q_{11}(z) (1, z, z^2) dz \quad A_{55} = \int_{-h/2}^{h/2} Q_{55}(z) dz \quad (2.10)$$

Also, the thermal force and resultant moment can be calculated as

$$(N_x^T, M_x^T) = \int_{-h/2}^{h/2} Q_{11}(z) \alpha(z) \Delta \theta (1, z) dz \quad (2.11)$$

Finally, the electrical force resultants can be written as

$$(N_x^e, M_x^e) = \int_{-h/2}^{h/2} e_{31}(z) E_z (1, z) dz \quad (2.12)$$

Substituting equations (2.7) and (2.8) into (2.6) and integrating with respect to z , and substituting of equation (2.9) and (2.10), the equilibrium equations for the beam have been derived as

$$N_{x,x} = 0 \quad Q_{x,x} + N_x w_{,xx} = 0 \quad M_{x,x} - Q_x = 0 \quad (2.13)$$

Substituting equation (2.9) into equation (2.13) and doing some simplifications, an ordinary differential equation with respect to displacement will be obtained. The final governing equation of the FGP beam based on Timoshenko assumptions is

$$w_{,xxxx} + \mu^2 w_{,xx} = 0 \quad (2.14)$$

where

$$\mu^2 = \frac{A_{11}N_x}{(B_{11}^2 - A_{11}D_{11})\left(1 + \frac{N_x}{K_s A_{55}}\right)} \quad (2.15)$$

Equation (2.14) is a fourth order ordinary differential equation which describes deflection of the beam.

2.2. Boundary conditions

The corresponding boundary conditions are considered as

$$\begin{aligned} N_x &= \bar{P} & \text{or} & \quad u = 0 \\ w_{,xxx} + \mu^2 w_{,x} &= \frac{\bar{R}\mu^2}{N_x} & \text{or} & \quad w = 0 \\ M_x &= \frac{1}{A_{11}}[(A_{11}D_{11} - B_{11}^2)\phi_{,x} + B_{11}P] - M_x^T - M_x^e = 0 & \text{or} & \quad \phi = 0 \end{aligned} \quad (2.16)$$

Using equations (2.9) and (2.16) yields

$$\bar{P} = P - N_x^T - N_x^e \quad \bar{M} = M - M_x^T - M_x^e \quad \bar{R} = R - R_x^T - R_x^e \quad (2.17)$$

in which the parameters P, R, M are the external axial force, reaction force from supports and external moment applied at the ends of the beam, respectively. Also, the parameters $\bar{P}, \bar{R}, \bar{M}$ are the axial resultant reaction force, resultant reactions from external supports and external resultant moment at the ends of the beam, respectively. The other parameters are the thermal and electrical resultant forces defined in Eqs. (2.11) and (2.12). The formulas for each type of boundary conditions are listed in Table 1.

Table 1. The boundary conditions for the FGP beam

Boundary conditions	$x = 0$ or l
Clamped	$w = \phi = 0$
Simply supported	$w = (A_{11}D_{11} - B_{11}^2)\phi_{,x} + B_{11}P - A_{11}(M_x^T + M_x^e) = 0$
Roller	$w_{,xxx} + \mu^2 w_{,x} = \phi = 0$

3. Solution

The exact solution to differential equation (2.14) based on the parameter μ , which depends on thickness and the resultant axial force of the beam, can be written as

$$w(x) = C_1 \sin(\mu x) + C_2 \cos(\mu x) + C_3 x + C_4 \quad (3.1)$$

where constants C_1-C_4 are calculated by using the boundary condition of the FGP beam. In order to deal with the constants, based on the Timoshenko beam theory and the number of the coefficient, we need to evaluate the deflection and slope of the beam in each boundary. Thus, the slope function can be presented using the deflection of the beam as

$$\phi(x) = \left(1 + \frac{N_x}{K_s A_{55}}\right)[-C_1 \mu \cos(\mu x) + C_2 \mu \sin(\mu x)] - C_3 \quad (3.2)$$

In this paper, stability of five types of boundary conditions is studied. The results show that instability occurs in two cases of boundary conditions (clamped-clamped (C-C) and clamped-

-roller (C-R)) while three others (simply supported-simply supported (S-S), simply supported-clamped (S-C), simply supported-roller (S-R)) are stable. For an example, the C-C condition is considered as a sample of instability in the beam. These results are the same for two different Euler-Bernoulli and Timoshenko beam theories and the obtained results can be validated by the data reported by Nasirzadeh *et al.* (2014). In Table 2, the effect of the boundary condition on stability of the FGP beam is abstracted.

Table 2. The effect of the boundary condition on stability of the FGP beam

Boundary conditions	C-C	C-R	S-S	S-C	S-R
Stability behavior	unstable	unstable	stable	stable	stable

To satisfy the boundary condition, the algebraic equation constants C_i are obtained using equation (2.18)

$$\begin{bmatrix} 0 & 1 & 0 & 1 \\ -\mu S & 0 & -1 & 0 \\ \sin(\mu L) & \cos(\mu L) & L & 1 \\ -\mu S \cos(\mu L) & \mu S \sin(\mu L) & -1 & 0 \end{bmatrix} \begin{bmatrix} C_1 \\ C_2 \\ C_3 \\ C_4 \end{bmatrix} = \begin{bmatrix} 0 \\ 0 \\ 0 \\ 0 \end{bmatrix} \quad (3.3)$$

where

$$S = 1 + \frac{N_x}{K_s A_{55}} \quad (3.4)$$

System of equations (2.20) has infinitely many non-trivial solutions if its coefficient matrix is singular. The non-trivial solution is obtained by equaling the determinant of the coefficient matrix to zero. By solving the obtained characteristic equation, it can be possible to determine the buckling load of the FGP beam for the C-C boundary condition. The characteristic equation of the coefficient matrix can be written as

$$S\mu(LS\mu \sin(\mu L) + 2 \cos(\mu L) - 2) = 0 \quad (3.5)$$

By solving equation (2.22), the buckling load of the FGP beam can be obtained as

$$(\bar{P})_{cr} = (P - N_x^T - N_x^e)_{cr} = \frac{\frac{4n^2\pi^2}{L^2}(B_{11}^2 - A_{11}D_{11})}{A_{11} - \frac{4n^2\pi^2}{L^2} \frac{B_{11}^2 - A_{11}D_{11}}{K_s A_{55}}} \quad n = 1, 2, \dots \quad (3.6)$$

Based on equation (2.23), the buckling load of the beam subjected to mechanical, thermal and electrical loads will be obtained. For the second example, the case of S-S boundary condition is considered as a sample of stable behavior of the structure. Like in the previous example, by applying the boundary conditions, the algebraic equations of the beam will be derived as

$$\begin{bmatrix} 0 & 1 & 0 & 1 \\ 0 & S\mu^2 & 0 & 0 \\ \sin(\mu L) & \cos(\mu L) & L & 1 \\ S\mu^2 \sin(\mu L) & S\mu^2 \cos(\mu L) & 0 & 0 \end{bmatrix} \begin{bmatrix} C_1 \\ C_2 \\ C_3 \\ C_4 \end{bmatrix} = \begin{bmatrix} 0 \\ 1 \\ 0 \\ 1 \end{bmatrix} \frac{A_{11}(M_x^T + M_x^e) - B_{11}P}{A_{11}D_{11} - B_{11}^2} \quad (3.7)$$

The above equation has not any non-trivial solution and hence the structure shows stable behavior. By solving equation (2.24), the deflection of the beam is obtained as

$$w(x) = \frac{F}{S\mu^2} \left(\frac{1 - \cos(\mu L)}{\sin(\mu L)} \sin(\mu x) + \cos(\mu x) - 1 \right) \quad (3.8)$$

in which

$$F = \frac{A_{11}(M_x^T + M_x^e) - B_{11}P}{A_{11}D_{11} - B_{11}^2} \quad (3.9)$$

It should be noted that the nonhomogeneous distribution of the material through thickness of the beam can lead to inhomogeneous boundary conditions, and so, the beam shows stable behavior.

3.1. Temperature field

In this paper, two kinds of thermal fields acting on the beam are investigated. In the first case, the beam is subjected to a uniform temperature field with the temperature rise of $\Delta\theta = \theta - \theta_0$, in which θ_0 is the initial temperature and θ is the final temperature imposed on the beam. In the second case, the beam is subjected to a linear temperature field through thickness of the beam. Using the assumption of a thin beam and solving the obtained heat transfer equation, the temperature distribution in the beam is derived as (Bodaghi *et al.*, 2014)

$$\theta = \theta_L + \theta_{UL}\left(\frac{1}{2} + \frac{z}{h}\right) \quad \theta_{UL} = \theta_U - \theta_L \quad \Delta\theta = \theta - \theta_0 \quad (3.10)$$

where θ_L and θ_U are temperatures of the lower and upper surfaces of the FGP beam, respectively.

4. Results and discussions

Consider a beam composed of a functionally graded material of PZT-4 and PZT-5 in the upper and lower surfaces, respectively. The properties of materials are listed in Table 3. In this Section, the buckling load of the FGP beam subjected to mechanical, thermal and electrical fields is studied. In the following Section, the results for Euler-Bernoulli and Timoshenko beams have been calculated and compared to each other. Moreover, the effect of uniform and linear thermal fields on the buckling load of the Timoshenko beam has been investigated. Finally, the critical values of the buckling load for the FGP beam with the clamped-clamped boundary conditions in thermal and electrical environment for different power law indexes and various aspect ratios will be studied.

Table 3. Thermal-electrical and mechanical properties of PZT-4 and PZT-5H (Komijani *et al.* 2013a)

Property	PZT-5H	PZT-4
Q_{11} [GPa]	60.6	81.3
Q_{55} [GPa]	23.0	25.6
e_{13} [C/m ²]	-16.604	-10.0
e_{15} [C/m ²]	44.9046	40.3248
k_{11} [(C ² /m ² N)·10 ⁻⁸]	1.5027	0.6712
k_{33} [(C ² /m ² N)·10 ⁻⁸]	2.554	1.0275
α [1/K]	10E-6	2E-6
$p_3 \cdot 10^{-5}$	0.548	2.5

At first, we compare our exact results with other data reported in the literature. Table 4 shows the buckling load of the piezoelectric beam for two different aspect ratios. The second solution is based on the finite element method. We used the two node Hermit elements and Euler-Bernoulli beam theory to model the beam. The results obtained by the FE method are

Table 4. Comparison of the buckling load (N/m) of the clamped-clamped piezoelectric beam versus aspect ratio

L/h	Exact value (our paper)	FEM results
25	3.1899E+06	3.1899E+06
50	7.9746E+05	7.9747E+05

compared with the exact solution which is obtained in this paper. As it is seen, the results for two distinct methods are in good agreement with each other.

Figure 2a shows the buckling load of the FGP beam versus the power low index k for different aspect ratios (L/h) for Euler-Bernoulli and Timoshenko beams. It is seen that by increasing the power law index k , the value of the buckling load increases. Also this figure shows that the load decreases with the increasing aspect ratio L/h . On the other hand, the differences between the buckling load obtained by using Euler-Bernoulli and Timoshenko beam theories are decreased when the ratio of L/h is increased. It is seen that the value of the resultant axial buckling load predicted by the Euler-Bernoulli theory is higher than that by the Timoshenko beam theory. The reason can be explained by considering the effect of shear stresses in the Timoshenko beam theory. In Fig. 2b, variation of the buckling load versus aspect ratio of the beam for various power low indexes is depicted. As it is seen, by decreasing the aspect ratio, the buckling load increases.

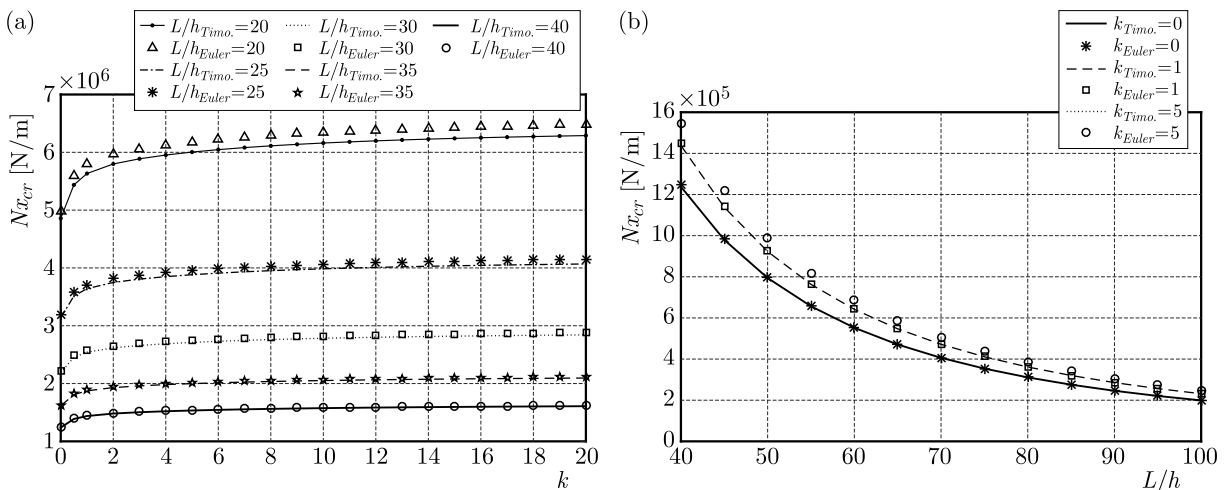


Fig. 2. (a) The effect of the power law index on the buckling load for various aspect ratios for Euler-Bernoulli and Timoshenko theories. (b) The effect of aspect ratios on the critical buckling load versus the power load index for Euler-Bernoulli and Timoshenko beam theories

In Figs. 3a and 3b, the effects of uniform and linear thermal fields on the buckling load of the beam are depicted. In the studied cases, the FGP beam exposed to a constant applied voltage ($V_0 = 500$ V) and the aspect ratio of the beam is ($L/h = 50$). The results show that the rate of change of the buckling load for power law indexes between zero to four is high, and for power indexes which are more than four is decreased and changes no more. Also it is seen that for a constant power law index, by increasing temperature in the beam, the buckling force decreases. The produced elongation caused by the temperature changes can be regarded as a reason for this phenomenon. It should be noted that, because of the acceptable conformity between the results of two theories, the mentioned points are same for the two beam theories.

Figures 4a and 4b show changes of the buckling load with respect to uniform temperature rise through thickness for different power law indexes of two theories. Because of the decreasing equivalent thermal expansion coefficient of the FGP beam by increasing of the power law index,

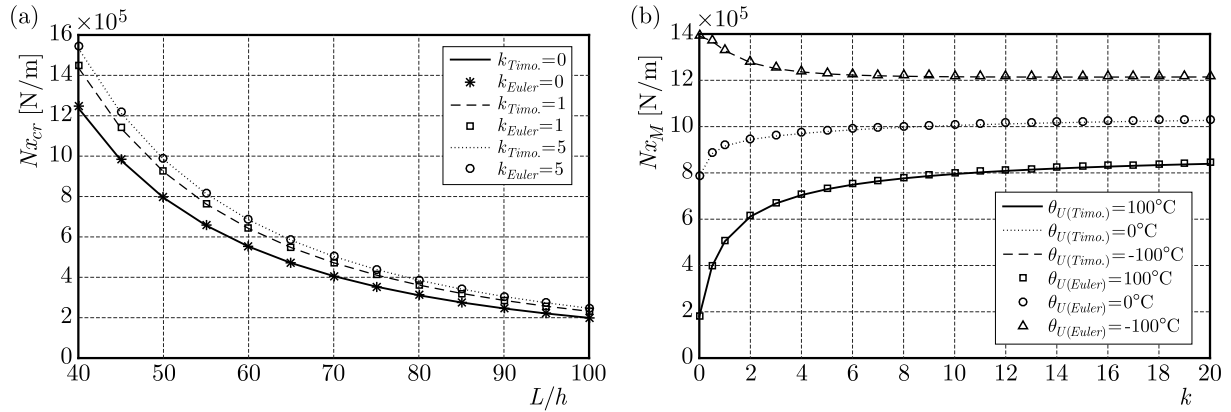


Fig. 3. (a) The effect of a constant thermal field on the buckling load with respect to the power index k for two theories. (b) The effect of a linear thermal field along thickness on the buckling load versus the power index k for two theories

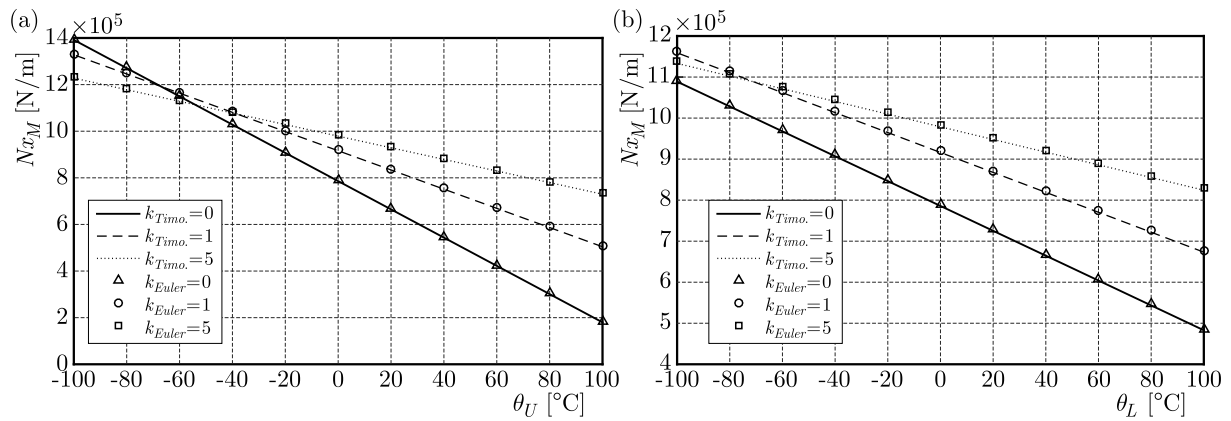


Fig. 4. (a) The effect of a constant thermal field on the buckling load for two theories for various power law indexes. (b) The effect of a linear thermal field on the buckling load for two theories for various power law indexes ($V_0 = 500$ v, $L/h = 50$)

the buckling load of the beam is decreased. Moreover, it should be noted that the intersection point of lines with various power indexes depends on the aspect ratio and thermal expansion coefficient of composed materials, and by changing of these parameters, this point is moved or eliminated.

In Fig. 5a, a comparison of the effects of the uniform and linear temperature rise through thickness of the Timoshenko beam on the buckling load is depicted. It can be seen that by increasing the temperature the critical buckling load is decreased. This phenomenon can be explained due to thermal stresses in the beam. The effect of the power law index on the critical buckling load for the uniform and linear temperature rise along the thickness of the beam for two theories are shown in Fig. 5b.

Figures 6, 7 and 8 show the effect of the power law index and applied voltage for the uniform and linear temperature rise on the critical buckling load of the beam. It can be inferred that in both conditions, by increasing the power law index, the critical buckling load is increased. Moreover, for a specified power law index, by decreasing the applied voltage, the value of critical buckling load increases; however it should be noted that the effect of voltage is negligible on the critical buckling load. Figure 6 shows the effect of uniform and linear temperature fields for different voltages on the critical buckling load. The most significant point is that the rate of buckling load variation by changing the applied voltage is almost negligible. It can be explained by the small value of the piezoelectric coefficient of the FGP beam.

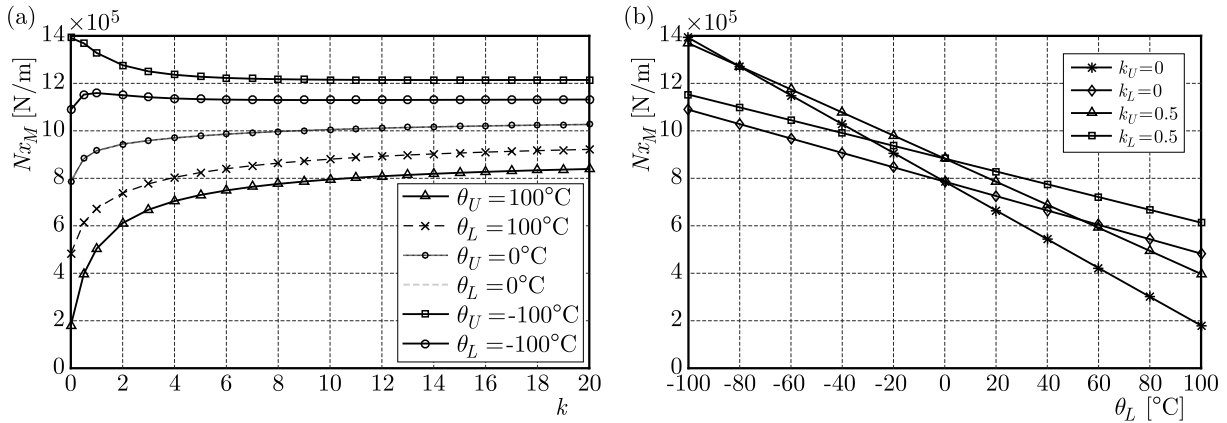


Fig. 5. (a) The effect of uniform and linear temperature fields on the buckling loads versus the power index for the Timoshenko beam. (b) The effect of uniform and linear thermal fields on the buckling load for various power indexes ($V_0 = 500$ V, $L/h = 50$)

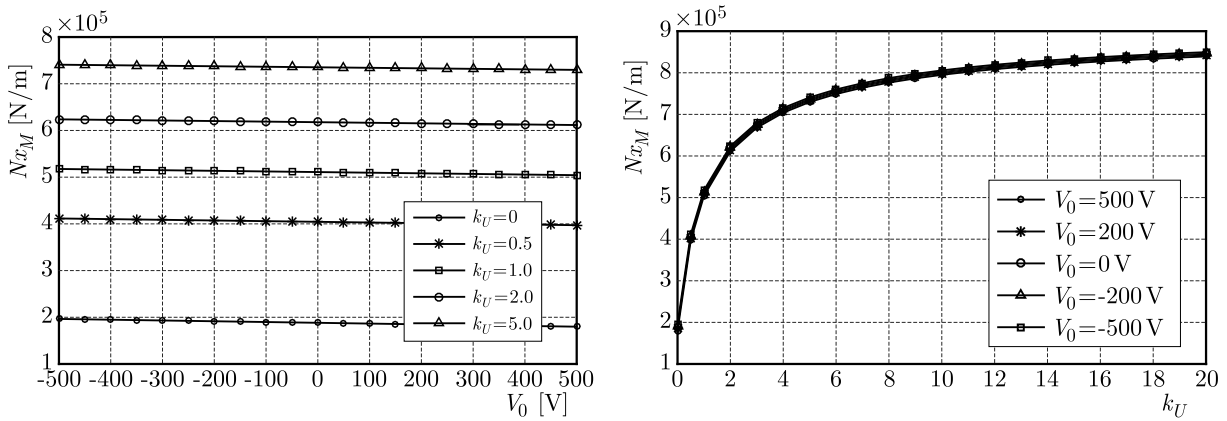


Fig. 6. The effect of voltage and power index on the critical buckling load for a uniform temperature rise

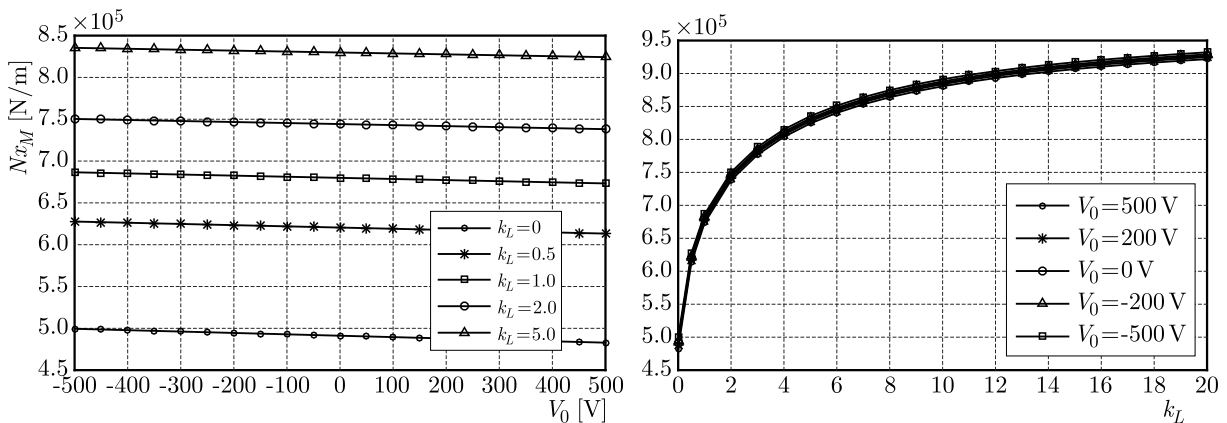


Fig. 7. The effect of voltage and power index on the critical buckling load for a linear temperature rise

Figure 9 shows the deflection of the FGPM beam with the S-S boundary condition versus the applied axial force. The beam is under a uniform thermal ($\Delta\theta = 100$) and electrical loading ($V_0 = 200$ V). This figure shows that by increasing the applied force, the deflection do not change, but in points closer to the bifurcation point of the beam the deflection sharply increases.

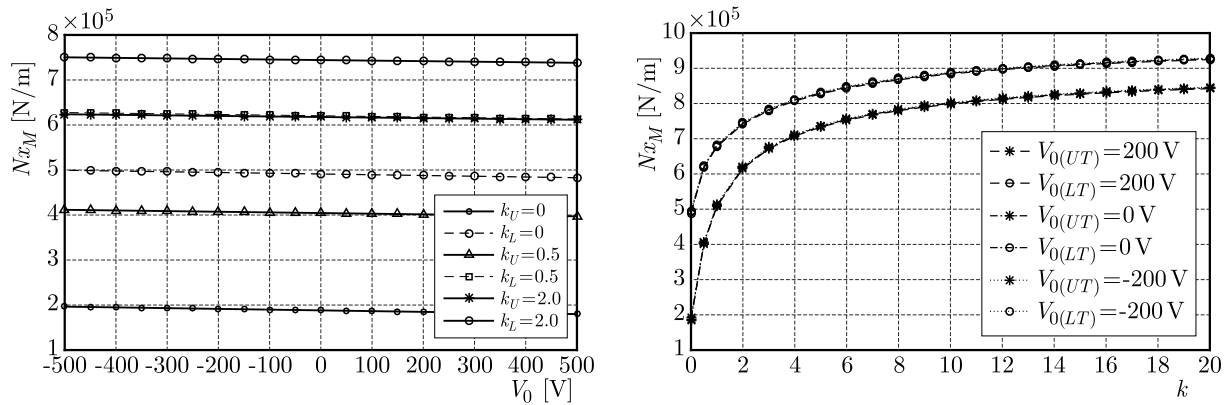


Fig. 8. The comparison of the critical buckling load for uniform and linear temperature field versus the applied voltage

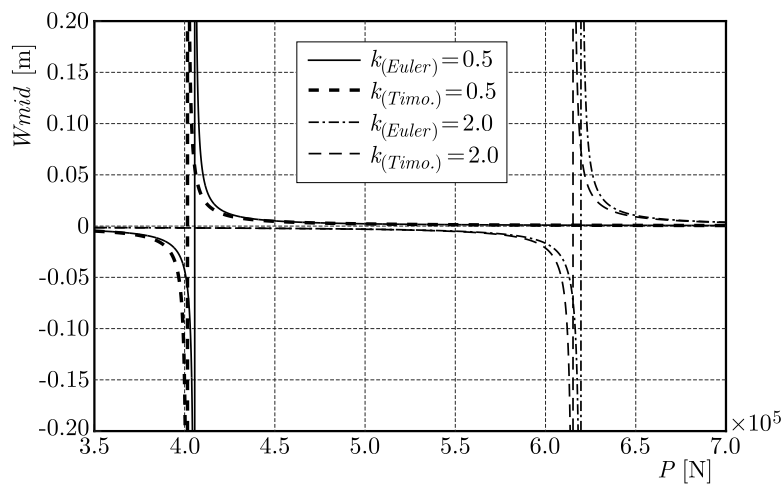


Fig. 9. Deflection of the SS beam under thermal ($\Delta\theta = 100^\circ\text{C}$) and voltage load ($V_0 = 200$ V)

5. Conclusions

In this paper, the stability and instability of FGP beams is investigated based on the Timoshenko beam theory. Considering different boundary conditions of the FGP beam the instability is shown for two cases of boundary conditions: clamped-clamped (C-C) and clamped-roller (C-R). The three others: simply supported-simply supported (S-S), simply supported-clamped (S-C), simply supported-roller (S-R) show stable behavior. For both boundary conditions which are unstable (C-C and C-R), the results show that the buckling load increases with the increasing power law index. Also, by increasing the temperature, the value of the buckling load decreases. In addition, a uniform temperature rise has greater effect on the buckling load than a linear temperature rise. Moreover, the temperature field is more effective than the electric field in the buckling load of the beam, and the electrical loading has not a significant effect on the buckling load of the FGP beam.

References

1. BALLAS R.G., 2007, *Piezoelectric Multilayer Beam Bending Actuators: Static and Dynamic Behavior and Aspects of Sensor Integration*, Springer
2. BATHE K.J., 1996, *Finite Element Procedures*, Prentice Hall

3. BODAGHI M., DAMANPACK A.R., AGHDAM M.M., SHAKERI M., 2014, Geometrically non-linear transient thermo-elastic response of FG beams integrated with a pair of FG piezoelectric sensors, *Composite Structures*, **107**, 48-59
4. DAVOODINIK A.R., RAHIMI G.H., 2011, Large deflection of flexible tapered functionally graded beam, *Acta Mechanica Sinica*, **27**, 5, 767-777
5. DOROUSHI A., ESLAMI M.R., KOMEILI, A., 2011. Vibration analysis and transient response of an FGPM beam under thermo-electro-mechanical loads using higher-order shear deformation theory, *Journal of Intelligent Material Systems and Structures*, **22**, 3, 231-243
6. ESFAHANI S.E., KIANI Y., ESLAMI M.R., 2013, Non-linear thermal stability analysis of temperature dependent FGM beams supported on non-linear hardening elastic foundations, *International Journal of Mechanical Sciences*, **69**, 10-20
7. FALLAH A., AGHDAM M.M., 2011, Nonlinear free vibration and post-buckling analysis of functionally graded beams on nonlinear elastic foundation, *European Journal of Mechanics-A/Solids*, **30**, 4, 571-583
8. FU Y., WANG J., MAO Y., 2012, Nonlinear analysis of buckling, free vibration and dynamic stability for the piezoelectric functionally graded beams in thermal environment, *Applied Mathematical Modelling*, **36**, 9, 4324-4340
9. KIANI Y., ESLAMI M.R., 2010, Thermal buckling analysis of functionally graded material beams, *International Journal of Mechanics and Materials in Design*, **6**, 3, 229-238
10. KOMIJANI M., KIANI Y., ESLAMI M.R., 2013a, Non-linear thermoelectrical stability analysis of functionally graded piezoelectric material beams, *Journal of Intelligent Material Systems and Structures*, **24**, 4, 399-410
11. KOMIJANI M., REDDY J.N., FERREIRA A.J.M., 2013b, Nonlinear stability and vibration of pre/post-buckled microstructure-dependent FGPM actuators, *Meccanica*, **49**, 2729-2745
12. LI S.R., BATRA R.C., 2013, Relations between buckling loads of functionally graded Timoshenko and homogeneous Euler-Bernoulli beams, *Composite Structures*, **95**, 5-9
13. LI S.R., ZHANG J.H., ZHAO Y.G., 2006, Thermal post-buckling of functionally graded material Timoshenko beams, *Applied Mathematics and Mechanics*, **27**, 803-810
14. NASIRZADEH R., BEHJAT B., KHARAZI M., 2014, Stability of FGP beams under thermo-electro-mechanical loading, *International Journal of Material Science Innovations*, **2**, 6, 164-177
15. PRADHAN S.C., MURMU T., 2009, Thermo-mechanical vibration of FGM sandwich beam under variable elastic foundations using differential quadrature method, *Journal of Sound and Vibration*, **321**, 1, 342-362
16. QIN Q.H., 2013, *Advanced Mechanics of Piezoelectricity*, Springer
17. WATTANASAKULPONG N., GANGADHARA PRUSTY B., KELLY D.W., 2011, Thermal buckling and elastic vibration of third-order shear deformable functionally graded beams, *International Journal of Mechanical Sciences*, **53**, 9, 734-743
18. YANG J.S., 2005, *Introduction to the Theory of Piezoelectricity*, Springer, New York
19. YING J., LÜ C.F., CHEN W.Q., 2008, Two-dimensional elasticity solutions for functionally graded beams resting on elastic foundations, *Composite Structures*, **84**, 3, 209-219.
20. ZHANG D.G., 2013, Nonlinear bending analysis of FGM beams based on physical neutral surface and high order shear deformation theory, *Composite Structures*, **100**, 121-126

NONCONSERVATIVE STABILITY OF VISCOELASTIC PLATES SUBJECT TO TRIANGULARLY DISTRIBUTED FOLLOWER LOADS

MOUAFO T.A. ROBINSON

*University of KwaZulu-Natal, Discipline of Mechanical Engineering, Durban, South Africa, and
University of Dschang, Department of Physics, Cameroon; e-mail: armandmouafo@yahoo.fr*

SARP ADALI

University of KwaZulu-Natal, Discipline of Mechanical Engineering, Durban, South Africa; e-mail: adali@ukzn.ac.za

Divergence and flutter instabilities of viscoelastic rectangular plates under triangularly distributed tangential follower loads are studied. Two sets of boundary conditions are considered, namely, simply supported plates and plates with a combination of clamped and simply supported edges. The constitutive relations for the viscoelastic plates are of Kelvin-Voigt type with the effect of viscoelasticity on stability studied numerically. The method of solution is differential quadrature which is employed to discretize the equation of motion and the boundary conditions leading to a generalized eigenvalue problem. After verifying the method of solution, numerical results are given for the real and imaginary parts of the eigenfrequencies to investigate flutter and divergence characteristics and dynamic stability of the plates with respect to various problem parameters.

Keywords: viscoelastic plates, dynamic stability, triangularly distributed follower load

1. Introduction

Dynamic stability of elastic structures subject to nonconservative loads is of practical importance in such fields as aerospace, mechanical and civil engineering. As a result, the subject has been studied extensively to quantify the behaviour of beams, plates and shells under follower forces. These forces can be concentrated, uniformly distributed or triangularly distributed depending on the specific application. They act in the tangential direction and are not derivable from a potential due to their nonconservative nature as presented in works by Kumar and Srivasta (1986), Przybylski (1999), Gajewski (2000), Krilov (2013).

Early work on the nonconservative instability under uniformly distributed follower loads mostly involved one dimensional elastic structures, namely, columns (Sugiyama and Kawagoe, 1975; Leipholz, 1975; Chen and Ku, 1991). Stability of columns under triangularly distributed loads was studied by Leipholz and Bhalla (1977), Sugiyama and Mladenov (1983) and Ryu *et al.* (2000). More recent studies on nonconservative loading include columns subject to uniformly distributed follower loads by Kim (2010), Kim *et al.* (2008) and Kazemi-Lari *et al.* (2013) and to triangularly distributed follower loads by Kim (2011). The follower force can also be realized by means of properly shaped loading heads which can affect the displacements of the loaded end as studied by Tomski and Szmidla (2004) and Tomski and Uzny (2013b). The installation of Tomski's head can lead to a loading force which is tangent to the end of the column and can be conservative (Tomski and Uzny, 2008, 2013a). The force in this case is directed to a constant point which becomes a pole for the loading. Introduction of Tomski's head can lead to new characteristic curves such as pseudo flutter and allows one to control the dynamic behavior of the system. Studies on nonconservative stability of two-dimensional structures mostly involved rectangular plates under follower loads (Culkowski and Reismann, 1977; Farshad, 1978; Adali,

1982) and under uniformly distributed tangential loads (Leipholz, 1978; Leipholz and Pfenndt, 1982, 1983; Wang and Ji, 1992).

Recent research on the stability of elastic plates under nonconservative loads includes works by Zuo and Shreyer (1996), Kim and Park (1998), Kim and Kim (2000), and Jayaraman and Struthers (2005). Dynamic stability of functionally graded plates under uniformly distributed axial loads was studied by Ruan *et al.* (2012) and shells by Toriki *et al.* (2014a,b). These studies neglected the effect of viscoelasticity on the stability of the columns and plates.

Dynamic stability of one-dimensional viscoelastic structures was the subject of the works by Marzani and Potapov (1999), Langthjem and Sugiyama (2000), Darabseh and Genin (2004), Zhuo and Fen (2005), Ilyasov and Ilyasova (2006) and Elfelsoufi and Azrar (2006). Recently, the dynamic stability of viscoelastic plates has been studied for a number of cases (Ilyasov and Aköz, 2000; Wang *et al.*, 2007, 2009, 2013; Zhou and Wang, 2014; Robinson and Adali, 2016). Vibrations of a simply supported plate with nonlinear strain-displacement relations and subject to a uniformly distributed tangential force were studied by Robinson (2013). Dynamic stability of viscoelastic shells was studied by Ilyasov (2010).

Although the dynamic stability under triangularly distributed tangential forces have been studied in the case of columns (see Leipholz and Bhalla, 1977; Sugiyama and Mladenov, 1983; Ryu *et al.*, 2000; Kim, 2011), dynamic stability of plates and, in particular, viscoelastic plates under this type of loading does not seem to be studied so far.

The present work extends the results of Robinson and Adali (2016) who studied nonconservative stability of viscoelastic plates with free edges and under uniformly distributed follower loads, to the case of plates with simply supported and simply supported-clamped plates and subject to triangularly distributed follower loads. Comparisons are given for the uniformly and triangularly distributed follower loads. The stability problem is solved for the simply supported plates and for plates with a combination of simple and clamped supports by the differential quadrature method. Divergence and flutter loads are determined and the effect of viscoelasticity and the boundary conditions on dynamic stability is investigated. The method of solution is verified against the known results in the literature.

2. Viscoelastic plate subject to triangularly distributed load

We consider a rectangular plate of uniform thickness h having dimensions $a \times b$ in the x and y directions, respectively (see Fig. 1). It is subject to a non-uniform tangential follower force $q_t = q_0a(1 - x/a)$.

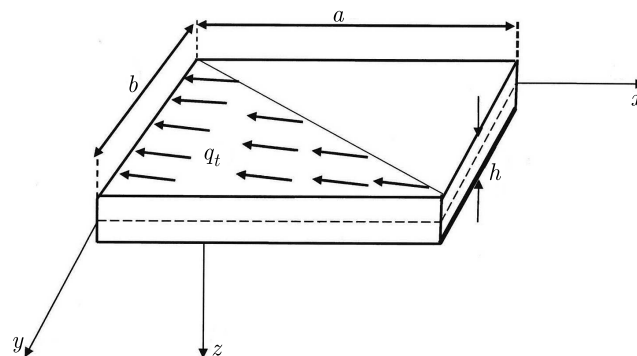


Fig. 1. Viscoelastic plate subjected to a triangular follower load

The material of the plate is viscoelastic which is expressed by the Kelvin-Voigt constitutive relations given by

$$\mathbf{s}_{ij} = 2G\mathbf{e}_{ij} + 2\eta\dot{\mathbf{e}}_{ij} \quad \boldsymbol{\sigma}_{ii} = 3K\boldsymbol{\varepsilon}_{ii} \quad (2.1)$$

where \mathbf{s}_{ij} and \mathbf{e}_{ij} are deviatoric tensors of stress and strain, respectively, and $\boldsymbol{\sigma}_{ii}$ and $\boldsymbol{\varepsilon}_{ii}$ are spherical tensors of stress and strain with η denoting the viscoelastic coefficient. The bulk modulus K and shear modulus G can be expressed in terms of Young's modulus E and Poisson's ratio ν as $K = E/3(1 - 2\nu)$ and $G = E/(1 + 2\nu)$. The equation of vibration of the viscoelastic plate subject to a triangular follower load is first obtained in the Laplace domain (see Wang *et al.*, 2007; Zhou and Wang, 2014). By the inverse Laplace transformation, the governing equation can be expressed in the time domain as

$$\frac{h^3}{12} \left(A_3 + A_4 \frac{\partial}{\partial t} + A_5 \frac{\partial^2}{\partial t^2} \right) \nabla^4 w + \left(A_1 + A_2 \frac{\partial}{\partial t} \right) \left(\frac{q_0(a-x)^2}{2} \frac{\partial^2 w}{\partial x^2} + \rho h \frac{\partial^2 w}{\partial t^2} \right) = 0 \quad (2.2)$$

where ρ is density of the plate and

$$\begin{aligned} A_1 &= 3K + 4G & A_2 &= 3K + 4G & A_3 &= 4\eta \\ A_4 &= 4G(3K + G) & A_5 &= \eta(8G + 12K) & A_6 &= 4\eta^2 \end{aligned} \quad (2.3)$$

and

$$\nabla^4 w = \frac{\partial^4 w}{\partial x^4} + 2 \frac{\partial^4 w}{\partial x^2 \partial y^2} + \frac{\partial^4 w}{\partial y^4} \quad (2.4)$$

After introducing dimensionless coefficients

$$X = \frac{x}{a} \quad Y = \frac{y}{b} \quad \bar{w} = \frac{w}{h} \quad \lambda = \frac{a}{b} \quad (2.5)$$

and

$$q = \frac{6q_0 a^4 (1 - \nu^2)}{E h^3} \quad \tau = \frac{th}{a^2} \sqrt{\frac{E}{12\rho(1 - \nu^2)}} \quad H = \frac{\eta h}{a^2} \sqrt{\frac{1}{12\rho(1 - \nu^2)E}} \quad (2.6)$$

the non-dimensional equation of motion is obtained as

$$\left(1 + g_1 \frac{\partial}{\partial \tau} + g_2 \frac{\partial^2}{\partial \tau^2} \right) \nabla^4 \bar{w} + \left(1 + g_3 \frac{\partial}{\partial \tau} \right) \left(q(1 - X)^2 \frac{\partial^2 \bar{w}}{\partial X^2} + \frac{\partial^2 \bar{w}}{\partial \tau^2} \right) = 0 \quad (2.7)$$

where

$$\begin{aligned} g_2 &= \frac{4(1 - 2\nu)(1 + \nu)^2}{3} H^2 & g_3 &= \frac{4(1 - 2\nu)(1 + \nu)}{3(1 - \nu)} H \\ \nabla^4 \bar{w} &= \frac{\partial^4 \bar{w}}{\partial X^4} + 2\lambda^2 \frac{\partial^4 \bar{w}}{\partial X^2 \partial Y^2} + \lambda^4 \frac{\partial^4 \bar{w}}{\partial Y^4} \end{aligned} \quad (2.8)$$

In equations (2.8), H is the dimensionless delay time of the material and τ is the dimensionless time defined in Eq. (2.6). Let

$$\bar{w}(X, Y, \tau) = W(X, Y) e^{j\omega\tau} \quad (2.9)$$

where $j = \sqrt{-1}$ and ω the dimensionless vibration frequency. Substitution of equation (2.9) into equation (2.7) yields the differential equation

$$(1 + g_1 j\omega + g_2 j^2 \omega^2) \nabla^4 W + (1 + g_3 j\omega) \left(q(1 - X)^2 \frac{\partial^2 W}{\partial X^2} + j^2 \omega^2 \right) = 0 \quad (2.10)$$

in terms of the space variables X and Y . The boundary conditions considered in the present work are the simply supported plates (SSSS) and plates with two opposite edges clamped and two others simply supported (CSCS).

SSSS boundary conditions are given by

$$\bar{w}(X, Y, \tau) = \begin{cases} \left. \frac{\partial^2 \bar{w}}{\partial X^2} \right|_{X=0,1} = 0 & \text{for } 0 \leq Y \leq 1 \\ \left. \frac{\partial^2 \bar{w}}{\partial Y^2} \right|_{Y=0,1} = 0 & \text{for } 0 \leq X \leq 1 \end{cases} \quad (2.11)$$

CSCS boundary conditions are given by

$$\bar{w}(X, Y, \tau) = \begin{cases} \left. \frac{\partial \bar{w}}{\partial X} \right|_{X=0,1} = 0 & \text{for } 0 \leq Y \leq 1 \\ \left. \frac{\partial^2 \bar{w}}{\partial Y^2} \right|_{Y=0,1} = 0 & \text{for } 0 \leq X \leq 1 \end{cases} \quad (2.12)$$

3. Differential quadrature (DQ) method

The DQ method involves approximating the partial derivatives of the function $W(X, Y)$ at a sample point (X_i, Y_j) by the weighted sum of the function W_{ij} (see Bert and Malik, 1996; Krowiak, 2008). Let the number of sample points denoted by N in the X direction and M in the Y direction. The r -th order partial derivative with respect to X , s -th order partial derivative with respect to Y and the $(r + s)$ -th order mixed partial derivative of $W(X, Y)$ with respect to both X and Y are discretely expressed at the point (X_i, Y_j) as

$$\begin{aligned} \frac{\partial^r W(X_i, Y_j)}{\partial X^r} &= \sum_{k=1}^N A_{ik}^{(r)} W_{kj} & \frac{\partial^s W(X_i, Y_j)}{\partial Y^s} &= \sum_{l=1}^M B_{jl}^{(s)} W_{il} \\ \frac{\partial^{r+s} W(X_i, Y_j)}{\partial X^r \partial Y^s} &= \sum_{k=1}^N A_{ik}^{(r)} \sum_{l=1}^M B_{jl}^{(s)} W_{kl} \end{aligned} \quad (3.1)$$

where $i = 1, 2, \dots, N$, $k = 1, 2, \dots, N - 1$, $j = 1, 2, \dots, M$ and $l = 1, 2, \dots, M - 1$.

For $r = s = 1$, the coefficients $A_{ik}^{(r)}$ and $B_{jl}^{(s)}$ are defined as

$$\begin{aligned} A_{ik}^{(1)} &= \begin{cases} \prod_{\mu=1, \mu \neq i}^N \frac{X_i - X_\mu}{(X_i - X_k) \prod_{\mu=1, \mu \neq k}^N (X_k - X_\mu)} & \text{for } i, k = 1, 2, \dots, N \quad (i \neq k) \\ \sum_{\mu=1, \mu \neq k}^N \frac{1}{X_i - X_\mu} & \text{for } i = 1, 2, \dots, N \quad (i = k) \end{cases} \\ B_{jl}^{(1)} &= \begin{cases} \prod_{\mu=1, \mu \neq j}^M \frac{Y_j - Y_\mu}{(Y_j - Y_l) \prod_{\mu=1, \mu \neq l}^M (Y_l - Y_\mu)} & \text{for } j, l = 1, 2, \dots, M \quad (j \neq l) \\ \sum_{\mu=1, \mu \neq j}^M \frac{1}{Y_j - Y_\mu} & \text{for } j = 1, 2, \dots, M \quad (j = l) \end{cases} \end{aligned} \quad (3.2)$$

For $r = 2, 3, \dots, N - 1$ and $s = 2, 3, \dots, M - 1$

$$\begin{aligned}
 A_{ik}^{(r)} &= \begin{cases} r \left(A_{ii}^{(r-1)} A_{ik}^{(1)} - \frac{A_{ik}^{(r-1)}}{X_i - X_k} \right) & \text{for } i, k = 1, 2, \dots, N \quad (i \neq k) \\ - \sum_{\mu=1, \mu \neq i}^N A_{i\mu}^{(r)} & \text{for } i = 1, 2, \dots, N \quad (i = k) \end{cases} \\
 B_{jl}^{(s)} &= \begin{cases} s \left(B_{jj}^{(s-1)} B_{jl}^{(1)} - \frac{B_{jl}^{(s-1)}}{Y_j - Y_l} \right) & \text{for } j, l = 1, 2, \dots, M \quad (j \neq l) \\ - \sum_{\mu=1, \mu \neq j}^M B_{j\mu}^{(s)} & \text{for } j = 1, 2, \dots, M \quad (j = l) \end{cases}
 \end{aligned} \tag{3.3}$$

The distribution of the grid points are taken as non-uniform, and for the simply supported plate, the grid points are specified as

$$\begin{aligned}
 X_1 = 0 \quad X_N = 1 \quad X_i &= \frac{1}{2} \left[1 - \cos \left(\frac{2i-3}{2N-4} \pi \right) \right] \quad \text{for } i = 2, 3, \dots, N-1 \\
 Y_1 = 0 \quad Y_M = 1 \quad Y_j &= \frac{1}{2} \left[1 - \cos \left(\frac{2j-3}{2N-4} \pi \right) \right] \quad \text{for } j = 2, 3, \dots, M-1
 \end{aligned} \tag{3.4}$$

For the plate with two opposite edges simply supported and other two edges clamped, the δ method combined with the weighted coefficient method is adopted. Thus, the grid points for the CSCS plate are given by

$$\begin{aligned}
 X_1 = 0 \quad X_2 = \delta \quad X_{N-1} = 1 - \delta \quad X_N = 1 \\
 X_i &= \frac{1}{2} \left[1 - \cos \left(\frac{i-2}{N-3} \pi \right) \right] \quad \text{for } i = 3, 4, \dots, N-2 \\
 Y_1 = 0 \quad Y_M = 1 \quad Y_j &= \frac{1}{2} \left[1 - \cos \left(\frac{2j-3}{2N-4} \pi \right) \right] \quad \text{for } j = 2, 3, \dots, M-1
 \end{aligned} \tag{3.5}$$

where $\delta \ll 1$. Using equation (3.1), the discretized form of differential equation (2.10) can be expressed as

$$\begin{aligned}
 c_1 j^3 W_{ij} \omega^3 + (c_2 S_{ij} + W_{ij}) j^2 \omega^2 + (c_3 S_{ij} \\
 + c_1 q (1 - X)^2 \sum_{k=1}^N A_{ik}^{(2)} W_{kj}) j \omega + q (1 - X)^2 \sum_{k=1}^N A_{ik}^{(2)} W_{kj} = 0
 \end{aligned} \tag{3.6}$$

where

$$\begin{aligned}
 S_{ij} &= \sum_{k=1}^N A_{ik}^{(4)} W_{kj} + 2\lambda^2 \sum_{l=1}^M B_{jl}^{(2)} \sum_{k=1}^N A_{ik}^{(2)} W_{kl} + \lambda^4 \sum_{l=1}^M B_{jl}^{(4)} W_{il} \\
 c_1 &= \frac{4(1-2\nu)(1+\nu)}{3(1-\nu)} H \quad c_2 = \frac{4(1-2\nu)(1+\nu)^2}{3} H^2 \quad c_3 = \frac{4(1-2\nu)(1+\nu)}{3} H
 \end{aligned}$$

The discretized form of boundary conditions (2.11) are given by

$$\begin{aligned}
 W_{1j} = W_{Nj} = W_{i1} = W_{iM} = 0 \quad \text{for } i = 1, 2, \dots, N \quad \wedge \quad j = 1, 2, \dots, M \\
 \sum_{k=1}^N A_{ik}^{(2)} W_{kj} = 0 \quad \text{for } i = 1, N \quad \wedge \quad j = 1, 2, \dots, M \\
 \sum_{l=1}^M B_{jl}^{(2)} W_{il} = 0 \quad \text{for } i = 1, 2, \dots, N \quad \wedge \quad j = 1, M
 \end{aligned} \tag{3.7}$$

The corresponding equations for boundary conditions (2.12) are

$$\begin{aligned}
 W_{1j} = W_{Nj} = W_{i1} = W_{iM} = 0 \quad & \text{for } i = 1, 2, \dots, N \quad \wedge \quad j = 1, 2, \dots, M \\
 \sum_{k=1}^N A_{ik}^{(1)} W_{kj} = 0 \quad & \text{for } i = 1, 2, \dots, N-1 \quad \wedge \quad j = 2, 3, \dots, M-2 \\
 \sum_{l=1}^M B_{jl}^{(2)} W_{il} = 0 \quad & \text{for } i = 1, 2, \dots, N \quad \wedge \quad j = 1, M
 \end{aligned} \tag{3.8}$$

4. Numerical results and discussion

The results for the viscoelastic plate subject to a triangularly distributed tangential force are given in comparison to the results for a viscoelastic plate subject to a uniformly distributed tangential force which was studied in Wang *et al.* (2007) and Zhou and Wang (2014). The results for the SSSS and CSCS boundary conditions are given in Table 1 for $H = 10^{-5}$ (nondimensional viscoelasticity coefficient). Table 1 shows that the flutter load, denoted by q_f , is higher in the case of the load having triangular distribution as expected. In Table 1, q_{d1} and q_{d2} denote the divergence loads of the 1st and 2nd modes, respectively.

Table 1. Comparison of flutter loads q of viscoelastic plates with $H = 10^{-5}$ for various aspect ratios

Aspect ratio λ	Boundary conditions	Uniformly distributed load, Wang <i>et al.</i> (2007)	Triangularly distributed load
1.0	SSSS	$q_{d1} = 67.5$ $q_{d2} = 132.1$	$q_{d1} = 95.1$ $q_{d2} = 225.1$
	CSCS	$q_{d1} = 143.5$ $q_f = 168.0$	$q_f = 226.0$
1.5	SSSS	$q_{d1} = 136.8$ $q_{d2} = 224.7$	$q_{d1} = 174.0$ $q_{d2} = 329.0$
	CSCS	$q_f = 202.8$	$q_f = 270.0$
2.0	SSSS	$q_{d1} = 224.8$ $q_{d2} = 340.5$	$q_{d1} = 273.04$ $q_{d2} = 453.2$
	CSCS	$q_f = 251.5$	$q_f = 333.0$

Figures 2-4 show the real and the imaginary parts of the first three frequencies plotted against the load q for uniformly and triangularly distributed tangential loads for the SSSS plates with $H = 10^{-5}$ and $\lambda = 1$, $\lambda = 1.5$ and $\lambda = 2$, respectively. The corresponding results for the imaginary part of the frequencies for $H = 10^{-3}$ are given in Figs. 5 and 6. It is noted that the results given in Figs. 2-6 for the uniformly distributed tangential load are the same as the ones given in Wang *et al.* (2007). As such, they provide the verification of the method of solution outlined in Section 3.

Comparisons of the loads with uniform and triangular distributions indicate that the results are qualitatively similar, but the magnitudes of the follower load causing divergence or flutter instability differ considerably. Comparisons between Figs. 2a, 3a, 4a ($H = 10^{-5}$) and Figs. 5a, 5b and 6 ($H = 10^{-3}$) indicate that the imaginary parts of the frequencies remain positive for $H = 10^{-3}$ up to the flutter load. The corresponding results for the CSCS plates with $H = 10^{-5}$ are given in Figs. 7-9 with $\lambda = 1$, $\lambda = 1.5$ and $\lambda = 2$, respectively. The results for the uniformly distributed tangential loads are also shown in the figures which verify the results of Wang *et al.*

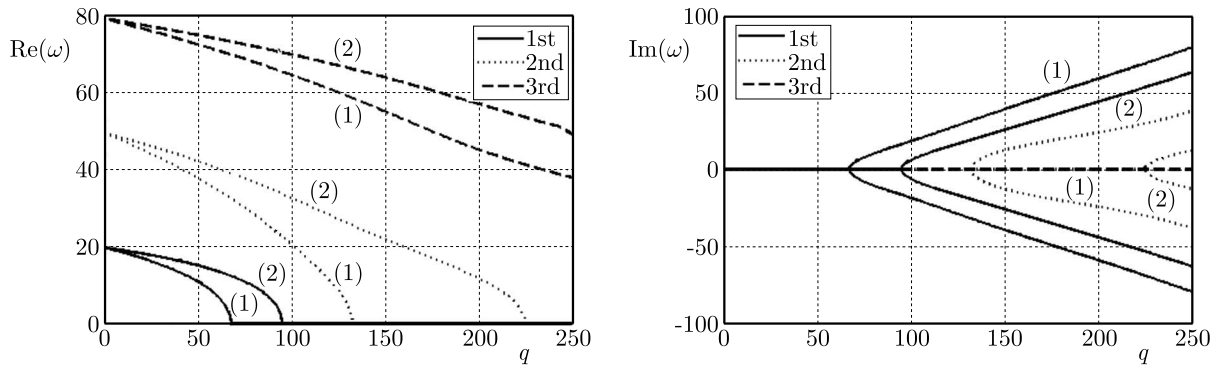


Fig. 2. First three frequencies of SSSS plate vs. follower force for $\lambda = 1$, $H = 10^{-5}$; (1) uniformly distributed load, (2) triangularly distributed load

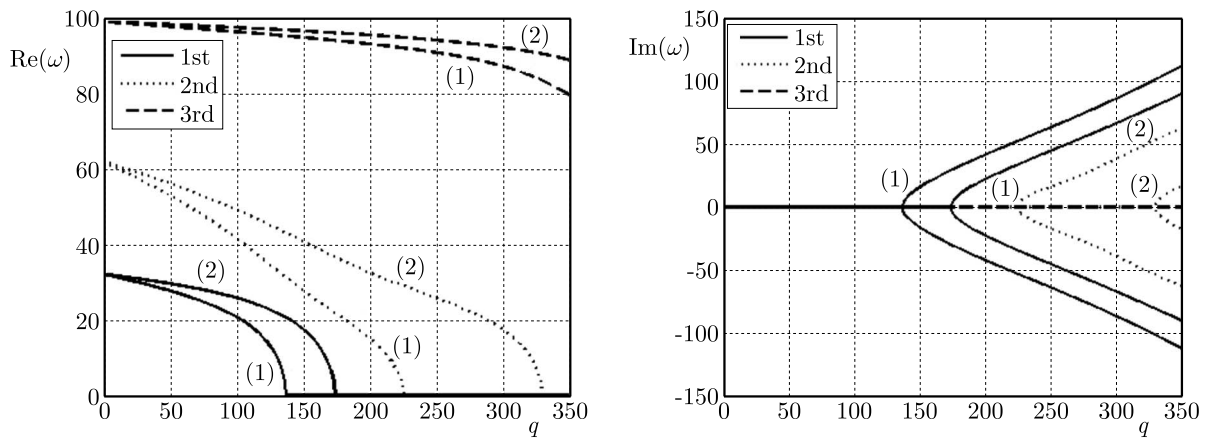


Fig. 3. First three frequencies of SSSS plate vs. follower force for $\lambda = 1.5$, $H = 10^{-5}$; (1) uniformly distributed load, (2) triangularly distributed load

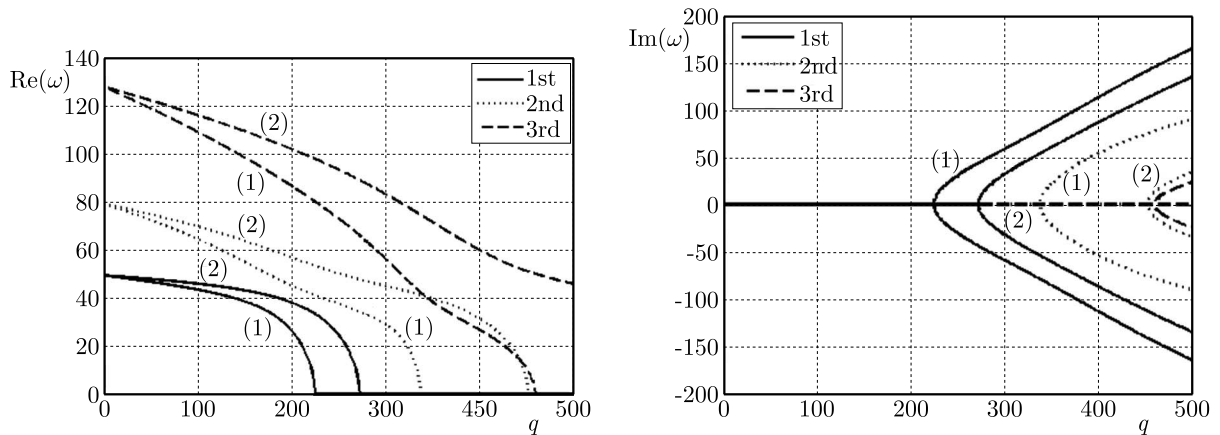


Fig. 4. First three frequencies of SSSS plate vs. follower force for $\lambda = 2$, $H = 10^{-5}$; (1) uniformly distributed load, (2) triangularly distributed load

(2007). In this case, it is observed that the real parts of the vibration modes behave differently as compared to the SSSS plates shown in Figs. 2-4. For the case $\lambda = 1$ (Fig. 7a), the real parts of the first and the third modes join to form a single mode. For $\lambda = 1.5$ and $\lambda = 2$, the first and the second modes join as shown in Figs. 8a and 9a, respectively. Thus, in the case of CSCS boundary conditions, there exists a threshold value q above which the first mode can join the second or third mode to form a single mode, and this value depends on the aspect ratio. Moreover, it is

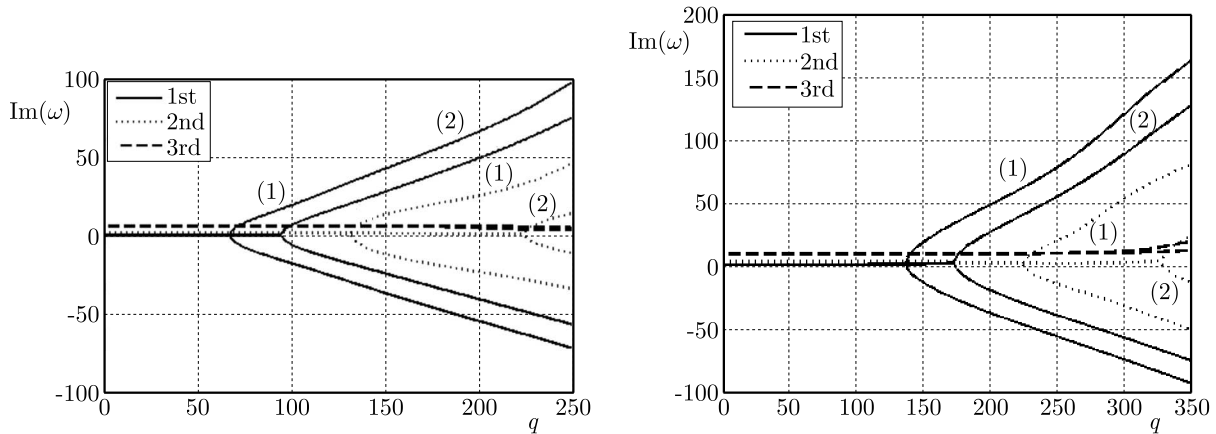


Fig. 5. Imaginary parts of frequencies of SSSS plate vs. follower force for (a) $\lambda = 1$ and (b) $\lambda = 1.5$, $H = 10^{-3}$; (1) uniformly distributed load, (2) triangularly distributed load

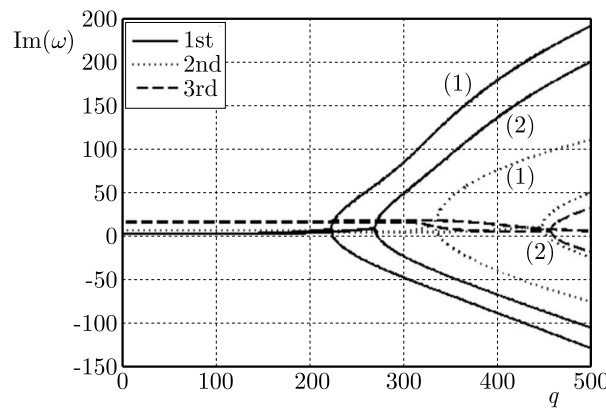


Fig. 6. Imaginary part of frequency of SSSS plate vs. follower force for $\lambda = 2$, $H = 10^{-3}$; (1) uniformly distributed load, (2) triangularly distributed load

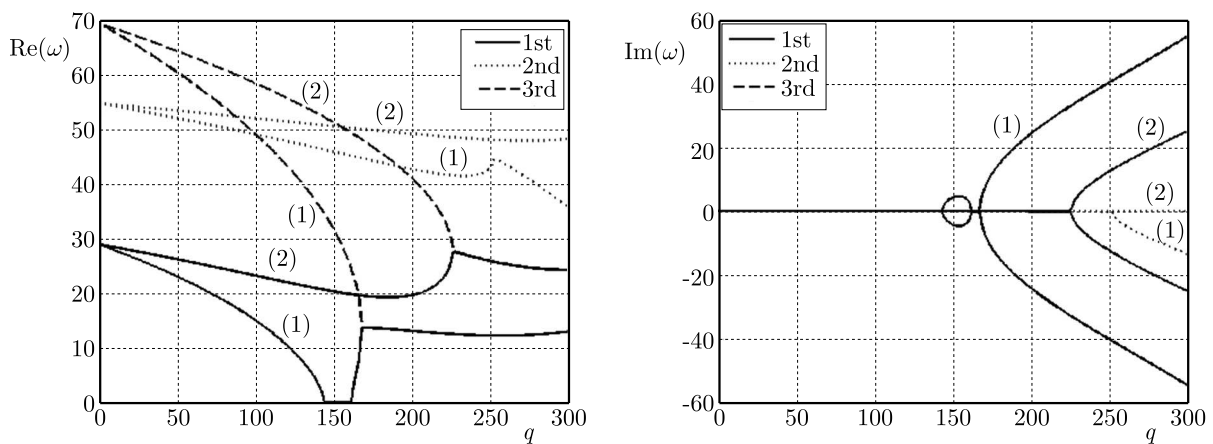


Fig. 7. First three frequencies of CSCS plate vs. follower force for $\lambda = 1$, $H = 10^{-5}$; (1) uniformly distributed load, (2) triangularly distributed load

observed that for the aspect ratios of $\lambda = 1.5$ and $\lambda = 2$, the plate does not show divergence instability and loses stability by flutter.

For the CSCS boundary conditions with $H = 10^{-3}$, the results are given in Figs. 10-12. For this value of $H = 10^{-3}$, the real parts of the frequencies do not form a single mode and the imaginary parts remain positive until the threshold values are exceeded and the flutter

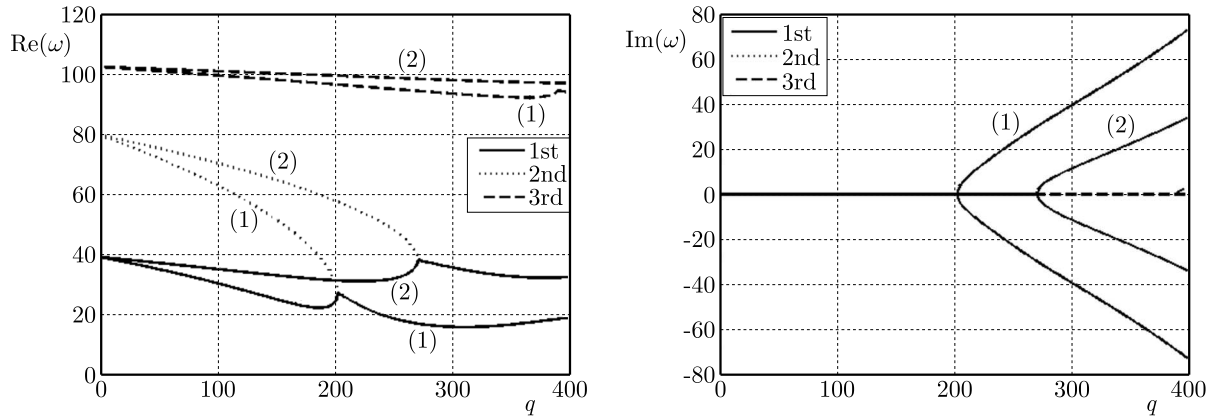


Fig. 8. First three frequencies of CSCS plate vs. follower force for $\lambda = 1.5$, $H = 10^{-5}$; (1) uniformly distributed load, (2) triangularly distributed load

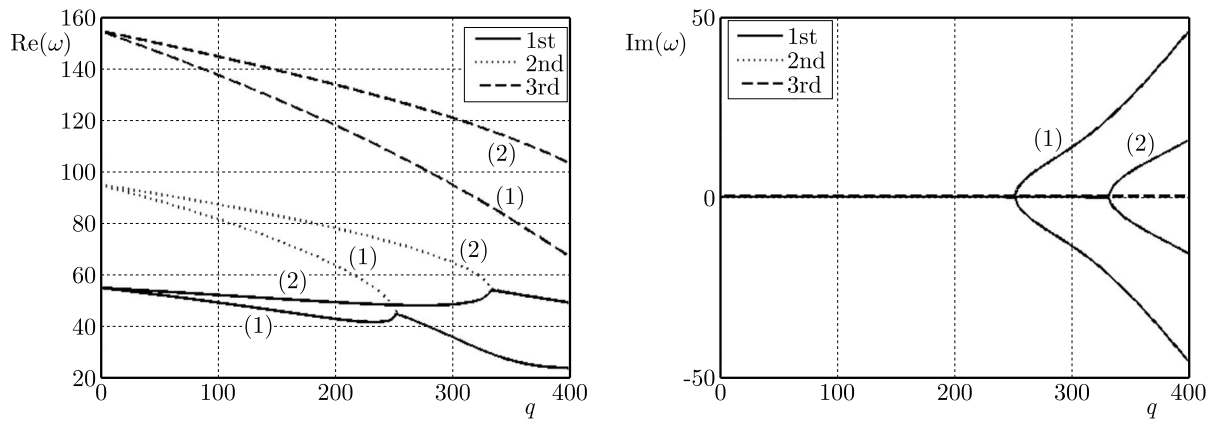


Fig. 9. First three frequencies of CSCS plate vs. follower force for $\lambda = 2$, $H = 10^{-5}$; (1) uniformly distributed load, (2) triangularly distributed load

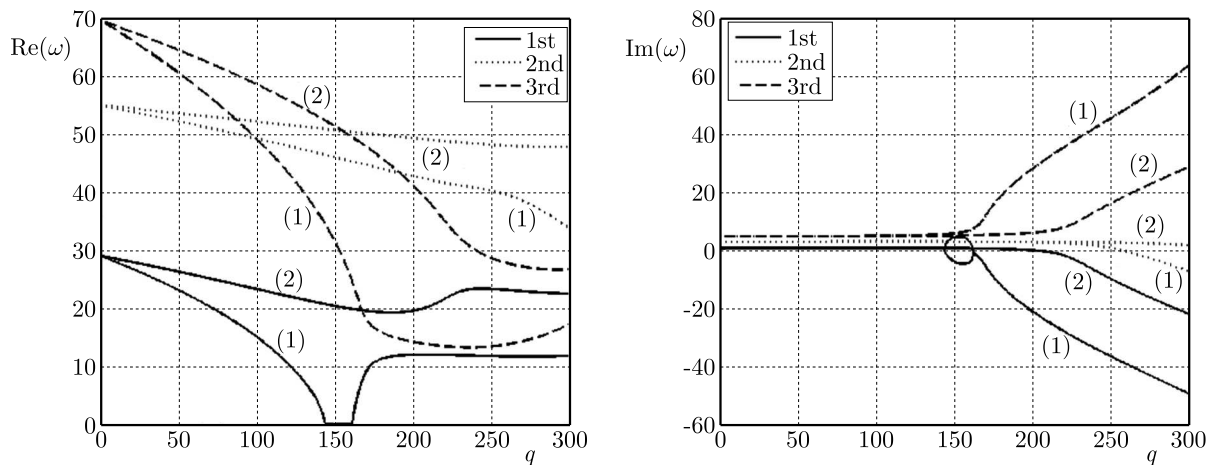


Fig. 10. First three frequencies of CSCS plate vs. follower force for $\lambda = 1$, $H = 10^{-3}$; (1) uniformly distributed load, (2) triangularly distributed load

instability occurs as shown in Figs. 10b, 11b and 12b. The imaginary parts of the frequencies exhibit negative values for $q \geq q_f$ leading to an exponential growth of the deflection.

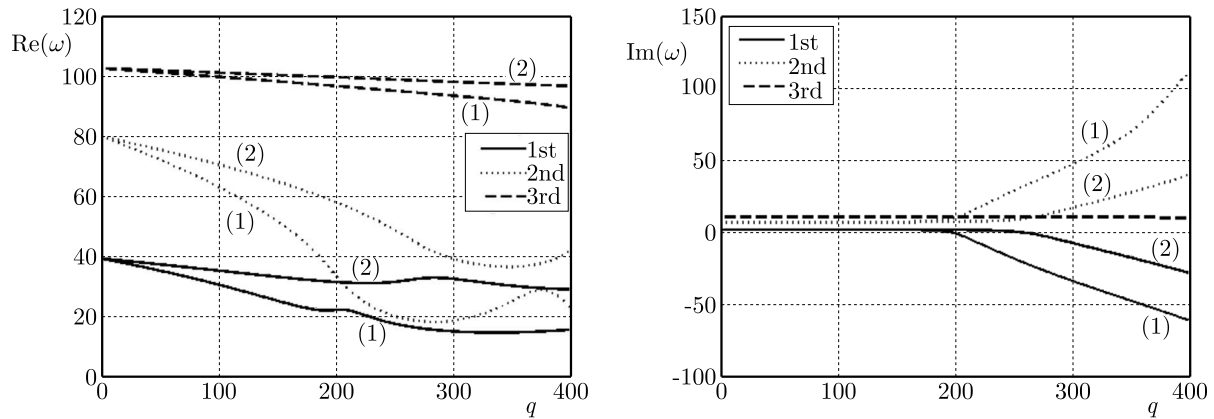


Fig. 11. First three frequencies of CSCS plate vs. follower force for $\lambda = 1.5$, $H = 10^{-3}$; (1) uniformly distributed load, (2) triangularly distributed load

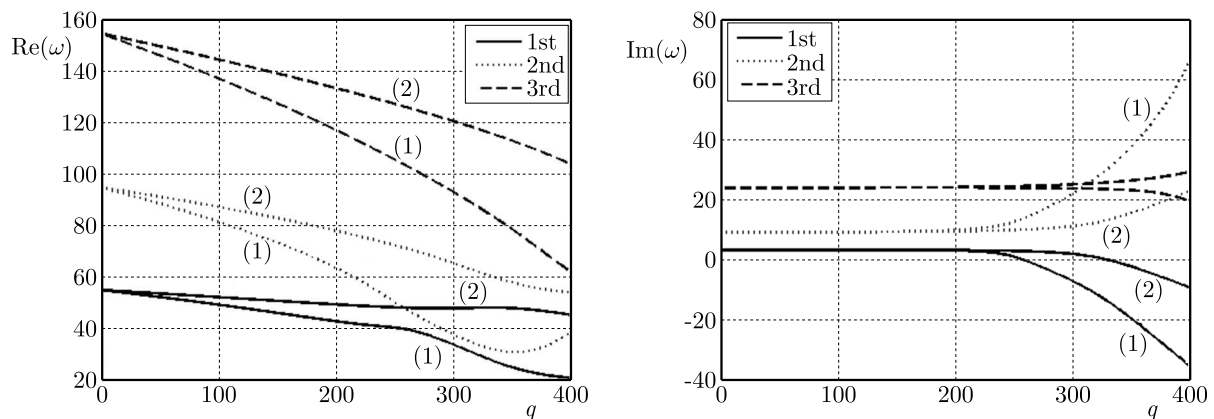


Fig. 12. First three frequencies of CSCS plate vs. follower force for $\lambda = 2$, $H = 10^{-3}$; (1) uniformly distributed load, (2) triangularly distributed load

5. Conclusions

The differential quadrature method is employed to study the dynamic stability of rectangular viscoelastic plates subject to triangularly distributed tangential follower loads. The Kelvin-Voigt viscoelastic model is taken as the constitutive equation of the plate. Two boundary conditions are investigated, namely, simple supports and a combination of simple and fixed supports. The solution is verified against the previous results obtained for SSSS and CSCS viscoelastic plates subject to uniformly distributed tangential loads by Wang *et al.* (2007).

Numerical results are given to study the effects of the aspect ratio and degree of viscoelasticity on the real and imaginary parts of the frequencies. The effect of uniformly and triangularly distributed follower loads on dynamic stability is compared numerically. It is observed that in the case of CSCS plates, the flutter instability occurs before the divergence instability for higher aspect ratios. In the case of SSSS plates, the degree of viscoelasticity does not affect the divergence load, but this effect is more pronounced for CSCS plates. At higher levels of viscoelasticity (higher values of H), the imaginary parts of the complex frequencies become positive rather than zero for low values of the follower load. The results obtained for the present case can be extended to different follower load cases and, in particular, to the cases where the direction of the load is controlled by a head (Tomski and Uzny, 2013b).

Acknowledgment

The research reported in this paper was supported by research grants from the University of KwaZulu-Natal (UKZN) and from National Research Foundation (NRF) of South Africa. The authors gratefully acknowledge the support provided by UKZN and NRF.

References

1. ADALI S., 1982, Stability of a rectangular plate under nonconservative and conservative forces, *International Journal of Solids and Structures*, **18**, 1043-1052
2. BERT C.W., MALIK M., 1996, Implementing multiple boundary conditions in the DQ solution of higher-order PDE's: Application to free vibration of plates, *International Journal of Numerical Methods in Engineering*, **39**, 1237-1258
3. CHEN L.-W., KU D.-M., 1991, Stability analysis of a Timoshenko beam subjected to distributed follower forces using finite elements, *Computers and Structures*, **41**, 813-819
4. CULKOWSKI P.M., REISMANN H., 1977, Plate buckling due to follower edge forces, *ASME Journal of Applied Mechanics*, **99**, 768-769
5. DARABSEH T.T., GENIN J., 2004, Dynamic stability of viscoelastic columns loaded by a follower force, *Journal of Mechanical Engineering Science*, **218**, 1091-1101
6. ELFELSOUFI Z., AZRAR L., 2006, Integral equation formulation and analysis of the dynamic stability of damped beams subjected to subtangential follower forces, *Journal of Sound and Vibration*, **296**, 690-713
7. FARSHAD M., 1978, Stability of cantilever plates subjected to biaxial subtangential loading, *Journal of Sound and Vibration*, **58**, 555-561
8. GAJEWSKI A., 2000, Vibrations and stability of a non-conservatively compressed prismatic column under nonlinear creep conditions, *Journal of Theoretical and Applied Mechanics*, **38**, 259-270
9. ILYASOV M.H., 2010, Parametric vibrations and stability of viscoelastic shells, *Mechanics of Time-Dependent Materials*, **14**, 153-171
10. ILYASOV M.H., AKÖZ Y.A., 2000, The vibration and dynamic stability of viscoelastic plates, *International Journal of Engineering Science*, **38**, 695-714
11. ILYASOV M.H., ILYASOVA N.M., 2006, Flutter of viscoelastic strips, *Mechanics of Time-Dependent Materials*, **10**, 201-213
12. JAYARAMAN G., STRUTHERS A., 2005, Divergence and flutter instability of elastic specially orthotropic plates subject to follower forces, *Journal of Sound and Vibration*, **281**, 357-373
13. KAZEMI-LARI M.A., GHAVANLOO E., FAZELZADEH S.A., 2013, Structural instability of carbon nanotubes embedded in viscoelastic medium and subjected to distributed tangential load, *Journal of Mechanical Science and Technology*, **27**, 2085-2091
14. KIM J.H., KIM H.S., 2000, A study on the dynamic stability of plates under a follower load, *Computers and Structures*, **74**, 351-363
15. KIM J.H., PARK J.H., 1998, On the dynamic stability of rectangular plates subjected to intermediate follower forces, *Journal of Sound and Vibration*, **209**, 882-888
16. KIM J.-O., LEE K.-S., LEE J.-W., 2008, Beam stability on an elastic foundation subjected to distributed follower force, *Journal of Mechanical Science and Technology*, **22**, 2386-2392
17. KIM N.I., 2010, Dynamic stability behavior of damped laminated beam subjected to uniformly distributed subtangential forces, *Composite Structures*, **92**, 2768-2780
18. KIM N.I., 2011, Divergence and flutter instability of damped laminated beams subjected to a triangular distribution of nonconservative forces, *Advances in Structural Engineering*, **14**, 1075-1091

19. KIRILLOV O.N., 2013, *Nonconservative Stability Problems of Modern Physics*, Walter de Gruyter GmbH, Berlin/Boston
20. KROWIAK A., 2008, Methods based on the differential quadrature in vibration analysis of plates, *Journal of Theoretical and Applied Mechanics*, **46**, 123-139
21. KUMAR A., SRIVASTA A.K., 1986, Stability of thin rectangular elastic plates under a follower force, *Mechanics Research Communications*, **13**, 165-168
22. LANGTHJEM M.A., SUGIYAMA Y., 2000, Dynamic stability of viscoelastic beam under follower forces, *Journal of Sound and Vibration* **238**, 809-851
23. LEIPHOLZ, H.H.E., 1975, An extremum principle for the buckling problem of the clamped-clamped rod subjected to tangential follower forces, *Mechanics Research Communications*, **2**, 119-123
24. LEIPHOLZ H.H.E., 1978, Stability of a rectangular simply supported plate subjected to nonincreasing tangential follower forces, *ASME Journal of Applied Mechanics*, **45**, 223-224
25. LEIPHOLZ H.H.E., BHALLA K., 1977, On the solution of the stability problem of elastic rods subjected to triangularly distributed tangential follower forces, *Ingenieur-Archiv*, **46**, 115-124
26. LEIPHOLZ, H.H.E., PFENDT F., 1982, On the stability of rectangular completely supported plates with uncoupled boundary conditions subjected to uniformly distributed follower forces, *Computer Methods in Applied Mechanics Engineering*, **30**, 19-52
27. LEIPHOLZ H.H.E., PFENDT F., 1983, Application of extended equations of Galerkin to stability problems of rectangular plates with free edges and subjected to uniformly distributed follower forces, *Computer Methods in Applied Mechanics and Engineering*, **37**, 341-365
28. MARZANI A., POTAPOV V.D., 1999, On the stability of a nonlinear viscoelastic rod subjected to a longitudinal force in the form of a random stationary process, *Mechanics of Time-Dependent Materials*, **2**, 335-349
29. PRZYBYLSKI J., 1999, Instability regions of a prestressed compound column subjected to a follower force, *Journal of Theoretical and Applied Mechanics*, **37**, 148-162
30. ROBINSON M.T.A., 2013, Nonlinear vibration of 2D viscoelastic plate subjected to tangential follower force, *Engineering Mechanics*, **20**, 59-74
31. ROBINSON M.T.A., ADALI S., 2016, Nonconservative stability of viscoelastic rectangular plates with free edges under uniformly distributed follower force, *International Journal of Mechanical Sciences*, **107**, 150-159
32. RUAN M., WANG Z.-M., WANG Y., 2012, Dynamic stability of functionally graded materials skew plates subjected to uniformly distributed tangential follower forces, *Journal of Vibration and Control*, **18**, 913-923
33. RYU B.J., SUGIYAMA Y., YIM K.B., LEE G.S., 2000, Dynamic stability of an elastically restrained column subjected to triangularly distributed subtangential forces, *Computers and Structures*, **76**, 611-619
34. SUGIYAMA Y., KAWAGOE H., 1975, Vibration and stability of elastic columns under the combined action of uniformly distributed vertical and tangential forces, *Journal of Sound and Vibration*, **38**, 341-355
35. SUGIYAMA Y., MLADENOV K.A., 1983, Vibration and stability of elastic columns subjected to triangularly distributed sub-tangential forces, *Journal of Sound and Vibration*, **88**, 447-457
36. TOMSKI L., SZMIDLA J., 2004, Vibration and stability of a column subjected to the generalised load by a force directed towards the pole, *Journal of Theoretical and Applied Mechanics*, **42**, 163-193
37. TOMSKI L., UZNY S., 2008, Free vibration and the stability of a geometrically non-linear column loaded by a follower force directed towards the positive pole, *International Journal of Solids and Structures*, **45**, 87-112
38. TOMSKI L., UZNY S., 2013a, Free vibrations and stability of a new slender system subjected to a conservative or non-conservative load, *ASCE Journal of Engineering Mechanics*, **139**, 1133-1148

39. TOMSKI L., UZNY S., 2013b, Vibrations and stability of a column subjected to the specific load realized by circular elements of heads, *Mechanics and Mechanical Engineering*, **17**, 197-206
40. TORKI M.E., KAZEMI M.T., HADDADPOUR H., MAHMOUDKHANI S., 2014a, Dynamic stability of cantilevered functionally graded cylindrical shells under axial follower forces, *Thin-Walled Structures*, **79**, 138-146
41. TORKI M.E., KAZEMI M.T., REDDY J.N., HADDADPOUD H., MAHMOUDKHANI S., 2014b, Dynamic stability of functionally graded cantilever cylindrical shells under distributed axial follower forces, *Journal of Sound and Vibration*, **333**, 801-817
42. WANG Y., WANG Z., ZU L., 2013, Stability of viscoelastic rectangular plate with a piezoelectric layer subjected to follower force, *Archive of Applied Mechanics*, **83**, 495-507
43. WANG Z.M., Ji Y.Z., 1992, The dynamic stability of rectangular plates under the action of tangential follower force, *Journal of Vibration Engineering*, **5**, 78-83
44. WANG Z.M., ZHOU Y.-F., WANG Y., 2007, Dynamic stability of non-conservative viscoelastic rectangular plate, *Journal of Sound and Vibration*, **307**, 250-264
45. WANG Z., WANG Y., GUO X., 2009, Dynamic stability of linearly varying thickness viscoelastic rectangular plate with crack and subjected to tangential follower force, *Applied Acoustics*, **70**, 845-856
46. ZHOU Y.-F., WANG Z.-M., 2014, Exact solutions for the stability of viscoelastic rectangular plate subjected to tangential follower force, *Archive of Applied Mechanics*, **84**, 1081-1089
47. ZHUO R.H., FEN S.Z., 2005, Dynamic stability of viscoelastic beam under follower force, *ASCE Journal of Engineering Mechanics*, **22**, 26-30
48. ZUO Q.H., SHREYER H.L., 1996, Flutter and divergence instability of nonconservative beams and plates, *International Journal of Solids and Structures*, **33**, 1355-1367

Manuscript received August 3, 2016; accepted for print April 7, 2017

ANALYTICAL EXPRESSIONS FOR EFFECTIVE WEIGHTING FUNCTIONS USED DURING SIMULATIONS OF WATER HAMMER

KAMIL URBANOWICZ

West Pomeranian University of Technology, Szczecin, Poland

e-mail: kamil.urbanowicz@zut.edu.pl

For some time, work has been underway aimed at significant simplification of the modelling of hydraulic resistance occurring in the water hammer while maintaining an acceptable error. This type of resistance is modelled using a convolution integral, among others, from local acceleration of a liquid and a certain weighting function. The recently completed work shows that during efficient calculations of the convolution integral, the effective weighting function used does not have to be characterised by large convergence with a classical function (according to Zielke during laminar flow and to Vardy-Brown during turbulent flow). However, it must be a sum of at least two or three exponential expressions so that the final results of the simulation could be considered as satisfactory. In this work, it has been decided to present certain analytical formulas using which it will be possible to determine the coefficients of simplified effective weighting functions in a simple direct way.

Keywords: unsteady flow, water hammer, convolution integral, frequency-dependent friction

1. Introduction

Unsteady flows occur in hydraulic systems, water supply systems, heating systems, thermal-hydraulic systems (cooling cores of nuclear power plants), etc., during start-up, braking or failure. Proper modelling of flows of liquids under pressure in such systems remains a significant challenge. Among the key issues widely discussed in new publications on the subject, special emphasis is placed on the correct modelling: of the time-varying hydraulic resistance (Vardy and Brown, 2003; Zarzycki *et al.*, 2011; Reddy *et al.*, 2012), cavitation (Zarzycki and Urbanowicz, 2006; Adamkowski and Lewandowski, 2009, 2012; Bergant *et al.*, 2006; Karadžić *et al.*, 2014; Soares *et al.*, 2015), the interaction between the liquid and walls of the conduit (Keramat *et al.*, 2012; Henclik, 2015; Zanganeh *et al.*, 2015), the viscoelastic phenomenon that occurs during the flow in a piping made of engineering polymers (Weinerowska-Bords, 2015; Soares *et al.*, 2012; Keramat *et al.*, 2013; Pezzinga *et al.*, 2014; Urbanowicz *et al.*, 2016). Taking into account all of the above phenomena while simulating unsteady flows has seemed impossible until recently. But now, thanks to the work carried out by Keramat and Tijsseling (2012) presented at the international conference on the analysis and damping of pressure surges associated with the phenomenon of water hammer (BHR Pressure Surges, Lisbon), we know that it is possible. In this general model, as well as in many others having a simplified design, the method of modelling of the time-varying hydraulic resistance has a very large impact on pressure runs.

During acceleration, deceleration or as a result of rapid suppression of the fluid flow resulting from quick valve closing (the so called water hammer effect occurs then), the friction of the fluid against pipe walls, as well as the internal friction between its elements, has a significant impact on transient flow parameters. It was already noted by Roiti, Helmholtz, Stearn and Gromeka in the first studies concerning unsteady fluid flow in pipes about 150 years ago. A rapid development of numerical methods in the 1950th and the 1960th, particularly development of the method

of characteristics being commonly used to date, induced further studies, the main objective of which was to properly describe the friction occurring during the flow in a mathematical manner.

At present, the models enabling the pipe wall shear stress to be simulated can be divided into two groups. The first group is simple models in which the stress is directly proportional to a momentary local and convective acceleration of the fluid. The model developed by a group of researchers under the leadership of Daily (1956), in which the stress depended only on momentary local acceleration of the fluid and a certain constant coefficient, is considered a prototype. The above model was developed with time by other researchers as Carstens and Roller, Safwat and Polder and Shuy and Apelt. A significant adjustment was introduced by Brunone *et al.* (1991), additionally making the stress conditional on momentary convective acceleration. Vítkovský *et al.* (2000) introduced a sign next to the convective derivative, while Laurerio and Ramos (2003) made a final adjustment of that model consisting in the splitting of the single constant coefficient k into two new coefficients k_t and k_x , which are to be found next to adequate velocity derivatives

$$\tau_w(t) = \frac{\lambda_q \rho v |v|}{8} + \frac{\rho D}{8} \left(k_t \frac{\partial v}{\partial t} + k_x c \frac{|v|}{v} \left| \frac{\partial v}{\partial x} \right| \right) \quad (1.1)$$

where: λ_q is the quasi-steady friction coefficient, ρ – liquid density, k_t and k_x – empirical coefficients, D – pipe inner diameter, v – velocity, t – time, c – pressure wave speed, x – distance along the pipe.

Ramos then numerically proved the impact of particular expressions of this solution on the phase shifts and the speed of pressure wave damping, whereas Reddy *et al.* (2012), based on known experimental results, presented a method consisting in the empirical selection of constants when calculating the coefficients k_t and k_x that are to be found in final solution (1.1). The models of the above group are limited due to the need for empirical determination of the coefficients k_t and k_x . There are no papers that would show details of their numerical implementation; besides, they are characterized by a limited qualitative compatibility of pressure course being modelled (Adamkowski and Lewandowski, 2006), which is their major disadvantage.

The second group of models consists of theoretical models being based on the so called convolution integral. The author of their prototype was Zielke (1968) who postulated

$$\tau_w(t) = \frac{4\mu}{R} v + \frac{2\mu}{R} \int_0^t w(t-u) \frac{\partial v}{\partial t}(u) du \quad (1.2)$$

where: μ is the dynamic viscosity coefficient, R – pipe inner radius, $w(t)$ – weighting function.

The convolutional integral, being a product of the weight function $w(t)$ and the momentary value of fluid acceleration, is the inverse Laplace transform from the expression describing the impedance of a hydraulic line. In laminar flows, this impedance is being calculated from a simple analytical formula introduced by Brown, whereas in the turbulent ones it has a very complex analytical and empirical form (empirical because an empirical distribution of the coefficient of turbulent viscosity in the pipe cross-section is needed to resolve it), the derivation of which was reached at the same time by Zarzycki (1997, 2000) and Vardy and Brown (1996, 2003, 2004).

The first numerical resolution of this integral being suitable for implementation in the method of characteristics was already shown in the work by Zielke (1968). Unfortunately, it was not suitable for effective calculations, therefore a few years later Trikha (1975) presented another numerical procedure based on a three term weighting function being constructed from exponential terms. Unfortunately, also Trikha made too many simplifications, thus – with time – other authors presented their revised versions of that procedure (Kagawa *et al.*, 1983; Schohl, 1993). Recently, Vardy and Brown (2010) noticed and corrected a significant error in the original procedure according to Zielke, consisting in approximation instead of integration of the

weight function in the dimensionless time interval from 0 to $\Delta\hat{t}$, but they did not present a revised effective calculation procedure. Such a procedure was, however, presented by Urbanowicz (2015).

It is also worth emphasising that Zarzycki (1997, 2000) as well as Vardy and Brown (1996, 2003, 2004) proved that solution in form of equation (1.2) may be also used for the modelling of turbulent unsteady flows, provided that an adequate weight function was going to be used.

Because all effective solutions are based on the weighting functions being a finite sum of exponential terms, the authors of effective numerical solutions frequently showed new forms of those functions in their papers referring to the modelling of laminar flow (Triakha 1975, Kagawa *et al.*, 1983; Schohl, 1993; Vítkovský *et al.*, 2004) or the turbulent one (Vítkovský *et al.*, 2004; Zarzycki *et al.*, 2011). Up to this day, the most accurate functions represented with an extended range of use were presented by Urbanowicz and Zarzycki (2012). They are very useful in all cases that require a complete weighting function, for example in the modeling of one-directional accelerated or decelerated flows. The coefficients describing the effective weighting functions in turbulent flow are closely dependent on the Reynolds number and the internal roughness of the pipe walls. For correct determination, the classical scaling procedure developed by Vítkovský *et al.* (2004) can be used, or the universal procedure (Urbanowicz *et al.*, 2012). The advantage of them is providing the shape of the effective weighting function compatible with the shape of the classical laminar weighting function presented by Zielke (1968) for the critical Reynolds number.

In this paper, analytical formulas that enable coefficients describing simplified effective weighting functions composed of two or three terms to be determined are presented. The method is responsible for offloading computer memory and accelerating the iterative computational process without losing accuracy. The exemplary results of simulation tests presented confirm high compatibility of the simulated courses (with the use of the weighting function with limited ranges and the same being characterized by a simple structure) with the experimental ones.

2. New idea

Recently completed studies have shown that unsteady flows can be modelled accurately using simplified effective weighting functions consisting of only two $k=2$ or three $k=3$ exponential expressions (Urbanowicz, 2015; Urbanowicz and Zarzycki, 2015)

$$w(t) = \sum_{i=1}^k m_i e^{-n_i \hat{t}} \quad (2.1)$$

where m_i and n_i are coefficients of effective weighting function, \hat{t} is the dimensionless time. These expressions are combined with the new improved method for calculating shear stress. Functions used in the studies are characterised by a limited yet essential range of application (Fig. 1).

The lower end of this range in the general case is set equal to the dimensionless time step $\Delta\hat{t}$, and the upper end to the multiplicity there of $10^3 \Delta\hat{t}$. The aforementioned time step in numerical calculations is calculated individually for all pressure conduits that retain their shape stability using the formula

$$\Delta\hat{t} = \frac{L}{f} \frac{\nu}{cR^2} \quad (2.2)$$

where: L is conduit length, ν – kinematic viscosity of liquid, f – number of analysed cross-sections.

Calculation of the coefficients m_i and n_i describing the previously analysed simplified effective weighting functions required the use of a numerical method developed in 2012 (Urbanowicz, 2012). Elimination in this work of the numerical procedure mentioned above at the stage of

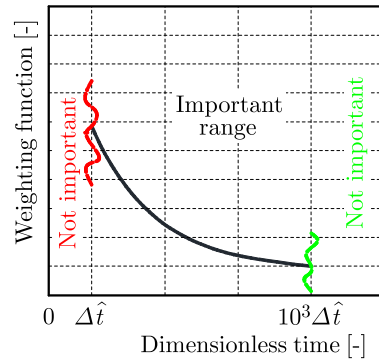


Fig. 1. Significant range of weighting functions

determining the weighting function coefficients reduces time needed for numerical computation, facilitating the modelling of unsteady flows to perform a simple verification of the effectiveness of the method presented in the work of Urbanowicz and Zarzycki (2015) and enabling simple implementation of this method in the existing commercial software by introducing a variable hydraulic resistance coefficient

$$\lambda_{(t+\Delta t)} = \lambda_{q,(t+\Delta t)} \quad (2.3)$$

$$+ \underbrace{\frac{16\nu}{R|v_{(t+\Delta t)}|v_{(t+\Delta t)}} \sum_{i=1}^j \underbrace{[y_i(t)A_i + \eta B_i(v_{(t+\Delta t)} - v_{(t)}) + (1 - \eta)C_i(v_{(t)} - v_{(t-\Delta t)})]}_{y_i(t+\Delta t)}}_{\lambda_{u,(t+\Delta t)}}$$

In the equation above, constants A_i , B_i and C_i depend only on coefficients m_i and n_i describing the effective weighting function and the dimensionless time step

$$A_i = e^{-n_i \Delta \hat{t}} \quad B_i = \frac{m_i}{n_i \Delta \hat{t}} (1 - A_i) \quad C_i = A_i B_i \quad (2.4)$$

3. Analytical approximate solution

Difficulties in widespread use of the simplified methodology presented in the work of Urbanowicz and Zarzycki (2015), arising from the need to use the numerical procedure (Urbanowicz, 2012), may discourage practical use of the solutions discussed. Therefore, to further simplify the modelling of unsteady resistance, analytical solutions will be presented that can help one to accurately calculate coefficients m_i and n_i of simplified effective weighting functions as a function of the dimensionless time step $\Delta \hat{t}$. The studies carried out previously (Urbanowicz, 2015; Urbanowicz and Zarzycki, 2015) indicate that the relative percentage error of effective weighting functions should not exceed 30% for the two-expression functions or 10% for three-expression functions and that the optimal range of applicability of these functions should be from $\Delta \hat{t}$ to $10^3 \Delta \hat{t}$. As can be seen in equation (2.2), the dimensionless time step $\Delta \hat{t}$ which is the starting point for the applicability of effective weighting functions assumes different values depending on the properties of flowing liquid, the conduit and the numerical method. Based on the analysis of practical and theoretical examples, the possible range of its variability can be specified using the domain of $\Delta \hat{t} \in [10^{-10}; 10^{-1}]$.

To determine the analytical function describing variation of the values of coefficients of two-expression effective weighting functions, it is necessary to first identify the set of values of these coefficients. For this purpose, the method discussed in 2012 was used (Urbanowicz, 2012).

When searching for an analytical solution for the effective two-expression functions, 93 sets of coefficients were determined (m_1, m_2, n_1, n_2) for the range from 10^{-10} every $10^{0.1}$ to $10^{-0.8}$. It is worth noting that for $\Delta\hat{t} = 10^{-0.8}$, the values of these coefficients coincided with the values known from the classical weighting function for laminar flow (i.e. weighting according to Zielke (1968)), i.e. $m_1 = 1$, $m_2 = 1$, $n_1 = 26.3744$, $n_2 = 70.8493$. In the case of effective three-expression functions, 89 sets of coefficients were determined $(m_1, m_2, m_3, n_1, n_2, n_3)$ for the range from 10^{-10} every $10^{0.1}$ to $10^{-1.2}$. The difference in the number of these sets resulted from the fact that in this case, already for $\Delta\hat{t} = 10^{-1.2}$, the values of these coefficients coincided with the values known from the classical weighting function for laminar flow, i.e. $m_1 = 1$, $m_2 = 1$, $m_3 = 1$, $n_1 = 26.3744$, $n_2 = 70.8493$, $n_3 = 135.0198$. Knowing all the above values, the next step was to adopt appropriate forms of analytic functions, which would accurately describe variability of these coefficients as a function of the dimensionless time step. Analysis of the variability of individual coefficients and the tests performed with other forms revealed that in the case of two-expression functions, their coefficients can be described using the formula

$$m_i, n_i = \sum_{i=1}^3 A_i \Delta\hat{t}^{B_i} + C \quad (3.1)$$

in the range of their linearity on a log-log graph (Fig. 2a) (interval for $\Delta\hat{t}$ from 10^{-10} to 10^{-4} , exceptionally for n_1 to 10^{-5}).

And the formula

$$m_i, n_i = \sum_{i=1}^4 D_i e^{-E_i \Delta\hat{t}} + F \quad (3.2)$$

for the range of their non-linearity on a log-log graph (Fig. 2b) (interval for $\Delta\hat{t}$ from 10^{-4} to ∞ , exceptionally for n_1 from 10^{-5} to ∞). On the graphs presented below (Figs. 2 and 3), the abbreviation ‘‘sol.’’ means that these are the coefficients calculated using the presented analytical formulas.

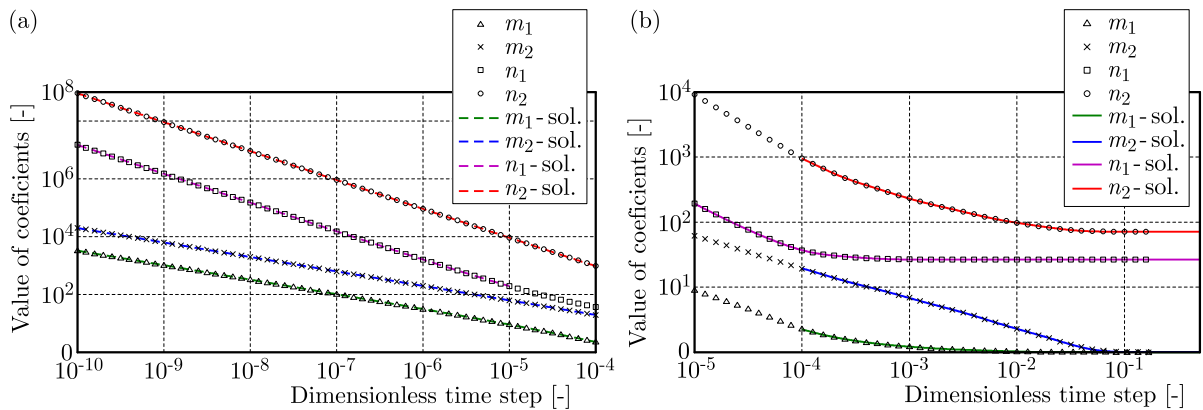


Fig. 2. Compatibility of the analytical solution – two-expression functions

To find definitive values of the coefficient of the functions adopted above, i.e. A_1, \dots, A_3 , B_1, \dots, B_3 and C , and D_1, \dots, D_4 , E_1, \dots, E_4 and F , the Curve Fitting Toolbox module implemented in MATLAB was used. The values of the estimated final coefficients are summarised in Table 1 and 2.

Analysis of the variability of individual coefficients m_1, \dots, m_3 and n_1, \dots, n_3 representing three-expression functions showed that the forms of analytical functions, which were assumed

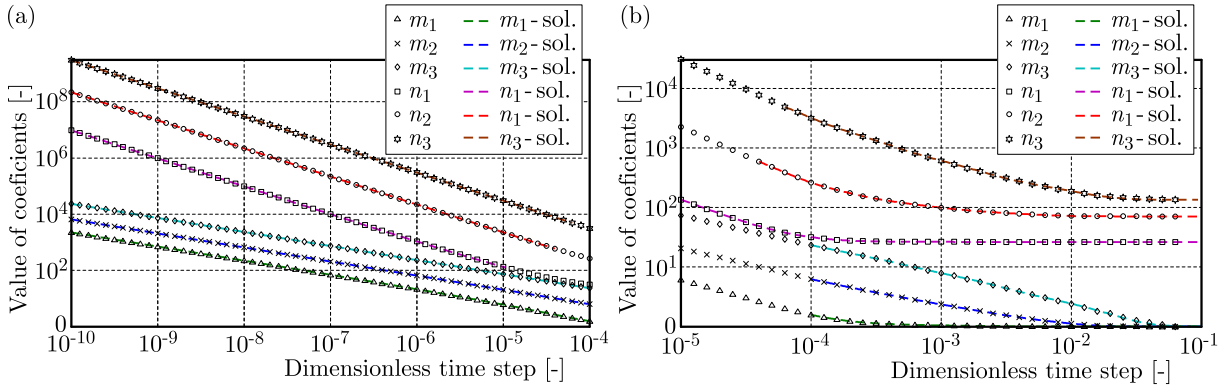


Fig. 3. Compatibility of the analytical solution – three-expression functions

Table 1. Coefficients of the analytical solution of effective two-expression functions for the range of small dimensionless time steps (Eq. (3.1))

Coeff.	m_1	m_2	n_1	n_2
	Interval [10^{-10} ; 10^{-4}]	Interval [10^{-10} ; 10^{-4}]	Interval [10^{-10} ; 10^{-5}]	Interval [10^{-10} ; 10^{-4}]
A_1	0.03234	0.1963	0.001476	0.09021
A_2	48.35	2.88	0.1203	0.382
A_3	9.717	-0.2661	526.7	223.1
B_1	-0.5	-0.5	-1	-1
B_2	0.5437	3.575	-0.5	-0.4592
B_3	3.85	5.276	0.5567	0.2615
C	-1.318	-0.2351	6.091	0

Table 2. Coefficients of the analytical solution of effective two-expression functions for the range of large dimensionless time steps (Eq. (3.2))

Coeff.	m_1	m_2	n_1	n_2
	Interval (10^{-4} ; ∞)	Interval (10^{-4} ; ∞)	Interval (10^{-5} ; ∞)	Interval (10^{-4} ; ∞)
D_1	0.1480	2.214	9.317	56.56
D_2	0.3227	4.155	87	136.5
D_3	0.8039	7.929	188.1	396.7
D_4	2.458	20.485	477.43	1903.3
E_1	188.8	62.02	4459	79.71
E_2	1316	386.6	29320	489.6
E_3	5728	2191	104300	2880
E_4	19270	12570	290500	15760
F	1	1	26.3744	70.8493

in the case discussed above, would also work. Thus, in range of its linearity on a log-log graph (Fig. 3a), the function sought has the form

$$m_i, n_i = \sum_{i=1}^4 A_i \Delta t^{B_i} \quad (3.3)$$

whereas for the range of non-linearity (Fig. 3b), we can describe it using the form exactly the same as in equation (3.2). In the case of the aforementioned analytical solution describing

coefficients of the effective three-expression weighting functions, much greater volatility of the dimensionless time was noted at which the functions describing individual coefficients correctly passed from the linear form (in log-log scale) to the non-linear form. Specific times of transition from one form to another are shown in Tables 3 and 4.

Table 3. Coefficients of the analytical solution of effective three-expression functions for the range of small dimensionless time steps (Eq. (3.3))

Coeff.	m_1	m_2	m_3	n_1	n_2	n_3
	Interval [10^{-10} ; 10^{-4}]	Interval [10^{-10} ; 10^{-4}]	Interval [10^{-10} ; 10^{-4}]	Interval [10^{-10} ; 10^{-5}]	Interval [10^{-10} ; $10^{-4.4}$]	Interval [10^{-10} ; $10^{-4.2}$]
A_1	0.02239	0.06549	0.2336	0.0009749	0.02208	0.3037
A_2	-1.123	-0.1334	11.52	0.09783	0.1233	0.1641
A_3	34.85	-2.54	-11.62	6.215	11.55	5.039
A_4	2.114e+06	2559	7.868	887.8	2025	1.011e+04
B_1	-0.5	-0.5	-0.5	-1	-1	-1
B_2	0	0	0	-0.5	-0.5	-0.5
B_3	0.5138	0.2948	0.0002657	0.001247	0.001441	-0.07303
B_4	1.789	2.894	3.297	0.5838	0.6193	0.6172

Table 4. Coefficients of the analytical solution of effective three-expression functions for the range of large dimensionless time steps (Eq. (3.2))

Coeff.	m_1	m_2	m_3	n_1	n_2	n_3
	Interval (10^{-4} ; ∞)	Interval (10^{-4} ; ∞)	Interval (10^{-4} ; ∞)	Interval (10^{-5} ; ∞)	Interval ($10^{-4.4}$; ∞)	Interval ($10^{-4.2}$; ∞)
D_1	0.02449	0.8285	3.272	1.16	26.05	216
D_2	0.06897	1.547	6.819	25.91	71.93	729.2
D_3	0.2359	2.776	13.42	96.44	263.8	2522
D_4	1.8429	5.9004	22.9793	251.6091	1427	12006.2
E_1	246	190.8	83.86	2939	314.5	140.2
E_2	995.2	907.7	645.4	1.792e+04	2054	969.4
E_3	4787	4112	3779	6.098e+04	1.09e+04	5460
E_4	1.696e+04	1.608e+04	1.895e+04	2e+05	4.32e+04	2.803e+04
F	1	1	1	26.3744	70.8493	135.0198

The maximum values of relative percentage errors, which are represented by the effective weighting functions determined using the above analytical formulas, calculated with reference to the classical function according to Zielke (1968) are illustrated in the chart below (Fig. 4). The graph shows that the maximum error for the dimensionless time step of $\Delta\hat{t} \approx 10^{-4}$ systematically decreases until reaching zero. Achieving the zero value is equivalent to overlapping of coefficients calculated using the analytical method with coefficients from the classical laminar weighting function according to Zielke.

With the use of the analytical formulas presented in this Section, it is possible only to determine coefficients that describe effective laminar functions. In a situation where there is turbulent flow, these coefficients have to be rescaled in accordance with the procedure described in (Vítkovský *et al.*, 2004; Urbanowicz *et al.*, 2012) for, as we know, the form of a classical turbulent weighting function according to Vardy and Brown (2007) is highly dependent on the Reynolds number.

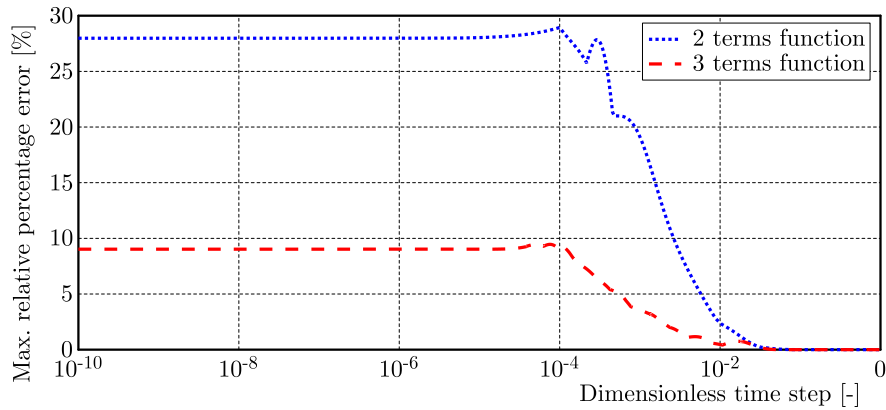


Fig. 4. Maximum relative percentage errors of weighting functions designated analytically

4. Example calculation results

To examine the impact of this new effective weighting function procedure presented in the previous Section, comparative studies for pure water hammer have been made. Basic continuity (4.1)₁ and momentum (4.1)₂ equations describing unsteady flow in a horizontal pipe are

$$\frac{\partial p}{\partial t} + \rho c^2 \frac{\partial v}{\partial x} = 0 \quad \frac{\partial p}{\partial x} + \rho \frac{\partial v}{\partial t} + \frac{2}{R} \tau_w = 0 \quad (4.1)$$

where: p is pressure, v – mean velocity in pipe cross-section.

To derive the above equations, the following assumptions are made: flow in the pipe is assumed as one-dimensional and the velocity distribution uniform over the pipe cross-section; the pipe walls and the fluid are assumed as linearly elastic (stress proportional to strain). Equations (4.1) have been solved using the well-known method of characteristics.

In this paper, the results of comparisons for two significant simulated and experimentally obtained pressure runs are presented. The experimental data have been obtained in a copper pipeline at the IMP in Gdańsk by Adamkowski and Lewandowski (2006) and previously published. All the details of the experimental test rig and the numerical procedures input data are presented in Table 5.

Table 5. Test rig details and input data for simulations

$L = 98.11 \text{ m}$, $\rho = 997.65 \text{ kg/m}^3$, $D = 0.016 \text{ m}$, $\nu = 9.493 \cdot 10^{-7} \text{ m}^2/\text{s}$, $f = 32$, $e = 0.001 \text{ m}$, $c = 1300 \text{ m/s}$			
v_0 [m/s]	Re_0 [-]	p_r [Pa]	Type of flow
0.066	1112	$1.265 \cdot 10^6$	laminar
0.94	15843	$1.264 \cdot 10^6$	turbulent

In the numerical analyses being made, the dimensionless time step amounted to

$$\Delta \hat{t} = \Delta t \frac{\nu}{R^2} = 3.5 \cdot 10^{-5}$$

where: $\Delta t = \Delta x/c = 0.0024 \text{ s}$ and $\Delta x = L/f = 3.066 \text{ m}$.

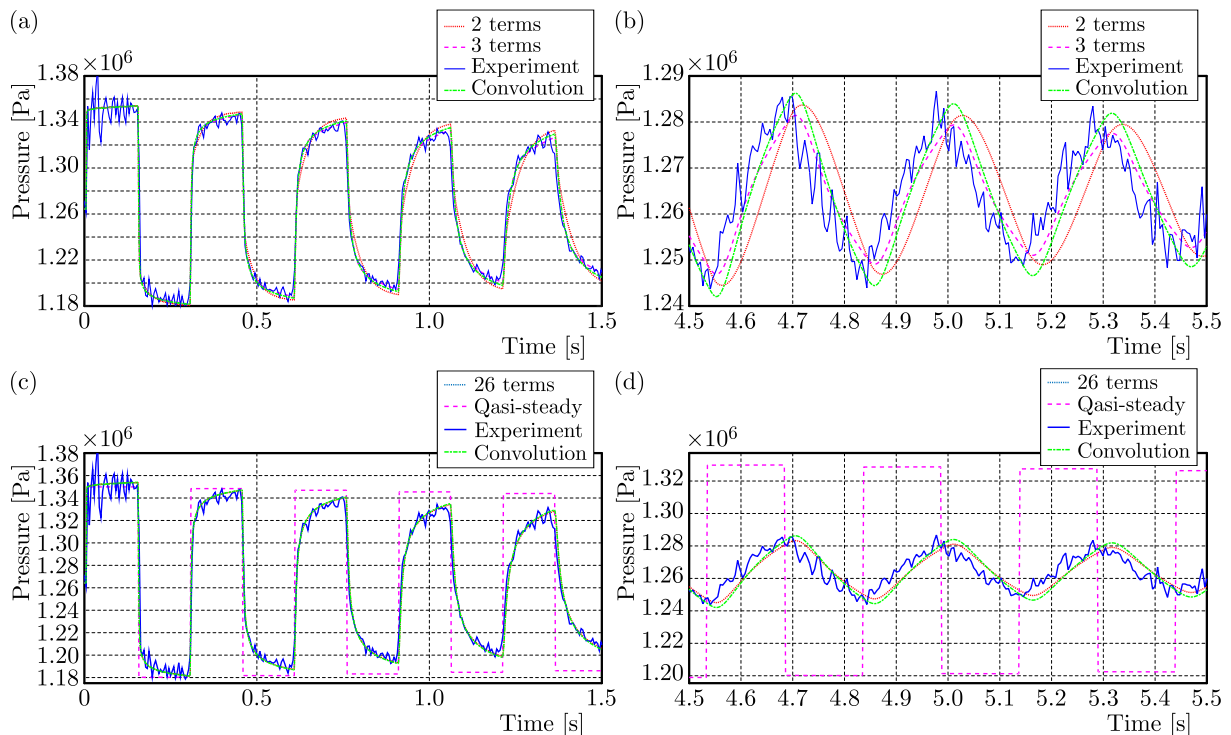
For the above dimensionless step, coefficients of optimum simplified effective weighting functions have been determined with the use of the procedure presented in this paper, see Table 6.

The coefficients for turbulent tests required the re-scaling. The details referring to the scaling procedure were discussed in the papers by Vítkovský *et al.* (2004) and Urbanowicz *et al.* (2012). Owing to the fact that the pipe walls are assumed to be rough ($k = 0.0000015 \text{ [m]}$), the coefficients

Table 6. Calculated weighting function coefficients

$L = 98.11 \text{ m}$, $\rho = 997.65 \text{ kg/m}^3$, $D = 0.016 \text{ m}$, $\nu = 9.493 \cdot 10^{-7} \text{ m}^2/\text{s}$, $f = 32$, $e = 0.001 \text{ m}$, $c = 1300 \text{ m/s}$						
m_1	m_2	m_3	n_1	n_2	n_3	type of flow – no terms
4.333	32.954	–	70.45	2636	–	laminar – 2 terms
2.864	10.816	39.43	52.92	666.9	8738	laminar – 3 terms
4.364	33.195	–	503.59	3069	–	turbulent – 2 terms
2.885	10.895	39.72	486.05	1100	9171	turbulent – 3 terms

m_i and n_i are scaled; the coefficients of exact weighting function according to Vardy and Brown (2007) are used for scaling. The coefficients of effective weighting function with extended range of applicability (26 terms), which with high accuracy corresponds to the classical weighting function according to Zielke (numerical calculations in this paper were also made using this function), were previously discussed in the paper by Urbanowicz and Zarzycki (2012). The results of numerical tests obtained are illustrated in Figs. 5 and 6.

Fig. 5. Results for laminar pipe flow ($Re = 1112$)

The main conclusions from the comparisons presented above are as follows:

- Simplified modelling with a new weighting function constructed with only two exponential terms is responsible for a gentle phase shift in the course being modelled. They are particularly visible in the final phase of flow deceleration (Figs. 5b and 6b). However, for the needs of engineering practice, the obtained results can be considered sufficient.
- Application of a new three term weighting function, the applicability range of which strictly depends on the hydraulic system analysed as well as on the numerical density of grid on the pipe length, allowed obtaining numerical results qualitatively compatible with the exact results of numerical tests (obtained using the exact extended 26 term weighting function and the full convolution based on the classical weighting function).

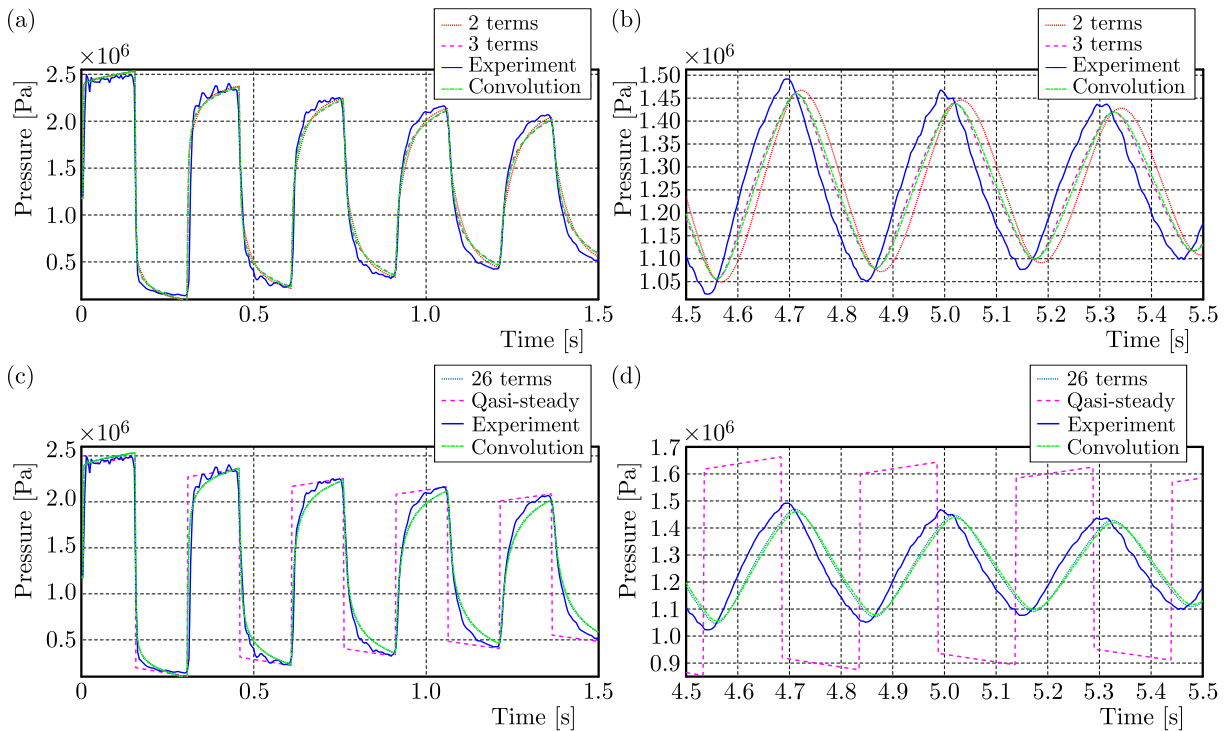


Fig. 6. Results for turbulent pipe flow ($Re = 15843$)

- c) Phase shifts between the experimental results and the numerical ones shown in Figs. 5b, 5d and 6b, 6d can be explained by a gentle variation in the speed of pressure wave propagation during recording of experimental courses. This variation of results may result from the impact of non-dissolved gases (air) found in the experimental system.

The simulation tests performed clearly show the impact of unsteady friction on the courses obtained as a result of examining the water hammer effect. The applied and very simplified weighting functions present themselves perfectly against the results obtained using only the quasi-steady model of friction. Thus, it is possible to safely recommend the presented procedure for engineers who are involved in protection of hydraulic systems against negative effects of the water hammer.

5. Summary

The analytical solutions presented in the paper allow one to quickly determine simplified forms of effective weighting functions composed of two or three exponential expressions. These correlations could be used in a simple manner by applying the instantaneous resistance coefficient (Eq. (2.3)) in commercial and custom computer programs used for the modelling of unsteady flows of liquids in conduits under pressure. The biggest problem associated with implementing the presented solution is the need to introduce into the program many constants estimated in this paper, which describe individual solutions. Another issue which the future user of the presented formulas should pay attention to, is the right choice of the method of the characteristics grid. With the range of application of effective weighting functions simplified in this manner, the number of computing sections should not be higher than $f=50$, because for this value, the instantaneous hydraulic resistance calculated is a function of velocity changes occurring in the last five periods of the water hammer.

References

1. ADAMKOWSKI A., LEWANDOWSKI M., 2006, Experimental examination of unsteady friction models for transient pipe flow simulation, *Journal of Fluids Engineering, ASME*, **128**, 6, 1351-1363
2. ADAMKOWSKI A., LEWANDOWSKI M., 2009, A new method for numerical prediction of liquid column separation accompanying hydraulic transients in pipelines, *Journal of Fluids Engineering, ASME*, **131**, 7, paper 071302
3. ADAMKOWSKI A., LEWANDOWSKI M., 2012, Investigation of hydraulic transients in a pipeline with column separation, *Journal of Hydraulic Engineering, ASCE*, **138**, 11, 935-944
4. BERGANT A., SIMPSON A.R., TIJSSELING A.S., 2006, Water hammer with column separation: A historical review, *Journal of Fluids and Structures*, **22**, 2006, 135-171
5. BRUNONE B., GOLIA U.M., GRECO M., 1991, Some remarks on the momentum equations for fast transients, *Proceedings of International Meeting on Hydraulic Transients with Column Separation, 9th Round Table, IAHR*, Valencia, Spain, 201-209
6. DAILEY J.W., HANKEY W.L., OLIVE R.W., JORDAAN J.M., 1956, Resistance coefficient for accelerated and decelerated flows through smooth tubes and orifices, *Journal of Basic Engineering, ASME*, **78**, 1071-1077
7. HENCLIK S., 2015, A numerical approach to the standard model of water hammer with fluid-structure interaction, *Journal of Theoretical and Applied Mechanics*, **53**, 3, 543-555
8. KAGAWA T., LEE I., KITAGAWA A., TAKENAKA T., 1983, High speed and accurate computing method of frequency-dependent friction in laminar pipe flow for characteristics method (in Japanese), *Transactions of the Japan Society of Mechanical Engineers, Part A*, **49**, 447, 2638-2644
9. KARADŽIĆ U., BULATOVIĆ V., BERGANT A., 2014, Valve-induced water hammer and column separation in a pipeline apparatus, *Strojniški vestnik – Journal of Mechanical Engineering*, **60**, 11, 742-754
10. KERAMAT A., TIJSSELING A.S., HOU Q., AHMADI A., 2012, Fluid-structure interaction with pipe-wall viscoelasticity during water hammer, *Journal of Fluids and Structures*, **28**, 1, 434-456
11. KERAMAT A., KOLAH A.G., AHMADI A., 2013, Waterhammer modelling of viscoelastic pipes with a time-dependent Poisson's ratio, *Journal of Fluids and Structures*, **43**, November, 164-178
12. KERAMAT A., TIJSSELING A.S., 2012, Waterhammer with column separation, fluid-structure interaction and unsteady friction in a viscoelastic pipe, *Proceedings of 11th International Conference on Pressure Surges*, BHR Group, Lisbon, Portugal, October 24-26, 443-460
13. LOUREIRO D., RAMOS H., 2003, A modified formulation for estimating the dissipative effect of 1-d transient pipe flow, [In:] *Pumps, Electromechanical Devices and Systems Applied to Urban Management*, Cabrera E. et al. (Edit.), A.A. Baklema Publishers, The Netherlands, 2, 755-763
14. PEZZINGA G., BRUNONE B., CANNIZZARO D., FERRANTE M., MENICONI S., BERNI A., 2014, Two-dimensional features of viscoelastic models of pipe transients, *Journal of Hydraulic Engineering*, **140**, 8, Art. No. 04014036
15. REDDY H.P., SILVA-ARAYA W.F., CHAUDHRY M.H., 2012, Estimation of decay coefficients for unsteady friction for instantaneous, acceleration-based models, *Journal of Hydraulic Engineering*, **138**, 260-271
16. SCHOHL G.A., 1993, Improved approximate method for simulating frequency – dependent friction in transient laminar flow, *Journal of Fluids Engineering, ASME*, **115**, September, 420-424
17. SOARES A.K., MARTINS N.M.C., COVAS D.I.C., 2012, Transient vaporous cavitation in viscoelastic pipes, *Journal of Hydraulic Research*, **50**, 2, 228-235
18. SOARES A.K., MARTINS N., COVAS D.I.C., 2015, Investigation of transient vaporous cavitation: experimental and numerical analyses, *Procedia Engineering*, **119**, 235-242
19. TRIKHA A.K., 1975, An efficient method for simulating frequency-dependent friction in transient liquid flow, *Journal of Fluids Engineering, ASME*, **97**, 1, 97-105
20. URBANOWICZ K., 2012, New approximation of unsteady friction weighting functions, *Proceedings of 11th International Conference on Pressure Surges*, Lisbon, Portugal, October 24-26, 477-492

21. URBANOWICZ K., 2015, Simple modelling of unsteady friction factor, *Proceedings of 12th International Conference on Pressure Surges*, Dublin, Ireland, 18-20 November, 113-130.
22. URBANOWICZ K., FIRKOWSKI M., ZARZYCKI Z., 2016, Modelling water hammer in viscoelastic pipelines: short brief, *Journal of Physics: Conference Series*, **760**, paper 012037
23. URBANOWICZ K., ZARZYCKI Z., 2012, New efficient approximation of weighting functions for simulations of unsteady friction losses in liquid pipe flow, *Journal of Theoretical and Applied Mechanics*, **50**, 2, 487-508
24. URBANOWICZ K., ZARZYCKI Z., 2015, Improved lumping friction model for liquid pipe flow, *Journal of Theoretical and Applied Mechanics*, **53**, 2, 295-305
25. URBANOWICZ K., ZARZYCKI Z., KUDŹMA S., 2012, Universal weighting function in modeling transient cavitating pipe flow, *Journal of Theoretical and Applied Mechanics*, **50**, 4, 889-902
26. VARDY A.E., BROWN J.M.B., 1996, On turbulent unsteady, smooth – pipe friction, *Proceedings of 7th International Conference on Pressure Surges*, BHR Group, Harrogate, United Kingdom, 289-311
27. VARDY A.E., BROWN J.M.B., 2003, Transient turbulent friction in smooth pipe flows, *Journal of Sound and Vibration*, **259**, 5, 1011-1036
28. VARDY A.E., BROWN J.M.B., 2004, Transient turbulent friction in fully rough pipe flows, *Journal of Sound and Vibration*, **270**, 233-257
29. VARDY A.E., BROWN J.M.B., 2007, Approximation of turbulent wall shear stresses in highly transient pipe flows, *Journal of Hydraulic Engineering*, **133**, 11, 1219-1228
30. VARDY A.E., BROWN J.M.B., 2010, Evaluation of unsteady wall shear stress by Zielke's method, *Journal of Hydraulic Engineering*, **136**, 453-456
31. VÍTKOVSKÝ J., LAMBERT M., SIMPSON A., BERGANT A., 2000, Advances in unsteady friction modeling in transient pipe flow, *Proceedings of 8th International Conference on Pressure Surges*, BHR Group, Hague, Holland, 471-482
32. VÍTKOVSKÝ J.P., STEPHENS M.L., BERGANT A., SIMPSON A.R., LAMBERT M.F., 2004, Efficient and accurate calculation of Zielke and Vardy–Brown unsteady friction in pipe transients, *Proceedings of 9th International Conference on Pressure Surges*, BHR Group, Chester, United Kingdom, 405-419
33. WEINEROWSKA-BORDS K., 2015, Alternative approach to convolution term of viscoelasticity in equations of unsteady pipe flow, *Journal of Fluids Engineering, ASME*, **137**, 5, paper 054501
34. ZANGANEH R., AHMADI A., KERAMAT A., 2015, Fluid-structure interaction with viscoelastic supports during waterhammer in a pipeline, *Journal of Fluids and Structures*, **54**, April, 215-234
35. ZARZYCKI Z., KUDŹMA S., URBANOWICZ K., 2011, Improved method for simulating transients of turbulent pipe flow, *Journal of Theoretical and Applied Mechanics*, **49**, 1, 135-158
36. ZARZYCKI Z., 1997, Hydraulic resistance of unsteady turbulent liquid flow in pipes, *Proceedings of 3rd International Conference on Water Pipeline Systems*, BHR Group, Hague, Holland, 163-178
37. ZARZYCKI Z., 2000, On weighting function for wall shear stress during unsteady turbulent flow, *Proceedings of 8th International Conference on Pressure Surges*, BHR Group, Hague, Holland, 39, 529-534
38. ZARZYCKI Z., URBANOWICZ K., 2006, Modelling of transient flow during water hammer considering cavitation in pressure pipes (in Polish), *Chemical and Process Engineering*, **27**, 3, 915-933
39. ZIELKE W., 1968, Frequency-dependent friction in transient pipe flow, *Journal of Basic Engineering, ASME*, **90**, 1, 109-115

FREE VIBRATION ANALYSIS OF POINT SUPPORTED RECTANGULAR PLATES USING QUADRATURE ELEMENT METHOD

AHMET ÇETKİN

Afyon Kocatepe University, Technical Education Faculty, Afyon, Turkey
e-mail: acetkin@aku.edu.tr

S. ORAK

Osmangazi University, Department of Mechanical Engineering, Eskisehir, Turkey
e-mail: sorak@ogu.edu.tr

In this study, the hybrid approach of the Quadrature Element Method (QEM) has been employed to generate solutions for point supported isotropic plates. The Hybrid QEM technique consists of a collocation method with the Galerkin finite element technique to combine the high accurate and rapid converging of Differential Quadrature Method (DQM) for efficient solution of differential equations. To present the validity of the solutions, the results have been compared with other known solutions for point supported rectangular plates. In addition, different solutions are carried out for different type boundary conditions, different locations and number of point supports. Results for the first vibration modes of plates are also tested using a commercial finite element code, and it is shown that they are in good agreement with literature.

Keywords: Quadrature Element Method, point support, plates, free vibration

1. Introduction

In the applications of modern structures, i.e. carousers, building floors, bridge decks, solar panels, aircraft and ship industries, bolted, riveted or spot-welded plate bodies are used. Designers have to know how these components change the dynamic characteristic of the structures. These types of engineering problems are known as point supported plate problems and they are frequently encountered in practice. Both analytical and numerical methods have been developed for the analysis of these problems. Although there are no exact solutions for these problems, various numerical approaches have been utilized. For example, Cox and Boxer (1960) used a finite difference method, Damle and Feeser (1972) used the finite element method, Fan and Cheung (1984) used the spline finite strip method, Huang and Thambiratnam (2001a) used the finite strip method, Guitierrez and Laura (1995) used the differential quadrature method, Zhao *et al.* (2002) used the discrete singular convolution method to solve the mentioned plate vibration problems. Because of its high accuracy, the Rayleigh-Ritz method has been the most frequently used analytical method to appeal for vibration analysis of plates, as Narita and Hodgkinson (2005) did. Also Gorman (1991) and Bapat and Suryanarayan (1989) utilized the superposition method and the flexibility function approach as analytical techniques, respectively.

Several functions are used for the analysis of free vibration of point supported rectangular plates. These include vibrating beam functions (Kerstens, 1979), B-spline functions (Mizusawa and Kajita, 1987)] and orthogonal polynomial functions (Kim and Dickinson, 1987). On the other hand, Liew and Lam (1994) applied a set of orthogonal plate functions generated by using the Gram-Schmidt orthogonality relationship to elastic point supported rectangular plates. Lee and Lee (1997) used a new type of the admissible function. Kitipornchai *et al.* (1994) and Liew *et al.* (1994) applied the Lagrange multiplier method and the constrain function method to

point supported Mindlin plates. Cheung and Zhou (1999, 2000) used the static beam function to composite plates and used the finite layer method to layered rectangular plates with point supports. Saadatpoure *et al.* (2000) studied vibration of plates having a general shape with internal point and line supports using the Galerkin method. Huang and Thambiratnam (2001b) applied a procedure incorporating the finite strip method together with spring systems for treating plates on elastic intermediate supports. Zhou (2002) used a set of static tapered beam functions which were the solutions of a tapered beam under a Taylor series of static loads developed as admissible functions for vibration analysis of point-supported rectangular plates with variable thickness in one or two directions. Again, Zhao *et al.* (2002) studied the problem of plate vibration under complex and irregular internal support conditions using the discrete singular convolution method. Kocatürk *et al.* (2004) used Lagrange equations to examine the steady state response to a sinusoidally varying force applied at the centre of a viscoelastically point-supported orthotropic elastic plate of rectangular shape with considered locations of added masses.

The Differential Quadrature Method (DQM) was proposed by Bellman and Casti (1971) in the early 1970's as an efficient numerical method to solve non-linear partial differential equations and applied to many areas of engineering problems. Especially, the Generalized Differential Quadrature Method (GDQM) has been used by various researches for efficient treatment of structural analysis problems. Analyses yielded good to excellent results for only a few discrete points due to the use of high order global basis functions in the computational domain. However, especially for real-world problems, DQM still lacks flexibility. Recently, Chen *et al.* (2000) extended the DQM to analysis of various structures and then it called the Quadrature Element Method (QEM). 49 degree of freedom (DOF) quadrature plate element was developed by Striz *et al.* (1994) to alleviate the lack of versatility and limitations of the existing high order series type approximation method. Different versions of the Differential Quadrature Method have been used for various applications. Hybrid approach was further developed by Han and Liew (1996) to solve the one-dimensional bending problem of the axisymmetric shear deformable circular plate, and by Liu and Liew (1998, 1999a,b) and Liu (2000) to solve two-dimensional bending and vibration problems of thick rectangular plates and polar plates having discontinuities. Wang and Gu (1997a,b) made an attempt to solve static problems of truss and beams and static and free vibration problems of thin plates. DQM was used by Liu and Liew (1999b) for the study of a two dimensional polar Reissner-Mindlin plate in the polar coordinate system by integrating the domain decomposition method (DDM). The Differential Quadrature Finite Difference Method (DQFDM) was proposed and applied by Chen (2004) for analysis of 2-D heat conduction in orthotropic media. Franciosi and Tomasiello (2004) applied a modified quadrature element method to perform static analysis of structures.

In this paper, the Quadrature Element Method is proposed and applied to analyze free vibration of point supported rectangular plates. Plates having different boundary conditions and various point topologies are studied. The results are compared with the studies using other approximating methods known in literature. First, interior and/or exterior point supported free plates and then, interior point supported plates having various boundary conditions are presented. Solutions are tested with the results of ABAQUS, a finite element program which has a wide spread use in the analysis of engineering problems.

2. Formulation of the quadrature plate element

The Hybrid Quadrature Element technique consists of a collocation method in conjunction with the Galerkin finite element technique to combines the high accuracy and rapid converging of DQM for efficient solution of differential equations with the generality of the finite element formulation (Chen *et al.*, 2000).

The quadrature plate element is closely related to the serendipity Lagrangian element, but it has internal points and basis functions of high order (Chen *et al.*, 2000). Numerical procedures are extensively used in the element formulation to circumvent the problems caused by the use of high order basis functions. C_0 and C_1 inter-element compatibilities are met exactly for the mid-surface, while the other C_2 or even C_3 compatibilities are closely approximated at each boundary by the use of moderately high order basis functions. The 25 node rectangular element is given in Fig. 1. This plate element has also 49 degrees of freedom. These degrees of freedom, which belong to the plate element, are given in Table 1 (Chen *et al.*, 2000; Quan and Chang, 1989).

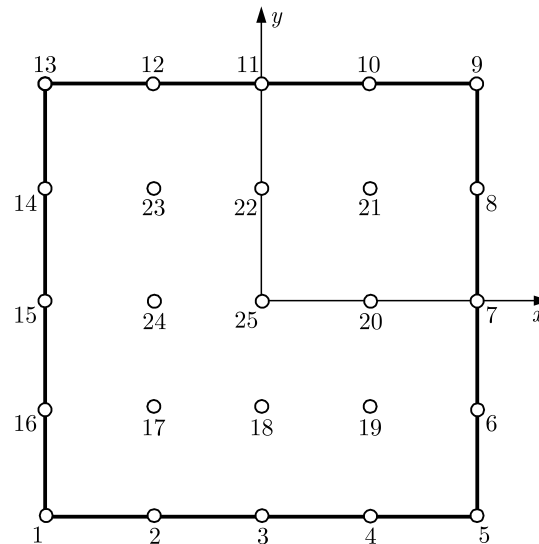


Fig. 1. Nodes of the Quadrature plate element

Table 1. Degrees of freedom for 25 node quadrature plate elements

Nodal number	DOF
1-5 9-13	$w, \frac{\partial w}{\partial x}, \frac{\partial w}{\partial y}, \frac{\partial^2 w}{\partial x \partial y}$
2-3-4 10-11-12	$w, \frac{\partial w}{\partial y}$
6-7-8 14-15-16	$w, \frac{\partial w}{\partial x}$
17-18-19 20-21-22 23-24-25	w

The displacements of 25 nodes and 49 degrees of the freedom quadrature plate element are expressed in terms of polynomial type basis functions, i.e.

$$\begin{aligned}
 w(x, y) = & \sum_{i=1,5,9,13} \left[N_{i1} w_i + N_{i2} \left(\frac{\partial w}{\partial x} \right)_i + N_{i3} \left(\frac{\partial w}{\partial y} \right)_i + N_{i4} \left(\frac{\partial^2 w}{\partial x \partial y} \right)_i \right] \\
 & + \sum_{i=2,3,4,10,11,12} \left[N_{i1} w_i + N_{i2} \left(\frac{\partial w}{\partial y} \right)_i \right] + \sum_{i=6,7,8,14,15,16} \left[N_{i1} w_i + N_{i2} \left(\frac{\partial w}{\partial x} \right)_i \right] \\
 & + \sum_{i=17,18,19,20,21,22,23,24,25} \left[N_{i1} w_i \right] = \mathbf{N} \mathbf{w}
 \end{aligned} \tag{2.1}$$

where N_{ij} is the shape function which can be determined from the specified collocation points, and $w_i, (\partial w/\partial x)_i, (\partial w/\partial y)_i, (\partial^2 w/\partial x\partial y)_i$ are local DOFs associated with the node i .

The governing equation of the isotropic thin plate in small deflection free vibration is given by

$$\frac{\partial^4 w}{\partial x^4} + 2\frac{\partial^4 w}{\partial x^2\partial y^2} + \frac{\partial^4 w}{\partial y^4} = \frac{\rho h\omega^2}{D}w \quad (2.2)$$

and Kirchhoff's plate theory, in which the bending strain of the element is given for an isotropic and homogeneous plate as

$$\boldsymbol{\varepsilon} = \begin{Bmatrix} \varepsilon_x \\ \varepsilon_y \\ \gamma_{xy} \end{Bmatrix} = -z \begin{Bmatrix} \frac{\partial^2 w}{\partial x^2} \\ \frac{\partial^2 w}{\partial y^2} \\ 2\frac{\partial^2 w}{\partial x\partial y} \end{Bmatrix} \quad (2.3)$$

If Eq. (2.1) and Eq. (2.3) are combined, the strain-displacement relationship is stated by

$$\boldsymbol{\varepsilon} = -z \begin{Bmatrix} \frac{\partial^2 w}{\partial x^2} \\ \frac{\partial^2 w}{\partial y^2} \\ 2\frac{\partial^2 w}{\partial x\partial y} \end{Bmatrix} \mathbf{N}\mathbf{w} = -z\mathbf{Q}\mathbf{w} \quad \text{for} \quad \mathbf{Q} = \begin{Bmatrix} \frac{\partial^2 w}{\partial x^2} \\ \frac{\partial^2 w}{\partial y^2} \\ 2\frac{\partial^2 w}{\partial x\partial y} \end{Bmatrix} \mathbf{N} \quad (2.4)$$

The stiffness matrix can be calculated for the area A

$$\mathbf{K} = \int_A \mathbf{Q}^T \mathbf{D} \mathbf{Q} dA \quad (2.5)$$

where \mathbf{D} is the rigidity matrix which can be calculated using constant thickness h , Poisson's ratio ν and the modulus of elasticity E

$$\mathbf{D} = \frac{Eh^2}{12(1-\nu^2)} \begin{bmatrix} 1 & \nu & 0 \\ \nu & 1 & 0 \\ 0 & 0 & (1-\nu)/2 \end{bmatrix} \quad (2.6)$$

The consistent mass matrix can be calculated as

$$\mathbf{M} = \int_A \mathbf{N}^T (\rho \mathbf{h}) \mathbf{N} dA \quad (2.7)$$

and the governing equation for plate free vibration can be written in the matrix form

$$(\mathbf{K}_s - \lambda^2 \mathbf{M}_s) \mathbf{w} = \mathbf{0} \quad (2.8)$$

where λ is the frequency parameter, and the subscribed s represents the whole discretized system.

3. Numerical application and discussions

Frequency parameters of free vibrations are described as $\lambda = \omega L^2 \sqrt{\rho h / D}$, where ω , L , ρ , h , D represent circular frequency, length of the plate, density, thickness and rigidity, respectively. In order to obtain more accurate results, QEM solutions have been carried out by using 2×2 and 4×4 differential quadrature plate elements joined side by side along the x and y directions. When a larger number of plate elements are used more accurate results can be obtained, but the solution can be obtained with a larger linear system of equations. If there are simply supported boundary conditions on all edges of the plate considered then the quadrature plate element has only 25 DOFs. In other words, a set of 25×25 linear equations system has to be solved for one plate element. The size of the linear equations system is set to 400×400 for the same procedure needed to solve with the same boundary conditions and the 4×4 plate element.

First, the number of plate elements that can be used for results having acceptable accuracy must be decided. Therefore, frequency parameters for three boundary conditions and four plate elements are obtained with QEM. Table 2 presents the frequency parameters λ of isotropic rectangular plates. It is interesting that acceptable accuracy results are obtained by QEM for all boundary conditions in the case of only one plate element.

Table 2. The first frequency parameters λ of isotropic square plates for some boundary conditions ($\lambda = \omega L^2 \sqrt{\rho h / D}$)

	Exact (Leissa, 1973)	Number of use DQ plate elements			
		1×1	2×2	3×3	4×4
S-S-S-S	19.73921	19.73921 ($7.0 \cdot 10^{-4}$)*	19.73921 ($2.2 \cdot 10^{-5}$)*	19.73921 ($4.3 \cdot 10^{-7}$)*	19.73921 ($1.6 \cdot 10^{-8}$)*
S-F-S-F	9.63138	9.63139	9.63138	9.63138	9.63138
S-C-S-S	23.64632	23.64700	23.64632	23.64632	23.64632

* Relative error in parenthesis has been evaluated using the analytical Leissa value ($2\pi^2$) [%]

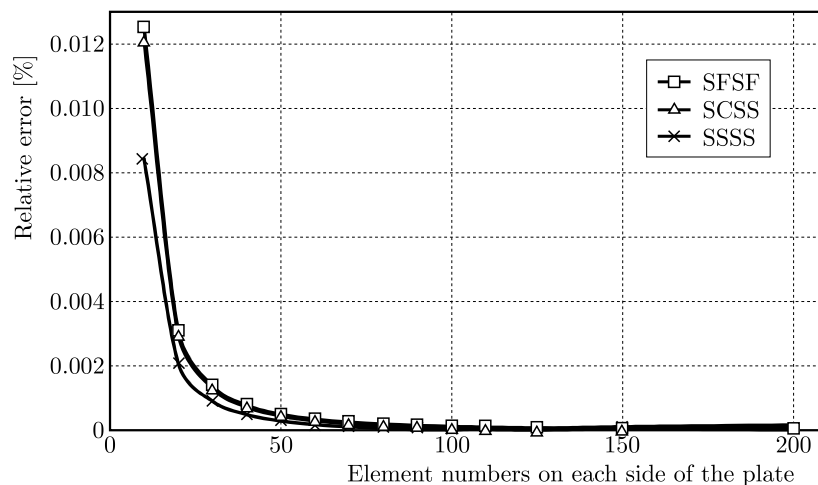


Fig. 2. Relative error determined by ABAQUS for different boundary conditions

Besides, the same boundary conditions given in Table 2 are solved using ABAQUS commercial finite codes. It is obvious that if more elements are used in computation, the error will be reduced. However, the required number of elements must be determined for acceptable accuracy. The variation of the relative error with selected degrees of freedom is given in Fig. 2 for different boundary conditions. Relative errors have been evaluated using the analytical results

of Leissa (1973). This % error value of the relative difference is defined as $(\text{Analytical Leissa value} - \text{ABAQUS result}) \times 100 / (\text{Analytical Leissa value})$. Naturally, the result changes when different boundary conditions are used. As in many literature sources the 4 node thin shell elements (S4R) are employed, the uniform mesh size and different element numbers on each side of the plate such as 10, 20, 50, 100, 200 and 400 scales are used to achieve convergent FEM solutions (Rui *et al.*, 2015, 2016). In this study, the results have been given for all values from 100 SR4 shell elements on each side of the plate. For these elements, there are approximately 49,800 DOFs. As shown in Fig. 2, the biggest % relative error for SFSF boundary conditions to the selected number of elements is 0.01%.

In order to simplify the visualisation of types of supports which are used in tables and figures, symbols in Table 3 are to be used. The number of elements used in ABAQUS should be determined to obtain an acceptable solution for simply supported rectangular plates with point supports at the centre, as this type of problems is found in numerous literature items. Simply supported rectangular plates with a point support at centre are shown in Fig. 3. The results of QEM (2×2 and 4×4) are presented in Table 4 with other solutions for which different methods are applied. For the first five frequency parameters λ , all results are also in good agreement. Especially, the results of the finite strip element method used by Huang and Thambiratnam (2001) are strongly in agreement with QEM. If it is assumed that the first mode is 49.483 as it was taken from results of Huang's solution (Huang and Thambiratnam, 2001), Fig. 4 shows the change in the results from ABAQUS solution as a function of the number of elements on each side of the plate. It can be seen that the relative error according to Huang's results is approximately 0.03% for 100 elements on each side of the plate.

Table 3. Simplified support type symbols

Symbol	Support types
Null	Free
//////	Fixed
- - - - -	Simply
o	Point

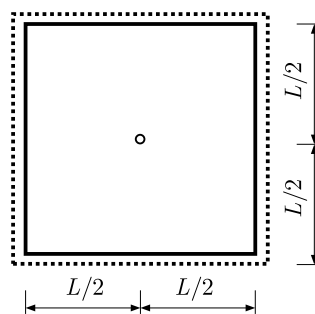


Fig. 3. Simply supported square plates with a point-support at center

As shown in Fig. 5, five boundary conditions and point support at the corner of the plate are considered. In Table 5, the results of Kim and Dickinson (1987) – orthogonal polynomial, Cheung and Zhou (2000) – static beam function, and Mizusawa and Kajita (1987) – finite spline, are presented. CFCE, CFSE, SFSF, CFFF, SFFF boundary conditions are considered and first five frequency parameters are presented. The natural frequencies are determined using both QEM and ABAQUS, and the obtained results are in good agreement with the analytical results reported in the literature.

Table 4. Frequency parameters λ of simply supported square plates with a point support at the center ($\lambda = \omega L^2 \sqrt{\rho h/D}$)

Method	λ_1	λ_2	λ_3	λ_4	λ_5
Venkateswara <i>et al.</i> (1973)	–	–	52.62	–	–
Lee and Lee (1977)	–	–	53.088	–	–
Leissa (1969)	49.3	–	–	–	–
Saadatpour <i>et al.</i> (2000)]	49.348	–	–	–	–
Fan and Cheung (1984)	49.35	49.35	52.78	78.96	98.71
Kim and Dickinson (1987)]	49.348	49.348	53.170	78.959	98.696
Huang and Thambiratnam (2001b)	49.348	49.351	52.667	78.959	98.711
Present (ABAQUS)	49.362	49.362	52.643	78.975	98.784
Present (QEM, 2×2)	49.348	49.348	52.851	78.957	98.711
Present (QEM, 4×4)	49.348	49.348	52.677	78.957	98.696

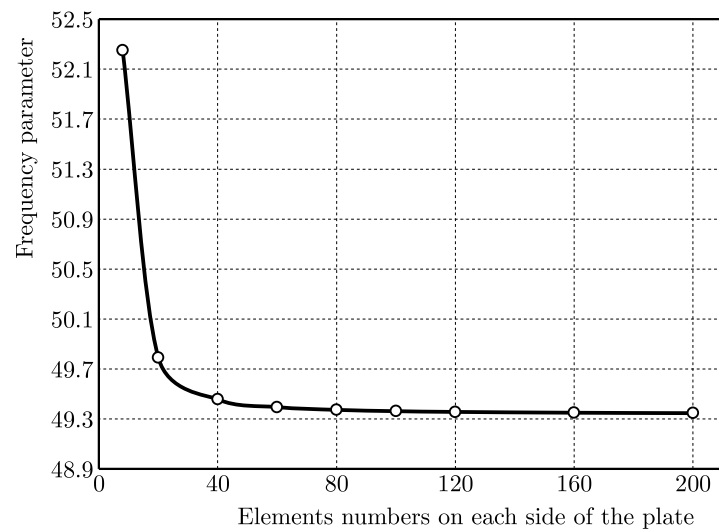


Fig. 4. First frequency parameters for simply supported square plate with a point support at center (ABAQUS solutions)

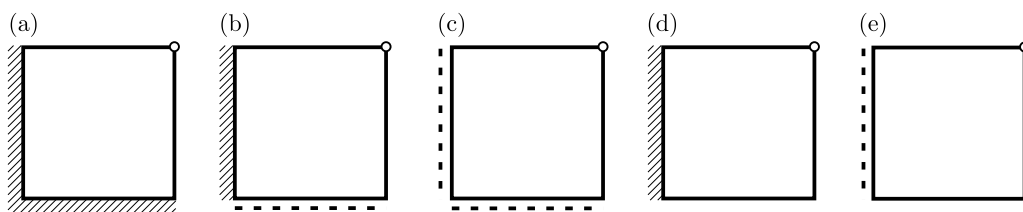


Fig. 5. Square plates with point supports at one corner for various boundary conditions

For several cases, the results for plates with point supports are compared with other values given in the literature. As shown in Fig. 6, plates with different numbers of point supports at the interior and/or boundary are considered. All results obtained from ABAQUS and QEM solutions are presented in Table 6. Kato and Honma (1998), Kim and Dickinson (1987) used Rayleigh-Ritz Method, Fan and Cheung (1984), Mizusawa and Kajita (1987) used Spline Finite Strip Element Method, Narita and Hodgkinson (2005) used Layerwise optimization method, Venkateswara *et al.* (1973) used Finite Element Method. Kocatürk *et al.* (2004) used the Lagrange Equation Method. The first five frequency parameters for eight different point supports situation are given in Table 6. It can be seen from Table 6, a very good agreement between QEM and those of

Table 5. Frequency parameters λ of square plates with point supports at one corner for various boundary conditions ($\lambda = \omega L^2 \sqrt{\rho h/D}$)

Fig.	Method	λ_1	λ_2	λ_3	λ_4	λ_5
5a	Cheung and Zhou (1999)	15.272	24.100	39.495	54.703	63.511
	Mizusawa and Kajita (1987)	15.12	23.70	39.37	53.53	62.54
	Kim and Dickinson (1987)	15.172	23.923	39.392	54.157	62.850
	Present (ABAQUS)	15.166	23.905	39.394	54.105	62.742
	Present (QEM, 2×2)	15.169	23.915	39.389	54.112	62.718
	Present (QEM, 4×4)	15.166	23.906	39.388	54.094	62.708
5b	Cheung and Zhou (1999)	12.021	21.348	35.140	47.916	58.903
	Mizusawa and Kajita (1987)	11.94	21.06	35.01	47.24	57.92
	Kim and Dickinson (1987)	11.940	21.175	35.015	47.398	58.144
	Present (ABAQUS)	11.939	21.167	35.018	47.399	58.096
	Present (QEM, 2×2)	11.939	21.172	35.014	47.393	58.076
	Present (QEM, 4×4)	11.939	21.167	35.014	47.388	58.069
5c	Cheung and Zhou (1999)	9.6801	17.496	30.713	44.178	51.873
	Mizusawa and Kajita (1987)	9.608	17.32	30.60	43.65	51.04
	Kim and Dickinson (1987)	9.6079	17.316	30.596	43.652	51.041
	Present (ABAQUS)	9.6079	17.317	30.598	43.663	51.058
	Present (QEM, 2×2)	9.6079	17.316	30.596	43.652	51.036
	Present (QEM, 4×4)	9.6079	17.316	30.596	43.652	51.035
5d	Cheung and Zhou (1999)	5.3351	16.054	22.000	29.536	43.894
	Mizusawa and Kajita (1987)	5.312	15.86	21.71	29.29	43.39
	Present (ABAQUS)	5.3261	15.912	21.813	29.403	43.499
	Present (QEM, 2×2)	5.3277	15.915	21.817	29.407	43.497
	Present (QEM, 4×4)	5.3268	15.912	21.812	29.403	43.494
5e	Cheung and Zhou (1999)	3.3395	12.033	17.419	25.886	38.982
	Mizusawa and Kajita (1987)	3.336	11.93	17.29	25.68	38.56
	Present (ABAQUS)	3.3357	11.927	17.293	25.681	38.561
	Present (QEM, 2×2)	3.3361	11.927	17.293	25.680	38.555
	Present (QEM, 4×4)	3.3361	11.927	17.293	25.679	38.555

Kato and Honma (1998), Kim and Dickinson (1987), Mizusawa and Kajita (1987), Narita and Hodgkinson (2005), Venkateswara *et al.* (1973), Kocatürk *et al.* (2004) are encountered.

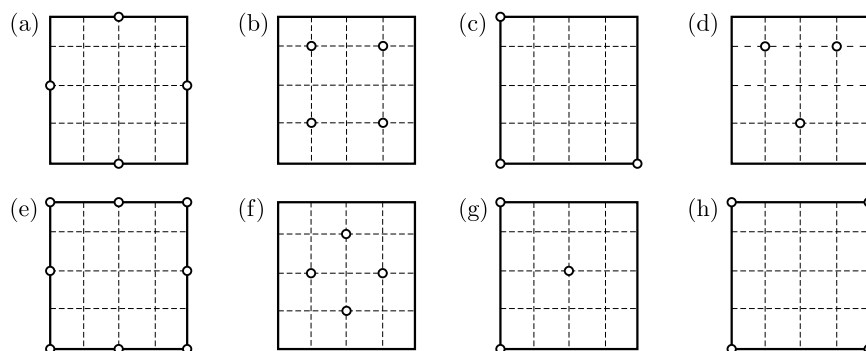


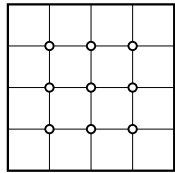
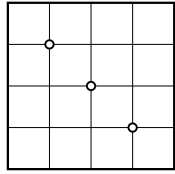
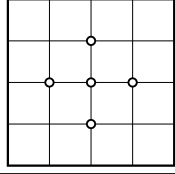
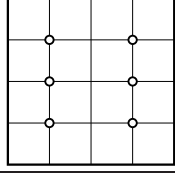
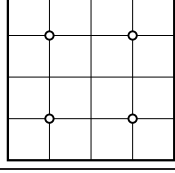
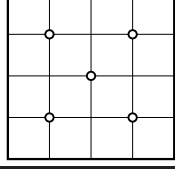
Fig. 6. Square plates with point supports

Table 6. Comparison of frequency parameters λ of square plates with point supports ($\lambda = \omega L^2 \sqrt{\rho h/D}$)

Fig.	Method	λ_1	λ_2	λ_3	λ_4	λ_5
6a	Kato and Honma (1998)	13.51	18.03	19.05	19.05	27.26
	Kim and Dickinson (1987)	13.47	18.03	18.93	18.93	27.05
	Fan and Cheung (1984)	13.47	17.85	18.79	18.79	26.92
	Narita and Hodgkinson (2005)	13.47	18.14	19.02	19.02	–
	Present (ABAQUS)	13.468	17.835	18.780	18.780	26.910
	Present (QEM)	13.468	17.841	18.786	18.786	26.913
6b	Narita and Hodgkinson (2005)	19.60	23.40	33.17	33.17	–
	Present (ABAQUS)	19.598	23.380	32.580	32.580	34.985
	Present (QEM)	19.596	23.378	32.597	32.597	35.013
6c	Narita and Hodgkinson (2005)	3.299	9.894	15.77	19.60	–
	Present (ABAQUS)	3.298	9.893	15.769	19.598	26.618
	Present (QEM)	3.298	9.893	15.770	19.596	26.616
6d	Narita and Hodgkinson (2005)	9.512	14.78	21.34	29.09	–
	Present (ABAQUS)	9.486	14.659	21.309	28.841	33.586
	Present (QEM)	9.487	14.662	21.307	28.847	33.604
6e	Kato and Honma (1998)	18.03	35.62	35.62	38.68	61.06
	Kim and Dickinson (1987)	18.03	35.17	35.17	38.43	60.58
	Fan and Cheung (1984)	17.85	34.89	34.89	38.43	60.12
	Present (ABAQUS)	17.837	34.884	34.884	38.440	60.101
	Present (QEM)	17.843	34.882	34.882	38.432	60.086
6f	Narita and Hodgkinson (2005)	13.47	17.09	18.65	18.65	–
	Present (ABAQUS)	13.468	17.029	18.275	18.275	39.185
	Present (QEM)	13.468	17.030	18.284	18.284	39.215
6g	Narita and Hodgkinson (2005)	6.641	6.736	19.60	19.75	–
	Present (ABAQUS)	6.638	6.700	19.489	19.598	24.639
	Present (QEM)	6.639	6.701	19.495	19.596	24.639
6h	Narita and Hodgkinson (2005)	7.112	15.77	15.77	16.90	–
	Cheung and Zhou (1999)	7.136	15.800	15.805	19.710	38.710
	Mizusawa and Kajita (1987)	7.111	15.77	15.77	19.60	38.43
	Kocatürk <i>et al.</i> (2004)	7.1109	–	–	19.596	–
	Venkateswara <i>et al.</i> (1973)	7.1109	–	–	19.596	–
	Present (ABAQUS)	7.1112	15.769	15.769	19.598	38.440
	Present (QEM)	7.1109	15.770	15.770	19.596	38.432

Various point support topologies and four different types of boundary conditions are considered as shown in Table 7. The minimum distances are $L/4$ since four quadrature plate elements are used for solutions. Seven different situations are considered and the first five frequency parameters are calculated. SSSS, CCCC, SCSC and FCFS type of boundary conditions are selected. Besides, the results of point supported free plates are given in Table 8. The first five frequency parameters are presented for point supports on the interior and/or boundary of plates. The differences between the results of QEM and ABAQUS solutions are approximately 0.1%

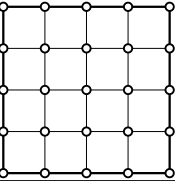
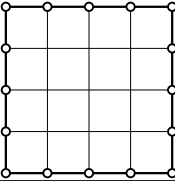
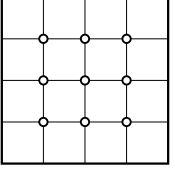
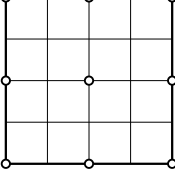
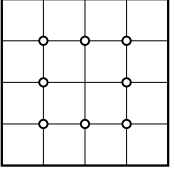
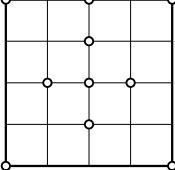
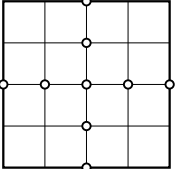
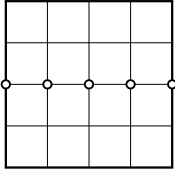
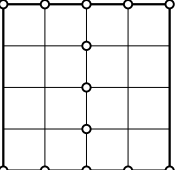
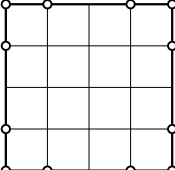
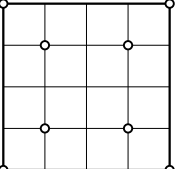
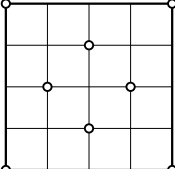
Table 7. Frequency parameters λ of square plates with point supports for four boundary conditions ($\lambda = \omega L^2 \sqrt{\rho h/D}$)

Support Position	Mod	S-S-S-S		C-C-C-C		C-S-C-S		F-C-F-S	
		QEM	ABAQUS	QEM	ABAQUS	QEM	ABAQUS	QEM	ABAQUS
	λ_1	167.78	168.08	187.97	188.10	170.35	170.64	48.538	48.515
	λ_2	167.78	168.08	187.97	188.10	184.95	184.97	50.128	50.086
	λ_3	182.71	182.74	207.96	207.92	185.99	186.13	82.215	82.172
	λ_4	182.71	182.74	215.98	215.71	205.14	205.04	82.772	82.712
	λ_5	197.39	197.65	242.16	242.60	206.70	206.96	133.17	133.19
	λ_1	49.348	49.362	73.394	73.437	60.807	60.829	26.227	26.222
	λ_2	62.106	62.071	86.985	86.931	73.233	73.194	33.799	33.787
	λ_3	91.269	91.232	105.57	105.55	100.02	99.999	61.801	61.796
	λ_4	98.696	98.784	131.58	131.76	115.97	116.083	66.573	66.574
	λ_5	128.30	128.38	151.28	151.16	141.12	140.983	77.381	77.385
	λ_1	78.957	78.975	108.22	108.27	94.586	94.625	42.012	41.987
	λ_2	91.269	91.228	121.28	121.25	104.68	104.66	42.899	42.859
	λ_3	91.269	91.228	121.28	121.24	110.16	110.10	58.187	58.196
	λ_4	101.69	101.61	139.20	139.12	120.37	120.30	61.114	61.109
	λ_5	167.78	168.08	204.49	204.88	170.35	170.64	99.245	99.301
	λ_1	67.760	67.759	74.089	74.075	71.703	71.701	38.804	38.798
	λ_2	91.269	91.232	105.57	105.55	104.68	104.66	48.538	48.515
	λ_3	131.52	131.51	162.74	162.81	162.17	162.25	77.124	77.123
	λ_4	167.78	168.08	187.97	188.10	170.33	170.64	80.303	80.260
	λ_5	167.78	168.08	207.05	207.49	193.81	193.78	82.215	82.172
	λ_1	52.677	52.644	55.185	55.150	53.966	53.931	38.203	38.193
	λ_2	91.269	91.232	105.57	105.55	92.350	92.298	41.679	41.647
	λ_3	91.269	91.232	105.57	105.55	104.68	104.66	52.440	52.410
	λ_4	98.696	98.784	131.58	131.76	110.61	110.70	77.139	77.137
	λ_5	146.83	146.80	180.45	180.55	168.11	168.16	79.983	79.957
	λ_1	91.269	91.232	105.57	105.55	92.350	92.298	39.993	39.972
	λ_2	91.269	91.232	105.57	105.55	103.43	103.33	41.679	41.647
	λ_3	98.696	98.784	116.08	115.81	104.68	104.66	75.963	75.960
	λ_4	104.81	104.58	131.58	131.76	120.48	120.44	79.983	79.957
	λ_5	167.78	168.07	207.05	207.49	170.35	170.64	96.537	96.564

4. Conclusions

The Quadrature Element Method is applied to analyze free vibration of point supported rectangular plates having different boundary conditions and various point topologies. The results are compared to other approximation methods. A very good agreement is observed with the data published in literature. A 25-node plate element is easier to process with commercial software. It is possible to apply the Quadrature Element Method to plates having more complex shapes and to obtain a better accuracy by means of joining plate elements side by side along the x and y directions.

Table 8. Frequency parameters of free square plates with point supports ($\lambda = \omega L^2 \sqrt{\rho h/D}$)

Support position	Mod	QEM	ABAQUS	Support position	Mod	QEM	ABAQUS
	λ_1	145.65	145.75		λ_1	19.543	19.588
	λ_2	145.65	145.75		λ_2	48.235	48.233
	λ_3	146.74	146.84		λ_3	48.235	48.233
	λ_4	149.25	149.21		λ_4	74.958	74.921
	λ_5	158.85	158.81		λ_5	94.207	94.234
	λ_1	32.646	32.627		λ_1	34.882	34.884
	λ_2	32.646	32.627		λ_2	34.882	34.884
	λ_3	33.114	33.083		λ_3	38.432	38.440
	λ_4	35.013	34.985		λ_4	41.089	41.066
	λ_5	39.215	39.185		λ_5	68.499	68.484
	λ_1	31.518	31.476		λ_1	38.432	38.412
	λ_2	32.646	32.627		λ_2	39.215	39.185
	λ_3	32.646	32.627		λ_3	39.870	39.839
	λ_4	35.013	34.985		λ_4	39.870	39.839
	λ_5	39.215	39.185		λ_5	41.093	41.042
	λ_1	13.468	13.412		λ_1	13.468	13.468
	λ_2	20.987	20.982		λ_2	13.856	13.855
	λ_3	20.987	20.982		λ_3	20.987	20.984
	λ_4	26.646	26.636		λ_4	34.801	34.804
	λ_5	69.265	69.286		λ_5	39.941	39.936
	λ_1	16.111	16.110		λ_1	17.929	17.926
	λ_2	22.635	22.631		λ_2	41.882	41.867
	λ_3	46.224	46.238		λ_3	41.882	41.867
	λ_4	49.757	49.762		λ_4	60.130	60.127
	λ_5	74.639	74.661		λ_5	74.958	74.921
	λ_1	19.596	19.598		λ_1	36.964	36.952
	λ_2	34.907	34.901		λ_2	38.432	38.440
	λ_3	34.907	34.901		λ_3	39.215	39.185
	λ_4	44.148	44.152		λ_4	39.870	39.839
	λ_5	55.391	55.340		λ_5	39.870	39.839

References

1. BAPAT A.V., SURYANARAYAN S., 1989, Flexibility function approach to vibration analysis of rectangular plates with arbitrary multiple point supports on the edges, *Journal of Sound and Vibration*, **128**, 209-233
2. BELLMAN R., CASTI J., 1971, Differential quadrature and long-term integration, *Journal of Mathematical Analysis and Applications*, **34**, 235-238
3. CHEN C.-N., 2004, DQEM and DQFDM irregular elements for analyses of 2-D heat conduction in orthotropic media, *Applied Mathematical Modeling*, **28**, 7, 617-638
4. CHEN W.L., STRIZ A.G., BERT C.W., 2000, High-accuracy plane stress and plate elements in the quadrature element method, *International Journal of Solids and Structures*, **37**, 627-647
5. CHEUNG Y.K., ZHOU D., 1999, Free vibration of rectangular composite plates with point-supports using static beam functions, *Composite Structures*, **44**, 2, 145-154
6. CHEUNG Y.K., ZHOU D., 2000, Free vibration of thick, layered rectangular plates with point supports by finite layer method, *International Journal of Solids and Structures*, **37**, 10, 1483-1499

7. COX H.L., BOXER J., 1960, Vibration of rectangular plates point-supported at the corners, *Aeronautical Quarterly*, **11**, 41-50
8. DAMLE S.K., FEESER L.J., 1972, Vibration of four point supported plates by a finite element method, *Journal of the Aeronautical Society of India*, **24**, 375-377
9. FAN S.C., CHEUNG Y.K., 1984, Flexural free vibrations of rectangular plates with complex support conditions, *Journal of Sound and Vibration*, **93**, 81-94
10. FRANCIOSI C., TOMASIELLO S., 2004, A modified quadrature element method to perform static analysis of structures, *International Journal of Mechanical Sciences*, **46**, 6, 945-959
11. GORMAN D.J., 1991, Analytical and experimental study of vibrating rectangular plates on rigid point supports, *AIAA Journal*, **29**, 8, 38-44
12. GU H.Z., WANG X.W., 1997, On the free vibration analysis of circular plates with stepped thickness over a concentric region by the quadrature element method, *Journal of Sound and Vibration*, **202**, 452-459
13. GUTIERREZ R.H., LAURA P.A.A., 1995, Analysis of vibrating, thin, rectangular plates with point-supports by the method of differential quadrature, *Ocean Engineering*, **22**, 101-103
14. HAN J.B., LIEW K.M., 1996, The differential quadrature element method (DQEM) for axisymmetric bending of thick circular plates, *Proceedings of the 3rd Asian-Pacific Conference on Computational Mechanics*, 2363-2368
15. HUANG M.H., THAMBIRATNAM D.P., 2001a, Analysis of plate resting on elastic supports and elastic foundation by finite strip method, *Computers and Structures*, **79**, 29-30, 2547-2557
16. HUANG M.H., THAMBIRATNAM D.P., 2001b, Free vibration analysis of rectangular plates on elastic intermediate supports, *Journal of Sound and Vibration*, **240**, 3 567-580
17. KATO Y., HONMA T., 1998, The Rayleigh-Ritz solution to estimate vibration characteristics of building floors, *Journal of Sound and Vibration*, **211**, 2, 195-206
18. KERSTENS J.G.M., 1979, Vibration of a rectangular plate supported at an arbitrary number of points, *Journal of Sound and Vibration*, **65**, 493-504
19. KIM C.S., DICKINSON S.M., 1987, Flexural vibration of rectangular plates with point supports, *Journal of Sound and Vibration*, **117**, 249-261
20. KITIPORNCHAI S., XIANG Y., LIEW K.M., 1994, Vibration of analysis of corner supported Mindlin plates of arbitrary shape using the Lagrange multiplier method, *Journal of Sound and Vibration*, **173**, 457-470
21. KOCATÜRK T., SEZER S., DEMİR C., 2004, Determination of the steady state response of viscoelastically point-supported rectangular specially orthotropic plates with added concentrated masses, *Journal of Sound and Vibration*, **278**, 4-5, 789-806
22. LEE L.T., LEE D.C., 1997, Free vibration of rectangular plates on elastic point supports with the application of a new type of admissible function, *Computer and Structures*, **65**, 2, 149-156
23. LEISSA A.W., 1969, Vibration of plates, NASA Sp160, U.S. Government Printing Office
24. LEISSA A.W., 1973, The free vibration of rectangular plates, *Journal of Sound and Vibration*, **31**, 3, 257-293
25. LIEW K.M., LAM K.Y., 1994, Effects of arbitrarily distributed elastic point constraints on vibrational behavior of rectangular plates, *Journal of Sound and Vibration*, **174**, 1, 23-36
26. LIEW K.M., XIANG Y., KITIPORNCHAI S., 1994, Vibration of Mindlin plates on point supports using constraint functions, *Journal of Engineering Mechanics*, **120**, 499-513
27. LIU F.-L., LIEW K.M., 1998, Static analysis of Reissner-Mindlin plates by differential quadrature element method, *ASME Journal of Applied Mechanics*, **65**, 705-710

28. LIU F.-L., LIEW K.M., 1999a, Differential quadrature element method: a new approach for free vibration analysis of polar Mindlin plates having discontinuities, *Computer Methods in Applied Mechanics and Engineering*, **179**, 3-4, 407-423
29. LIU F.-L., LIEW K.M., 1999b, Differential quadrature element method for static analysis of Reissner-Mindlin polar plates, *International Journal of Solids and Structures*, **36**, 5101-5123
30. LIU F.-L., 2000, Rectangular thick plates on Winkler foundation: differential quadrature element solutions, *International Journal of Solids and Structures*, **37**, 12, 1743-1763
31. MIZUSAWA T., KAJITA T., 1987, Vibration of skew plates resting on point supports, *Journal of Sound and Vibration*, **115**, 243-251
32. NARITA Y., HODGKINSON J.M., 2005, Layerwise optimisation for maximizing the fundamental frequencies of point-supported rectangular laminated composite plates, *Composite Structures*, **69**, 2, 127-135
33. QUAN J.R., CHANG C.T., 1989, New insights in solving distributed system equations by the quadrature method. I – Analysis, *Computers and Chemical Engineering*, **13**, 7, 779-788
34. RUI L., BO W., GANG L., BIN T., 2016, Hamiltonian system-based analytic modeling of the free rectangular thin plates' free vibration, *Applied Mathematical Modelling*, **40**, 2, 984-992
35. RUI L., BO W., GANG L., JIAHUI D., XIAOTING A., 2015, Analytic free vibration solutions of rectangular thin plates point-supported at a corner, *International Journal of Mechanical Sciences*, **96-97**, 199-205
36. SAADATPOUR M.M., AZHARI M., BRADFORD M.A., 2000, Vibration analysis of simply supported plates of general shape with internal point and line supports using the Galerkin method, *Engineering Structures*, **22**, 9, 1180-1188
37. STRIZ A.G., CHEN W., BERT C.W., 1994, Static analysis of structures by the quadrature element method (QEM), *International Journal of Solids and Structures*, **31**, 20, 2807-2818
38. VENKATESWARA R.G., RAJU I.S., MURTY G.K., 1973, Vibration of rectangular plates with mixed boundary conditions, *Journal of Sound and Vibration*, **30**, 257-260
39. WANG X.W., GU H.Z., 1997, Static analysis of frame structure by the differential quadrature element method, *International Journal of Numerical Methods in Engineering*, **40**, 759-772
40. ZHAO Y.B., WEI G.W., XIANG Y., 2002, Plate vibration under irregular internal supports, *International Journal of Solids and Structures*, **39**, 5, 361-1383
41. ZHOU D., 2002, Vibrations of point-supported rectangular plates with variable thickness using a set of static tapered beam functions, *International Journal of Mechanical Sciences*, **44**, 1, 149-164

ULTIMATE STATE BOUNDEDNESS OF UNDERACTUATED SPACECRAFT SUBJECT TO AN UNMATCHED DISTURBANCE

ROUZBEH MORADI, ALIREZA ALIKHANI

*Aerospace Research Institute (Ministry of Science, Research and Technology), Tehran, Iran
e-mail: roozbeh_moradi_aerospace@yahoo.com; aalikhani@ari.ac.ir (corresponding author)*

MOHSEN FATHI JEGARKANDI

*Department of Aerospace Engineering, Sharif University of Technology, Tehran, Iran
e-mail: fathi@sharif.edu*

Ultimate state boundedness for underactuated spacecraft subject to large non-matched disturbances is attained. First, non-smooth time-invariant state feedback control laws that make the origin asymptotically stable are obtained. Then, the controller is extended to make the closed-loop system globally uniformly ultimately bounded under the following conditions: 1) the disturbances acting on the directly actuated states are known and 2) the disturbance acting on the unactuated state is bounded and its profile need not be known. Finally, numerical simulations are presented to verify the analytical results. A large step disturbance is considered, and it is shown that the proposed controller makes the closed-loop system globally uniformly ultimately bounded. The proposed method is rather general and can be extended to other systems.

Keywords: underactuated spacecraft stabilization, non-matched disturbances, global uniform ultimate boundedness

1. Introduction

A mechanical system is underactuated when the number of independent control inputs is less than the number of degrees of freedom to be controlled. Considering the stabilization of such systems, an extensive amount of studies has been published in the literature. Choukchou-Braham *et al.* (2013), Olfati-Saber (2001), Aneke (2003), Spong (1998), Fantoni and Lozano (2002) and Liu and Yu (2013) are just a few examples.

The linearized model of a majority of underactuated systems, especially in the absence of gravitational terms, is not controllable near equilibrium points (Choukchou-Braham *et al.*, 2013). This leads to the well-known fact that most underactuated systems do not satisfy Brockett's necessary condition for smooth feedback stabilization (Choukchou-Braham *et al.*, 2013). In order to deal with this problem, non-smooth feedbacks have been proposed to stabilize underactuated mechanical systems (Reyhanoglu *et al.*, 2000).

In addition to the smoothness of feedback control laws, underactuation leads to another important challenge: attenuation of disturbances. The severity of this problem increases when the disturbances are non-matched, i.e. $\text{span}\{P\} \notin \text{span}\{B\}$, where P and B are the disturbance and control matrices, respectively (Astolfi and Rapaport, 1998).

Reducing the effects of disturbances on the stabilization of underactuated spacecraft has been considered by several papers. Astolfi and Rapaport (1998) considered robust stabilization of the angular velocity of a rigid body subject to external disturbances using L_2 -gain analysis. Several propositions were proved, and the robust stabilization problem was solved in a region having a hole. Floquet *et al.* (2000) used higher order sliding mode control (variable structure

control) to make the origin asymptotically stable for underactuated spacecraft within a finite time. However, it was assumed that no disturbance was exerted on the unactuated axis, i.e. they satisfied matching conditions. Karami and Sassani (2000) used the backstepping technique to asymptotically stabilize the angular velocity and attitude of underactuated spacecraft. The considered step disturbance had a very low magnitude. Zhang *et al.* (2008) considered the spin stabilization problem of underactuated spacecraft subject to sinusoidal disturbances. All of the disturbances were considered to be sinusoidal. Wang *et al.* (2003) considered stabilization of the angular velocity and attitude of underactuated spacecraft under sinusoidal disturbance. Although three exogenous disturbances were considered to be exerted on the spacecraft, the controller design was based on matched type disturbances.

In this paper, a new method is proposed to find non-smooth time-invariant state feedback control laws for underactuated spacecraft. Then, the controller is extended to make the closed-loop system globally uniformly ultimately bounded (GUUB). The proposed method is based on a combination of feedback linearization and Lyapunov stability theory. To avoid singularity of control inputs near the equilibrium points, a thin boundary layer is defined. It is assumed that outside the boundary layer, the extended controller is applied to the system. However, inside the boundary layer, the terms leading to singularity are canceled.

The present paper has two contributions: First, the proposed method is rather general and can be extended to other systems and second, the large step disturbance is considered to verify the controller performance. Most of the previous works have considered sinusoidal disturbances, which are not as severe as the step disturbance for the underactuated spacecraft.

The rest of this paper consists of the following sections: Section 2 provides non-smooth time-invariant state feedback control of underactuated spacecraft. In Section 3, the controller is extended to make the closed-loop system GUUB subject to non-matched disturbances. Finally, Section 4 presents numerical simulations and discussions to verify the analytical results.

2. Time-invariant non-smooth state feedback control of underactuated spacecraft

In the principal coordinate system, the rigid spacecraft angular velocity equations are described by the following expressions (Sidi, 2000)

$$\begin{aligned} \dot{p} &= \alpha_1 qr + u_1 + d_p & d_p &= \frac{T_{dp}}{J_x} \\ \dot{q} &= \alpha_2 pr + u_2 + d_q & d_q &= \frac{T_{dq}}{J_y} \\ \dot{r} &= \alpha_3 pq + u_3 + d_r & d_r &= \frac{T_{dr}}{J_z} \end{aligned} \quad (2.1)$$

where $[p, q, r]$ are angular velocities of the spacecraft, $[u_1, u_2, u_3]$ are normalized control inputs and $[T_{dp}, T_{dq}, T_{dr}]$ are external disturbances. α_1, α_2 and α_3 are fractions of moments of inertia and are assumed to be constant. Their values are obtained from the following set of equations

$$\alpha_1 = \frac{J_y - J_z}{J_x} \quad \alpha_2 = \frac{J_z - J_x}{J_y} \quad \alpha_3 = \frac{J_x - J_y}{J_z} \quad (2.2)$$

where $[J_x, J_y, J_z]$ are principal moments of inertia of the rigid body along the principal body axis. The relation between control moments and inputs are given by the following equations

$$u_1 = \frac{M_x}{J_x} \quad u_2 = \frac{M_y}{J_y} \quad u_3 = \frac{M_z}{J_z} \quad (2.3)$$

$[M_x, M_y, M_z]$ are three control moments acting on the spacecraft, and are assumed to be produced by thrusters.

Without loss of generality, it is assumed that the third state (r) is unactuated ($u_3 = 0$). On the other hand, it is assumed that $\alpha_i \neq 0 \forall i = 1, 2, 3$.

For now, the disturbances are not considered in the controller design. Therefore, Eqs. (2.1) will be simplified to Eqs. (2.4)

$$\dot{p} = \alpha_1 qr + u_1 \quad \dot{q} = \alpha_2 pr + u_2 \quad \dot{r} = \alpha_3 pq \quad (2.4)$$

In order to obtain a virtual control input for r , q is bisected into two parts

$$q = aq_1 + bq_2 \quad a, b \in R \quad (2.5)$$

a and b are constant real numbers that are presented to show that any linear combination of q_1 and q_2 will lead to the same results. This fact will be confirmed shortly.

Inserting q into the second and third rows of Eqs. (2.4) leads to

$$\dot{p} = \alpha_1 qr + u_1 \quad a\dot{q}_1 = \alpha_2 pr + u_2 - b\dot{q}_2 \quad \dot{r} = \alpha_3 p(aq_1 + bq_2) \quad (2.6)$$

The following definition is introduced

$$\dot{q}_2 = w \quad (2.7)$$

w is a scalar variable that is used to stabilize the unactuated state (r). The goal is now to determine q_2 that forces r to approach the origin. This q_2 is denoted as $q_{2,des}$.

In order for r to be exponentially stabilized, the following relation must hold

$$\dot{r} = -k_r r \quad (2.8)$$

Considering the last row of Eqs. (2.6) and (2.8), the following equation is obtained

$$-k_r r = \alpha_3 p(aq_1 + bq_{2,des}) \quad (2.9)$$

Solving for $q_{2,des}$ results in

$$q_{2,des} = \frac{1}{b}\phi - \frac{a}{b}q_1 \quad (2.10)$$

where $\phi = -k_r r / (\alpha_3 p)$.

It can be easily shown that

$$\lim_{t \rightarrow \infty} q = \lim_{t \rightarrow \infty} \phi \quad (2.11)$$

Therefore, it is possible to tune the controller parameters to make sure that the steady-state value of q becomes zero.

Now, the following linear combination of q_2 and $q_{2,des}$ is introduced to transform Eqs. (2.6) into a virtually fully actuated form

$$z = cq_2 + dq_{2,des} \quad c, d \in R \quad (2.12)$$

c and d are constant real numbers, and their values have direct influence on the stability and performance of the closed-loop system. The validity and importance of this statement will become clear at the end of this Section. As stated previously, $q_{2,des}$ is the virtual control input.

Note 1: If $c = -d$ and $z = 0$, q_2 will be equal to $q_{2,des}$, which is the ideal case. This is equivalent to saying that the stabilization of z is equivalent to the stabilization of r . According to this point, the equation for \dot{r} will be replaced by \dot{z} .

Differentiating Eq. (2.12) with respect to time together with Eq. (2.7) results in

$$\dot{z} = c\dot{q}_2 + d\dot{q}_{2,des} = cw + d\dot{q}_{2,des} \quad (2.13)$$

Replacing the third equation of Eqs. (2.6) with Eq. (2.13) leads to

$$\dot{p} = \alpha_1 qr + u_1 \quad \dot{q}_1 = \frac{1}{a}(\alpha_2 pr + u_2 - b\dot{q}_2) \quad \dot{z} = cw + d\dot{q}_{2,des} \quad (2.14)$$

The time derivative of $q_{2,des}$ can be obtained by partial differentiation of Eq. (2.10)

$$\dot{q}_{2,des} = \frac{1}{b} \frac{\partial \phi}{\partial p} \dot{p} - \frac{a}{b} \dot{q}_1 \quad (2.15)$$

It is assumed that $(\partial \phi / \partial r) / \dot{r} \approx 0$ in comparison to the other terms. The reason for this assumption is to rewrite \dot{z} in terms of the original variables.

Using Eqs. (2.5), (2.7), (2.15) and performing some mathematical operations, along with the third row of Eqs. (2.4), \dot{z} will be simplified to

$$\dot{z} = (c + d)w + \frac{d}{b} \frac{\partial \phi}{\partial p} \dot{p} - \frac{d}{b} \dot{q}_1 \quad (2.16)$$

Therefore, the entire set of Eqs. (2.14) in a virtually fully actuated form will be given as

$$\dot{p} = \alpha_1 qr + u_1 \quad \dot{q}_1 = \frac{1}{a}(\alpha_2 pr + u_2 - bw) \quad \dot{z} = (c + d)w + \frac{d}{b} \frac{\partial \phi}{\partial p} \dot{p} - \frac{d}{b} \dot{q}_1 \quad (2.17)$$

According to the third row, in order for z to be stabilizable, c should not be equal to $-d$. However, this is in contradiction with the previously made conclusion (Note 1). In order to alleviate this problem, it will be assumed that $c \approx -d$.

Using feedback linearization and expecting exponential convergence from z i.e. $\dot{z} = -k_z z$, w is obtained as follows

$$w = \frac{1}{c + d} \left(-k_z z - \frac{d}{b} \frac{\partial \phi}{\partial p} \dot{p} + \frac{d}{b} \dot{q}_1 \right) \quad (2.18)$$

Inserting w in the second equation of Eqs. (2.17), u_2 is obtained as follows

$$u_2 = a\dot{q}_1 - \alpha_2 pr + \frac{b}{c + d} \left(-k_z z - \frac{d}{b} \frac{k_p k_r (-r)}{\alpha_3 p} - \frac{d}{b} k_q q \right) \quad (2.19)$$

Using Eq. (2.12) and considering the fact that $\lim_{t \rightarrow \infty} q_{2,des} = 0$, the above equation is simplified to

$$u_2 = a\dot{q}_1 - \alpha_2 pr + \frac{b}{c + d} \left(-k_z c q_2 - \frac{d}{b} \frac{k_p k_r (-r)}{\alpha_3 p} - \frac{d}{b} k_q q \right) \quad (2.20)$$

The reason for assuming $\lim_{t \rightarrow \infty} q_{2,des} = 0$ can be inferred from Eq. (2.10). ϕ is a function that can converge to zero through tuning the controller parameters ($k_p < k_r$ or equivalently, the convergence rate of p less than the convergence rate of r). On the other hand, according to the dynamics imposed on q_1 ($\dot{q}_1 = -k_{q1} q_1$), this variable will also converge to zero. Considering these facts, u_2 is

$$u_2 = -ak_{q1} q_1 - \alpha_2 pr - \frac{b}{c + d} k_z c q_2 - \frac{d}{c + d} \frac{k_p k_r (-r)}{\alpha_3 p} - \frac{d}{c + d} k_q q \quad (2.21)$$

Assuming $k_{q_1} = [c/(c+d)]k_z = [c/(c+d)]k_q$ and according to Eq. (2.5), the final equation for u_1 and u_2 is

$$u_1 = -k_p p - \alpha_1 q r \quad u_2 = -k_q q - \alpha_2 p r + \frac{d}{c+d} \frac{k_p k_r r}{\alpha_3 p} \quad (2.22)$$

Since the procedure used to obtain this controller is based on linear state bisection (Eq. (2.5)), this controller is called LSB.

In accordance with Eq. (2.22), u_2 consists of two parts

$$u_{2_1} = -k_q q - \alpha_2 p r \quad u_{2_2} = \frac{d}{c+d} \frac{k_p k_r r}{\alpha_3 p} \quad (2.23)$$

u_{2_1} and u_{2_2} are used to stabilize q and r , respectively. The form of u_2 is consistent with the one proposed by Reyhanoglu (1996).

According to Eqs. (2.23), u_2 does not depend on a and b . According to Eq. (2.1), the components of d_p and d_q can be easily counteracted by the direct control input vectors, u_1 and u_2 . Therefore, the component of disturbances on the unactuated state (d_r) plays the key role in the controller design.

Non-smooth time-invariant state feedback control laws (Eq. (2.22)) make the origin asymptotically stable for the disturbance-free system (Eqs. (2.4)). In the next Section, this controller is extended to provide GUUB, in the presence of non-matched disturbances.

3. Underactuated spacecraft angular velocity ultimate boundedness in presence of non-matched disturbances

Definition 1 (Astolfi and Rapaport (1998)): The disturbances are non-matched when $\text{span}\{P\} \notin \text{span}\{B\}$, where P and B are the disturbance and control matrices, respectively.

Assumption 1: d_p and d_q can be unbounded, but should be known.

Assumption 2: d_r should be bounded, and its maximum value should be known.

In order to extend the controller and to ensure that the states are GUUB, the following procedure is proposed:

- 1) Since u_2 has been selected to stabilize r , u_1 is used to provide GUUB.
- 2) A candidate Lyapunov function (CLF) is proposed.
- 3) The derivative of this CLF along the trajectories of the closed-loop system is evaluated.
- 4) u_1 is used to ensure GUUB of the states for the perturbed closed-loop system.

Consider Eqs. (2.4) with disturbances

$$\dot{p} = u_1 + \alpha_1 q r + d_p \quad \dot{q} = u_2 + \alpha_2 p r + d_q \quad \dot{r} = \alpha_3 p q + d_r \quad (3.1)$$

It has been shown in Section 2 that u_1 and u_2 (Eq. (2.22)) make the origin asymptotically stable for Eqs. (3.1) without the presence of disturbances.

After eliminating d_p and d_q using direct control inputs, the closed-loop system will be

$$\dot{p} = u'_1 \quad \dot{q} = -k_q q + \frac{d}{c+d} \frac{k_p k_r r}{\alpha_3 p} \quad \dot{r} = \alpha_3 p q + d_r \quad (3.2)$$

Now, the goal is to find u'_1 that makes the closed-loop system GUUB.

In order to solve this problem, the following CLF is proposed

$$V = \frac{1}{2} \begin{bmatrix} p & q & r \end{bmatrix} \begin{bmatrix} k_p & 0 & 0 \\ 0 & k_q & 0 \\ 0 & 0 & k_r \end{bmatrix} \begin{bmatrix} p \\ q \\ r \end{bmatrix} = \frac{1}{2}(k_p p^2 + k_q q^2 + k_r r^2) \quad (3.3)$$

The derivative of V along the trajectories (Eqs. (3.2)) is given by

$$\begin{aligned} \dot{V} &= \frac{\partial V}{\partial x} \dot{x} = k_p p u'_1 - k_q^2 q^2 + \frac{d}{c+d} \frac{k_p k_q k_r r q}{\alpha_3 p} + \alpha_3 k_r p q r + k_r r d_r \\ &\leq k_p p u'_1 - k_q^2 q^2 + \frac{d}{c+d} \frac{k_p k_q k_r r q}{\alpha_3 p} + \alpha_3 k_r p q r + k_r r M_d \end{aligned} \quad (3.4)$$

where M_d is the maximum absolute value of d_r . If u'_1 is selected as

$$u'_1 = \frac{1}{k_p p} \left(-\frac{d}{c+d} \frac{k_p k_q k_r r q}{\alpha_3 p} - \alpha_3 k_r p q r - k_p^2 p^2 - k_r^2 r^2 \right) \quad p \neq 0 \quad (3.5)$$

\dot{V} will result in the following equation

$$\dot{V} \leq -k_p^2 p^2 - k_q^2 q^2 - k_r^2 r^2 + k_r r M_d = -w_2(x) + k_r r M_d \quad (3.6)$$

Since

$$-w_2(x) \leq -\min(k_p^2, k_q^2, k_r^2) \|x\|_2^2 \quad (3.7)$$

and at the same time $r \leq \|x\|_2$, \dot{V} will satisfy the following inequality

$$\dot{V} \leq -\min(k_p^2, k_q^2, k_r^2) \|x\|_2^2 + k_r M_d \|x\|_2 \quad (3.8)$$

Therefore, if the following inequality holds

$$M_d \leq \frac{\min(k_p^2, k_q^2, k_r^2)}{2k_r} \|x\|_2 \quad (3.9)$$

equivalently

$$\|x\|_2 \geq \frac{2k_r}{\min(k_p^2, k_q^2, k_r^2)} M_d \quad (3.10)$$

\dot{V} will satisfy the following relation

$$\dot{V} \leq -\frac{1}{2} \min(k_p^2, k_q^2, k_r^2) \|x\|_2^2 = -w_1(x) \quad (3.11)$$

where $w_1(x)$ is a positive definite function. Equations (3.3) and (3.11) confirm that the conditions of theorem 4.18 (Khalil, 2001) are satisfied. This means that the states of Eqs. (3.2) become GUUB for the state-feedback control law given by Eq. (3.5).

An important parameter is introduced: thp_0 or the thicknesses of the boundary layer. This parameter is selected such that the control inputs never reach the singular point and, at the same time, the states reach the vicinity of equilibrium points with good quality.

Note 2: In order to make the control input (Eq. (3.5)) smoother, especially near the equilibrium point, the terms that contain p in their denominator are neglected. As will be shown in the simulation Section, this simplification leads to more implementable control inputs and still provides GUUB of the states.

Depending on the magnitude of p and the value chosen for thp_0 , two different cases occur during simulations:

— for $|p| > thp_0$

$$\begin{aligned} u_1 &= \frac{-\alpha_3 k_r q r}{k_p} - k_p p - \alpha_1 q r - d_p \\ u_2 &= -k_q q + \frac{d}{c+d} \frac{k_p k_r r}{\alpha_3 p} - \alpha_2 p r - d_q \end{aligned} \quad (3.12)$$

— for $|p| \leq thp_0$

$$\begin{aligned} u_1 &= \frac{-\alpha_3 k_r q r}{k_p} - k_p p - \alpha_1 q r - d_p \\ u_2 &= -k_q q - \alpha_2 p r - d_q \end{aligned} \quad (3.13)$$

The above controllers are extended forms of LSB. Therefore, they will be called ELSB. In order to verify the analytical results, several simulations are carried out, and the results are presented in the next Section.

4. Simulations

The system and controller parameters are presented in Table 1. c and d are selected as 1 and -0.94 to -0.90 , respectively.

Table 1. System and controller parameters

Initial conditions [deg/s]	Boundary layer thickness [deg/s]	Controller coefficients	Moments of inertia [kg m ²]
$p_0 = 8$		$k_p = 0.05$	$J_x = 449.5$
$q_0 = -6$	$thp_0 = 0.1$	$k_q = 0.1$	$J_y = 264.6$
$r_0 = 7$		$k_r = 0.1$	$J_z = 312.5$

Three scenarios are considered for simulation. These scenarios are presented in Table 2.

Table 2. Simulation scenarios

Scenario	Controller	Disturbance
First scenario	LSB	step
Second scenario	ELSB	step
Third scenario	LSB	sinusoidal

A comparison of the first and second scenarios analyzes the capabilities of the LSB and ELSB in dealing with a large step disturbance. A comparison of the first and third scenarios shows severity of the step disturbance compared to the sinusoidal disturbance.

First scenario

The component of disturbances exerted on the unactuated axis is considered as the following step function

$$d_r = \frac{1}{J_z} \quad (4.1)$$

Therefore, the external disturbance (T_{dr}) exerted on the unactuated axis is 1 N m.

As stated in *Assumption 1*, the disturbances exerted on the actuated states are not important as long as they are known. Therefore, they are not considered here.

The LSB response is illustrated in Figs. 1 and 2.

As illustrated in Fig. 1, LSB is not able to provide GUUB for the states. The reason can be explained by Eq. (2.22). The controller tries to make the origin an asymptotically stable equilibrium for the closed-loop system. However, due to the presence of a large step disturbance on the unactuated axis, r increases in an unacceptable way. This important example shows the adverse effects of not considering large non-matched disturbances in the controller design. Due to the non-smooth nature of the control inputs, a jump in the control moment is observed (Fig. 2).

Note 3: In order to reduce the adverse effects of sudden changes in the control moments and to make them more implementable, thickness of the boundary layer should increase, at the expense of less response quality.

Second scenario

In order to provide GUUB, the ELSB is used. The response and control moments of this controller are illustrated in Figs. 3 and 4:

According to Fig. 3, the ELSB makes the closed-loop system GUUB. As stated in Note 2, the simplifications have led to implementable control moments. At the same time, the states are bounded.

Third scenario

It is assumed that the following sinusoidal disturbance is exerted on the unactuated axis

$$d_r = \frac{1}{J_z} \sin\left(\frac{2\pi}{50}t\right) \quad (4.2)$$

In comparison to Eq. (4.1), the amplitudes of the disturbances are the same.

The results of the simulation are shown in Figs. 5 and 6.

A comparison of Fig. 1 and Fig. 5 shows that the closed-loop system is bounded for the sinusoidal disturbance. However, for the step disturbance, the response of the unactuated axis becomes unbounded.

Finally, it can be concluded that the LSB makes the origin asymptotically stable for the disturbance-free closed-loop system. Therefore, in the absence of non-matched disturbances, the origin is asymptotically stable. However, this controller will not provide satisfactory performance when large non-matched disturbances are considered. On the other hand, the ELSB attenuates the effects of non-matched disturbances and makes the closed-loop system GUUB.

5. Conclusion

A mechanical system is underactuated when the number of independent control inputs is less than the number of degrees of freedom to be controlled. The presence of uncontrollable modes in their linearized models prevents them from being smooth state feedback stabilizable. The problems increase when disturbances, especially of the non-matched type, enter into the problem. In this paper, non-smooth time-invariant state feedback control laws have been obtained that made the origin asymptotically stable for underactuated spacecraft. Then, these control laws have been extended to make the closed-loop system GUUB. Simulation results have been presented to verify the analytical solutions.

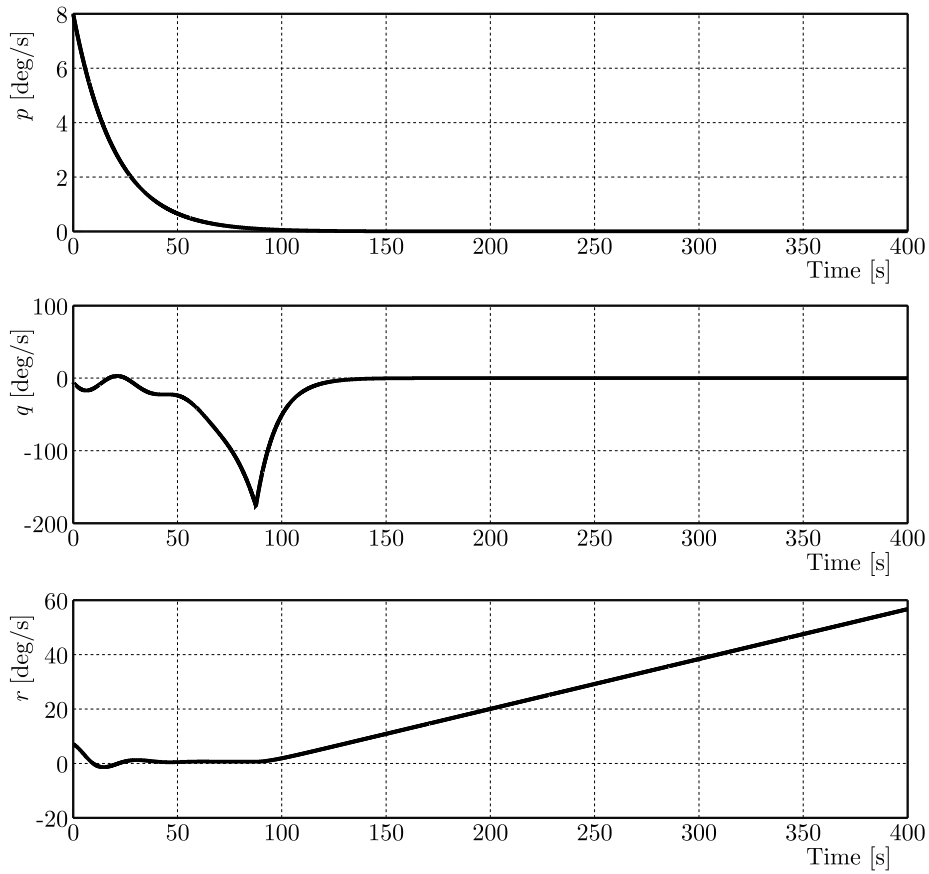


Fig. 1. Response of the LSB (first scenario)

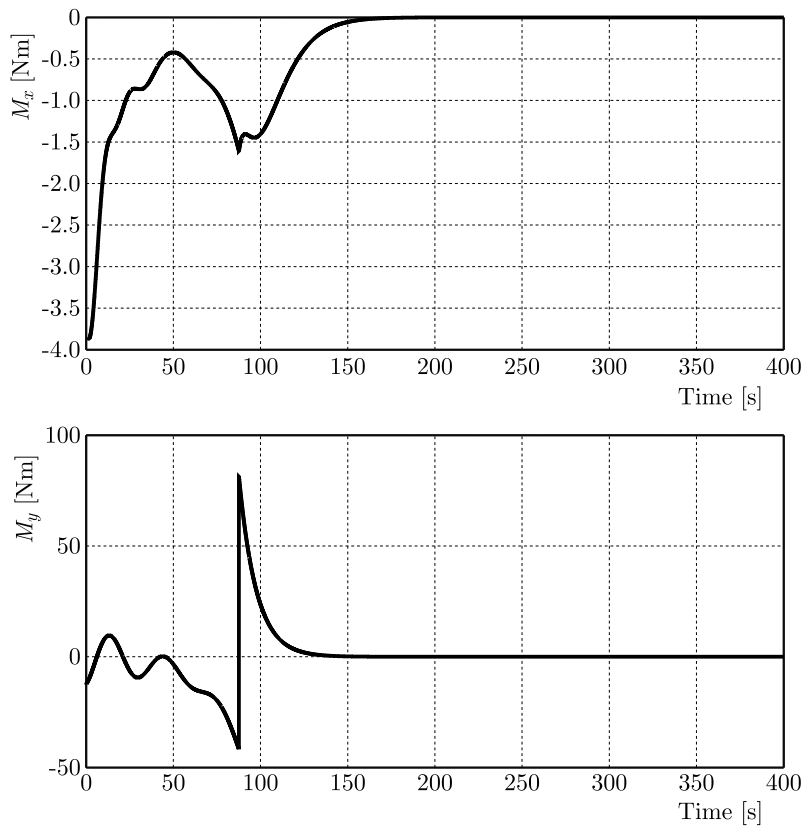


Fig. 2. Control moments

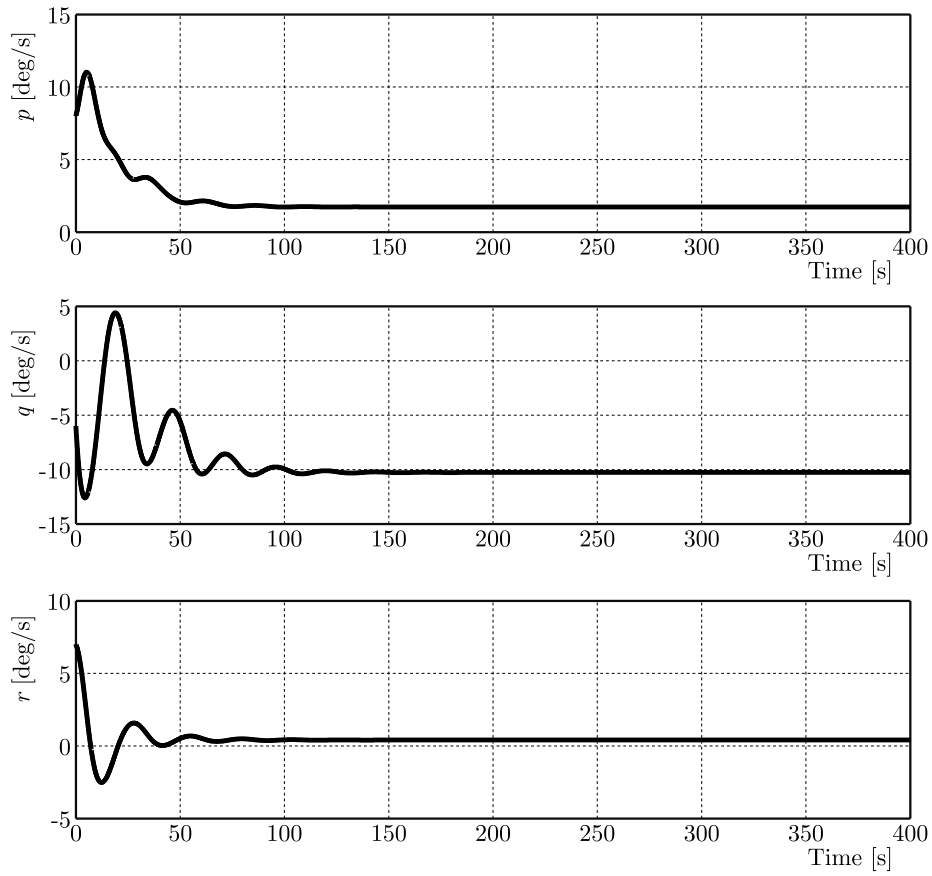


Fig. 3. Response of the ELSB (second scenario)

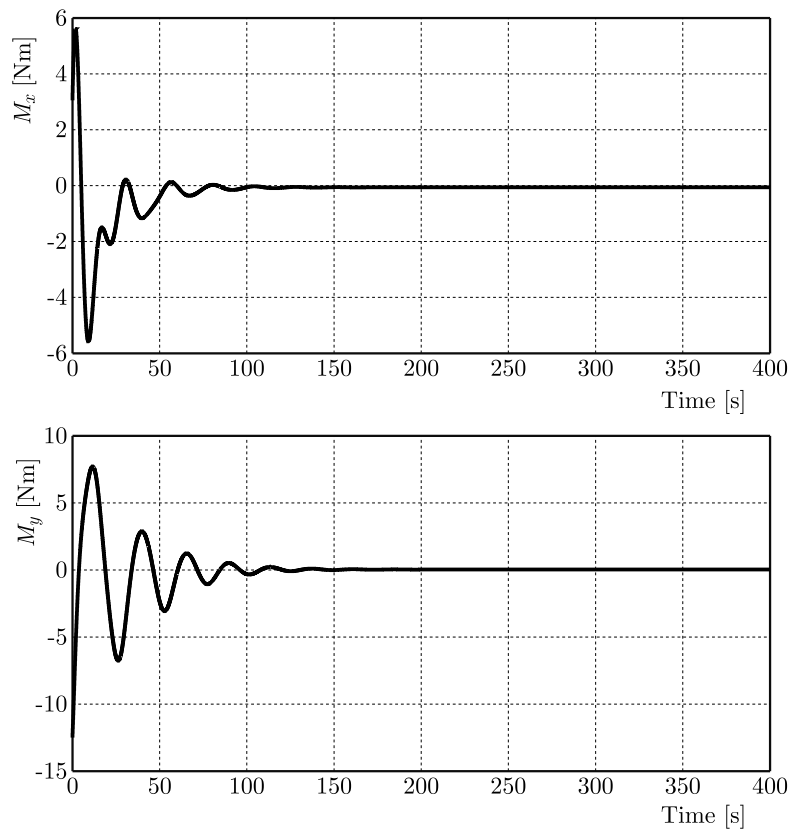


Fig. 4. Control moments

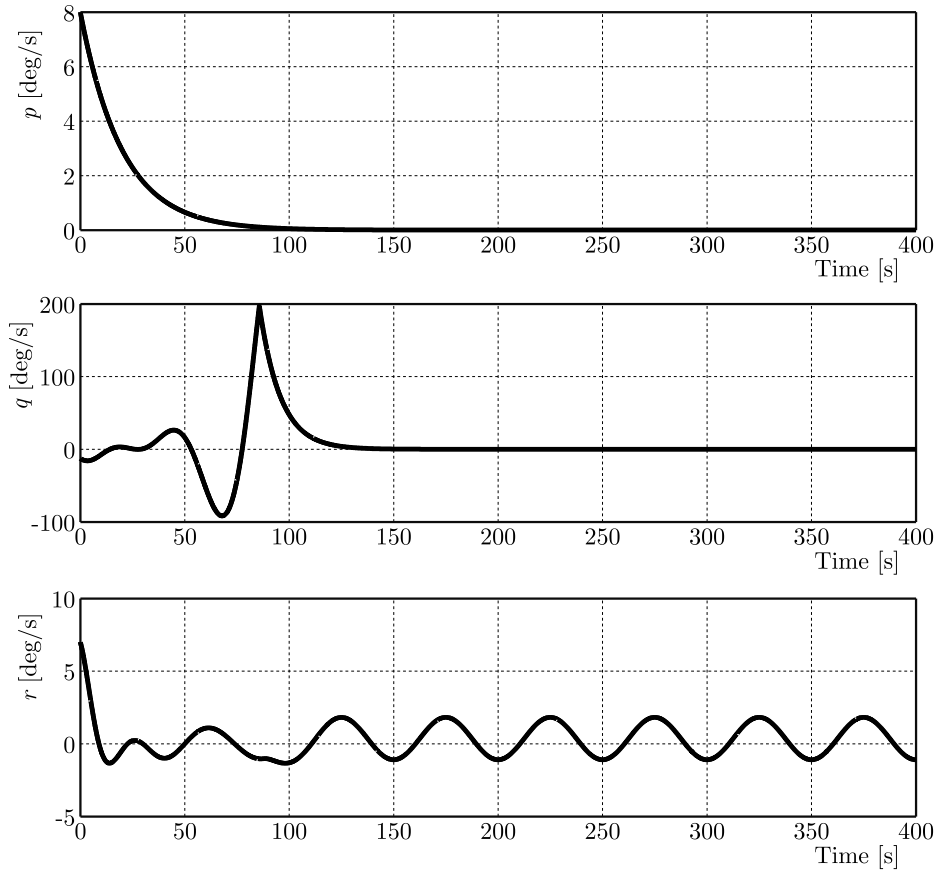


Fig. 5. Response of the LSB (third scenario)

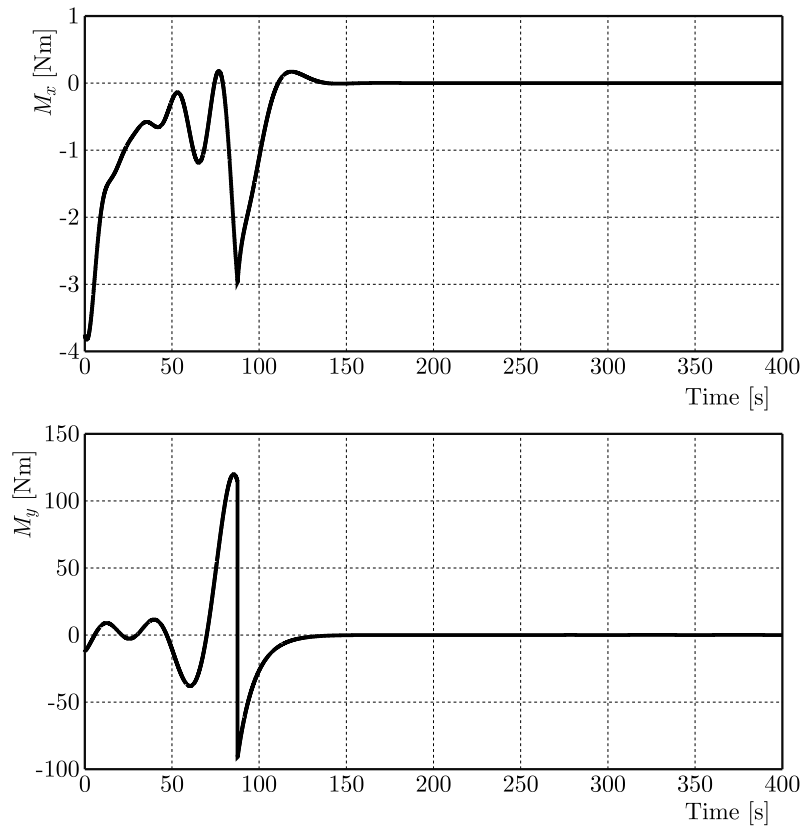


Fig. 6. Control moments

References

1. ANEKE N.P.I., 2003, *Control of Underactuated Mechanical Systems*, Eindhoven: Technische Universiteit Eindhoven, DOI: 10.6100/IR559509
2. ASTOLFI A., RAPAPORT A., 1998, Robust stabilization of the angular velocity of a rigid body, *Systems and Control Letters*, **34**, 5, 257-264, DOI: 10.1016/S0167-6911(98)00031-0
3. CHOUKCHOU-BRAHAM A., CHERKI B., DJEMAI M., BUSAWON K., 2013, *Analysis and Control of Underactuated Mechanical Systems*, Springer, DOI: 10.1007/978-3-319-02636-7
4. FANTONI I., LOZANO R., 2002, *Nonlinear Control for Underactuated Mechanical Systems*, Springer-Verlag London, Communication and Control Engineering, ISBN: 978-1-4471-1086-6, DOI: 10.1007/978-1-4471-0177-2
5. FLOQUET T., PERRUQUETTI W., BARBOT J.P., 2000, Angular velocity stabilization of a rigid body via VSS control, *Journal of Dynamic Systems, Measurement, and Control*, **122**, 4, 669-673, DOI:10.1115/1.1316787
6. KARAMI M.A., SASSANI F., 2007, Nonlinear attitude control of an underactuated spacecraft subject to disturbance torques, *Proceedings of the American Control Conference*, 3150-3155, DOI: 10.1109/ACC.2007.4283042
7. KHALIL H., 2000, *Nonlinear Systems*, Prentice Hall, Third Edition, ISBN: 0-13-067389-7
8. LIU Y., YU H., 2013, A survey of underactuated mechanical systems, *IET Control Theory and Applications*, **7**, 7, 921-935, DOI: 10.1049/iet-cta.2012.0505
9. OLFATI-SABER R., 2001, Nonlinear control of underactuated mechanical systems with application to robotics and aerospace vehicles, Ph.D. Thesis, MIT University
10. REYHANOGLU M., 1996, Discontinuous feedback stabilization of the angular velocity of a rigid body with two control torques, *Proceedings of the 36th IEEE Conference on Decision and Control*, **3**, 2692-2694, DOI: 10.1109/CDC.1996.573511
11. REYHANOGLU M., CHO S., MCCLAMROCH H.N., 2000, Discontinuous feedback control of a special class of underactuated mechanical systems, *International Journal of Robust and Nonlinear Control*, **10**, 4, 265-281, DOI: 10.1002/(SICI)1099-1239(20000415)10:4<265::AID-RNC470>3.0.CO;2-N
12. SIDI M.J., 2000, *Spacecraft Dynamics and Control: A Practical Engineering Approach*, Cambridge Aerospace Series 7, ISBN: 0-521-55072-6
13. SPONG M.W., 1998, Underactuated mechanical systems, *Control Problems in Robotics and Automation, Lecture Notes in Control and Information Sciences*, **230**, 135-150, DOI: 10.1007/BFb0015081
14. WANG D., JIA Y., JIN L., XU S., 2013, Control analysis of an underactuated spacecraft under disturbance, *Acta Astronautica*, **83**, 44-53, DOI: 10.1016/j.actaastro.2012.10.029
15. ZHANG H.H., WANG F., TRIVAILO P.M., 2008, Spin-axis stabilization of underactuated rigid spacecraft under sinusoidal disturbance, *International Journal of Control*, **81**, 12, 1901-1909, DOI: 10.1080/00207170801930217

EIGENVALUE APPROACH TO NANOBEAM IN MODIFIED COUPLE STRESS THERMOELASTIC WITH THREE-PHASE-LAG MODEL INDUCED BY RAMP TYPE HEATING

RAJNEESH KUMAR

Kurukshetra University, Department of Mathematics, Kurukshetra, India
e-mail: rajneesh_kuk@rediffmail.com

SHALOO DEVI

Himachal Pradesh University, Department of Mathematics and Statistics, Shimla, India
e-mail: shaloosharma2673@gmail.com

This article deals with the study of a thermoelastic nanobeam in a modified couple stress theory subjected to ramp-type heating. The mathematical model is prepared for the nanobeam in thermoelastic three-phase-lag. The Laplace transform and the eigenvalue approach are used to find the displacement component, lateral deflection, temperature change and axial stress of the thermoelastic beam. The general algorithm of the inverse Laplace transform is developed to compute results numerically. The comparison of three-phase-lag, dual-phase-lag and GN-III (1993) models are represented, and their illustration is depicted graphically. This study finds the applications in engineering, medical science, sensors, etc.

Keywords: modified couple stress thermoelastic, eigenvalue approach, nanobeam

1. Introduction

Cosserat and Cosserat (1909) developed a mathematical model for a couple stress theory in which kinematical quantities are the displacement and material microrotation. Yang *et al.* (2002) proposed a modified couple stress theory in which the couple stress tensor was symmetric and required only one material length parameter to capture the size effect which was caused by micro-structure. Various authors studied different problems in a modified couple stress theory (2008, 2011-2015).

Tzou (1995a,b, 1997) proposed a dual-phase-lag model by modifying the classical Fourier law by an approximation with two different time translations: a phase-lag of the heat flux τ_q and a phase-lag of the temperature gradient τ_θ . Tzou (1995b) supported that model by experimental results. A review of five theories of thermoelasticity was given by Hetnarski and Ignaczak (1999). Roychoudhuri (2007) developed a three-phase-lag model for a thermoelastic material. In that model, the Fourier law of heat conduction was modified by introducing three different phase-lags for the heat flux vector, temperature gradient and thermal displacement component gradient. Quintanilla and Racke (2008) investigated stability of the three-phase-lag heat conduction equation and the relations among three material parameters. Kumar *et al.* (2012) studied wave propagation in an anisotropic viscoelastic medium with the three-phase-lag model of thermoelasticity. Sur and Kanoria (2014) examined vibration of a gold nanobeam induced by a ramp-type laser pulse under the three-phase-lag model.

The significance of using the eigenvalue approach is to reduce the problem on the vector-matrix differential equation to algebraic eigenvalue problems. Thus the solutions for the field variables are obtained by determining eigenvalues and the corresponding eigenvectors. In this approach, the physical quantities are directly involved in the formulation of the problem and,

as such, the boundary and initial conditions can be applied directly. The problem of micropolar thermoelasticity without energy dissipation by employing the eigenvalue approach was studied by Kumar *et al.* (2007). Zang and Fu (2012) constructed a new beam model for a viscoelastic micro-beam based on a modified couple stress theory.

Abouelregal and Zenkour (2014) investigated the problem of an axially moving microbeam subjected to a sinusoidal pulse heating and an external transverse excitation with one relaxation time using the Laplace transform. Zenkour and Abouelregal (2015) investigated the problem of a thermoviscoelastic orthotropic continuum with a cylindrical hole and variable thermal conductivity under three-phase-lag model and solved the physical quantities by the Laplace transform technique. The effects of hall current and rotation in a modified couple stress theory subjected to the ramp type loading in the context of theory of generalized thermoelastic diffusion was presented by Kumar and Devi (2015). Thermoelastic interaction in a thermally conducting cubic crystal subjected to the ramp-type heating was investigated by Abbas *et al.* (2015). Reddy *et al.* (2016) discussed the problem of functionally graded circular plates with the modified couple stress theory by using the finite element method. On the basis of global local theory, a model for the composite laminated Reddy plate of a new modified couple-stress theory was developed by Chen and Wang (2016). Zenkour and Abouelregal (2016) discussed vibration of functionally graded microbeams by using the Green-Naghdi thermoelasticity theory (1993) and the Laplace transform.

The present investigation deals with a thermoelastic nanobeam in the modified couple stress theory induced by the ramp-type heating in the three-phase-lag model. The non-dimensional equations are written in form of the Laplace transform which is solved by the eigenvalue approach. The expressions of the displacement component, lateral deflection, temperature change and axial stress are computed numerically and then represented graphically. Particular cases of interest are deduced from the present investigation.

2. Basic equations

Following Yang *et al.* (2002) and Roychoudhuri (2007), the constitutive relations, equations of motion and the equation of heat conduction in the modified couple stress generalized thermoelasticity with three-phase-lag model in the absence of body forces are:

— constitutive relations

$$\begin{aligned} t_{ij} &= \lambda e_{kk} \delta_{ij} + 2\mu e_{ij} - \frac{1}{2} e_{kij} m_{lk,l} - \beta_1 T \delta_{ij} & m_{ij} &= 2\alpha \chi_{ij} \\ \chi_{ij} &= \frac{1}{2} (\omega_{i,j} + \omega_{j,i}) & \omega_i &= \frac{1}{2} e_{ipq} u_{q,p} \end{aligned} \quad (2.1)$$

— equations of motion

$$\left(\lambda + \mu + \frac{\alpha}{4} \Delta \right) \nabla (\nabla \cdot \mathbf{u}) + \left(\mu - \frac{\alpha}{4} \Delta \right) \nabla^2 \mathbf{u} - \beta_1 \nabla T = \rho \ddot{\mathbf{u}} \quad (2.2)$$

— equation of heat conduction with three-phase-lag

$$\left[K^* \left(1 + \tau_\nu \frac{\partial}{\partial t} \right) + K \frac{\partial}{\partial t} \left(1 + \tau_T \frac{\partial}{\partial t} \right) \right] \Delta T = \left(1 + \tau_q \frac{\partial}{\partial t} + \frac{\tau_q^2}{2} \frac{\partial^2}{\partial t^2} \right) \left(\rho c_e \frac{\partial^2 T}{\partial t^2} + T_0 \beta_1 \frac{\partial^2}{\partial t^2} (\nabla \cdot \mathbf{u}) \right) \quad (2.3)$$

where t_{ij} are components of the stress tensor, λ and μ are Lamé's constants, δ_{ij} is Kronecker's delta, $e_{ij} = (u_{i,j} + u_{j,i})/2$ are components of the strain tensor, e_{ijk} is the alternate tensor, m_{ij} are components of the couple-stress, $\beta_1 = (3\lambda + 2\mu)\alpha_t$. Here α_t are coefficients of linear thermal expansion and diffusion, respectively, T is temperature change, χ_{ij} is symmetric curvature, $\omega_{ij} = (u_{j,i} - u_{i,j})/2$ are components of rotation, ω_i is the rotational vector, α is the couple

stress parameter and $\mathbf{u} = [u_1, u_2, u_3]$ is the displacement component, ρ is density, Δ is the Laplacian operator, ∇ is del operator. K is the coefficient of thermal conductivity, K^* is the material characteristic constant of the theory, c_e is the specific heat at a constant strain, T_0 is the reference temperature assumed to be such that $T/T_0 \ll 1$. τ_T , τ_q and τ_ν are the phase lags of the temperature gradient, of the heat flux and of the thermal displacement component gradient, respectively, such that $\tau_\nu < \tau_T < \tau_q$.

3. Formulation of the problem

Consider a homogeneous, isotropic, rectangular modified couple stress thermoelastic beam having dimensions of length ($0 \leq x \leq L$), width ($-d/2 \leq y \leq d/2$) and thickness ($-h/2 \leq z \leq h/2$) (Fig. 1). Let us take the x -axis along length of the beam, the y -axis along width and z -axis along thickness, representing the axis of material symmetry. Therefore, any plane cross-section initially perpendicular to the axis of the beam remains plane and perpendicular to the neutral surface during bending. According to the Euler-Bernoulli theory for a small deflection in a simple bending problem, the displacement components are given by

$$u(x, y, z, t) = -z \frac{\partial w}{\partial x} \quad v(x, y, z, t) = 0 \quad w(x, y, z, t) = w(x, t) \quad (3.1)$$

where $w(x, t)$ is lateral deflection of the beam and t is time. The one-dimension stress component t_x , with the aid of equations (2.1)₁ and (3.1), yields

$$(3.2)t_x = -(\lambda + 2\mu)z \frac{\partial^2 w}{\partial x^2} - \beta_1 T \quad (3.2)$$

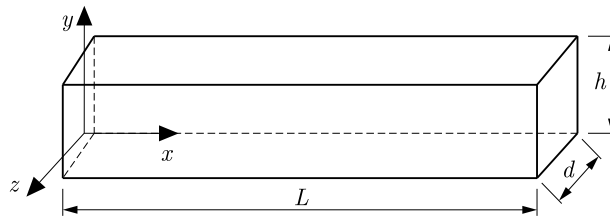


Fig. 1. Schematic figure of the beam

The flexural moment of the cross-section of the beam is given by

$$M = M_\sigma + M_m = d \left(\int_{-h/2}^{h/2} t_x z \, dz + \int_{-h/2}^{h/2} m_{xy} \, dz \right) \quad (3.3)$$

where M_σ and M_m are components of the bending moment due to the classic stress and couple stress tensors, respectively.

Making use of the value of t_x and m_{xy} from (3.2) and (2.1)₂ in (3.3), with the aid of (3.1), yield

$$M = - \left[(\lambda + 2\mu) \frac{dh^3}{12} + \alpha A \right] \frac{\partial^2 w}{\partial x^2} - \beta_1 d \int_{-h/2}^{h/2} T z \, dz \quad (3.4)$$

Following Rao (2007), the equation of transverse motion of the beam is given by

$$\frac{\partial^2 M}{\partial x^2} - \rho A \frac{\partial^2 w}{\partial t^2} = 0 \quad (3.5)$$

where $A = dh$ is the cross-sectional area of the beam.

For a very thin beam, assuming that the temperature increment varies in terms of the $\sin(pz)$ function along thickness of the beam, where $p = \pi/h$ as

$$T(x, z, t) = T_1(x, t) \sin(pz) \quad (3.6)$$

Substituting the value of M from (3.4) into equation (3.5), with the aid of equation (3.6), yields

$$\left[(\lambda + 2\mu) \frac{dh^3}{12} + \alpha A \right] \frac{\partial^4 w}{\partial x^4} + \beta_1 d \frac{\partial^2 T_1}{\partial x^2} \int_{-h/2}^{h/2} z \sin(pz) dz + \rho A \frac{\partial^2 w}{\partial t^2} = 0 \quad (3.7)$$

Multiplying heat conduction equation (2.3), after using equation (3.1), by z and integrating them with respect to the interval $(-h/2, h/2)$, and with the use of equation (3.6), we obtain

$$\begin{aligned} & \left[K^* \left(1 + \tau_\nu \frac{\partial}{\partial t} \right) + K \frac{\partial}{\partial t} \left(1 + \tau_T \frac{\partial}{\partial t} \right) \right] \left(\frac{\partial^2 T_1}{\partial x^2} - p^2 T_1 \right) \\ & = \left(1 + \tau_q \frac{\partial}{\partial t} + \frac{\tau_q^2}{2} \frac{\partial^2}{\partial t^2} \right) \left(\rho c_e \frac{\partial^2 T_1}{\partial t^2} - \frac{\beta_1 T_0 p^2 h^3}{24} \frac{\partial^4 w}{\partial x^2 \partial t^2} \right) \end{aligned} \quad (3.8)$$

To facilitate solution, the following dimensionless quantities are introduced

$$\begin{aligned} x' &= \frac{x}{L} & (z', u', w') &= \frac{(z, u, w)}{h} & (\tau'_\nu, \tau'_T, \tau'_q, t') &= \frac{(\tau_\nu, \tau_T, \tau_q, t)\nu}{L} \\ T'_1 &= \frac{\beta_1 T_1}{E} & (M', M'_T) &= \frac{(M, M_T)}{dEh^2} & t'_x &= \frac{t_x}{E} \\ \nu^2 &= \frac{E}{\rho} & K^* &= \frac{c_e(\lambda + 2\mu)}{4} \end{aligned} \quad (3.9)$$

Making use of equation (3.9) in (3.7) and (3.8), after surpassing the primes, we obtain

$$\begin{aligned} & \frac{\partial^4 w}{\partial x^4} + a_1 \frac{\partial^2 T_1}{\partial x^2} + a_2 \frac{\partial^2 w}{\partial t^2} = 0 \\ & \left[a_3 \left(1 + \tau_\nu \frac{\partial}{\partial t} \right) + \frac{\partial}{\partial t} \left(1 + \tau_T \frac{\partial}{\partial t} \right) \right] \left(\frac{\partial^2 T_1}{\partial x^2} - a_4 T_1 \right) \\ & = \left(1 + \tau_q \frac{\partial}{\partial t} + \frac{\tau_q^2}{2} \frac{\partial^2}{\partial t^2} \right) \left(a_5 \frac{\partial^2 T_1}{\partial t^2} - a_6 \frac{\partial^2 w}{\partial x^2 \partial t^2} \right) = 0 \end{aligned} \quad (3.10)$$

where

$$\begin{aligned} a_1 &= \frac{2dEL}{p^2 \left[(\lambda + 2\mu) \frac{dh^3}{12} + \alpha A \right]} & a_2 &= \frac{\rho A \nu^2 L^2}{(\lambda + 2\mu) \frac{dh^3}{12} + \alpha A} & a_3 &= \frac{K^* L}{K \nu} \\ a_4 &= \frac{p^2}{L^2} & a_5 &= \frac{\rho c_e \nu L}{K} & a_6 &= \frac{\beta_1^2 T_0 \nu p^2 h^3}{24KE} \end{aligned}$$

4. Problem solution

The Laplace transform is defined as

$$L\{f(t)\} = \int_0^\infty e^{-st} f(t) dt = \bar{f}(s) \quad (4.1)$$

where s is the Laplace transform parameter.

Applying the Laplace transform defined by equation (4.1) to equations (3.10) and (3.11), gives

$$\frac{d^4\bar{w}}{dx^4} + a_1\frac{d^2\bar{T}_1}{dx^2} + a_2s^2\bar{w} = 0 \quad \frac{d^2\bar{T}_1}{dx^2} - a_4\bar{T}_1 = a_7s^2\bar{T}_1 - a_8s^2\frac{d^2\bar{w}}{dx^2} \quad (4.2)$$

where

$$\begin{aligned} \bar{\tau}_q &= 1 + \tau_q s + \frac{\tau_q^2}{2}s^2 & \bar{\tau}_\nu &= 1 + \tau_\nu s & \bar{\tau}_T &= 1 + \tau_T s \\ a_7 &= \frac{a_5\bar{\tau}_q}{a_3\bar{\tau}_\nu + s\bar{\tau}_T} & a_8 &= \frac{a_6\bar{\tau}_q}{a_3\bar{\tau}_\nu + s\bar{\tau}_T} \end{aligned}$$

The set of equations (4.2) can be written as

$$\frac{d^2\bar{v}}{dx^2} = -a_9\bar{w} + a_{10}\bar{v} - a_{11}\bar{T}_1 \quad \frac{d^2\bar{T}_1}{dx^2} = -a_{12}\bar{v} + a_{13}\bar{T}_1 \quad (4.3)$$

where

$$\begin{aligned} \frac{d^2\bar{w}}{dx^2} &= \bar{v} & a_9 &= a_2s^2 & a_{10} &= a_1a_8s^2 \\ a_{11} &= a_1(a_4 + a_7s^2) & a_{12} &= a_8s^2 & a_{13} &= a_4 + a_7s^2 \end{aligned}$$

The system of equations (4.4) can be written in a matrix form as

$$D\mathbf{V}(x, s) = \mathbf{A}\mathbf{V}(x, s) \quad (4.4)$$

where

$$\mathbf{V} = \begin{bmatrix} \mathbf{U} \\ D\mathbf{U} \end{bmatrix} \quad \mathbf{U} = \begin{bmatrix} \bar{w} \\ \bar{v} \\ \bar{T}_1 \end{bmatrix} \quad \mathbf{A} = \begin{bmatrix} \mathbf{O} & \mathbf{I} \\ \mathbf{A}_1 & \mathbf{O} \end{bmatrix} \quad \mathbf{A}_1 = \begin{bmatrix} 0 & 1 & 0 \\ -a_9 & a_{10} & -a_{11} \\ 0 & -a_{12} & a_{13} \end{bmatrix} \quad (4.5)$$

and $D = d/dz$, \mathbf{I} is the identity matrix of the order 3, \mathbf{O} is a null matrix of the order 3.

We take the solution to equation (4.4) as

$$\mathbf{V}(x, s) = \mathbf{X}_r(x, s)e^{\lambda z} \quad (4.6)$$

such that

$$\mathbf{A}(x, s)\mathbf{V}(x, s) = \lambda\mathbf{V}(x, s) \quad (4.7)$$

which leads to the eigenvalue approach. The characteristic equation of the matrix \mathbf{A} can be written as

$$\lambda^6 - G_1\lambda^4 + G_2\lambda^2 - G_3 = 0 \quad (4.8)$$

where

$$G_1 = a_{10} + a_{13} \quad G_2 = a_9 + a_{10}a_{13} - a_{11}a_{12} \quad G_3 = a_9a_{13}$$

The characteristic roots of equation (4.6) are also the eigenvalues of the matrix \mathbf{A} . The eigenvectors $\mathbf{X}(x, s)$ corresponding to the eigenvalue λ_r can be determined by solving the homogeneous equations

$$(\mathbf{A} - \lambda\mathbf{I})\mathbf{X}(x, s) = \mathbf{0} \quad (4.9)$$

The set of eigenvectors $\mathbf{X}_r(x, s)$ may be obtained as

$$\mathbf{X}_r(x, s) = \begin{bmatrix} \mathbf{X}_{r1}(x, s) \\ \mathbf{X}_{r2}(x, s) \end{bmatrix} \quad \mathbf{X}_{r1}(x, s) = \begin{bmatrix} b_r \\ c_r \\ d_r \end{bmatrix} \quad \mathbf{X}_{r2}(x, s) = \lambda_r \mathbf{X}_{r1}(x, s)$$

for $\lambda = \lambda_r, r = 1, 2, 3$ and

$$\mathbf{X}_j(x, s) = \begin{bmatrix} \mathbf{X}_{j1}(x, s) \\ \mathbf{X}_{j2}(x, s) \end{bmatrix} \quad \mathbf{X}_{j1}(x, s) = \begin{bmatrix} b_r \\ c_r \\ d_r \end{bmatrix} \quad \mathbf{X}_{j2}(x, s) = \lambda_j \mathbf{X}_{j1}(x, s)$$

for $j = r + 4, \lambda = -\lambda_r, r = 1, 2, 3$ and

$$b_r = -a_{11} \quad c_r = -a_{11}\lambda_r^2 \quad d_r = \lambda_r^4 - a_{10}\lambda_r^2 + a_9$$

The solution to equation (4.6) reduces to

$$\mathbf{V} = \sum_{r=1}^3 B_r \mathbf{X}_r(x, s) e^{-\lambda_r x} + \sum_{r=1}^3 B_{r+3} \mathbf{X}_{r+3}(x, s) e^{\lambda_r x} \tag{4.10}$$

where $B_i (i = 1, \dots, 6)$ are arbitrary constants.

Thus, the field quantities can be written as

$$(\bar{w}, \bar{v}, \bar{T}_1)(x, s) = \sum_{r=1}^3 (b_r, c_r, d_r) B_r e^{-\lambda_r x} + \sum_{j=1}^3 (b_{j+3}, c_{j+3}, d_{j+3}) B_{j+3} e^{\lambda_j x} \tag{4.11}$$

5. Initial and boundary conditions

Both initial and boundary conditions should be considered to solve the problem. The initial conditions of the problem are taken in the form as

$$w(x, t) \Big|_{t=0} = \frac{\partial w(x, t)}{\partial t} \Big|_{t=0} = 0 \quad T_1(x, t) \Big|_{t=0} = \frac{\partial T_1(x, t)}{\partial t} \Big|_{t=0} = 0 \tag{5.1}$$

Let us consider a nanobeam with both ends are simply supported

$$w(0, t) = 0 \quad \frac{\partial^2 w(0, t)}{\partial x^2} = 0 \quad w(L, t) = 0 \quad \frac{\partial^2 w(L, t)}{\partial x^2} = 0 \tag{5.2}$$

We consider the side of the nanobeam $x = 0$ being thermally loaded by ramp-type heating incidents into the surface of the nanobeam

$$T_1(0, t) = g_0 \begin{cases} 0 & t \leq 0 \\ t/t_0 & 0 < t \leq t_0 \\ 1 & t > t_0 \end{cases} \tag{5.3}$$

where t_0 is a non-negative constant called the ramp type parameter and g_0 is a constant.

We also assume that the other side of the nanobeam $x = L$ is thermally insulated, and there is no variation of temperature on it, which this means that the following relation will be satisfied

$$\frac{dT_1(L, t)}{dx} = 0 \tag{5.4}$$

Applying the Laplace transform defined by equation (4.1) to boundary conditions (5.2)-(5.4), we obtain

$$\begin{aligned} \bar{w}(0, s) = 0 \quad \frac{d^2 \bar{w}(0, s)}{dx^2} = 0 \quad \bar{T}_1(0, s) = g_0 \left(\frac{1 - e^{-st_0}}{t_0 s^2} \right) \\ \bar{w}(1, s) = 0 \quad \frac{d^2 \bar{w}(1, s)}{dx^2} = 0 \quad \frac{d \bar{T}_1(1, s)}{dx} = 0 \end{aligned} \quad (5.5)$$

The values of displacement \bar{u} and axial stress \bar{t}_x are then obtained

$$\begin{aligned} \bar{u}(x, s) = z \left(\sum_{i=1}^3 \lambda_i b_i B_i e^{-\lambda_i x} - \sum_{i=1}^3 \lambda_i b_{i+3} B_{i+3} e^{\lambda_i x} \right) \\ \bar{t}_x(x, s) = - \left[\sum_{i=1}^3 \left(\frac{\lambda + 2\mu}{E} z \lambda_i^2 b_i + d_i \sin(pz) \right) B_i e^{-\lambda_i x} \right. \\ \left. + \sum_{i=1}^3 \left(\frac{\lambda + 2\mu}{E} z \lambda_i^2 b_{i+3} + d_{i+3} \sin(pz) \right) B_{i+3} e^{\lambda_i x} \right] \end{aligned} \quad (5.6)$$

Making use of the value of \bar{w} and \bar{T}_1 from (4.11) in boundary conditions (5.5), with the aid of equations (5.6), after some calculations, we find the expressions of the displacement component, lateral deflection, temperature change and axial stress of the beam as

$$\begin{aligned} (\bar{u}, \bar{w})(x, s) = \sum_{i=1}^3 (z \lambda_i, 1) b_i B_i e^{-\lambda_i x} + \sum_{i=1}^3 (-\lambda_i, 1) b_{i+3} B_{i+3} e^{\lambda_i x} \\ (\bar{T}_1, \bar{t}_x)(x, s) = \sum_{i=1}^3 (d_i, M_i) B_i e^{-\lambda_i x} + \sum_{i=1}^3 (d_{i+3}, M_{i+3}) B_{i+3} e^{\lambda_i x} \end{aligned} \quad (5.7)$$

where

$$B_i = \frac{\Delta_i}{\Delta} \quad i = 1, \dots, 6$$

and

$$\begin{aligned} \sum_{i=1}^3 M_i = - \left(\frac{\lambda + 2\mu}{E} z \lambda_i^2 b_i + d_i \sin(pz) \right) \quad \sum_{i=1}^3 M_{i+3} = - \left(\frac{\lambda + 2\mu}{E} z \lambda_i^2 b_{i+3} + d_{i+3} \sin(pz) \right) \\ \Delta = \begin{bmatrix} b_1 & b_2 & b_3 & b_4 & b_5 & b_6 \\ b_1 e^{-\lambda_1} & b_2 e^{-\lambda_2} & b_3 e^{-\lambda_3} & b_4 e^{\lambda_2} & b_5 e^{\lambda_2} & b_6 e^{\lambda_2} \\ b_1 \lambda_1^2 & b_2 \lambda_2^2 & b_3 \lambda_3^2 & b_4 \lambda_1^2 & b_5 \lambda_2^2 & b_6 \lambda_3^2 \\ b_1 \lambda_1^2 e^{-\lambda_1} & b_2 \lambda_2^2 e^{-\lambda_2} & b_3 \lambda_3^2 e^{-\lambda_3} & b_4 \lambda_1^2 e^{-\lambda_1} & b_5 \lambda_2^2 e^{-\lambda_2} & b_6 \lambda_3^2 e^{-\lambda_3} \\ d_1 & d_2 & d_3 & d_4 & d_5 & d_6 \\ -d_1 \lambda_1 e^{-\lambda_1} & -d_2 \lambda_2 e^{-\lambda_2} & -d_3 \lambda_3 e^{-\lambda_3} & -d_4 \lambda_1 e^{\lambda_1} & d_5 \lambda_2 e^{\lambda_2} & d_6 \lambda_3 e^{\lambda_3} \end{bmatrix} \end{aligned}$$

where Δ_i ($i = 1, \dots, 6$) are obtained by replacing the i -th column with $[0, 0, 0, 0, g_0((1 - e^{-st_0})/(t_0 s^2)), 0]^T$ in Δ_i .

6. Particular cases

(i) Dual-phase-lag model

If $K^* = \tau_\nu = 0$, in equations (5.7), we obtain the corresponding results for modified couple stress thermoelastic materials with the dual-phase-lag model of thermoelasticity.

(ii) GN-III model

In the absence of $\tau_\nu = \tau_T = \tau_q = \tau_q^2 = 0$ in equations (5.7), we obtain the corresponding results for modified couple stress thermoelastic materials with energy dissipation in the context of GN-III theory of thermoelasticity.

(iii) If we take $\alpha = 0$ in equations (5.7), we obtain the corresponding results for thermoelastic materials with the three-phase-lag model of thermoelasticity. Our results in a special case are similar to those obtained by Sur and Kanoria (2014).

7. Inversion of the Laplace transform

We have obtained solutions for the displacement component, lateral deflection, temperature change and axial stress in the Laplace transform domain (x, s) . We shall now briefly outline the numerical inversion method used to find the solution in the physical domain. Let $\bar{f}(s)$ be the Laplace transform of a function $f(t)$. To obtain the solution of the problem in the physical domain, we invert the Laplace transform by using the method described by Kumar (2016).

8. Numerical results and discussion

We have chosen gold (Au) as the material for numerical computations. The physical data for gold are given by Sur and Kanoria (2014): $\lambda = 198$ GPa, $\mu = 27$ GPa, $\alpha_t = 14.2 \cdot 10^{-6} \text{ K}^{-1}$, $\rho = 1930 \text{ kg/m}^3$, $T_0 = 0.293 \cdot 10^3 \text{ K}$, $\nu = 0.44$, $K = 200 \text{ W/(mK)}$, $c_e = 130 \text{ J/(kg K)}$, $\alpha = 2.5 \text{ kg m/s}^2$, $t = 1.5 \text{ s}$, $\tau_\nu = 0.02 \text{ s}$, $\tau_T = 0.03 \text{ s}$, $\tau_q = 0.04 \text{ s}$, $g_0 = 1$, $t_0 = 0.2$, $L = 1$, $d = 1$, $h = 10$.

Numerical computations have been carried out with the help of MATLAB software. By using this software, the displacement component, lateral deflection, temperature change, thermal stress, bending moment and axial stress with respect to distance are computed numerically and shown graphically in Figs. 2-7. In Figs. 2-4, the small dash line (- - -) corresponds to the three-phase-lag model (TPL), small dash line with the centre symbol (- - * - -) corresponds to the dual-phase-lag model (DPL) and a small dash line with the centre symbol (- - o - -) corresponds to the GN-III model respectively. Similarly, Figs. 5-7, the small dash line (- - -) corresponds to $t_0 = 0.2$, small dash line with the centre symbol (- - * - -) corresponds to $t_0 = 0.4$, the small dash line with the centre symbol (- - o - -) corresponds to $t_0 = 0.6$.

Figure 2a shows the variation of the displacement component with respect to length of the beam for different models. The behavior and variation are similar for all the cases but with differences in their magnitudes. However, the values of the GN-III model are greater than compared to DPL and TPL models. Figure 2b depicts the variation of lateral deflection with respect to length of the beam for the three-phase-lag, dual-phase-lag and GN-III models. It is observed that the lateral deflection decreases for smaller values of length and oscillates for higher values of length for all TPL, DPL and GN-III models.

Figure 3a presents the variation of axial stress with respect to length of the beam for TPL, DPL, GN-III models. As seen in the figure, the axial stress decreases smoothly in the whole region for all cases. Also, it is noticed that the axial stress has a large value for the three-phase-lag (TPL) and dual-phase-lag (DPL) thermoelastic beams as compared to that for the GN-III thermoelastic beam. Figure 3b shows the variation of temperature change with respect to length of the beam for different thermoelastic (TPL, DPL, GN-III) models. It is observed from the figure that the behavior and variation are oscillatory in nature with fluctuating values in all the cases.

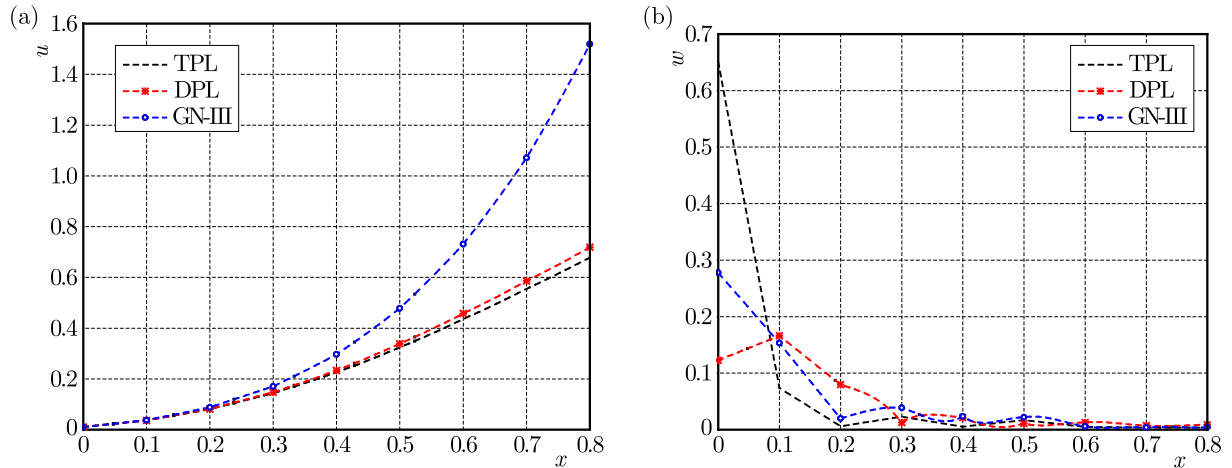


Fig. 2. (a) Displacement component u and (b) lateral deflection w with respect to distance x for different phase lag theories of thermoelasticity

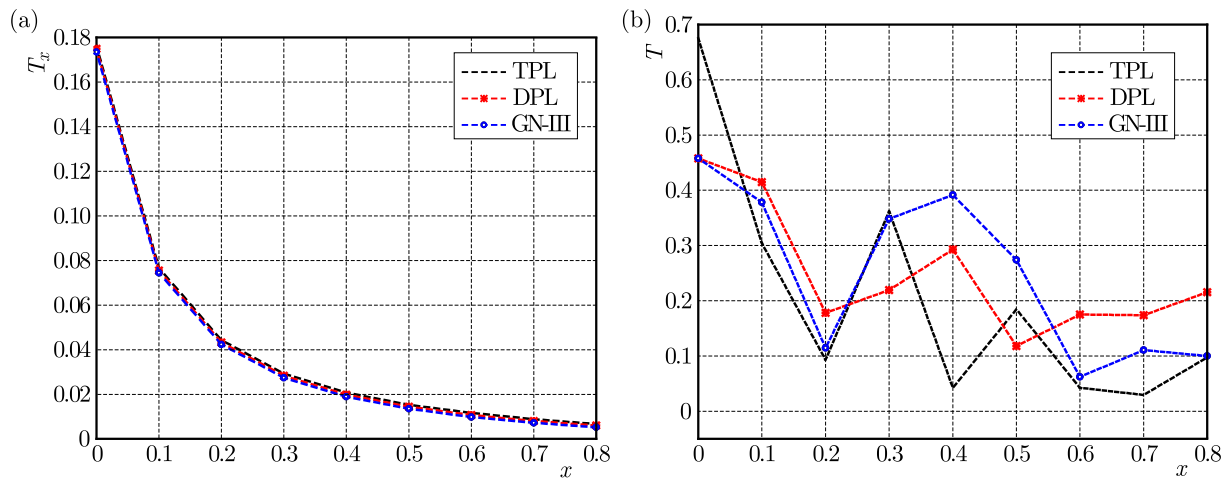


Fig. 3. (a) Axial stress T_x and (b) temperature change T with respect to distance x for different phase lag theories of thermoelasticity

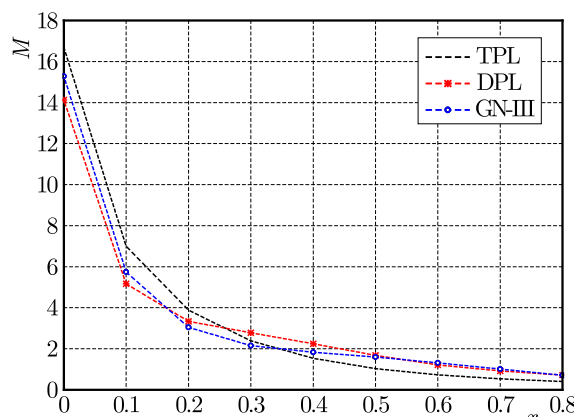


Fig. 4. Bending moment M with respect to distance x for different phase lag theories of thermoelasticity

Figure 4 shows the variation of bending moment with respect to length of the beam for different thermoelastic models. It is clearly seen in the figure that the value of bending moment decreases with a decrease in the value of length for all the cases of phase lag theories of thermoelasticity. Also, the value of bending moment is higher in the range $0 \leq x \leq 0.25$ for $t_0 = 0.2$ and smaller for $t_0 = 0.4, 0.6$ in the remaining range.

Figure 5a shows the variation of lateral deflection with respect to length of the beam for different values of the ramp type parameter. Initially, the lateral deflection decreases with a difference in the ramp type parameter up to $x \leq 0.3$ and then remains stable in the range $0.3 < x \leq 0.8$. Figure 5b presents the variation of temperature change with respect to length of the beam for different values of the ramp type parameter. The behavior and variation are oscillatory in nature for all the cases of the ramp type parameter.

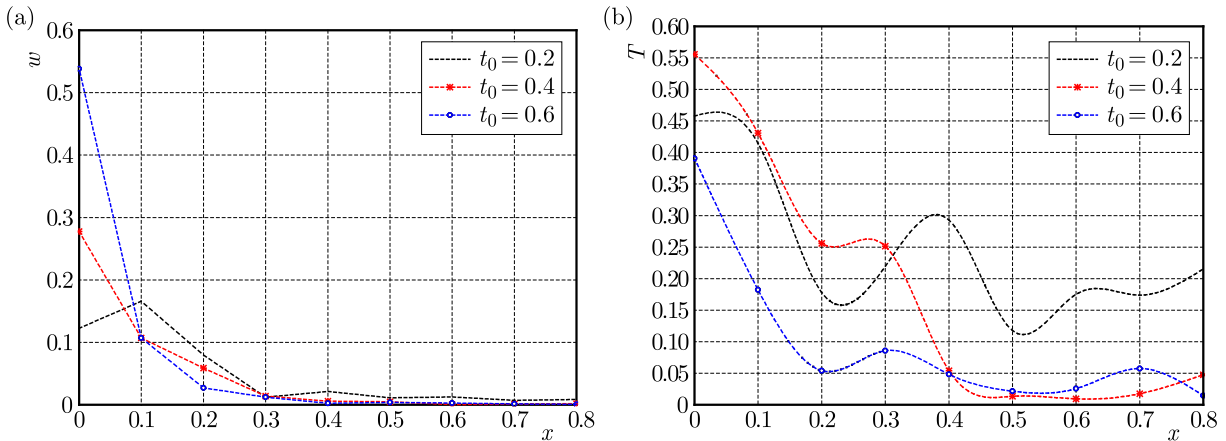


Fig. 5. (a) Lateral deflection w and (b) temperature change T with respect to length x for different values of the ramp type parameter

Figure 6a shows the variation of axial stress with respect to length of the beam for different values of the ramp type parameter. The value of axial stress decreases monotonically with an increase in length. Also, the value of axial stress for $t_0 = 0.2$ is greater than that the ramp type parameter $t_0 = 0.4, 0.6$.

Figure 6b depicts the variation of displacement component with respect to length of the beam for different values of the ramp type parameter. The displacement component increases with an increase in length.

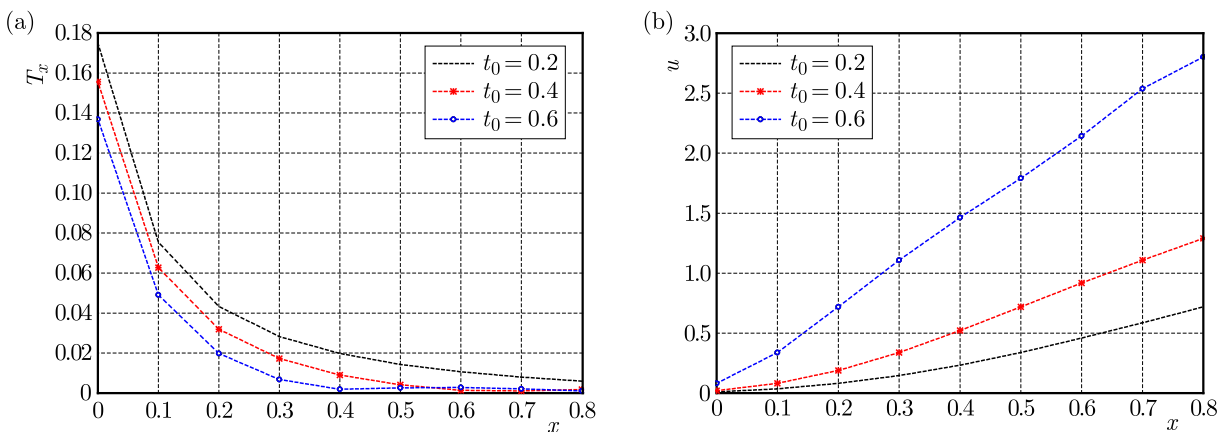


Fig. 6. (a) Axial stress T_x and (b) displacement component u with respect to distance x for different values of the ramp type parameter

Figure 7a represents the variation of bending moment with respect to length of the beam for different values of the ramp type parameter. The bending moment smoothly decreases with a decrease in the value of length. The value of the bending moment is greater for $t_0 = 0.2$ up to the value of $x = 0.25$ in comparison with that for $t_0 = 0.4, 0.6$, but shows opposite behavior in the remaining range. Figure 7b depicts the variation of thermal stress with respect to length of the beam for different values of the ramp type parameter. The oscillatory behavior is shown for

all the cases of ramp type parameters. It is clear from the figure that the value of thermal stress for $t_0 = 0.6$ is less in the range $0 \leq x \leq 0.5$ but reversed behavior is shown for $t_0 = 0.2, 0.4$ in the considered region.

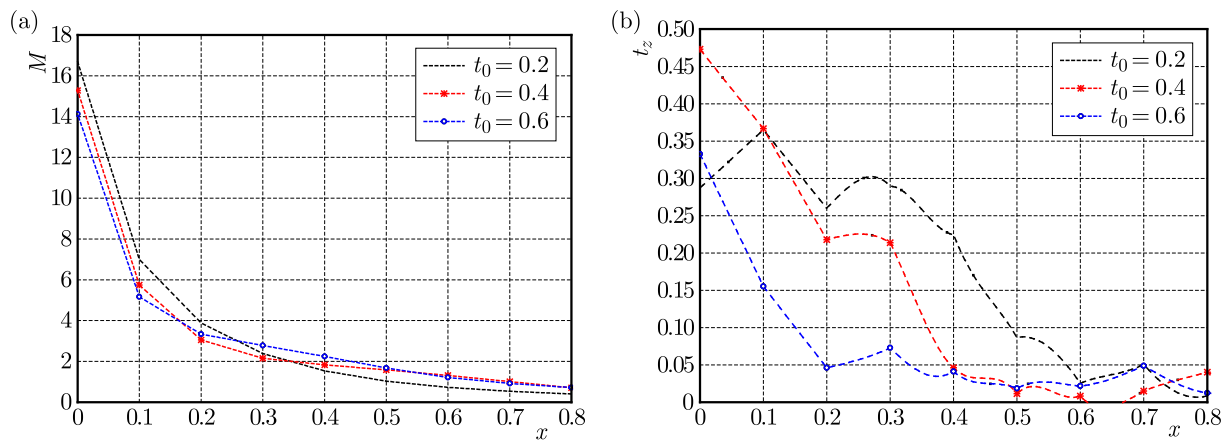


Fig. 7. (a) Bending moment M and (b) thermal stress t_z with respect to distance x for different values of the ramp type parameter

9. Conclusions

In the present study, the effects of three-phase-lag, dual-phase-lag and GN-III on the displacement component, lateral deflection, axial stress, bending moment and temperature change are derived numerically and presented graphically. The effect of the ramp type parameter is shown graphically for lateral deflection, bending moment, displacement component, axial stress, thermal stress and temperature change. The Euler Bernoulli beam assumption and the Laplace transform technique are used to write the basic governing equations in form of vector-matrix differential equations which are then calculated by the eigenvalue approach. A numerical technique has been adopted to determine solutions in the physical domain. It is observed from the obtained figures that the displacement component increases with a increase in length for all the three-phase-lag, dual-phase-lag and GN-III models but opposite behavior is observed for the axial stress. It is also noticed that the values of displacement component and axial stress for the three-phase-lag thermoelastic model is greater in comparison with the dual-phase-lag and GN-III models. The lateral deflection and temperature change are oscillatory in nature but differ in their magnitude values for all the cases. The method used in the present study is applicable to a wide range of mathematical problems in the field of thermodynamics, thermoelasticity and couple stress theory. This study also find various applications to applied mathematics, mechanical engineering, geophysical and industrial sectors.

References

1. ABBAS I.A., KUMAR R., RANI L., 2015, Thermoelastic interaction in a thermally conducting cubic crystal subjected to ramp-type heating, *Applied Mathematics and Computation*, **254**, 360-369
2. ABOUELREGAL A.E., ZENKOUR A.M., 2014, Effect of phase lags on thermoelastic functionally graded microbeams subjected to ramp-type heating, *Iranian Journal of Science and Technology: Transactions of Mechanical Engineering*, **38**, M2, 321-335
3. ASGHARI M., 2012, Geometrically nonlinear micro-plate formulation based on the modified couple stress theory, *International Journal of Engineering Science*, **51**, 292-309

4. COSSERAT E., COSSERAT F., 1909, *Theory of Deformable Bodies*, Hermann et Fils, Paris
5. CHEN W., LI L., XU M., 2011, A modified couple stress model for bending analysis of composite laminated beams with first order shear deformation, *Composite Structures*, **93**, 2723-2732
6. CHEN W., WANG Y., 2016, A model of composite laminated Reddy plate of the global-local theory based on new modified couple-stress theory, *Mechanics of Advanced Materials and Structures*, **23**, 6, 636-651
7. DARIJANI H., SHAHDADI A.H., 2015, A new shear deformation model with modified couple stress theory for microplates, *Acta Mechanica*, **226**, 2773-2788
8. GREEN A.E., NAGHDI P.M., 1993, Thermoelasticity without energy dissipation, *Journal of Elasticity*, **31**, 189-209
9. HETNARSKI R.B., IGNACZAK J., 1999, Generalized thermoelasticity, *Journal of Thermal Stresses*, **22**, 451-476
10. KUMAR R., 2016, Response of thermoelastic beam due to thermal source in modified couple stress theory, *Computational Methods in Science and Technology*, **22**, 2, 87-93
11. KUMAR R., CHAWLA V., ABBAS I.A., 2012, Effect of viscosity on wave propagation in anisotropic thermoelastic medium with three-phase-lag model, *Theoretical and Applied Mechanics*, **39**, 4, 313-341
12. KUMAR R., DEVI S., 2015, Interaction due to Hall current and rotation in a modified couple stress elastic half-space due to ramp-type loading, *Computational Methods in Science and Technology*, **21**, 4, 229-240, DOI:10.12921/cmst.2015.21.04.007.
13. KUMAR R., SINGH R., CHADHA T.K., 2007, Eigenvalue approach to micropolar thermoelasticity without energy dissipation, *Indian Journal of Mathematics*, **49**, 3, 355-369
14. MA H.M., GAO X.L., REDDY J.N., 2008, A microstructure-dependent Timoshenko beam model based on a modified couple stress theory, *Journal of the Mechanics and Physics of Solids*, **56**, 3379-3391
15. MOHAMMAD-ABADI M., DANESHMEHR A.R., 2014, Size dependent buckling analysis of micro beams based on modified couple stress theory with high order theories and general boundary conditions, *International Journal of Engineering Science*, **74**, 1-14
16. QUINTANILLA R., RACKE R.A., 2008, Note on stability in three-phase-lag heat conduction, *International Journal of Heat Mass Transfer*, **51**, 1/2, 24-29
17. RAO S.S., 2007, *Vibration of Continuous Systems*, John Wiley & Sons, Inc. Hoboken, New Jersey
18. REDDY J.N., ROMANOFF J., LOYA J.A., 2016, Nonlinear finite element analysis of functionally graded circular plates with modified couple stress theory, *European Journal of Mechanics – A/Solids*, **56**, 92-104
19. REZAZADEH G., VAHDAT A.S., TAYEFEH-REZAEI S., CETINKAYA C., 2012, Thermoelastic damping in a micro-beam resonator using modified couple stress theory, *Acta Mechanica*, **223**, 6, 1137-1152
20. ROYCHOUDHURI S.K., 2007, On a thermoelastic three-phase-lag model, *Journal of Thermal Stresses*, **30**, 231-238
21. SIMSEK M., REDDY J.N., 2013, Bending and vibration of functionally graded microbeams using a new higher order beam theory and the modified couple stress theory, *International Journal of Engineering Science*, **64**, 37-53
22. SUR A., KANORIA M., 2014, Vibration of a gold-nanobeam induced by ramp type laser pulse three-phase-lag model, *International Journal of Applied Mathematics and Mechanics*, **10**, 5, 86-104
23. TZOU D.Y., 1995a, A unified field approach for heat conduction from micro to macroscales, *ASME Journal of Heat Transfer*, **117**, 8-16

24. TZOU D.Y., 1995b, Experiments support for the lagging behaviour in heat propagation, *Journal of Thermophysics and Heat Transfer*, **9**, 686-693
25. TZOU D.Y., 1997, *Macro to Microscale Heat Transfer: the Lagging Behaviour*, Series in Chemical and Mechanical Engineering, Taylor & Francis, Washington, DC
26. YAGHOUB T.B., FAHIMEH M., HAMED R., 2015, Free vibration analysis of size-dependent shear deformable functionally graded cylindrical shell on the basis of modified couple stress theory, *Composite Structures*, **120**, 65-78
27. YANG F., CHONG A.C.M., LAM D.C.C., TONG P., 2002, Couple stress based strain gradient theory for elasticity, *International Journal of Solids and Structures*, **39**, 2731-2743
28. YONG-GANG W., WEN-HUI L., LIU N., 2015, Nonlinear bending and post-buckling of extensible microscale beams based on modified couple stress theory, *Applied Mathematical Modelling*, **39**, 117-127
29. ZANG J., FU Y., 2012, Pull-in analysis of electrically actuated viscoelastic microbeams based on a modified couple stress theory, *Meccanica*, **47**, 1649-1658
30. ZENKOUR A.M., ABOUELREGAL A.E., 2015, Effects of phase-lags in a thermoviscoelastic orthotropic continuum with a cylindrical hole and variable thermal conductivity, *Archives of Mechanics*, **67**, 6, 457-475
31. ZENKOUR A.M., ABOUELREGAL A.E., 2016, Effect of ramp-type heating on the vibration of functionally graded microbeams without energy dissipation, *Mechanics of Advanced Materials and Structures*, **23**, 5, 529-537

Manuscript received September 16, 2016; accepted for print April 31, 2017

ON THE OPTIMUM ABSORBER PARAMETERS: REVISING THE CLASSICAL RESULTS

VOLODYMYR PUZYROV

*Donetsk National University, Department of Higher Mathematics and Methodology of Teaching, Donetsk, Ukraine
e-mail: doe.seldon@gmail.com*

JAN AWREJCEWICZ

*Lodz University of Technology, Department of Automation, Biomechanics and Mechatronics, Łódź, Poland
e-mail: awrejcew@p.lodz.pl*

The dynamic vibration absorber is a kind of mechanical device with inertia, stiffness, and damping. Once connected to a given structure or machine, it is capable of absorbing vibratory energy. As a result, the primary system can be protected from excessively high vibration levels. In this paper, we deal with classical Den Hartog's model to clarify the known results and improve the mathematical component of this approach. We suggest the optimal choice of absorber parameters, which is slightly different and more general analytical approach. The comparison of two methods of optimization is carried out, and the corresponding error of calculus is estimated.

Keywords: dynamic vibration absorber, Den Hartog's model, frequency-amplitude curve, optimization

1. Introduction

The problem of elimination or reduction of undesired vibration in various technical systems has long history and great achievements. The concept of vibration control is widely accepted nowadays and has been applied in many different areas, such as civil, mechanical, and aeronautical engineering. Passive vibration control is the most widespread, and effective methods are available. The typical simplest and most reliable device is the dynamic vibration absorber (DVA) or tuned-mass damper (TMD). A simple DVA consists of a mass and a spring. When the primary system is excited by a harmonic force, its vibration can be suppressed by attaching a DVA. The main purpose of adding the secondary oscillator is to move the resonant frequency of the mechanical system away from the operating frequency of the vibratory force. So, the system becomes a 2-DOF (degree of freedom) mechanical system, but with coincidence of the exciting frequency with one of the two natural frequencies it will be again at resonance. To eliminate this effect, a damper is added to the DVA (Fig. 1).

The idea of vibration control was originally proposed by Frahm (1911), and many various DVA configurations were designed during the past century (Ormondroyd and Den Hartog, 1928; Brock, 1946; Mead, 2000; Hunt, 1979; Korenev and Reznikov, 1993; Viet *et al.*, 2011; Marano *et al.*, 2007). Good surveys on the subject were presented in (Johnson, 1995; Sun *et al.*, 1995). With reference to the DVA optimal design, the first criterion was offered by Ormondroyd and Den Hartog (1928). This criterion concerned the minimization of the system response with respect to the stationary harmonic excitation with the most "dangerous" frequency value which results in the largest increase of the amplitude.

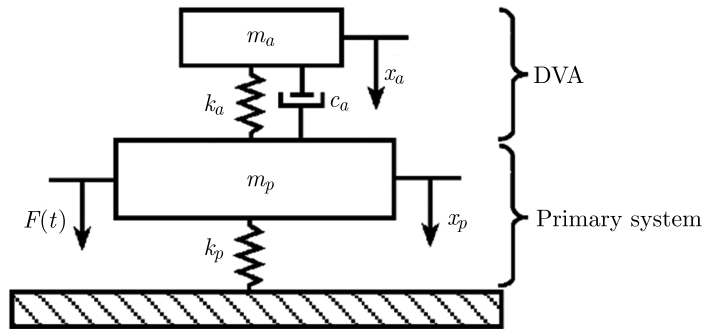


Fig. 1. Damped DVA connected to a primary system

2. Formulation of the problem

The equations of motion of the mechanical system under consideration are

$$\begin{aligned} m_p \ddot{x}_p + c_a(\dot{x}_p - \dot{x}_a) + k_p x_p + k_a(x_p - x_a) &= F_0 e^{i\omega t} \\ m_a \ddot{x}_a + c_a(\dot{x}_a - \dot{x}_p) + k_a(x_a - x_p) &= 0 \end{aligned} \quad (2.1)$$

In this formulation, we use the notions according to (Johnson, 1995), $F(t) = F_0 e^{i\omega t}$ is a harmonic excitation force acting on the primary system.

The amplitudes of steady state harmonic responses are

$$\begin{aligned} X_p &= F_0 \frac{k_a - m_a \omega^2 + i\omega c_a}{(k_p - m_p \omega^2)(k_a - m_a \omega^2) - m_a k_a \omega^2 + i\omega c_a (k_p - m_p \omega^2 - m_a \omega^2)} \\ X_a &= -F_0 \frac{k_a + i\omega c_a}{(k_p - m_p \omega^2)(k_a - m_a \omega^2) - m_a k_a \omega^2 + i\omega c_a (k_p - m_p \omega^2 - m_a \omega^2)} \end{aligned} \quad (2.2)$$

In terms of dimensionless parameters, we can rewrite

$$\frac{|X_p|}{(X_p)_{st}} = \sqrt{\frac{(2\zeta g)^2 + (g^2 - \eta^2)^2}{(2\zeta g)^2 (g^2 - 1 + \mu g^2) + [\mu \eta^2 g^2 + (g^2 - 1)(g^2 - \eta^2)]}} \quad (2.3)$$

where $\mu = m_a/m_p$ is the mass ratio; $\omega_a = \sqrt{k_a/m_a}$ – undamped natural frequency of the DVA considered separately; $\omega_p = \sqrt{k_p/m_p}$ – undamped natural frequency of the primary system considered separately; $\eta = \omega_a/\omega_p$ – tuning factor; $g = \omega/\omega_p$ – forcing frequency ratio; $\zeta = c_a/(2m_a\omega_p)$ – damping ratio; $(X_p)_{st} = F_0/k_p$ – static displacement of the primary mass.

Many methods of optimization have been developed to opportunely design this vibration control technique. In the classical textbook on mechanical vibrations, Den Hartog (1940) pointed out a remarkable feature: for any fixed values of η and μ , curves (2.3) intersect in two points P and Q (named “invariant points”), as shown in Fig. 2, independently of the value of ζ . These points are situated close enough to the peaks of the frequency-amplitude curve. Den Hartog suggested to choose the parameter η to equalize ordinates of P and Q . Secondly, ζ was taken to satisfy the condition of “almost horizontal” tangents in the invariant points. Thus the values

$$\eta_{opt} = \frac{1}{1 + \mu} \quad \zeta_{opt} = \sqrt{\frac{3\mu}{8(1 + \mu)^3}} \quad (2.4)$$

were obtained.

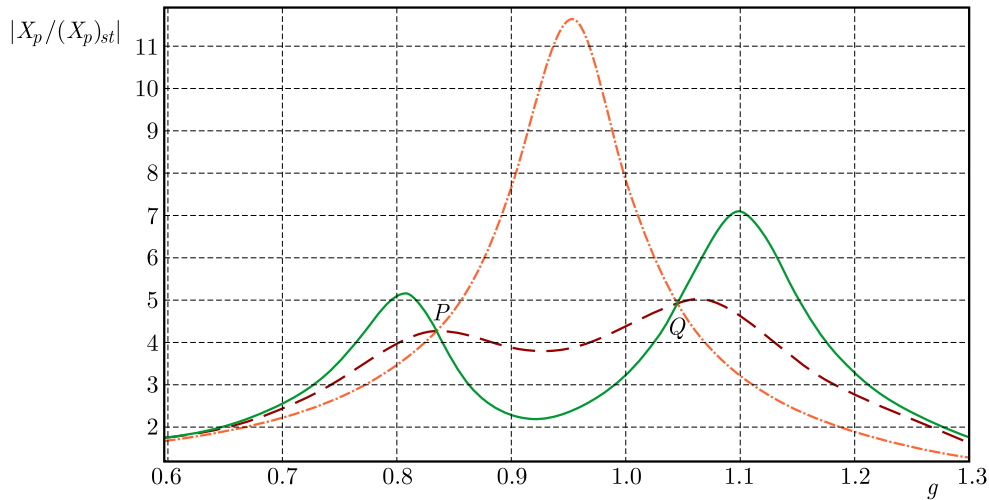


Fig. 2. Invariant points for $\eta = 0.9$, $\mu = 0.1$. Solid line $\zeta = 0.027$, long dash line $\zeta = 0.16$, dot-dash line $\zeta = 0.5$

3. Mathematical analysis of the problem

The approach of Den Hartog has undoubted advantages: simplicity, which is essential for applied researchers, and rather high accuracy, as was shown in numerical simulations. At the same time, it is possible to note two drawbacks of this approach. The first one is the absence of analytical assessment of the difference between the maximum response value proposed and the true value. The second is that the scheme of determining the optimal values is based on the existence of invariant points, which is an exception rather than the rule. For example, this approach does not fit in the case when the main body is damped itself (Warbrton and Ayorinde, 1980), or for sky-hooked (Griffin *et al.*, 2002; Liu and Liu, 2005) DVA. So, in such cases, one have to rely upon numerical methods for optimization. It should be added that from the theoretical viewpoint, the question on the existence of the exact solution of the problem in an algebraic form is not closed.

Considering the above-mentioned, our aims are: 1) to provide a more general approach which does not rely on exclusive properties of (2.3) (invariant points existence); 2) to evaluate the error of formulas (2.4).

At the beginning, let us consider a function

$$f(\mu, \delta, h, \gamma) = \frac{h\gamma + (\gamma - \delta)^2}{h\gamma(\gamma + \mu\gamma - 1)^2 + [\mu\delta\gamma - (\gamma - 1)(\gamma - \delta)]^2} \tag{3.1}$$

which we believe is more suitable for the analysis. Here

$$\delta = \eta^2 \quad h = 4\zeta^2 \quad \gamma = g^2 \quad f = \left(\frac{|X_p|}{(X_p)_{st}} \right)^2 \tag{3.2}$$

Obviously, the optimization of function (2.3) is the same as function (3.1). The optimal values from (2.4) in the new notions are

$$\delta = \frac{1}{(1 + \mu)^2} \quad h = \frac{3\mu}{2(1 + \mu)^3} \tag{3.3}$$

The typical shapes of the surface $f(\gamma, \mu)$ with fixed values δ, h are presented in Fig. 3.

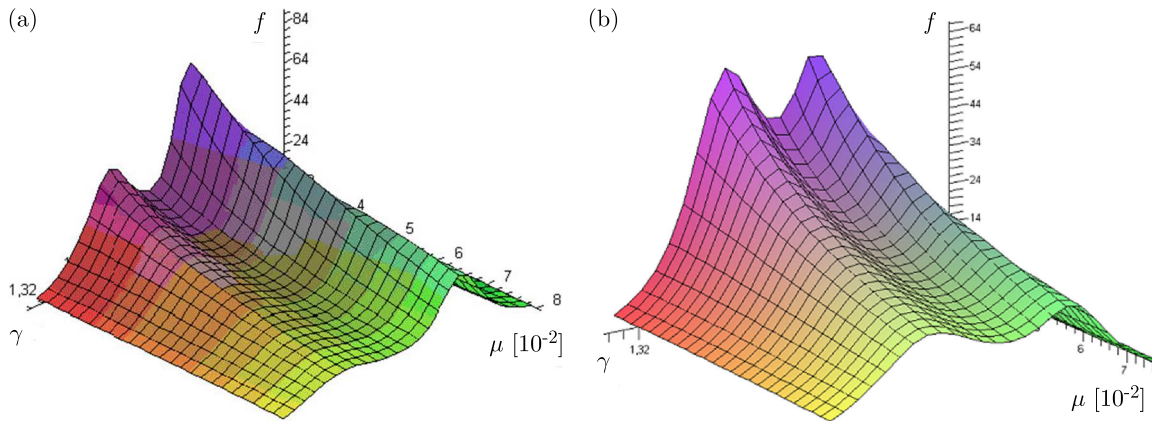


Fig. 3. Typical character of surface (3.1): (a) $\delta = 1 - 2.5\mu$, $h = 0.5$, (b) according to Eqs. (3.3)

It is remarkable that for any given set of (δ, h, μ) , zeros of the derivative $df/d\gamma$ lead to the following equation

$$\begin{aligned} &\gamma^5 - \gamma^4[4\delta - 2h + \mu(\delta - h) - \frac{1}{2}h\mu^2] + \gamma^3[6\delta^2 + 4\delta - 4h\delta + h^2 - 2h + 2\mu(2\delta^2 - 3h\delta + h^2) \\ &\quad - h\mu^2(2\delta - h)] - \gamma^2[4\delta^3 - 2h\delta^2 + 6\delta^2 - 4h\delta + h^2 + \mu(5\delta^3 - 4h\delta^2 + \delta^2 - 3h\delta + h^2)] \\ &\quad + \gamma\delta^2[\delta^2 + 4\delta - 2h + 2\mu(\delta^2 + \delta - h) + \mu^2\delta^2] - \delta^4(1 + \mu) = 0 \end{aligned} \tag{3.4}$$

This equation of the 5-th order cannot be solved in an explicit form and, therefore, there is no way to make a conclusion on the maximum value of f . Because of this, we require an indirect method to achieve our goal.¹

Let $f_0 = 1/\kappa$ be some fixed number. Then the equation $f = f_0$ is equivalent to the following polynomial equation

$$\begin{aligned} u(\gamma) = &\gamma^4 + (h + h\mu^2 + 2h\mu - 2 - 2\delta - 2\mu\delta)\gamma^3 + (\mu^2\delta^2 + 4\delta - 2h + 2\mu\delta - 2h\mu + 1 \\ &+ \delta^2 - \kappa + 2\mu\delta^2)\gamma^2 + (h - 2\delta^2 - 2\mu\delta^2 + 2\delta\kappa - 2\delta - h\kappa)\gamma + \delta^2 - \delta^2\kappa = 0 \end{aligned} \tag{3.5}$$

In the case when curve (3.1) has two peaks, for some values of κ the line

$$f = \frac{1}{\kappa} \tag{3.6}$$

intersects this curve four times, and equation (3.5) has four real positive roots. Otherwise, when line (3.6) is above curve (3.1), equation (3.5) has no positive roots. On the assumption that both peaks have the same height, we conclude that this is a borderline between two cases. In other words, the discriminant of the polynomial $u(\gamma)$ is equal to zero, and (3.5) has two pairs of multiple roots. Thereby, there exist such expressions $M(\mu, \delta, h)$, $N(\mu, \delta, h)$ that

$$u(\gamma) = (\gamma^2 + M\gamma + N)^2 \quad M^2 - 4N > 0 \tag{3.7}$$

Then, we conclude from (3.7) that

$$\begin{aligned} &(-2\delta + 2\mu h + \mu^2 h - 2\mu\delta - 2M - 2 + h)\gamma^3 \\ &\quad + (1 + 2\mu\delta^2 + 2\mu\delta - 2h - \kappa + 4\delta + \delta^2 - 2\delta N - 2\mu h + \mu^2\delta^2 - M^2)\gamma^2 \\ &\quad + (-2\delta^2 - h\kappa + 2\delta\kappa - 2\delta MN - 2\delta + h - 2\mu\delta^2)\gamma + \delta^2(1 - \kappa) - N^2 = 0 \end{aligned}$$

¹An approach based on investigation of equation (3.4) with Taylor expansions representation was presented in (Pozdniakovich and Puzyrov, 2009). It allowed one to achieve some progress, comparatively with (3.3), but again, no explicit form and error estimation were gained.

Now we have a system of four equations with five variables κ, δ, h, M, N , and can consistently find

$$\begin{aligned} \kappa &= 1 - \left(\frac{N}{\delta}\right)^2 & h &= \frac{2[(1 + \mu)\delta + M + 1]}{(1 + \mu)^2} \\ M &= -\frac{\delta^2(1 + \mu)^3 + \mu\delta N^2(1 + \mu) - N^2}{N[\delta(1 + \mu)^2 - N]} \end{aligned} \tag{3.8}$$

The last equation is

$$\begin{aligned} &(\delta - N)[\delta^9(1 + \mu)^6 + \delta^8 N(1 + \mu)^6 - 4\delta^7 N(1 + \mu)^4 - 4\delta^6 N^2(1 + \mu)^4 \\ &+ 2\delta^5 N^2(1 + \mu)^2(3 + \mu) + 2\delta^4 N^3(1 + \mu)^2(3 + \mu) - 4\delta^3 N^3(1 + \mu) \\ &- 2\delta^2 N^4(2 + 2\mu + \mu^2) + \delta N^4 + N^5] = 0 \end{aligned} \tag{3.9}$$

Condition (3.9) gives an equation of the 9-th order on δ (and 5-th order on N), but with the substitution

$$\delta = \frac{\delta_1}{(1 + \mu)^2} \quad N = \frac{N_1 \delta_1^2}{(1 + \mu)^2} \tag{3.10}$$

it may be rewritten as

$$\begin{aligned} &N_1^2 \delta_1^2 [N_1^4(1 + \mu)^2 - 2N_1^3(2 + 2\mu + \mu^2) + 2N_1^2(3 + \mu) - 4N_1 + 1] + 2N_1^4 \mu^2 \delta_1 \\ &- [N_1^4(1 + \mu)^2 - 4N_1^3(1 + \mu) + 2N_1^2(3 + \mu) - 4N_1 + 1] = 0 \end{aligned}$$

The last one being factorized as

$$\begin{aligned} &(N_1 \delta_1 - 1) \{ \delta_1 [N_1^4(1 + \mu)^2 - 2N_1^3(2 + 2\mu + \mu^2) + 2N_1^2(3 + \mu) - 4N_1 + 1] \\ &+ [N_1^4(1 + \mu)^2 - 4N_1^3(1 + \mu) + 2N_1^2(3 + \mu) - 4N_1 + 1] \} = 0 \end{aligned}$$

finally leads to

$$\begin{aligned} &(1 - N_1 \delta_1) \left\{ -N_1 \delta_1 [\mu \sqrt{N_1^3} 2(\sqrt{2} - \sqrt{N_1}) - (1 - N_1)^2] [\mu \sqrt{N_1^3} 2(\sqrt{2} + \sqrt{N_1}) + (1 - N_1)^2] \right. \\ &\left. + [\mu N_1^2 + (1 - N_1)^2]^2 \right\} = 0 \end{aligned} \tag{3.11}$$

Evidently,

$$\mu \sqrt{N_1^3}(\sqrt{2} + \sqrt{N_1}) + (1 - N_1)^2 > 0 \quad [\mu N_1^2 + (1 - N_1)^2]^2 > 0$$

and, due to the condition $\kappa > 0$, the expression in the first square brackets must be positive to fulfill (3.11). With this, we have the following restrictions on N_1

$$N_1 \delta_1 < 1 \quad \mu \sqrt{N_1^3}(\sqrt{2} - \sqrt{N_1}) > (1 - N_1)^2 \tag{3.12}$$

So, we have

$$\delta_1(N_1) = \frac{2\mu^2 N_1^2}{2\mu^2 N_1^3 - [\mu N_1^2 + (1 - N_1)^2]^2} - \frac{1}{N_1} \tag{3.13}$$

and now we can find the maximum of κ , i.e. the minimum of $\varphi(N_1) = N/\delta = N_1 \delta_1(N_1)$

$$\frac{d\varphi}{dN_1} = 2\mu^2 N_1^2 \frac{(1 + \mu)^2 N_1^4 - 2(3 + \mu) N_1^2 + 8N_1 - 3}{\{2\mu^2 N_1^3 - [\mu N_1^2 + (1 - N_1)^2]^2\}^2}$$

The numerator has two real and two complex roots

$$\frac{\sqrt{4+3\mu}-1}{1+\mu} \quad - \quad \frac{\sqrt{4+3\mu}+1}{1+\mu} \quad \frac{1+i\sqrt{\mu}}{1+\mu} \quad \frac{1-i\sqrt{\mu}}{1+\mu}$$

Only the first of them is positive and for any given value of μ provides the absolute minimum of the function $\varphi(N_1)$.

Substituting $N_1 = (\sqrt{4+3\mu}-1)/(1+\mu)$ in (3.13), after simplifications we get

$$\delta_1^* = \frac{8}{3} \frac{16 + 23\mu + 9\mu^2 + 2(2 + \mu)\sqrt{4 + 3\mu}}{64 + 80\mu + 27\mu^2} \tag{3.14}$$

The last expression is obviously positive, so the second inequality in (3.12) holds. Now we verify the first one. It leads to

$$N = \frac{64}{3} \frac{64 + 112\mu + 61\mu^2 + 9\mu^3 + (64 + 136\mu + 103\mu^2 + 27\mu^3)\sqrt{4 + 3\mu}}{(1 + \mu)^2(64 + 80\mu + 27\mu^2)} < \delta \tag{3.15}$$

Eliminating the square root, one may see that

$$729\mu^6 + 5778\mu^5 + 19279\mu^4 + 32758\mu^3 + 27809\mu^2 + 9344\mu > 0$$

So, for any $\mu > 0$ we have $N < \delta$, and (3.12) are fulfilled. Finally, we have

$$\delta^* = \frac{8}{3} \frac{16 + 23\mu + 9\mu^2 + 2(2 + \mu)\sqrt{4 + 3\mu}}{(1 + \mu)^2(64 + 80\mu + 27\mu^2)} \tag{3.16}$$

$$h^* = \frac{2}{3} \frac{64 + 248\mu + 255\mu^2 + 81\mu^3 - 2(16 + 20\mu + 9\mu^2)\sqrt{4 + 3\mu}}{(64 + 80\mu + 27\mu^2)(1 + \mu)^3}$$

and respectively

$$\eta^* = 2\sqrt{\frac{2}{3} \frac{16 + 23\mu + 9\mu^2 + 2(2 + \mu)\sqrt{4 + 3\mu}}{(1 + \mu)^2(64 + 80\mu + 27\mu^2)}} \tag{3.17}$$

$$\zeta^* = \sqrt{\frac{64 + 248\mu + 255\mu^2 + 81\mu^3 - 2(16 + 20\mu + 9\mu^2)\sqrt{4 + 3\mu}}{6(64 + 80\mu + 27\mu^2)(1 + \mu)^3}}$$

which determine the optimal values of stiffness and damping for DVA. For $\mu = 0.1$, the curve $f(\gamma)$ in the vicinity of peaks is presented in Figs. 4a and 4b for both cases – according to (3.3) and (3.16).

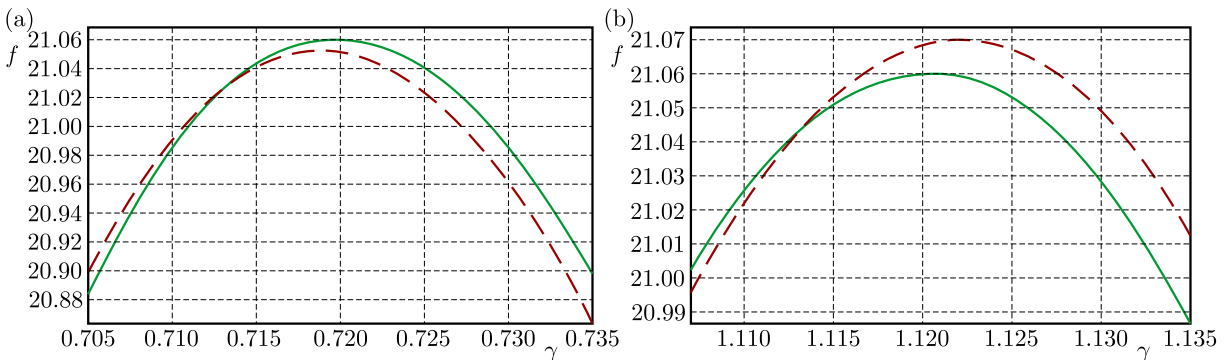


Fig. 4. Frequency-amplitude curve in the neighbourhood of peaks. Long dash line – according to (3.3), solid line – according to (3.16)

Also, substituting δ and N into (3.8)₂, we get

$$M = -\frac{414\mu^2 + 1104\mu + 768 + (54\mu^2 + 168\mu + 192)\sqrt{4 + 3\mu}}{9(1 + \mu)(64 + 80\mu + 27\mu^2)} \tag{3.18}$$

The rigorous mathematical proof of the fact that any pair of δ , h which differs from (3.16) is worse (gives larger maximum of f) is too cumbersome to be given here. But, at least, this verification versus pair (3.3) is rather simple. Indeed, substituting (3.3) and (3.16) one after the other in (3.4), we determine the extremal values of γ for each case separately with the help of Taylor expansions by $\sqrt{\mu}$

$$\begin{aligned} \gamma_1^{upon(3.3)} &= 1 - \frac{\sqrt{2}}{2}\sqrt{\mu} - \frac{7}{8}\mu - \frac{139\sqrt{2}}{256}(\sqrt{\mu})^3 + \frac{1797}{2058}\mu^2 + \dots \\ \gamma_2^{upon(3.3)} &= 1 + \frac{\sqrt{2}}{2}\sqrt{\mu} - \frac{7}{8}\mu + \frac{139\sqrt{2}}{256}(\sqrt{\mu})^3 + \frac{1797}{2058}\mu^2 + \dots \\ \gamma_1^{upon(3.16)} &= 1 - \frac{\sqrt{2}}{2}\sqrt{\mu} - \frac{7}{8}\mu - \frac{37\sqrt{2}}{64}(\sqrt{\mu})^3 + \frac{107}{128}\mu^2 + \dots \\ \gamma_1^{upon(3.16)} &= 1 + \frac{\sqrt{2}}{2}\sqrt{\mu} - \frac{7}{8}\mu + \frac{37\sqrt{2}}{64}(\sqrt{\mu})^3 + \frac{107}{128}\mu^2 + \dots \end{aligned}$$

And then, we may estimate the gain of using the values by (3.16)

$$\begin{aligned} \max f^{upon(3.3)} - \max f^{upon(3.16)} &= f(\gamma_2^{upon(3.3)}) - f(\gamma_2^{upon(3.16)}) \\ &= \frac{5\sqrt{2}}{256}\sqrt{\mu} + \frac{101}{8192}\mu + \frac{9859\sqrt{2}}{131072}\mu^2 + \dots \end{aligned} \tag{3.19}$$

Numerically, such verification is even easier – we may just combine (3.1) with condition (3.4) for both cases separately and plot the curve

$$\psi(\mu) = \max f^{upon(3.3)} - \max f^{upon(3.16)}$$

This curve is presented in Fig. 5, the dash line corresponds to $\gamma_1^{upon(3.3)}$, so the distance between the two branches is the height difference between the two peaks for case (3.3).

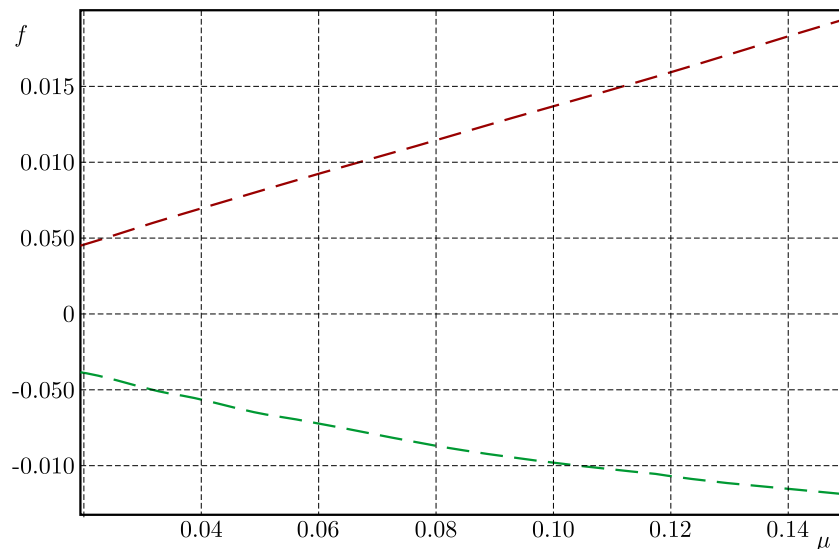


Fig. 5. Difference in f_{max} values for two cases

As the last step, let us write down the analytical expression for $|X_p|/(X_p)_{st}$. Substituting δ^* , h^* according to (3.16) and $\gamma_2 = (-M + \sqrt{M^2 - 4N})/2$ in f , we have

$$\left(\frac{|X_p|}{(X_p)_{st}}\right)^2 = f^* = \frac{A + BR}{C + DR}$$

where

$$\begin{aligned} A &= 2(A_0 + A_1 r) & B &= 3(1 + \mu)\sigma(B_0 + B_1 r) & C &= 2(C_0 + C_1 r) \\ D &= 3(1 + \mu)\sigma(D_0 + D_1 r) & R &= \sqrt{M^2 - 4N} & r &= \sqrt{4 + 3\mu} \\ \sigma &= 64 + 80\mu + 27\mu^2 \end{aligned}$$

Here, the polynomial coefficients are given by formulas

$$\begin{aligned} A_0 &= 8192 + 57856\mu + 145536\mu^2 + 181000\mu^3 + 122048\mu^4 + 43764\mu^5 + 7083\mu^6 + 243\mu^7 \\ A_1 &= -4096 - 8960\mu - 1152\mu^2 + 13252\mu^3 + 15443\mu^4 + 7149\mu^5 + 1242\mu^6 \\ B_0 &= 64 + 376\mu + 564\mu^2 + 331\mu^3 + 69\mu^4 & B_1 &= -32 + 4\mu + 63\mu^2 + 46\mu^3 + 9\mu^4 \\ C_0 &= \mu^2(1437696 + 5792256\mu + 9830592\mu^2 + 8976744\mu^3 + 4645404\mu^4 + 1291545\mu^5 \\ &\quad + 150903\mu^6) \\ C_1 &= \mu^2(387072 + 1278720\mu + 1804896\mu^2 + 1411020\mu^3 + 652725\mu^4 + 170586\mu^5 + 19683\mu^6) \\ D_0 &= \mu^2(155713536 + 906854400\mu + 2321104896\mu^2 + 3410021376\mu^3 + 3146726016\mu^4 \\ &\quad + 1871659224\mu^5 + 705324672\mu^6 + 157181148\mu^7 + 17380089\mu^8 + 531441\mu^9) \\ D_1 &= \mu^2(35389440 + 177389568\mu + 397799424\mu^2 + 529362432\mu^3 + 463738176\mu^4 \\ &\quad + 275945292\mu^5 + 108628209\mu^6 + 25572591\mu^7 + 2716254\mu^8) \end{aligned}$$

Eliminating the root R from the denominator, we have

$$(AC - BDR^2) + (BC - AD)R$$

in the numerator, and multiplier before R must be zero, because of $f(\gamma_2^{\text{upon}(3.16)}) = f(\gamma_1^{\text{upon}(3.16)})$, i.e. f^* is an even function of R (direct calculation confirms this fact). To simplify the fraction obtained, we also need to eliminate the ‘‘small’’ root r from the denominator. The final expression

$$\frac{|X_p|}{(X_p)_{st}} = \sqrt{\frac{(8 + 9\mu)^2(16 + 9\mu) - 128\sqrt{(4 + 3\mu)^3}}{27\mu^2(32 + 27\mu)}} \quad (3.20)$$

is a quite remarkable recognition because reduction of the fraction is possible only at the final stage, and the denominator before this reduction is the polynomial of the 48-th(!) order in μ .

4. Conclusion

We have discussed the problem of selection of optimal parameters of a DVA according to the classical Den Hartog model (Den Hartog, 1940). We have shown that the solution may be given in an accurate algebraic form which updates somewhat the known result. The analytical approach presented here may be more applicable for solving problems connected with the use of passive damping devices. We have also compared the results of two approaches and determined the error estimation which has been illustrated by the corresponding frequency-amplitude curves.

References

1. BROWN S., SAN DIEGO S. ET AL. (EDIT.), 2002, *Encyclopedia of Vibrations*, Academic Press, 1685 p.
2. BROCK J.E., 1946, A note on the damped vibration absorber, *Journal of Applied Mechanics*, **68**, A-284
3. DEN HARTOG J.P., 1940, *Mechanical Vibrations*, 2nd ed., McGraw-Hill, New York
4. FRAHM H., 1911, Device for damping vibration bodies, US Patent No. 989/959, 1911
5. GRIFFIN S., GUSSY J., LANE S.A., HENDERSON B.K., SCIULLI D., 2002, Virtual skyhook vibration isolation system, *Journal of Vibration and Acoustics*, **124**, 63-67
6. HUNT J.B., 1979, *Dynamic Vibration Absorbers*, Mechanical Engineering Publications, London
7. JOHNSON C.D., 1995, Design of passive damping systems, *Journal of Vibration and Acoustics*, **117(B)**, 171-175
8. KORENEV B.G., REZNIKOV L.M., 1993, *Dynamic Vibration Absorbers*, Wiley, New York
9. LIU K., LIU J., 2005, The damped dynamic vibration absorbers: revisited and new result, *Journal of Sound and Vibration*, **284**, 1181-1189
10. MARANO G.C., GRECO R., TRENTADUE F., CHIAIA B., Constrained reliability-based optimization of linear tuned mass dampers for seismic control, *International Journal of Solids and Structures*, **44**, 22/23, 7370-7388
11. MEAD D.J., 2000, *Passive Vibration Control*, John Wiley & Sons Ltd, Chichester, West Sussex, England
12. ORMONDROYD J., DEN HARTOG J.P., 1928, The theory of the vibration absorber, *Transactions of the American Society of Mechanical Engineers*, **49**, A9-22
13. POZDNIAKOVICH A.E., PUZYROV V.E., 2009, On the choice of the parameters of the dynamical vibration absorber, *Mekhanika Tverdogo Tela*, **39**, 167-172
14. SUN J.Q., JOLLY M.R., NORRIS M.A., 1995, Passive, adaptive and active tuned vibration absorbers survey, *Transactions of the ASME*, **117**, 4, 234-242
15. VIET L.D., ANH N.D., MATSUHISA H., 2011, The effective damping approach to design a dynamic vibration absorber using Coriolis force, *Journal of Sound and Vibration*, **330**, 1904-1916
16. WARBURTON G.B., AYORINDE E.O., 1980, Optimum absorber parameters for simple systems, *Earthquake Engineering and Structural Dynamics*, **8**, 197-217

APPLICATION OF THE LATTICE BOLTZMANN METHOD TO THE FLOW PAST A SPHERE

ADAM KAJZER, JACEK POZORSKI

Institute of Fluid-Flow Machinery, Polish Academy of Sciences, Gdańsk, Poland

e-mail: adkajzer@gmail.com; jp@imp.gda.pl

The results of fully resolved simulations and large eddy simulations of bluff-body flows obtained by means of the Lattice Boltzmann Method (LBM) are reported. A selection of Reynolds numbers has been investigated in unsteady laminar and transient flow regimes. Computed drag coefficients of a cube have been compared with the available data for validation purposes. Then, a more detailed analysis of the flow past a sphere is presented, including also the determination of vortex shedding frequency and the resulting Strouhal numbers. Advantages and drawbacks of the chosen geometry implementation technique, so called “staircase geometry”, are discussed. For the quest of maximum computational efficiency, all simulations have been carried out with the use of in-house code executed on GPU.

Keywords: bluff-body flow, Lattice Boltzmann Method, Large Eddy Simulation, GPU computing

1. Introduction

Computational Fluid Dynamics (CFD) is of higher and higher importance in science and engineering as it allows one to predict flow phenomena in investigated systems without carrying out experiments that tend to be increasingly costly and time consuming. The most popular CFD approach is the Finite Volume Method (FVM), see Versteeg and Malalasekera (2007), especially when the computational domain geometry is complex. The FVM is very well validated and has become an industrial standard in a wide range of applications. On the other hand, recent rapid developments in computer technology including Graphics Processing Units (GPU) and availability of high-level programming tools have made massive parallel computing relatively easy and inexpensive nowadays. This is an incentive to revisit the formulation of numerical schemes and algorithms.

The Lattice Boltzmann Method (LBM) is an alternative approach in CFD. Thanks to its explicit and local character (Succi, 2001), LBM is straightforward to parallelize, e.g., on the GPUs (Schoenherr *et al.*, 2011). The important feature of the method is that it also allows easy handling of complex geometries. Satisfactory results obtained by means of LBM have been reported for various compressible and incompressible, turbulent, single- and multiphase flows (Arcidiacono *et al.*, 2007; Chang *et al.*, 2013; Prasianakis and Karlin, 2008; Pourmirzaagha *et al.*, 2015). In a comprehensive paper by Hoelzer and Sommerfeld (2009), directly relevant for the present work, LBM was applied to the prediction of forces and moments acting on finite-size particles. Also, reactive flow phenomena including combustion, heat transfer and flows through porous media can be successfully simulated with the Lattice Boltzmann approach (Chiavazzo *et al.*, 2010; Arcidiacono *et al.*, 2008; Prasianakis and Karlin, 2007; Grucelski and Pozorski, 2015). Thus, it is worth to investigate different LBM approaches and implementation techniques to make it more and more accurate without sacrificing computational efficiency.

In this paper, we present LBM simulations of a flow around a sphere in both laminar and turbulent regimes. The investigated case is well validated experimentally (Achenbach, 1972, 1974; Sakamoto and Haniu, 1990), so it is often treated as a benchmark for computational approaches (Jones and Clarke, 2008). The main aim of this work is to investigate LBM capability to predict macroscopic flow quantities (i.e. the drag coefficient and Strouhal number) for the “staircase geometry” scheme applied on a uniform lattice. This approach is the simplest possible way of spatial discretisation of the body geometry in LBM and allows one to efficiently parallelize the implementation of boundary conditions and evaluation of hydrodynamic forces. To the best of the authors’ knowledge, the use of simplified geometry in the turbulent flow regime is a novel aspect of this work. Researchers investigated also more sophisticated methods, i.e. interpolation of the body boundary (Mei *et al.*, 2002). Stiebler *et al.* (2011) presented an LBM simulation of the flow around a sphere with the use of local discretisation refinement. In the present work, simulations have been carried out for a selection of Reynolds numbers varying from 30 up to 10^4 . Large eddy simulation (LES) has been implemented according to the sub-grid scale (SGS) turbulence model of Smagorinsky (1963) that already had given good results in simulation of the turbulent Taylor-Green vortex (Kajzer *et al.*, 2014).

2. Lattice Boltzmann Method and implementation details

2.1. Fundamentals of the method

The LBM is based on the kinetic theory of gases. The discretised Boltzmann equation is solved (instead of the Navier-Stokes equations) for discrete velocity distribution functions $f_\alpha(\mathbf{x}, t)$, in further sections also called populations. The spatial discretisation is done on a regular cubic grid; moreover, only a finite number of directions and magnitudes (indexed by α) are allowed in the microscopic velocity field. In this paper, we present results obtained with a code implementing the $D3Q15$ lattice scheme, i.e., $D = 3$ dimensions and $Q = 15$ allowed directions. Also popular, due to its better accuracy and only slightly higher computational cost, is the $D3Q19$ model. All formulations and proofs of statements recalled in this Section can be found in the book of Succi (2001).

The discretised Boltzmann equation with the Bhatnagar-Gross-Krook closure for the collision operator takes the following form

$$f_\alpha(\mathbf{x} + \Delta t \mathbf{e}_\alpha, t + \Delta t) - f_\alpha(\mathbf{x}, t) = \tau^{-1} (f_\alpha^{eq}(\mathbf{x}, t) - f_\alpha(\mathbf{x}, t)) \quad (2.1)$$

where α is the index of the velocity direction ($\alpha = 0, 1, \dots, Q - 1$), τ is the nondimensional relaxation time and \mathbf{e}_α is the lattice velocity in the direction α . The equilibrium distributions $f_\alpha^{eq}(\mathbf{x}, t)$, or more precisely $f_\alpha^{eq}(\rho(\mathbf{x}, t), \mathbf{u}(\mathbf{x}, t))$, corresponding to the density ρ and macroscopic velocity \mathbf{u} at the lattice node \mathbf{x} at the time t , are calculated as follows

$$f_\alpha^{eq}(\rho, \mathbf{u}) = w_\alpha \rho \left(1 + \frac{3}{c^2} \mathbf{e}_\alpha \cdot \mathbf{u} + \frac{9}{2c^4} (\mathbf{e}_\alpha \cdot \mathbf{u})^2 - \frac{3}{2c^2} \mathbf{u} \cdot \mathbf{u} \right) \quad (2.2)$$

where $\rho = \sum_{\alpha=0}^{Q-1} f_\alpha$ is the fluid density, $\mathbf{u} = \rho^{-1} \sum_{\alpha=0}^{Q-1} f_\alpha \mathbf{e}_\alpha$ is the macroscopic fluid velocity, w_α is a weighting coefficient (depending on the lattice type $DnQm$), $c = \Delta x / \Delta t$ is the lattice speed.

The discretised Boltzmann equation is solved in two steps, called respectively the collision step and the propagation step

$$\begin{aligned} \tilde{f}_\alpha(\mathbf{x}, t) &= f_\alpha(\mathbf{x}, t) + \tau^{-1} (f_\alpha^{eq}(\mathbf{x}, t) - f_\alpha(\mathbf{x}, t)) \\ f_\alpha(\mathbf{x} + \Delta t \mathbf{e}_\alpha, t + \Delta t) &= \tilde{f}_\alpha(\mathbf{x}, t) \end{aligned} \quad (2.3)$$

The explicit and local character of LBM is visible in the above equations: the collision step involves values of the flow fields (through f^{eq}) and populations at a single node only, and the propagation step consists in copying the post-collision populations to proper neighbouring nodes. In our implementation, $\Delta x = \Delta t = 1$ which results in $c = 1$. The pressure field is obtained from the following equation of state: $p = \rho c_s^2$, where the speed of sound is $c_s = c/\sqrt{3}$. It can be shown that \mathbf{u} and p satisfy the Navier-Stokes equations with the kinematic viscosity $\nu = (\tau - 1/2)c_s^2 \Delta t$ with an error $\mathcal{O}(\text{Ma}^2)$.

2.2. Boundary conditions

As the discretised Boltzmann equation solves for the discrete velocity distribution functions, proper boundary conditions on these distributions have to be enforced to retrieve the physical behaviour of the fluid in the macroscopic sense (i.e., velocity and pressure). All types of boundary conditions used in presented simulations are widely described by Succi (2001). The easiest way to implement the immersed body geometry is to project it on regular lattice nodes. The lattice nodes are then marked with respective flags, “fluid” and “solid”, say. That is why this variant is called “staircase geometry” (mesh-fitted surface of the body). Such an approach enables explicit use of the so-called bounce-back (BB) boundary condition. The populations outcoming from the solid nodes to the fluid nodes are replaced by populations moving in the opposite direction. This scheme makes the code efficient as it does not require any interpolation steps. Unfortunately, it is of the first order of accuracy in the described case (i.e. when the solid wall coincides with the lattice nodes). The inflow boundary condition corresponds to the constant velocity vector normal to the inflow plane, and the density (thus the pressure) is resultant. It is achieved by enforcing the populations to be in the equilibrium state $f_\alpha(\mathbf{x}_{in}, t) = f_\alpha^{eq}(\mathbf{x}_{in}, t)$ with \mathbf{x}_{in} being the inlet nodes, corresponding to the inflow velocity and the resulting density. The outflow boundary condition forces the density (and pressure) to be constant and the velocity gradient to vanish. It is realized by setting the populations in equilibrium related to the reference density ρ_0 and the velocity values in nodes preceding to the outflow plane in the normal direction $-\mathbf{e}_{n,out}$, pointing towards the domain interior: $f_\alpha(\mathbf{x}_{out}, t) = f_\alpha^{eq}(\mathbf{x}_{out} - \Delta t \mathbf{e}_{n,out}, t)$, where \mathbf{x}_{out} are the outflow nodes. On the domain side boundaries, the symmetry plane boundary condition is imposed (this is achieved by mirror reflection of proper populations), and the density is resultant. Some other approaches to inflow and outflow conditions can be found in (Grucelski and Pozorski, 2013).

2.3. Force evaluation

Hydrodynamic forces acting on the sphere are calculated by means of the momentum exchange method. We decided to use this method although it is proposed for cases with boundary nodes lying exactly halfway between the lattice nodes. Mei *et al.* (2002) raised some questions about the required body discretisation resolution as a function of the Reynolds number when using this method. It utilises only the advection and collision distribution functions (f_α and \tilde{f}_α) without the necessity of computing the pressure and shear stress. The total force \mathbf{F} acting on the immersed body is calculated as follows

$$\mathbf{F} = \sum_{\mathbf{x}_{sf}} \sum_{\alpha} (f_{-\alpha}(\mathbf{x}_{sf}) + \tilde{f}_\alpha(\mathbf{x}_{sf})) \mathbf{e}_\alpha \quad (2.4)$$

where \mathbf{x}_{sf} denotes the fluid nodes that have at least one solid neighbour, and the subscript $-\alpha$ is defined by $\mathbf{e}_{-\alpha} = -\mathbf{e}_\alpha$.

2.4. Large Eddy Simulation in LBM

LES is a method of turbulence modelling that resolves spatially filtered flow fields (Aubard *et al.*, 2013; Sagaut and Grohens, 1999). The method can be implemented as a local increase of the kinematic viscosity ν

$$\nu_{eff} = \nu + \nu_{sgs} \quad (2.5)$$

where ν_{eff} is the effective local viscosity and ν_{sgs} denotes the turbulent (or sub-grid scale, SGS) viscosity which in the model of Smagorinsky (1963) is computed as

$$\nu_{sgs} = (C_S \Delta)^2 |S| \quad (2.6)$$

where Δ is the filter size, $|S| = \sqrt{2S_{ij}S_{ij}}$ and $S_{ij} = \frac{1}{2} \left(\frac{\partial u_i}{\partial x_j} + \frac{\partial u_j}{\partial x_i} \right)$ is the strain rate tensor, C_S is a constant, most often equal to 0.17.

We present now the application of the Smagorinsky SGS model to LBM (Chang *et al.*, 2013; Stiebler *et al.*, 2011). In the lattice Boltzmann method, the kinematic viscosity of the fluid ν is uniquely linked with the relaxation time τ . The effective relaxation time is determined as

$$\tau_{eff} = 3(\nu + \nu_{sgs}) \frac{\Delta t}{(\Delta x)^2} + \frac{1}{2} \quad (2.7)$$

It can be shown that

$$\nu_{sgs} = (C_S \Delta)^2 |S| = \frac{1}{6} \left(\sqrt{\tau^2 + \frac{18(C_S \Delta)^2 |P|}{\rho}} - \tau \right) \quad (2.8)$$

where $|P| = \sqrt{2P_{ij}P_{ij}}$ with $P_{ij} = \sum_{\alpha} e_{\alpha i} e_{\alpha j} (f_{\alpha} - f_{\alpha}^{eq})$ being the stress tensor. Combining Eqs. (2.7) and (2.8), we obtain

$$\tau_{eff} = \frac{\tau}{2} \left(1 + \sqrt{1 + \frac{18(C_S \Delta)^2 P}{\rho \tau^2}} \right) \quad (2.9)$$

In our implementation of LES in the LBM, we set $\Delta = \Delta x$.

3. Flow cases and results

3.1. Validation case: flow past a cube

In order to validate the computer implementation, we made a simulation of the flow around a cube, as the solid boundary is exactly modelled within the “staircase geometry” approach. All computations have been carried out with the use of an in-house LBM code written in NVIDIA CUDA-C language and executed on NVIDIA GeForce series GPU. The code does not involve external libraries or user-defined data structures – only CUDA built-in types are used. The spatial resolution was set to $644 \times 244 \times 244$ nodes in the x, y and z directions respectively, resulting in about 38 million of nodes which exploited all available GPU memory (6 GB). The cube centre was placed at $x = 160$ l.u. (lattice units) and the cube edge was 32 l.u. Setting the inflow speed to 0.0289 l.u. resulted in $Ma < 0.1$ (while the lattice sound speed $c_s \approx 0.57$) in the whole domain so the flow could be treated as incompressible. The computations were carried out at Reynolds numbers $Re = 50, 100, 200, 300$ (fully resolved simulations) and 10^4 (LES), where $Re = U_{in} D / \nu = 3U_l N / (\tau - 0.5)$ with D being the cube edge size (characteristic length) in physical units, where U_{in} is the inlet speed in physical units, U_l is the inlet speed in lattice units,

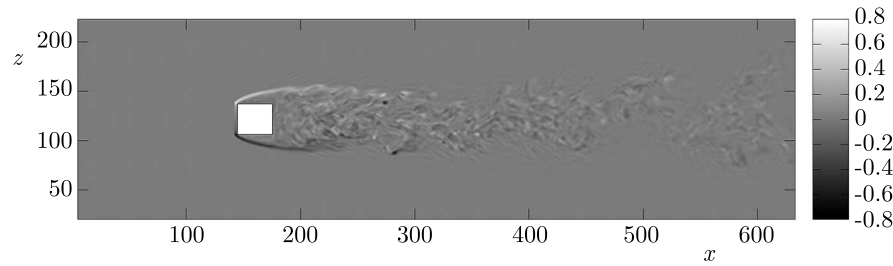


Fig. 1. A snapshot of the vorticity y -component in the flow past a cube at $Re = 10^4$ (cross-section normal to the y -axis in the symmetry plane, $t^+ = 95$)

N is the number of lattice nodes per cube characteristic length. The obtained y component of vorticity field at $Re = 10^4$ at non-dimensional time $t^+ = 95$ (statistically steady state), where $t^+ = tU_l/N$ with t being the time in l.u., is shown in Fig. 1.

In Fig. 2, the results of the computed drag coefficient C_D are shown. It is calculated as $C_D = 2F_x/\rho U_l^2 S$, where F_x is the force acting on the cube in the x -direction, see Eq. (2.4), ρ is the density, U_l is the inflow speed in l.u. and S is the cross-section area of the cube in l.u. At $Re = 50, 100, 200$ and 300 , the computed drag is in very good agreement with the data reported by Saha (2004) obtained by means of the MAC (Marker And Cell) method. His results were summarised in the form of correlation $C_D = (24/Re)(1 + 0.232 \cdot Re^{0.628})$. For Reynolds numbers above 300 in the transient flow regime, some scattered data on the drag coefficient are available, but no precise values or correlations are given (Hoelzer and Sommerfeld, 2009). In the turbulent regime, at $Re = 10^4$, the drag coefficient is slightly overestimated in comparison to the Re -independent value $C_D = 1.05 \pm 0.05$ given by Holmes *et al.* (2004). The reason of this discrepancy is discussed in the next Section.

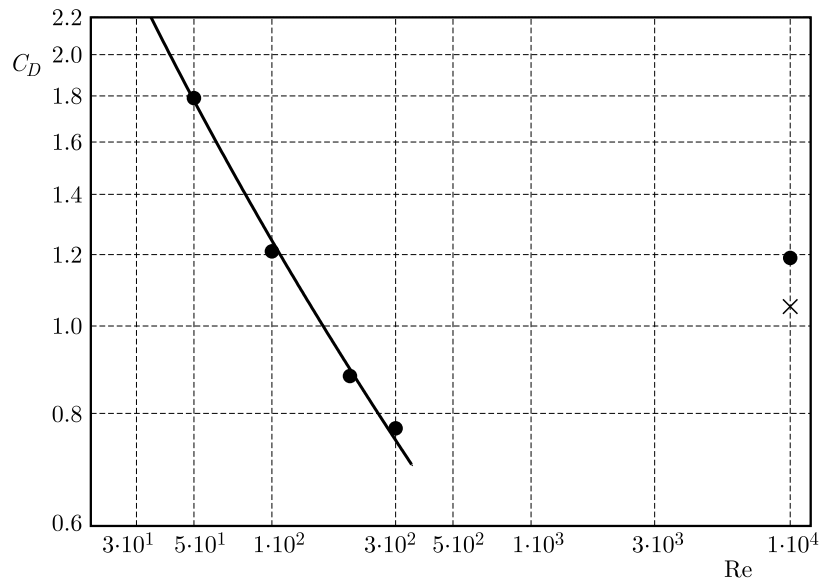


Fig. 2. Drag coefficient of cube; ●: present LBM results; —: approximation of numerical results given by Saha (2004) for laminar flow; ×: $C_D = 1.05 \pm 0.05$, valid for the turbulent regime

3.2. Flow past a sphere

After the validation tests presented above, simulations of the flow past a body of simplest curvilinear geometry – a sphere – have been carried out. The sphere diameter was set to 32 lattice units which resulted in domain blockage about 1.3% (defined as the ratio of cross-stream areas

of the sphere and the domain). All other parameters were set to the same values as in the simulations of the flow past a cube. Computations without turbulence modelling at $Re = 30, 50, 100, 300$ and 500 were performed. In Table 1, the computed drag coefficients are compared with the experimental correlation reported by Clift *et al.* (1978). The computed drag coefficients are in good agreement with the experimental results up to $Re = 300$ (see Fig. 3). At $Re = 500$, the error is more significant, which suggests that the simulation is underresolved. Therefore, at higher Reynolds numbers ($10^3, 3 \cdot 10^3$ and 10^4), the LES model (described in Sec. 2.4) was used. In Fig. 4, the map of the ratio of the turbulent-to-molecular viscosity ν_{sgs}/ν is shown at $Re = 10^3$. It is clearly visible that the resolution used in these simulations is barely sufficient since the maximum values of the SGS viscosity are comparable to the molecular viscosity. At $Re = 10^4$, the values of ν_{sgs} can locally be even one order of magnitude higher than ν in the vicinity of the sphere surface, which means that the boundary layer is not adequately resolved. Arguably, this explains the overestimation of the drag coefficient. Moreover, since we are close to the stability limit of computations, some artefacts are visible in the upstream region in Fig. 4 due to the weakly compressible nature of LBM. Computations at higher Reynolds numbers (above 10^4 , not shown in Fig. 3) reveal that the drag coefficient remains almost constant. This effect is expected since capturing these slight differences, in particular a correct prediction of the drag crisis at $Re \sim 2 \cdot 10^4$, would require very fine meshes (Rodriguez *et al.*, 2013).

Table 1. Computed and experimental drag coefficients C_D of the sphere. At $Re = 10^3$ and above, the LES approach has been applied

Re	exp. data	LBM (rel. error in %)
30	2.12	2.08 (1.9%)
50	1.57	1.55 (1.3%)
100	1.09	1.08 (1.0%)
300	0.65	0.67 (3.1%)
500	0.55	0.59 (7.3%)
10^3 (LES)	0.47	0.55 (17%)
$3 \cdot 10^3$ (LES)	0.40	0.53 (33%)
10^4 (LES)	0.41	0.54 (32%)

The frequency spectra of velocity in the wake area have also been calculated in order to obtain the Strouhal number defined as

$$St = \frac{f_0 D}{U_{in}} \quad (3.1)$$

where f_0 denotes the frequency of vortex shedding, D is the sphere diameter and U_{in} is the inflow velocity. The frequency spectra of the cross-stream velocity components were obtained by means of FFT. The velocity probes were placed at $\mathbf{x} = \mathbf{x}_c + x_p \mathbf{x}_0 + y_p \mathbf{y}_0 + z_p \mathbf{z}_0$, where \mathbf{x}_c denotes the position of the sphere centre, $\mathbf{x}_0, \mathbf{y}_0, \mathbf{z}_0$ are axes unit vectors, and $x_p = 3.0D$, $y_p = 0.3D$ and $z_p = 0.5D$. The spectra were computed at $Re = 10^3$ and $Re = 10^4$. Figure 5 shows the computed spectra of the y -component of velocity, $F[u_y]$, as a function of the dimensionless frequency $f^* = fD/U_{in}$.

The obtained results match quite well the experimental data at $Re = 10^3$. Sakamoto and Haniu (1990) reported $St = 0.18-0.20$ with $\sim 4\%$ measurement errors, while the present LBM result is $St = 0.19$. At $Re = 10^4$, the spectrum has significant amplitudes also at higher frequencies, which is an expected result as the wake becomes more turbulent than at $Re = 10^3$. Moreover, it is hard to distinguish a clearly dominating frequency in the neighbourhood of $f^* = 0.2$ (obtained in experiments), although the highest value is achieved at $f^* = 0.17$. This result should however be taken with care since the simulation is underresolved.

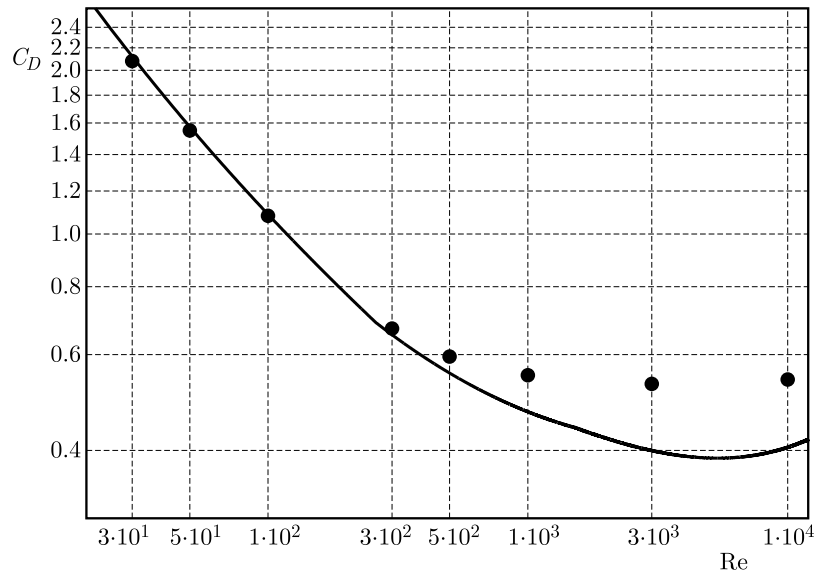


Fig. 3. Drag coefficient of the sphere. \bullet : present LBM computations; $—$: approximation of experimental results according to Clift *et al.* (1978)

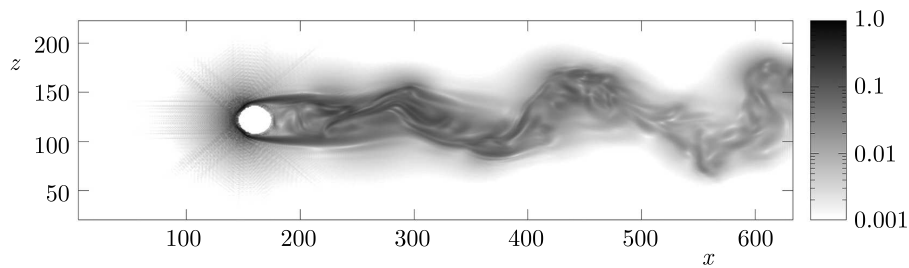


Fig. 4. The grayscale map of ν_{sgs}/ν at $Re = 10^3$ at non-dimensional time $t^+ = 95$

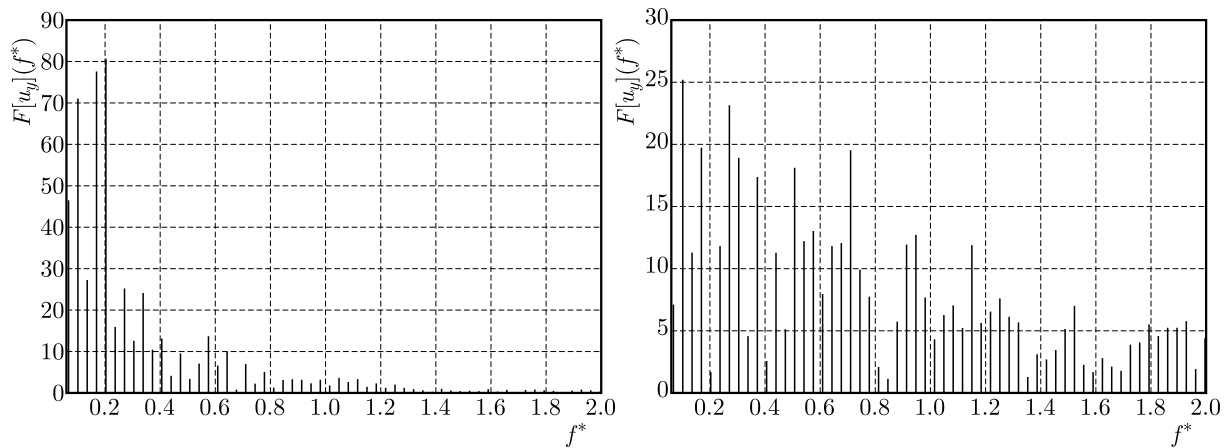


Fig. 5. The spectrum of the y -component of velocity obtained in LBM simulations expressed in terms of the dimensionless frequency f^* at $Re = 10^3$ (left) and $Re = 10^4$ (right)

4. Conclusions and perspectives

The methods presented in this paper allow one to accurately predict the flow past simple bluff bodies in terms of the drag force and the Strouhal number in the range of low and moderate Reynolds numbers. In the transitional and turbulent regimes, we have added the LES closure for non-resolved flow scales. In the case of a turbulent flow, it would be however necessary to

introduce a local lattice refinement to solve the boundary layer and wake with sufficient accuracy. Further validation of the presented methods should involve study of more complex phenomena in bluff-body flows, e.g. wake dynamics and structures which were investigated in an experimental way by Klotz *et al.* (2014) and Szaltys *et al.* (2011).

The presented implementation of boundary conditions, force evaluation and turbulence model do not deprive LBM from its explicit local character, so the problem size (the number of lattice nodes N , say) does not have a big impact on the total simulation time as the computational complexity remains of $\mathcal{O}(N)$. These features of LBM make it incomparably faster than other methods, even up to two orders of magnitude faster than FVM executed on a single multicore CPU of comparable cost with a similar programming effort (Kajzer *et al.*, 2014). Introduction of the block-wise refinement will not require modification of the presented approaches. However, it will make the implementation slightly more complicated in comparison to the homogenous lattice.

Summarising, the Lattice Boltzmann Method seems to be a promising tool for external flow computations in a wide range of Reynolds numbers.

Acknowledgments

The authors would like to thank Dr Arkadiusz Grucelski (IMP PAN Gdańsk) and an unknown Referee for their insightful remarks and helpful suggestions.

References

1. ACHENBACH E., 1972, Experiments on the flow past spheres at very high Reynolds numbers, *Journal of Fluid Mechanics*, **54**, 565-575
2. ACHENBACH E., 1974, Vortex shedding from sphere, *Journal of Fluid Mechanics*, **62**, 209-221
3. ARCIDIACONO S., MANTZARAS J., KARLIN I.V., FROUZAKIS C., 2007, Lattice Boltzmann method for the simulation of multi-component mixtures, *Physical Review E*, **76**, 046703
4. ARCIDIACONO S., MANTZARAS J., KARLIN I.V., 2008, Lattice Boltzmann method for the simulation of catalytic reactions, *Physical Review E*, **78**, 046771
5. AUBARD G., VOLPIANI P.S., GLOERFELT X., ROBINET J.C., 2013, Comparison of subgrid-scale viscosity models and selective filtering strategy for large-eddy simulations, *Flow, Turbulence and Combustion*, **91**, 497-518
6. CHANG S.C., YANG Y.T., CHEN C.K., CHEN W.L., 2013, Application of the lattice Boltzmann method combined with large-eddy simulations to turbulent convective heat transfer, *International Journal of Heat and Mass Transfer*, **66**, 338-348
7. CHIAVAZZO E., KARLIN I.V., GORBAN A.N., BOULOUCHOS K.B., 2010, Coupling of the model reduction technique with the lattice Boltzmann method for combustion simulations, *Combustion and Flame*, **157**, 1833-1849
8. CLIFT R., GRACE J. R., WEBER M.E., 1978, *Bubbles, Drops, and Particles*, Academic, New York
9. GRUCELSKI A., POZORSKI J., 2013, Lattice Boltzmann simulations of flow past an obstacle and in simple porous media, *Computers and Fluids*, **71**, 406-416
10. GRUCELSKI A., POZORSKI J., 2015, Lattice Boltzmann simulations of heat transfer in flow past a cylinder and in simple porous media, *International Journal of Heat and Mass Transfer*, **86**, 139-148
11. HOELZER A., SOMMERFELD M., 2009, Lattice Boltzmann simulations to determine drag, lift and torque acting on non-spherical particles, *Computers and Fluids*, **38**, 572-589
12. HOLMES J., ENGLISH E., LETCHFORD C., 2004, Aerodynamic forces and moments on cubes and flat plates, with applications to wind-borne debris, *Fifth International Colloquium on Bluff Body Aerodynamics and Applications*, Ottawa, Canada, 11-15 July 2004

13. JONES D.A., CLARKE D.B., 2008, *Simulation of Flow Past a Sphere using the Fluent Code*, Defence Science and Technology Organisation, Maritime Platforms Division, Victoria, Australia
14. KAJZER A., POZORSKI J., SZEWC K., 2014, Large-eddy simulations of 3D Taylor-Green vortex: comparison of Smoothed Particle Hydrodynamics, Lattice Boltzmann and Finite Volume methods, *Journal of Physics: Conference Series*, **530**, 012019
15. KLOTZ L., GOUJON-DURAND S., ROKICKI J., WESFREID J.E., 2014, Experimental investigation of flow behind a cube for moderate Reynolds numbers, *Journal of Fluid Mechanics*, **750**, 73-98
16. MEI R., YU D., SHYY W., LUO L.-S., 2002, Force evaluation in the lattice Boltzmann method involving curved geometry, *Physical Review E*, **65**, 0412037
17. POURMIRZAAGHA H., AFROUZI H.H., MEHRIZI A.A., 2015, Nano-particles transport in a concentric annulus: a Lattice-Boltzmann approach, *Journal of Theoretical and Applied Mechanics*, **53**, 683-695
18. PRASIANAKIS N., KARLIN I.V., 2007, Lattice Boltzmann simulation of thermal flows on standard lattices, *Physical Review E*, **76**, 016702
19. PRASIANAKIS N., KARLIN I.V., 2008, Lattice Boltzmann simulation of compressible flows on standard lattices, *Physical Review E*, **78**, 016704
20. RODRIGUEZ I., LEHMKUHL O., BORRELL R., PANIAGUA L., PEREZ-SEGARRA C.D., 2013, High performance computing of the flow past a circular cylinder, *Procedia Engineering*, **63**, 166-172
21. SAGAUT P., GROHENS R., 1999, Discrete filters for large eddy simulation, *International Journal of Numerical Methods in Fluids*, **31**, 1195-1220
22. SAHA A.K., 2004, Three-dimensional numerical simulations of the transition of flow past a cube, *Physics of Fluids*, **16** 5, 1630-1646
23. SAKAMOTO H., HANIU H., 1990, A study on vortex shedding from spheres in a uniform flow, *Journal of Fluids Engineering*, **112**, 4, 386-392
24. SCHLICHTING H., 1979, *Boundary-Layer Theory*, 7th ed., McGraw-Hill, New York
25. SCHOENHERR M., KUCHER K., GEIER M., STIEBLER M., FREUDIGER S., KRAFCZYK M., 2011, Multi-thread implementations of the lattice Boltzmann method on non-uniform grids for CPUs and GPUs, *Computers and Mathematics with Applications*, **61**, 3730-3743
26. SMAGORINSKY J., 1963, General circulation experiments with the primitive equations, *Monthly Weather Review*, **91**, 3, 99-164
27. STIEBLER M., KRAFCZYK M., FREUDIGER S., GEIER M., 2011, Lattice Boltzmann large eddy simulation of subcritical flows around a sphere on non-uniform grids, *Computers and Mathematics with Applications*, **61**, 3475-3484
28. SUCCI S., 2001, *The Lattice Boltzmann Method for Fluid Dynamics and Beyond*, Clarendon Press, Oxford
29. SZALTYS P., CHRUST M., PRZADKA A., GOUJON-DURAND S., TUCKERMAN L.S., WESFREID J.E., 2011, Nonlinear evolution of instabilities behind spheres and disks, *Journal of Fluids and Structures*, **28**, 483-487
30. VERSTEEG H.K., MALALASEKERA W., 2007, *An Introduction to Computational Fluid Dynamics: the Finite Volume Method*, Pearson Education Ltd., Harlow, England, New York

UBIQUITIFORMAL FRACTURE ENERGY

ZHUO-CHENG OU, MIN YANG, GUAN-YING LI, ZHUO-PING DUAN, FENG-LEI HUANG

State Key Laboratory of Explosion Science and Technology, School of Mechatronics, Beijing Institute of Technology, Beijing, China; e-mail: zcou@bit.edu.cn

The ubiquitous fracture energy is proposed in the paper and its explicit expression is obtained. Moreover, the numerical results for concrete are found to be in good agreement with those for the critical strain energy release rate. The discrepancy between the numerical results of the traditional fracture energy and the critical strain energy release rate can be explained reasonably, which implies that the ubiquitous fracture energy should be taken as an available fracture parameter of materials. Finally, it is numerically found for some concrete that there is not size effect for the ubiquitous fracture energy.

Keywords: fractal, ubiquitous, fracture energy, size effect

1. Introduction

As is well known, pioneered by the work of Mandelbrot *et al.* (1984), the fractality of fracture surfaces in various kinds of materials such as concrete (Saouma *et al.*, 1990; Saouma and Barton, 1994), steel (Mandelbrot *et al.*, 1984; Underwood, 1986), ceramic (Mecholsky, 1989) and rock (Krohn and Thompson, 1986; Radlinski *et al.*, 1999) has been verified experimentally, which has gradually lead to the establishment of the emergent fractal fracture mechanics over the past three decades. Naturally, it is a reasonable desire that some important physical concepts or parameters in the classical fracture mechanics can be extended directly into the fractal one but, unfortunately, this is not the case sometimes. For example, fracture energy or, more scholarly, the strain energy release rate, is one of the significant properties characterizing the fracture property of materials in the classical fracture mechanics and defined as the energy required to create a unit new crack surface (in integral dimension of $D = 2$). However, it seems that there exists an intrinsic difficulty for extending such a traditional concept in the classical fracture mechanics into the fractal fracture mechanics, because of singularity of the integral dimensional measure or the immeasurability of the corresponding fractal such as the so-called fractal fracture energy. That is to say, the integral dimensional measures or, intuitively, the area of all the fractal fracture surfaces tend in general to infinity, which makes all the traditional fracture energy vanishing. In fact, over the past decades, to overcome such a difficulty and well describe fractal characteristics of a fractal crack as a direct extension of the concept of traditional fracture energy, some new density kinds of fractal fracture energy parameters defined on a unit fractal measure were proposed, such as the specific energy-absorbing capacity of unit fractal measure (Borodich, 1992, 1997, 1999), fractal fracture energy (Bažant, 1995, 1997a,b) as well as the renormalized fractal fracture energy (Carpinteri, 1994; Carpinteri and Ferro, 1994; Carpinteri *et al.*, 2002), which have been used widely in practical applications. However, as was pointed out recently by Ou *et al.* (2014), such a concept of the fractal fracture energy seems now to be a little questionable, because these fractal fracture energies are both difficult to be determined in practice and lack unambiguous physical meanings (Bažant and Yavari, 2005). More importantly, such defined fractal fracture parameters are not appropriate to be taken as a measure of strength or toughness of materials. On account of that the comparison between the

measures of two objects in different dimensions is radically meaningless, while the traditional fracture energy is indeed an important characteristic parameter of materials. For example, one can say that the material with a higher fracture energy has higher a load bearing capacity. Addison (2000) tried to deal with such an issue for fractal cracks by using the concept of so-called pre-fractal fracture surfaces. With the aid of a new-defined hypervolume, Addison (2000) obtained the ratio of the area of the pre-fractal fracture surface to the original smooth cross-sectional area of the specimens. Taking the ratio as a modified factor, the pre-fractal fracture energy was obtained but, certainly, the fractal fracture energy was still divergent and hence could not be determined. Moreover, it was also found by Addison (2000) that the values of the pre-fractal fracture energy were remarkably coincident with the critical strain energy release rate determined by the fracture toughness relation, in which the fracture toughness and the elastic modulus were determined experimentally (Swartz and Kan, 1992). Although, as concluded by Addison (2000), the pre-fractal fracture energy can be a true material constant, it should be noticed that the formulation of the pre-fractal fracture energy under the concept of fractals is a little miscellaneous and the hypervolume of a fractal object seems to have no physical significance, and then becomes unnecessary.

As above mentioned, there are some intrinsic difficulties in the practical engineering applications of fractals, especially when the measure of the considered object must be taken into account. As was pointed out further by Ou *et al.* (2014), the fractal approximation of a physical object in nature is unreasonable because of divergence of the integral dimensional measure of the fractal. Moreover, to cover the shortage in fractal applications, a new concept of a ubiquitous form was proposed by Ou *et al.* (2014). It is believed that a real physical or geometrical object in nature should be ubiquitous rather than fractal. According to Ou *et al.* (2014), a ubiquitous form can be defined as a finite order self-similar (or self-affine) physical configuration constructed usually by a finite iterative procedure and, moreover, under the concept of the ubiquitous form, the singularity of the integral dimensional measure or the immeasurability of the fractal disappears.

In this paper, therefore, the fracture energy and its size effects are re-analyzed based on the concept of the ubiquitous form. A ubiquitous form fracture energy is proposed and its explicit expression is obtained. Subsequently, the calculated numerical results of the ubiquitous form fracture energy for concrete are compared with those for the critical strain energy release rate calculated by using the well-known fracture toughness relation. Furthermore, a similar size effect of the fracture energy to that derived by fractal theory is also obtained. This article is divided into four sections. After this brief introduction, the ubiquitous form fracture energy and the size effect of the fracture energy are presented in Section 2. In Section 3, numerical results for the ubiquitous form fracture energy are presented together with a brief discussion and, finally, some conclusions are drawn out in Section 4.

2. Ubiquitous form fracture energy of concrete

In the classical fracture mechanics, the fracture energy G is defined as the released energy W divided by the opened fracture area A , namely

$$G = \frac{W}{A} \quad (2.1)$$

Thus, for a specimen with a smooth square cross-section of side length l , $A = l^2$, the traditional fracture energy is

$$G = \frac{W}{l^2} \quad (2.2)$$

On the other hand, when taking the same cross-section as a ubiquitous surface, the ubiquitous area A_{uf} is

$$A_{uf} = l^D \delta_{min}^{2-D} \quad (2.3)$$

where D is the complexity of the ubiquitous and, according to Ou *et al.* (2014), the value of D for the ubiquitous is equal to the fractal dimension of its associated fractal. δ_{min} is the lower bound to scale invariance for the ubiquitous, which is believed to be related to the microstructure of the object under consideration.

Substituting Eq. (2.3) into Eq. (2.1), the ubiquitous fracture energy G_{uf} of a material can be defined as

$$G_{uf} = \frac{W}{l^D} \delta_{min}^{2-D} \quad (2.4)$$

Moreover, the relationship between the ubiquitous fracture energy and the traditional one can be obtained directly from Eqs. (2.4) and (2.2), as

$$\frac{G_{uf}}{G} = \left(\frac{l}{\delta_{min}} \right)^{2-D} \quad (2.5)$$

It is seen from Eq. (2.5) that, unlike the fractal fracture energy (Borodich, 1992, 1997, 1999; Bažant, 1995, 1997a,b; Carpinteri, 1994; Carpinteri and Ferro, 1994; Carpinteri *et al.*, 2002), the ubiquitous fracture energy G_{uf} can be obtained directly from physical and geometrical properties of the object under consideration, and then such a ubiquitous fracture energy can be taken as a reasonable material parameter, as was proposed by Addison (2000). However, on the one hand, Addison (2000) reached this conclusion via the concept of a pre-fractal, which implied that the fracture surface was of fractal, i.e. the fracture surface had fractional dimension. On the contrary, the concept of the ubiquitous emphasizes the integral dimension feature of a real object in nature, that is, all the real fracture surfaces are of integral dimension 2. On the other hand, the pre-fractal fracture energy has to be determined via an ambiguous parameter, namely, the hypervolume V^* , which is unnecessary in the determination of the ubiquitous fracture energy.

Furthermore, it is believed that there is a size effect for the traditional fracture energy G , which can be easily obtained from Eq. (2.5). Considering two specimens in different sizes l_1 and l_2 , respectively, there are

$$\frac{G_{uf}}{G_1} = \left(\frac{l_1}{\delta_{min}} \right)^{2-D} \quad \frac{G_{uf}}{G_2} = \left(\frac{l_2}{\delta_{min}} \right)^{2-D} \quad (2.6)$$

where G_1 and G_2 are the corresponding traditional fracture energies for the two specimens, respectively. And then the size effect can be presented simply as

$$\frac{G_1}{G_2} = \left(\frac{l_1}{l_2} \right)^{D-2} \quad (2.7)$$

In fact, Carpinteri and Ferro (1994), Carpinteri and Chiaia (1995) also obtained such a relationship from fractal theory based on the concept of renormalized fracture energy. However, similarly to the concept of the hypervolume used by Addison (2000), the renormalization fracture energy has also no clear physical meaning, and it is difficult to be determined in practice.

3. Numerical results and discussions

In Eq. (2.5), both the traditional fracture energy G and the complexity D can be determined experimentally. For concrete material, the lower bound to scale invariance δ_{min} can be empirically related to the tensile strength f_t (Li, 2014) as

$$\delta_{min} = 221.28 f_t^{-3.24} \quad (3.1)$$

where the units of δ_{min} and f_t are μm and MPa , respectively.

To investigate numerically the properties of the ubiquitous fracture energy, concrete materials presented in Swartz and Kan (1992) as well as by Saouma *et al.* (1990, 1991) and Saouma and Barton (1994) are used. The corresponding material properties as well as the calculated values of δ_{min} from Eq.(3.1) are listed in Tables 1 and 2, respectively. For convenience, according to Addison (2000), the complexities used for the concrete materials presented by Swartz and Kan (1992) are all taken to be $D = 2.1$. In the tables, E is the elastic modulus and K_{IC} is the fracture toughness.

Table 1. Experimental data (Swartz and Kan, 1992) and the corresponding lower bound to scale invariance

Specimen	l [cm]	E [GPa]	K_{IC} [MPa $\sqrt{\text{m}}$]	G [N/m]	f_t [MPa]	δ_{min} [μm]
NC-.64	12.7	31.0	1.015	99.0	5.1	1.1
HC-.64	12.7	35.0	1.327	144.4	6.0	0.7
NP-.64	12.7	32.7	1.078	99.9	5.4	1.0
NP-.30	12.7	37.2	1.392	127.4	8.0	0.3
HC-.30	12.7	38.2	1.676	166.8	8.0	0.3
NC-.30	12.7	41.6	1.439	119.0	8.4	0.2

Table 2. Experimental data (Saouma *et al.*, 1990, 1991; Saouma and Barton, 1994) and the corresponding lower bound to scale invariance

Specimen	l [cm]	E [GPa]	D [-]	K_{IC} [MPa $\sqrt{\text{m}}$]	G [N/m]	f_t [MPa]	δ_{min} [μm]
S32A	40.64	16.9	2.1	0.89	224.6	2.67	9.2
S32B	40.64	16.9	2.098	1.0	205.3	2.67	9.2
S32C	40.64	16.9	2.117	1.1	238.6	2.67	9.2
S52A	67.74	16.9	2.073	1.16	205.3	2.67	9.2
SS32A	40.64	23.2	2.08	1.4	303.5	3.96	2.6
SS32B	40.64	23.2	2.085	1.25	249.1	3.96	2.6
S33A	40.64	16.5	2.097	0.99	212.3	2.41	12.8
S33B	40.64	16.5	2.109	0.88	221.1	2.41	12.8
S33C	40.64	16.5	2.103	1.28	245.6	2.41	12.8
S53A	67.74	16.5	2.082	0.98	236.8	2.41	12.8

The numerical results of the ubiquitous fracture energy calculated by using Eq. (2.5) for the two materials are presented in Figs. 1a and 1b, respectively. For the sake of comparison and discussions, the numerical results of both the traditional fracture energy G and the critical strain energy release rate G_c calculated from the fracture toughness relation $G_c = K_{IC}^2/E$ are also presented in Figs. 1a and 1b.

It can be seen from both Figs. 1a and 1b that the numerical result of the ubiquitous fracture energy G_{uf} is in good agreement with that of the critical strain energy release rate G_c calculated from the fracture toughness relation and, as usual, far from that of the fracture energy G . As is well known, the discrepancy between the calculated results of the critical strain energy release rate G_c from the fracture toughness K_{IC} and the experimental data of G has been perplexing researchers for a long time. It was conjectured that, in general, the assumption of linear elasticity is not a so good approximation to describe physical properties of real

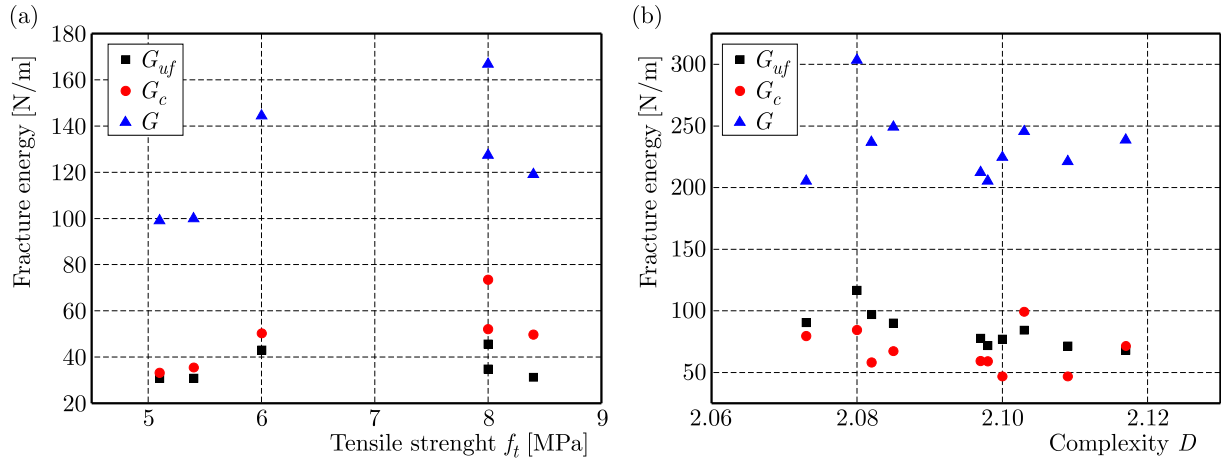


Fig. 1. Ubiquitiformal fracture energy G_{uf} for concrete: (a) Swartz and Kan (1992),
(b) Saouma *et al.* (1990, 1991), Saouma and Barton (1994)

materials, because the relation for fracture toughness is derived from rationalistic deduction on the assumption of linear elasticity. It seems now that the above mentioned discrepancy can be reasonably explained based on the ubiquitiformal fracture energy as follows. In fact, in the proper sense, the fracture energy G is obtained by the ratio of the work done by the external traction to the area of the fracture surface, which hence represents the average energy release rate for creating the fracture surface and characterizes a global fracture property of the material under consideration. On the other hand, however, the critical strain energy release rate G_c is the critical crack-tip energy release rate, which describes the local fracture property of materials. Thus, it can be realized that the discrepancy between the values of the fracture energy G and the critical strain energy release rate G_c should result from two uncertainties coming from the two physical variables G and G_c , respectively. One is the accuracy of the calculation results of the area of the fracture surface for the fracture energy G , and the other one is the availability of the assumption of linear elasticity for deduction of the critical strain energy release rate G_c as inferred in the past. Obviously, based on large volumes of the experimental variations as above mentioned, the real fracture surface should be ubiquitiformal rather than smooth. Therefore, it must be questionable to calculate the area of the fracture surface under the smooth surface assumption, and instead of which, the concept of the ubiquitiform surface must be taken into account. Considering further the agreement of the calculated numerical results of the ubiquitiformal fracture energy G_{uf} and that of the critical strain energy release rate G_c , it can be believed that the above mentioned discrepancy is indeed resulted from the incorrect calculation of the area of the fracture surface on the smooth surface assumption and that the ubiquitiformal fracture energy G_{uf} is superior to the traditional fracture energy G . Moreover, it should be pointed out here that the fact that the numerical result of the ubiquitiformal fracture energy G_{uf} is in good agreement with that of the critical strain energy release rate G_c calculated from the fracture toughness relation also implies that the opened area of the fracture surface is more important than the well-known crack-tip stress singularity in the description of the fracture process in materials. This can be demonstrated further as follows. On the one hand, G_c comes from the rigorous theoretical analysis of the crack-tip stress singularity on the assumption of linear elasticity. On the other hand, a ubiquitiformal crack will include a number of smaller cracks distributed in different lengths and directions, which obviously may result in much more complexity in the crack-tip stress singularity. However, although it does not take the complicated crack-tip stress singularity into account, the numerical results of the ubiquitiformal fracture energy calculated directly via the area of the ubiquitiformal fracture surface can still be in good agreement with that of the critical strain energy release rate, which just verifies the importance of the area.

Nay more, unlike the fracture energy G , for some concrete materials, the ubiquitous fracture energy G_{uf} seems to have not the size effect, which is shown in Table 3 by taking the concrete presented by Carpinteri and Ferro (1994) as an example. The material properties as well as the calculated values of both δ_{min} and G_{uf} are listed in Table 3, where G_m and G_{ufm} are the mean values of the fracture energy G and the ubiquitous fracture energy G_{uf} , respectively; $E_r(G)$ and $E_r(G_{uf})$ are the relative errors of G and G_{uf} , respectively. It can be seen that the relative errors of the ubiquitous fracture energy $E_r(G_{uf})$ are all within the range of 10% for varying sizes of the specimens, while that of the traditional fracture energy $E_r(G)$ can reach up to 30%.

Table 3. Experimental data (Carpinteri and Ferro, 1994) and the corresponding ubiquitous fracture energy

l [cm]	f_t [MPa]	δ_{min} [μm]	D [-]	G [N/m]	G_m [N/m]	$E_r(G)$ [%]	G_{uf} [N/m]	G_{ufm} [N/m]	$E_r(G_{uf})$ [%]
5	4.25	2.04	2.38	83	109	-31	1.78	1.97	-10
10	3.78	2.98	2.38	102	109	-7	1.94	1.97	-2
20	3.64	3.37	2.38	142	109	23	2.18	1.97	10

In addition, it can be seen from Eq. (2.5) that the lower bound to scale invariance δ_{min} can introduce some errors to the calculation of the area of the ubiquitous fracture surface A_{uf} and then affect the calculation results of the ubiquitous fracture energy G_{uf} . In the following, it will be numerically demonstrated that such an influence can be neglected. Denote the true value and the actual value of the lower bound to scale invariance by δ_{min} and δ'_{min} , respectively, the corresponding areas of the ubiquitous fracture surface by A_{uf} and A'_{uf} , and the relative error of δ_{min} and of the ubiquitous area A_{uf} by $E_r(\delta_{min})$ and $E_r(A_{uf})$, respectively, one can obtain the relation between the two relative errors from Eq. (2.3), as

$$\begin{aligned}
 E_r(\delta_{min}) &= \frac{\delta'_{min} - \delta_{min}}{\delta_{min}} = \frac{\delta'_{min}}{\delta_{min}} - 1 \\
 E_r(A_{uf}) &= \frac{A'_{uf} - A_{uf}}{A_{uf}} = \left(\frac{\delta'_{min}}{\delta_{min}}\right)^{2-D} - 1 = [E_r(\delta_{min}) + 1]^{2-D} - 1
 \end{aligned}
 \tag{3.2}$$

Thus, from Eqs. (3.2), the relative error $E_r(A_{uf})$ only depends on the relative error $E_r(\delta_{min})$ and the complexity D . For example, for $D = 2.1$, taking a larger value of the relative error of the lower bound to scale invariance $E_r(\delta_{min}) = 50\%$, it can be calculated from Eqs. (3.2) that $E_r(A_{uf}) = -3.97\%$, which is obviously an acceptable error in most engineering applications.

4. Conclusion

Based on the new concept of ubiquitous, namely, all the real physical or geometrical objects in nature are ubiquitous, the fracture energy, one of the important mechanical properties in the fracture mechanics, is re-examined in this study. Instead of the traditional fracture energy G for the smooth crack configuration, the concept of the ubiquitous fracture energy G_{uf} is proposed. Because of the integral dimension characteristic of a ubiquitous crack or the corresponding ubiquitous fracture surface, an explicit expression for the ubiquitous fracture energy can be obtained, which is intrinsically different from the case for a fractal crack because of the singularity of the integral dimension of fractals. Moreover, it is found that the calculated numerical results of the ubiquitous fracture energy are in good agreement with those for the critical strain energy release rate G_c calculated from the fracture toughness relation, $G_c = K_{IC}^2/E$. Consequently, the perplexity over a long period of time about the discrepancy

between the experimental data of the traditional fracture energy G and the calculated results of the critical strain energy release rate G_c by using the fracture toughness relation can be reasonably explained. That is, the fracture surfaces generated in a real material cannot be thought of as a smooth configuration but, instead, it must be a ubiquitiformal one, and then, instead of the traditional fracture energy, the ubiquitiformal fracture energy must be adopted in practical engineering applications. In addition, it should be pointed out that the agreement between the numerical results of G_{uf} and G_c also implies that the created area of the fracture surface will play a more important role than the crack-tip stress singularity to characterize the fracture process in materials. Finally, unlike the traditional fracture energy, for some concrete materials, it is verified numerically that there is not size effect for the ubiquitiformal fracture energy, which, certainly, should be further theoretically studied in future.

Acknowledgements

The project has been supported by both the National Natural Science Foundation of China under Grant 11221202 and the National Science Foundation of China under Grant 11390362.

References

1. ADDISON P.S., 2000, The geometry of prefractal renormalization: Application to crack surface energies, *Fractals*, **8**, 2, 147-153
2. BAŽANT Z.P., 1995, Scaling of quasi-brittle fracture and the fractal question, *ASME Journal of Materials and Technology*, **117**, 361-367
3. BAŽANT Z.P., 1997a, Scaling in nonlinear fracture mechanics, *IUTAM Symposium on Nonlinear Analysis of Fracture*, University of Cambridge, 3-7 September 1995, J.R. Willis (Edit.), Kluwer Academic Publishers, Dordrecht, 1-12
4. BAŽANT Z.P., 1997b, Scaling of quasibrittle fracture: hypotheses of invasive and lacunar fractality, their critique and Weibull connection, *International Journal of Fracture*, **29**, 1699-1709
5. BAŽANT Z.P., YAVARI A., 2005, Is the cause of size effect on structural strength fractal or energetic-statistical?, *Engineering Fracture Mechanics*, **72**, 1-31
6. BORODICH F.M., 1992, Fracture energy in a fractal crack propagating in concrete or rock, *Doklady Rossiyskoy Akademii Nauk*, **325**, 6, 1138-1141
7. BORODICH F.M., 1997, Some fractal models of fracture, *Journal of the Mechanics and Physics of Solids*, **45**, 2, 239-259
8. BORODICH F.M., 1999, Fractals and fractal scaling in fracture mechanics, *International Journal of Fracture*, **95**, 1-4, 239-259
9. CARPINTERI A., 1994, Fractal nature of material microstructure and size effects on apparent mechanical properties, *Mechanics of Materials*, **18**, 2, 89-101
10. CARPINTERI A., CHIAIA B., 1995, Multifractal nature of concrete fracture surfaces and size effects on nominal fracture energy, *Materials and Structures*, **28**, 435-443
11. CARPINTERI A., FERRO G., 1994, Size effects on tensile fracture properties: a unified explanation based on disorder and fractality of concrete microstructure, *Materials and Structures*, **27**, 563-571
12. CARPINTERI A., PUZZI S., 2008, Self-similarity in concrete fracture: size-scale effects and transition between different collapse mechanisms, *International Journal of Fracture*, **154**, 1-2, 167-175
13. KROHN C.E., THOMPSON A.H., 1986, Fractal sandstone pores: Automated measurements using scanning-electron-microscope images, *Physical Review B*, **33**, 6366-6374
14. LI G.Y., 2014, Research on basic theory of ubiquitiform and some aspects of its application (in Chinese), PhD Thesis, Beijing Institute of Technology, Beijing

15. MANDELBROT B.B., PASSOJA D.E., PAULLAY A.J., 1984, Fractal character of fracture surfaces of metals, *Nature*, **308**, 721-722
16. MECHOLSKY J.J., PASSOJA D.E., FEINBERG-RINGLE K.S., 1989, Quantitative analysis of brittle fracture surfaces using fractal geometry, *Journal of the American Ceramic Society*, **72**, 60-65
17. OU Z.-C., LI G.-Y., DUAN Z.-P., HUANG F.-L., 2014, Ubiquitiform in applied mechanics, *Journal of Theoretical and Applied Mechanics*, **52**, 1, 37-46
18. RADLIŃSKI A.P., RADLIŃSKA E.Z., AGAMALIAN M., WIGNALL G.D., LINDNER P., RANDL O.G., 1999, Fractal geometry of rocks, *Physical Review Letters*, **31**, 163-172
19. SAOUMA V.E., BARTON C.C., 1994, Fractals, fractures, and size effects in concrete, *Journal of Engineering Mechanics*, **120**, 4, 835-854
20. SAOUMA V.E., BARTON C.C., GAMALELDIN N.A., 1990, Fractal characterization of fracture surfaces in concrete, *Engineering Fracture Mechanics*, **35**, 1-3, 47-53
21. SAOUMA V.E., BROZ J.J., BRÜHWILER E., BOGGS H.L., 1991, Effect of aggregate and specimen size on fracture properties of dam concrete, *Journal of Materials in Civil Engineering ASCE*, **3**, 3, 204-218
22. SWARTZ S., KAN Y.C., 1992, The influence of aggregate/paste bonding and strength of mode I fracture mechanics properties of concrete, [In:] *Fracture Mechanics of Concrete Structures*, Bažant Z.P. (Edit.), Elsevier Applied Science, London, 437-442
23. UNDERWOOD E.E., 1986, Fractals in fractography, *Materials Science and Engineering A*, **80**, 1-14

Manuscript received December 14, 2016; accepted for print April 24, 2017

INFORMATION FOR AUTHORS

Journal of Theoretical and Applied Mechanics (JTAM) is devoted to all aspects of solid mechanics, fluid mechanics, thermodynamics and applied problems of structural mechanics, mechatronics, biomechanics and robotics. Both theoretical and experimental papers as well as survey papers can be proposed.

We accept articles in English only. The text of a *JTAM* paper should not exceed **12 pages of standard format A4** (11-point type size, including abstract, figures, tables and references), short communications – **4 pages**.

The material for publication should be sent to the Editorial Office via electronic journal system: <http://www.ptmts.org.pl/jtam/index.php/jtam>

Papers are accepted for publication after the review process. Blind review model is applied, which means that the reviewers' names are kept confidential to the authors. The final decision on paper acceptance belongs to the Editorial Board.

After qualifying your paper for publication we will require L^AT_EX or T_EX or Word document file and figures.

The best preferred form of figures are files obtained by making use of editorial environments employing vector graphics:

- generated in CorelDraw (*.cdr), AutoCad and ArchiCad (*.dwg) and Adobe Illustrator (*.ai). We require original files saved in the standard format of the given program.
- generated by calculation software (e.g. Mathematica) – we need files saved in *.eps or *.pdf formats.
- made in other programs based on vector graphics – we ask for *.eps, *.wmf, *.svg, *.psfiles.

Any figures created without application of vector graphics (scans, photos, bitmaps) are strongly encouraged to be supplied in *.jpg, *.tif, *.png formats with resolution of at least 300 dpi.

Requirements for paper preparation

Contents of the manuscripts should appear in the following order:

- Title of the paper
- Authors' full name, affiliation and e-mail
- Short abstract (**maximum 100 words**) and 3-5 key words (**1 line**)
- Article text (equations should be numbered separately in each section; each reference should be cited in the text by the last name(s) of the author(s) and the publication year)
- References in alphabetical order. See the following:
 1. Achen S.C., 1989, A new boundary integral equation formulation, *Journal of Applied Mechanics*, **56**, 2, 297-303
 2. Boley B.A., Weiner J.H., 1960, *Theory of Thermal Stresses*, Wiley, New York
 3. Canon W., 1955, Vibrations of heated beams, Ph.D. Thesis, Columbia University, New York
 4. Deresiewicz H., 1958, Solution of the equations of thermoelasticity, *Proceedings of Third U.S. National Congress of Applied Mechanics*, 287-305
- Titles of references originally published not in English, should be translated into English and formulated as follows:
 5. Huber M.T., 1904, Specific work of strain as a measure of material effort (in Polish), *Czasopismo Techniczne*, **XXII**, 3, 80-81

All the data should be reported in **SI units**.

Contents

Attia Hili M., Bouaziz S., Haddar M. — Stability analysis and dynamic behaviour of a flexible asymmetric rotor supported by active magnetic bearings	751
Mirsalimov V.M., Mustafayev A.B. — Effect of induced temperature field on development of curvilinear crack with bonds between the faces in end zones	765
Sado D., Freundlich J., Bobrowska A. — Chaotic vibration of an autoparametrical system with the spherical pendulum	779
Suchocki C. — Finite element implementation of slightly compressible and incompressible first invariant-based hyperelasticity: theory, coding, exemplary problems	787
Zandavi S.M. — Surface-to-air missile path planning using genetic and PSO algorithms	801
Mohammadi Esfarjani S., Salehi M., Ghassemi A. — Effect of the multiple damages and temperature changes on the natural frequency	813
Ziaee S. — Linear free vibration of graphene sheets with nanopore via Aifantis theory and Ritz method	823
Ciesielski M. — Application of the alternating direction implicit method for numerical solution of the dual phase lag equation	839
Mohammdimehr M., Rostami R. — Bending, buckling, and forced vibration analyses of nonlocal nanocomposite microplate using TSDT considering MEE properties dependent to various volume fractions of CoFe_2O_4 - BaTiO_3	853
Bentahar M., Benzaama H., Bentoumi M., Mokhtari M. — A new automated stretching finite element method for 2D crack propagation	869
Dastjerdi S., Lotfi M., Jabbarzadeh M. — Nonlocal analysis of single and double-layered graphene cylindrical panels and nano-tubes under internal and external pressures considering thermal effects	883
Barboteu M., Djehaf N., Shillor M., Sofonea M. — Modeling and simulations for quasistatic frictional contact of a linear 2D bar	897
Bera T.K., Dixit S., Bhattacharya A., Kumar D., Samantaray A.K. — Thermal modelling, simulation and experimental validation of heat accumulation in a framed glass cabin	911
Taktak W., Taktak R., Haddar N., Elleuch R. — Study of the influence of cold working on mechanical behavior and ductile fracture of 5754 aluminum alloy: experimental and numerical simulations	823
Abouelregal A.E., Zenkour A.M. — Thermoelastic response of nanobeam resonators subjected to exponential decaying time varying load	937
Klanner M., Ellermann K. — Solutions of vibration problems for thin infinite plates subjected to harmonic loads	949
Malik B., Akhtar S., Masood J. — Influence of flight control law on spin dynamics of aerodynamically asymmetric aircraft	963
Orzechowski G., Frączek J. — Volumetric locking suppression method for nearly incompressible nonlinear elastic multi-layer beams using ANCF elements	977
Lisowski F. — The specific dynamic capacity of a planetary roller screw with random deviations of the thread pitch	991
Nasirzadeh R., Behjat B., Kharazi M., Khabazaghdam A. — Investigation of boundary condition effects on the stability of FGP beams in thermal environment	1003
Robinson M.T.A., Adali S. — Nonconservative stability of viscoelastic plates subject to triangularly distributed follower loads	1015
Urbanowicz K. — Analytical expressions for effective weighting functions used during simulations of water hammer	1029
Çetkin A., Orak S. — Free vibration analysis of point supported rectangular plates using quadrature element method	1041
Moradi R., Alikhani A., Jegarkandi M.F. — Ultimate state boundedness of underactuated spacecraft subject to an unmatched disturbance	1055
Kumar R., Devi S. — Eigenvalue approach to nanobeam in modified couple stress thermoelastic with three-phase-lag model induced by ramp type heating	1067
Puzyrov V., Awrejcewicz J. — On the optimum absorber parameters: revising the classical results	1081
Kajzer A., Pozorski J. — Application of the Lattice Boltzmann Method to the flow past a sphere	1091
Ou Z.-C., Yang M., Li G.-Y., Duan Z.-P., Huang F.-L. — Ubiquitiformal fracture energy	1101